What causes Long Covid? Three theories emerge p. 1261

Ocean oil slicks abounding pp. 1266 & 1300

Piezoelectric, conductive robotic metamaterials pp. 1272 & 1287

Science

$15
17 JUNE 2022
science.org

AAAS

GLACIER BEARS

A newly identified polar bear population sheds light on the future pp. 1267 & 1333

CONTENTS

17 JUNE 2022 • VOLUME 376
ISSUE 6599

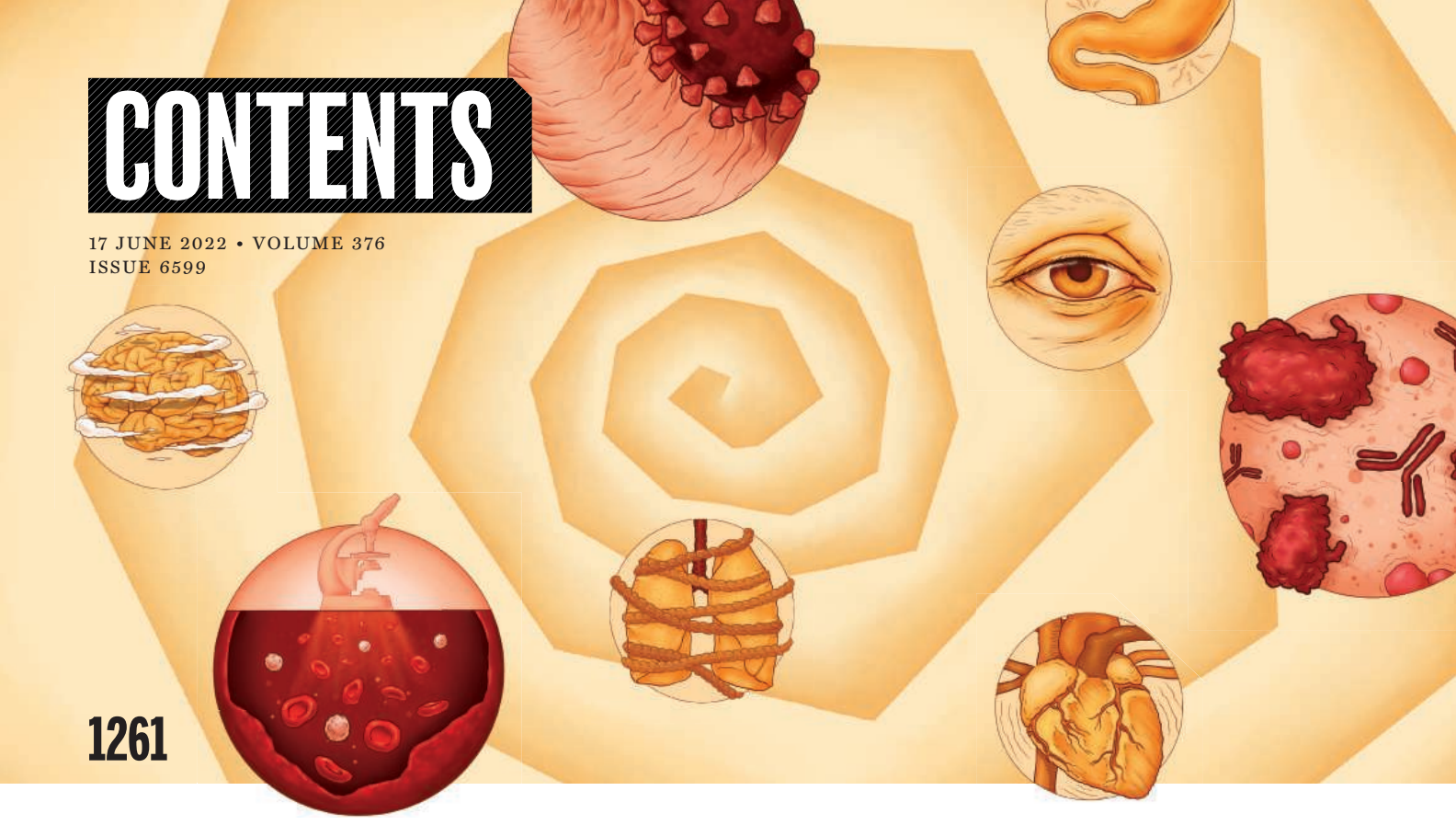

1261

NEWS

IN BRIEF

1250 News at a glance

IN DEPTH

1253 The triumph and tragedy of the Higgs boson
Ten years ago, physicists found what they predicted. Little new has followed
By A. Cho

1254 Ancient DNA reveals Black Death source
Graves in Kyrgyzstan hold early victims of plague that swept medieval Europe
By A. Gibbons

1256 Studies tying weather extremes to global warming gain rigor
Record-shattering events spur climate attribution advances *By P. Voosen*

1257 Upstart DNA sequencers could be a 'game changer'
Increasing potential for fast, cheap genomes may break open biology's bottleneck and broaden clinical uses
By E. Pennisi

1258 Monkeypox could establish new reservoirs in animals
Concern grows that virus will get footholds in species outside Africa
By J. Cohen

1260 Telescope in India snares light in spinning mercury
Inexpensive "liquid mirrors" could be used in giant telescopes on the Moon *By D. Clery*

FEATURES

1261 Clues to Long Covid
Scientists strive to unravel what is driving disabling symptoms *By J. Couzin-Frankel*

1262 Glacial pace for U.S. Long Covid grants
By M. Wadman
PODCAST

INSIGHTS

PERSPECTIVES

1266 Oil at sea—how much is too much?
The anthropogenic share of marine oil discharge is much larger than previously thought *By I. Leifer*
REPORT p. 1300

1267 A new polar bear population
Can the international conservation agreement protect these bears?
By E. Peacock
REPORT p. 1333

1269 Chip-scale power booster for light
A miniature amplifier with high power is realized with an ion-doped waveguide
By J. Kim
REPORT p. 1309

1270 Modifying insulin to improve performance
A platform to enable precise modifications of insulin could improve drug functionality
By N.-P. Lin and D. H.-C. Chou
REPORT p. 1321

1271 Cellular cross-talk in heart repair
The cytokine meteorin-like (METRNL) improves cardiac function after heart attack in mice *By D. Srivastava*
REPORT p. 1343

1272 Turning materials into robots
Researchers showcase a 3D-printed millirobot made out of multifunctional metamaterials
By A. Rafsanjani
RESEARCH ARTICLE p. 1287

POLICY FORUM

1274 Get law enforcement out of biospecimen authentication
Use of DNA markers in research that are used in law enforcement risks undermining public trust and participation *By D. J. H. Mathews and N. Ram*
PODCAST

BOOKS *ET AL.*

1277 Confronting the climate crisis
Leading literary writers explore what it means to live on a changing planet *By J. Swift*

1278 Peter Higgs and his eponymous particle
A new biography juxtaposes the physicist's life story with the search for the Higgs boson
By S. Mitton

ILLUSTRATIONS BY ASHLEY MASTIN

LETTERS

1279 Shrinking aquifers and land subsidence in Iran
By M. Negahdary

1279 Biotechnology ethics for food and agriculture
By C. Kendig et al.

1280 Broaden chemicals scope in biodiversity targets
By G. Sigmund et al.

RESEARCH

IN BRIEF

1281 From *Science* and other journals

RESEARCH ARTICLES

1284 Cell biology
Control of meiotic chromosomal bouquet and germ cell morphogenesis by the zygotene cilium *A. Mytlis* et al.
RESEARCH ARTICLE SUMMARY; FOR FULL TEXT: DOI.ORG/10.1126/SCIENCE.ABH3104

1285 Innate immunity
Human OTULIN haploinsufficiency impairs cell-intrinsic immunity to staphylococcal α-toxin
A. N. Spaan et al.
RESEARCH ARTICLE SUMMARY; FOR FULL TEXT: DOI.ORG/10.1126/SCIENCE.ABM6380

1286 Neurodevelopment
Spatial centrosome proteome of human neural cells uncovers disease-relevant heterogeneity *A. C. O'Neill* et al.
RESEARCH ARTICLE SUMMARY; FOR FULL TEXT: DOI.ORG/10.1126/SCIENCE.ABF9088

1287 Robotic materials
Design and printing of proprioceptive three-dimensional architected robotic metamaterials *H. Cui* et al.
PERSPECTIVE p. 1272

1293 Plant science
A genetic module at one locus in rice protects chloroplasts to enhance thermotolerance *H. Zhang* et al.

REPORTS

1300 Oil pollution
Chronic oiling in global oceans
Y. Dong et al.
PERSPECTIVE p. 1266

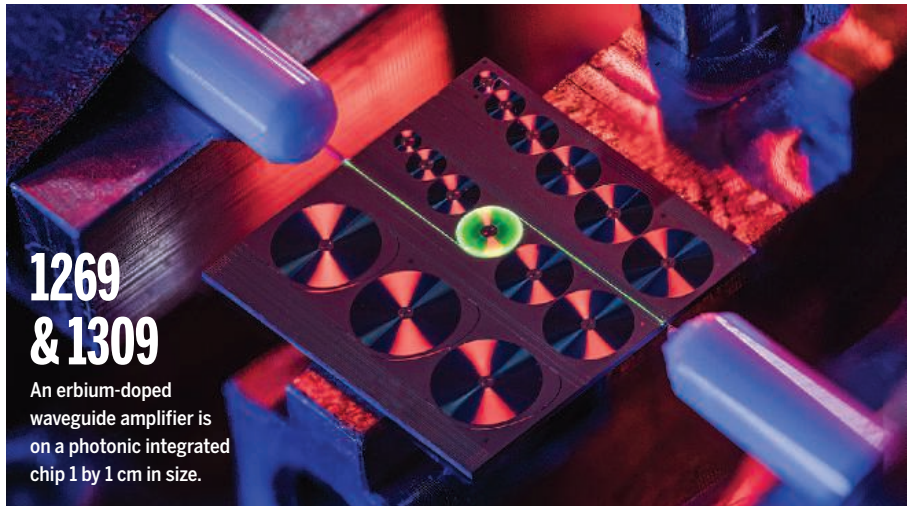

1269 & 1309
An erbium-doped waveguide amplifier is on a photonic integrated chip 1 by 1 cm in size.

1305 Quantum gases
Spin-charge separation in a one-dimensional Fermi gas with tunable interactions
R. Senaratne et al.

1309 Photonics
A photonic integrated circuit–based erbium-doped amplifier
Y. Liu et al.
PERSPECTIVE p. 1269

1313 Transcription
Structural basis of nucleosome retention during transcription elongation
M. Filipovski et al.

1317 Historical drought
Droughts and societal change: The environmental context for the emergence of Islam in late Antique Arabia
D. Fleitmann et al.

1321 Bioconjugation
A chemoenzymatic strategy for site-selective functionalization of native peptides and proteins *A. Fryszkowska* et al.
PERSPECTIVE p. 1270

1327 Coronavirus
Analysis of 6.4 million SARS-CoV-2 genomes identifies mutations associated with fitness
F. Obermeyer et al.

1333 Conservation
Glacial ice supports a distinct and undocumented polar bear subpopulation persisting in late 21st-century sea-ice conditions
K. L. Laidre et al.
PERSPECTIVE p. 1267

1338 Molecular biology
Structure of the mammalian ribosome as it decodes the selenocysteine UGA codon
T. Hilal et al.

1343 Heart repair
Meteorin-like promotes heart repair through endothelial KIT receptor tyrosine kinase
M. R. Reboll et al.
PERSPECTIVE p. 1271

DEPARTMENTS

1248 Editorial
G7: Balance security and collaboration
By H. G. Broadman and C. Abdallah

1249 Editorial
A future for Ukrainian science
By J. Duszyński et al.

1350 Working Life
More than my hands *By I. Smolensky*

ON THE COVER

A previously unidentified population of polar bears documented on the southeast coast of Greenland uses glacier ice to survive despite limited access to sea ice. This small, genetically distinct group of polar bears displays foraging strategies that could facilitate persistence in a warming world. See pages 1267 and 1333. *Photo: Carsten Egevang*

Science Careers 1348

SCIENCE (ISSN 0036-8075) is published weekly on Friday, except last week in December, by the American Association for the Advancement of Science, 1200 New York Avenue, NW, Washington, DC 20005. Periodicals mail postage (publication No. 484460) paid at Washington, DC, and additional mailing offices. Copyright © 2022 by the American Association for the Advancement of Science. The title SCIENCE is a registered trademark of the AAAS. Domestic individual membership, including subscription (12 months): $165 ($74 allocated to subscription). Domestic institutional subscription (51 issues): $2212; Foreign postage extra: Air assist delivery: $98. First class, airmail, student, and emeritus rates on request. Canadian rates with GST available upon request, GST #125488122. Publications Mail Agreement Number 1069624. **Printed in the U.S.A.**
Change of address: Allow 4 weeks, giving old and new addresses and 8-digit account number. **Postmaster:** Send change of address to AAAS, P.O. Box 96178, Washington, DC 20090–6178. **Single-copy sales:** $15 each plus shipping and handling available from backissues.science.org; bulk rate on request. **Authorization to reproduce** material for internal or personal use under circumstances not falling within the fair use provisions of the Copyright Act can be obtained through the Copyright Clearance Center (CCC), www.copyright.com. The identification code for *Science* is 0036-8075. *Science* is indexed in the *Reader's Guide to Periodical Literature* and in several specialized indexes.

PHOTO: LABORATORY OF PHOTONICS AND QUANTUM MEASUREMENTS (LPQM). EPFL. © NIELS ACKERMANN

EDITORIAL

G7: Balance security and collaboration

Harry G. Broadman is a managing director at Berkeley Research Group LLC, Washington, DC, USA, and a faculty member at Johns Hopkins University School of Advanced International Studies, Washington, DC, USA. hbroadman@thinkbrg.com

Chaouki Abdallah is a professor of Electrical and Computer Engineering and executive vice president for research at the Georgia Institute of Technology, Atlanta, GA, USA. ctabdallah@gatech.edu

Increased government scrutiny of cross-border university research relationships, tightened export controls on technologies, and strengthened national regimes regulating technology-related foreign direct investment are now priorities for most democracies. These policy changes are motivated by the common goal of shoring up economic and national security. But the approaches are neither uniform nor harmonized, even among the relatively homogeneous G7 nations, undermining cross-border research and development (R&D) collaboration. When the leaders of G7 meet in late June in Schloss Elmau, Germany, they should make it a priority to coordinate controls on knowledge flows and technology. They need to act together to demonstrate how democracies can counter illicit activities for acquiring technologies.

The issue of research security bubbled up on university campuses in the US almost 5 years ago as questions about technology exports to, and acquisitions of US firms by, China raised concerns about the economic, military, and intelligence vulnerabilities of G7 nations. Then in February 2022, Russia invaded Ukraine. Many of the world's liberal democracies banded together—in record time and a highly coordinated fashion—to impose far-reaching export controls to prevent advanced technology products from reaching Russia. Democracies in general, and the G7 in particular, have awoken to the fact that they have the means and powerful new motivations to more carefully control the diffusion of dual-use knowledge and advanced technologies to adversaries.

The result is looming changes—in law and enforcement—of national policies in advanced democracies. The new approaches fall to different governmental entities, depending on whether the policy is the granting of export licenses; agency clearance of inbound—and likely soon even outbound—foreign direct investment; or the funding of university research. The result—leading democratic states rapidly inventing or strengthening technology-protection polices with little multilateral consultation—is predictable: regulatory confusion for both researchers and companies engaged in cross-border activity, and a reduction in international flows of scientific and engineering knowledge and personnel.

There are huge and long-term costs to innovation and economic growth of allies taking distinct approaches to export controls, placing limits on university-based open research collaboration between domestic and foreign scientists, or imposing constraints on foreign direct investment. All three of these national security policies can substantially affect beneficial cross-border research collaboration and commercial exchange in advanced technologies. But they are rarely considered together. They should be. Ensuring such integration is where the G7 must lead. Indeed, the G7 needs to act rapidly.

Because of the decentralized nature of the changes required, it is hard to know whether this imperative will even be recognized as an emerging problem when the G7 leaders meet later this month. Whereas balancing research security and openness in research was identified as a key topic in the "Research Compact" unveiled by the G7 at last year's summit in Cornwall, UK, there does not appear to be any focus planned on the impact of tightening the downstream—and arguably far more important—technology export controls and foreign direct investment regulations.

> "...G7...needs... a process to separate high-risk from low-risk commercial technology exchanges..."

The first step is for the G7 to agree on the principles of a new regime: making the implementation of national regulations smarter about global knowledge networks, coordinating to facilitate openness among the G7 nations and control at the interface between those within the group and those outside; and ensuring harmonization that supports cross-border collaboration in public and private R&D and innovation within the G7.

The G7 leaders cannot design such a regime during their 2022 summit, but they can agree that it needs to be done on a priority basis and formally launch the process of creating modernized, enforceable, cross-border science and technology agreements governing not just government-to-government research exchanges but also setting out a process to separate high-risk from low-risk commercial technology exchanges and foreign direct investments. And they need to be quick, as the sovereign-to-sovereign agreements among the G7 must be in place soon so that other liberal democracies can align their policies and practices with the G7.

The G7 should lead democracies out of the thicket of conflicting, collaboration-dampening, and national approaches to protecting the technology-dependent aspect of economic and national security.

–Harry G. Broadman and Chaouki Abdallah

10.1126/science.add3956

A future for Ukrainian science

As the war in Ukraine enters its fourth month, Russian forces continue to destroy the nation's scientific institutions and infrastructure, signaling Russia's intent to obliterate the future for Ukraine. In Kharkiv, for instance, the renowned Institute of Physics and Technology and its newly built Neutron Source nuclear facility have been heavily damaged. Even the Plant Production Institute with its underground national seed bank—one of the world's largest—has been bombed. At the Chernobyl nuclear labs, Russian forces have looted or destroyed hundreds of computers, radiation dosimeters, and irreplaceable software and equipment. Although the response to each international science crisis is necessarily unique, the US National Academy of Sciences is once again joining with international and regional partners to support beleaguered colleagues, as it did last year in the successful extraction and resettlement of Afghanistan scientists at risk from the Taliban. To that end, the national science academies of Poland, Ukraine, and the United States recently convened a meeting of leaders from several national science academies (including the presidents of Germany's Leopoldina science academy, the Royal Danish Academy of Sciences and Letters, and the ALLEA European Federation of Academies of Sciences and Humanities, and leaders from the Royal Society of the United Kingdom) to explore how the global science community can best help Ukraine. The resulting 10-point action plan for the world's research community aims to help meet several immediate needs and also provide the building blocks for revitalizing Ukrainian science in the future.

> **"It is...vital that science be a cornerstone of any postwar reconstruction..."**

The plan seeks to support researchers working within Ukrainian institutions, as well as their teams—whether within Ukraine or in neighboring countries—both scientifically and financially so that these generations of researchers will not be lost to science or to Ukraine. Along with the traditional types of support provided by international cooperation and collaboration, funders are considering developing grant programs for joint research, particularly if conducted inside Ukraine. Some journal publishers have waived Ukraine's institutional subscription charges and author publication charges, and scientific societies are considering temporarily suspending membership dues. Such steps open the opportunity to immediately increase connections of Ukrainian researchers to thriving international research communities. It is also vital that science be a cornerstone of any postwar reconstruction of Ukraine.

There is also an urgent need for donated instruments, including various types of microscopes, spectrometers, and materials testing machines to keep these researchers productive. At the same time, many female scholars forced to flee, most with children, need temporary research positions and financial support for themselves and their research teams until they can return home. The Polish Academy of Sciences and the US National Academy of Sciences have partnered to place temporarily some 220 Ukrainian researchers in Polish science institutions and provide financial support so that they can continue to make valuable contributions to research. Programs like this will hopefully expand within Poland and into other European countries such as Germany, the United Kingdom, and Denmark while allowing these scientists to retain their Ukrainian science affiliations until they can return home.

Lessons learned during the COVID-19 pandemic can also be applied to help Ukrainian researchers form virtual networks with international colleagues, with intentional encouragement from institutions and researchers. These efforts cost little but would keep these scientists engaged and involved.

Once the war is over, it is hoped that Ukraine will swiftly begin the monumental task of rebuilding. National science academies around the world should advocate that international aid to Ukraine be directed to rebuilding science infrastructure alongside other critical needs such as transportation, energy, and health care. Rebuilding Ukrainian science should not concentrate on replicating what was lost, but on equipping the country's scientific enterprise to meet shared 21st-century challenges—such as preparing for future pandemics, fighting climate change, and sharing the benefits of science equally and equitably.

The stakes of the war in Ukraine are high—the future of democracy in Europe is at risk. The global science community should not only help guarantee that Ukrainian science remains a vital source of national advancement, but also ensure that it is part of international science so that its values of collaboration, cooperation, and mutual trust continue to contribute to a better world.

–Jerzy Duszyński, Marcia McNutt, Anatoly Zagorodny

Jerzy Duszyński
is the president of the Polish Academy of Sciences, Warsaw, Poland.
president@pan.pl

Marcia McNutt
is the president of the US National Academy of Sciences, Washington, DC, USA.
mmcnutt@nas.edu

Anatoly Zagorodny
is the president of the National Academy of Sciences of Ukraine, Kyiv, Ukraine.
azagorodny@bitp.kiev.ua

Published online 13 June 2022; 10.1126/science.add4088

14.5% Portion of the world's population likely infected by Lyme disease. The estimate comes from a meta-analysis in *BMJ Global Health* of 89 studies involving 158,287 people that examined the presence of blood antibodies. Prevalence has grown since 2010.

IN BRIEF

Edited by **Jeffrey Brainard**

ASTRONOMY

Dust grain hits Webb space telescope

One mirror segment of NASA's James Webb Space Telescope was struck by a micrometeoroid last month, leading to a "marginally detectable effect" on its data collection, the agency said last week. Launched nearly 6 months ago, Webb has a 6.5-meter, gold-coated mirror made of 18 hexagonal segments. Mission planners expected many specks of high-speed space dust to ding Webb during its lifetime and simulated their impact using spare mirror segments. Operators recorded four small strikes during Webb's deployment and commissioning phase. NASA estimated the speck that struck it in May was larger, but less than 0.1 millimeter wide. The telescope is designed to withstand many such hits, and engineers have already adjusted the shape and position of the affected mirror segment to mitigate distortion from the damage; NASA says the telescope's performance still exceeds all mission requirements.

U.S. nixes funding Russia work

WAR | The U.S. government last week said it will not fund new collaborations with research institutions affiliated with Russia's government and individuals working at those institutions, in response to Russia's 24 February invasion of Ukraine. The 11 June announcement comes months after several European nations went further, freezing existing collaborations. The U.S. policy allows existing joint projects to continue until completed. Some U.S. institutions have already voluntarily canceled existing collaborations with Russian universities; for example, in February the Massachusetts Institute of Technology pulled out of one with the Skolkovo Institute of Science and Technology, which MIT had helped found.

Don't rule out lab leak, panel says

COVID-19 | In yet another attempt to determine the origin of the pandemic, a new group of experts convened by the World Health Organization (WHO) last week issued a preliminary report that calls for further study of several ideas, including the contentious one that SARS-CoV-2 might have escaped from a lab in Wuhan, China. An earlier WHO-organized commission drew controversy in 2021 by ranking the lab-leak notion "extremely unlikely" and not a priority for further study. Its successor, the Scientific Advisory Group for the Origins of Novel Pathogens (SAGO), says the idea can't be ruled out, although "the strongest evidence" supports the hypothesis that the virus jumped from animals to humans, SAGO's chair, South African virologist Marietjie Venter, said at a 9 June press conference. China has rejected the lab-leak theory, and panel members from China, Brazil, and Russia said they see no reason to study it further. SAGO also proposes a more careful examination of the possibility that SARS-CoV-2 jumped into humans at a Wuhan market that sold several mammalian species susceptible to the virus.

Marine canyon to be preserved

CONSERVATION | President Joe Biden's administration last week proposed to make Hudson Canyon, an underwater chasm in the Atlantic Ocean, a national marine sanctuary. It would join a handful of other federally protected reserves off the eastern seaboard of the United States. The largest underwater canyon in this region, Hudson Canyon is roughly 160 kilometers southeast of New York City. It plunges to 4000 meters at its deepest point, and its drop below the surrounding seabed rivals the Grand Canyon's depth. Hudson Canyon is home to more than 200 species of fish and other organisms, such as sperm whales, cold water corals, and sea turtles, some classified as vulnerable, and is dotted by shipwrecks. The designation would not automatically ban commercial fishing; federal officials plan to finalize allowed human activities after a 90-day comment period.

Land-use maps pick up speed

REMOTE SENSING | Researchers studying the ecological and environmental changes wrought by humanity now will have access to sharper and more frequently updated maps of Earth's surface, categorized by land-use types such as trees, built-up areas, and bare land. The World Resources Institute (WRI) and Google last week unveiled Dynamic World, a project that publishes global, digital land-use maps as frequently as every 2 days at resolutions as fine as 10 meters. By comparison, many countries

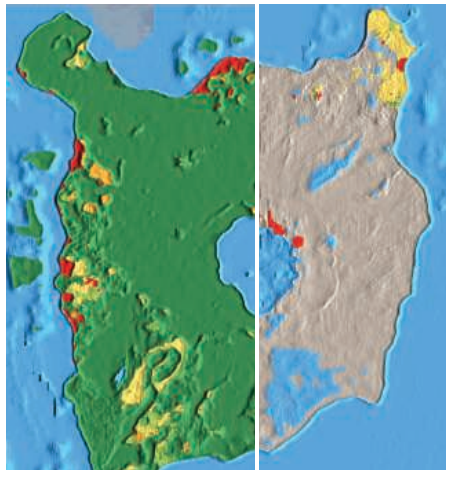

A map of land types shows the Taal volcano in the Philippines before (left) and after it erupted in 2020. Green represents trees; gray, bare land.

MAPS: IMAGERY © 2022/CNES; AIRBUS/LANDSAT; COPERNICUS

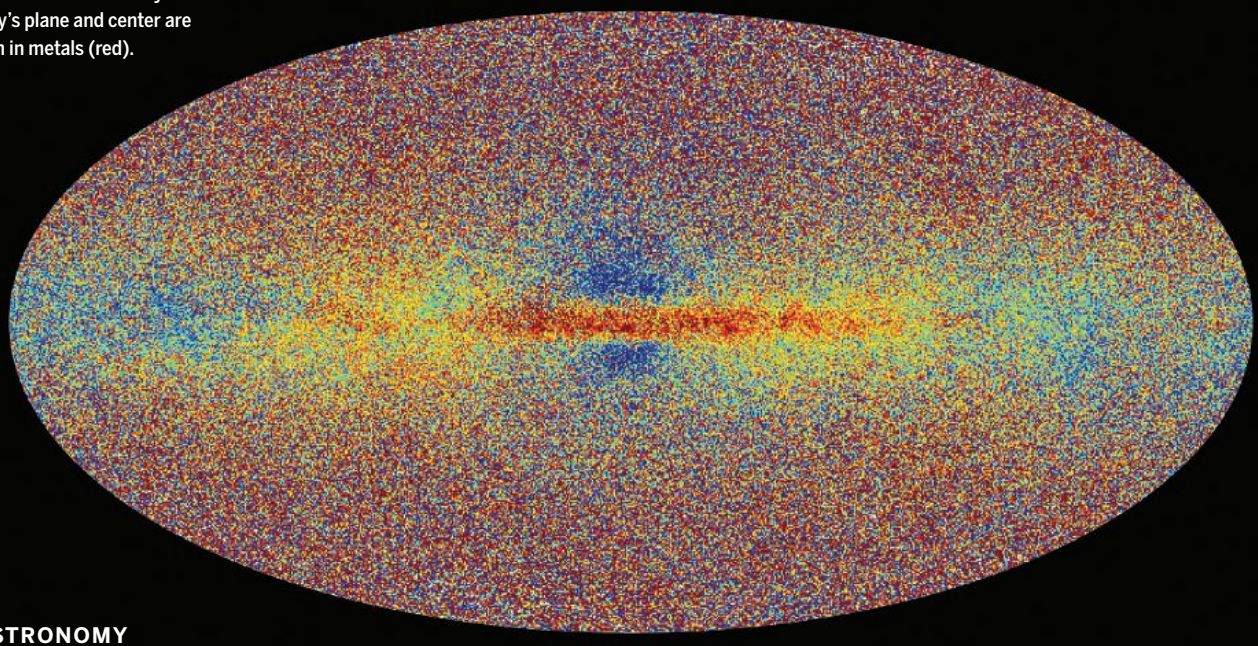

Stars close to the Milky Way's plane and center are rich in metals (red).

IMAGE: © ESA/GAIA/DPAC/CC BY-SA 3.0 IGO

ASTRONOMY

Star mapper provides Milky Way portrait

The European Space Agency's Gaia satellite has now mapped almost 2 billion of the Milky Way's stars, logging their positions, speeds, temperatures, and other parameters—and allowing astronomers to chart the Galaxy's structure and evolution. Last week, operators released the third major trove of data, including lists of 800,000 binary stars, 10 million variable stars, and, within the Solar System, 156,000 asteroids and rocky bodies. Launched in 2013, Gaia has already uncovered new nearby satellite galaxies, fast-moving stars escaping the Milky Way, and evidence of past galaxies that merged with ours. The new data show thousands of stars are convulsed by giant, violent waves. And, for the first time, the data also include spectra—breakdowns of starlight—that point to chemical compositions. Stars forge heavier elements and disperse them when they explode; the elements are taken up by subsequent generations of stars. Mapping that information shows the abundance of heavy elements is highest in the Galaxy's central disk, where stars live fast and die young.

have produced maps with no better than 30-meter resolution and only update them annually, reflecting the time it takes to identify land types. Some regional maps are revised monthly, but even that pace is too slow to capture rapid change from wildfire or flooding. The new maps are based on imagery from the European Space Agency's Sentinel-2 satellites; Google tailored artificial intelligence algorithms to estimate probable land-cover types, a method described last week in *Nature Scientific Data*.

U.K. eyes scrutiny of foreign ties

POLICY | U.K. universities may be forced to declare funding of more than £75,000 from "foreign actors," under proposed legislation. The law, which aims to protect free speech in higher education, would also give the government new powers to police the effects of university funding from countries such as China and Russia. It would exempt countries in the European Union and NATO, as well as those belonging to the Academic Technology Approval Scheme, a U.K. program to weed out foreign students who may pose a national security threat. The move follows concerns about foreign influence on U.K. universities, including Chinese efforts to block discussions of controversial topics, such as Taiwan and the treatment of Uighur Muslims. The legislation would also ban Confucius Institutes—Chinese centers of language and culture that have been closed in the United States.

Storm watchers fail to reach orbit

METEOROLOGY | A rocket launch carrying two small hurricane-monitoring satellites for NASA ended in disappointment on 12 June. Rocketmaker Astra said the rocket's second stage malfunctioned after liftoff; the CubeSats likely fell into the ocean and were destroyed. It was the fifth failure out of seven orbital launch attempts by the fledgling company. The satellites were the first two of six planned CubeSats, each the size of a shoebox, in NASA's $30 million TROPICS mission. Mission managers intend to use microwave radiometers to see through clouds and measure the temperature and moisture of tropical storms. The fleet would improve forecasts of hurricane intensity by observing storms as often as every 50 minutes. The mission can still achieve many of its science goals with just four satellites, which Astra rockets are also supposed to launch.

Rename monkeypox strains?

INFECTIOUS DISEASES | Identifying monkeypox strains by their place of origin in Africa is "discriminatory and stigmatizing," says an international group of researchers who have urged an overhaul of how the fast-spreading virus is named. Years ago, researchers divided monkeypox viruses into two "clades," or

branches, named after the regions—West Africa and the Congo Basin—where many were first found. (The two clades differ in their genomes and the severity of disease caused.) But monkeypox needs a new, "practical and neutral system of nomenclature," the international group argues in a preprint posted last week on a virology website. They suggest renaming the Congo Basin and West African clades as 1 and 2, respectively, and creating a separate clade, 3, for the current human outbreak strains, given their differences from those in the other two. The outbreak's origin remains unknown. The call to rename the clades echoes debates over the names of other diseases and pathogens; one such recent discussion led to the current nomenclature for SARS-CoV-2 variants, with Greek letters replacing geographical names like the Wuhan or South African strain.

China to grow journal portfolio

SCIENTIFIC PUBLISHING | China plans to launch 50 new English-language academic journals in the next year in an ambitious expansion of its program to create world-class publications, Zhang Yuzhuo of the China Association for Science and Technology (CAST) said at a press conference last week. Since 2019, the Chinese government has supported establishing up to 30 new journals each year. This year, CAST is accepting proposals in fields ranging from astronomy and artificial intelligence to public health and software engineering. Each approved new journal will get a one-time grant of $74,000 to help cover startup costs. The plan has also provided grants to 250 existing publications to support training staff and upgrading websites. The journals' improving quality has attracted more submissions and led to rising citation counts, says Xiaotian Chen, a librarian at Bradley University. Chen says *Cell Research*, *Molecular Plant*, and *National Science Review* are examples of Chinese journals that have gained international stature.

U.S. ends travel testing rule

COVID-19 | People bound for the United States and its territories no longer need to test for the pandemic coronavirus ahead of traveling, President Joe Biden's administration announced last week. Since January 2021, the Centers for Disease Control and Prevention (CDC) had mandated that those flying into the country, including U.S. citizens, present a negative SARS-CoV-2 test result obtained no more than 24 hours prior to their arrival. (Those who had been infected with the virus in the 90 days prior to travel had to show proof they had recovered.) The testing requirement could now be lifted because "the COVID-19 pandemic has now shifted to a new phase," given broad uptake of vaccines and high immunity levels, CDC's announcement stated. An agency official said CDC plans to re-evaluate its decision in 90 days. It will monitor viral variants of concern and reinstate the testing mandate if needed.

Troubled beagle facility to close

ANIMAL WELFARE | A facility that has bred thousands of beagles for medical research and been criticized for more than 70 violations of the U.S. Animal Welfare Act (AWA) will be shut down, its owner, contract research organization Inotiv, said this week. CEO Robert Leasure cited the growing cost of fixing the problems at the Cumberland, Virginia, establishment. The decision came 2 months after Virginia enacted a law that prevents facilities from selling dogs or cats for research if they sustain a single, serious violation of the AWA after June 2023. In a first for a research breeding facility, the Department of Justice last month sued Inotiv subsidiary Envigo, which operates the facility, seeking to force AWA compliance and seized 446 puppies and dogs that veterinarians said were "in acute distress." In a 13 June hearing, attorneys for the government and the company sparred over whether it should be allowed to sell about 3000 dogs there to research clients or be compelled to give them away for adoption.

NASA steps into UFO hunt

FRONTIERS | NASA said last week it will spend up to $100,000 to gather data relevant to understanding "unidentified aerial phenomena," more commonly known as UFOs. The civilian agency has typically eschewed any studies of UFOs; only in recent years has it resumed funding research in the broader field of the search for extraterrestrial intelligence (SETI). The project parallels separate efforts by the U.S. Department of Defense to document and categorize UFO reports, after Congress directed it to create a permanent office for UFO investigations. NASA's independent study team will be led by astrophysicist David Spergel, president of the Simons Foundation. Thomas Zurbuchen, NASA's associate administrator for science, described the new effort as complementary to its existing SETI research, which looks for "technosignatures" of advanced civilizations in astronomical observations. "NASA believes that the tools of scientific discovery are powerful and apply here also," Zurbuchen said in a statement.

IN FOCUS Cactus bees (*Diadasia rinconis*) swarm in a mating ball in Texas in a photo that won the Grand Prize in the annual BigPicture competition, run by the California Academy of Sciences. Cactus bees are mostly solitary.

PHOTO: KARINE AIGNER/THIS GALLERY WAS ORIGINALLY PUBLISHED BY POWERED BY THE CALIFORNIA ACADEMY OF SCIENCES. AND MEDIA PARTNER OF THE BIGPICTURE NATURAL WORLD PHOTOGRAPHY COMPETITION.

SCIENCE.ORG/NEWS
Read more news from *Science* online.

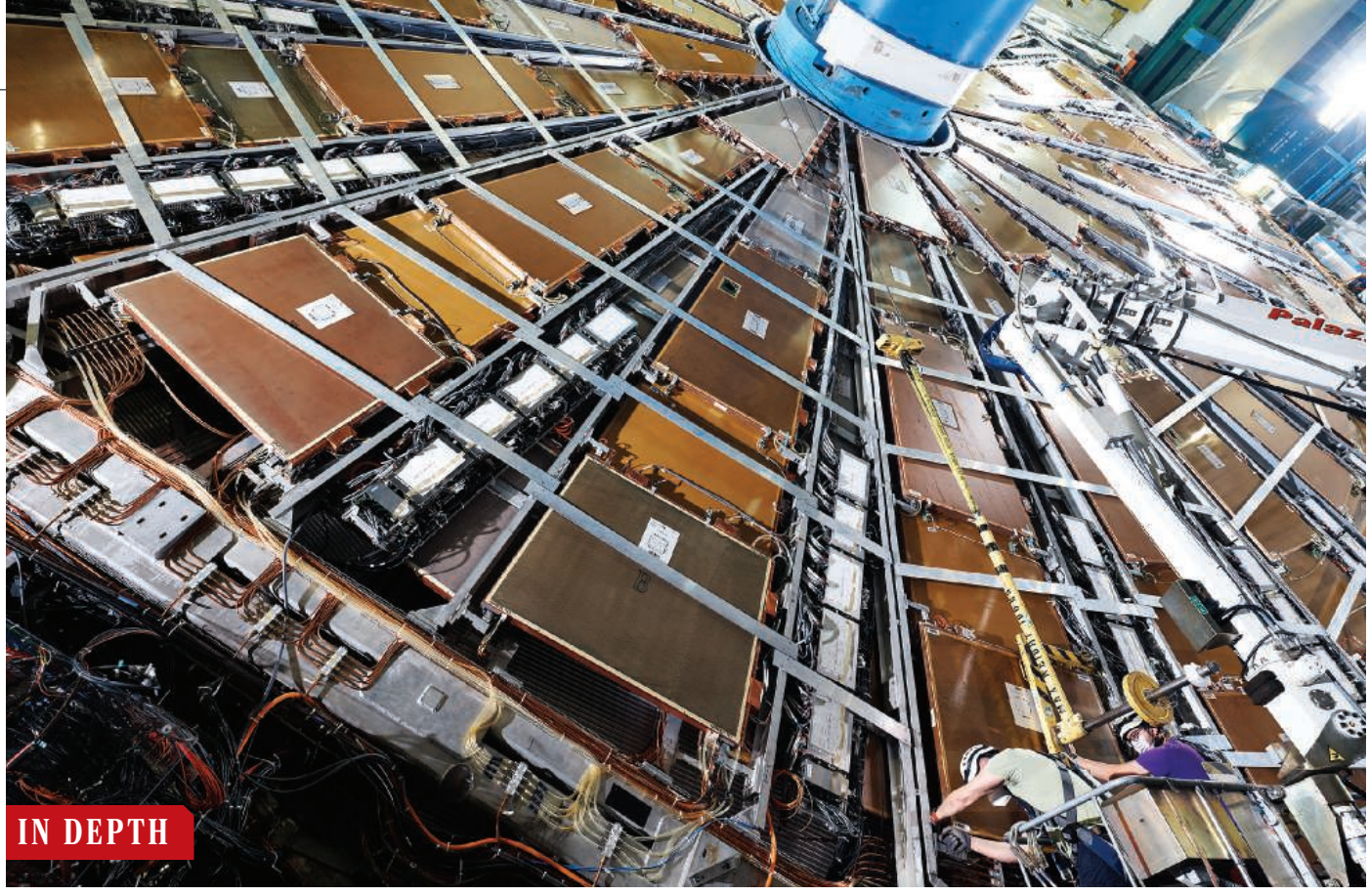

IN DEPTH

ATLAS (above) and the other particle detectors fed by Europe's Large Hadron Collider should resume taking data next month.

PHOTO: MAXIMILIEN BRICE/CERN

PARTICLE PHYSICS

The triumph and tragedy of the Higgs boson

Ten years ago, physicists found what they predicted. Little new has followed

By **Adrian Cho**

A decade ago, particle physicists thrilled the world. On 4 July 2012, 6000 researchers working with the world's biggest atom smasher, the Large Hadron Collider (LHC) at the European particle physics laboratory, CERN, announced they had discovered the Higgs boson, a massive, fleeting particle key to their abstruse explanation of how other fundamental particles get their mass. The discovery fulfilled a 45-year-old prediction, completed a theory called the standard model, and thrust physicists into the spotlight.

Then came a long hangover. Before the 27-kilometer-long ring-shaped LHC started to take data in 2010, physicists fretted that it might produce the Higgs and nothing else, leaving no clue to what lies beyond the standard model (*Science*, 23 March 2007, p. 1657). So far, that nightmare scenario is coming true. "It's a bit disappointing," allows Barry Barish, a physicist at the California Institute of Technology. "I thought we would discover supersymmetry," the leading extension of the standard model.

It's too early to despair, many physicists say. After 3 years of upgrades, the LHC is now powering up for the third of five planned runs, and some new particle could emerge in the billions of proton-proton collisions it will produce every second. In fact, the LHC should run for another 16 years, and with further upgrades should collect 16 times as much data as it already has. All those data could reveal subtle signs of novel particles and phenomena.

Still, some researchers say the writing is on the wall for collider physics. "If they don't find anything, this field is dead," says Juan Collar, a physicist at the University of Chicago who hunts dark matter in smaller experiments. John Ellis, a theorist at King's College London, says hopes of a sudden breakthrough have given way to the prospect of a long, uncertain grind toward discovery. "It's going to be like pulling teeth, not like teeth falling out."

Since the 1970s, physicists have been locked in a wrestling match with the standard model. It holds that ordinary matter consists of lightweight particles called up quarks and down quarks—which bond in trios to make protons and neutrons—along with electrons and featherweight particles called electron neutrinos. Two sets of heavier particles lurk in the vacuum and can be blasted into fleeting existence in particle collisions. All interact by exchanging other particles: The photon conveys the electromagnetic force, the gluon carries the strong force that binds quarks, and the massive W and Z bosons carry the weak force.

The standard model describes everything scientists have seen at particle colliders so far. Yet it cannot be the ultimate theory of nature. It leaves out the force of gravity, and it doesn't include mysterious, invisible dark matter, which appears to outweigh ordinary matter in the universe six to one.

The LHC was supposed to break that impasse. In its ring, protons circulating in opposite directions crash together at energies nearly seven times as high as at any previous collider, enabling the LHC to produce particles too massive to be made elsewhere.

A decade ago many physicists envisioned quickly spotting marvels including new force-carrying particles or even mini–black holes. "One would drown in supersymmetric particles," recalls Beate Heinemann, director of particle physics at the German laboratory DESY. Finding the Higgs would take longer, physicists predicted.

Instead, the Higgs appeared in a relatively speedy 3 years—in part because it is somewhat less massive than many physicists expected, about 133 times as heavy as a proton, which made it easier to produce. And 10 years after that monumental discovery, no other new particle has emerged.

That dearth has undermined two of physicists' cherished ideas. A notion called naturalness suggested the low mass of the Higgs more or less guaranteed the existence of new particles within the LHC's grasp. According to quantum mechanics, any particles lurking "virtually" in the vacuum will interact with real ones and affect their properties. That's exactly how virtual Higgs bosons give other particles their mass.

That physics cuts both ways, however. The Higgs boson's mass ought to be pulled dramatically upward by other standard model particles in the vacuum—especially the top quark, a heavier version of the up quark that weighs 184 times as much as the proton. That doesn't happen, so theorists have reasoned that at least one other new particle with a similar mass and just the right properties—in particular, a different spin—must exist in the vacuum to "naturally" counter the effects of the top quark.

> **"If they don't find anything, this field is dead."**
>
> **Juan Collar**, University of Chicago

The theoretical concept known as supersymmetry would supply such particles. For every known standard model particle, it posits a heavier partner with a different spin. Lurking in the vacuum, those partners would not only keep the Higgs's mass from running away, but would also help explain how the Higgs field, which pervades the vacuum like an unextinguishable electric field, came into being. Supersymmetric particles might even account for dark matter.

But instead of those hoped-for particles, what have emerged in the past decade are tantalizing anomalies—small discrepancies between observations and standard model predictions—that physicists will explore in the LHC's next 3-year run. For example, in 2017, physicists working with LHCb, one of four large particle detectors fed by the LHC, found that B mesons, particles that contain a heavy bottom quark, decay more often to an electron and a positron than to a particle called a muon and an antimuon. The standard model says the two rates should be the same, and the difference might be a hint of supersymmetric partners, Ellis says.

Similarly, experiments elsewhere suggest the muon might be very slightly more magnetic than the standard model predicts (*Science*, 9 April 2021, p. 113). That anomaly can be explained by the existence of exotic particles called leptoquarks, which might already be hiding undetected in the LHC's output, Ellis says.

The Higgs itself provides other avenues of exploration, as any difference between its observed and predicted properties would signal new physics. For example, in August 2020, teams of physicists working with the LHC's two biggest detectors, ATLAS and CMS, announced that both had spotted the Higgs decaying to a muon and an antimuon. If the rate of that hard-to-see decay varies from predictions, the deviation could point to new particles hiding in the vacuum, says Marcela Carena, a theorist at Fermi National Accelerator Laboratory.

Those searches likely won't yield dramatic "Eureka!" moments, however. "There's a shift towards very precise measurements of subtle effects," Heinemann says. Still, Carena says, "I very much doubt that in 20 years, I will say, 'Oh, boy, after the Higgs discovery we learned nothing new.'"

Others are less sanguine about LHC experimenters' chances. "They're facing the desert and they don't know how wide it is," says Marvin Marshak, a physicist at the University of Minnesota, Twin Cities, who studies neutrinos using other facilities. Even optimists say that if the LHC finds nothing new, it will be harder to convince the governments of the world to build the next bigger, more expensive collider to keep the field going.

For now, many physicists at the LHC are just excited to get back to smashing protons. During the past 3 years, scientists have upgraded the detectors and reworked the lower energy accelerators that feed the collider. The LHC should now run at a more constant collision rate, effectively increasing the flow of data by as much as 50%, says Mike Lamont, director of accelerators and beams at CERN.

Accelerator physicists have been slowly tuning up the LHC's beams for months, Lamont says. Only when the beams are sufficiently stable will they turn on the detectors and resume taking data. Those switches should flip on 5 July, 10 years and 1 day after the announcement of the Higgs discovery, Lamont says. "It's good to be going into some sustained running." ■

INFECTIOUS DISEASE

Ancient DNA reveals Black Death source

Graves in Kyrgyzstan hold early victims of plague that swept medieval Europe

By **Ann Gibbons**

The Syriac engraving on the medieval tombstone was tantalizing: "This is the tomb of the believer Sanmaq. [He] died of pestilence." Sanmaq, who was buried in 1338 near Lake Issyk Kul in what is now northern Kyrgyzstan, was one of many victims of the unnamed plague. By scrutinizing field notes and more photos from the Russian team that had excavated the graves in the 1880s, historian Philip Slavin found that at least 118 people from Sanmaq's Central Asian trading community died in the epidemic.

Slavin was on the trail of the origin of the Black Death, which devastated Europe a decade after the Kyrgyzstan burials. But he knew the medieval diagnosis of "pestilence" encompassed many horrific diseases. "I was almost 100% certain it was the beginning of the Black Death," says Slavin, a medieval historian at the University of Stirling. "But there was no way to prove it without DNA."

Now, Slavin is senior author of a new study of ancient DNA from the "pestilence" victims showing they were indeed infected with the bacterium, *Yersinia pestis*, that caused the Black Death. The strain that killed them was ancestral to all the strains that rampaged across Europe a decade later and continued to kill for the next 500 years. The bacterium jumped from rodents to humans just before the Kyrgyzstan burials, perhaps after sudden changes in rainfall or temperature, the researchers propose this week in *Nature*.

"This is the place where it all started—the Wuhan of the Black Death," says senior author and paleogeneticist Johannes Krause of the Max Planck Institute for Evolutionary Anthropology.

The finding confirms some other researchers' hunches about Central Asia as a source for the Black Death strain, and pinpoints a precise time and place. "There's not much doubt about it—[the region is] where you have lots of reservoirs of the plague," says

A decade ago many physicists envisioned quickly spotting marvels including new force-carrying particles or even mini–black holes. "One would drown in supersymmetric particles," recalls Beate Heinemann, director of particle physics at the German laboratory DESY. Finding the Higgs would take longer, physicists predicted.

Instead, the Higgs appeared in a relatively speedy 3 years—in part because it is somewhat less massive than many physicists expected, about 133 times as heavy as a proton, which made it easier to produce. And 10 years after that monumental discovery, no other new particle has emerged.

That dearth has undermined two of physicists' cherished ideas. A notion called naturalness suggested the low mass of the Higgs more or less guaranteed the existence of new particles within the LHC's grasp. According to quantum mechanics, any particles lurking "virtually" in the vacuum will interact with real ones and affect their properties. That's exactly how virtual Higgs bosons give other particles their mass.

That physics cuts both ways, however. The Higgs boson's mass ought to be pulled dramatically upward by other standard model particles in the vacuum—especially the top quark, a heavier version of the up quark that weighs 184 times as much as the proton. That doesn't happen, so theorists have reasoned that at least one other new particle with a similar mass and just the right properties—in particular, a different spin—must exist in the vacuum to "naturally" counter the effects of the top quark.

> **"If they don't find anything, this field is dead."**
>
> **Juan Collar**, University of Chicago

The theoretical concept known as supersymmetry would supply such particles. For every known standard model particle, it posits a heavier partner with a different spin. Lurking in the vacuum, those partners would not only keep the Higgs's mass from running away, but would also help explain how the Higgs field, which pervades the vacuum like an unextinguishable electric field, came into being. Supersymmetric particles might even account for dark matter.

But instead of those hoped-for particles, what have emerged in the past decade are tantalizing anomalies—small discrepancies between observations and standard model predictions—that physicists will explore in the LHC's next 3-year run. For example, in 2017, physicists working with LHCb, one of four large particle detectors fed by the LHC, found that B mesons, particles that contain a heavy bottom quark, decay more often to an electron and a positron than to a particle called a muon and an antimuon. The standard model says the two rates should be the same, and the difference might be a hint of supersymmetric partners, Ellis says.

Similarly, experiments elsewhere suggest the muon might be very slightly more magnetic than the standard model predicts (*Science*, 9 April 2021, p. 113). That anomaly can be explained by the existence of exotic particles called leptoquarks, which might already be hiding undetected in the LHC's output, Ellis says.

The Higgs itself provides other avenues of exploration, as any difference between its observed and predicted properties would signal new physics. For example, in August 2020, teams of physicists working with the LHC's two biggest detectors, ATLAS and CMS, announced that both had spotted the Higgs decaying to a muon and an antimuon. If the rate of that hard-to-see decay varies from predictions, the deviation could point to new particles hiding in the vacuum, says Marcela Carena, a theorist at Fermi National Accelerator Laboratory.

Those searches likely won't yield dramatic "Eureka!" moments, however. "There's a shift towards very precise measurements of subtle effects," Heinemann says. Still, Carena says, "I very much doubt that in 20 years, I will say, 'Oh, boy, after the Higgs discovery we learned nothing new.'"

Others are less sanguine about LHC experimenters' chances. "They're facing the desert and they don't know how wide it is," says Marvin Marshak, a physicist at the University of Minnesota, Twin Cities, who studies neutrinos using other facilities. Even optimists say that if the LHC finds nothing new, it will be harder to convince the governments of the world to build the next bigger, more expensive collider to keep the field going.

For now, many physicists at the LHC are just excited to get back to smashing protons. During the past 3 years, scientists have upgraded the detectors and reworked the lower energy accelerators that feed the collider. The LHC should now run at a more constant collision rate, effectively increasing the flow of data by as much as 50%, says Mike Lamont, director of accelerators and beams at CERN.

Accelerator physicists have been slowly tuning up the LHC's beams for months, Lamont says. Only when the beams are sufficiently stable will they turn on the detectors and resume taking data. Those switches should flip on 5 July, 10 years and 1 day after the announcement of the Higgs discovery, Lamont says. "It's good to be going into some sustained running." ■

INFECTIOUS DISEASE

Ancient DNA reveals Black Death source

Graves in Kyrgyzstan hold early victims of plague that swept medieval Europe

By **Ann Gibbons**

The Syriac engraving on the medieval tombstone was tantalizing: "This is the tomb of the believer Sanmaq. [He] died of pestilence." Sanmaq, who was buried in 1338 near Lake Issyk Kul in what is now northern Kyrgyzstan, was one of many victims of the unnamed plague. By scrutinizing field notes and more photos from the Russian team that had excavated the graves in the 1880s, historian Philip Slavin found that at least 118 people from Sanmaq's Central Asian trading community died in the epidemic.

Slavin was on the trail of the origin of the Black Death, which devastated Europe a decade after the Kyrgyzstan burials. But he knew the medieval diagnosis of "pestilence" encompassed many horrific diseases. "I was almost 100% certain it was the beginning of the Black Death," says Slavin, a medieval historian at the University of Stirling. "But there was no way to prove it without DNA."

Now, Slavin is senior author of a new study of ancient DNA from the "pestilence" victims showing they were indeed infected with the bacterium, *Yersinia pestis*, that caused the Black Death. The strain that killed them was ancestral to all the strains that rampaged across Europe a decade later and continued to kill for the next 500 years. The bacterium jumped from rodents to humans just before the Kyrgyzstan burials, perhaps after sudden changes in rainfall or temperature, the researchers propose this week in *Nature*.

"This is the place where it all started—the Wuhan of the Black Death," says senior author and paleogeneticist Johannes Krause of the Max Planck Institute for Evolutionary Anthropology.

The finding confirms some other researchers' hunches about Central Asia as a source for the Black Death strain, and pinpoints a precise time and place. "There's not much doubt about it—[the region is] where you have lots of reservoirs of the plague," says

physical anthropologist Barbara Bramanti of the University of Ferrara.

In European historical accounts, the Black Death appears first in 1346 at ports on the Black Sea. Within a year it was in Europe, where scholars estimate it killed more than half of the population by 1353. In 1894, microbiologists identified *Y. pestis* as the cause. Ever since, they have debated where and when the deadly strain was born, considering China, Central Asia, India, and Genghis Khan's armies marching from Mongolia.

In 2020, a new analysis of more than 1300 modern and ancient genomes of *Y. pestis* narrowed the options. A team led by microbiologist Mark Achtman of the University of Warwick used a new software tool to sort all known strains of *Y. pestis* from humans and host animals into a family tree showing their evolution over 5500 years, starting with strains that were not closely related to the Black Death strain.

One branch of the tree underwent a "big bang" explosion of diversity at the time of the Black Death, creating a starlike pattern of four new lineages of *Y. pestis* whose descendant strains still persist in 40 species of rodents around the world. One of those lineages was the source of the Black Death and later outbreaks in Europe until the 18th century. The ancestral strain of this lineage was "literally the mother of them all," Krause says.

Geneticists knew this mother strain did not arise in Europe, because the strains found in Black Death victims there differed by two mutations from the putative ancestral genome, says paleogeneticist Maria Spyrou of the University of Tübingen, who had been Krause's postdoc. "We knew the European genomes were very close to origins of the Black Death, but not quite there," she says. Several teams suspected the source was in Central Asia, where strains from rodents were the closest genetic match to the mother genome. But no one had DNA data on strains from human victims of the right time period.

Then Krause and Spyrou heard Slavin give a talk about the tombstones. When he reported that the people had died of "pestilence," they each immediately thought, "We should do DNA!" Krause recalls.

Working with Slavin and Russian collaborators including Valeri Khartanovich of the Peter the Great Museum of Anthropology and Ethnography, where the Issyk Kul skulls were stored, Spyrou extracted DNA from the pulp of seven individuals' teeth and found three were infected with *Y. pestis*. She was able to reconstruct a high-quality genome of the ancient strain that killed them.

That strain "fell exactly on the origin point of that big bang event" in the evolution of *Y. pestis*, Spyrou says. "That was incredibly exciting."

The strain was closely related to ones found in rodents near Issyk Kul today. The authors suggest it spilled over to humans, perhaps from a marmot, which are abundant in the Tian Shan mountain region of northern Kyrgyzstan, southern Kazakhstan, and northwestern China. Sudden changes in rainfall or temperature could have led to surges in local rodent populations and the fleas or other insects they harbor. More rodents and their pests meant more opportunities to hop to a new host—humans—and adapt to it, says population biologist Nils Christian-Stenseth of the University of Oslo, who has shown a correlation between outbreaks of plague and warm, wet weather in Central Asia. He adds: "There are many good possibilities for plague reservoirs; you have the great gerbils, marmots, voles."

The remaining mystery, he says, is how the Black Death traveled 3500 kilometers from Central Asia to the Black Sea, where historical accounts describe the Mongolian army hurling the bodies of plague victims into the besieged city of Caffa in Crimea in 1346 in an early form of biological warfare.

The meticulous archaeological records for each Kyrgyzstan grave offer hints, Slavin says. Many people were buried with pearls, coins, and other goods from the Indian Ocean, the Mediterranean, and Iran; some were apparently traders. As they traveled, their camel wagons may have harbored rats and fleas, long considered likely vectors for plague.

Another paper, in *Nature Communications* last month, suggests rats were perfectly positioned to help spread the Black Death. A team led by archaeologist David Orton of the University of York used the diversity of ancient DNA in rat bones to trace the ups and downs of black rat populations through history. In Europe, one population collapsed with the fall of the Roman Empire but was replaced by another in the 13th century, when growing cities offered new food and shelter for the rodents. Black rats and their fleas were everywhere at that time, Krause says, especially aboard ships traveling between the Black Sea and Mediterranean ports—the route the Black Death evidently followed.

Meanwhile, the Issyk Kul graveyard is giving names and identities to the first known victims of the Black Death. "To actually have *Y. pestis* from incredibly well dated burials is really exciting," says bioarchaeologist Sharon De Witte of the University of South Carolina, Columbia. "We can clarify what other disease they were infected with and look at the biosocial factors that might have shaped risk of death in that first wave."

As for Slavin, he's still marveling at the discovery. "This was one of my dreams, to solve this outstanding puzzle." ■

Deadly spread

A new study pinpoints the first known cases of the plague that caused the Black Death, in people buried in 1338 near Lake Issyk Kul in today's Kyrgyzstan. A decade later, bubonic plague had devastated Europe.

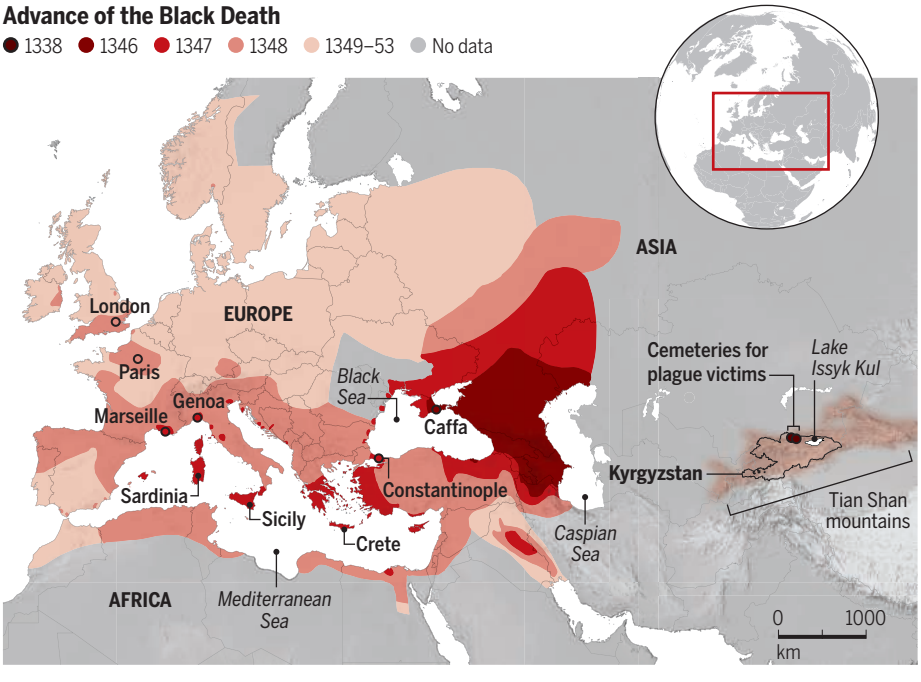

CREDITS: (MAP) K. FRANKLIN/*SCIENCE*; (DATA) OLE J. BENEDICTOW, *THE COMPLETE HISTORY OF THE BLACK DEATH* (2021)

The 2021 Pacific Northwest heat wave was unique, making it tough to assess climate change's role.

PHOTO: MARANIE STAAB/BLOOMBERG/GETTY IMAGES

CLIMATE CHANGE

Studies tying weather extremes to global warming gain rigor

Record-shattering events spur climate attribution advances

By **Paul Voosen**

In June 2021, a jet stream charged with heat and chaotic energy from a nearby cyclone stalled over the Pacific Northwest. The mass of trapped air baked the already hot landscape below to a record 49.6°C. More than 1000 people died from heat exposure.

Scientists quickly began working to figure out how much of the blame for the heat wave could be laid to global warming. But the heat was so unusual, the weather so weird, that it broke their methods. "It challenged our techniques, our climate models, and our statistical analysis methods," says Michael Wehner, a climate scientist at Lawrence Berkeley National Laboratory who participates in the World Weather Attribution (WWA) initiative. WWA ultimately issued a statement, finding the heat wave was "virtually impossible" without global warming. But, Wehner admits, that statement masked plenty of doubts. "We sort of kludged it."

Next time, he and fellow modelers expect to do better.

Critics complain that extreme event attribution, as the effort is known, overemphasizes public communications and underestimates uncertainty. But new approaches promise to increase the field's rigor and more precisely capture the relationship between climate change and extreme weather—even for events so extreme that there is no historical record for comparison.

In one existing method, researchers use climate models to simulate decades of climate history under current conditions and in preindustrial times, before warming set in. They tally up weather events that are similar to the extreme at hand in the two simulations and compare the frequencies to see whether warming increased the odds of the event occurring. In a second method, they shorten the timescale and run a model several hundred times under current and preindustrial conditions to see how often the extreme event would occur in each world. In a third method, researchers force models to re-create the actual atmospheric conditions recorded in the few years leading up to an event, then see how they unfold in counterfactual worlds with less warming. Although this "storyline" approach doesn't show how much more likely global warming made the extreme event, it does offer clues to how much worse it was because of warming.

By highlighting how the slow process of climate change can affect dangerous weather, these techniques have "revolutionized our ability to communicate the findings of climate science to the public," says Wim Thiery, a climate scientist at the Free University of Brussels. The results are increasingly being considered as evidence in lawsuits seeking damages for fossil fuel emissions and in the push for wealthy countries to pay for their role in worsening global warming. And the studies have led to new insights, Wehner says, for instance by showing that warming can increase hurricane flooding even more than expected and exposing how poorly models handle local causes of heat waves.

But these efforts rely on climate models with known biases that often fail to capture the detailed, local weather phenomena behind a heat wave or a flood. As a result, attribution studies that conclude, for example, that an event was 10.9 times more likely because of warming risk a false precision, says Markus Donat, a climate scientist at the Barcelona Supercomputing Center. "I don't think such a quantification factor means anything."

Because of such criticisms, WWA no longer relies on a single climate model, says Friederike Otto, a climatologist at Imperial College London; instead, it uses a suite of models to compare extreme events in preindustrial and greenhouse climates. The group has also standardized how it defines and categorizes an extreme event, a choice that's critical when hunting for and tallying up similar events in the models.

Yet these methods still falter with weather so extreme that it appears unprecedented, such as the Pacific Northwest heat wave. Such weather doesn't necessarily signal a new climate state; weather is so chaotic that even centuries of records can miss what's possible, says Laura Suarez-Gutierrez, a climate scientist who studies heat extremes at the Max Planck Institute for Meteorology. "Our range of events we can look at in the real world are so limited."

A method called "ensemble boosting" described last month at the annual meeting of the European Geosciences Union (EGU) could help modelers dissect such singular events. A team led by Erich Fischer, a climate modeler at ETH Zürich, has run a climate model many times over, looking for heat extremes similar to the 2021 heat wave. In a few instances, the model produced a heat wave resembling the real event, though not quite as extreme. The team took those outliers and rewound the model, perturbing the atmospheric conditions a few weeks before the heat wave to introduce more chaos and see whether they could produce events more like the real one. "We're trying to push the model to the most extreme state," Fischer says. In future research, he says, modelers could create such an ensemble of artificial scenarios for both current and preindustrial atmospheres. Then they could analyze these outliers and say whether global warming made the heat wave worse.

Other techniques forgo models entirely. Davide Faranda, a climate scientist at the University of Paris-Saclay, compares recent records of sea level air pressure to records from 1950–79, when warming was only getting started. He says these pressure analogs reflect large-scale air flows that can drive extreme events such as the Pacific Northwest heat wave. The method ensures that comparisons are like-to-like, unlike the model techniques, which might sometimes hinge on comparisons of regional rainfall, which can have diverse causes—a thunderstorm or a hurricane, for example. And it identifies when a weather event is truly new, resulting from chaotic pressure flows unseen in past records—which makes it statistically impossible to say whether climate change made the event more likely. In a preprint posted in February, Faranda and colleagues applied the method to maps of pressure leading up to a series of 2021 extremes, including flooding in Germany. They found the rainfall from similar extreme events has increased in modern times, a sign that warming made the flooding worse.

Finally, one group of researchers, led by Nicholas Leach, a graduate student at the University of Oxford, is betting that detailed weather forecasting models can give a more precise picture of global warming's role in weather than coarser climate models. They simulated the 2021 Pacific Northwest heat wave with the world-leading model of the European Centre for Medium-Range Weather Forecasts. After lowering carbon dioxide levels and removing human-driven heat from the ocean, the model reproduced a similar heat wave, although the highs were 2°C or so cooler than in the actual event, the team reported last month at the EGU meeting. The model's many runs for each scenario will allow them to assess whether climate change made the heat wave more likely. But WWA's statement that the event was "virtually impossible" without warming was likely an overreach, Leach says. "We don't find that in our model."

Such advances are encouraging government agencies to move into attribution studies. The National Oceanic and Atmospheric Administration, for example, has funded a pilot study on rapid attribution using its operational forecast model and climate models. The effort will seek to tease out the influence not only of global warming, but also of large-scale weather patterns like El Niño. Thiery can see a day coming where weather forecasters might incorporate an attribution like Leach's into their everyday work. "You can imagine a weather forecaster saying this heat wave is coming and it's 2°C warmer because of climate change." ■

PHOTO: JUSUN/ISTOCK.COM

GENOMICS

Upstart DNA sequencers could be a 'game changer'

Increasing potential for fast, cheap genomes may break open biology's bottleneck and broaden clinical uses

By **Elizabeth Pennisi**

For DNA sequencing, this "is the year of the big shake-up," says Michael Snyder, a systems biologist at Stanford University. Sequencing is crucial to fields from basic biology to virology to human evolution, and its importance keeps growing. Clinicians are clamoring to harness it for early detection of cancer and other diseases, and biologists are finding ever more ways to use genomics to study single cells. But for years, most sequencing has relied on machines from a single company, Illumina.

Last week, however, a young company called Ultima Genomics said at a meeting in Orlando, Florida, that with new twists on existing technologies, it could provide human genomes for $100 a pop, one-fifth the going rate. Several other companies also promised faster, cheaper sequencing at the same meeting, Advances in Genome Biology and Technology. This year, key patents protecting Illumina's sequencing technology will expire, paving the way for more competition, including from a Chinese company, MGI, which last week announced it would begin to sell its machines in the United States this summer. "We may be on the brink of the next revolution in sequencing," says Beth Shapiro, an evolutionary biologist at the University of California, Santa Cruz (UCSC).

Most sequencing companies, including Illumina, which has controlled 80% of the global market, depend on "sequencing by synthesis." The DNA to be deciphered is separated into single strands, which are usually chopped into short pieces and mounted on a surface—often a tiny bead—in a container called a flow cell. Each single strand fragment serves as a template to guide the synthesis of a strand with complementary bases, supplied one at a time to channels of beads. Because each added base has been modified to glow, a camera can record where it attaches—and hence the identity of the corresponding base on the original strand. The steps are repeated until the new DNA strand is complete.

Ultima streamlined the process by spraying the DNA-laden beads by the billions onto round silicon wafers the size of dessert plates. Nozzles above each wafer gently squirt out bases and other reagents, which spread thinly and evenly across the wafer as it rotates, reducing the amount of these expensive materials needed. Instead of moving back and forth across under the camera, the disk moves in a spiral, akin to how a compact disk is played, which speeds up imaging. It's "clever engineering [that] avoids a lot of complex plumbing," says Mark Akeson, a molecular biologist at UCSC. A neural network program rapidly turns imaging data into a sequence.

The sequencing chemistry is different as well. Only a few bases carry fluorescent tags,

The more than 3 billion letters in the human genome can now be sequenced for $100, several companies claim.

reducing costs. Moreover, the bases lack the usual stop signal, which ensures no extra bases latch on. Without these "terminators," the growing chain can sometimes add multiple bases at once, speeding the process. "Many of these innovations are used elsewhere, but they seem to have come together very nicely here," says Jay Shendure,

Other techniques forgo models entirely. Davide Faranda, a climate scientist at the University of Paris-Saclay, compares recent records of sea level air pressure to records from 1950–79, when warming was only getting started. He says these pressure analogs reflect large-scale air flows that can drive extreme events such as the Pacific Northwest heat wave. The method ensures that comparisons are like-to-like, unlike the model techniques, which might sometimes hinge on comparisons of regional rainfall, which can have diverse causes—a thunderstorm or a hurricane, for example. And it identifies when a weather event is truly new, resulting from chaotic pressure flows unseen in past records—which makes it statistically impossible to say whether climate change made the event more likely. In a preprint posted in February, Faranda and colleagues applied the method to maps of pressure leading up to a series of 2021 extremes, including flooding in Germany. They found the rainfall from similar extreme events has increased in modern times, a sign that warming made the flooding worse.

Finally, one group of researchers, led by Nicholas Leach, a graduate student at the University of Oxford, is betting that detailed weather forecasting models can give a more precise picture of global warming's role in weather than coarser climate models. They simulated the 2021 Pacific Northwest heat wave with the world-leading model of the European Centre for Medium-Range Weather Forecasts. After lowering carbon dioxide levels and removing human-driven heat from the ocean, the model reproduced a similar heat wave, although the highs were 2°C or so cooler than in the actual event, the team reported last month at the EGU meeting. The model's many runs for each scenario will allow them to assess whether climate change made the heat wave more likely. But WWA's statement that the event was "virtually impossible" without warming was likely an overreach, Leach says. "We don't find that in our model."

Such advances are encouraging government agencies to move into attribution studies. The National Oceanic and Atmospheric Administration, for example, has funded a pilot study on rapid attribution using its operational forecast model and climate models. The effort will seek to tease out the influence not only of global warming, but also of large-scale weather patterns like El Niño. Thiery can see a day coming where weather forecasters might incorporate an attribution like Leach's into their everyday work. "You can imagine a weather forecaster saying this heat wave is coming and it's 2°C warmer because of climate change." ■

PHOTO: JUSUN/ISTOCK.COM

GENOMICS

Upstart DNA sequencers could be a 'game changer'

Increasing potential for fast, cheap genomes may break open biology's bottleneck and broaden clinical uses

By **Elizabeth Pennisi**

For DNA sequencing, this "is the year of the big shake-up," says Michael Snyder, a systems biologist at Stanford University. Sequencing is crucial to fields from basic biology to virology to human evolution, and its importance keeps growing. Clinicians are clamoring to harness it for early detection of cancer and other diseases, and biologists are finding ever more ways to use genomics to study single cells. But for years, most sequencing has relied on machines from a single company, Illumina.

Last week, however, a young company called Ultima Genomics said at a meeting in Orlando, Florida, that with new twists on existing technologies, it could provide human genomes for $100 a pop, one-fifth the going rate. Several other companies also promised faster, cheaper sequencing at the same meeting, Advances in Genome Biology and Technology. This year, key patents protecting Illumina's sequencing technology will expire, paving the way for more competition, including from a Chinese company, MGI, which last week announced it would begin to sell its machines in the United States this summer. "We may be on the brink of the next revolution in sequencing," says Beth Shapiro, an evolutionary biologist at the University of California, Santa Cruz (UCSC).

Most sequencing companies, including Illumina, which has controlled 80% of the global market, depend on "sequencing by synthesis." The DNA to be deciphered is separated into single strands, which are usually chopped into short pieces and mounted on a surface—often a tiny bead—in a container called a flow cell. Each single strand fragment serves as a template to guide the synthesis of a strand with complementary bases, supplied one at a time to channels of beads. Because each added base has been modified to glow, a camera can record where it attaches—and hence the identity of the corresponding base on the original strand. The steps are repeated until the new DNA strand is complete.

Ultima streamlined the process by spraying the DNA-laden beads by the billions onto round silicon wafers the size of dessert plates. Nozzles above each wafer gently squirt out bases and other reagents, which spread thinly and evenly across the wafer as it rotates, reducing the amount of these expensive materials needed. Instead of moving back and forth across under the camera, the disk moves in a spiral, akin to how a compact disk is played, which speeds up imaging. It's "clever engineering [that] avoids a lot of complex plumbing," says Mark Akeson, a molecular biologist at UCSC. A neural network program rapidly turns imaging data into a sequence.

The sequencing chemistry is different as well. Only a few bases carry fluorescent tags,

The more than 3 billion letters in the human genome can now be sequenced for $100, several companies claim.

reducing costs. Moreover, the bases lack the usual stop signal, which ensures no extra bases latch on. Without these "terminators," the growing chain can sometimes add multiple bases at once, speeding the process. "Many of these innovations are used elsewhere, but they seem to have come together very nicely here," says Jay Shendure,

a geneticist and technology developer at the University of Washington (UW), Seattle.

Ultima CEO Gilad Almogy and his colleagues demonstrated the technology's potential in four preprints posted in late May on bioRxiv. In one, they and colleagues at the Broad Institute of MIT and Harvard used their machine to sequence more than 224 already-sequenced human genomes and found their results on par with previous work. The three other studies showed the technology can evaluate a single cell's repertoire of expressed genes, the effects of mutations, and epigenetics—chemical modifications of DNA that affect gene activity.

Until now, cost has limited such single-cell studies, causing a bottleneck in research. But Snyder found Ultima's low-cost approach enabled him to sequence multiple colon cancer cells to document how one DNA modification, methylation, changes as colon cancer develops.

In another preprint, Joshua Levin and his Broad Institute colleagues tested the ability of the Ultima technology to identify active genes in single blood cells as indicated by the genes' RNA transcripts. The team found Ultima's machine identified those genes about as well as Illumina's did. And, he adds, "It's a game changer due to the lower cost."

Florence Chardon, a UW genomics graduate student who modifies DNA with the genome editor CRISPR, is excited by that prospect. "The less expensive [sequencing] gets, the more accessible this kind of research is to more labs and more people," she says.

But Lior Pachter, a computational biologist at the California Institute of Technology, has reservations about the new technology. He and graduate student A. Sina Booeshaghi looked at one of the most active genes in blood cells from Levin's team, a possible cancer biomarker also known for producing a protein athletes sometimes inject to illegally enhance their performance. The Ultima technology sometimes missed the active gene, Pachter says. The "error rate was very high, and the performance was very poor."

The gene has a stretch in which the same base is repeated eight times, and Ultima admits long repeats can undermine the accuracy of its reads. Looking elsewhere in the Ultima sequence, Pachter found errors when one base was repeated just three times. He notes that a human genome contains at least 1.4 million of these so-called homopolymers. Still, he says, "For some applications, you don't need perfect sequences."

Pachter and others also take issue with the touted $100 cost. That figure only covers reagents, not the labor, pre- and post-sequencing steps, and initial outlay for the machine, the price of which has not been released. Even if the $100 figure is real, it may not be unique: Other companies are also promising $100 per human genome.

One is MGI, a subsidiary of Chinese sequencing giant BGI. MGI's technology is similar to Illumina's, but it increases accuracy by adding all four bases at once as it sequences DNA. To track which bases are incorporated, it uses antibodies, which are brighter and less expensive than fluorescent dyes. Illumina, too, is promising lower costs, and at the meeting it introduced new chemistries to increase accuracy and flexibility.

For this bargain rate to be realized, Ultima and MGI both require filling their sequencers to capacity with hundreds of genomes. But high-throughput sequencing "is not always good for clinical practice even if it is good economics," says Greg Elgar, a genome biologist at Genomics England, because sometimes a physician needs just one or a few people's genomes analyzed. Other companies with new flow cells and chemistries can economically sequence small numbers of genomes. At last week's meeting, Element Biosciences CEO Molly He reported the company is now shipping benchtop sequencers that can sequence three human genomes at a time, at a cost of $560 each. Another company, Singular Genomics, also promises benchtop technology that doesn't require high throughput for cost savings.

"We may be on the brink of the next revolution in sequencing."
Beth Shapiro, University of California, Santa Cruz

These machines, like those from Illumina, MGI, and Ultima, all decipher short fragments of DNA. But for the past 7 years, two companies, Pacific Biosciences and Oxford Nanopore Technologies, have worked on sequencing "long reads," thousands of bases long, which leave fewer partial sequences to piece together into a full genome. The technologies "can sequence the native DNA molecule, in all its glory," Elgar says. They have struggled with low accuracy and high cost, but he says they are on their way to becoming practical tools.

Don't count the sequencing giant Illumina out just yet. Its scientists "probably have kept a couple of cards in their back pocket" to keep their position in the market strong, says Albert Vilella, a bioinformatician and genomics consultant in Cambridge, England. Nonetheless, Illumina faces unprecedented competition, he adds. "It's time to look at the [DNA sequencing] landscape with fresh eyes." ■

INFECTIOUS DISEASE

Monkeypox could establish new reservoirs in animals

Concern grows that virus will get footholds in species outside Africa

By **Jon Cohen**

Eleven days after being bitten by one of her pet prairie dogs, a 3-year-old girl in Wisconsin on 24 May 2003 became the first person outside of Africa to be diagnosed with monkeypox. Two months later, her parents and 69 other people in the United States had suspected or confirmed cases of this disease, which is caused by a relative of the much deadlier smallpox virus. The monkeypox virus is endemic in parts of Africa, and rodents imported from Ghana had apparently infected captive prairie dogs from North America when an animal distributor in Texas housed them together.

The outbreak now underway has affected more people outside of Africa than ever before—more than 1800 cases as of 14 June, on multiple continents, many of them men who have sex with men. But like the 2003 episode, today's surge has raised a possibility that makes researchers gulp: Monkeypox virus could take up permanent residence in wildlife outside of Africa, forming a reservoir that could lead to repeated human outbreaks.

No animal reservoir currently exists outside of Africa, but the U.S. outbreak of 2003 was a close call, some scientists suspect, especially because nearly 300 of the animals from Ghana and the exposed prairie dogs were never found. "We narrowly escaped having monkeypox establish itself in a wild animal population" in North America, suggests Anne Rimoin, an epidemiologist at the University of California, Los Angeles, who long has studied the disease in the Democratic Republic of the Congo (DRC).

In the end, however, surveys of wild animals in Wisconsin and Illinois never found monkeypox virus, none of the infected humans passed on the disease to other people, and worries about this exotic outbreak

a geneticist and technology developer at the University of Washington (UW), Seattle.

Ultima CEO Gilad Almogy and his colleagues demonstrated the technology's potential in four preprints posted in late May on bioRxiv. In one, they and colleagues at the Broad Institute of MIT and Harvard used their machine to sequence more than 224 already-sequenced human genomes and found their results on par with previous work. The three other studies showed the technology can evaluate a single cell's repertoire of expressed genes, the effects of mutations, and epigenetics—chemical modifications of DNA that affect gene activity.

Until now, cost has limited such single-cell studies, causing a bottleneck in research. But Snyder found Ultima's low-cost approach enabled him to sequence multiple colon cancer cells to document how one DNA modification, methylation, changes as colon cancer develops.

In another preprint, Joshua Levin and his Broad Institute colleagues tested the ability of the Ultima technology to identify active genes in single blood cells as indicated by the genes' RNA transcripts. The team found Ultima's machine identified those genes about as well as Illumina's did. And, he adds, "It's a game changer due to the lower cost."

Florence Chardon, a UW genomics graduate student who modifies DNA with the genome editor CRISPR, is excited by that prospect. "The less expensive [sequencing] gets, the more accessible this kind of research is to more labs and more people," she says.

But Lior Pachter, a computational biologist at the California Institute of Technology, has reservations about the new technology. He and graduate student A. Sina Booeshaghi looked at one of the most active genes in blood cells from Levin's team, a possible cancer biomarker also known for producing a protein athletes sometimes inject to illegally enhance their performance. The Ultima technology sometimes missed the active gene, Pachter says. The "error rate was very high, and the performance was very poor."

The gene has a stretch in which the same base is repeated eight times, and Ultima admits long repeats can undermine the accuracy of its reads. Looking elsewhere in the Ultima sequence, Pachter found errors when one base was repeated just three times. He notes that a human genome contains at least 1.4 million of these so-called homopolymers. Still, he says, "For some applications, you don't need perfect sequences."

Pachter and others also take issue with the touted $100 cost. That figure only covers reagents, not the labor, pre- and post-sequencing steps, and initial outlay for the machine, the price of which has not been released. Even if the $100 figure is real, it may not be unique: Other companies are also promising $100 per human genome.

One is MGI, a subsidiary of Chinese sequencing giant BGI. MGI's technology is similar to Illumina's, but it increases accuracy by adding all four bases at once as it sequences DNA. To track which bases are incorporated, it uses antibodies, which are brighter and less expensive than fluorescent dyes. Illumina, too, is promising lower costs, and at the meeting it introduced new chemistries to increase accuracy and flexibility.

For this bargain rate to be realized, Ultima and MGI both require filling their sequencers to capacity with hundreds of genomes. But high-throughput sequencing "is not always good for clinical practice even if it is good economics," says Greg Elgar, a genome biologist at Genomics England, because sometimes a physician needs just one or a few people's genomes analyzed. Other companies with new flow cells and chemistries can economically sequence small numbers of genomes. At last week's meeting, Element Biosciences CEO Molly He reported the company is now shipping benchtop sequencers that can sequence three human genomes at a time, at a cost of $560 each. Another company, Singular Genomics, also promises benchtop technology that doesn't require high throughput for cost savings.

"We may be on the brink of the next revolution in sequencing."
Beth Shapiro, University of California, Santa Cruz

These machines, like those from Illumina, MGI, and Ultima, all decipher short fragments of DNA. But for the past 7 years, two companies, Pacific Biosciences and Oxford Nanopore Technologies, have worked on sequencing "long reads," thousands of bases long, which leave fewer partial sequences to piece together into a full genome. The technologies "can sequence the native DNA molecule, in all its glory," Elgar says. They have struggled with low accuracy and high cost, but he says they are on their way to becoming practical tools.

Don't count the sequencing giant Illumina out just yet. Its scientists "probably have kept a couple of cards in their back pocket" to keep their position in the market strong, says Albert Vilella, a bioinformatician and genomics consultant in Cambridge, England. Nonetheless, Illumina faces unprecedented competition, he adds. "It's time to look at the [DNA sequencing] landscape with fresh eyes." ■

INFECTIOUS DISEASE

Monkeypox could establish new reservoirs in animals

Concern grows that virus will get footholds in species outside Africa

By **Jon Cohen**

Eleven days after being bitten by one of her pet prairie dogs, a 3-year-old girl in Wisconsin on 24 May 2003 became the first person outside of Africa to be diagnosed with monkeypox. Two months later, her parents and 69 other people in the United States had suspected or confirmed cases of this disease, which is caused by a relative of the much deadlier smallpox virus. The monkeypox virus is endemic in parts of Africa, and rodents imported from Ghana had apparently infected captive prairie dogs from North America when an animal distributor in Texas housed them together.

The outbreak now underway has affected more people outside of Africa than ever before—more than 1800 cases as of 14 June, on multiple continents, many of them men who have sex with men. But like the 2003 episode, today's surge has raised a possibility that makes researchers gulp: Monkeypox virus could take up permanent residence in wildlife outside of Africa, forming a reservoir that could lead to repeated human outbreaks.

No animal reservoir currently exists outside of Africa, but the U.S. outbreak of 2003 was a close call, some scientists suspect, especially because nearly 300 of the animals from Ghana and the exposed prairie dogs were never found. "We narrowly escaped having monkeypox establish itself in a wild animal population" in North America, suggests Anne Rimoin, an epidemiologist at the University of California, Los Angeles, who long has studied the disease in the Democratic Republic of the Congo (DRC).

In the end, however, surveys of wild animals in Wisconsin and Illinois never found monkeypox virus, none of the infected humans passed on the disease to other people, and worries about this exotic outbreak

evaporated. Will North and South America, Europe, Asia, and Australia—all of which have reported monkeypox cases in this outbreak—be similarly fortunate this time?

Viruses frequently pingpong between humans and other species. Although COVID-19 is widely thought to have resulted from SARS-CoV-2 jumping from a bat or other host into people, humans have, in "reverse zoonoses," also infected white-tailed deer, minks, cats, and dogs with the virus. One study in Ohio found antibodies to SARS-CoV-2 in more than one-third of 360 wild deer sampled. And in past centuries, when humans carried plague and yellow fever to new continents, those pathogens created reservoirs in rodents and monkeys, respectively—which later infected humans again.

As this outbreak of monkeypox expands, the virus has an unprecedented opportunity to establish itself in non-African species, which could infect humans and provide greater opportunity for more dangerous variants to evolve. "Monkeypox reservoirs in wild animals outside of Africa is a scary scenario," says Bertram Jacobs, a virologist at Arizona State University (ASU), Tempe, who studies vaccinia, the poxvirus that served as the smallpox vaccine and helped eradicate that devastating virus from humans.

Public health officials in several countries have advised people who have monkeypox lesions to avoid contact with their pets. Some 80% of the cases have occurred in Europe, and the European Food Safety Authority said no pets or wild animals had been infected as of 24 May. But it added that "close collaboration between human and veterinary public health authorities is needed to manage exposed pets and prevent the disease from being transmitted to wildlife."

The possibility that humans infected with monkeypox virus will spread it to wildlife outside of Africa "warrants serious concern," says William Karesh, a veterinarian at the EcoHealth Alliance who on 2 June spoke about this possibility at a consultation on monkeypox research organized by the World Health Organization. For now, he says, the limited number of human cases reduces the odds. But pet rodents are a particular worry, as is the sheer number of wild ones—they make up 40% of all mammals—that frequently raid trash and could become infected by contaminated waste. "That's a lot of opportunity," he says.

Studies have yet to pinpoint the African reservoir of the monkeypox virus. Although a lab in Copenhagen, Denmark, in 1958 first identified it in research monkeys from Asia, scientists now believe the primates caught it from an African source. Since the first human case was reported in 1970, in the DRC (then Zaire), all could be tied to the virus spilling over from animals in Africa.

So far, however, only six wild animals trapped in Africa have yielded the virus: three rope squirrels, a Gambian rat, a shrew, and a sooty mangabey monkey. Antibodies to the monkeypox virus are most abundant in African squirrels. "We still poorly understand the current reservoir other than it's rodents," says Grant McFadden, a poxvirus researcher who is also based at ASU.

The Kautzer family, shown here in June 2003 with their prairie dog Chuckles, were all infected by monkeypox 1 month earlier by a second pet prairie dog that died.

PHOTO: MIKE ROEMER/GETTY IMAGES

But it's clear monkeypox can infect many other kinds of animals in the wild and captivity. A 1964 outbreak in a Rotterdam, Netherlands, zoo sickened giant anteaters, orangutans, gorillas, chimpanzees, a gibbon, and a marmoset. Researchers have intentionally infected many lab animals, including rabbits, hamsters, guinea pigs, and chickens, although the virus doesn't reliably cause disease in several of them.

For many viruses, a lock-and-key relationship between viral surface proteins and receptors on host cells determines which animals it can infect; the spike protein of SARS-CoV-2, for example, latches onto angiotensin-converting enzyme 2, a protein that studs a variety of cells in humans, minks, cats, and many other species. But poxviruses don't seem to require specific host receptors, enabling many to infect a wide range of mammalian cells. Vaccinia, the smallpox vaccine virus, can even infect fruit flies in addition to cows and people, notes David Evans, a poxvirus researcher at the University of Alberta, Edmonton. Bernard Moss, a virologist at the U.S. National Institute of Allergy and Infectious Diseases (NIAID), has posited that some poxviruses have proteins on their surfaces that form a "hydrophobic face," a water-repelling area that can bind nonspecifically to hydrophilic cell membranes and initiate the infection process.

But whether a poxvirus can thrive in an infected cell and, ultimately persist in a species to create a reservoir depends on how well it fends off the host's immune attacks. Poxviruses have a relatively large complement of genes, about 200, and roughly half undermine a host's immune response. "Some viruses run and hide or are stealthy, avoiding direct contact with elements of the immune system," McFadden says. "Poxviruses by and large stand up and fight."

Their defense against host immunity appears to rely heavily on a family of genes scattered around their genomes that code for poorly understood proteins containing domains known as ankyrin repeats. Poxvirus proteins containing these repeats act as "molecular flypaper," Evans says, glomming onto host proteins involved with coordinating the immune response. "Orthopoxviruses have these arrays of ankyrin repeats, and most of them, we don't really know what they target," Evans says. "But the bottom line is those probably hold the key to trying to understand why it is some of these viruses have the host range that they do."

Variola, the smallpox virus, appears to have lost many of these immune-evasion genes. It only persists in humans and has no animal reservoir, which was why the global vaccination campaign could eradicate it. Monkeypox is clearly more promiscuous. But there's no telling whether it is capable of creating reservoirs in non-African wildlife. "One of the challenges has been a lack of interest," says Lisa Hensley, a microbiologist at the U.S. Department of Agriculture who began doing monkeypox research in 2001 as part of a U.S. Army lab.

Hensley, who worked on monkeypox at NIAID for nearly a decade and collaborated with Rimoin, urges people to keep an open mind about how the virus behaves and what it might do next. "We're recognizing that this is a disease we need to worry about and that we really don't know as much as we think we know." ■

ASTRONOMY

Telescope in India snares light in spinning mercury

Inexpensive "liquid mirrors" could be used in giant telescopes on the Moon

By **Daniel Clery**

A unique telescope that focuses light with a slowly spinning bowl of liquid mercury instead of a solid mirror has opened its eye to the skies above India. Such telescopes have been built before, but the 4-meter-wide International Liquid Mirror Telescope (ILMT) is the first large one to be purpose-built for astronomy, at the kind of high-altitude site observers prize—the 2450-meter Devasthal Observatory in the Himalayas.

Although its users must satisfy themselves with only looking straight up, the $2 million instrument, built by a consortium from Belgium, Canada, and India, is much cheaper than telescopes with glass mirrors. A stone's throw from ILMT is the 3.6-meter, steerable Devasthal Optical Telescope (DOT), built by the same Belgian company at the same time—but for $18 million. "Simple things are often the best," says Project Director Jean Surdej of the University of Liège. Some astronomers say liquid mirrors are the perfect technology for a giant telescope on the Moon that could see back to the time of the universe's very first stars.

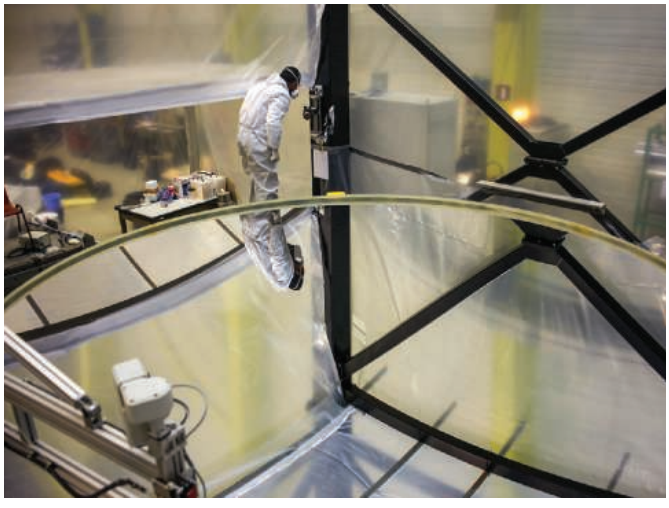

The International Liquid Mirror Telescope relies on a spinning dish containing 50 liters of mercury.

When a bowl of reflective liquid mercury is rotated, the combination of gravity and centrifugal force pushes the liquid into a perfect parabolic shape, exactly like a conventional telescope mirror—but without the expense of casting a glass mirror blank, grinding its surface into a parabola, and coating it with reflective aluminum.

ILMT was originally dreamt up in the late 1990s. The dish-shaped vessel that holds the mercury was delivered to India in 2012, but construction of the telescope enclosure was delayed. Then researchers found they didn't have enough mercury. As they waited for more, the COVID-19 pandemic struck, making travel to India impossible. Finally, in April, the team set 50 liters of mercury spinning, creating a parabolic layer 3.5 millimeters thick. After such a long gestation, "we're all very happy," says team member Paul Hickson of the University of British Columbia, Vancouver.

Staring straight up, the rotating mirror will see a swath of sky almost as wide as the full Moon while Earth's rotation scans it across the heavens from dusk to dawn. "You just turn it on and let it go," Hickson says. Objects appear as long streaks in the image; the separate pixels can be added together afterward to create a single long exposure. Because the telescope sees roughly the same strip of sky on successive nights, exposures from many nights can be added together to get extremely sensitive images of faint objects.

Alternatively, one night's image can be subtracted from the next's to see what has changed, revealing transient objects such as supernovae and quasars, the bright hearts of distant galaxies that wax and wane as supermassive black holes consume matter. Surdej also wants to hunt for gravitational lenses, in which the gravity of a galaxy or galaxy cluster bends the light of a more distant object like a giant magnifying glass. ILMT's sensitive measurement of the objects' brightness can reveal the mass distribution of the lens galaxies. A study suggested as many as 50 lenses might be visible in ILMT's view of the sky.

Conventional survey telescopes, such as the Zwicky Transient Facility in California and the upcoming Vera C. Rubin Observatory in Chile, cover much more of the sky. But they are unlikely to return to the same patch every single night to search for changes. "We're forced to have a niche," Hickson says. ILMT has the added strength of sitting next to DOT, which is equipped with instruments that can rapidly scrutinize any fleeting objects discovered by its next-door neighbor. This tag-team approach "is more comprehensive, and scientifically more rich," says Dipankar Banerjee, director of the Aryabhatta Research Institute of Observational Sciences, which runs the Devasthal Observatory.

If ILMT is a success, Surdej says the technology could be scaled up to build much larger liquid mirrors on the Moon, an attractive location for giant telescopes because it is less seismically active than Earth and has no atmosphere. On Earth, the Coriolis effect, from the planet's rotation, would warp the motion of the mercury in mirrors larger than 8 meters. But the Moon rotates more slowly, allowing much larger liquid mirrors—although not of mercury. It is too heavy to transport to the Moon and would freeze at night and evaporate during the day. But more than a decade ago, liquid mirror pioneer Ermanno Borra of Laval University showed that "ionic liquids," lightweight molten salts with low freezing points, would survive lunar conditions and could be made reflective with a thin coating of silver.

In the 2000s, both NASA and the Canadian Space Agency commissioned studies of lunar liquid mirror telescopes but didn't go any further. Astronomers hope the current interest in Moon exploration and the cheap launches offered by rocket companies such as SpaceX will spur a revival. In 2020, a team at the University of Texas, Austin, proposed the Ultimately Large Telescope, a 100-meter liquid mirror that would stare constantly at the same patch of sky for years on end from one of the Moon's poles. Such a giant could gather the faint trickle of photons from the very first stars that lit up the universe, before galaxies even existed. Veteran mirrormaker Roger Angel of the University of Arizona says there is "a unique niche for a big [liquid] mirror that goes beyond what others can do." ■

PHOTO: ANNA AND JEAN SURDEJ

CLUES TO LONG COVID

Scientists strive to unravel what is driving disabling symptoms

By **Jennifer Couzin-Frankel**; *Illustrations by* **Ashley Mastin**

They span three continents, but a trio of researchers who've never met share a singular focus made vital by the still-raging pandemic: deciphering the causes of Long Covid and figuring out how to treat it.

Almost 2 years ago in Italy, pediatric infectious disease doctor Danilo Buonsenso, who works at Gemelli University Hospital, started to see children who, months after mild infections with SARS-CoV-2, were still short of breath and had crushing fatigue and other symptoms. He now suspects that, in some of them, the cells and tissues that control blood flow are damaged and the blood's tendency to clot is amplified. Minute blood clots, leftover from the viral assault or fueled by its aftermath, might be gumming up the body's circulation, to disastrous effect from the brain to joints. "In some patients we have specific areas where no blood flow comes in" or the flow is reduced, Buonsenso says. Is that driving their lingering symp-

toms? "I can't say this is the truth, of course. But this makes sense."

Meanwhile, in the United States, microbiologist Amy Proal can't stop thinking about a second leading Long Covid theory: that the coronavirus keeps hurting people by stubbornly enduring in the body, even after acute infection passes. Studies have shown "the virus is capable of persistence in a wide range of body sites," especially nerves and other tissues, says Proal, who works at the PolyBio Research Foundation, a nonprofit in Washington state. She recently caught COVID-19 for the third time.

Down under in Australia, immunologist Chansavath Phetsouphanh of the University of New South Wales, Sydney, is chasing a third lead, motivated by what the blood of Long Covid patients has divulged: an immune system gone haywire even 8 months after they'd first tested positive. He had assumed that immune cells galvanized to fight off infection would have calmed down over that time span. So, "It was a surprise that these cells did not recover," says Phetsouphanh, who is working to set up an international Long Covid collaboration.

For each of these researchers—and many others exploring the causes of Long Covid—untangling the complex syndrome, with a still-evolving definition, is a laborious, step-wise process. First, they must show that a possible contributor—such as minuscule clots, lingering virus, or immune abnormalities—crops up disproportionately in people with Long Covid. Then comes the hard part: proving that each of these traits, alone or in combination, explains why the coronavirus has rendered millions of people shadows of their former selves.

All agree that solo operators are unlikely. Lingering virus, for example, could attack the circulatory system, triggering blood clots or chronic inflammation. "I see this as a triangle," Buonsenso says, with each trigger potentially explaining, or even amplifying, the others.

A final challenge is identifying treatments that ease or reverse these abnormalities and help patients feel better. In the United Kingdom, home to a widely praised effort to identify immediate COVID-19 treatments, researchers are launching a clinical trial that will be among the largest worldwide to test potential Long Covid therapies in a randomized, statistically robust manner. But more such studies are needed—and time is of the essence (see sidebar, below). In May, the U.S. Centers for Disease Control and Prevention reported that a review of the medical records of nearly 2 million people suggested at least one in five of those diagnosed with COVID-19 had developed conditions characteristic of Long Covid. Other studies have found roughly similar rates. Some recent research suggests the risk for vaccinated people is somewhat lower, but vaccination's power to head off the syndrome remains uncertain.

> **"I consider Long Covid to be a massive emergency."**
>
> **Amy Proal**, PolyBio Research Foundation

For Proal and others, fitting the puzzle pieces together is of urgent concern. "I consider Long Covid to be a massive emergency," she says.

TINY BLOOD CLOTS

In Rome, Buonsenso is using a sophisticated medical imaging technique to better understand the role of blood clots. Called a SPECT-CT scan, it combines two different types of images: a single-photon emission computed tomography scan, which uses a radiotracer injected into a person's veins to provide pictures of blood flow, and a standard CT scan for information about lung structure. By merging these, doctors can see which parts of the lungs aren't getting normal blood flow.

So far, Buonsenso has scanned the lungs of 11 youngsters who have severe Long Covid, including irregular heartbeats and breathlessness during exercise. In six children, the lungs appeared normal. In the other five, the images were striking: Where there should have been bright oranges and yellows, signifying pulsing blood, one lung was nearly completely blue, indicating little flow. Buonsenso believes tiny blood clots or chronic damage to the lining of

Glacial pace for U.S. Long Covid grants

By **Meredith Wadman**

David Putrino, a neurophysiologist at the Icahn School of Medicine at Mount Sinai, labored through his holiday last Christmas to write a grant application for urgently needed Long Covid research. With colleagues, he hoped to tap into $1.15 billion in funding that Congress granted the National Institutes of Health (NIH) in 2020, as Long Covid emerged as a major public health problem. NIH had solicited grant applications in December 2021, just weeks before their January due date. The agency said it planned to issue decisions by late March.

But as of 10 June, Putrino was still waiting to hear whether NIH will fund his effort to discover whether microclots might be a meaningful diagnostic biomarker for many types of Long Covid. "Maybe they should hire people who are dedicated to accelerating these programs," says Putrino, who specializes in rehabilitation medicine. "[Long Covid] is a national crisis. This does not deserve to be somebody's second or third job. What we need from the NIH right now is their full attention."

Putrino's is not the lone complaint about NIH's management of Long Covid research—an initiative dubbed RECOVER, for Researching COVID to Enhance Recovery. RECOVER's flagship, an observational study of up to 40,000 people, has come under fire from patient advocates and some scientists who say it lacks transparency and is moving far too slowly—a ponderous battleship when a fleet of hydroplanes is what's needed. As of 6 June, the study had signed up 3712 adults, or 21% of its adult enrollment target of 17,680. Among children, numbers are even lower, with 98 children in a study aiming to enroll 19,500 of them.

Critics note that other countries have been more nimble. By July 2021, the United Kingdom had funded 15 Long Covid research projects aimed at diagnosis and treatment. A recent independent review published by the Rockefeller Foundation found that, as of February, NIH had funded just eight of the 200 Long Covid trials listed in the database ClinicalTrials.gov; the trials are being run in many countries.

NIH acknowledges the critiques and says it has already "obligated or committed" the $1.15 billion, slated to be spent over 4 years. But the scope of the project prevents it from sprinting, Walter Koroshetz, director of NIH's National Institute of Neurological Disorders and Stroke and a co-chair of the RECOVER initiative, implied in a talk to a panel of advisers to the NIH director on 9 June. "You can't believe what a big lift this has been," he told the advisers. RECOVER "is engineered to really not leave any stone unturned."

NIH added in a statement that it expects to announce winners of the long-awaited January funding within 2 weeks. And the agency says it has dedicated multiple staff to RECOVER, reinforced by other NIH experts and the outside firm Deloitte. But given the growing concern about Long Covid—one recent report estimated one in five U.S. COVID-19 survivors is afflicted—U.S. researchers say more urgency is needed (see main story, p. 1261).

RECOVER's longitudinal study aims to discover the biological roots of Long Covid and describe its prevalence, risk factors, and

blood vessels may be impairing blood flow. He and his colleagues published their first evidence of such damage, in a 14-year-old girl, in July 2021 in *The Lancet Child & Adolescent Health*.

The knotty question is what to do next. Buonsenso's patients don't meet the current criteria for taking anticoagulant drugs that prevent blood clots or keep them from getting bigger, because no clots are visible on their scans. "You either say, 'I'm sorry, but I can't do anything outside of a study,' or you are kind of a not-scared doctor with reciprocal trust with the patient and family, and together make a decision," Buonsenso says.

With seriously ill children and their desperate parents in front of him, Buonsenso didn't want to wait to launch a clinical trial. He and the families instead decided to do what they could. All five patients are now taking anticoagulants—which carry the risk of severe bleeding—under close monitoring.

He's heartened by their progress. Several are back in school, playing sports, and spending time with friends. Two have been rescanned. A teenager who still suffers from symptoms showed little improvement. But in another, whose symptoms have largely resolved, the images looked nearly normal. The other three will be rescanned this summer.

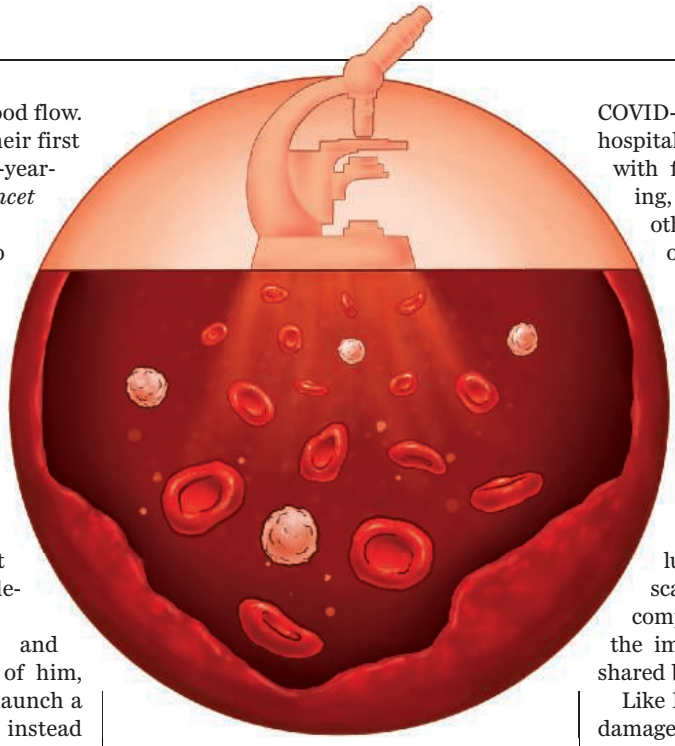

ILLUSTRATION: A. MASTIN/*SCIENCE*

Of course, he can't be sure those who improved did so because of the treatment. That's why he is hoping for resources to establish a Long Covid clinical trial that would include a placebo group.

Like other doctors, Buonsenso has been inspired by Long Covid patients who have lobbied hard for treatments and shared successes and failures on social media. Marta Esperti, a 34-year-old graduate student now living in Paris, is one of them. Struck by COVID-19 more than 2 years ago, she wasn't hospitalized but months later struggled with fatigue, breathlessness when walking, persistent fever, joint pain, and other symptoms. Yet bloodwork and other medical tests, such as x-rays of her lungs, were largely normal. Esperti kept pushing for answers. Then, in the spring of 2021, "I received a call from the pulmonologist saying, 'Listen, I want you to do another test.'"

Esperti was one of the first Long Covid patients in Europe to receive a lung SPECT-CT scan, and it looked just like the compromised lungs of the sick children Buonsenso scanned later. "My right lung is almost completely blue," she says. She posted the images on Twitter, where they were shared by thousands of people.

Like Buonsenso, Esperti's doctors believe damage to tiny blood vessels and minuscule clots are the culprit. The theory of persistent microclots gained further credence in the summer of 2021, when Resia Pretorius, a physiologist at Stellenbosch University in South Africa, and her colleagues reported in *Cardiovascular Diabetology* that such clots could linger in the blood of Long Covid patients. Her team found signs of excessive blood clotting in 11 people with Long Covid, but not in healthy people or another group with type 2 diabetes, whom they used for comparison.

symptoms. It will also include clinical trials of treatments and preventives, which NIH hopes to launch by fall.

"Everybody is working as fast as possible but this is a monster of a study," says immunologist Janko Nikolich-Žugich of the University of Arizona College of Medicine, Tucson, a principal investigator for a RECOVER arm in Arizona. "It has been a nightmare to both put together and to run … in part because Long Covid comes in so many flavors."

A year ago NIH awarded New York University's (NYU's) Grossman School of Medicine a huge chunk—$448 million—of its Long Covid funding to run the longitudinal study, through subawards NYU made to more than 24 institutions. NYU declined to make RECOVER investigators available for interviews or respond to written questions about the study.

Meanwhile, extramural scientists not involved in RECOVER are finding other ways to fund research, because NIH has put out few new requests for applications since it first launched the initiative. Michael VanElzakker, a neuroscientist at Massachusetts General Hospital, was already using a rare, sophisticated brain scanner to run a battery of tests on cognitive function in people with myalgic encephalomyelitis/chronic fatigue syndrome when the pandemic descended. As a result, he says, "I have a whole neuroimaging pipeline that's ripe for Long Covid people to go through." But he's relying on charitable donations, because "there's not really a way to apply for [NIH] Long Covid funding per se." He recently applied for a general NIH neuroscience grant but worries his proposal won't fare well when "binned in with somebody who's got a model of ALS [amyotrophic lateral sclerosis]."

Others complain about NIH's opaqueness. For instance, the RECOVER website does not list award amounts to institutions subcontracted through NYU, or tally how much has been spent. "I wish there was more transparency regarding instruments, enrollment, data, and where and when and with whom the money has been invested and what it has yielded so far," says Harlan Krumholz, a cardiologist at the Yale School of Medicine. He co-authored Rockefeller's policy briefing, which excoriated NIH's Long Covid response. NIH says it is working to add grant funding and other details to its searchable public database, REPORTER.

Still others remain frustrated by NIH's tight application deadlines. For example, on 27 April the agency announced a competition for funding for Long Covid clinical trials—with a preferred submission deadline of 19 May. "I decided not to apply because the deadline" was so short, one prominent immunologist says.

But Nikolich-Žugich says the agency is doing the best it can. "I have seen an incredible number of people from the NIH work incredibly hard on all of this on very compressed timelines," he says.

Mady Hornig, a neuropsychiatrist at Columbia University who has Long Covid and is a patient representative in RECOVER, notes NIH must balance moving quickly with preserving rigor. The goal of the fast funding turnarounds "is a really laudable one: not to be slowed down by the usual NIH cycle and still allow for high-quality peer review," she says. Still, she agrees that when it comes to funding research on this mysterious condition, "There have been a few hiccups along the way."

Koroshetz said last week that NIH is doing its all. "We're hoping we can … really make a difference to people. And the sooner the better."

One challenge facing clinicians keen to hunt for microclots in blood is that detecting them is a laborious process, although Pretorius is working to make it more accessible to doctors. SPECT-CT scans identify clots indirectly, based on blood flow abnormalities.

The work by Pretorius and others fits an emerging pattern in which the biology of acute and chronic COVID-19 appears to overlap. Early in the pandemic, doctors recognized blood clots as a signature of early, severe illness: Many hospitalized patients had clots in their lungs, brain, and elsewhere. Even people with milder disease were at heightened risk of heart attacks and strokes in the weeks following infection.

"The two diseases"—acute COVID-19 and Long Covid—"aren't very different," posits David Lee, an emergency medicine doctor at New York University Grossman School of Medicine. He suspects microclots explain many chronic symptoms. At least 70% of Long Covid patients have respiratory problems, he estimates, and at least 30% suffer from dysautonomia, in which abnormalities in the autonomic nervous system disrupt heart rate, breathing, and digestive function. Many suffer from fatigue and what's often called "brain fog." Tiny clots in the brain could explain cognitive troubles, Lee notes; or clots may kill small fiber nerve cells and drive dysautonomia.

But solid evidence that microclots cause Long Covid symptoms is still lacking. To learn more, Lee launched a study of 20 Long Covid patients with respiratory symptoms and 20 healthy volunteers who had COVID-19 and recovered. The participants will undergo SPECT-CT scans to see whether any of them have disrupted lungs. If abnormalities on the scans are unique to some with Long Covid, that could be a step toward identifying subsets of patients.

"I oscillate in my excitement" for different Long Covid theories, says David Putrino, a neurophysiologist and rehabilitation medicine specialist at the Icahn School of Medicine at Mount Sinai. He is studying several possible mechanisms for why symptoms can linger or even worsen after an infection. Right now, his enthusiasm for the microclot hypothesis is running high, thanks in part to a collaboration with Pretorius and others; that team has preliminary data to suggest the amount of microclots in blood correlates with the severity of some Long Covid symptoms, such as cognitive deficits.

Putrino is now running a small study of Long Covid patients with microclots in blood plasma, testing whether apheresis, which filters blood and reinfuses it, improves their symptoms. Any results, though, will be "very preliminary," he cautions. Apheresis can "filter out lots of things in the blood" that also might fuel symptoms.

PERSISTENT VIRUS

The idea that lingering virus might be a Long Covid culprit solidified for Proal in late 2021, thanks in part to an autopsy study that captured her attention. Researchers from the U.S. National Institutes of Health described in a preprint their analysis of tissues from 44 people who had been infected. Most had died from COVID-19 but five had mild or even asymptomatic infection and had succumbed to something else. All 44 still harbored viral RNA in their body, including in the brain, muscle, gut, and lungs. Many organs also had evidence of replicating virus.

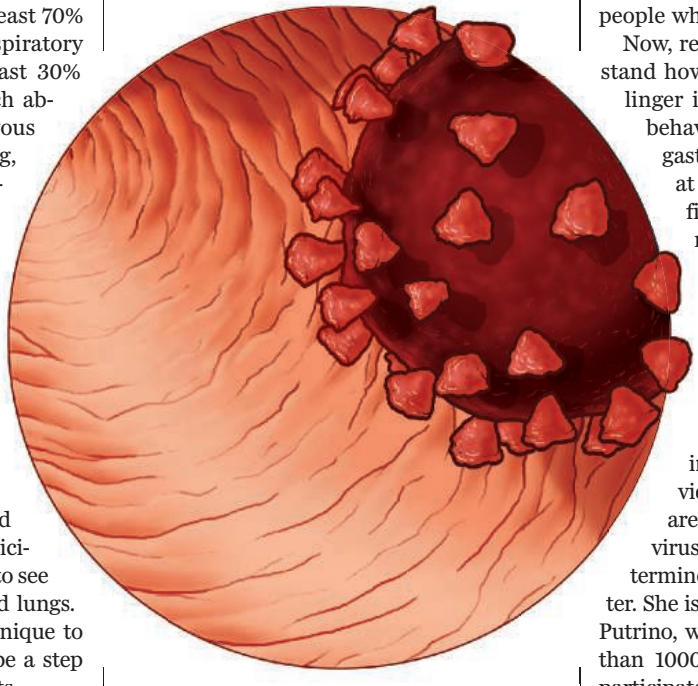

The study established that replicating copies of the virus could persist. But it didn't focus on people with Long Covid, making it difficult to establish a link.

Other studies are now trying to do that by comparing those with Long Covid and other cohorts, including people who have recovered from COVID-19. In one, gastroenterologist Herbert Tilg at the Medical University of Innsbruck set out to look for molecular traces of virus in the gut, a favorite hunting ground for researchers studying SARS-CoV-2. That's because the gut is far easier for doctors to access than many other organs, such as the lungs or the brain, and is thought likelier to harbor virus than blood, which tends to clear a pathogen more quickly.

Tilg recruited 46 people who'd had COVID-19 months earlier, 21 of whom had at least one symptom of Long Covid. All the volunteers had inflammatory bowel disease and were scheduled for routine endoscopies. (Most were in remission.) Tilg used that procedure to gather extra tissue samples and probe for signs of the coronavirus. The bottom line: All of those with Long Covid symptoms harbored viral RNA or, in some cases, viral proteins. Among those who'd recovered from acute COVID-19, 11 had traces of virus, too, whereas another 14 had no virus that Tilg could find. He and colleagues published their study in May in *Gastroenterology*.

"Our paper is a clinical observation," he stresses, and doesn't prove that lingering virus is harming people. That said, Tilg was surprised by the presence of persistent virus in people with Long Covid symptoms, and its absence in many previously infected people who felt fine.

Now, researchers like Tilg want to understand how the small amounts of virus that linger in tissue reserves such as the gut behave. Tilg and Saurabh Mehandru, a gastroenterologist and immunologist at Mount Sinai who was among the first to find signs of persistent virus in COVID-19 survivors, haven't been able to culture the virus from gut tissue in the lab—which would confirm that the virus is replicating. But such culturing can be tough, even in acute cases of COVID-19.

A key question is whether lingering virus is driving illness in Long Covid patients. Proal and her colleagues are trying to definitively tie persistent virus to Long Covid symptoms—or determine that the theory doesn't hold water. She is working with Mehandru and with Putrino, who has access to a cohort of more than 1000 Long Covid patients who could participate in new studies. The team is planning colonoscopies to look for virus in intestinal cells, and also wants to scrutinize the activity of immune cells that populate the region. Are these cells in a heightened state of alert, for example, suggesting the viral particles are setting them off? In some patients, Mehandru has noted immune responses in the gut, but says the work is preliminary.

Ideally, this deep dive into the gut's biology would be paired with a clinical trial examining whether antiviral drugs can beat back Long Covid symptoms. Participants could be studied before and after a course of antivirals, to see whether they clear any signs of virus in their gut and whether that matches up with changes in symptoms. "That's the trial I'd love to see happen," Putrino says.

ILLUSTRATION: A. MASTIN/*SCIENCE*

So far it hasn't, to the frustration of many in the Long Covid research and advocacy communities. "The patients are really, really desperate," says Francisco Tejerina, an HIV researcher at Gregorio Marañón Hospital in Madrid, who has detected viral RNA in the stool, urine, and blood plasma of people with Long Covid. He worries about people experimenting on their own with therapies, including antivirals, that may be useless, or worse, dangerous. "They want something now," he says. "I understand that."

HAYWIRE IMMUNE SYSTEM

As the pursuit of blood clots and viral fragments intensifies, a third track is both intersecting with those themes and making inroads on its own: the immune system, which some researchers believe could help bind together disparate observations. One idea, Phetsouphanh says, is that in some COVID-19 patients an immune system revved up and destabilized by the coronavirus attack may be unable to reset itself to idle.

To test that, he and colleagues gathered blood from 31 Long Covid patients, who all had fatigue or other characteristic symptoms at least 3 months after infection, and analyzed dozens of immune markers. "We were uncertain what we would find," Phetsouphanh says. The result was striking. Essentially, Long Covid patients had an immune system in constant high alert, the team reported in January in *Nature Immunology*.

White blood cells that typically recruit other cells to sites of infection were highly activated, which may explain why the patients' levels of interferons, proteins the body makes to fight invaders, were sky high 8 months after infection. The participants also had a dearth of inactivated T cells and B cells, a population of cells that normally putters about awaiting instruction to counter pathogens. Collectively this signaled chronic inflammation, which can cause a host of health problems.

Phetsouphanh and his colleagues also found these immune signatures were unique to their Long Covid cohort: They didn't appear in people who'd had the virus but recovered, or in those who'd been infected with different coronaviruses.

Other groups are also finding myriad immune system abnormalities long after a SARS-CoV-2 infection. In January, immunologist Akiko Iwasaki at the Yale School of Medicine, neuroscientist Michelle Monje at Stanford Medicine, and their colleagues reported in a preprint that mice given the coronavirus in their nose to mimic a mild infection developed inflammation in the brain, as well as loss of myelin, which insulates nerves and helps them transmit signals. In the mice, inflammation struck the brain even though the researchers couldn't find virus there. Furthermore, when the group compared blood samples from 48 people with Long Covid who had cognitive impairments and 15 Long Covid patients who did not, they found higher levels of inflammatory markers in the first group, suggesting chronic inflammation may be driving these neurological symptoms.

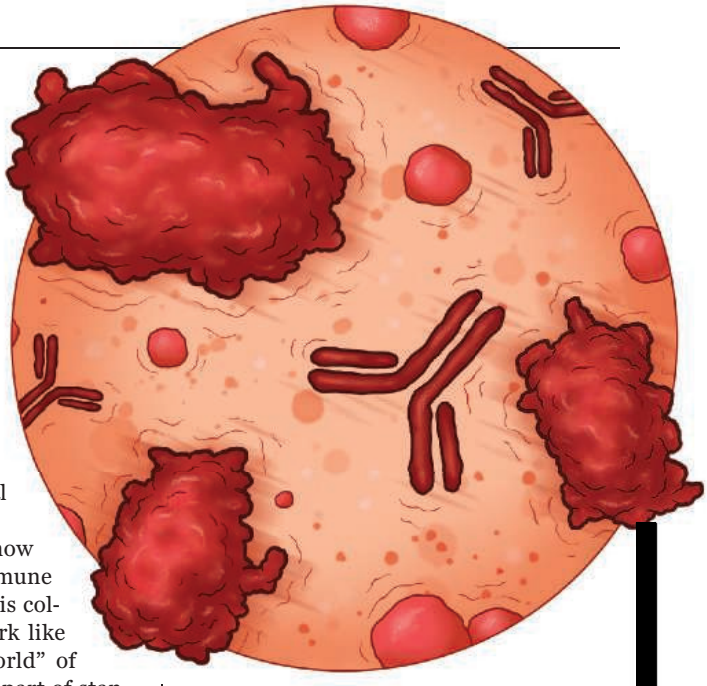

Such work highlights "how little we know about immune function," says Putrino, who is collaborating with Iwasaki. Work like hers is "opening up this world" of immune markers that aren't part of standard blood tests but may be critical to understanding the syndrome.

Increasingly, researchers want to fine-tune how they classify people with Long Covid, differentiating subsets based on symptoms, biology, or both. In a way, "the biggest obstacle that we are facing is we gave it one name, we gave it the name of Long Covid, which implies that it is one disease," says Chahinda Ghossein, a physician and heart disease researcher at Maastricht University and co-leader of a 15,000-patient Long Covid study in the Netherlands. "All the studies being performed show us that it is not."

One of the first large efforts to define subgroups, in part by testing potential treatments, will begin to enroll patients this month in the United Kingdom. Called STIMULATE-ICP (Symptoms, Trajectory, Inequalities and Management: Understanding Long-COVID to Address and Transform Existing Integrated Care Pathways), it will recruit 4500 Long Covid patients. Each will be randomly assigned one of three potential therapies: an anticlotting drug called rivaroxaban, an anti-inflammatory called colchicine, or a pair of antihistamines, famotidine and loratadine. (Antihistamines can quell a type of inflammation called mast-cell activation.) The project will include imaging as well as the collection of blood and tissue samples for a biobank. Organizers also have the option of adding up to three additional treatments.

Amitava Banerjee, a cardiologist at University College London, leads the study, and his colleague Emma Wall at UCL and the Francis Crick Institute is overseeing the treatment element. Both say it's crucial to test Long Covid therapies in trials before prescribing them en masse to patients.

"If you follow social media, you might think we've cracked it," Banerjee says, referring to anecdotal reports of vastly improved Long Covid symptoms, after, say, taking anticoagulants or antiviral drugs. Those narratives can offer important clues, he says, stressing that working with and listening to patients is invaluable. (Every component of STIMULATE-ICP includes a patient advocate.) But, "We've got to be really humble" about what we know, Banerjee adds.

After months of delays, the trial is "close to the start line," he says, but "we should have been there months ago." Trials for drugs to treat acute COVID-19 were fast-tracked, while "Long Covid is joining the queue with everything else" in medicine, Banerjee laments.

Esperti's story underscores the work to be done. She's been taking anticoagulant drugs for more than a year, and can now work, swim, drive, and cook—all previously impossible tasks. But she still can't run or carry heavy objects, and she suffers from sporadic fatigue. She was hit by a second bout of COVID-19 in December 2021 that left her severely debilitated, but she improved after a fourth dose of vaccine in late March.

Mysteries remain. A repeat SPECT-CT scan 3 months after she started taking the drugs showed no change in her lungs, though her lung function has improved. "I thought all I have to do is take anticoagulants" and recovery would be quick, she says. Esperti suspects that, like peeling the layers of an onion, she's unraveled one trigger for her symptoms only to come upon another she can't yet decode. It's another chapter in the annals of Long Covid—a narrative researchers are doggedly trying to change. ■

ILLUSTRATION: A. MASTIN/*SCIENCE*

toms? "I can't say this is the truth, of course. But this makes sense."

Meanwhile, in the United States, microbiologist Amy Proal can't stop thinking about a second leading Long Covid theory: that the coronavirus keeps hurting people by stubbornly enduring in the body, even after acute infection passes. Studies have shown "the virus is capable of persistence in a wide range of body sites," especially nerves and other tissues, says Proal, who works at the PolyBio Research Foundation, a nonprofit in Washington state. She recently caught COVID-19 for the third time.

Down under in Australia, immunologist Chansavath Phetsouphanh of the University of New South Wales, Sydney, is chasing a third lead, motivated by what the blood of Long Covid patients has divulged: an immune system gone haywire even 8 months after they'd first tested positive. He had assumed that immune cells galvanized to fight off infection would have calmed down over that time span. So, "It was a surprise that these cells did not recover," says Phetsouphanh, who is working to set up an international Long Covid collaboration.

For each of these researchers—and many others exploring the causes of Long Covid—untangling the complex syndrome, with a still-evolving definition, is a laborious, step-wise process. First, they must show that a possible contributor—such as minuscule clots, lingering virus, or immune abnormalities—crops up disproportionately in people with Long Covid. Then comes the hard part: proving that each of these traits, alone or in combination, explains why the coronavirus has rendered millions of people shadows of their former selves.

All agree that solo operators are unlikely. Lingering virus, for example, could attack the circulatory system, triggering blood clots or chronic inflammation. "I see this as a triangle," Buonsenso says, with each trigger potentially explaining, or even amplifying, the others.

A final challenge is identifying treatments that ease or reverse these abnormalities and help patients feel better. In the United Kingdom, home to a widely praised effort to identify immediate COVID-19 treatments, researchers are launching a clinical trial that will be among the largest worldwide to test potential Long Covid therapies in a randomized, statistically robust manner. But more such studies are needed—and time is of the essence (see sidebar, below). In May, the U.S. Centers for Disease Control and Prevention reported that a review of the medical records of nearly 2 million people suggested at least one in five of those diagnosed with COVID-19 had developed conditions characteristic of Long Covid. Other studies have found roughly similar rates. Some recent research suggests the risk for vaccinated people is somewhat lower, but vaccination's power to head off the syndrome remains uncertain.

> **"I consider Long Covid to be a massive emergency."**
>
> **Amy Proal**, PolyBio Research Foundation

For Proal and others, fitting the puzzle pieces together is of urgent concern. "I consider Long Covid to be a massive emergency," she says.

TINY BLOOD CLOTS

In Rome, Buonsenso is using a sophisticated medical imaging technique to better understand the role of blood clots. Called a SPECT-CT scan, it combines two different types of images: a single-photon emission computed tomography scan, which uses a radiotracer injected into a person's veins to provide pictures of blood flow, and a standard CT scan for information about lung structure. By merging these, doctors can see which parts of the lungs aren't getting normal blood flow.

So far, Buonsenso has scanned the lungs of 11 youngsters who have severe Long Covid, including irregular heartbeats and breathlessness during exercise. In six children, the lungs appeared normal. In the other five, the images were striking: Where there should have been bright oranges and yellows, signifying pulsing blood, one lung was nearly completely blue, indicating little flow. Buonsenso believes tiny blood clots or chronic damage to the lining of

Glacial pace for U.S. Long Covid grants

By **Meredith Wadman**

David Putrino, a neurophysiologist at the Icahn School of Medicine at Mount Sinai, labored through his holiday last Christmas to write a grant application for urgently needed Long Covid research. With colleagues, he hoped to tap into $1.15 billion in funding that Congress granted the National Institutes of Health (NIH) in 2020, as Long Covid emerged as a major public health problem. NIH had solicited grant applications in December 2021, just weeks before their January due date. The agency said it planned to issue decisions by late March.

But as of 10 June, Putrino was still waiting to hear whether NIH will fund his effort to discover whether microclots might be a meaningful diagnostic biomarker for many types of Long Covid. "Maybe they should hire people who are dedicated to accelerating these programs," says Putrino, who specializes in rehabilitation medicine. "[Long Covid] is a national crisis. This does not deserve to be somebody's second or third job. What we need from the NIH right now is their full attention."

Putrino's is not the lone complaint about NIH's management of Long Covid research—an initiative dubbed RECOVER, for Researching COVID to Enhance Recovery. RECOVER's flagship, an observational study of up to 40,000 people, has come under fire from patient advocates and some scientists who say it lacks transparency and is moving far too slowly—a ponderous battleship when a fleet of hydroplanes is what's needed. As of 6 June, the study had signed up 3712 adults, or 21% of its adult enrollment target of 17,680. Among children, numbers are even lower, with 98 children in a study aiming to enroll 19,500 of them.

Critics note that other countries have been more nimble. By July 2021, the United Kingdom had funded 15 Long Covid research projects aimed at diagnosis and treatment. A recent independent review published by the Rockefeller Foundation found that, as of February, NIH had funded just eight of the 200 Long Covid trials listed in the database ClinicalTrials.gov; the trials are being run in many countries.

NIH acknowledges the critiques and says it has already "obligated or committed" the $1.15 billion, slated to be spent over 4 years. But the scope of the project prevents it from sprinting, Walter Koroshetz, director of NIH's National Institute of Neurological Disorders and Stroke and a co-chair of the RECOVER initiative, implied in a talk to a panel of advisers to the NIH director on 9 June. "You can't believe what a big lift this has been," he told the advisers. RECOVER "is engineered to really not leave any stone unturned."

NIH added in a statement that it expects to announce winners of the long-awaited January funding within 2 weeks. And the agency says it has dedicated multiple staff to RECOVER, reinforced by other NIH experts and the outside firm Deloitte. But given the growing concern about Long Covid—one recent report estimated one in five U.S. COVID-19 survivors is afflicted—U.S. researchers say more urgency is needed (see main story, p. 1261).

RECOVER's longitudinal study aims to discover the biological roots of Long Covid and describe its prevalence, risk factors, and

blood vessels may be impairing blood flow. He and his colleagues published their first evidence of such damage, in a 14-year-old girl, in July 2021 in *The Lancet Child & Adolescent Health*.

The knotty question is what to do next. Buonsenso's patients don't meet the current criteria for taking anticoagulant drugs that prevent blood clots or keep them from getting bigger, because no clots are visible on their scans. "You either say, 'I'm sorry, but I can't do anything outside of a study,' or you are kind of a not-scared doctor with reciprocal trust with the patient and family, and together make a decision," Buonsenso says.

With seriously ill children and their desperate parents in front of him, Buonsenso didn't want to wait to launch a clinical trial. He and the families instead decided to do what they could. All five patients are now taking anticoagulants—which carry the risk of severe bleeding—under close monitoring.

He's heartened by their progress. Several are back in school, playing sports, and spending time with friends. Two have been rescanned. A teenager who still suffers from symptoms showed little improvement. But in another, whose symptoms have largely resolved, the images looked nearly normal. The other three will be rescanned this summer.

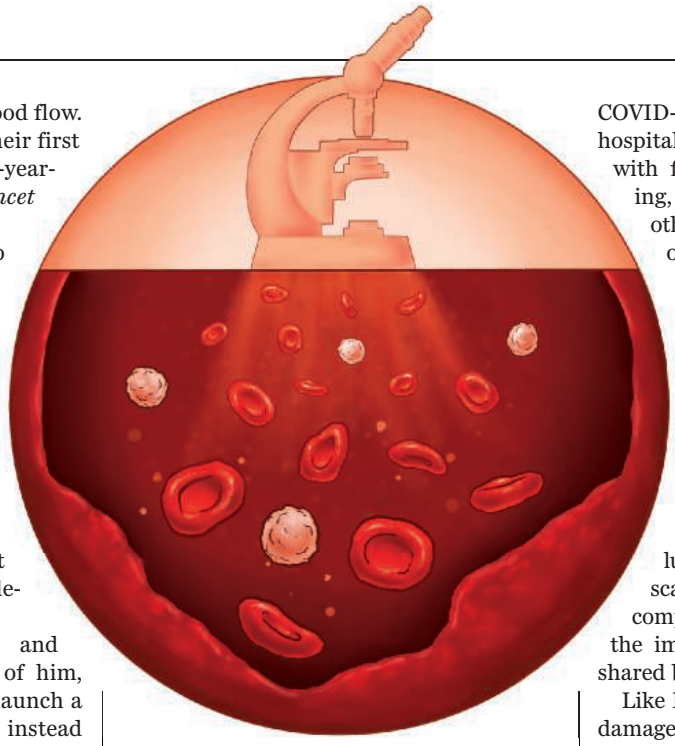

ILLUSTRATION: A. MASTIN/*SCIENCE*

Of course, he can't be sure those who improved did so because of the treatment. That's why he is hoping for resources to establish a Long Covid clinical trial that would include a placebo group.

Like other doctors, Buonsenso has been inspired by Long Covid patients who have lobbied hard for treatments and shared successes and failures on social media. Marta Esperti, a 34-year-old graduate student now living in Paris, is one of them. Struck by COVID-19 more than 2 years ago, she wasn't hospitalized but months later struggled with fatigue, breathlessness when walking, persistent fever, joint pain, and other symptoms. Yet bloodwork and other medical tests, such as x-rays of her lungs, were largely normal. Esperti kept pushing for answers. Then, in the spring of 2021, "I received a call from the pulmonologist saying, 'Listen, I want you to do another test.'"

Esperti was one of the first Long Covid patients in Europe to receive a lung SPECT-CT scan, and it looked just like the compromised lungs of the sick children Buonsenso scanned later. "My right lung is almost completely blue," she says. She posted the images on Twitter, where they were shared by thousands of people.

Like Buonsenso, Esperti's doctors believe damage to tiny blood vessels and minuscule clots are the culprit. The theory of persistent microclots gained further credence in the summer of 2021, when Resia Pretorius, a physiologist at Stellenbosch University in South Africa, and her colleagues reported in *Cardiovascular Diabetology* that such clots could linger in the blood of Long Covid patients. Her team found signs of excessive blood clotting in 11 people with Long Covid, but not in healthy people or another group with type 2 diabetes, whom they used for comparison.

symptoms. It will also include clinical trials of treatments and preventives, which NIH hopes to launch by fall.

"Everybody is working as fast as possible but this is a monster of a study," says immunologist Janko Nikolich-Žugich of the University of Arizona College of Medicine, Tucson, a principal investigator for a RECOVER arm in Arizona. "It has been a nightmare to both put together and to run … in part because Long Covid comes in so many flavors."

A year ago NIH awarded New York University's (NYU's) Grossman School of Medicine a huge chunk—$448 million—of its Long Covid funding to run the longitudinal study, through subawards NYU made to more than 24 institutions. NYU declined to make RECOVER investigators available for interviews or respond to written questions about the study.

Meanwhile, extramural scientists not involved in RECOVER are finding other ways to fund research, because NIH has put out few new requests for applications since it first launched the initiative. Michael VanElzakker, a neuroscientist at Massachusetts General Hospital, was already using a rare, sophisticated brain scanner to run a battery of tests on cognitive function in people with myalgic encephalomyelitis/chronic fatigue syndrome when the pandemic descended. As a result, he says, "I have a whole neuroimaging pipeline that's ripe for Long Covid people to go through." But he's relying on charitable donations, because "there's not really a way to apply for [NIH] Long Covid funding per se." He recently applied for a general NIH neuroscience grant but worries his proposal won't fare well when "binned in with somebody who's got a model of ALS [amyotrophic lateral sclerosis]."

Others complain about NIH's opaqueness. For instance, the RECOVER website does not list award amounts to institutions subcontracted through NYU, or tally how much has been spent. "I wish there was more transparency regarding instruments, enrollment, data, and where and when and with whom the money has been invested and what it has yielded so far," says Harlan Krumholz, a cardiologist at the Yale School of Medicine. He co-authored Rockefeller's policy briefing, which excoriated NIH's Long Covid response. NIH says it is working to add grant funding and other details to its searchable public database, REPORTER.

Still others remain frustrated by NIH's tight application deadlines. For example, on 27 April the agency announced a competition for funding for Long Covid clinical trials—with a preferred submission deadline of 19 May. "I decided not to apply because the deadline" was so short, one prominent immunologist says.

But Nikolich-Žugich says the agency is doing the best it can. "I have seen an incredible number of people from the NIH work incredibly hard on all of this on very compressed timelines," he says.

Mady Hornig, a neuropsychiatrist at Columbia University who has Long Covid and is a patient representative in RECOVER, notes NIH must balance moving quickly with preserving rigor. The goal of the fast funding turnarounds "is a really laudable one: not to be slowed down by the usual NIH cycle and still allow for high-quality peer review," she says. Still, she agrees that when it comes to funding research on this mysterious condition, "There have been a few hiccups along the way."

Koroshetz said last week that NIH is doing its all. "We're hoping we can … really make a difference to people. And the sooner the better."

PERSPECTIVES

OCEANOGRAPHY

Oil at sea—how much is too much?

The anthropogenic share of marine oil discharge is much larger than previously thought

By **Ira Leifer**

Natural oil seepage from seafloor petroleum hydrocarbon reservoirs is a chemical stress on marine life (*1*). It also is a chemosynthetic energy source that allows the existence of chemosynthetic lifeforms and communities. These hydrocarbon emissions drive ecological adaptations and support high biomass (*2*). Additional oil enters the ocean from accidental and operational releases and primarily manifests as chronic and transient slicks found along shipping lanes and in coastal waters (*3*). Trends for small oil releases have been unclear because of the paucity of monitoring methods. Satellite synthetic aperture radar (SAR) is highly promising for monitoring small spills and oil seepage slicks. On page 1300 of this issue, Dong *et al.* (*3*) find that oil slicks are far more widespread than prior estimates (*1*). They analyzed more than 500,000 satellite SAR images from 2014 to 2019 and found over 450,000 oil slicks, with the vast majority originating from anthropogenic releases or discharges.

Slicks were found over hotspots associated with natural marine seepage, offshore oil production, and shipping lanes. Dong *et al.* found that natural seeps contributed 6% in 2014 to 2019, whereas anthropogenic discharges, such as those from ships, oil platforms, and pipelines, contributed 94%. This finding was a notable change compared to the roughly 50/50 split during the 1990s (*1*). This change likely resulted in part from shipping expansion during recent decades, particularly in developing countries' waters. This latest assessment of the marine anthropogenic oil budget implies substantial, yet poorly characterized, ecological implications.

Insights into the ecological implications of anthropogenic marine oil emissions are provided by natural marine oil seepage studies (*4*). The resulting ecosystem adaptations depend on the hydrocarbon flux, persistence, and composition. These vary spatially and alter the community species composition based on the balance between toxicity and bioavailable energy. For example, the decrease in seep hydrocarbon concentration with distance from the seabed source correlates to community composition shifts along this gradient (*5*). Most seep ecosystem studies focus on deepsea systems far below the photic zone (*6*). Oil seepage also affects shallow communities where there is competition with species that utilize sunlight-derived energy (*2, 4*). Given that most anthropogenic oil slicks occur in shallow coastal waters (*3*), improving understanding of shallow seep ecosystems is highly relevant.

Seepage ecosystem studies largely have focused on the lowest chemosynthetic trophic level of the food chain, microbes (*6*). The seep microbiome supports the next trophic food chain level—namely, the sediment seep communities, which include copepods, nematodes, foraminifera, and higher trophic levels of macrofauna, such as tubeworms, bivalves, and sponges. These species dominate the seep community and support predatory and mobile feeders such as shrimp, crabs, and fish (*6*). Seep communities have high-density biomass compared to the surrounding seabed, albeit at reduced species diversity (*7*). Still, solely seep-dependent species are constrained to the vicinity of the area of active seepage (*8*); their presence is a strong indicator of natural seepage (*5*). These seep communities could play a critical role in the survival of opportunistic mobile predators, such as during periods of food scarcity—similar to "watering holes" during the dry season in the African savannah (*2*). Researchers also have proposed that seepage plays a role in the food needs of whales in the Gulf of Mexico (*2*).

The seep community specializes or adapts according to their surroundings. For example, seep communities in the deep sea often have seep specialist organisms that leverage the ecosystem niches created by the seep

Bubbleology Research International, Solvang, CA, USA.
Email: ira.leifer@bubbleology.com

PHOTO: CHRIS GRAYTHEN/GETTY IMAGES

bioavailable energy and the toxicity of the seep petroleum. Such seep specialists compete poorly against nonspecialists outside the seep environs and against species that opportunistically use both chemosynthetic-derived and Sun-derived energy at shallow seepage sites (*9*).

As the already dominant anthropogenic petroleum footprint continues expanding, these chemosynthetic niches grow at the expense of endangered and protected species and ecosystems. This threat occurs both directly by toxicity and indirectly by ecosystem adaptations that shift species composition—as is observed in seep communities. Such shifts affect the food supply of predators such as fish and crabs, which also are under stress from non-oil pollution and factors like ocean acidification and warming oceans.

In response, laws, regulations, and policies globally seek to minimize anthropogenic releases (*10*). Mitigation falls into two distinct approaches: proactively—through regulation; and reactively—through oil spill response and penalties. The latter's success is mixed at best for large offshore spills (*11*), with mitigation approaches having negative environmental impacts that should be assessed against natural mitigation (*12*). However, societal concerns inevitably also influence response decisions (and regulation development and implementation).

After analyzing >500,000 satellite images of global oceans, Dong *et al.* found more than 450,000 oil slicks, which cover a much larger area than prior estimates, with more than 90% coming from human activities.

Dong *et al.* report that connecting slicks to shipborne sources was difficult to infeasible—a critical factor in effective regulatory enforcement. Dense SAR coverage of coastal waters, as implemented by CleanSeaNet for Europe, combined with ship time-history and back-trajectory modeling, can connect slicks to their sources. CleanSeaNet spill detection is backed up by marine and airborne patrol dispatch within 3 hours (*13*). According to some estimates (*14*), North Sea bird oilings decreased by up to an order of magnitude during the 2000s, depending on species. This encouraging decrease corresponded to the program's implementation.

Successful regulations must shift the balance from the operational cost of pollution toward compliance costs. Effective enforcement is key. Penalties and enforcement likelihood need to exceed the maintenance and retrofit costs to incentivize against operational oil releases. Moreover, the development of effective regulation requires meaningful progress metrics, which currently are largely absent. Here, satellite SAR provides a globally available tool to support environmental management and spill response to reduce anthropogenic oil and its impacts.

The current understanding of the ecological impacts of the typical small marine oil releases is poor. Given the overlap, this highlights the need for studies of shallow, coastal seepage ecosystems where most releases occur. Marine ecosystems face numerous growing and synergistic threats. Thus, protecting chemosynthetic and nonchemosynthetic ecosystems requires an improved understanding of their resiliency and fragility. ■

REFERENCES AND NOTES

1. National Research Council, *Oil in the Sea III: Inputs, Fates, and Effects* (National Academies Press, 2003).
2. I. Leifer, A. Judd, J. A. Hildebrand, *Oceanogr. Fish.* **4**, 555636 (2017).
3. Y. Dong, Y. Liu, C. Hu, I. R. MacDonald, Y. Lu, *Science* **376**, 1300 (2022).
4. I. Leifer, *Geofluids* **2019**, 1 (2019).
5. E. E. Cordes *et al.*, *Mar. Ecol. (Berl.)* **31**, 51 (2010).
6. S. B. Joye, *Annu. Rev. Earth Planet. Sci.* **48**, 205 (2020).
7. J. R. Bourque *et al.*, *Deep Sea Res. 2 Top. Stud. Oceanogr.* **137**, 42 (2017).
8. L. Menot *et al.*, *Mar. Ecol. (Berl.)* **31**, 78 (2010).
9. R. B. Spies, D. J. Desmarais, *Mar. Biol.* **73**, 67 (1983).
10. P. Li *et al.*, *Mar. Pollut. Bull.* **110**, 6 (2016).
11. D. S. Etkin, T. J. Nedwed, *Mar. Pollut. Bull.* **163**, 111848 (2021).
12. B. Péquin *et al.*, *Mar. Pollut. Bull.* **176**, 113464 (2022).
13. G. Hajduch, in *Remote Detection and Maritime Pollution: Chemical Spill Studies*, S. Le Floch, F. Muttin, Eds. (Wiley, 2020), pp. 77–86.
14. K. Camphuysen, M. Heubeck, in *Oil Pollution in the North Sea*, A. Carpenter, Ed. (Springer International, 2016), pp. 193–208.

10.1126/science.abp8666

ECOLOGY AND EVOLUTION

A new polar bear population

Can the international conservation agreement protect these bears?

By **Elizabeth Peacock**

In 1965, in Fairbanks, Alaska, biologists from around the Circumpolar North convened the First International Scientific Meeting on the Polar Bear (*1*). Scientists from the USSR, the United States, Denmark, Norway, and Canada gathered in urgency, in the midst of the Cold War, to strategize how to protect the polar bear, whose populations were declining rapidly because of hunting for sport. This landmark meeting led to the 1973 international Agreement on the Conservation of Polar Bears (hereafter, the Agreement), one of the first international wildlife agreements and the first political agreement among Arctic nations. The Agreement promised to protect polar bears from unregulated harvest and to collaborate on a global scale on research and conservation (*1*). On page 1333 of this issue, Laidre *et al.* (*2*) testify to the Agreement and the enduring hope of those scientists who met in Fairbanks in a paramount global collaboration.

The original Agreement was a resounding success, resulting both in the rebound of polar bear populations from the hunting of the mid-20th century [e.g., (*3*)] and in global scientific collaboration [e.g., (*4*)]. The Polar Bear Specialist Group, now under the auspices of the International Union for Conservation of Nature (*1*), continues to meet every 3 to 4 years to give updates on the research and management of the global populations of polar bears.

Through Laidre *et al.*'s collection of data in difficult field conditions in a remote corner of the globe and through analysis of 37 years of data from the circumpolar Arctic collected by hundreds of technicians and biologists, often at risk to their own lives, a new and distinctive polar bear population—the 20th—has been identified in southeast Greenland (see the photo). Laidre *et al.* detail the characteristics of this population of polar bears, which diverged from other populations just a few

Department of Emergency Medicine, Emory University School of Medicine, Atlanta, GA. USA. Email: elizabeth.peacock@emory.edu

bioavailable energy and the toxicity of the seep petroleum. Such seep specialists compete poorly against nonspecialists outside the seep environs and against species that opportunistically use both chemosynthetic-derived and Sun-derived energy at shallow seepage sites (*9*).

As the already dominant anthropogenic petroleum footprint continues expanding, these chemosynthetic niches grow at the expense of endangered and protected species and ecosystems. This threat occurs both directly by toxicity and indirectly by ecosystem adaptations that shift species composition—as is observed in seep communities. Such shifts affect the food supply of predators such as fish and crabs, which also are under stress from non-oil pollution and factors like ocean acidification and warming oceans.

In response, laws, regulations, and policies globally seek to minimize anthropogenic releases (*10*). Mitigation falls into two distinct approaches: proactively—through regulation; and reactively—through oil spill response and penalties. The latter's success is mixed at best for large offshore spills (*11*), with mitigation approaches having negative environmental impacts that should be assessed against natural mitigation (*12*). However, societal concerns inevitably also influence response decisions (and regulation development and implementation).

After analyzing >500,000 satellite images of global oceans, Dong *et al.* found more than 450,000 oil slicks, which cover a much larger area than prior estimates, with more than 90% coming from human activities.

Dong *et al.* report that connecting slicks to shipborne sources was difficult to infeasible—a critical factor in effective regulatory enforcement. Dense SAR coverage of coastal waters, as implemented by CleanSeaNet for Europe, combined with ship time-history and back-trajectory modeling, can connect slicks to their sources. CleanSeaNet spill detection is backed up by marine and airborne patrol dispatch within 3 hours (*13*). According to some estimates (*14*), North Sea bird oilings decreased by up to an order of magnitude during the 2000s, depending on species. This encouraging decrease corresponded to the program's implementation.

Successful regulations must shift the balance from the operational cost of pollution toward compliance costs. Effective enforcement is key. Penalties and enforcement likelihood need to exceed the maintenance and retrofit costs to incentivize against operational oil releases. Moreover, the development of effective regulation requires meaningful progress metrics, which currently are largely absent. Here, satellite SAR provides a globally available tool to support environmental management and spill response to reduce anthropogenic oil and its impacts.

The current understanding of the ecological impacts of the typical small marine oil releases is poor. Given the overlap, this highlights the need for studies of shallow, coastal seepage ecosystems where most releases occur. Marine ecosystems face numerous growing and synergistic threats. Thus, protecting chemosynthetic and nonchemosynthetic ecosystems requires an improved understanding of their resiliency and fragility. ■

REFERENCES AND NOTES

1. National Research Council, *Oil in the Sea III: Inputs, Fates, and Effects* (National Academies Press, 2003).
2. I. Leifer, A. Judd, J. A. Hildebrand, *Oceanogr. Fish.* **4**, 555636 (2017).
3. Y. Dong, Y. Liu, C. Hu, I. R. MacDonald, Y. Lu, *Science* **376**, 1300 (2022).
4. I. Leifer, *Geofluids* **2019**, 1 (2019).
5. E. E. Cordes *et al.*, *Mar. Ecol. (Berl.)* **31**, 51 (2010).
6. S. B. Joye, *Annu. Rev. Earth Planet. Sci.* **48**, 205 (2020).
7. J. R. Bourque *et al.*, *Deep Sea Res. 2 Top. Stud. Oceanogr.* **137**, 42 (2017).
8. L. Menot *et al.*, *Mar. Ecol. (Berl.)* **31**, 78 (2010).
9. R. B. Spies, D. J. Desmarais, *Mar. Biol.* **73**, 67 (1983).
10. P. Li *et al.*, *Mar. Pollut. Bull.* **110**, 6 (2016).
11. D. S. Etkin, T. J. Nedwed, *Mar. Pollut. Bull.* **163**, 111848 (2021).
12. B. Péquin *et al.*, *Mar. Pollut. Bull.* **176**, 113464 (2022).
13. G. Hajduch, in *Remote Detection and Maritime Pollution: Chemical Spill Studies*, S. Le Floch, F. Muttin, Eds. (Wiley, 2020), pp. 77–86.
14. K. Camphuysen, M. Heubeck, in *Oil Pollution in the North Sea*, A. Carpenter, Ed. (Springer International, 2016), pp. 193–208.

10.1126/science.abp8666

ECOLOGY AND EVOLUTION

A new polar bear population

Can the international conservation agreement protect these bears?

By **Elizabeth Peacock**

In 1965, in Fairbanks, Alaska, biologists from around the Circumpolar North convened the First International Scientific Meeting on the Polar Bear (*1*). Scientists from the USSR, the United States, Denmark, Norway, and Canada gathered in urgency, in the midst of the Cold War, to strategize how to protect the polar bear, whose populations were declining rapidly because of hunting for sport. This landmark meeting led to the 1973 international Agreement on the Conservation of Polar Bears (hereafter, the Agreement), one of the first international wildlife agreements and the first political agreement among Arctic nations. The Agreement promised to protect polar bears from unregulated harvest and to collaborate on a global scale on research and conservation (*1*). On page 1333 of this issue, Laidre *et al.* (*2*) testify to the Agreement and the enduring hope of those scientists who met in Fairbanks in a paramount global collaboration.

The original Agreement was a resounding success, resulting both in the rebound of polar bear populations from the hunting of the mid-20th century [e.g., (*3*)] and in global scientific collaboration [e.g., (*4*)]. The Polar Bear Specialist Group, now under the auspices of the International Union for Conservation of Nature (*1*), continues to meet every 3 to 4 years to give updates on the research and management of the global populations of polar bears.

Through Laidre *et al.*'s collection of data in difficult field conditions in a remote corner of the globe and through analysis of 37 years of data from the circumpolar Arctic collected by hundreds of technicians and biologists, often at risk to their own lives, a new and distinctive polar bear population—the 20th—has been identified in southeast Greenland (see the photo). Laidre *et al.* detail the characteristics of this population of polar bears, which diverged from other populations just a few

Department of Emergency Medicine, Emory University School of Medicine, Atlanta, GA. USA. Email: elizabeth.peacock@emory.edu

hundred years ago. The southeast Greenland population's functional isolation is further supported by the following: an expansive analysis of movement data from bears wearing GPS collars; the demography of observed, biopsied, and captured bears; sea ice dynamics observed from satellite images; and hunting patterns of local Inuit. Through sophisticated habitat analysis, natural history observation, and embrace of traditional ecological knowledge, the authors recognized a previously unreported polar bear behavior—namely, the use of fresh ice at the marine terminal glacial fronts, also known as glacial mélange, as a platform to hunt seals. This glacial mélange enables the bears to succeed in a region where current sea ice conditions would not allow the bears to persist otherwise. This demonstrates that the habitat of southeast Greenland bears is already a climate refugium, suggesting that this behavioral attribute has served as a buffer against local extinction. If the prolonged persistence of polar bears in high Arctic sea ice refugia is possible, it would likely require similar behavioral plasticity.

Laidre *et al*. have identified a distinctive and isolated population of polar bears in southeast Greenland.

Polar bears have been observed to display varied behaviors elsewhere, for example, in the southern Beaufort population in Alaska, where the bears are shifting from sea ice to land maternity dens (*5*), and in the Barents Sea, east of the Norwegian archipelago Svalbard, where bears have developed separate sea ice and coastal life histories (*6*). Indeed, whereas the ringed seal (*Pusa hispida*) is the most common prey of polar bears, diverse diets do exist, and populations with more diverse diets are expected to be less vulnerable to climate change (*7*). Polar bears of the Davis Strait in Labrador were determined to be less vulnerable with their more diverse diet (*7*), and indeed their survival rates have been tied to a less common prey—the harp seal (*Pagophilus groenlandicus*) (*3*).

Yet the polar bear's long generation time will challenge its ability to adapt under natural selection at a rate as fast as the climate is changing. In other words, as sea ice (and glacial mélange) disappears, so will the polar bear (*1*). Animals with a long generation time have evolved low variance in survival and reproduction because the population growth rate is most sensitive to these vital rates. In polar bears, the most influential parameter is the survival rate of adult females (*8*). These vital rates are under strong natural selection and provide a buffer against typical environmental variation.

Although Laidre *et al*. found that southeast Greenland's bears have adult female body mass, litter sizes, and cub survival rates comparable to other populations, the bears have substantially fewer adult females with newborn cubs in the spring. The authors suggest that this may be due to mate-finding difficulties in the small population (estimated to be in the hundreds). However, the density of bears in this relatively small area (27,749 km^2; ~8 bears per 1000 km^2) is on par with other polar bear densities (*9*) and unlikely to be low enough now to affect their ability to find mates (*10*).

Alternatively, the fewer females with newborns in southeast Greenland could be attributed to prudent parenting (*11*)—deferred breeding to avoid trading on survival—possibly through resorption of a pregnancy in the fall based on body condition, which is a known phenomenon in polar bears (*12*). An examination of long-lived Antarctic mammals and birds found much support for this demographic-buffering hypothesis during rapid sea ice decline, except for the Antarctic fur seal (*Arctocephalus gazella*), which showed both decreasing adult female survival and propensity to breed. But could such demographic buffering of adult survival in southeast Greenland mitigate the effects of rapid habitat change on population growth, or have polar bears' vital rates evolved to be too constrained? More work is necessary to estimate the survival of adult bears in southeast Greenland to answer this question.

The question of plasticity versus adaptation in the polar bear's changing environment is just one question in polar bear ecology that has been generated by Laidre *et al*.'s expansive research on the southeast Greenland population. Will the population continue to persist in a refugium without sea ice habitat, and does southeast Greenland represent a fifth distinct ecoregion of polar bears (*13*)? Further, ecologists could study southeast Greenland as a model refugium for areas of the high Arctic that have been proposed as climate refugia.

Notwithstanding interesting future research, the conservation of southeast Greenland's bears is imperative for their intrinsic value, genetic diversity, and distinctive ecology. In 1993, the task for collaboration among the world's polar bear scientists and managers was refocused with the warning of potential impacts of climate warming on polar bears (*14*), many of which have unfortunately been subsequently demonstrated [e.g., (*15*)]. It is unclear whether the Agreement, which had been so successful in bringing back the global populations from overharvest, will be an adequate mechanism to protect polar bears in the face of reduced habitat due to climate change. The population of southeast Greenland is a small, genetically distinct group of bears with a distinctive ecology. In the conservation of this polar bear population, we find an explicit test of the modern influence of the half-century-old international Agreement on the Conservation of Polar Bears. ■

REFERENCES AND NOTES

1. P. Prestrud, I. Stirling, *Aquat. Mamm.* **20**, 113 (1994).
2. K. L. Laidre *et al*., *Science* **376**, 1333 (2022).
3. E. Peacock *et al*., *J. Wildl. Manage.* **77**, 463 (2013).
4. G. M. Durner *et al*., *Ecol. Monogr.* **79**, 25 (2009).
5. A. S. Fischbach, S. C. Amstrup, D. C. Douglas, *Polar Biol.* **30**, 1395 (2007).
6. M. Mauritzen, A. E. Derocher, Ø. Wiig, *Can. J. Zool.* **79**, 1704 (2001).
7. S. G. Hamilton, A. E. Derocher, *Anim. Conserv.* **22**, 83 (2018).
8. M. K. Taylor *et al*., *J. Wildl. Manage.* **51**, 811 (1987).
9. M. K. Taylor, J. Lee, *Arctic* **48**, 147 (1995).
10. P. K. Molnár, M. A. Lewis, A. E. Derocher, *PLOS ONE* **9**, e85410 (2014).
11. J. Forcada, P. N. Trathan, E. J. Murphy, *Glob. Change Biol.* **14**, 2473 (2008).
12. A. E. Derocher, I. Stirling, D. Andriashek, *Can. J. Zool.* **70**, 561 (1992).
13. S. C. Amstrup, B. G. Marcot, D. C. Douglas, in *Arctic Sea Ice Decline: Observations, Projections, Mechanisms, and Implications*, E. T. DeWeaver *et al*., Eds. (Geophysical Monograph Series, vol. 180, American Geophysical Union, 2008), pp. 213–268.
14. I. Stirling, A. Derocher, *Arctic* **46**, 240 (1993).
15. E. V. Regehr *et al*., *J. Wildl. Manage.* **71**, 2673 (2007).

ACKNOWLEDGMENTS

I thank A. Chavez, P. Fine, H. Neville, and M. Obbard for constructive comments. I dedicate this article to those polar bear biologists who lost their lives collecting some of the global samples: Malcolm Ramsay (1949–2000), Stuart Innes (1953–2000), John Bevins (1955–1990), George Menkens (1957–1990), and Markus Dyck (1966–2021).

10.1126/science.abq5267

PHOTO: CARSTEN EGEVANG

PHOTONICS

Chip-scale power booster for light

A miniature amplifier with high power is realized with an ion-doped waveguide

By **Jungwon Kim**

Telecommunications, the internet, and various streaming services are all made possible by ultrabroadband optical fiber networks that span more than a million kilometers and connect the globe. Erbium-doped fiber amplifiers (EDFAs) are one of the most important technologies for global data transfer (*1*). Mears *et al.* demonstrated EDFAs in 1987 (*2*), which not only unlocked the full potential of ultrahigh data-rate optical transfer over a long fiber, but also advanced high-performance laser sources, such as mode-locked erbium-doped fiber lasers and frequency combs (*3*). On page 1309 of this issue, Liu *et al.* (*4*) report the realization of an ultracompact chip-scale version of the EDFAs, with a performance already comparable to that of commercially available EDFA modules.

Given the enormous success of ion-doped fiber amplifiers, a reasonable next step is to use the same ion doping in a smaller integrated waveguide device for chip-scale amplification. Since the 1990s (*5*), many attempts were made to realize chip-scale erbium-doped waveguide amplifiers (*6*). However, it turned out to be quite challenging to make a waveguide amplifier that competes with the well-established EDFAs. The most problematic of several interconnected issues was the substantial waveguide loss, which limited the length of a usable ion-doped waveguide and therefore the achievable output power level. Whereas the waveguide amplifiers had a decent net gain for small input signal power, the output power has mostly been less than a milliwatt. As a result, a high-power and low-noise on-chip amplifier has been a missing element for photonic integrated circuits.

Liu *et al.* have solved this long-standing problem and report a record-high output-power erbium-doped waveguide amplifier (see the photo). The maximum on-chip output power of 145 mW is obtained when 2.61 mW of input power is applied under 245 mW of pump power. This high output power, as well as a high power conversion efficiency of ~60%, could be achieved by a tiny photonic chip with a 21-cm-long erbium-doped silicon nitride waveguide. The authors were able to pack a spiral of erbium-doped silicon nitride waveguide up to 50 cm long in a compact footprint of only 1.2 mm by 3.6 mm.

Crucial to this breakthrough was the ability to make an ultralow-loss silicon nitride waveguide. By exploiting their earlier work (*7*), Liu *et al.* show only a 5 dB/m loss in their silicon nitride waveguide. After the ion implantation and subsequent processes, this ultralow waveguide loss was maintained, allowing the amplification process to achieve a more than 30-dB on-chip small-signal net gain.

Liu *et al.* further show two applications of their on-chip erbium-doped waveguide amplifier by amplifying the output of their microcombs (*8*). Microcombs can generate a soliton pulse train with a repetition rate of tens to hundreds of gigahertz, but their output power is limited to only tens to hundreds of microwatts, necessitating amplification in almost every application. The authors' first demonstration was low-noise microwave generation, in which a higher optical power is required to scale the noise floor in the optical-to-electronic conversion process at the photodiode (*9*). The authors could scale the phase noise floor of the generated microwave by 40 dB using the on-chip amplifier, suggesting that complete on-chip photonic microwave generation might be one step closer. The second demonstration was the direct amplification of more than 20 wavelength-division multiplexing (WDM) channels for data transmission over a 1-km-long fiber link, indicating the viability of compact chip-scale amplification for telecommunication networks.

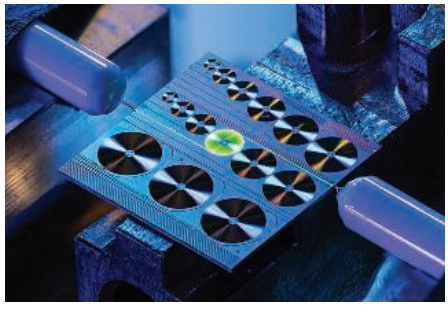

Shown is an erbium-doped waveguide amplifier on a photonic integrated chip of 1-cm–by–1-cm size, with green emission from optically excited erbium ions.

One intriguing potential for this on-chip waveguide amplifier is an on-chip femtosecond mode-locked laser. Although microcombs can generate optical pulses with a repetition rate of tens of gigahertz and higher, scaling their repetition rate below 10 GHz is difficult. For generating ultralow-noise optical pulses with repetition rates ranging from a few megahertz to a few gigahertz, mode-locked fiber lasers (*10*) with a footprint of tens of centimeters on each side have been extensively developed to the commercial level and widely used. The erbium-doped waveguide amplifier might allow the implementation of such ultralow-noise mode-locked lasers on a chip with a footprint of less than a square centimeter. One obstacle that remains is managing the strong nonlinearity in a silicon nitride waveguide. Finding a way to actively tame and utilize the nonlinearity using a combination of waveguide dispersion engineering and filtering might lead to different and interesting on-chip mode-locked lasers.

The on-chip amplifier does require an off-chip pump diode and a pump-coupling fiber coupler (WDM coupler). This means that the entire amplifier unit is not completely on a chip yet. However, given the rapid advances in heterogeneous integration capabilities (*11*, *12*), a full on-chip amplifier might also be possible. Because the main techniques of ion doping and ultralow-loss silicon nitride waveguide fabrication are mature, large-volume manufacturing of such devices should be possible. Finally, the doping strategy can be extended to a variety of different forms. For example, codoping with other rare-earth ions or heterogeneous integration with thin-film lithium niobate will result in amplification of different wavelength ranges or improved compatibility for microwave photonic system on a chip, respectively. ■

REFERENCES AND NOTES

1. E. Desurvire *et al.*, *Erbium-Doped Fiber Amplifiers: Device and System Developments* (Wiley, 2002).
2. R. J. Mears *et al.*, in *Optical Fiber Communication* (1987 OSA Technical Digest Series, Optical Publishing Group, 1987), paper WI2.
3. B. R. Washburn *et al.*, *Opt. Lett.* **29**, 250 (2004).
4. Y. Liu *et al.*, *Science* **376**, 1309 (2022).
5. Y. C. Yan *et al.*, *Appl. Phys. Lett.* **71**, 2922 (1997).
6. J. Bradley, M. Pollnau, *Laser Photonics Rev.* **5**, 368 (2011).
7. J. Liu *et al.*, *Nat. Commun.* **12**, 2236 (2021).
8. A. Pasquazi *et al.*, *Phys. Rep.* **729**, 1 (2018).
9. H. Jiang *et al.*, *IEEE Photonics J.* **3**, 1004 (2011).
10. J. Kim, Y. Song, *Adv. Opt. Photonics* **8**, 465 (2016).
11. B. Stern *et al.*, *Nature* **562**, 401 (2018).
12. C. Xiang *et al.*, *Science* **373**, 99 (2021).

ACKNOWLEDGMENTS

I thank the National Research Foundation of Korea (2021R1A2B5B03001407 and 2021R1A5A1032937) for support.

10.1126/science.abq8422

Korea Advanced Institute of Science and Technology (KAIST), Daejeon 34141, South Korea. Email: jungwon.kim@kaist.ac.kr

PHOTO: LABORATORY OF PHOTONICS AND QUANTUM MEASUREMENTS (LPQM), EPFL/© NIELS ACKERMANN

MEDICINE

Modifying insulin to improve performance

A platform to enable precise modifications of insulin could improve drug functionality

By **Nai-Pin Lin** and **Danny Hung-Chieh Chou**

The emergence of protein therapeutic drugs presents an opportunity for site-specific chemical modifications to improve their functionality. For example, insulin derivatives can provide pharmacokinetic benefits over native insulin for people with type 1 diabetes (*1*). Most new insulin analogs are produced by total chemical synthesis, and the long ad hoc approaches to add modifications impede scaling up production for future pharmaceutical applications (*2*). A systematic functionalization approach will facilitate access to new insulin derivatives with high efficiency and scalability. On page 1321 of this issue, Fryszkowska *et al.* (*3*) demonstrate that the three amino groups in insulin can be selectively modified to establish a complete combination of insulin analogs, providing a platform for functionalization that could be applied to other protein therapeutics.

Insulin is an anabolic peptide hormone that promotes glucose uptake, glycogenesis, lipogenesis, and protein synthesis. It is injected subcutaneously to treat diabetes. Pharmacokinetically, it has a short half-life, which can be extended through insulin modifications. For example, insulin can be engineered to have a longer serum half-life through increased binding to serum albumin. There are three amines—reactive groups used for modifications—in insulin, including two amino termini of the A and B chains and a Lys^{29} on the B chain. To selectively modify amino groups, nearly all reported methods can only target one or a few amines among all available amino groups, with limited scalability (*4, 5*). US Food and Drug Administration (FDA)–approved insulin drugs, such as insulin detemir and insulin degludec, have aliphatic modifications at the Nε amino group of the only lysine residue, which increase their affinity with serum albumin. However, there are still no efficient methods for selective modifications on the two amino-terminal amino groups on large scales (*6, 7*). It is even more difficult to achieve multiple modifications.

Penicillin G acylase (PGA) is an enzyme that performs acylation and hydrolysis on amino groups. Fryszkowska *et al.* used directed evolution techniques to identify multiple PGA variants that can either selectively protect native insulin at the Nε amino group of lysine, on the amino terminus of either chain, or selectively deprotect the fully protected insulin on the Nε amino group of lysine and on the amino terminus of either chain. The set of PGA variants can generate all possible monoprotected insulin analogs, three diprotected insulin analogs on any two amino groups, and the triprotected insulin analogs through only one enzymatic step, and are highly scalable. Using this toolbox, the synthesis of antidiabetic insulin candidates, MK-1092 and MK-5160 (*8*), was achieved through a systematic selective protection-conjugation-deprotection pipeline on large scales. MK-1092 and MK-5160 are dimeric insulin and demonstrate partial agonistic properties and metabolic benefits in mouse models of diabetes. This work demonstrates the feasibility of modifying any amino group on insulin with high efficiency and substantially broadens access to insulin bioconjugates for future studies.

This suite of PGA variants also extends the scope of insulin derivatives to enable new features beyond improved pharmacokinetics. An insulin analog modified with both a diol and a phenylboronic acid group on two separate amino groups was recently reported (*9*). This dual-modified insulin analog can undergo conformational changes in the presence of fructose. This is an important milestone toward the development of glucose-responsive insulin, a much-anticipated therapy that could avoid dangerous side effects of current therapy such as hypoglycemia. However, its synthesis includes multiple steps of protein expression, proteolysis, and chemical modifications with limited efficiency. The PGA variants developed by Fryszkowska *et al.*

Stanford University, School of Medicine, Palo Alto, CA, USA.
Email: dannychou@stanford.edu

A toolkit for insulin modifications

Multiple penicillin G acylase (PGA) variants were generated by Fryszkowska *et al.* to specifically modify each of the three NH_2 groups in insulin. This enables the addition of new properties to insulin, including partial insulin receptor activation, glucose responsiveness, glucose-sensitive mannose receptor binding (to regulate insulin availability), and extended serum half-life.

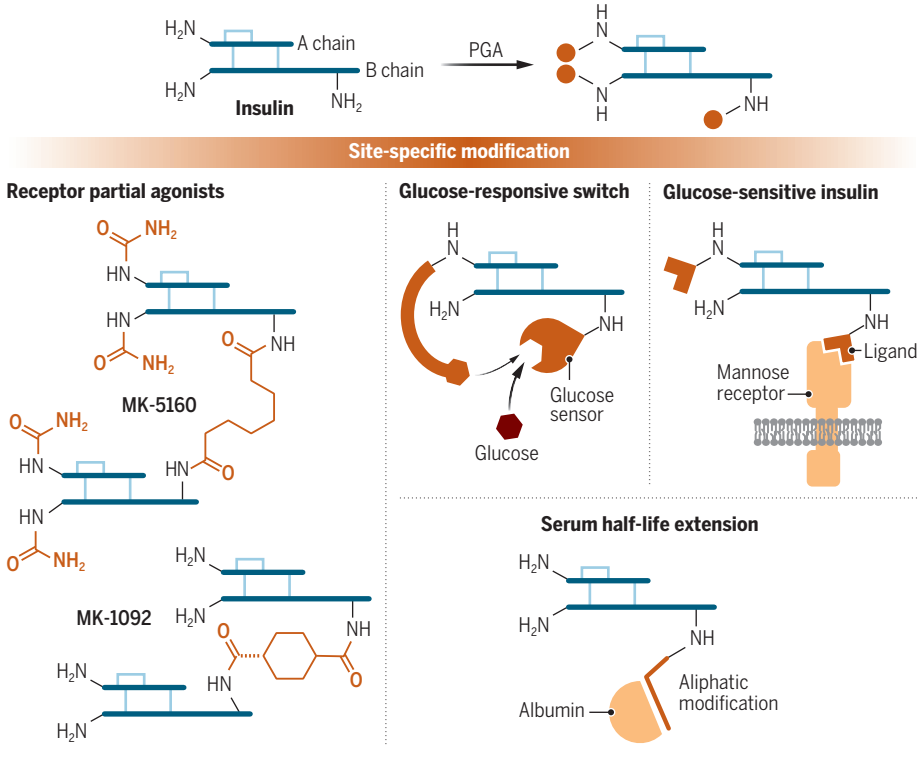

GRAPHIC: KELLIE HOLOSKI/*SCIENCE* BASED ON N.-P. LIN AND D.

could therefore facilitate access to sophisticated insulin derivatives and speed up the discovery of glucose-responsive insulin by adding glucose-recognizing groups.

The study of Fryszkowska *et al.* opens the door to the development of new therapeutic proteins with modifications that can be manufactured at large scales (see the figure). There remain challenges with the current suite of PGA variants. In the case of insulin, there is increasing interest in modifications of the carboxyl terminal of the A chain, which would not affect receptor binding affinity and would tolerate larger modifications such as the addition of antibody fragments (*10*). A new PGA variant is likely required to selectively modify the amino group on an added lysine residue in this region. Furthermore, the three amino groups on insulin are either on or close to the terminal ends. It remains to be seen whether new PGA variants can selectively recognize and modify lysine residues in the middle of a protein, further enhancing the scope of applications.

This work presents tremendous protein therapeutic opportunities beyond insulin. One intriguing target is interleukin-2 (IL-2), an FDA-approved drug since 1992 that is used to treat metastatic renal cell carcinoma. Incorporating unnatural amino acids to allow the addition of polyethylene glycol (PEG), engineered IL-2 with site-specific PEGylation enhanced antitumor properties in mice (*11*). Engineered PGA variants may lead to new IL-2 derivatives without the need to engineer proteins with unnatural amino acids. Glucagon-like peptide 1 (GLP-1) is a gut hormone involved in metabolic regulation and satiety. Recently, modified GLP-1 drugs, such as semaglutide that has aliphatic modifications on lysine for half-life extension, have shown clinical success for treating diabetes and obesity, demonstrating how chemical modifications can provide better clinical outcomes (*12*). With this new platform, more peptide and protein derivatives are expected to be developed. ■

REFERENCES AND NOTES

1. C. Mathieu, P. J. Martens, R. Vangoitsenhoven, *Nat. Rev. Endocrinol.* **17**, 715 (2021).
2. X. Xiong *et al.*, *Nat. Chem. Biol.* **18**, 511 (2022).
3. A. Fryszkowska *et al.*, *Science* **376**, 1321 (2022).
4. M. J. Matos *et al.*, *J. Am. Chem. Soc.* **140**, 4004 (2018).
5. R. Adakkattil, K. Thakur, V. Rai, *Chem. Rec.* **21**, 1941 (2021).
6. D. Chen, M. M. Disotuar, X. Xiong, Y. Wang, D. H. Chou, *Chem. Sci.* **8**, 2717 (2017).
7. L. Purushottam *et al.*, *Nat. Commun.* **10**, 2539 (2019).
8. D. A. Pissarnitski *et al.*, *J. Med. Chem.* **65**, 5593 (2022).
9. Y. S. Chen *et al.*, *Proc. Natl. Acad. Sci. U.S.A.* **118**, e2103518118 (2021).
10. T. M. Tagmose *et al.*, *J. Med. Chem.* **65**, 2633 (2022).
11. J. L. Ptacin *et al.*, *Nat. Commun.* **12**, 4785 (2021).
12. J. P. H. Wilding *et al.*, *N. Engl. J. Med.* **384**, 989 (2021).

10.1126/science.abq7217

MEDICINE

Cellular cross-talk in heart repair

The cytokine meteorin-like (METRNL) improves cardiac function after heart attack in mice

By **Deepak Srivastava**[1,2,3,4]

Heart disease is the number one cause of death worldwide, and more than 25 million survivors suffer from heart failure, most commonly because of vascular occlusion that causes damage to the heart. The heart has limited capacity to regenerate after damage, but stimulation of new blood vessel formation (angiogenesis) after a heart attack, or myocardial infarction, is an essential part of the repair process and might be a therapeutic approach to improve heart function after injury. On page 1343 of this issue, Reboll *et al.* (*1*) show that upon cardiac injury in mice, monocytes and macrophages migrate to the heart, where they secrete the cytokine meteorin-like (METRNL), which stimulates the expansion of a subset of vascular endothelial cells expressing the KIT receptor, resulting in an angiogenic response that limits damage. They show that METRNL is a ligand for KIT, whose activation is necessary for the normal angiogenic response after myocardial infarction and could be harnessed for therapeutic intervention.

"...delivering the meteorin-like (METRNL) protein increased angiogenesis and improved cardiac function in mice after acute myocardial infarction."

Heart disease comes in many flavors, including cardiomyopathies resulting from intrinsic muscle defects, structural anomalies, and ischemic heart disease involving insufficient blood flow to the heart resulting in myocardial infarction. Each of these can cause heart failure, where the heart's pumping is insufficient to meet the body's demands. The interest in stimulating cardiac angiogenesis in ischemic heart disease has a long history (*2*). Initial efforts to promote angiogenesis with vascular endothelial growth factor A (VEGFA) met with difficulty related to the use of first-generation viral vectors and the development of fragile vessels. More recently, messenger RNA delivery of VEGFA has been tested in preclinical models and is advancing in clinical trials (*3*).

Reboll *et al.* built on the recognition that cell-cell communication between myeloid cells in the heart and other nonmyocytes may play a role in the injury response (*4*). Circulating monocytes and macrophages are recruited to sites of cardiac injury, where they secrete factors that act non–cell autonomously to affect cardiac remodeling. The authors searched for secreted proteins that might mediate aspects of this cellular cross-talk in mouse infarcts and in human tissue from patients with acute myocardial infarction, and they found that METRNL expression was prominently increased. Cells expressing METRNL were located near blood vessels, suggesting that they may affect angiogenesis. Using mice with genetic ablation of *Metrnl* and mice receiving bone marrow cells lacking *Metrnl*, the authors show that METRNL produced by circulating myeloid cells that take up residence in the heart is necessary for the normal angiogenic response during cardiac repair (see the figure). Notably, delivering the METRNL protein increased angiogenesis and improved cardiac function in mice after acute myocardial infarction.

Although METRNL has previously been described as a secreted immunomodulatory cytokine (*5*), and one with cardioprotective features (*6*), its receptor had not been identified. Through a variety of approaches, Reboll *et al.* demonstrate that METRNL is a ligand for the KIT receptor, which also responds to the secreted protein stem cell factor (SCF) (*7*). SCF functions to maintain KIT-expressing hematopoietic stem cells during development and for maintenance in their bone marrow niche. Both METRNL and SCF could stimulate expansion of KIT-expressing mouse endothelial cells and did so through activation of similar downstream signaling pathways involving AKT phosphorylation.

[1]Gladstone Institutes, San Francisco, CA, USA. [2]Roddenberry Stem Cell Center at Gladstone, San Francisco, CA, USA. [3]Department of Pediatrics, University of California San Francisco, San Francisco, CA, USA. [4]Department of Biochemistry and Biophysics, University of California San Francisco, San Francisco, CA, USA. Email: dsrivastava@gladstone.ucsf.edu

could therefore facilitate access to sophisticated insulin derivatives and speed up the discovery of glucose-responsive insulin by adding glucose-recognizing groups.

The study of Fryszkowska *et al.* opens the door to the development of new therapeutic proteins with modifications that can be manufactured at large scales (see the figure). There remain challenges with the current suite of PGA variants. In the case of insulin, there is increasing interest in modifications of the carboxyl terminal of the A chain, which would not affect receptor binding affinity and would tolerate larger modifications such as the addition of antibody fragments (*10*). A new PGA variant is likely required to selectively modify the amino group on an added lysine residue in this region. Furthermore, the three amino groups on insulin are either on or close to the terminal ends. It remains to be seen whether new PGA variants can selectively recognize and modify lysine residues in the middle of a protein, further enhancing the scope of applications.

This work presents tremendous protein therapeutic opportunities beyond insulin. One intriguing target is interleukin-2 (IL-2), an FDA-approved drug since 1992 that is used to treat metastatic renal cell carcinoma. Incorporating unnatural amino acids to allow the addition of polyethylene glycol (PEG), engineered IL-2 with site-specific PEGylation enhanced antitumor properties in mice (*11*). Engineered PGA variants may lead to new IL-2 derivatives without the need to engineer proteins with unnatural amino acids. Glucagon-like peptide 1 (GLP-1) is a gut hormone involved in metabolic regulation and satiety. Recently, modified GLP-1 drugs, such as semaglutide that has aliphatic modifications on lysine for half-life extension, have shown clinical success for treating diabetes and obesity, demonstrating how chemical modifications can provide better clinical outcomes (*12*). With this new platform, more peptide and protein derivatives are expected to be developed. ■

REFERENCES AND NOTES

1. C. Mathieu, P. J. Martens, R. Vangoitsenhoven, *Nat. Rev. Endocrinol.* **17**, 715 (2021).
2. X. Xiong *et al.*, *Nat. Chem. Biol.* **18**, 511 (2022).
3. A. Fryszkowska *et al.*, *Science* **376**, 1321 (2022).
4. M. J. Matos *et al.*, *J. Am. Chem. Soc.* **140**, 4004 (2018).
5. R. Adakkattil, K. Thakur, V. Rai, *Chem. Rec.* **21**, 1941 (2021).
6. D. Chen, M. M. Disotuar, X. Xiong, Y. Wang, D. H. Chou, *Chem. Sci.* **8**, 2717 (2017).
7. L. Purushottam *et al.*, *Nat. Commun.* **10**, 2539 (2019).
8. D. A. Pissarnitski *et al.*, *J. Med. Chem.* **65**, 5593 (2022).
9. Y. S. Chen *et al.*, *Proc. Natl. Acad. Sci. U.S.A.* **118**, e2103518118 (2021).
10. T. M. Tagmose *et al.*, *J. Med. Chem.* **65**, 2633 (2022).
11. J. L. Ptacin *et al.*, *Nat. Commun.* **12**, 4785 (2021).
12. J. P. H. Wilding *et al.*, *N. Engl. J. Med.* **384**, 989 (2021).

10.1126/science.abq7217

MEDICINE

Cellular cross-talk in heart repair

The cytokine meteorin-like (METRNL) improves cardiac function after heart attack in mice

By **Deepak Srivastava**[1,2,3,4]

Heart disease is the number one cause of death worldwide, and more than 25 million survivors suffer from heart failure, most commonly because of vascular occlusion that causes damage to the heart. The heart has limited capacity to regenerate after damage, but stimulation of new blood vessel formation (angiogenesis) after a heart attack, or myocardial infarction, is an essential part of the repair process and might be a therapeutic approach to improve heart function after injury. On page 1343 of this issue, Reboll *et al.* (*1*) show that upon cardiac injury in mice, monocytes and macrophages migrate to the heart, where they secrete the cytokine meteorin-like (METRNL), which stimulates the expansion of a subset of vascular endothelial cells expressing the KIT receptor, resulting in an angiogenic response that limits damage. They show that METRNL is a ligand for KIT, whose activation is necessary for the normal angiogenic response after myocardial infarction and could be harnessed for therapeutic intervention.

"...delivering the meteorin-like (METRNL) protein increased angiogenesis and improved cardiac function in mice after acute myocardial infarction."

Heart disease comes in many flavors, including cardiomyopathies resulting from intrinsic muscle defects, structural anomalies, and ischemic heart disease involving insufficient blood flow to the heart resulting in myocardial infarction. Each of these can cause heart failure, where the heart's pumping is insufficient to meet the body's demands. The interest in stimulating cardiac angiogenesis in ischemic heart disease has a long history (*2*). Initial efforts to promote angiogenesis with vascular endothelial growth factor A (VEGFA) met with difficulty related to the use of first-generation viral vectors and the development of fragile vessels. More recently, messenger RNA delivery of VEGFA has been tested in preclinical models and is advancing in clinical trials (*3*).

Reboll *et al.* built on the recognition that cell-cell communication between myeloid cells in the heart and other nonmyocytes may play a role in the injury response (*4*). Circulating monocytes and macrophages are recruited to sites of cardiac injury, where they secrete factors that act non–cell autonomously to affect cardiac remodeling. The authors searched for secreted proteins that might mediate aspects of this cellular cross-talk in mouse infarcts and in human tissue from patients with acute myocardial infarction, and they found that METRNL expression was prominently increased. Cells expressing METRNL were located near blood vessels, suggesting that they may affect angiogenesis. Using mice with genetic ablation of *Metrnl* and mice receiving bone marrow cells lacking *Metrnl*, the authors show that METRNL produced by circulating myeloid cells that take up residence in the heart is necessary for the normal angiogenic response during cardiac repair (see the figure). Notably, delivering the METRNL protein increased angiogenesis and improved cardiac function in mice after acute myocardial infarction.

Although METRNL has previously been described as a secreted immunomodulatory cytokine (*5*), and one with cardioprotective features (*6*), its receptor had not been identified. Through a variety of approaches, Reboll *et al.* demonstrate that METRNL is a ligand for the KIT receptor, which also responds to the secreted protein stem cell factor (SCF) (*7*). SCF functions to maintain KIT-expressing hematopoietic stem cells during development and for maintenance in their bone marrow niche. Both METRNL and SCF could stimulate expansion of KIT-expressing mouse endothelial cells and did so through activation of similar downstream signaling pathways involving AKT phosphorylation.

[1]Gladstone Institutes, San Francisco, CA, USA. [2]Roddenberry Stem Cell Center at Gladstone, San Francisco, CA, USA. [3]Department of Pediatrics, University of California San Francisco, San Francisco, CA, USA. [4]Department of Biochemistry and Biophysics, University of California San Francisco, San Francisco, CA, USA. Email: dsrivastava@gladstone.ucsf.edu

Notably, the phosphoproteomic signatures stimulated by METRNL and SCF were distinct from those induced by VEGFA in endothelial cells, suggesting that although METRNL and VEGFA can trigger expansion of endothelial cells, they may have distinct functions during angiogenesis. Although SCF could stimulate endothelial cell proliferation, it was not up-regulated after injury in vivo in mice or in ex vivo human samples and therefore did not substitute for METRNL after infarction. Only a specific subset of the monocyte and macrophage population secreted high amounts of METRNL [marked by high expression of C-C chemokine receptor 2 (CCR2)], and only a subset of vascular endothelial cells were responsive and expressed the KIT receptor. How injury is sensed and results in repair in the setting of chronic ischemia where there is not an acute injury.

Despite these questions, it is intriguing to consider METRNL as a potential systemic biologic therapy in the setting of acute myocardial infarction to limit the damage caused by coronary occlusive events. Fortunately, in most cases, patients can be quickly revascularized through placement of coronary stents, but for those who are unable to seek medical care in time, proangiogenic therapies could be valuable. In other more-chronic cases of cardiac ischemia, vascular narrowing is sometimes not amenable to intervention with stents, in which case a robust proangiogenic therapy could be even more important. However, it remains to be seen whether endothelial cells express KIT in a chronic setting, METRNL activation in specific cells will be an important area of further study, as will investigations regarding the mechanisms underlying the expansion in KIT$^+$ endothelial cells after injury.

Unlike past treatment with VEGFA in animals that involved direct intramyocardial injection, it is noteworthy that systemic delivery of METRNL with an infusion pump had sufficient effects on the cardiac angiogenic response in mice. Given the likelihood that METRNL also induces KIT$^+$ endothelial cell proliferation in other organs, it will be interesting to know whether systemic delivery induces angiogenesis outside the heart. Because there are fewer KIT$^+$ endothelial cells at baseline, it is possible that in the uninjured setting, endothelial cells are unable to respond to METRNL, in which case METRNL would be relatively inert. Although this may be beneficial, it may also limit utility for heart which would be a prerequisite to METRNL activity. Nevertheless, the discovery of the myeloid-endothelial interaction and the central role of METRNL-KIT signaling is exciting and opens new avenues for both understanding injury responses and developing therapies for heart disease. ■

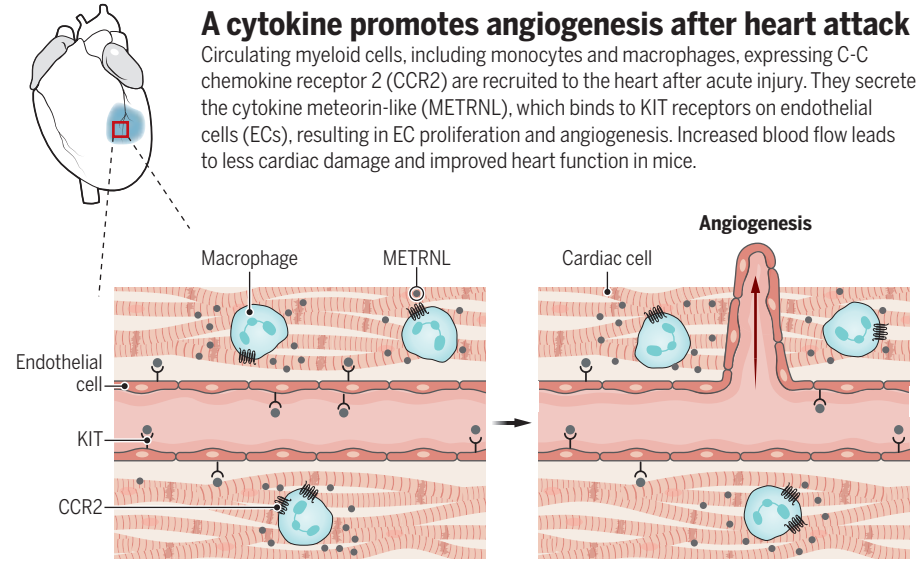

A cytokine promotes angiogenesis after heart attack

Circulating myeloid cells, including monocytes and macrophages, expressing C-C chemokine receptor 2 (CCR2) are recruited to the heart after acute injury. They secrete the cytokine meteorin-like (METRNL), which binds to KIT receptors on endothelial cells (ECs), resulting in EC proliferation and angiogenesis. Increased blood flow leads to less cardiac damage and improved heart function in mice.

REFERENCES AND NOTES

1. M. R. Reboll *et al.*, *Science* **376**, 1343 (2022).
2. S. Ylä-Herttuala, A. H. Baker, *Mol. Ther.* **25**, 1095 (2017).
3. A. Collén *et al.*, *Nat. Rev. Drug Discov.* **21**, 79 (2022).
4. F. K. Swirski, M. Nahrendorf, *Nat. Rev. Immunol.* **18**, 733 (2018).
5. I. Ushach *et al.*, *J. Immunol.* **201**, 3669 (2018).
6. C. Rupérez *et al.*, *J. Exp. Med.* **218**, e20201206 (2021).
7. K. L. Kim *et al.*, *Arterioscler. Thromb. Vasc. Biol.* **39**, 2120 (2019).

ACKNOWLEDGMENTS

D.S. is supported by grants from the National Institutes of Health National Heart, Lung, and Blood Institute. D.S. is a cofounder, shareholder, and director of Tenaya Therapeutics.

10.1126/science.adc8698

METAMATERIALS

Turning materials into robots

Researchers showcase a 3D-printed millirobot made out of multifunctional metamaterials

By **Ahmad Rafsanjani**

Instead of building a robot with separate parts that provide different functions, a robot built with multifunctional metamaterials has certain advantages (*1*). A metamaterial is a synthetic structure made of repeating patterns designed to exhibit desired macroscopic properties. Unlike bulk materials, the behavior of metamaterials is governed by their engineered architecture rather than purely driven by their material makeup. Additive manufacturing techniques, such as 3D printing, have accelerated the fabrication of intricate metamaterials at increasingly smaller scales with unprecedented functionalities. Building robots has traditionally relied on assembling discrete actuators, sensors, microprocessors, and power supplies. Robotic metamaterials challenge this paradigm by conceiving autonomy into the periodic structure of metamaterials. On page 1287 of this issue, Cui *et al.* (*2*) present the design and methods for 3D printing a mobile robotic metamaterial that can navigate autonomously and interact with its surroundings.

Historically, the research of metamaterials has primarily focused on optical applications, such as metamaterials with tunable optical properties beyond the capabilities of ordinary lenses and mirrors (*3*). However, in recent years, researchers have increasingly turned to adopting this design rationale in other domains. Examples include mechanical metamaterials that can convert linear motion into rotation without using transmission gears (*4*) or a swarm of tessellated robots that enable on-demand adjustment of bulk properties such as stiffness or deformation (*5*, *6*). Another route to creating robotic metamaterials is the embodi-

Center for Soft Robotics, SDU Biorobotics, The Maersk McKinney Moller Institute, University of Southern Denmark, Odense, Denmark. Email: ahra@mmmi.sdu.dk

GRAPHIC: N. DESAI/*SCIENCE*

Notably, the phosphoproteomic signatures stimulated by METRNL and SCF were distinct from those induced by VEGFA in endothelial cells, suggesting that although METRNL and VEGFA can trigger expansion of endothelial cells, they may have distinct functions during angiogenesis. Although SCF could stimulate endothelial cell proliferation, it was not up-regulated after injury in vivo in mice or in ex vivo human samples and therefore did not substitute for METRNL after infarction. Only a specific subset of the monocyte and macrophage population secreted high amounts of METRNL [marked by high expression of C-C chemokine receptor 2 (CCR2)], and only a subset of vascular endothelial cells were responsive and expressed the KIT receptor. How injury is sensed and results in repair in the setting of chronic ischemia where there is not an acute injury.

Despite these questions, it is intriguing to consider METRNL as a potential systemic biologic therapy in the setting of acute myocardial infarction to limit the damage caused by coronary occlusive events. Fortunately, in most cases, patients can be quickly revascularized through placement of coronary stents, but for those who are unable to seek medical care in time, proangiogenic therapies could be valuable. In other more-chronic cases of cardiac ischemia, vascular narrowing is sometimes not amenable to intervention with stents, in which case a robust proangiogenic therapy could be even more important. However, it remains to be seen whether endothelial cells express KIT in a chronic setting, METRNL activation in specific cells will be an important area of further study, as will investigations regarding the mechanisms underlying the expansion in KIT$^+$ endothelial cells after injury.

Unlike past treatment with VEGFA in animals that involved direct intramyocardial injection, it is noteworthy that systemic delivery of METRNL with an infusion pump had sufficient effects on the cardiac angiogenic response in mice. Given the likelihood that METRNL also induces KIT$^+$ endothelial cell proliferation in other organs, it will be interesting to know whether systemic delivery induces angiogenesis outside the heart. Because there are fewer KIT$^+$ endothelial cells at baseline, it is possible that in the uninjured setting, endothelial cells are unable to respond to METRNL, in which case METRNL would be relatively inert. Although this may be beneficial, it may also limit utility for heart which would be a prerequisite to METRNL activity. Nevertheless, the discovery of the myeloid-endothelial interaction and the central role of METRNL-KIT signaling is exciting and opens new avenues for both understanding injury responses and developing therapies for heart disease. ■

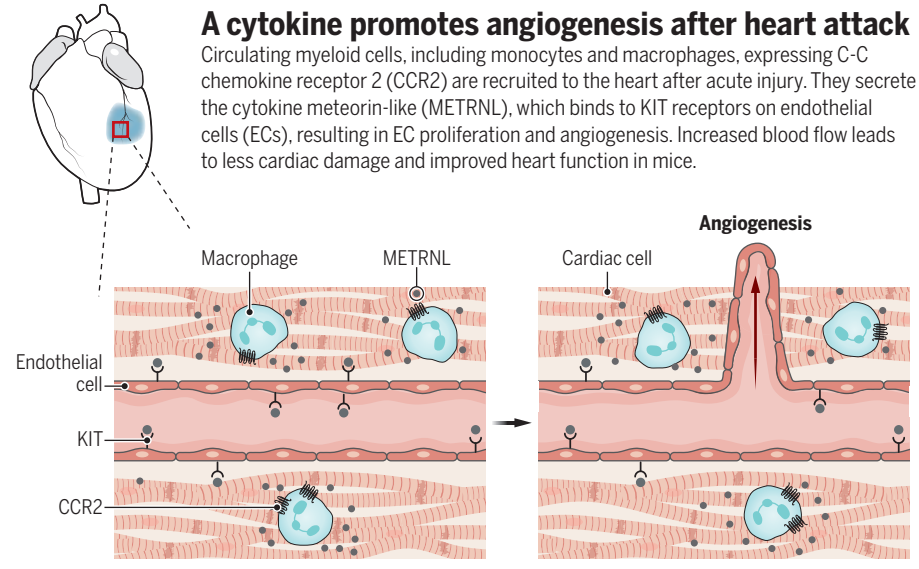

A cytokine promotes angiogenesis after heart attack

Circulating myeloid cells, including monocytes and macrophages, expressing C-C chemokine receptor 2 (CCR2) are recruited to the heart after acute injury. They secrete the cytokine meteorin-like (METRNL), which binds to KIT receptors on endothelial cells (ECs), resulting in EC proliferation and angiogenesis. Increased blood flow leads to less cardiac damage and improved heart function in mice.

REFERENCES AND NOTES

1. M. R. Reboll *et al.*, *Science* **376**, 1343 (2022).
2. S. Ylä-Herttuala, A. H. Baker, *Mol. Ther.* **25**, 1095 (2017).
3. A. Collén *et al.*, *Nat. Rev. Drug Discov.* **21**, 79 (2022).
4. F. K. Swirski, M. Nahrendorf, *Nat. Rev. Immunol.* **18**, 733 (2018).
5. I. Ushach *et al.*, *J. Immunol.* **201**, 3669 (2018).
6. C. Rupérez *et al.*, *J. Exp. Med.* **218**, e20201206 (2021).
7. K. L. Kim *et al.*, *Arterioscler. Thromb. Vasc. Biol.* **39**, 2120 (2019).

ACKNOWLEDGMENTS

D.S. is supported by grants from the National Institutes of Health National Heart, Lung, and Blood Institute. D.S. is a cofounder, shareholder, and director of Tenaya Therapeutics.

10.1126/science.adc8698

METAMATERIALS

Turning materials into robots

Researchers showcase a 3D-printed millirobot made out of multifunctional metamaterials

By **Ahmad Rafsanjani**

Instead of building a robot with separate parts that provide different functions, a robot built with multifunctional metamaterials has certain advantages (*1*). A metamaterial is a synthetic structure made of repeating patterns designed to exhibit desired macroscopic properties. Unlike bulk materials, the behavior of metamaterials is governed by their engineered architecture rather than purely driven by their material makeup. Additive manufacturing techniques, such as 3D printing, have accelerated the fabrication of intricate metamaterials at increasingly smaller scales with unprecedented functionalities. Building robots has traditionally relied on assembling discrete actuators, sensors, microprocessors, and power supplies. Robotic metamaterials challenge this paradigm by conceiving autonomy into the periodic structure of metamaterials. On page 1287 of this issue, Cui *et al.* (*2*) present the design and methods for 3D printing a mobile robotic metamaterial that can navigate autonomously and interact with its surroundings.

Historically, the research of metamaterials has primarily focused on optical applications, such as metamaterials with tunable optical properties beyond the capabilities of ordinary lenses and mirrors (*3*). However, in recent years, researchers have increasingly turned to adopting this design rationale in other domains. Examples include mechanical metamaterials that can convert linear motion into rotation without using transmission gears (*4*) or a swarm of tessellated robots that enable on-demand adjustment of bulk properties such as stiffness or deformation (*5*, *6*). Another route to creating robotic metamaterials is the embodi-

Center for Soft Robotics, SDU Biorobotics, The Maersk McKinney Moller Institute, University of Southern Denmark, Odense, Denmark. Email: ahra@mmmi.sdu.dk

GRAPHIC: N. DESAI/*SCIENCE*

ment of "robotic tasks" in the structure. For example, one can design a metamaterial whose deformation can be controlled with electrical signals, which can be used to construct prosthetics with less mechanical parts prone to failure. Piezoelectric materials, such as lead-zirconate-titanate (PZT), can generate electricity under mechanical stress and deform when connected to an electric field. However, high stiffness, heavy weight, and small electric field–induced strain impede the immediate application of materials such as PZT as a robotic limb.

Cui *et al.* developed an approach for a rational design of piezoelectric metamaterials made of passive, piezo-active, and conductive phases that can perform a handful of robotic tasks (see the photo). A desired deformation mode, such as a twist, was approximated with the motion of some discrete planes passing through the structure. In turn, the allowed motion of these planes would inform how the structural phases, actuators, and electrodes should be organized within the piezoelectric metamaterial to generate the targeted movement. In the classical theory of elasticity, the deformation of an elastic material is characterized by extension, compression, and shearing. Cui *et al.* applied the micropolar elasticity that extends classical elasticity by incorporating rotations on top of translations. This approach enables a more comprehensive evaluation of macroscopic expansion, shear, twist, and flexure of piezoelectric metamaterials to their microarchitecture, polarization, and the applied electric field.

To put their design strategy to the test, Cui *et al.* used a multimaterial stereolithography system with spatially programmed electrostatic charges and fabricated 3D ceramic lattices decorated with conductive metals and piezoelectric properties in selected regions. The resulting structure is a robotic metamaterial that uses two-way conversion of an electric field to a mechanical strain for generating movement and sensing. The inverse piezoelectric effect gives the robot actuation capability, whereas direct and bidirectional piezoelectric effects enable feedback control through proprioception (self-monitoring) and exteroception (contact detection and remote sensing), respectively. The topology of metamaterials allowed placing electrodes directly onto piezo-active struts that induced a stronger electric field and amplified the actuation strain. A proof-of-concept steerable multigait millirobot fabricated with the piezoelectric metamaterials showed the ability to move forward, turn, jump, carry cargo, and avoid obstacles.

Cui *et al.* artfully interweaved actuation and perception in a lightweight miniature composite 3D lattice that moves around and senses its surroundings. The authors then took steps toward an untethered implementation by devising an onboard control system and power supply. Such system-level integration, although rare, should be strongly encouraged to tap into the full potential of fast-developing robotic materials in real-world scenarios and identify their shortcomings. Considering the mobile piezoelectric metamaterials discussed here, the wiring of piezo-active elements is still a limiting factor to enhancing their versatility, and distributing power and decentralizing control are remaining barriers to overcome. Despite these limitations, the authors demonstrated that when mobility and untethered autonomy are not essential, a single piece of piezoelectric architecture can serve as a compact 3D printed manipulator with six degrees of freedom—that is, with the ability to extend translationally along all three axes and twist rotationally around all three axes.

The study of Cui *et al.* highlights a broader view of "robotic materials" in which the boundary between materials and machines becomes indiscernible and embodied intelligence evolves into a sought-after material property (*7*). Additive manufacturing of piezoelectric metamaterials may lead to materializing fully integrated robots that might eventually walk straight out of a 3D printer (*8*). Despite being made of hard ceramics, harnessing the internal architecture of metamaterials for feedback control of deformation can inform the design of continuum and soft robots (*9*). The rational design approach for piezoelectric metamaterials can motivate the development of soft robotic metamaterials through the use of much softer electroactive polymers or magnetorheological elastomers. Although integrating embedded electronics into metamaterials remains a burden for some time, recent progress in distributed energy systems (*10*) can guide generating, storing, and harvesting power within robotic metamaterials. Cui *et al.* bring robotic metamaterials closer to biological systems, one function at a time. ■

Materializing robots by robotizing matter

The 3D-printable multifunctional metamaterial designed by Cui *et al.* can be used to construct simple and autonomous millirobots without the need for complicated assembly of multiple moving parts.

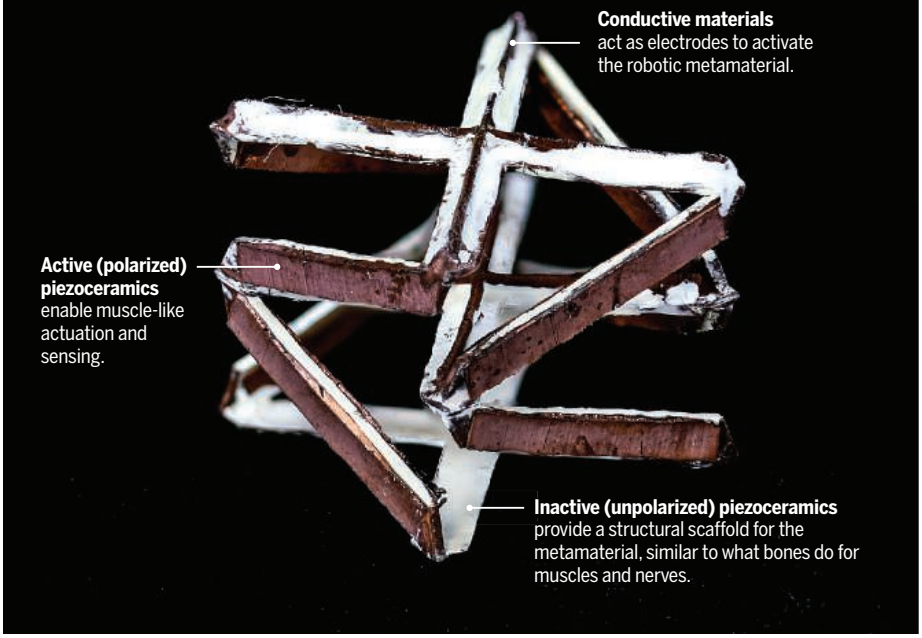
Conductive materials act as electrodes to activate the robotic metamaterial.
Active (polarized) piezoceramics enable muscle-like actuation and sensing.
Inactive (unpolarized) piezoceramics provide a structural scaffold for the metamaterial, similar to what bones do for muscles and nerves.

GRAPHIC: C. SMITH/*SCIENCE*; (PHOTO) CUI *ET AL.*

REFERENCES AND NOTES

1. M. A. McEvoy, N. Correll, *Science* **347**, 1261689 (2015).
2. H. Cui *et al.*, *Science* **376**, 1287 (2022).
3. V. M. Shalaev *et al.*, *Opt. Lett.* **30**, 3356 (2005).
4. T. Frenzel, M. Kadic, M. Wegener, *Science* **358**, 1072 (2017).
5. C. Luo *et al.*, *Mater. Horiz.* **7**, 229 (2020).
6. M. Brandenbourger *et al.*, *Nat. Commun* **10**, 4608 (2019).
7. R. L. Truby, *Acc. Mater. Res* **2**, 854 (2021).
8. H. Lipson, *3D Print Addit. Manuf.* **2**, 41 (2015).
9. A. Rafsanjani, K. Bertoldi, A. R. Studart, *Sci. Robot.* **4**, eaav7874 (2019).
10. C. A. Aubin *et al.*, *Nature* **602**, 393 (2022).

ACKNOWLEDGMENTS

A.R. was supported by the Villum Young Investigator grant 37499.

10.1126/science.abq4102

POLICY FORUM

PUBLIC TRUST

Get law enforcement out of biospecimen authentication

Use of DNA markers in research that are used in law enforcement risks undermining public trust and participation

By **Debra J. H. Mathews**[1,2] *and* **Natalie Ram**[3]

In response to long-standing challenges in biomedical research arising from misidentification of cell lines, the research community has broadly adopted a human tissue authentication standard based on a well-characterized set of short tandem repeats (STRs). But in so doing, the research community has largely settled on the same genetic markers for authentication purposes that are used by law enforcement around the globe for forensic DNA analysis. This serious misstep could undermine public trust in science and may inhibit the recruitment of research participants, particularly those from historically marginalized groups—many of which are disproportionately represented in the criminal legal system and law enforcement databases. Authentication of research tissues is critically important, but using preexisting law enforcement marker kits may have serious and undesirable effects that could have been, and could still be, avoided by developing an independent marker set or technology for scientific research purposes, distinct and apart from the forensic set.

The problem of cell culture misidentification has been recognized since the 1950s and was brought into sharp relief in the 1960s and 1970s with the repeated discovery and demonstration that assumed independent cell lines were in fact all HeLa (*1*). The proposed solution to this substantial and urgent problem was cell line authentication: standardized genetic typing to enable verification that the biospecimen in hand is from the correct individual, and to ensure its identity and integrity over time, throughout use, development of derivatives (such as cell lines, derived tissues, and organoids), and distribution to collaborators and the broader scientific community.

[1]Berman Institute of Bioethics, Johns Hopkins University, Baltimore, MD, USA. [2]Department of Genetic Medicine, Johns Hopkins University, Baltimore, MD, USA. [3]Carey School of Law, University of Maryland, Baltimore, MD, USA. Email: dmathews@jhu.edu

In response to this concern, international standards for cell line authentication have been developed, and many journals require authentication before publication. A 2007 notice from the US National Institutes of Health (NIH) about the importance of cell line authentication was motivated by legitimate and long-standing concerns about the relationship between cell line misidentification and the reproducibility of research results, noting, "Improper characterization [of cultured cells] can impede efforts to replicate published findings and therefore the advancement of science" (*2*). In 2015, the NIH began requiring "authentication of key biological and/or chemical resources," including cell lines and other human tissues (*3*).

Although the NIH does not require a particular approach to authentication of research tissues, since 2011 and updated most recently in 2021, the American National Standards Institute (ANSI) has published authentication standards (*4*), focused on the typing of STRs. STRs are regions of short, repeated DNA sequences, the length of which are highly variable between individuals. By typing multiple STRs, researchers can easily differentiate one individual's biospecimen from another's. In addition to the efficiency and effectiveness of STR profiling for research authentication, this technology is also the most convenient and least expensive because of the widespread availability of extensively validated commercial STR profiling kits.

This strong commercial market for STR kits existed long before the authentication standards for research purposes. It was born from and tailored to law enforcement's interest in matching crime scene DNA samples to DNA samples from arrestees and convicted offenders. The US government operates the Combined DNA Index System (CODIS), a database developed and maintained by the Federal Bureau of Investigation (FBI), through which local, state, and federal law enforcement entities can already compare crime scene DNA to more than 19 million known DNA profiles on a routine basis (*5*). These DNA profiles identify individuals arrested for or convicted of specified offenses. Given the existing standards and the products available to meet those standards, commercial authentication kits now sold for medical and scientific research across the market are based on the markers used for CODIS.

That the research community has largely settled on the same genetic markers for authentication purposes that law enforcement uses for CODIS and other global law enforcement databases is, in some ways, unsurprising. Using CODIS markers enabled researchers to hit the ground running, without delays and financial investment associated with identifying additional, distinct markers or technologies for authentication purposes.

But as a result, NIH's authentication guidelines will lead to increasing numbers of researchers developing and reporting information about research subjects that corresponds precisely to the data that law enforcement typically uses to develop an investigative lead. The same is true for researchers across Europe and in Japan, where similar overlap exists between CODIS markers, local law enforcement markers, and those currently used for biospecimen authentication in research (*6*). Although there is variation in which and how many total markers are used by law enforcement in each country, a core set of seven markers (plus Amelogenin) is shared across the United States, the European Union, the United Kingdom, and Interpol, which includes 84 member countries from around the world.

UNNECESSARY RISKS

Data collection for biomedical research and for law enforcement are typically based on very different justifications and have very different goals and systems of governance. Protective silos have been built and bolstered to keep data generated by and for these particular kinds of activities quite separate. However, with this overlap of authentication efforts and CODIS, the boundary between biomedical research and law enforcement appears to be weakening. Of note, this weakening is asymmetric because historically, the FBI has largely been unwilling to permit researchers to access CODIS profiles to conduct certain kinds of research that could enhance, for example, understanding of match frequencies or the likelihood of false matches, which would presumably help further the stated goals of law enforcement rather than frustrate or harm them.

We identify three clear risks with persisting in the use of CODIS markers for research authentication, then offer a path forward for authentication of research tissues that di-

verges from the established and likely stable path of law enforcement, maximizes benefit, and minimizes potential harm.

Undermines efforts to recruit research participants from historically marginalized and excluded groups that are underrepresented in research

Genetic research and resources are composed largely of individuals of European descent (*7*), leaving the vast genetic variation present in non-European populations understudied, poorly understood, and unavailable for the development of targeted genetic therapies. It is increasingly recognized that more must be done to diversify all aspects of genetic research, including the individuals who are recruited and who ultimately enroll as research participants. Qualitative research suggests that past exploitation—including in the infamous Tuskegee syphilis study and of individuals such as Henrietta Lacks and her family, as well as current structural racism within research and health systems affecting communities of color—undermine the willingness of individuals from historically marginalized communities to participate in research (*8*). Concomitantly, racial disparities have been repeatedly demonstrated across multiple components of the criminal legal system, including in policing, arrests, charging, and sentencing (*9*)—and subsequently in CODIS. CODIS aggregates profiles for nearly all convicted (and many arrested) persons throughout the United States, and so disparities in the earlier stages of the criminal legal system are replicated in CODIS.

When the language used to describe people and samples in research is the language of law enforcement, that is likely to affect how potential research participants frame and understand the research enterprise and the risks it may entail. For populations disproportionately targeted by law enforcement (and thus disproportionately represented in law enforcement DNA databases, among other harms), the effect is likely to be negative.

That runs counter to the goals of authentication itself and the interests of science. Authentication is intended to ensure that research can be replicated and reproduced, which also helps ensure that participants' tissue and data are used in scientifically rigorous research. Thus, authentication can be a tool for building trust with research participants. But using a law enforcement tool to further biomedical research goals is likely to have the opposite result, raising questions about the trustworthiness of science by creating an indelible link between research and law enforcement data. Even if law enforcement never exploits that link, the fact of its existence may well erode trust and undermine efforts to recruit research participants on a broader scale. In other words, language matters.

Risks drawing increased law enforcement interest in gaining access to these research data

Law enforcement entities have repeatedly demonstrated an interest in and willingness to exploit genetic data for investigative purposes, with little regard for the origin of that data or the expectations of its progenitors. Consider two recent examples. The advent of investigative genetic genealogy by using consumer genetic data has whetted law enforcement appetite to use non-CODIS DNA repositories to generate genetic leads (*10*). Using consumer genetics platforms such as GEDmatch and FamilyTreeDNA, law enforcement and private companies have been able to compare crime scene DNA to consumer DNA profiles, investigate resulting familial connections, and—in more than 200 cases so far—make arrests. Meanwhile, investigators in San Francisco recently made headlines for using genetic data collected from sexual assault victims to identify at least one such victim as a suspect in an unrelated crime (*11*).

Authentication of human biospecimens is critically important, but some approaches may cause more harm than good.

PHOTO: TEK IMAGE/SCIENCE SOURCE

Such examples conflict with a principle, enshrined in federal law, that special standards of confidentiality ought to apply to sensitive, identifiable research data. Under federal law, the NIH issues Certificates of Confidentiality to federally funded and non–federally funded researchers alike. The relevant statute provides that researchers with a Certificate "shall not, in any Federal, State, or local civil, criminal, administrative, legislative, or other proceeding, disclose or provide" identifiable, sensitive data they hold about research subjects (*12*). Certificates were enacted precisely to shield sensitive research data from law enforcement use. Yet not every researcher will have a Certificate, know its terms, or enforce it as required, and the enforceability of a Certificate in the face of a law enforcement demand remains uncertain (*13*). Moreover, it is unclear whether biobanks are appropriate recipients of a Certificate at all, even though they are repositories of vast quantities of sensitive, identifiable data.

The tension—between law enforcement appetite to access additional sources of genetic data for investigative purposes and the legal and ethical commitment that research data demand special protections—indicates a need to erect practical (as well as legal) barriers to law enforcement use of genetic data where that use would be inappropriate, such as in the context of research.

The use of CODIS markers for research authentication may accomplish the opposite. Requiring researchers to generate data that are directly relevant to and usable by law enforcement may well invite law enforcement interest in this source of genetic data. Indeed, some cell banks post CODIS marker data alongside the cell lines in their publicly available catalogs. Guarding patients' and research subjects' identifying information so as to reduce reidentification risks is unlikely to be sufficient protection in this circumstance. Researchers have repeatedly demonstrated that reidentification of genetic data is possible (*14*). Further, were law enforcement to document a close or exact match between a research authentication profile and a crime scene DNA profile, a court might well order disclosure of identifying information associated with that biological material.

To be sure, any authentication technology or marker set will produce data that may attract law enforcement interest. But that risk is exacerbated when the data generated are in a form that law enforcement is likely to deem relevant and straightforward to use, provided that reidentification can be ordered or accomplished.

Imposes additional potential harms on already vulnerable populations, particularly children

Among other things, public biobanks (such as newborn screening programs), academic biobanks, and commercial biobanks

often include samples from infants and children. This may include healthy infants and children enrolled in genetic research by their parents, often with an intended benefit to a sick sibling. Genomic sequencing projects have also enrolled healthy infants and children.

Genetic research has usually been classified as no more than minimal risk, suggesting that enrollment of all children in such research should be permissible. But given rapid changes in genetic technology and the research, commercial/consumer, and law enforcement landscapes, it may no longer be the case that such research should be considered minimal risk under current regulations. Traditional barriers to the movement of data from research to consumer to law enforcement uses have already begun to break down, as the use of consumer genetics data to solve crimes demonstrates (*10*). The use of CODIS markers as a matter of course for research authentication heightens the risks and potentially shifts the risk-benefit calculation of research participation. For healthy children, this increased risk (in the absence of benefit) could make their participation in such research ethically problematic. This same logic may also apply to a "Not Human Subject Research" designation for secondary use of unconsented clinical samples.

INNOVATE FOR INDEPENDENCE

Risks and difficulties surrounding research use of CODIS markers are not inevitable. Although the adoption of CODIS markers for research authentication purposes is the path of least resistance, it is not the only path. There is no scientific reason that the research community should be locked into law enforcement's STR platform for authentication at all. Ideally, researchers should work toward a platform-agnostic method of authentication that is more flexible and open to innovation—and completely independent of CODIS.

Innovation in developing STR profiles is not only possible, it is practicable. Take two examples. When the forensic community determined that additional STRs would enhance its law enforcement work, it set about identifying those STRs. Today, CODIS profiles consist of 20 STR markers rather than the original 13. Further, these are not the only reliable and effective STRs for verifying identity. When the Coriell Institute for Medical Research, which had long used a locally developed (non-CODIS) six-marker set (plus Amelogenin) for authentication and quality control, was preparing to transition to a new, more robust set of markers for this purpose, it recognized the risks of adopting the CODIS markers. As such, Coriell developed and validated a new multiplexed STR-based assay for internal use that runs on the same platform as the original set and does not include CODIS markers. In combination, these marker sets are able to distinguish all 48,000 related and unrelated samples in the repository used for validation, demonstrating similar discriminating power to that of the CODIS-associated STRs for purposes of avoiding misidentification (*15*).

Given the forces aligned in favor of using CODIS (and other global law enforcement) markers for authentication, moving away from these markers is daunting to be sure. Alternatives must be developed and validated. A market must be built to bring the per-sample cost down. Legacy samples would need to be retyped. And those in a position to establish standards [such as ANSI and the National Institute of Standards and Technology (NIST)], fund research (such as NIH), publish research, and steward biospecimen collections would need to commit to facilitating and incentivizing the shift.

But transitioning away from CODIS markers would enable the research community, in this one way, to bolster rather than erode trust—and it is the right thing to do, regardless of how frequently law enforcement might pursue research authentication data for investigative purposes. Insofar as law enforcement actively seeks to exploit research data, making that use more time-consuming and expensive by requiring different markers to be analyzed, may dissuade that use from becoming routine. Even if law enforcement never pursues this use, eliminating the direct link between law enforcement and research would avoid the harm caused by the perception that link may create.

STRENGTHEN SILOS

The first step that needs to be taken is for biospecimen and cell line repositories and other relevant entities to immediately remove all CODIS-based authentication data from their websites, making the information available only upon request. In addition, a working group should be established to include representatives from NIH, ANSI, NIST, and other stakeholder groups to begin to identify viable alternatives. These could include non-CODIS STRs, such as the assay developed by Coriell, or another technology, such as single-nucleotide polymorphisms. These initial actions will ameliorate immediate potential harm and give us a basis for the path forward.

In many instances, the dissolution of barriers between siloed data is warranted and advances the interests of both science and patients; but the disparate justifications for collection, regulations, and norms that govern samples in the criminal legal system and in research require that the silos around these samples and the data derived from them be strengthened, not dissolved. The forensic DNA in CODIS is legally compelled from individuals who have been accused or convicted of crimes, and it is used without consent against the individual from whom it was taken. Paradigmatically, research samples (and the cell lines derived from them) are donated by volunteers who consent to participate in research because they believe in and endorse the goals of the research and because they trust the person asking them to participate. Authentication of biospecimens is and remains crucial for sound scientific research. But appropriating law enforcement tools to serve research goals undermines both consent and trust. As we have learned repeatedly over the past 2 years, trust in science is critical to both individual and public health. ■

REFERENCES AND NOTES

1. American Type Culture Collection Standards Development Organization Workgroup ASN, *Nat. Rev. Cancer* **10**, 441 (2010).
2. N. Ruiz Bravo, M. Gottesman, "Notice regarding authentication of cultured cell lines" (NIH, 2007); https://grants.nih.gov/grants/guide/notice-files/not-od-08-017.html.
3. NIH, Enhancing Reproducibility through Rigor and Transparency (9 June 2015); https://grants.nih.gov/grants/guide/notice-files/NOT-OD-15-103.html.
4. ANSI, *Authentication of Human Cell Lines: Standardization of Short Tandem Repeat (STR) Profiling* (ANSI, 2021); https://webstore.ansi.org/Standards/ATCC/ANSIATCCASN00022021.
5. FBI, "CODros. Inf. Serv. – NDros. Inf. Serv. Statistics" (October 2021); https://www.fbi.gov/services/laboratory/biometric-analysis/codis/ndis-statistics.
6. European Network of Forensic Science Institutes (ENFSI) DNA Working Group, "DNA database management review and recommendations" (ENFSI, 2019); https://enfsi.eu/wp-content/uploads/2021/09/ENFSI-DOCUMENT-ON-DNA-DATABASE-MANAGEMENT-2019.pdf.
7. A. B. Popejoy, S. M. Fullerton, *Nature* **538**, 161 (2016).
8. J. Jaiswal, P. N. Halkitis, *Behav. Med.* **45**, 79 (2019).
9. M. B. Kovera, *J. Soc. Sci.* **75**, 1139 (2019).
10. N. Ram, C. J. Guerrini, A. L. McGuire, *Science* **360**, 1078 (2018).
11. T. Abdollah, "Rape survivors, child victims, consensual sex partners: San Francisco police have used DNA from all of them for 7 years," *USA Today*, 23 February 2022.
12. Public Health Service Act § 301(d), 42 U.S.C. § 241(d)(1)(D).
13. L. E. Wolf *et al.*, *J. Empir. Res. Hum. Res. Ethics* **7**, 1 (2012).
14. M. Gymrek, A. L. McGuire, D. Golan, E. Halperin, Y. Erlich, *Science* **339**, 321 (2013).
15. G. Smith *et al.*, *Biopreserv. Biobank.* **19**, 438 (2021).

ACKNOWLEDGMENTS

From 2014 to 2020, D.J.H.M. was a member of the Scientific Advisory Committee of the National Institute of General Medical Sciences Human Genetic Cell Repository at the Coriell Institute for Medical Research. N.R. is supported by a Greenwall Foundation Faculty Scholars grant. The authors thank L. Brody and N. Turan for their critical support of and feedback on this work.

10.1126/science.abo5386

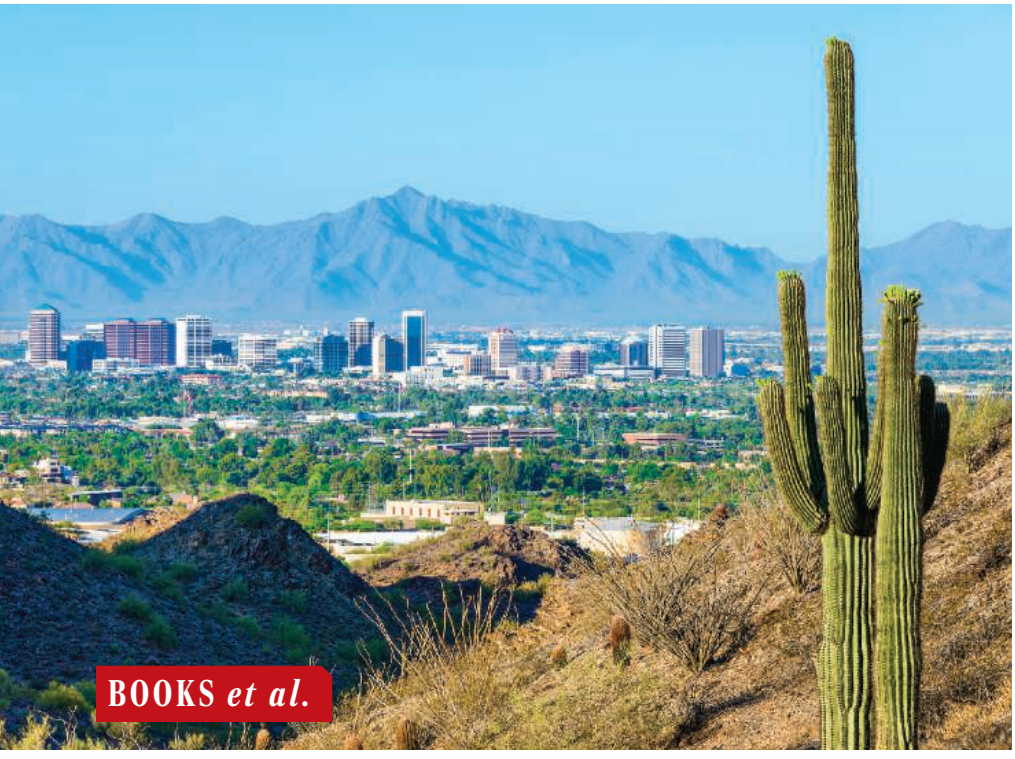

BOOKS *et al.*

The future of a defining feature of the American West, the saguaro cactus (*Carnegiea gigantea*), is uncertain.

ENVIRONMENTAL STUDIES

Confronting the climate crisis

Leading literary writers explore what it means to live on a changing planet

By **Joseph Swift**

In ancient times, it was common to divine the future by watching animal behavior. For example, an unexpected appearance of a bear or a serpent could indicate the will of the gods. As we slide further into a future of climate change, there is no shortage of such omens. Around the world, animals are acting unusually—ticks are migrating northward into Canada, swarms of jellyfish are invading the Sea of Japan, and bats are dying in the thousands in eastern Australia.

We do not need superstition to guess what type of future these animals are pointing to; climate science has provided a clear answer for decades. But given what the evidence predicts, one wonders whether its magnitude can be explained in scientific terms alone. To capture the impact of climate change in all its existential proportions, we might need methods more ancient than modern science. Drawing on storytelling, lived experience, and even a bit of superstition, *The World As We Knew It* is a collection of essays from leading literary writers that does just that, confronting climate change with a wider vocabulary than science affords.

The World As We Knew It: Dispatches From a Changing Climate
Amy Brady and Tajja Isen, Eds.
Catapult, 2022. 288 pp.

Each essay in the book serves as a type of local dispatch, with the authors sharing how climate change has shaped their own sense of place and self. On the surface, what they choose to share can appear unrelated and even irrelevant—readers learn about nuclear contamination, Arizona cacti, mold allergies, dam building, grief, commune life, raising children, and, of course, COVID-19. But as a collection, these narratives work together to shift the audience's perception of the environment, unsettling assumptions that it is something to be controlled or conquered.

For example, in her essay "What We Don't Talk About When We Talk About Antarctica," Elizabeth Rush asks why Antarctica is still romanticized as a place to demonstrate one's personal endurance, as though the continent exists only as a setting for a form of extreme boot camp. Similarly, in "Come Hell," Lacy M. Johnson hints that if religion treats the biosphere as a sort of endowment, we can become ambivalent to its destruction, because, regardless, "we please God when we use His gifts."

Even as they challenge the ways we rationalize our relationship with nature, the book's authors do not attempt to promote an alternate philosophy. While they fan out to assess other ways of knowing, such as what we can learn from feminism or Indigenous peoples, their musings point only toward encouraging ideas, not concrete solutions.

Instead, they tend to provide readers a sense of climate change as something that is both inescapable and unconcerned with human endeavors. Importantly, they lead their audience to this understanding without using alarmist language, and in doing so, the vague sense of panic their writing instills hits deeper, throwing into relief how much we would rather distract ourselves from the fact that we are not in control. After all, if we really believe there is a climate emergency, why do we spend so much time thinking about cryptocurrency, how many airline miles we have, or a journal's impact factor?

It is tricky to articulate this sort of irony, and, wisely, most of the authors of this collection do not try to define it directly. Instead, they opt for gentle observation. For example, in "Starshift," Gabrielle Bellot examines her own train of thought, showing how it is possible to worry both about the growing intensity of Caribbean hurricanes and whether it is time to go out and buy new underwear.

Some essays miss the mark, evoking an overwhelming sense of dread that blunts their intended message. And while the contributing authors are by some measures diverse, most have been plucked from a narrow political stratum. This is problematic, as discourse on science is weakened when constrained to one part of the intelligentsia.

But aside from these shortcomings, *The World As We Knew It* is resoundingly articulate about climate change in ways that dispassionate scientific inquiry cannot be. By taking a more off-the-cuff approach, the essay collection is so razor sharp, one feels it has a chance of reaching even the most hardened climate skeptic. ■

The reviewer is at the Salk Institute for Biological Studies, La Jolla, CA 92037, USA. Email: jswift@salk.edu

10.1126/science.abp8954

PHOTO: DSZC/ISTOCK.COM

SCIENCE LIVES

Peter Higgs and his eponymous particle

A new biography juxtaposes the physicist's life story with the search for the Higgs boson

By **Simon Mitton**

Frank Close's new biography of Peter Higgs opens with a telling incident: the physicist's disappearance on the day the Nobel committee announced that he was one of the two 2013 physics laureates. The favorite for the 2013 award had silently slipped away from his Edinburgh apartment, anxious to escape media attention. He had forewarned his department that on the fateful day he would be in the Scottish Highlands. This was a bluff to throw nosy newshounds off his scent. After a refreshing three-mile stroll to the Firth of Forth, he lunched alone at a seafood restaurant, leaving his colleagues to field a blizzard of media calls.

Elusive: How Peter Higgs Solved the Mystery of Mass is notable for its moderation and objectivity. Two narratives are niftily interwoven, one exploring the private world of the modest physicist and the second charting the timeline (almost half a century) of the public search for the elusive boson that would bear his name.

Close sensitively illustrates how the circumstances of Higgs's early life, which included ill health and frequent absences from school, left an indelible mark on his adult persona, characterized by shyness, extreme modesty, and a love of solitude.

From his father's cast-off engineering textbooks, the eager youngster discovered the world of mathematics. Self-taught, he mastered calculus, algebra, and trigonometry years ahead of his age group. This formative learning would later flourish as a lifelong passion for deep scholarship and intensive study.

In high school, Higgs became intrigued by the name Paul Dirac, which featured prominently on the honors board. Curious to learn more of this alumnus, he turned to Max Born's *Atomic Physics*, for its accessible account of Dirac's discoveries in quantum mechanics. He read with amazement of Dirac's prescient conjecture of the existence of antimatter, which Carl Anderson confirmed from observations of positron tracks in a cloud chamber. Decades later, he pinpointed this as a turning point of his life in physics.

Higgs graduated first-class from King's College London in 1950 and earned his doctorate in 1954 for theoretical research on the spectroscopy of organic molecules. Thereafter he focused on quantum field theory but failed to write anything of consequence for several years.

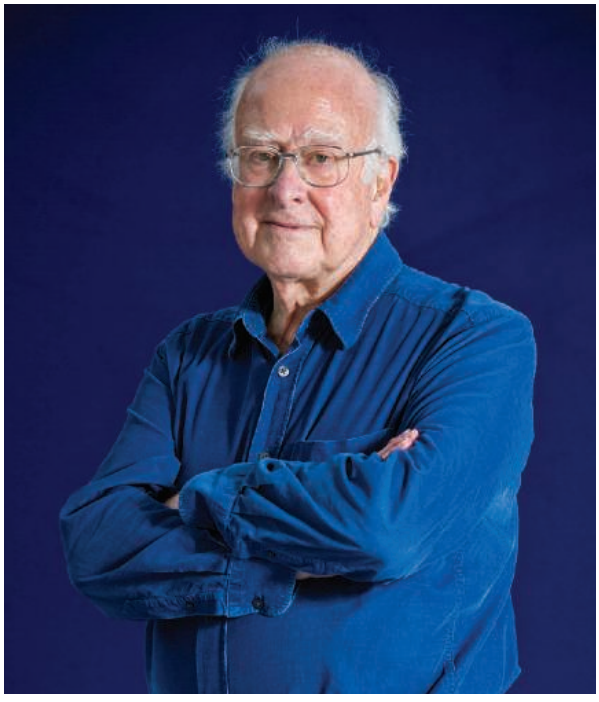

Higgs credited his fortuitous prediction to a flash of insight.

The middle section of the book, with its vivid account of the parlous state of particle physics theory in the mid-1960s, gives the context in which Higgs found himself. Here, Close's description of the mathematical manipulations employed by Higgs and others will challenge readers not already at ease with quantum mechanics and the standard model of particle physics. He offers useful tutorials and a couple of appendices that may help those who have the time for a second or third reading. Better still, just skip to the epilogue for the author's delightful overview in plain English.

Elusive: How Peter Higgs Solved the Mystery of Mass
Frank Close
Basic Books, 2022.
304 pp.

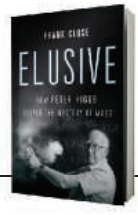

Higgs and many rivals struggled to comprehend the fundamental particles and forces of our Universe. All attempts to unify the electromagnetic and the weak nuclear forces failed. A fault lurked somewhere in the modeling, which predicted that the particles (bosons) mediating the weak interaction had zero mass. Higgs viewed the concept of a massless boson as ridiculous, intuiting that modelers were overlooking something. But what?

After 3 years of fruitless attempts to unpick the mistakes others had made, Higgs found the error in a flash of insight, spotting that the leading contender had neglected the influence of electromagnetism. It took him a weekend to plug that gap by invoking a hypothetical quantum field to generate mass. Later, he articulated his surmise as "the only really original idea I've *ever* had."

Higgs became aware of rivals who were postulating that an unusual quantum field had endowed bosons with mass. Luckily, he published first and suggested that the massive boson could be identified from its decay products. However, his papers failed to gain traction, because the Higgs mass creation mechanism had the appearance of a mathematical fudge.

Higgs instinctively adopted a low profile until 1967, when Steven Weinberg enthusiastically cited Higgs *et al.* for their exorcising of massless bosons. By the mid-1970s, the path to a mathematically tidy (renormalizable) standard model was clear. The task that then lay ahead was finding the Higgs boson, a totem by which the validity of the standard model would be judged. Close concludes his biography with an eyewitness account of the momentous day, 4 July 2012, when CERN applauded the discovery of "a particle compatible with the Higgs boson." ■

10.1126/science.abq4315

The reviewer is a life fellow of St Edmund's College, University of Cambridge, Cambridge CB3 0BN, UK. Email: sam11@cam.ac.uk

PHOTO: COLIN MCPHERSON/CORBIS/GETTY IMAGES

Sinking land and fissures in Iran could lead to a humanitarian crisis.

PHOTO: AP IMAGES

Edited by **Jennifer Sills**

Shrinking aquifers and land subsidence in Iran

More than 98% of Iran's 1.648 million km² of land faces land subsidence (*1*, *2*). Internationally, a rate of subsidence greater than 4 mm per year (*3*) is considered a crisis; Iran's land is sinking at an astonishing rate of 6 cm per year (*1*) as a result of 25 years of water level decline in the plains (*2*, *4*). Dam construction, climate change, inefficient water consumption by agriculture and industries, and the use of underground aquifers as sources for illegal agricultural water extraction wells all continue to deplete Iran's water table (*5*, *6*). Iran must address its water levels before subsidence leads to a humanitarian crisis.

In urban areas, subsidence will damage buildings, bridges, transportation lines, and energy transmission lines as well as reduce the earthquake resistance of buildings (*1*, *2*). Historical monuments are also at risk. Moreover, continued water level declines will reduce the ground's water permeability and turn fertile plains into barren deserts.

Subsidence can be managed and controlled with proper monitoring. To address the problem, Iran should save water by adopting mechanized irrigation in agriculture and managing wells to prevent illegal water extraction. Farmers should use cultivation patterns that maximize water efficiency in the production of crops. Where possible, agricultural products should be cultivated in greenhouses, which use less water than traditional farming (*7*). Finally, to protect the aquifers in the plains from further water loss, Iran should facilitate the transfer of industries with high water consumption to the shores of the Caspian Sea or the Persian Gulf, where desalination technologies can provide adequate water (*8*).

Masoud Negahdary
Department of Fundamental Chemistry, Institute of Chemistry, University of São Paulo, São Paulo, Brazil. Email: mnegahdary@iq.usp.br

REFERENCES AND NOTES

1. A. Shahidi, "Land subsidence swallows Iran: Out of 609 plains in the country, 400 plains are in critical condition," *Tasnim News* (2022); www.tasnimnews.com/fa/news/1400/12/25/2682940 [in Persian].
2. M. Amighpey, "Land subsidence crisis in 8 provinces; most dangerous areas of Tehran announced," *Khabara Online* (2021); www.khabaronline.ir/news/1569061 [in Persian].
3. M. M. Ashnani *et al.*, *J. Environ. Sci. Technol.* **22**, 253 (2020).
4. S. T. Loghmani Khouzani *et al.*, *Wat. Int.* **47**, 181 (2022).
5. G. Herrera-García *et al.*, *Science* **371**, 34 (2021).
6. M. Bagheri-Gavkosh *et al.*, *Sci. Tot. Environ.* **778**, 146193 (2021).
7. "The role of greenhouses in reducing agricultural water consumption," *IRNA News Agency* (2019); www.irna.ir/news/83169422 [in Persian].
8. M. Qadir *et al.*, *Unconventional Water Resources* (Springer International Publishing, 2022).

10.1126/science.add1263

Biotechnology ethics for food and agriculture

In January, the National Bioengineered Food Disclosure Law (NBFDL) went into effect, requiring all US food manufacturers to disclose whether their products contain bioengineered ingredients (*1*). However, the law is the subject of debate, with critics arguing that it inhibits rather than increases transparency around the use of biotechnology in food (*2*). Given the importance of the agbiotech industry, the Biden-Harris administration should develop an agricultural biotechnology advisory commission devoted to inclusive deliberation on ethics and governance in agricultural and food biotechnology.

The NBFDL is consistent with the US Department of Agriculture's (USDA's) Sustainable, Ecological, Consistent, Uniform, Responsible, Efficient (SECURE) rule (*3*), which exempts many gene-edited crop traits from regulation and allows companies to self-regulate. Similarly, the NBFDL grants exemptions from labeling for processed foods with trace percentages (<5%) of genetic material and allows for disclosure through QR codes rather than through a clearly identifiable symbol that can be read directly on a package. Several lawsuits alleging deficiencies in the governance of genetically engineered crops and food animals are making their way through the court system (*2*, *4*).

The United States has appointed a bioethics commission in the past, but no commission has been formed since 2017 (*5*). The urgency of reinstating the commission has been highlighted by National Academy of Sciences President Marcia McNutt and National Academy of Medicine President Victor J. Dzau (*5*, *6*). The need for a commission addressing ethics in public health, biomedicine, and climate science signals that we should also create bioethics commissions for other areas, including agriculture biotechnology.

Commissions focusing on agricultural bioethics have never existed in the United States, but they have been successfully developed elsewhere. The Norwegian Biotechnology Advisory Board has recommended a forward-looking regulatory framework for genetically modified organism use and gene editing in agriculture based on extensive public consultation (*7*). The UK's Nuffield Council on Bioethics, an independent forum funded by the Medical Research Council and the Wellcome Trust, has published a series of reports on the social and ethical issues related to genome editing and farmed animal breeding, elicited public responses to proposed regulation changes, and facilitated public dialogues on genome editing in farm animals (*8*). The United States should use these examples as models for the establishment of a presidential bioethics commission that addresses critical issues and

promotes inclusive engagement around biotechnology in food and agriculture.

Catherine Kendig[1]*, Theresa Selfa[2], Paul B. Thompson[1,3,4]
[1]Department of Philosophy, Michigan State University, East Lansing, MI 48824, USA. [2]Department of Environmental Studies, State University of New York College of Environmental Science and Forestry, Syracuse, NY 13210, USA. [3]Department of Agricultural, Food, and Resource Economics, Michigan State University, East Lansing, MI 48824, USA. [4]Department of Community Sustainability, Michigan State University, East Lansing, MI 48824, USA.
*Corresponding author. Email: kendig@msu.edu

REFERENCES AND NOTES

1. USDA, Agricultural Marketing Service, BE Disclosure (2022); www.ams.usda.gov/rules-regulations/be.
2. G. Jaffe, J. Kuzma, "New bioengineered (aka GM) food disclosure law: Useful information or consumer confusion?" Food and Drug Law Institute (2021); www.fdli.org/2021/04/new-bioengineered-aka-gm-food-disclosure-law-useful-information-or-consumer-confusion.
3. USDA, Animal and Plant Health Inspection Service, SECURE Rule Text Only (2021); www.aphis.usda.gov/aphis/ourfocus/biotechnology/biotech-rule-revision/secure-rule/secure-text/sr-text.
4. S. Davies, "Lawsuit challenges Trump-era overhaul of USDA's biotech regulation," *AgriPulse* (2021); www.agri-pulse.com/articles/16221-lawsuit-challenges-trump-rule-on-biotechplants.
5. "NAS and NAM presidents, other experts urge Biden administration to reinstate presidential bioethics commission," (National Academies, 2022); www.nationalacademies.org/news/2022/03/nas-and-nam-presidents-other-experts-urge-biden-administration-to-reinstate-presidential-bioethics-commission.
6. S. Wolf *et al.*, "Recommending a new presidential bioethics commission" (National Academies, 2022); https://nationalacademies.org/docs/D8822B76BACDA83FD980DFCE49DEA32747F272C9B624.
7. Bioteknologirådet, "A forward-looking regulatory framework for GMO" (2019); www.bioteknologiradet.no/2019/03/a-forward-looking-regulatory-framework-for-gmo/.
8. Nuffield Council on Bioethics, "Genome editing and farmed animal breeding: Social and ethical issues" (Nuffield Council on Bioethics, 2021); www.nuffieldbioethics.org/publications/genome-editing-and-farmed-animals.

10.1126/science.add1403

Broaden chemicals scope in biodiversity targets

On 21 June, the next round of negotiations on the post-2020 global biodiversity framework will be held in Nairobi (*1*). In the draft document (*2*) listing 21 targets, target 7 addresses chemical pollution by explicitly mentioning nutrients, pesticides, and plastic waste. Limiting this target's scope to these three groups does not do justice to the immense variety of anthropogenic chemicals polluting the environment (*3*), which also include, for example, toxic metals, industrial chemicals, chemicals from consumer products, and pharmaceuticals (*4*), as well as the (often unknown) transformation products of substances from each group (*5*). We urge the negotiators to broaden the scope of target 7 to reflect the complexity of chemical pollution.

Both direct and indirect impacts of chemical pollutants on organisms in the environment can lead to population instability, possibly resulting in the decline or even extinction of vulnerable species. Chemical pollutants can also cause undesired shifts in community composition and/or function, which can affect ecosystem services (*6*). Biological adaptation to chemical exposure may decrease genetic diversity, reducing resilience to future stressors, such as global warming and other aspects of global change (*7*). Thus, to focus solely on nutrients and pesticides would detract attention from myriad potential interactions, beyond eutrophication and acute toxicity, which could negatively affect biodiversity and ecosystems at large.

Chemical pollution mitigation plans should address pharmaceutical waste.

Understanding environmental exposures and their consequences is a formidable task because of the variety of pollutants and multitude of potential impacts, as well as the fact that chemicals occur in mixtures and act in conjunction with other stressors (*7*, *8*). To comprehensively address these complex interactions, joint efforts by interdisciplinary teams of researchers are essential. Neither the scientific community nor research funders have fully recognized or adequately responded to this necessity yet.

Environmental pollution by anthropogenic chemicals has been recognized as a major agent of global change (*9*). The continuous rise in the creation, production, and use of chemicals far outpaces humanity's capacity to assess their hazards and risks to human health and the environment (*10*, *11*). To tackle the global threats of chemical pollution, countries around the world have recently agreed on creating an intergovernmental science-policy panel on chemicals and waste, charged with consolidating existing knowledge to inform policymakers (*12*). The available evidence already justifies targeting a wider scope of chemical pollutants for strategies and action to be implemented in the post-2020 global biodiversity framework.

Gabriel Sigmund[1], Marlene Ågerstrand[2], Tomas Brodin[3], Miriam L. Diamond[4], Walter R. Erdelen[5], David C. Evers[6], Adelene Lai[7,8], Matthias C. Rillig[9], Andreas Schäffer[10], Anna Soehl[11], João Paulo M. Torres[12], Zhanyun Wang[13], Ksenia J. Groh[14]*
[1]Centre for Microbiology and Environmental Systems Science, University of Vienna, 1090 Wien, Austria. [2]Department of Environmental Science, Stockholm University, SE-106 91 Stockholm, Sweden. [3]Department of Wildlife, Fish, and Environmental Studies, Swedish University of Agricultural Sciences, SLU Umeå, Sweden. [4]Department of Earth Sciences and School of the Environment, University of Toronto, Toronto, ON M5S 3B1, Canada. [5]Ostrhauderfehn, Lower Saxony, Germany. [6]Biodiversity Research Institute, Portland, ME 04103, USA. [7]Luxembourg Centre for Systems Biomedicine, University of Luxembourg, 4367 Belvaux, Luxembourg. [8]Institute for Inorganic and Analytical Chemistry, Friedrich-Schiller University, 07743 Jena, Germany. [9]Freie Universität Berlin, 14195 Berlin, Germany. [10]Institute for Environmental Research, Rhenish-Westphalian Technical University (RWTH) Aachen University, 52074 Aachen, Germany. [11]International Panel on Chemical Pollution, 8092 Zürich, Switzerland. [12]Laboratório de Radioisótopos Eduardo Penna Franca, Instituto de Biofísica Carlos Chagas Filho, Universidade Federal do Rio de Janeiro, Rio de Janeiro 21941-902, Brazil. [13]Technology and Society Laboratory, Swiss Federal Laboratories for Materials Science and Technology (EMPA), 9014 St. Gallen, Switzerland. [14]Department of Environmental Toxicology, Swiss Federal Institute of Aquatic Science and Technology (EAWAG), 8600 Dübendorf, Switzerland.
*Corresponding author.
Email: ksenia.groh@eawag.ch

REFERENCES AND NOTES

1. Convention on Biological Diversity (CBD), "Fourth meeting of the Open-Ended Working Group on the Post-2020 Global Biodiversity Framework, 21–26 June 2022, Nairobi, Kenya" (2022); www.cbd.int/article/notification2022-024.
2. CBD, "A new global framework for managing nature through 2030: First detailed draft agreement debuts" (2021); www.cbd.int/article/draft-1-global-biodiversity-framework.
3. K. Groh, C. vom Berg, K. Schirmer, A. Tlili, *Environ. Sci. Technol.* **56**, 707 (2022).
4. Z. Wang, G. W. Walker, D. C. G. Muir, K. Nagatani-Yoshida, *Environ. Sci. Technol.* **54**, 2575 (2020).
5. B. I. Escher, K. Fenner, *Environ. Sci. Technol.* **45**, 3835 (2011).
6. M. Saaristo *et al.*, *Proc. R. Soc. B Biol. Sci.* **285**, 20181297 (2018).
7. M. C. Rillig *et al.*, *Science* **366**, 886 (2019).
8. A. Schaeffer *et al.*, *Sci. Tot. Environ.* **568**, 1076 (2016).
9. E. S. Bernhardt *et al.*, *Front. Ecol. Environ.* **15**, 84 (2017).
10. R. Naidu *et al.*, *Environ. Int.* **156**, 106616 (2021).
11. L. Persson *et al.*, *Environ. Sci. Technol.* **56**, 1510 (2022).
12. Z. Wang *et al.*, *Science* **371**, 774 (2021).

COMPETING INTERESTS

A. Soehl is an independent contractor supporting the work of Green Science Policy Institute.

10.1126/science.add3070

PHOTO: GOU YIGE/AFP/GETTY IMAGES

RESEARCH

IN *SCIENCE* JOURNALS

Edited by
Michael Funk

QUANTUM GASES

Separating spin and charge

In one-dimensional fermionic systems, spin and charge excitations can decouple from each other. This so-called spin-charge separation has been detected in solids and cold-atom systems held in optical lattices. Senaratne *et al*. observed spin-charge separation in one-dimensional Fermi gases of lithium atoms in the absence of a lattice structure within the gas. The researchers were able to excite the spin and charge excitation modes independently from each other and measure their velocities as a function of the strength of the atomic interactions. —JS *Science*, abn1719, this issue p. 1305

Artist's conception of a spin excitation propagating through a one-dimensional gas of fermionic atoms

ILLUSTRATION: ELLA MARU STUDIO, COURTESY OF R. HULET/RICE UNIVERSITY

TRANSCRIPTION

When Pol II meets nucleosome

Eukaryotic cells organize their large genomes into a compacted structure called chromatin. The condensed structure of chromatin, with its fundamental unit, the nucleosome, represents a challenge to nucleic acid–transacting machines including RNA polymerase II (Pol II), the enzyme responsible for the transcription of most protein-coding genes. How RNA Pol II overcomes nucleosomes without disrupting chromatin organization remains unknown. Using cryo–electron microscopy, Filipovski *et al*. provide structural snapshots of a complex between mammalian RNA Pol II and a nucleosome that show how previously transcribed DNA rewraps the nucleosome. The finding provides a structural basis of how nucleosomes, and consequently epigenetic marks, are retained during transcription. —DJ

Science, abo3851, this issue p. 1313

CORONAVIRUS

First off the COVID block

The severe acute respiratory syndrome coronavirus 2 (SARS-CoV-2) pandemic has been characterized by waves of transmission initiated by new variants replacing older ones. Given this pattern of emergence, there is an obvious need for the early detection of novel variants to prevent excess deaths. Obermeyer *et al*. have developed a Bayesian model to compare relative transmissibility of all viral lineages. Using this model, emerging lineages can be spotted together with the mutations that contribute toward transmissibility, not only in Spike, but also in other viral proteins. The model can prioritize lineages as they emerge for public health concern. —CA

Science, abm1208, this issue p. 1327

MOLECULAR BIOLOGY

How to make selenoproteins

In all domains of life, the essential trace element selenium is incorporated into selenoproteins as the amino acid selenocysteine during protein translation. Specialized protein and RNA factors assist selenocysteine transfer RNA to reinterpret specific UGA codons, not as a signal to end protein synthesis, but rather as a sign for selenocysteine insertion. Hilal *et al*. used cryo–electron microscopy to trap and visualize the mammalian ribosome as it decodes the selenocysteine UGA codon. An unforeseen extended network of interactions between key molecular players facilitates the recoding event, thereby providing a basis for further

studies of this fundamental biological process. —DJ

Science, abg3875, this issue p. 1338

BIOLOGY

A tractable lead for lupus

Lack of optimal immune defense functions and thus increased risk for infections is a known issue for patients with systemic lupus erythematosus (SLE), adding an additional possible complication to an already often-severe systemic autoimmune disease. Chen *et al.* found that the cell surface enzyme CD38 compromises mitochondrial fitness by suppressing mitophagy in $CD8^+$ T cells from lupus patients. Administration of a CD38 enzymatic inhibitor reverses cytotoxic T cell defects, which are thought to be a cause of the impaired immune function. Because CD38 inhibitors are available for the clinical setting, this finding opens up interesting new avenues to hopefully restore immune function in SLE patients. —MGvH

Sci. Adv. 10.1126/sciadv.abo4271 (2022).

HEART REPAIR

Meteorin-like signals through KIT

The adult mammalian heart has limited regenerative capacity and heals by scar formation after myocardial infarction. Effective repair of the injured heart entails a vigorous angiogenic response that mitigates scarring and helps to preserve pump function. Reboll *et al*. identified the myeloid cell-derived cytokine meteorin-like (METRNL) protein as being a critical driver of postinfarction angiogenesis and a high-affinity ligand for the stem cell factor receptor KIT (see the Perspective by Srivastava). METRNL promotes infarct repair in mice by selectively expanding the KIT-expressing endothelial cell population in the infarct border zone. Failure to mount this KIT-dependent angiogenic response provokes severe postinfarction heart failure. METRNL provides a mechanism for activating endothelial KIT signaling after tissue injury. —BAP

Science, abn3027, this issue p. 1343; see also adc8698, p. 1271

CANCER IMMUNOLOGY

Engulfing to improve radiation

Despite the wide use of radiation therapy (RT) in colorectal cancer, many patients experience progression at non-irradiated sites of disease. Hsieh *et al.* used mouse modeling and human cancer cell lines to show that RT increased the expression of the cell surface markers CD47 and PD-L1 in a DNA repair signaling–dependent manner. Targeting these pathways with antibodies against their ligands, SIRPα and PD-1, in combination with RT, led to clearance of primary tumors and robust abscopal effects. This triple combination depended on host STING expression, leading to improved tumor cell phagocytosis and subsequent cross-priming of tumor antigen–specific T cells. These data suggest that targeting immune checkpoints and phagocytosis during RT may help in the treatment of patients with colorectal cancer. —DAE

Sci. Immunol. **7**, eabl9330 (2022).

HISTORICAL DROUGHT

Arabian aridity

Islam emerged in the Arabian Peninsula in the early seventh century CE after a period of profound societal changes. What was the environmental context of that emergence? Fleitmann *et al*. present a hydroclimate record of Southern Arabia showing that droughts plagued the region throughout the sixth century CE. They suggest that increasing aridity and declining agricultural yields may have contributed to demise of Himyar, the dominant power in Arabia at that time. —HJS

Science, abg4044, this issue p. 1317

IN OTHER JOURNALS

Edited by **Caroline Ash** *and* **Jesse Smith**

PHOTO: BLICKWINKEL/ALAMY STOCK PHOTO

SPECIES INTERACTIONS

Mismatches matter

As the climate changes, interacting species often respond differently to changing seasonal cues. This phenomenon can lead to phenological mismatches in which temporal decoupling between species occurs, such as predators emerging before or after their prey. Wilde *et al*. investigated how phenological mismatches caused by earlier insect emergence influence the growth and survival of chicks of the Hudsonian godwit (*Limosa haemastica*, an Alaskan shorebird shown here). The young godwits' growth and survival were highest during periods of high insect abundance, but chicks also required larger insects as they grew. Thus, the consumer's population success depends not just on synchrony with its prey, but also on overlap between individuals' changing resource needs and the quantity and quality of available resources. —BEL

Ecology 10.1002/ecy.3743 (2022).

IMMUNOLOGY

A Pten-tial cause of autoimmunity?

Although platelets are mostly known for their role in clotting, they also have immunoregulatory functions. Hyperactive platelets are associated with several autoimmune diseases. Chen *et al.* report that mice with hyperactive platelets develop severe age-related autoimmune and lymphoproliferative disease. Platelet-specific deletion of a gene called phosphatase and tensin homolog (*Pten*) results in excessive platelet aggregation

ALSO IN *SCIENCE* JOURNALS

Edited by **Michael Funk**

CELL BIOLOGY

Making a chromosomal bouquet

During meiosis, chromosomal pairing requires microtubule-dependent telomere tethering and rotation on the nuclear envelope, a process that also drives chromosome homology searches. Formation of the structure called the "zygotene chromosomal bouquet" involves telomere pulling toward the centrosome. Mytlis *et al*. describe the so-called "zygotene cilium," which helps to ensure chromosomal bouquet formation and germ cell morphogenesis in zebrafish and mouse oocytes. The cilium anchors the centrosome, allowing it to resist telomere pulling, and is essential for bouquet and synaptonemal complex formation and successful oogenesis. —SMH and BAP

Science, abh3104, this issue p. 1284

INNATE IMMUNITY

Human OTULIN haploinsufficiency

The interindividual clinical variability upon infection with *Staphylococcus aureus* in otherwise healthy people is poorly understood. Using human genetic approaches, Spaan *et al*. found a genome-wide enrichment for rare heterozygous OTULIN variants in a cohort of patients with severe staphylococcal disease. Autosomal-dominant OTULIN deficiency operates by haploinsufficiency and is phenocopied in patients with the more common 5p− (or Cri du Chat) chromosomal deletion syndrome. OTULIN haploinsufficiency underlies staphylococcal necrosis of the skin and lungs by increasing the susceptibility of tissue-resident, nonhematopoietic cells to the major staphylococcal virulence factor α-toxin. Naturally elicited α-toxin–neutralizing antibodies apparently rescue the disorder and contribute to incomplete clinical penetrance. —SMH

Science, abm6380, this issue p. 1285

PLANT SCIENCE

Heat tolerance in rice

Too much heat can damage a plant's chloroplasts, driving yield down when temperatures exceed a crop's normal tolerance. Zhang *et al*. identified a locus with two genes that together enhance rice thermotolerance. The ubiquitin ligase activity of Thermo-tolerance 3.1 (TT3.1) drove degradation of TT3.2, a chloroplast precursor protein that can trigger chloroplast damage in the context of heat stress. Together, these protein products respond to heat and control the damage. —PJH

Science, abo5721, this issue p. 1293

NEURODEVELOPMENT

RNA modification hub at the centrosome

The centrosome acts as the cell's microtubule-organizing center, supporting cell division and the extension of cilia and neurites. Newly born neurons require the microtubule-organizing activity of centrosomes to migrate away from their birthplace at the ventricle. O'Neill *et al*. analyzed the centrosome proteome of human induced pluripotent stem cell–derived neural stem cells and neurons. The neural centrosome proteome contains a variety of RNA-binding/modifying proteins, including an RNA-splicing factor mutation that is linked to periventricular heterotopia. —PJH

Science, abf9088, this issue p. 1286

ROBOTIC MATERIALS

Form and function all in one

Piezoelectric actuators are one route to driving motion in robotic systems. However, one typically needs either multiple crystals or engineered structures to allow motion with multiple degrees of freedom. Cui *et al*. designed architected materials composed of conductive and piezoelectric materials that couple electric field and mechanical strain (see the Perspective by Rafsanjani). The authors engineered these three-dimensional materials to be capable of a variety of motions and transducer functions by using additive manufacturing to build the complex shapes. They demonstrate their functionality for actuation and sensing in a unified miniaturized mobile robot that can move, sense, and perform feedback control. —MSL

Science, abn0090, this issue p. 1287; see also abq4102, p. 1272

OIL POLLUTION

Slick findings

Ocean oil slicks may have natural or anthropogenic sources, but how many occur, how extensive they are, and in what proportions they happen are unclear. Dong *et al*. present a global oil slick map and a detailed inventory of static-and-persistent sources for the period between 2014 and 2019 (see the Perspective by Leifer). They observed a highly uneven distribution of slicks, with most of them located within 160 kilometers of coastlines and along shipping routes. Anthropogenic sources constitute the overwhelming majority of cases, and their numbers show that their contribution may have been significantly underestimated in the past. —HJS

Science, abm5940, this issue p. 1300; see also abp8666, p. 1266

PHOTONICS

On-chip optical amplification

The success of long-haul optical communications and our information society is largely due to the invention of the erbium-doped fiber amplifier. Because the need for faster chips is expected to see a shift from electronics- to photonics-based technologies, erbium ions could form the basis for amplification in optical integrated circuits. Liu *et al*. used an ultra-low-loss silicon nitride photonic integrated circuit with a waveguide length up to 0.5 meters and erbium ion implantation to fabricate an erbium-doped waveguide amplifier on a compact photonic chip (see the Perspective by Kim). Operating in the continuous-wave regime and providing large optical gain in the telecommunication bands, the results are promising for device applications. —ISO

Science, abo2631, this issue p. 1309; see also abq8422, p. 1269

CONSERVATION

A new hope

Polar bears are one of the most mentioned—and iconic—potential victims of climate change. Most polar bears rely on sea ice to hunt, so the current and predicted reductions in sea ice occurrence and persistence are likely to have major impacts on their survival. Laidre *et al*. describe the discovery of an isolated population of polar bears from southeastern Greenland that is much less reliant on sea ice, instead existing at the terminal end of a glacier and relying on resources from this glacial-freshwater mélange (see the Perspective by Peacock). Discovery of this population suggests both that such environments might serve as refugia for polar bears and that conservation of this new population is essential. —SNV

Science, abk2793, this issue p. 1333; see also abq5267, p. 1267

BIOCONJUGATION

Enzymes for tailored insulin derivatives

The development of drugs based on protein hormones such as insulin is a challenge

because many of the usual tools in organic synthesis are either not compatible with folded proteins or lack selectivity when redundant functional groups are present. Fryszkowska *et al*. generated a panel of enzymes that selectively modify one or more of the three amine groups of insulin, adding or removing protecting groups (see the Perspective by Lin and Chou). The enzymatically functionalized molecules can then be modified by electrophilic reagents to produce homogeneous insulin conjugates. The authors also demonstrate enzymatic activity on a range of bioactive peptides, suggesting that biocatalytic approaches may help in the development of potential peptide-based therapeutics or probes. —MAF

Science, abn2009, this issue p. 1321; see also abq7217, p. 1270

PHYSIOLOGY

Hearing better with TRα1 signaling

Mutations that affect the thyroid hormone receptor TRβ cause resistance to thyroid hormone and have been associated with deafness. Affortit *et al.* demonstrated hearing loss that worsened with age in juvenile mice with a frameshift mutation (similar to disease-associated mutations in humans) in the gene encoding the related thyroid hormone receptor isoform TRα1. The cochlear outer hair cells in these mice were abnormally oriented or absent and showed mislocalization of a prosurvival factor for outer hair cells and increased signs of oxidative stress. —AMV

Sci. Signal. **15**, eabj4583 (2022).

HEART MUSCLE DISEASE

Conditional cardioprotection

Phosphodiesterase 5 (PDE5) inhibition has been shown to have inconsistent cardioprotective effects. Pofi *et al.* conducted a small phase 4 trial to assess sex differences in cardiac remodeling in patients with diabetes and diabetic cardiomyopathy treated with the PDE5 inhibitor tadalafil. They observed an improvement in cardiac shortening and torsion in men but not women, but the circulating small noncoding RNA hsa-miR-199-5p was reduced and the protein Klotho was increased with treatment in both sexes. Certain populations of monocytes were also altered with treatment. These results highlight the importance of considering sex-specific differences in treatment response. —CC

Sci. Transl. Med. **14**, eabl8503 (2022).

GENETICS

How trypanosomes go quiet

The parasite *Trypanosoma brucei* causes sleeping sickness, which can be fatal. At a critical density, the parasite differentiates into a quiescent stumpy form. This transition promotes host survival but also facilitates trypanosome transmission. Guegan *et al.* conducted RNA sequencing in *T. brucei* to identify 1428 previously unknown long noncoding RNA (lncRNA) genes. They found that one of these genes, named *grumpy*, promotes differentiation into the quiescent form, and that this process is mediated by a small nucleolar RNA (snoRNA) encoded within the lncRNA. The snoRNA binds to the mRNAs of at least two genes that regulate stumpy differentiation, enhancing their expression. Overexpression of *grumpy* reduces parasitemia in infected mice, indicating that trypanosome lncRNAs regulate parasite-host interactions. —DLD

Sci. Adv. 10.1126/sciadv.abn2706 (2022).

studies of this fundamental biological process. —DJ

Science, abg3875, this issue p. 1338

BIOLOGY

A tractable lead for lupus

Lack of optimal immune defense functions and thus increased risk for infections is a known issue for patients with systemic lupus erythematosus (SLE), adding an additional possible complication to an already often-severe systemic autoimmune disease. Chen *et al.* found that the cell surface enzyme CD38 compromises mitochondrial fitness by suppressing mitophagy in $CD8^+$ T cells from lupus patients. Administration of a CD38 enzymatic inhibitor reverses cytotoxic T cell defects, which are thought to be a cause of the impaired immune function. Because CD38 inhibitors are available for the clinical setting, this finding opens up interesting new avenues to hopefully restore immune function in SLE patients. —MGvH

Sci. Adv. 10.1126/sciadv.abo4271 (2022).

HEART REPAIR

Meteorin-like signals through KIT

The adult mammalian heart has limited regenerative capacity and heals by scar formation after myocardial infarction. Effective repair of the injured heart entails a vigorous angiogenic response that mitigates scarring and helps to preserve pump function. Reboll *et al*. identified the myeloid cell-derived cytokine meteorin-like (METRNL) protein as being a critical driver of postinfarction angiogenesis and a high-affinity ligand for the stem cell factor receptor KIT (see the Perspective by Srivastava). METRNL promotes infarct repair in mice by selectively expanding the KIT-expressing endothelial cell population in the infarct border zone. Failure to mount this KIT-dependent angiogenic response provokes severe postinfarction heart failure. METRNL provides a mechanism for activating endothelial KIT signaling after tissue injury. —BAP

Science, abn3027, this issue p. 1343; see also adc8698, p. 1271

CANCER IMMUNOLOGY

Engulfing to improve radiation

Despite the wide use of radiation therapy (RT) in colorectal cancer, many patients experience progression at non-irradiated sites of disease. Hsieh *et al.* used mouse modeling and human cancer cell lines to show that RT increased the expression of the cell surface markers CD47 and PD-L1 in a DNA repair signaling–dependent manner. Targeting these pathways with antibodies against their ligands, SIRPα and PD-1, in combination with RT, led to clearance of primary tumors and robust abscopal effects. This triple combination depended on host STING expression, leading to improved tumor cell phagocytosis and subsequent cross-priming of tumor antigen–specific T cells. These data suggest that targeting immune checkpoints and phagocytosis during RT may help in the treatment of patients with colorectal cancer. —DAE

Sci. Immunol. **7**, eabl9330 (2022).

HISTORICAL DROUGHT

Arabian aridity

Islam emerged in the Arabian Peninsula in the early seventh century CE after a period of profound societal changes. What was the environmental context of that emergence? Fleitmann *et al*. present a hydroclimate record of Southern Arabia showing that droughts plagued the region throughout the sixth century CE. They suggest that increasing aridity and declining agricultural yields may have contributed to demise of Himyar, the dominant power in Arabia at that time. —HJS

Science, abg4044, this issue p. 1317

IN OTHER JOURNALS

Edited by **Caroline Ash** *and* **Jesse Smith**

PHOTO: BLICKWINKEL/ALAMY STOCK PHOTO

SPECIES INTERACTIONS

Mismatches matter

As the climate changes, interacting species often respond differently to changing seasonal cues. This phenomenon can lead to phenological mismatches in which temporal decoupling between species occurs, such as predators emerging before or after their prey. Wilde *et al*. investigated how phenological mismatches caused by earlier insect emergence influence the growth and survival of chicks of the Hudsonian godwit (*Limosa haemastica*, an Alaskan shorebird shown here). The young godwits' growth and survival were highest during periods of high insect abundance, but chicks also required larger insects as they grew. Thus, the consumer's population success depends not just on synchrony with its prey, but also on overlap between individuals' changing resource needs and the quantity and quality of available resources. —BEL

Ecology 10.1002/ecy.3743 (2022).

IMMUNOLOGY

A Pten-tial cause of autoimmunity?

Although platelets are mostly known for their role in clotting, they also have immunoregulatory functions. Hyperactive platelets are associated with several autoimmune diseases. Chen *et al.* report that mice with hyperactive platelets develop severe age-related autoimmune and lymphoproliferative disease. Platelet-specific deletion of a gene called phosphatase and tensin homolog (*Pten*) results in excessive platelet aggregation

and secretion of cytokines that promote the development of T follicular helper (Tfh) cells. Tfh cells support B cell antibody production in lymphoid germinal centers. Future studies will be needed to test whether platelet-mediated enhancement of Tfh cell activity is a hallmark of any autoimmune diseases in humans. —STS

Nat Commun **13**, 2762 (2022).

MICROBIOME

Microbiome and statins

Statins, or HMG-CoA reductase inhibitors, are cholesterol-reducing drugs that are among the most prescribed medications. Their effectiveness and side effects are very heterogeneous. Human gut bacteria are known to metabolize statins in vitro, and their prevalence is also heterogeneous. In people prescribed known doses of statins, Wilmanski *et al*. showed that blood concentrations of the metabolite 3-hydroxy-3-methylglutarate-coenzyme-A (HMG), the natural substrate for HMG-CoA reductase, is potentially a serum biomarker for statin responses. Further, shotgun sequencing of stool samples found that people on statins who were enriched for *Bacteroides* gut bacteria tended to have greater risk of metabolic disruption than those with a preponderance of *Firmicutes* bacteria. —YN

Med 10.1016/j.medj.2022.04.007 (2022).

NEURONAL CELL BIOLOGY

An axonal laddER

Neuronal axons contain their own complement of cytoplasmic organelles, including endoplasmic reticulum (ER). It is challenging to explain how ER tubules are packed into the elongated axon of a neuronal cell. Zamponi *et al.* examined the ER in developing mammalian axons at nanometer resolution. The axonal ER intercalates and engages in close contacts with individual microtubules to make the "rungs" of ladder-like structures. In developing neurons, the ER axonal ladder acts as a reservoir for key components of the calcium-handling machinery. The ER-shaping protein Reticulon 2 (Rtn2) influences the architecture and dynamics of the ladder by linking ER tubules to kinesin motors on microtubules. Mutant Rtn2, which is linked to hereditary spastic paraplegia, disrupts the ladder by competing for kinesin binding, and thus impairs ER trafficking in axons. —SMH

Dev. Cell 10.1016/j.devcel.2022.05.002 (2022).

2D MATERIALS

Excitons confined

Using electric fields to confine neutral objects such as excitons, which consist of an electron and a hole, can be tricky. Thureja *et al.* used the Stark effect, which is the shifting of energy levels in the presence of electric fields, to engineer the confinement of excitons in monolayer molybdenum diselenide. The researchers applied an inhomogeneous in-plane electric field, which induced a permanent dipole moment for excitons, creating a potential minimum at the position of the field maximum. The repulsive interaction of excitons with free carriers further contributed to the confinement. This resulted in the quantization of exciton motional states, which was detected by measuring the sample's optical response. The technique may be useful in applications, as well as in fundamental studies. —JS

Nature 10.1038/s41586-022-04634-z (2022).

CHEMISTRY

N with four phenyls

Salts with nitrogen bound to four carbons are extremely common and find use in a variety of cleaning products. Surprisingly, however, the simple cation in which all four substituents are phenyl rings has eluded full characterization. The chief problem has been that the triphenylamine precursor is not sufficiently reactive to add the fourth ring. Fujita *et al.* surmounted that problem by appending (and later removing) *tert*-butyl substituents to the rings and applying radical coupling to form the fourth nitrogen–carbon bond. The cation, paired with a borate, crystallized with the rings canted in S_4 symmetry. —JSY

Nat. Commun. 10.1038/s41467-022-30282-y (2022).

OZONE HOLE

A bumpy road

The Antarctic stratospheric ozone hole has gradually been shrinking due to the decrease in anthropogenic emissions of ozone-depleting substances. However, in 2020 and 2021, it grew again to sizes among the largest on record. What was the reason for this? Yook *et al.* suggest that its growth was the result of the injection of anomalously large amounts of aerosols into the stratosphere by two episodic events: the Australian bushfires of 2020 and the volcanic eruption of La Soufriere on Saint Vincent in 2021. Southern Hemisphere surface climate also seems to have been influenced by these ozone holes. —HJS

Geophys. Res. Lett. 10.1029/2022GL098064 (2022).

PHOTO: ORVIL SAMUEL/AP IMAGES

The 2021 eruption of the La Soufriere volcano on the Caribbean island of Saint Vincent helped to increase the size of the Antarctic ozone hole later that year.

RESEARCH ARTICLE SUMMARY

NEURODEVELOPMENT

Spatial centrosome proteome of human neural cells uncovers disease-relevant heterogeneity

Adam C. O'Neill†, Fatma Uzbas†, Giulia Antognolli†, Florencia Merino†, Kalina Draganova, Alex Jäck, Sirui Zhang, Giorgia Pedini, Julia P. Schessner, Kimberly Cramer, Aloys Schepers, Fabian Metzger, Miriam Esgleas, Pawel Smialowski, Renzo Guerrini, Sven Falk, Regina Feederle, Saskia Freytag, Zefeng Wang, Melanie Bahlo, Ralf Jungmann, Claudia Bagni, Georg H. H. Borner, Stephen P. Robertson, Stefanie M. Hauck, Magdalena Götz*

INTRODUCTION: The centrosome is an interaction hub composed of two centrioles surrounded by pericentriolar material that collectively exerts many pancellular functions, such as cell division, cell migration, and cilia formation. The centrosome acts as the main microtubule-organizing center (MTOC) in many cells, including stem and progenitor cells, but loses this activity often during differentiation. Very little is known, however, about the extent of its cell type–specific composition and function. Individual proteins have been found to be specific to the centrosome of, for example, neural stem cell subtypes, but whether these are exceptions or the rule is unknown.

RATIONALE: To assess any potential cell type–specific functions of the centrosome, its composition needs to be further investigated. However, no comprehensive proteome of neural centrosomes exists to date, and hence, the differences in centrosome composition between neural and other cell types are unknown. Likewise, the extent of the changes in this organelle's distinct makeup during the differentiation of neural stem cells to neurons has not been explored. Because centrosome dysfunction is also linked to many neurodevelopmental conditions, information from such analysis could identify yet unknown disease associations.

RESULTS: To map the centrosome proteome of human neural stem cells and neurons, we chose a spatial proteomic approach to identify not only which proteins are present at this organelle but also where they are localized. Specifically, we selected 10 bait proteins known to localize to distinct sites of the centrosome, immunoprecipitated them from induced pluripotent stem cell–derived neural stem cells and neurons, and reproducibly determined their interactome with mass spectrometry. Interrogation of their interacting partners revealed diversity at this organelle, in which around 60% of the centrosome proteins had not yet been detected at the centrosome in other cell types. Furthermore, upon neuronal differentiation, more than half of these proteins become exchanged for new interactions at specific localizations within the centrosome. The neural centrosome proteomes comprise significantly enriched Gene Ontology terms of RNA-interacting proteins that were not observed in other cell types. Overlapping the neural stem cell and neuron centrosome proteomes with gene variants observed in patients with neurodevelopmental conditions of unknown etiology highlights specific and significant enrichment in epilepsy patients for the neuronal and, in periventricular heterotopia (PH), for the neural stem cell centrosome proteome. With respect to PH, we explored the effect of one candidate variant within the ubiquitously expressed gene that encodes the pre-mRNA processing factor 6 (PRPF6). We chose this candidate because several members of the PRPF6 complex were detected at the neural stem cell centrosome and had variants associated with PH. We show that the specific mutation of PRPF6 recapitulates aspects of the disease phenotype with ectopic cell localization in the periventricular region of the developing mouse cortex. Expression of the mutated form of PRPF6 results in misregulated splicing of, among others, the microtubule-associated protein kinase *Brsk2*. Coexpression of the correctly spliced form—but not the misspliced form, which lacks exon 19—with the mutant PRPF6 rescued the aberrant cell accumulation at the ventricle. The localization of *Brsk2* mRNA at the centrosome is consistent with a role for PRPF6 in bringing its splicing targets to the centrosome for local translation and fine tuning of microtubule function at the centrosome for proper migration out of the periventricular region.

CONCLUSION: Centrosome composition differs between cell types, offering a diversity that is important for development and disease. The ubiquitously expressed protein PRPF6 is enriched at the centrosome in neural stem cells but not neurons, which causes, when mutated, a PH-like phenotype. The extensive characterization of centrosome proteins unraveled in this study provides a rich resource with which to explore further disease associations and cell type– and stage-specific functions. ■

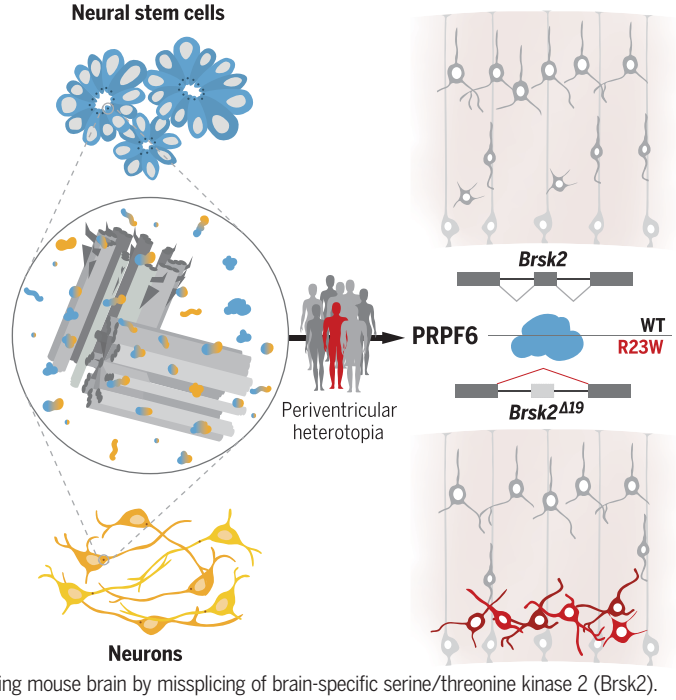

Neural centrosome proteome identifies disease candidates. Spatial proteomics of human neural stem cell and neuronal centrosomes uncovers cell type–specific protein hubs. Overlapping the proteomes with de novo mutations identified in patients with neurodevelopmental diseases revealed cell type–specific disease associations, enabling prioritization of disease variants. Among those, the expression of the PH-associated mutant R23W [in which arginine (R) at position 23 is replaced with tryptophan (W); red] PRPF6 (blue) recapitulated the periventricular cellular misplacement in the developing mouse brain by missplicing of brain-specific serine/threonine kinase 2 (Brsk2).

The list of author affiliations is available in the full article online.
***Corresponding author. Email: magdalena.goetz@helmholtz-muenchen.de**
†These authors contributed equally to this work.
Cite this article as A. C. O'Neill *et al.*, *Science* 376, eabf9088 (2022). DOI: 10.1126/science.abf9088

READ THE FULL ARTICLE AT
https://doi.org/10.1126/science.abf9088

RESEARCH ARTICLE

NEURODEVELOPMENT

Spatial centrosome proteome of human neural cells uncovers disease-relevant heterogeneity

Adam C. O'Neill[1,2]†, Fatma Uzbas[1,2]†, Giulia Antognolli[1,2]†, Florencia Merino[1,2]†, Kalina Draganova[1,2], Alex Jäck[1,2], Sirui Zhang[3,4,5], Giorgia Pedini[6], Julia P. Schessner[7], Kimberly Cramer[7,8], Aloys Schepers[9]‡, Fabian Metzger[10]§, Miriam Esgleas[1,2], Pawel Smialowski[1,2], Renzo Guerrini[11], Sven Falk[1,2], Regina Feederle[9,12], Saskia Freytag[13,14], Zefeng Wang[3,4,5], Melanie Bahlo[13,14], Ralf Jungmann[7,8], Claudia Bagni[6,15], Georg H. H. Borner[7], Stephen P. Robertson[16], Stefanie M. Hauck[10], Magdalena Götz[1,2,12]*

The centrosome provides an intracellular anchor for the cytoskeleton, regulating cell division, cell migration, and cilia formation. We used spatial proteomics to elucidate protein interaction networks at the centrosome of human induced pluripotent stem cell–derived neural stem cells (NSCs) and neurons. Centrosome-associated proteins were largely cell type–specific, with protein hubs involved in RNA dynamics. Analysis of neurodevelopmental disease cohorts identified a significant overrepresentation of NSC centrosome proteins with variants in patients with periventricular heterotopia (PH). Expressing the PH-associated mutant pre-mRNA-processing factor 6 (PRPF6) reproduced the periventricular misplacement in the developing mouse brain, highlighting missplicing of transcripts of a microtubule-associated kinase with centrosomal location as essential for the phenotype. Collectively, cell type–specific centrosome interactomes explain how genetic variants in ubiquitous proteins may convey brain-specific phenotypes.

The centrosome acts as a hub for the cytoskeleton and regulates many processes in development (*1*). It is composed of two centrioles of differing maturity, called the mother and daughter centrioles (*2*). Microtubules are anchored at the more mature mother centriole through its subdistal appendages (*3*). This feature is central to the function of the centrosome as the primary microtubule-organizing center (MTOC) in animal cells (*4*, *5*). Centrosomal MTOC activity changes during development, increasing, for example, in delaminating neural stem cells (NSCs) and decreasing in migrating neurons, a process that is regulated by the newly identified centrosomal protein formerly named AT-hook-containing transcription factor (AKNA) (*6*). Although centrosome proteomes have been cataloged for cancer cells and *Drosophila* (*7*–*10*), the dynamic relationship of AKNA with the centrosome highlights the need to comprehensively investigate the potential heterogeneity of centrosome interactors in brain cells. We identified the centrosome proteome of human NSCs and neurons, showing their cell type–specific relevance to the neurodevelopmental disorder periventricular heterotopia (PH).

Results

Spatial centrosome proteome of NSCs and neurons

To investigate the centrosome proteome of human NSCs and neurons, induced pluripotent stem cells (iPSCs) were differentiated toward a dorsal forebrain identity (Fig. 1A) (*11*). At day 15 of differentiation, almost all cells (96.6%) were PAX6$^+$ NSCs (Fig. 1, B and D, and fig. S1A), whereas neurons reached high purity at around day 40 (Fig. 1, C and D, and fig. S1A) and exhibited known centrosome dynamics, such as NINEIN loss from this organelle (Fig. 1, E to G) (*12*). We therefore chose these time points to probe the centrosome proteomes of NSCs and neurons by using mass spectrometry.

To inform about the spatial distribution of the interactors at the centrosome, we designed an affinity purification strategy that targets 10 different "bait" proteins essential for correct centrosome function, each localizing at different regions within this organelle (Fig. 1H) (*13*). In NSC cultures harvested at day 15 from four biological replicates, 1401 high-confidence interactions comprising 751 proteins were identified, including many centrosomal proteins from curated reference lists and previous studies (*14*–*18*), thus underscoring the robustness of the approach (Fig. 1H; figs. S1, D to F, and S2H; and table S1). We detected 480 proteins that were not allocated to the centrosome in previously studied cell types (Fig. 1I). As expected, the NSC centrosome proteome is enriched for Gene Ontology (GO) terms related to cell division and microtubule organization, among others (Table 1). However, among the highly significant GO terms (*P* values are provided in Table 1) were also mRNA processing, splicing, and metabolism, which were not present in previous centrosome datasets analyzed in the same manner (Table 1 and table S4). Overlapping protein-protein interaction networks of multiple baits can inform on spatial distribution and organellar dynamics (*19*). We therefore clustered the protein interactions for these 10 bait proteins within a force-directed layout by use of Cytoscape. Bait-prey positions within the network are dependent on their common interactions with other bait proteins, as shown in the spatial projection (Fig. 1, L and M). This revealed enrichment of RNA-interacting proteins at specific baits, including the subdistal appendage proteins centrosomal protein of 170 kDa (CEP170) and outer dense fiber of sperm tails 2 (ODF2) (Fig. 1M). Centrosome localization of these RNA-interacting proteins was not dependent on microtubules because they persisted in the centrosome interactome of NSCs after treatment with microtubule-depolymerizing nocodazole (fig. S3 and tables S1 and S3). Thus, the centrosome interactors detected in NSCs may shed light on brain-specific functions at the centrosome.

To ask whether these interactions were brain-specific or NSC-specific, we applied affinity purification of the same 10 bait proteins in neurons, collected at day 40 of iPSC differentiation (Fig. 1, C and D). This revealed 786 proteins enriched at the centrosome in neurons (Fig. 1, H and J, and tables S2 and S3), with about half of the centrosome interactome present only at one stage—59% in neurons and 57% in NSCs (Fig. 1K). Of these, the majority (64 and 57% in NSCs and neurons, respectively) were not present in other centrosome datasets (Fig. 1, I to K). RNA-related

[1]Physiological Genomics, Biomedical Center (BMC), Ludwig-Maximilians-Universitaet (LMU), Großhaderner Straße 9, 82152 Planegg-Martinsried, Germany. [2]Institute of Stem Cell Research, Helmholtz Center Munich, German Research Center for Environmental Health, Großhaderner Straße 9, 82152 Planegg-Martinsried, Germany. [3]CAS Key Laboratory of Computational Biology, Biomedical Big Data Center, Shanghai Institute of Nutrition and Health, Chinese Academy of Sciences, Shanghai 200031, China. [4]University of Chinese Academy of Sciences, Chinese Academy of Sciences, Shanghai 200031, China. [5]CAS Center for Excellence in Molecular Cell Science, Chinese Academy of Sciences, Shanghai 200031, China. [6]Department of Biomedicine and Prevention, University of Rome Tor Vergata, Via Montpellier 1, 00133 Rome, Italy. [7]Max Planck Institute of Biochemistry, Martinsried, Germany. [8]Faculty of Physics and Center for Nanoscience, LMU, Munich, Germany. [9]Monoclonal Antibody Core Facility, Institute for Diabetes and Obesity, Helmholtz Center Munich, German Research Center for Environmental Health, 85764 Neuherberg, Germany. [10]Research Unit Protein Science and Metabolomics and Proteomics Core, Helmholtz Centre Munich, German Research Center for Environmental Health, 85764 Neuherberg, Germany. [11]Neuroscience Department, Children's Hospital Meyer–University of Florence, Florence, Italy. [12]SYNERGY, Excellence Cluster of Systems Neurology, Biomedical Center, LMU, Planegg-Martinsried, Germany. [13]Personalised Oncology Division, The Walter and Eliza Hall Institute of Medical Research, Parkville, VIC 3052, Australia. [14]Department of Medical Biology, University of Melbourne, Melbourne, VIC 3010, Australia. [15]Department of Fundamental Neurosciences, University of Lausanne, Rue du Bugnon 9, 1005 Lausanne, Switzerland. [16]Department of Women's and Children's Health, Dunedin School of Medicine, University of Otago, Dunedin, New Zealand.
†These authors contributed equally to this work. ‡Present address: Institute of Epigenetics and Stem Cells, Helmholtz Zentrum München, Marchioninistrasse 25, 81377 München, Germany. §Deceased.
*Corresponding author. Email: magdalena.goetz@helmholtz-muenchen.de

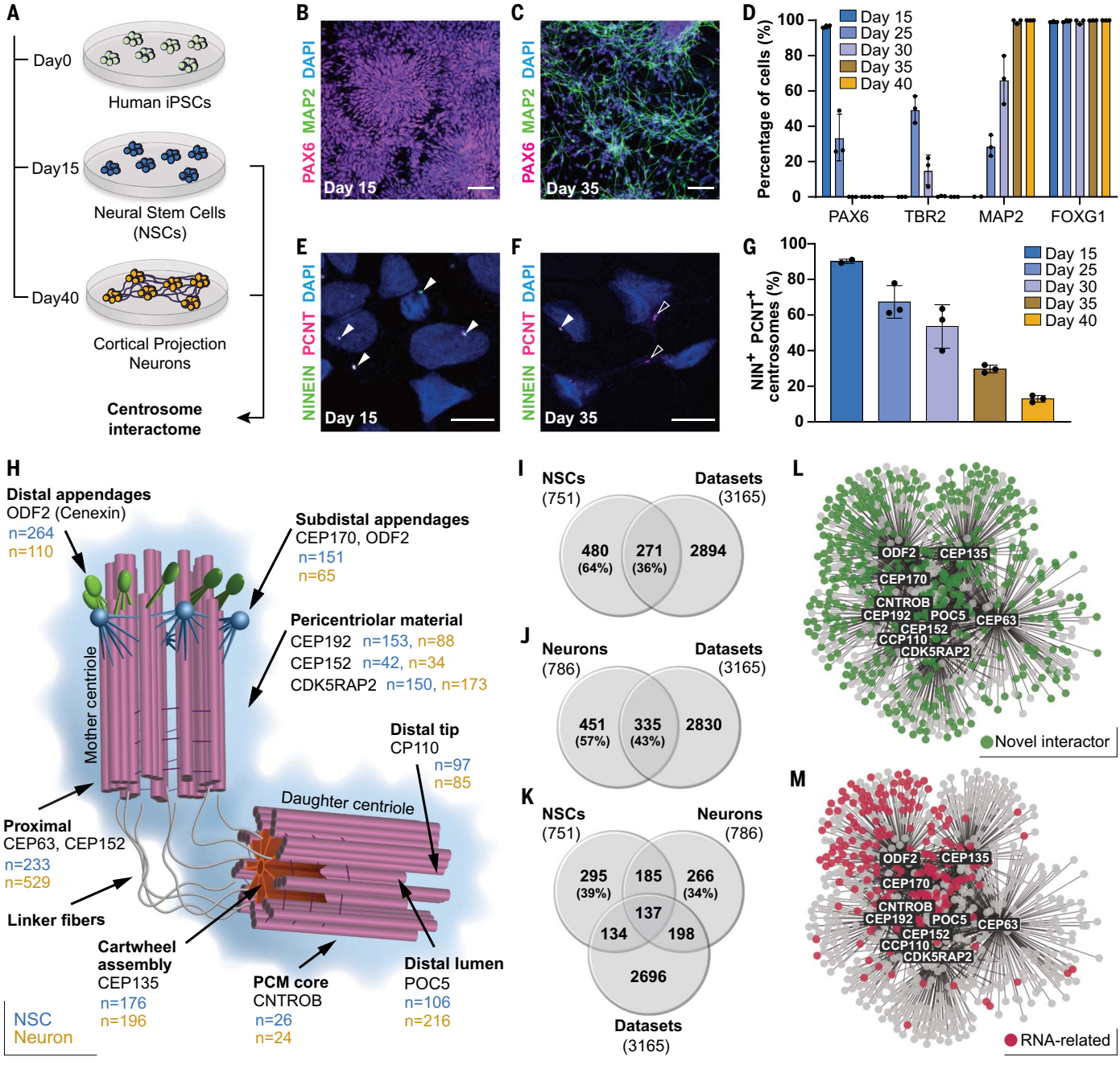

Fig. 1. Spatiotemporal profiling of the neural centrosome interactome. (**A**) Schematic overview of the study design. (**B** to **G**) Immunostainings of human iPSC-derived cells at the stages indicated for antigens indicated on the left, quantified in (D) and (G). Scale bars, (B) and (C) 50 μm; (E) and (F) 10 μm. (**H**) Schematic representation of the mammalian centrosome with the position of the 10 bait proteins indicated, informed by (*13*, *64*), and the number of interactors (*n*) in NSCs (blue) and neurons (yellow). (**I** to **K**) Comparison of the iPSC-derived (I) NSC and (J) neuron centrosome-interactome, with the pooled human centrosome protein list derived from curated databases (*14*, *17*, *18*) and previously published BioID screens (*15*, *16*) and (K) with each other. (**L** and **M**) Force-directed bait-prey interactome of NSCs, with (L) previously unidentified interactors [not found in the datasets in (I) to (K)] (green) and (M) proteins associated with splicing and RNA export-related GO terms (red) highlighted.

functions, such as RNA localization or RNA metabolic processes, remained the top GO terms in both neural proteomes (Table 1 and tables S4 and S8), with RNA splicing selectively enriched in the NSC centrosome proteome (Table 1 and figs. S2, A to F), comprising a complex of pre-mRNA-processing factor 6 (PRPF6), apoptotic chromatin condensation inducer 1 (ACIN1), DEAD-box helicase 23 (DDX23), and protein virilizer homolog (VIRMA/KIAA1429).

Visualization of the spatial centrosome interactomes shows that changes during neuronal differentiation are bait-specific (Fig. 2A; specificity of baits at the centrosome is provided in fig. S4). Most interactors lost during differentiation (significantly enriched at the centrosome in NSCs, but no longer in neurons) are associated with the baits ODF2 and CEP170 at the subdistal appendages and the baits CDK5 regulatory subunit associated protein 2 (CDK5RAP2) and centrosomal protein of

Table 1. GO enrichment for this and previous centrosome databases. Numbers indicate the false discovery rate (FDR) for each term in each dataset indicated (stringency cutoff, 5%). Terms are sorted in ascending order of the FDR difference between NSC and neurons. Complete lists of GO terms are provided in tables S4 and S8.

GO identifier	GO biological process	NSCs	Neurons	Curated databases	BioID screens
GO:0008380	RNA splicing	2.4×10^{-107}*	2.02×10^{-34}		
GO:0016071	mRNA metabolic process	2.4×10^{-107}*	2.19×10^{-66}		
GO:0006405	RNA export from nucleus	4.85×10^{-29}*	2.83×10^{-8}		
GO:0031503	Protein-containing complex localization	6.55×10^{-25}	2.25×10^{-8}	1.39×10^{-16}	3.87×10^{-12}
GO:0006403	RNA localization	2.79×10^{-31}*	5×10^{-17}*		1.21×10^{-6}
GO:0051301	Cell division	2.18×10^{-6}	0.00093	1.39×10^{-38}	7.55×10^{-22}
GO:0071826	Ribonucleoprotein complex subunit organization	1.56×10^{-30}	4.08×10^{-28}		
GO:0000278	Mitotic cell cycle	1.13×10^{-12}	1.18×10^{-14}	2.55×10^{-59}	1.74×10^{-29}
GO:0007018	Microtubule-based movement		0.006	4.69×10^{-58}	7.06×10^{-10}
GO:0007163	Establishment or maintenance of cell polarity		0.0015	1.24×10^{-5}	1.97×10^{-9}
GO:0031023	Microtubule organizing center organization	5.62×10^{-7}	2.16×10^{-10}	9.55×10^{-31}	2.28×10^{-17}
GO:0007098	Centrosome cycle	4.7×10^{-7}	1.28×10^{-10}	6.23×10^{-31}	7.97×10^{-16}
GO:0030705	Cytoskeleton-dependent intracellular transport	0.0078	7.14×10^{-8}	1.25×10^{-26}	9.92×10^{-13}
GO:0030048	Actin filament-based movement		7.33×10^{-6}		
GO:0033119	Negative regulation of RNA splicing		7.07×10^{-6}		
GO:0002252	Immune effector process	0.0022	7.77×10^{-9}		0.0314
GO:0006417	Regulation of translation	2.23×10^{-16}	3.55×10^{-24}		0.0231
GO:0032886	Regulation of microtubule-based process	0.039	5.51×10^{-10}	1.45×10^{-28}	1.52×10^{-12}
GO:0007399	Nervous system development		5.29×10^{-9}	1.96×10^{-12}	1.34×10^{-5}
GO:0000226	Microtubule cytoskeleton organization	4.23×10^{-12}	1.91×10^{-20}	4.03×10^{-94}	6.97×10^{-38}
GO:0070507	Regulation of microtubule cytoskeleton organization	0.0161	1.41×10^{-11}	1.05×10^{-24}	1.89×10^{-16}
GO:0051640	Organelle localization	3.83×10^{-8}	1.14×10^{-19}	2.78×10^{-49}	3.1×10^{-51}
GO:0030036	Actin cytoskeleton organization		4.29×10^{-14}*		6.97×10^{-6}
GO:0030030	Cell projection organization	0.0013	7.58×10^{-19}	2.56×10^{-83}	5.51×10^{-30}
GO:0060271	Cilium assembly	0.00011	5.16×10^{-20}	1.7×10^{-106}	2.71×10^{-35}
GO:0097711	Ciliary basal body-plasma membrane docking	4.86×10^{-11}	6.19×10^{-27}	7.96×10^{-42}	2.94×10^{-39}
GO:0008104	Protein localization	3.16×10^{-10}	4.06×10^{-34}	1.96×10^{-33}	8.16×10^{-52}
GO:0007010	Cytoskeleton organization	3.83×10^{-12}	1.24×10^{-37}	1.37×10^{-60}	5.64×10^{-40}
GO:0006996	Organelle organization	4.42×10^{-14}	9.78×10^{-41}	1.4×10^{-76}	2.32×10^{-61}
GO:0000184	Nuclear-transcribed mRNA catabolic process, nonsense-mediated decay	1.32×10^{-10}	1.36×10^{-42}*		
GO:0006612	Protein targeting to membrane		1.15×10^{-33}*		
GO:0072599	Establishment of protein localization to endoplasmic reticulum		9.06×10^{-40}*		
GO:0006413	Translational initiation	1.83×10^{-10}	2.54×10^{-51}*		

*The notable terms for either cell type.

192 kDa (CEP192) associated with the pericentriolar material (Fig. 2A). This fits with the known loss of centrosome MTOC activity during neuronal differentiation (*6*, *20*), the reduction of CEP170 at the centrosome during cell differentiation, and the role of CEP192 in controlling the balance of centrosomal and noncentrosomal MTOC (*21*–*23*). Centrosome interactors gained in neurons were often associated with centrosomal protein of 63 kDa (CEP63), forming interactions with the actin network and included RNA-interacting proteins enriched at different baits (Fig. 2B and fig. S2) as compared with those in NSCs (Fig. 1M).

Although these dynamic changes imply confidence in the selectivity of the centrosome interactors, we further probed this by comparing with the total cellular proteome (*24*, *25*) of NSCs and neurons differentiated from the same human iPSC line by using the protocol described above. Most of the proteins detected as significantly enriched at the centrosome in neurons, but not NSCs (or vice versa), were not regulated between these cell types within the total proteomes, including proteins further highlighted in this study (fig. S2, I and J). The overall abundance of bait proteins did not change between NSCs and neurons either, with the exception of CEP170 and Centrobin (CNTROB), which are higher in neurons (fig. S2J), but their number of interactors was reduced in neurons or remained the same, respectively (Fig. 1D). Consistent with the lower number of interactors of CEP170 (fig. S1D), its centrosomal association has been shown previously to decrease during differentiation (*23*), and we also found reduced levels at the centrosome by means of immunostaining (fig. S4). Overall, these data corroborate the specificity of the centrosome enrichment in different cell types.

Because the above data suggest neural cell–type specificity of centrosome-interacting proteins with a preponderance to RNA binding and RNA-processing factors in both neural cell types, we next validated sets of those with immunostaining (Fig. 2, C to H, and fig. S5, K to Q) or Western blotting after coimmunoprecipitation with the respective bait proteins (Fig. 2, I to K, and fig. S5, A to J). The centrosome association of the exon-junction proteins (MAGOH

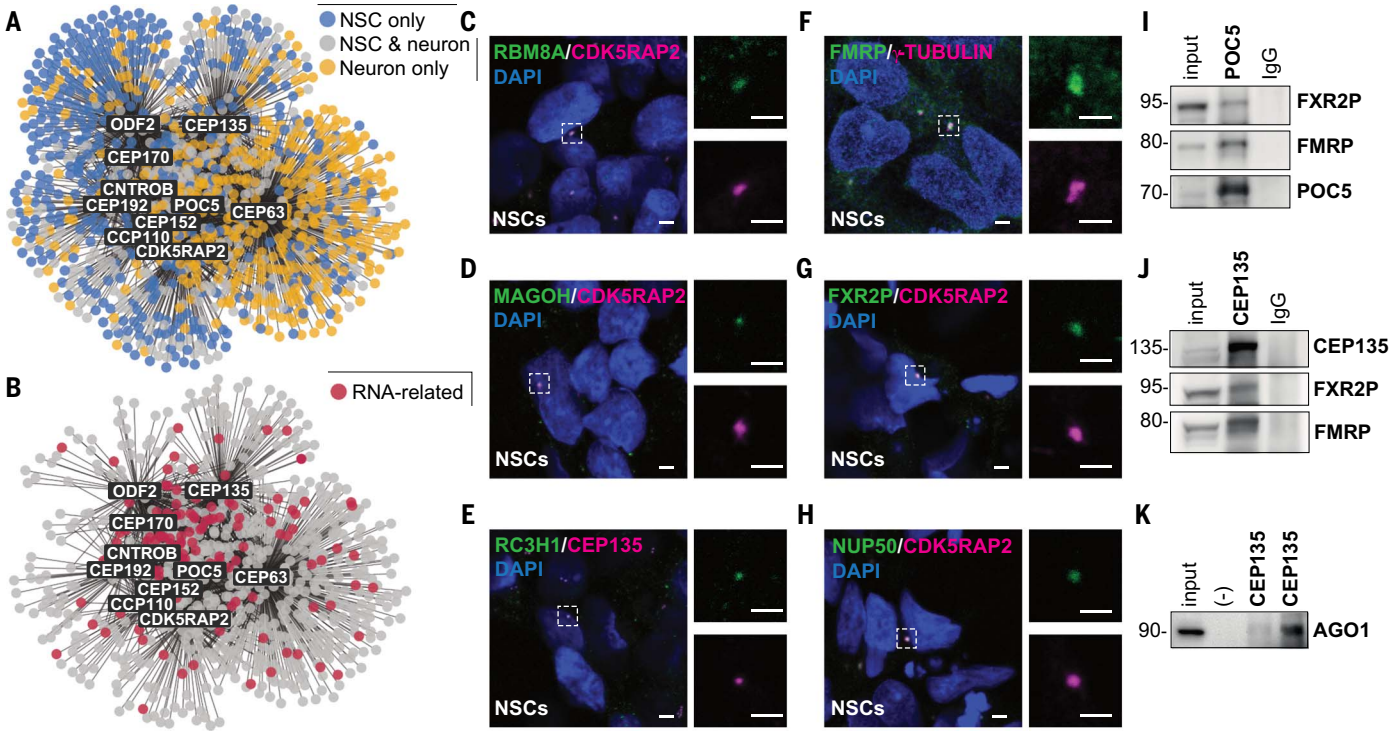

Fig. 2. Cell type–specific RNA-processing proteins at the centrosomes. (**A**) Combined view of the force-directed bait-prey interactomes of the NSC and neuron centrosomes. (**B**) Proteins associated with splicing and RNA export-related GO terms (red) at the neuronal centrosome (NSCs are provided in Fig. 1M). (**C** to **H**) Immunostainings confirming the localization of selected RNA binding proteins at the centrosome in human iPSC-derived NSCs at day 16. White dashed boxes outline colocalization of the proteins indicated in green, with the centrosomal markers in magenta shown to the right in higher magnification. Scale bars, 2.5 μm. (**I** to **K**) Coimmunoprecipitation with bait proteins followed by Western blotting of the indicated preys to validate the liquid chromatography–mass spectrometry (LC-MS)/MS findings. [(I) and (J)] FMRP and FXR2P were pulled down by bait proteins POC5 and CEP135 at day 15, and (K) AGO1 was pulled down by CEP135 at day 35. Further confirmations are available in fig. S5.

Table 2. Overlapping neurodevelopmental disease cohorts and centrosome proteomes. Shown is analysis of the de novo variants per disease gene set per protein list, assessed by means of exact binomial test with Benjamini-Hochberg correction. *P* values were calculated by means of exact binomial test (two-tailed) with Benjamini-Hochberg correction (FDR 0.05). ASD, autism spectrum disorder; PH, periventricular nodular heterotopia; ID, intellectual disability; EE, epileptic encephalopathy; PMG, polymicrogyria.

	Centrosome datasets (*n* = 3165)			NSCs (*n* = 751)			NSCs microtubule-independent (*n* = 625)			Neurons (*n* = 786)		
Disease gene-set*	Expected events	Observed events	*P* value	Expected events	Observed events	*P* value	Expected events	Observed events	*P* value	Expected events	Observed events	*P* value
ASD (*n* = 1918)	285	453	3.26×10^{-23}†	78	135	9.16×10^{-9}†	63	112	6.37×10^{-8}†	76	152	1.16×10^{-14}†
EE (*n* = 356)	53	58	0.5702	14	20	0.1726	12	18	0.1200	14	23	0.0333†
ID (*n* = 192)	29	50	0.0002†	8	13	0.1086	6	9	0.3806	8	18	0.0016†
PH (*n* = 202)	30	34	0.7147	8	16	0.0273†	7	15	0.0104†	8	10	0.4653
PMG (*n* = 86)	13	11	0.7612	3	5	0.4020	3	4	0.3695	3	7	0.1061

*Number of individuals (*n*). †Significant *P* values.

and RBM8A), RNA binding protein Roquin-1 (RC3H1), translation regulators FMRP and FXR2P, RNA processing complex member AGO1, and the nucleoporin NUP50 (Fig. 2, C to K, and fig. S5) [other nucleoporins at the centrosome are available in (*26*)] was confirmed in cultured cells and human fetal cortex samples (fig. S5, I and J). For the latter, we chose gestational week 18 as a later stage of cortex neurogenesis, with many neurons still migrating, which would be most comparable with the stages analyzed in vitro. Thus, three sets of analyses confirm the reliability and specificity of our centrosome interactome analysis.

Significant overlap with specific neurodevelopmental disease cohorts

We next asked whether these neural proteome datasets could be used to inform on genetic variants of unknown etiological relevance in individuals with neurodevelopmental disease. The proteins identified in our centrosome

Table 3. PH-associated de novo variants within individual bait interactomes. Analysis of de novo variants for PH gene-set within the proteome of individual baits in NSCs, assessed by means of exact binomial test with Benjamini-Hochberg correction (FDR 0.05).

NSC, all		NSC, microtubule-independent	
Bait protein	***P* value**	**Bait protein**	***P* value**
CDK5RAP2 (*n* = 150)	0.3318	CDK5RAP2 (*n* = 97)	0.7846
Centrobin (*n* = 26)	0.3808	Centrobin (*n* = 3)	0.0751
CEP63 (*n* = 233)	0.8336	CEP63 (*n* = 176)	0.7785
CEP135 (*n* = 176)	0.3000	CEP135 (*n* = 158)	0.3627
CEP152 (*n* = 42)	1	CEP152 (*n* = 29)	1
CEP170 (*n* = 151)	0.0220*	CEP170 (*n* = 119)	0.0074*
CEP192 (*n* = 153)	0.1634	CEP192 (*n* = 112)	0.0202*
CP110 (*n* = 97)	0.3855	CP110 (*n* = 84)	0.4209
ODF2 (*n* = 264)	0.0107*	ODF2 (*n* = 220)	0.0047*
POC5 (*n* = 106)	0.7534	POC5 (*n* = 86)	0.8335

*Significant *P* values.

proteomes and other publicly available centrosome interactors (*14*–*18*) were overlaid with genes harboring rare de novo variants (DNVs) identified in patients with various neurodevelopmental disorders that still await genetic diagnosis (*27*–*34*). Comparing the overlap of the centrosome proteomes with neurodevelopmental disease cohorts identified several significant overlaps (Table 2 and table S5) that are beyond that expected from natural genetic variation (*35*). First, we observed that autism spectrum disorder (ASD) DNVs showed significant enrichment in all centrosome datasets, supporting pancellular centrosome proteins in disease etiology. Another significant association was observed between DNVs in patients with intellectual disability (ID) and both published centrosome datasets and our neuronal centrosome proteome. Because neurons do not divide, neuronal centrosomes may be particularly relevant for ID owing to their role in cilia formation and function. Conversely, only the NSC centrosome proteome was significantly enriched for proteins encoded by loci with DNVs in the PH cohort databases (Table 2). The failure of some cells to move away from the ventricular lining in PH (*36*) may relate to the centrosomal MTOC activity in NSCs mediating delamination of cells from the ventricle (*6*, *37*). Consistent with this hypothesis, the majority (88%) of the NSC centrosome proteins with DNVs in PH were associated with baits located at microtubule-anchoring centrosome positions (Table 3 and table S5). Almost all (15 of 16) of these proteins driving the PH association were interacting with the centrosome in a microtubule-independent manner (still present in the nocodazole-treated condition) and hence are direct centrosome interactors. Taken together, these data suggest a link between our neural centrosome data and specific neurodevelopmental diseases, with proteins of the NSC and neuronal centrosome proteome enriched in distinct disease cohorts.

PRPF6 variant recapitulates aspects of PH

To determine whether centrosome association of certain proteins indeed helps prioritize DNVs with functional relevance, we investigated the dynamic enrichment of PH DNVs within the centrosome proteomes. Among the microtubule-independent NSC centrosome interactors with PH DNVs, we found four members of an RNA-processing complex: ACIN1, DDX23, KIAA1429, and PRPF6 (Table 2 and tables S1 and S3). Members of this complex were significantly enriched within a set of 40 candidate PH genes whose expression patterns mimic those of known PH loci within human brain transcriptomic data, supporting a relationship to the disease (fig. S6, A and B, and table S6). This prompted us to focus our analysis on the ubiquitously expressed protein PRPF6 because its centrosomal localization along with its associated PH interactors may explain how mutations in this complex induce neurodevelopmental phenotypes. As predicted by the proteome analysis and confirmed with down-regulation, PRPF6 is enriched at the centrosome of NSCs and binds centrosomal and RNA-interacting proteins (Fig. 3, A to F, and fig. S6, E to H). Affinity purification of the RNA binding protein PRPF6 within the human iPSC-derived NSCs pulled down 297 proteins, of which 111 were shared with centrosome proteome (tables S1 and S7), and included a protein complex significantly enriched for genes with DNVs in patients with PH (fig. S6C). This reinforces the plausibility of a contribution of PRPF6 centrosomal localization to the disease phenotype caused by this otherwise ubiquitous protein.

The DNV in *PRPF6* was identified in a male patient born from healthy nonconsanguineous parents, was diagnosed with delayed developmental milestones, and had experienced a single convulsive seizure at 3 years of age. He had severe ID and was nonverbal. Head circumference was at the seventh percentile; brain magnetic resonance imaging (MRI) showed bilateral PH with mildly enlarged Sylvian fissures, and mild frontal lobe and cerebellar hypoplasia. Specifically, the patient has a single, rare (not observed in large genomic sequence datasets) de novo missense variant [c.67C>T, p.Arg23Trp; RefSeq NM_012469.4 (GRCh37)] localized in the Prp1 domain of PRPF6 that directly targets RNA for splicing (*38*). The variant is predicted to be deleterious on the basis of the high Polyphen score and low residual variation intolerance score (*32*).

In the developing mouse brain, *Prpf6* is expressed in both neurons and progenitors (fig. S6D), which is consistent with its overall ubiquitous expression (*39*). Following previous modeling of PH in the developing mouse brain (*40*–*42*), we used in utero electroporation (IUE) to introduce constructs expressing either control [green fluorescent protein (GFP)], wild type ($PRPF6^{WT}$), or $PRPF6^{R23W}$ mutant [in which arginine (R) at position 23 is replaced with tryptophan (W)] into the mouse cortex at embryonic day 13 (E13) (fig. S7, A to C). Analysis at 3 days after electroporation (at E16) showed significantly more GFP^+ cells expressing $PRPF6^{R23W}$ in the periventricular area (Bins 1 and 2, comprising the ventricular and subventricular zones, respectively), with fewer cells reaching the neuronal layers in the cortical plate (Bins 4 and 5) relative to the cells expressing the wild-type form (fig. S7, A to D). Most of the cells expressing $PRPF6^{R23W}$ that were stuck in the subventricular zone succumbed to cell death (fig. S7, E to H), and by 5 days after electroporation at E18, most GFP^+ cells had reached the outer bins in all three conditions (Fig. 3, G to J). However, a significantly increased fraction of cells expressing $PRPF6^{R23W}$ remained located at the periventricular area (Fig. 3, I and J) in a pattern reminiscent of the heterotopia in PH patients. Although this phenotype may not reflect all aspects detected in human patients, the finding of only a minority of cells placed ectopically in periventricular regions, whereas most made it into a normal-appearing grey matter, reflects a common hallmark in PH.

Immunostainings for the NSC marker PAX6, the progenitor marker TBR2, and the neuronal marker TBR1 revealed the mixed composition of the periventricular GFP^+ cells in all three conditions at E18 (Fig. 3, K to S). Most were $PAX6^+$ (Fig. 3, K to M and Q), many were $TBR2^+$ (Fig. 3, K to M and R), and some were $TBR1^+$ (Fig. 3, N to P and S). However, the proportion of $PAX6^+$ NSCs was significantly decreased, whereas neurons were increased in the $PRPF6^{R23W}$ condition (Fig. 3, Q and S). Thus, deficits in delamination and/or migration

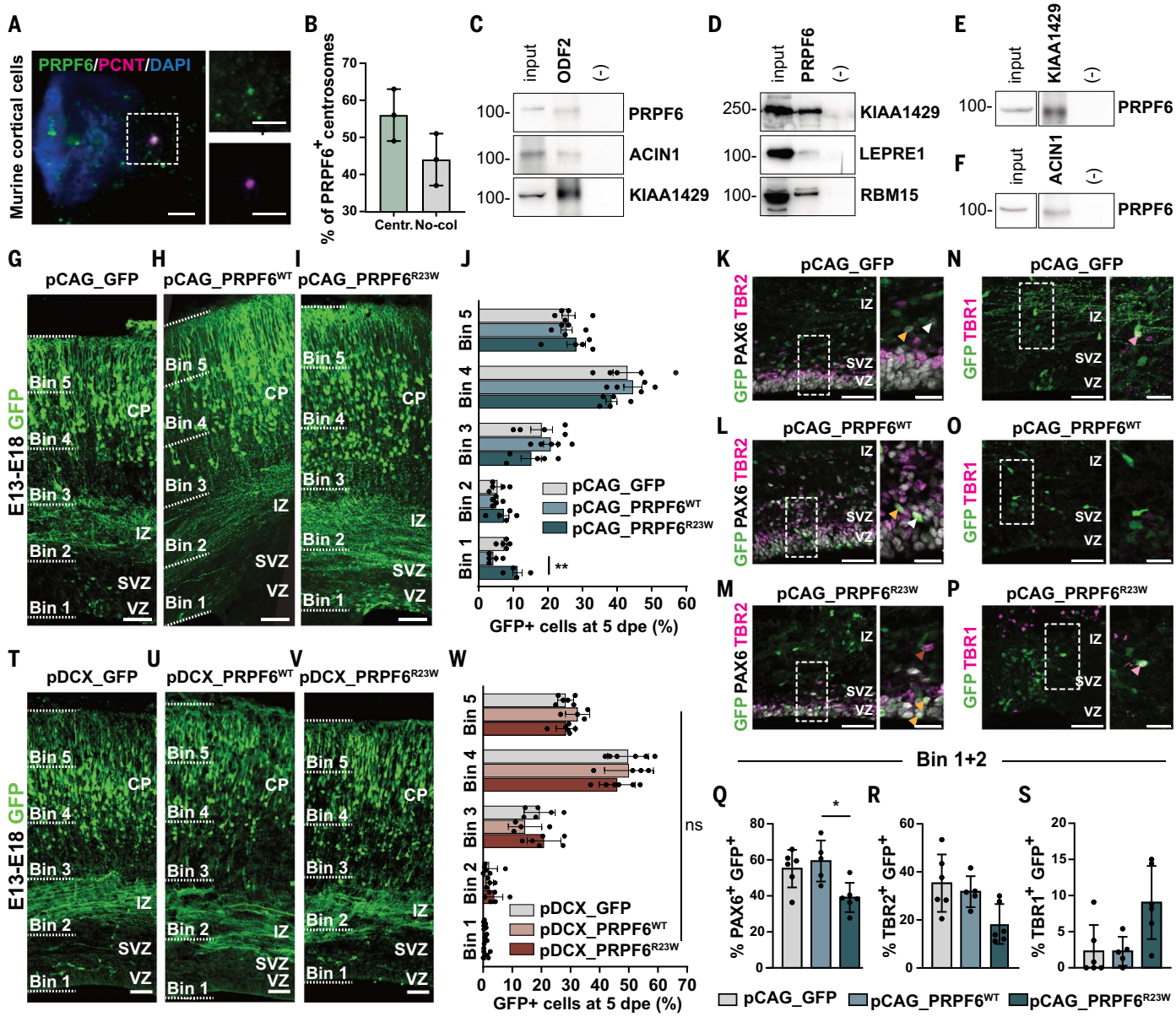

Fig. 3. Centrosomal PRPF6 and its role in PH. (**A**) E14 mouse cortical cells at 3 days in vitro stained as indicated, and (**B**) colocalization quantified (n = 300 in three independent replicates indicated as mean ± SD). Scale bars, 2.5 μm. (**C** to **F**) Coimmunoprecipitation (immunoprecipitation indicated at top) followed by Western blot (antibodies indicated at right) from day 15 iPSC-derived NSCs. (**G** to **I**, **K** to **P**, and **T** to **V**) Coronal sections of E18 mouse cerebral cortices electroporated at E13 with [(G), (K), (N), and (T)] GFP-only control, [(H), (L), (O), and (U)] PRPF6^{WT}, or [(I), (M), (P), and (V)] PRPF6^{R23W} under [(G) to (I) and (K) to (P)] CAG or [(T) to (V)] doublecortin promoter, immunostained as indicated. (**J**) Quantification of (G) to (I) and (**W**) Quantification of (T) to (V). (**Q** and **R**) Quantification of (K) to (M) and (**S**) Quantification of (N) to (P) for GFP$^+$ cells double-positive for the respective markers in Bin 1 and Bin 2; n = embryo; mean ± SD; unpaired two-tailed Kruskal-Wallis test followed with Dunn's multiple comparison; *P < 0.05. Scale bars, (G) to (I) and (T) to (V), 100 μm; (K) to (P), left, 50 μm; (K) to (P), right, 20 μm. Arrows in the periventricular region indicated in (K) to (P) represent double-positive (yellow, white, and pink) or triple-positive (red) cells. VZ, ventricular zone; SVZ, subventricular zone; IZ, intermediate zone; CP, cortical plate; dpe, days post-electroporation.

rather than a failure to differentiate seem to be involved in the periventricular cell positioning. Therefore, we aimed to determine whether the ectopic positioning would also occur when GFP, PRPF6^{WT}, and PRPF6^{R23W} were expressed only in young neurons and differentiating progenitors under the doublecortin regulatory elements (*6*). IUE at E13 followed by analysis at E18 showed no significant difference in the distribution of GFP$^+$ cells for any of the conditions and no ectopic cells in the lower bins (Fig. 3, T to W), suggesting that placement of cells expressing mutant PRPF6 in the periventricular region occurs at earlier stages, before neuronal differentiation. This finding is in agreement with the preferential interaction of the PRPF6 splicing complex with the NSC compared with the neuronal centrosome.

Correctly spliced Brsk2 rescues PRPF6-induced PH

To better understand the etiology of this phenotype, we explored the role of PRPF6 as a

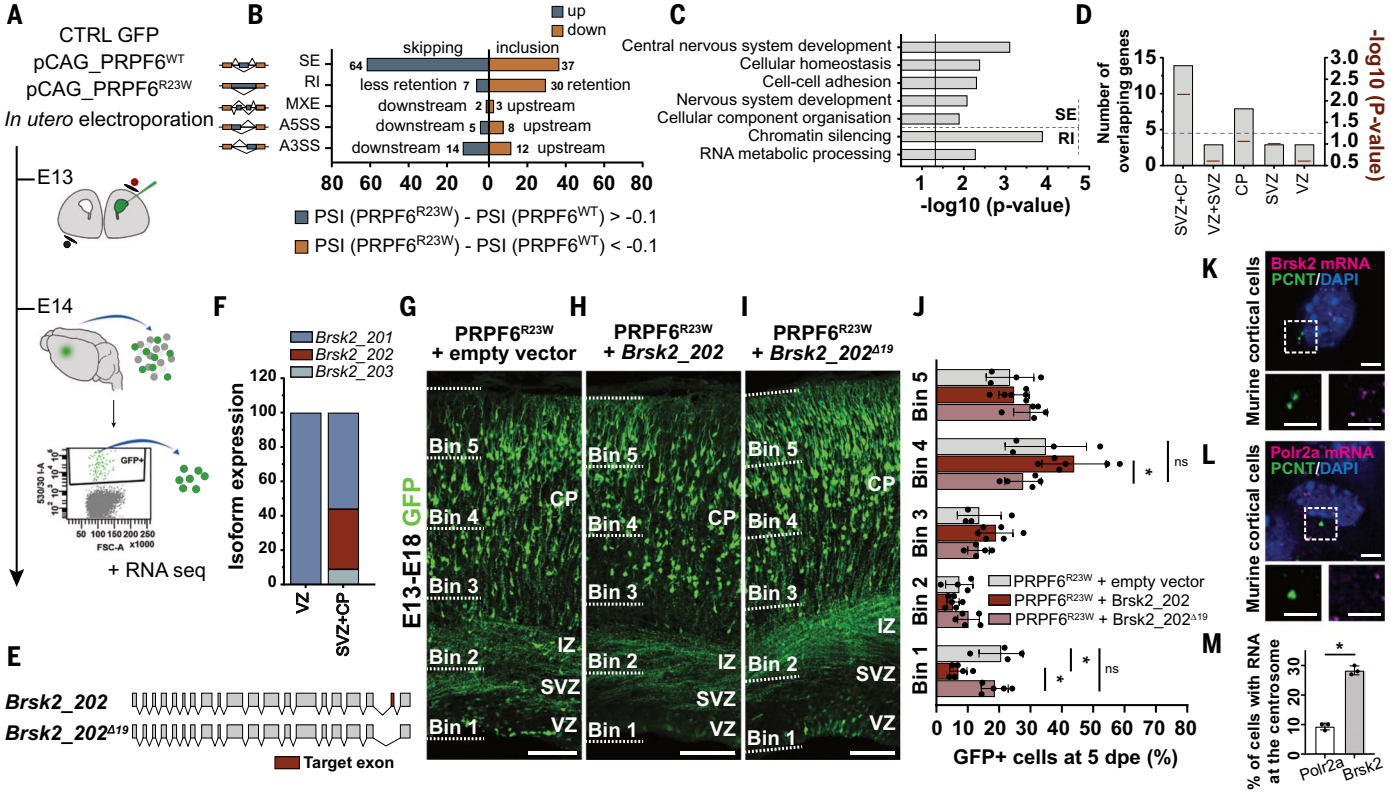

Fig. 4. PRPF6^{R23W} affects splicing in the PH phenotype. (**A**) Schematic representation of the experimental protocol. (**B**) Summary of the splicing changes (indicated as numbers) in cells expressing PRPF6^{R23W} versus PRPF6^{WT}. SE, skipped exon; RI, intron retention; MXE, mutually exclusive exon; A5SS, alternative donor site; A3SS, alternative acceptor site. PSI; percent spliced-in. (**C**) GO analysis (biological processes) of genes with SE or RI in PRPF6^{R23W} versus PRPF6^{WT}-expressing cells. (**D**) Quantification of the number of genes differentially spliced and preferentially expressed in the indicated regions. *P* values with scale are shown on right *y* axis as red bars (Fisher's Exact test, two-tailed, with Benjamini-Hochberg correction). (**E**) Exons (boxes) encoding the *Brsk2_202* transcript isoforms (red; skipped exon in PRPF6^{R23W} cells), introns (lines). (**F**) Regional expression of Brsk2 isoforms (*23*). (**G** to **I**) Coronal sections of E18 mouse cortices coelectroporated at E13 as indicated at top. (**J**) Quantification of (G) to (I) (*n* = embryo; mean ± SD; unpaired two-tailed Kruskal-Wallis test followed with Dunn's multiple comparison; **P* < 0.05). (**K** and **L**) Single-molecule FISH (magenta) and immunostaining in embryonic mouse cortical cells (3 days in vitro). The white dashed boxes are expanded in the bottom insets. (**M**) Quantification of (K) and (L) (*n* = 300 cells from three independent cultures; mean ± SD; unpaired one-tailed Mann-Whitney test; * *P* < 0.05). Scale bars, (G) to (I) 100 μm; (K) and (L) 2.5 μm. Abbreviations are as in Fig. 3.

regulator of the spliceosome machinery (*38*, *43*). To do so, we performed RNA-sequencing on flow cytometry–purified GFP^{+} cells at 1 day after electroporation (at E14), before any phenotype could be observed (Fig. 4A and fig. S8, A to D). Only two genes (VCAM1 and a collagen) were differentially expressed between PRPF6^{WT}- and PRPF6^{R23W}-expressing cells (fig. S8E). Using the mixture-of-isoforms (MISO) statistical model, which assigns a "percentage spliced in" (PSI) value to each splicing event (*44*), and choosing the stringent Bayes factor >5, a total of 182 alternative splice events in 166 separate genes were found to be significantly changed between PRPF6^{WT} with PRPF6^{R23W} GFP^{+} cells (Fig. 4B). These changes encompassed all types of alternative splicing events: 101 alternative cassette exons, 37 intron retention events, five mixed spliced events, as well as 13 and 26 events for alternative donor and acceptor sites, respectively (Fig. 4B). Cells expressing PRPF6^{R23W} showed a bias toward two categories: cassette exon-skipping and intron retention (Fig. 4B), as validated with quantitative reverse transcription polymerase chain reaction (RT-PCR) (fig. S8F). This is consistent with the role of PRPF6 as a core splicing component.

GO term analysis for the genes identified with skipped exons (SEs) or retained introns (RIs) revealed enrichment for categories governing central nervous system development and cell-cell adhesion among SE genes, whereas RI genes were enriched for chromatin silencing and RNA metabolic processing (Fig. 4C). To probe when the genes misspliced upon PRPF6^{R23W} expression may have the greatest effect, we examined their expression using data from the developing mouse cortex (*45*). This showed that genes with skipped exons induced by expression of PRPF6^{R23W} were enriched for loci with significantly greater expression during migration (Fig. 4D). To prioritize possible candidate genes mediating the PH phenotype, we combined the two main enrichment analyses from Fig. 4, C and D, which identified *Ctip2* and *Brsk2*. We selected *Brsk2* because it encodes the SAD-A kinase phosphorylating microtubule-associated proteins (MAPs), regulating microtubule dynamics (*46*, *47*) and neuronal migration in the developing cerebral cortex (*48*).

Of the three *Brsk2* isoforms expressed within the developing mouse brain (*23*), *exon 19* of isoform *Brsk2_202* [RefSeq NM_001009930.3 (GRCh37)] is skipped in the mutant condition (Fig. 4E and fig. S8L). *Brsk2_202* is expressed in cells that leave the ventricle, whereas the isoform *Brsk2_201* [RefSeq NM_001009929.3 (GRCh37)] is expressed in all zones [data are from (*23*)] (Fig. 4F). To test whether *Brsk2_202* plays a role in mediating exit from the ventricular region, PRPF6^{R23W} and *Brsk2_202* were coelectroporated at E13. This resulted in correct cellular distribution within the developing cortex 5 days after electroporation (at

E18) (Fig. 4, G to J), whereas coelectroporation of the misspliced *Brsk2_202* lacking *exon 19* (Brsk2_202$^{\Delta 19}$) did not rescue the PRPF6^{R23W} periventricular phenotype (Fig. 4, I and J). These data implicate the deficiency of this isoform in cells failing to leave the periventricular region and link microtubule-associated processes in migration out of the periventricular region in causing PH phenotypes.

These findings prompted the question of whether NSC centrosome-associated proteins in the highest enrichment category, "splicing," bring their target RNAs to the centrosome. Splicing normally takes place in the nucleus, but the dynamic centrosome association of the PRPF6 complex (which includes ACIN1, DDX23, and KIAA1429 as well as exon junction complex proteins) suggests that RNA processing, transport, and/or translation modulation may be locally regulated by PRPF6. Consistent with this, we detected *Brsk2* RNA by means of single-molecule fluorescence in situ hybridization (FISH) and high-resolution imaging in the proximity of the centrosome in 28.3% of mouse embryonic cortex cells compared with control *Polr2a* RNA (9.3%) (Fig. 4, K to M). RNAs encoding centrosomal proteins have been found at the centrosome in a polysome and translation-related manner (*49*, *50*). These data are consistent with a role of the PRPF6 RNA binding and RNA-processing protein complex at the centrosome, shedding light on how a mutation of this ubiquitous protein causes a phenotype in the developing brain.

Discussion

We used affinity-based proteomics on human iPSC-derived NSCs and neurons targeting 10 core proteins to obtain a spatial portrait of the centrosome proteome. This led to the discovery of hundreds of neural centrosome interactors that were not reported in other centrosome proteomes. Further, this work uncovered dynamic changes of more than half of the centrosome proteome at specific baits during neuronal differentiation. Overlaying this interactome with DNVs of unknown importance from distinct neurodevelopmental disorders identified an enrichment for variants found in individuals with PH within the NSC centrosome proteome. This overlap was not observed for other cell types, including neurons profiled with the same method, which supports centrosome cell-type specificity to be relevant for neurodevelopmental disorders. The centrosome localization of interactors was not restricted to mitosis—as described, for example, for transcriptional regulators localizing to the centrosome or spindle apparatus in mitosis (*51*)—but was rather found in interphase, like AKNA (*6*). Significant enrichment of RNA binding and RNA-processing proteins is prominent in the neural centrosome proteome, and their disease relevance is highlighted by the splicing complex formed by PRPF6 with ACIN1, DDX23, and KIAA1429. Modeling the disease contribution of the PRPF6 mutation detected in a PH patient, our work indicates how ubiquitously expressed genes can contribute to specific disease phenotypes through differential protein network interactions across cell types.

We report the predominance of RNA binding and RNA-modifying proteins, including factors involved in mRNA splicing, RNA transport, and regulation of translation at the neural centrosome proteome, which were not detected in other centrosome proteomes. For example, the three fragile X syndrome proteins—FXR1P, FXR2P, and FMRP—regulate several RNA processes, including translation, transport, and editing (*52*–*57*). Given their link to ASD, exploring their centrosomal function in neural iPSC-derived cells as well as in fetal tissue could elucidate the neurodevelopmental contribution to this condition. Roquin-1 is an RNA binding protein that mediates degradation of its targets and was also detected and validated at the neural centrosome, along with its interactor NUFIP2 (*58*). The recently shown binding of Roquin-1 to *Akna* RNA (*59*) would be consistent with a role in regulating centrosomal MTOC through RNA regulation at the centrosome. Specific mRNA transcripts have been shown to localize at this organelle (such as *PCNT*) (*50*, *60*, *61*), where their local protein translation is detected (*62*). We demonstrated that the RNA for a MAP kinase (SAD-A encoded by *Brsk2*), a splicing target of the PRPF6 complex, also localizes to the centrosome, expanding the concept of function of specific RNAs at this location.

The concept of regulating centrosomal MTOC activity also through local RNAs is further supported by the localization of most of the proteins with PH variants at centrosome baits of the appendages or pericentriolar material (PCM) where microtubules are anchored, including all components of the PRPF6 complex. Centrosomal MTOC activity has been shown to be essential for newly born basal progenitors to migrate away from the brain's ventricle (*6*, *37*). The PRPF6 complex interacts with the centrosome components involved in regulating MTOC, with the de novo PRPF6^{R23W} variant identified in a patient with PH increasing the number of cells remaining in the periventricular region (*6*, *37*). Like AKNA, PRPF6 localizes to the centrosome during interphase and promotes cells' migrating out of the periventricular region. For both proteins, this role occurs before neuronal differentiation because expression under a neuronal promoter failed to elicit a phenotype. The rescue of the heterotopia only with the correctly spliced form of *Brsk2*, but not the one lacking exon 19, further supports the functional relevance of these proteins and their target RNAs at the centrosome for disease. Nascent proteins may exert local functions such as phosphorylation of dynamic microtubule-associated components at the centrosome [reviewed in (*63*)]. Thus, localization of ubiquitously expressed proteins from the PRPF6 complex at the centrosome in NSCs, but not other cells, correlates with their involvement in PH. This not only identifies the microtubule-anchoring region of the centrosome as a hub for PH disease variants but also sheds light on how mutations in genes that encode widely expressed proteins can lead to disorders restricted to the developing brain.

Methods summary

Cell culture

Cortical NSCs and neurons were differentiated from human iPSC lines by using a dual-SMAD inhibition protocol (*11*) with modifications. Cellular identity was confirmed with quantitative RT-PCR and immunostaining.

Coimmunoprecipitation

For proteome analysis, cells were harvested at days 15 (NSCs) or 40 (neurons) of differentiation after treatment with dimethyl sulfoxide (DMSO) or 3.3 μM nocodazole (NSCs only). Cell lysates, each containing 5 mg total protein, were incubated for 1 hour with one of the 10 centrosomal bait antibodies and 2 more hours after adding Protein A and Protein G Dynabeads, with end-to-end rotation at 4°C. Immunoprecipitated lysates were washed with lysis buffer, dissociated by boiling in Laemmli buffer, and stored at −80°C until mass spectometry. Using the same procedure, negative controls were prepared for each of the four replicates parallel to the samples, but bait antibodies were omitted.

Mass spectrometry

Immunoprecipitates were analyzed with mass spectrometry, followed by processing with MaxQuant software (1.6.17.0). Protein enrichment within each immunoprecipitation was calculated with Perseus software (1.6.14.0) by using LFQ intensities through unpaired one-tailed Student's *t* test against the negative controls. GO enrichment of the protein lists was calculated by using the Search Tool for the Retrieval of Interacting Genes/Proteins (STRING) database.

Burden analysis

Disease set enrichment analyses were carried out by using exact binomial test (two-tailed) with Benjamini-Hochberg correction as described previously (*35*), using published de novo variants for ASD, PH, ID, epileptic encephalopathy (EE), and polymicrogyria (PMG) (*27*–*34*).

Immunostaining and single-molecule FISH

Cortical sections and cells were incubated overnight in blocking solution and primary

antibody at 4°C. The day after, they were stained with secondary antibodies diluted in blocking solution and incubated for 1 to 2 hours. For single-molecule FISH combined immunofluorescence, cells were incubated with primary antibody in bovine serum albumin (BSA) and Triton X-100 in 1× phosphate-buffered saline (PBS) and stained with secondary antibodies as described above. After secondary antibody incubation, cells were hybridized with RNA probes overnight at 37°C and thoroughly washed before embedding. Nuclei were visualized by using 4′,6-diamidino-2-phenylindole (DAPI).

Western blot

Immunoprecipitated samples were ran on 6 to 12% SDS gels (depending on the protein size) and then transferred to nitrocellulose membranes. For immunodetection, membranes were first blocked for 1 hour, incubated overnight with primary antibodies, and then washed three times with 1× tris-buffered saline–Polysorbate 20 (TBST) before being incubated with horseradish peroxidase (HRP)–coupled secondary antibodies. The blots were visualized by means of the enhanced chemiluminesence (ECL) method, using a ChemiDoc instrument.

IUE

Endotoxin-free vectors were diluted to 0.5 to 0.7 μg/μl each in 0.9% NaCl and mixed with Fast green, and 1 μl of mix was injected into the ventricles of embryos at E13 in the uterus of anesthetized C57/Bl6 mice and electroporated. Embryonic brains were dissected 1, 3, or 5 days after electroporation and fixed with 4% paraformaldehyde (PFA) in 1× PBS for 2 hours (1 day after electroporation), 4 hours (3 days after electroporation), or 6 hours (5 days after electroporation). For analysis, embryos from at least two females were used, and quantifications were made from two to three coronal sections from four to six embryos. Statistical differences were assessed by means of unpaired Kruskal-Wallis tests followed by Dunn's multiple comparison correction.

REFERENCES AND NOTES

1. M. Wilsch-Bräuninger, W. B. Huttner, Primary cilia and centrosomes in neocortex development. *Front. Neurosci.* **15**, 755867 (2021). doi: 10.3389/fnins.2021.755867; pmid: 34744618
2. P. Gönczy, G. N. Hatzopoulos, Centriole assembly at a glance. *J. Cell Sci.* **132**, jcs228833 (2019). doi: 10.1242/jcs.228833; pmid: 30787112
3. C. Vineethakumari, J. Lüders, Microtubule anchoring: Attaching dynamic polymers to cellular structures. *Front. Cell Dev. Biol.* **10**, 867870 (2022). doi: 10.3389/fcell.2022.867870; pmid: 35309944
4. N. Delgehyr, J. Sillibourne, M. Bornens, Microtubule nucleation and anchoring at the centrosome are independent processes linked by ninein function. *J. Cell Sci.* **118**, 1565–1575 (2005). doi: 10.1242/jcs.02302; pmid: 15784680
5. M. Piel, P. Meyer, A. Khodjakov, C. L. Rieder, M. Bornens, The respective contributions of the mother and daughter centrioles to centrosome activity and behavior in vertebrate cells. *J. Cell Biol.* **149**, 317–330 (2000). doi: 10.1083/jcb.149.2.317; pmid: 10769025
6. G. Camargo Ortega *et al.*, The centrosome protein AKNA regulates neurogenesis via microtubule organization. *Nature* **567**, 113–117 (2019). doi: 10.1038/s41586-019-0962-4; pmid: 30787442
7. J. S. Andersen *et al.*, Proteomic characterization of the human centrosome by protein correlation profiling. *Nature* **426**, 570–574 (2003). doi: 10.1038/nature02166; pmid: 14654843
8. L. Gheiratmand *et al.*, Spatial and proteomic profiling reveals centrosome-independent features of centriolar satellites. *EMBO J.* **38**, e101109 (2019). doi: 10.15252/embj.2018101109; pmid: 31304627
9. H. Müller *et al.*, Proteomic and functional analysis of the mitotic Drosophila centrosome. *EMBO J.* **29**, 3344–3357 (2010). doi: 10.1038/emboj.2010.210; pmid: 20818332
10. G. Sauer *et al.*, Proteome analysis of the human mitotic spindle. *Mol. Cell. Proteomics* **4**, 35–43 (2005). doi: 10.1074/mcp.M400158-MCP200; pmid: 15561729
11. Y. Shi, P. Kirwan, F. J. Livesey, Directed differentiation of human pluripotent stem cells to cerebral cortex neurons and neural networks. *Nat. Protoc.* **7**, 1836–1846 (2012). doi: 10.1038/nprot.2012.116; pmid: 22976355
12. D. K. Moss *et al.*, Ninein is released from the centrosome and moves bi-directionally along microtubules. *J. Cell Sci.* **120**, 3064–3074 (2007). doi: 10.1242/jcs.010322; pmid: 17698918
13. G. A. Pihan, Centrosome dysfunction contributes to chromosome instability, chromoanagenesis, and genome reprograming in cancer. *Front. Oncol.* **3**, 277 (2013). doi: 10.3389/fonc.2013.00277; pmid: 24282781
14. J. M. C. Alves-Cruzeiro, R. Nogales-Cadenas, A. D. Pascual-Montano, CentrosomeDB: A new generation of the centrosomal proteins database for *Human* and *Drosophila melanogaster*. *Nucleic Acids Res.* **42**, D430–D436 (2014). doi: 10.1093/nar/gkt1126; pmid: 24270791
15. E. N. Firat-Karalar, N. Rauniyar, J. R. Yates3rd, T. Stearns, Proximity interactions among centrosome components identify regulators of centriole duplication. *Curr. Biol.* **24**, 664–670 (2014). doi: 10.1016/j.cub.2014.01.067; pmid: 24613305
16. G. D. Gupta *et al.*, A dynamic protein interaction landscape of the human centrosome-cilium interface. *Cell* **163**, 1484–1499 (2015). doi: 10.1016/j.cell.2015.10.065; pmid: 26638075
17. E. Sjöstedt *et al.*, An atlas of the protein-coding genes in the human, pig, and mouse brain. *Science* **367**, eaay5947 (2020). doi: 10.1126/science.aay5947; pmid: 32139519
18. T. J. van Dam, G. Wheway, G. G. Slaats, M. A. Huynen, R. H. Giles; SYSCILIA Study Group, The SYSCILIA gold standard (SCGSv1) of known ciliary components and its applications within a systems biology consortium. *Cilia* **2**, 7 (2013). doi: 10.1186/2046-2530-2-7; pmid: 23725226
19. E. Lundberg, G. H. H. Borner, Spatial proteomics: A powerful discovery tool for cell biology. *Nat. Rev. Mol. Cell Biol.* **20**, 285–302 (2019). doi: 10.1038/s41580-018-0094-y; pmid: 30659282
20. M. Stiess *et al.*, Axon extension occurs independently of centrosomal microtubule nucleation. *Science* **327**, 704–707 (2010). doi: 10.1126/science.1182179; pmid: 20056854
21. M. P. Gavilan *et al.*, The dual role of the centrosome in organizing the microtubule network in interphase. *EMBO Rep.* **19**, e45942 (2018). doi: 10.15252/embr.201845942; pmid: 30224411
22. B. P. O'Rourke *et al.*, Cep192 controls the balance of centrosome and non-centrosomal microtubules during interphase. *PLOS ONE* **9**, e101001 (2014). doi: 10.1371/journal.pone.0101001; pmid: 24971877
23. X. Zhang *et al.*, Cell-type-specific alternative splicing governs cell fate in the developing cerebral cortex. *Cell* **166**, 1147–1162.e15 (2016). doi: 10.1016/j.cell.2016.07.025; pmid: 27565344
24. D. N. Itzhak, S. Tyanova, J. Cox, G. H. Borner, Global, quantitative and dynamic mapping of protein subcellular localization. *eLife* **5**, e16950 (2016). doi: 10.7554/eLife.16950; pmid: 27278775
25. D. N. Itzhak *et al.*, A mass spectrometry-based approach for mapping protein subcellular localization reveals the spatial proteome of mouse primary neurons. *Cell Rep.* **20**, 2706–2718 (2017). doi: 10.1016/j.celrep.2017.08.063; pmid: 28903049
26. R. W. Wong, New activities of the nuclear pore complexes. *Cells* **10**, 2123 (2021). doi: 10.3390/cells10082123; pmid: 34440892
27. J. de Ligt *et al.*, Diagnostic exome sequencing in persons with severe intellectual disability. *N. Engl. J. Med.* **367**, 1921–1929 (2012). doi: 10.1056/NEJMoa1206524; pmid: 23033978
28. A. S. Allen *et al.*, De novo mutations in epileptic encephalopathies. *Nature* **501**, 217–221 (2013). doi: 10.1038/nature12439; pmid: 23934111
29. A. S. Allen *et al.*, Diverse genetic causes of polymicrogyria with epilepsy. *Epilepsia* **62**, 973–983 (2021). doi: 10.1111/epi.16854; pmid: 33818783
30. M. Fromer *et al.*, De novo mutations in schizophrenia implicate synaptic networks. *Nature* **506**, 179–184 (2014). doi: 10.1038/nature12929; pmid: 24463507
31. F. F. Hamdan *et al.*, De novo mutations in moderate or severe intellectual disability. *PLOS Genet.* **10**, e1004772 (2014). doi: 10.1371/journal.pgen.1004772; pmid: 25356899
32. E. L. Heinzen *et al.*, De novo and inherited private variants in MAP1B in periventricular nodular heterotopia. *PLOS Genet.* **14**, e1007281 (2018). doi: 10.1371/journal.pgen.1007281; pmid: 29738522
33. E. T. Lim *et al.*, Rates, distribution and implications of postzygotic mosaic mutations in autism spectrum disorder. *Nat. Neurosci.* **20**, 1217–1224 (2017). doi: 10.1038/nn.4598; pmid: 28714951
34. A. Rauch *et al.*, Range of genetic mutations associated with severe non-syndromic sporadic intellectual disability: An exome sequencing study. *Lancet* **380**, 1674–1682 (2012). doi: 10.1016/S0140-6736(12)61480-9; pmid: 23020937
35. K. E. Samocha *et al.*, A framework for the interpretation of de novo mutation in human disease. *Nat. Genet.* **46**, 944–950 (2014). doi: 10.1038/ng.3050; pmid: 25086666
36. E. Parrini *et al.*, Periventricular heterotopia: Phenotypic heterogeneity and correlation with Filamin A mutations. *Brain* **129**, 1892–1906 (2006). doi: 10.1093/brain/awl125; pmid: 16684786
37. I. Kasioulis, R. M. Das, K. G. Storey, Inter-dependent apical microtubule and actin dynamics orchestrate centrosome retention and neuronal delamination. *eLife* **6**, e26215 (2017). doi: 10.7554/eLife.26215; pmid: 29058679
38. M. Lützelberger *et al.*, The N-terminus of Prp1 (Prp6/U5-102 K) is essential for spliceosome activation in vivo. *Nucleic Acids Res.* **38**, 1610–1622 (2010). doi: 10.1093/nar/gkp1155; pmid: 20007600
39. D. J. Di Bella *et al.*, Molecular logic of cellular diversification in the mouse cerebral cortex. *Nature* **595**, 554–559 (2021). doi: 10.1038/s41586-021-03670-5; pmid: 34163074
40. L. Broix *et al.*, Mutations in the HECT domain of NEDD4L lead to AKT-mTOR pathway deregulation and cause periventricular nodular heterotopia. *Nat. Genet.* **48**, 1349–1358 (2016). doi: 10.1038/ng.3676; pmid: 27694961
41. S. Cappello *et al.*, Mutations in genes encoding the cadherin receptor-ligand pair DCHS1 and FAT4 disrupt cerebral cortical development. *Nat. Genet.* **45**, 1300–1308 (2013). doi: 10.1038/ng.2765; pmid: 24056717
42. A. Carabalona *et al.*, A glial origin for periventricular nodular heterotopia caused by impaired expression of Filamin-A. *Hum. Mol. Genet.* **21**, 1004–1017 (2012). doi: 10.1093/hmg/ddr531; pmid: 22076441
43. G. Tanackovic *et al.*, A missense mutation in PRPF6 causes impairment of pre-mRNA splicing and autosomal-dominant retinitis pigmentosa. *Am. J. Hum. Genet.* **88**, 643–649 (2011). doi: 10.1016/j.ajhg.2011.04.008; pmid: 21549338
44. Y. Katz, E. T. Wang, E. M. Airoldi, C. B. Burge, Analysis and design of RNA sequencing experiments for identifying isoform regulation. *Nat. Methods* **7**, 1009–1015 (2010). doi: 10.1038/nmeth.1528; pmid: 21057496
45. S. A. Fietz *et al.*, Transcriptomes of germinal zones of human and mouse fetal neocortex suggest a role of extracellular matrix in progenitor self-renewal. *Proc. Natl. Acad. Sci. U.S.A.* **109**, 11836–11841 (2012). doi: 10.1073/pnas.1209647109; pmid: 22753484
46. A. P. Barnes *et al.*, LKB1 and SAD kinases define a pathway required for the polarization of cortical neurons. *Cell* **129**, 549–563 (2007). doi: 10.1016/j.cell.2007.03.025; pmid: 17482548
47. M. Kishi, Y. A. Pan, J. G. Crump, J. R. Sanes, Mammalian SAD kinases are required for neuronal polarization. *Science* **307**, 929–932 (2005). doi: 10.1126/science.1107403; pmid: 15705853

48. K. Nakanishi *et al*., Isozyme-specific role of SAD-A in neuronal migration during development of cerebral cortex. *Cereb. Cortex* **29**, 3738–3751 (2019). doi: 10.1093/cercor/bhy253; pmid: 30307479
49. P. V. Ryder, J. Fang, D. A. Lerit, *centrocortin* RNA localization to centrosomes is regulated by FMRP and facilitates error-free mitosis. *J. Cell Biol.* **219**, e202004101 (2020). doi: 10.1083/jcb.202004101; pmid: 33196763
50. G. Sepulveda *et al*., Co-translational protein targeting facilitates centrosomal recruitment of PCNT during centrosome maturation in vertebrates. *eLife* **7**, e34959 (2018). doi: 10.7554/eLife.34959; pmid: 29708497
51. M. P. Somma *et al*., Moonlighting in mitosis: Analysis of the mitotic functions of transcription and splicing factors. *Cells* **9**, 1554 (2020). doi: 10.3390/cells9061554; pmid: 32604778
52. C. Bagni, R. S. Zukin, A synaptic perspective of fragile X syndrome and autism spectrum disorders. *Neuron* **101**, 1070–1088 (2019). doi: 10.1016/j.neuron.2019.02.041; pmid: 30897358
53. D. Cook *et al*., FXR1P limits long-term memory, long-lasting synaptic potentiation, and de novo GluA2 translation. *Cell Rep.* **9**, 1402–1416 (2014). doi: 10.1016/j.celrep.2014.10.028; pmid: 25456134
54. J. K. Davis, K. Broadie, Multifarious functions of the fragile X mental retardation protein. *Trends Genet.* **33**, 703–714 (2017). doi: 10.1016/j.tig.2017.07.008; pmid: 28826631
55. E. Fernández *et al*., FXR2P exerts a positive translational control and is required for the activity-dependent increase of PSD95 expression. *J. Neurosci.* **35**, 9402–9408 (2015). doi: 10.1523/JNEUROSCI.4800-14.2015; pmid: 26109663
56. L.-J. Pilaz, A. L. Lennox, J. P. Rouanet, D. L. Silver, Dynamic mRNA transport and local translation in radial glial progenitors of the developing brain. *Curr. Biol.* **26**, 3383–3392 (2016). doi: 10.1016/j.cub.2016.10.040; pmid: 27916527
57. L.-J. Pilaz, D. L. Silver, Moving messages in the developing brain-emerging roles for mRNA transport and local translation in neural stem cells. *FEBS Lett.* **591**, 1526–1539 (2017). doi: 10.1002/1873-3468.12626; pmid: 28304078
58. G. Behrens, V. Heissmeyer, Cooperation of RNA-binding proteins—A focus on roquin function in T cells. *Front. Immunol.* **13**, 839762 (2022). doi: 10.3389/fimmu.2022.839762; pmid: 35251035
59. K. P. Hoefig *et al*., Defining the RBPome of primary T helper cells to elucidate higher-order Roquin-mediated mRNA regulation. *Nat. Commun.* **12**, 5208 (2021). doi: 10.1038/s41467-021-25345-5; pmid: 34471108
60. S. Hassine *et al*., Staufen1 localizes to the mitotic spindle and controls the localization of RNA populations to the spindle. *J. Cell Sci.* **133**, jcs247155 (2020). doi: 10.1242/jcs.247155; pmid: 32576666
61. A. Safieddine *et al*., A choreography of centrosomal mRNAs reveals a conserved localization mechanism involving active polysome transport. *Nat. Commun.* **12**, 1352 (2021). doi: 10.1038/s41467-021-21585-7; pmid: 33649340
62. D. Iaconis *et al*., The centrosomal OFD1 protein interacts with the translation machinery and regulates the synthesis of specific targets. *Sci. Rep.* **7**, 1224 (2017). doi: 10.1038/s41598-017-01156-x; pmid: 28450740
63. M. W. Breuss, I. Leca, T. Gstrein, A. H. Hansen, D. A. Keays, Tubulins and brain development—The origins of functional specification. *Mol. Cell. Neurosci.* **84**, 58–67 (2017). doi: 10.1016/j.mcn.2017.03.002; pmid: 28347630
64. R. Uzbekov, I. Alieva, Who are you, subdistal appendages of centriole? *Open Biol.* **8**, 180062 (2018). doi: 10.1098/rsob.180062; pmid: 30045886

ACKNOWLEDGMENTS

We thank V. Heissmeyer for Roquin-1 and NUFIP2 antibodies, M. Kiebler for Stau2 antibodies, I. Solovei for Lamin-A antibodies, and M.-E. Torres-Padilla for CRABP2 antibodies; D. L. Silver for suggestions on exon-junction complex proteins; M. Drukker and E. Rusha (HMGU) for the iPSC lines; and M. Bürkle and I. Mühlhahn for their excellent technical help with Western Blotting and cloning, respectively. We are particularly grateful to G. Camargo Ortega and T. Mikeladze-Dvali for providing great centrosome expertise, to G. Camargo Ortega for excellent comments on the manuscript, and to M. Puglisi for help with the graphical abstract. **Funding:** A.C.O. was supported by a Philip Wrightson Postdoctoral Fellowship from the Neurological Foundation of New Zealand. Funding for this work was provided from the ERC (advanced grant NeuroCentro, 885382 to M.G.), the EU (NSC-Reconstruct, 874758, to M.G.), the German Research Foundation [Go 640 12/1, 14/2; Synergy (EXC 2145/ID 390857198), SFB870 to M.G.], and Curekids and the Health Research Council of NZ (to S.P.R.). R.G. was supported by Tuscany Region Call for Health 2018 (grant DECODE-EE), Z.W. was supported by NSFC (grant 31730110), and M.B. was supported by an Australian National Health and Medical Research Council (NHMRC) Fellowship (110297). Funding to C.B. was from PRIN2017 201789LFKB, Telethon GGP20137, and SNSF 310030-182651. This work was also supported by the NHMRC Independent Research Institute Infrastructure Support Scheme (IRIISS to M.B.). J.P.S. and G.H.H.B. were supported by the Max Planck Society for the Advancement of Science, and we thank M. Mann for his continued support. The human embryonic and fetal material was provided by the Human Developmental Biology Resource (https://www.hdbr.org). **Author contributions:** M.G. conceived and designed the project together with A.C.O.; A.C.O. and F.U. performed the NSC and neuron centrosome bait immunoprecipitations, respectively, and F.U. analyzed mass spectrometry data. F.Met. and S.M.H. performed mass spectrometry and informed on proteomics. J.P.S. performed mass spectrometry to determine the overall proteomes of neurons and NSCs; J.P.S. and G.H.H.B. jointly performed the corresponding data analyses. G.A. assessed PRPF6 function in vitro and centrosomal localization across cell-types; K.C. and G.A. performed FISH experiments with guidance by R.J.; F.U., K.D., and G.A. validated centrosome interactors, supervised by M.G., and G.P. by C.B., and K.D. validated PRPF6 interactors and aided in fluorescence-activated cell sorting (FACS) analysis with A.C.O; A.C.O and F.Mer. performed all in vivo experiments, which were also analyzed by A.J.; A.J. analyzed NINEIN dynamics in vitro; A.C.O. and S.Fr. performed analysis on human brain transcriptomic data, with supervision from M.B.; A.S. and R.F. generated monoclonal PRPF6 and NUP50 antibodies; R.G. and S.P.R. contributed clinical phenotyping; and S.P.R. contributed whole-exome sequencing data. M.E. produced PRPF6 constructs; S.Z. and Z.W. performed splicing analysis; P.S. analyzed *Brsk2* isoform expression dynamics; A.C.O. and M.G. wrote the manuscript, and all authors contributed corrections and comments. **Competing interests:** The authors declare no competing interests. **Data and materials availability:** Raw and processed mass spectrometry proteomics data have been deposited to the ProteomeXchange Consortium through the Proteomics Identification Database (PRIDE; https://www.ebi.ac.uk/pride) with the accession number: PXD031936 (https://doi.org/10.6019/PXD031936). The RNA-sequencing data discussed in this manuscript is deposited in NCBI's Gene Expression Omnibus (NCBI-GEO) and is accessible under the Series: GSE201954 (https://www.ncbi.nlm.nih.gov/geo/query/acc.cgi?acc=GSE201954). All other data are in the main paper or supplementary materials. **License information:** Copyright © 2022 the authors, some rights reserved; exclusive licensee American Association for the Advancement of Science. No claim to original US government works. https://www.science.org/about/science-licenses-journal-article-reuse

SUPPLEMENTARY MATERIALS

science.org/doi/10.1126/science.abf9088
Materials and Methods
Figs. S1 to S8
References (*65*–*85*)
Tables S1 to S8
MDAR Reproducibility Checklist

View/request a protocol for this paper from *Bio-protocol*.

Submitted 27 November 2020; resubmitted 31 December 2021
Accepted 5 May 2022
10.1126/science.abf9088

RESEARCH ARTICLE SUMMARY

CELL BIOLOGY

Control of meiotic chromosomal bouquet and germ cell morphogenesis by the zygotene cilium

Avishag Mytlis†, Vineet Kumar†, Tao Qiu†, Rachael Deis, Neta Hart, Karine Levy, Markus Masek, Amal Shawahny, Adam Ahmad, Hagai Eitan, Farouq Nather, Shai Adar-Levor, Ramon Y. Birnbaum, Natalie Elia, Ruxandra Bachmann-Gagescu, Sudipto Roy, Yaniv M. Elkouby*

INTRODUCTION: Meiosis is a cellular program that is essential for producing haploid gametes and is conserved in sexually reproducing organisms. A hallmark of meiosis is chromosomal pairing through synaptonemal complexes and meiotic cohesins, which is required for the execution of homologous recombination. However, nuclear events of meiosis occur in the cellular context of a differentiating gamete, where chromosomal pairing depends on cytoplasmic counterparts. In pairing, telomeres perform a unique function: They slide on perinuclear microtubules, shuffling chromosomes and mechanically driving their homology searches. Telomeres tether to Sun/Kash complexes on the nuclear envelope (NE), which associate with perinuclear microtubules (MTs) through dynein. This facilitates telomere rotations around the NE, which in turn shuffle chromosomes, driving their search for homologs. The perinuclear MTs at these stages emanate from the centrosome MT organizing center. Ultimately, rotating telomeres are pulled toward the centrosome and cluster on this side of the NE while looping their chromosomes to the other side, a configuration called the zygotene chromosomal bouquet. These telomere dynamics are essential for pairing and fertility. The bouquet, discovered in 1900, is universally conserved and was proposed as a hub for chromosomal pairing. Nevertheless, how cytoplasmic counterparts of bouquet formation are mechanically regulated has remained enigmatic.

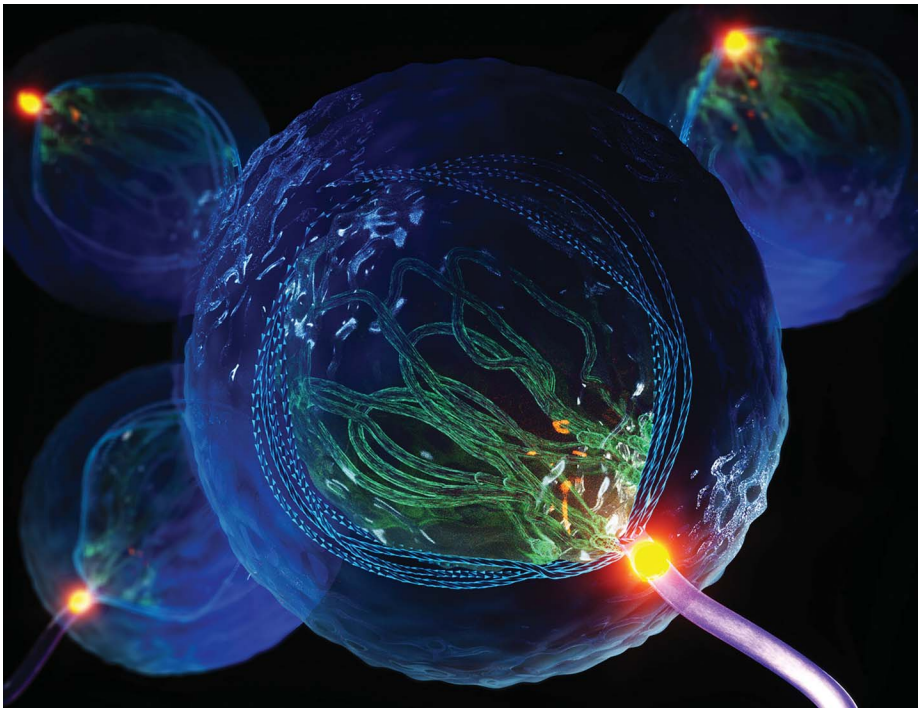

Zygotene bouquet–stage oocyte. Shown is an oocyte at the zygotene bouquet stage, where chromosomes (green) are tethered on the NE through their telomeres, which cluster apposing the centrosome (yellow circle), with their free looping ends facing the other side. The bouquet cytoplasmic machinery is shown as a cable system composed of the perinuclear MTs (blue cables) that are organized from the centrosome, which connects to the zygotene cilium (purple cable).

RATIONALE: Here, we report the "zygotene cilium," a previously unrecognized cilium, in oocytes. Using quantitative three-dimensional confocal image analysis, serial block-face scanning electron microscopy, and live microscopy, we characterized in zebrafish the intracellular and intercellular organization of the zygotene cilium, as well as its developmental stage–specific formation during oogenesis. We show that the zygotene cilium specifically connects to the bouquet centrosome, constituting a cable system of the cytoplasmic bouquet machinery. Furthermore, zygotene cilia extend throughout the germline cyst, a conserved germ cell organization. We reasoned that the zygotene cilium could regulate bouquet formation and germline cyst cellular organization.

RESULTS: We analyzed multiple viable *loss-of-function* mutations in zebrafish ciliary genes that in humans cause ciliopathies, genetic disorders that are caused by ciliary defects, including *cep290*, *kif7*, and *cc2d2a*. Using these mutants, as well as laser-induced excision of the zygotene cilium and live time-lapse imaging, we demonstrate that the organelle is essential for chromosomal bouquet and synaptonemal complex formation, germline cyst morphogenesis, ovarian development, and fertility. Mechanistically, we provide evidence that the cilium functions by anchoring the bouquet centrosome to counterbalance telomere rotation and pulling. We further show that the bouquet configuration is required for proper synaptonemal complex formation. Loss of the zygotene cilium resulted in bouquet and germline cyst perturbations that in turn induced oocyte apoptosis. Crossing the ciliary mutants to *tp53* mutant fish demonstrated that they induce P53-dependent apoptosis, likely by activating a meiotic checkpoint. Ultimately, loss of the zygotene cilium leads to ovarian dysgenesis and deficient fertility in adult females. We also show that the zygotene cilium is conserved in both male and female meiosis in zebrafish, as well as in mammals.

CONCLUSION: Our work uncovers the concept of the cilium as a critical player in meiosis and provides evidence that the bouquet is functionally required for synaptonemal complex formation. Our findings further shed new light on reproduction phenotypes in ciliopathies and propose a cellular paradigm that cilia can control chromosomal dynamics. ■

The list of author affiliations is available in the full article online.
*Corresponding author. Email: yaniv.elkouby@mail.huji.ac.il
†These authors contributed equally to this work.
Cite this article as A. Mytlis *et al.*, *Science* **376**, eabh3104 (2022). DOI: 10.1126/science.abh3104

READ THE FULL ARTICLE AT
https://doi.org/10.1126/science.abh3104

CREDIT: ILLUSTRATION BY ELLA MARU STUDIO

RESEARCH ARTICLE

CELL BIOLOGY

Control of meiotic chromosomal bouquet and germ cell morphogenesis by the zygotene cilium

Avishag Mytlis[1,2]†, Vineet Kumar[1,2]†, Tao Qiu[3]†, Rachael Deis[1,2], Neta Hart[1,2], Karine Levy[1,2], Markus Masek[4,5], Amal Shawahny[1,2], Adam Ahmad[1,2], Hagai Eitan[1,2], Farouq Nather[1,2], Shai Adar-Levor[6], Ramon Y. Birnbaum[6], Natalie Elia[6], Ruxandra Bachmann-Gagescu[4,5], Sudipto Roy[3,7,8], Yaniv M. Elkouby[1,2]*

A hallmark of meiosis is chromosomal pairing, which requires telomere tethering and rotation on the nuclear envelope through microtubules, driving chromosome homology searches. Telomere pulling toward the centrosome forms the "zygotene chromosomal bouquet." Here, we identified the "zygotene cilium" in oocytes. This cilium provides a cable system for the bouquet machinery and extends throughout the germline cyst. Using zebrafish mutants and live manipulations, we demonstrate that the cilium anchors the centrosome to counterbalance telomere pulling. The cilium is essential for bouquet and synaptonemal complex formation, oogenesis, ovarian development, and fertility. Thus, a cilium represents a conserved player in zebrafish and mouse meiosis, which sheds light on reproductive aspects in ciliopathies and suggests that cilia can control chromosomal dynamics.

Meiosis is a cellular program essential for producing haploid gametes, conserved in sexually reproducing organisms. During prophase stages of meiosis, induced double-strand breaks must be repaired, and their repair through homologous recombination requires the pairing of homologous chromosomes and formation of the synaptonemal complex (SC). The SC is composed of SC proteins Sycp1 to Sycp3 that assemble between chromosomes and along their axes (*1*). Together with meiotic cohesins, these connect homologous chromosomes and hold them together for the execution of recombination (*1*, *2*), and recent breakthroughs have revealed their structure and functions (*1*–*8*).

However, the nuclear events of meiosis occur in the cellular context of a differentiating gamete (*9*), where chromosomal pairing depends on cytoplasmic counterparts. In pairing, telomeres perform a unique function: At the leptotene stage, telomeres tether to Sun/Kash complexes on the nuclear envelope (NE), which associate with perinuclear microtubules (MTs) through dynein (*10*–*17*). This facilitates telomere rotations around the NE during the leptotene-zygotene stages (fig. S1A), which in turn shuffle chromosomes, driving their search for homologs. The perinuclear MTs at these stages emanate from the centrosome MT-organizing center (MTOC) (*16*, *18*, *19*) (fig. S1A). Ultimately, rotating telomeres are pulled toward the centrosome and cluster on this side of the NE while looping their chromosomes to the other side, a configuration called the zygotene chromosomal bouquet (*20*, *21*) (fig. S1A). These telomere dynamics are essential for synapsis, homologous recombination, and fertility (*10*–*17*). Telomere clustering is thought to stabilize initial pairing between homologous chromosomes, and in zebrafish, the bouquet was proposed as a hub for chromosomal pairing (*22*). It was shown that double-strand breaks cluster at subtelomeric regions and that Sycp3 and Sycp1 first load adjacent to clustered telomeres specifically at the bouquet stages, from which they extend along chromosomal axes (*22*, *23*) (fig. S1A).

The bouquet configuration was discovered in 1900 (*20*) and is conserved from yeast to mammals (*10*–*17*). However, how the cytoplasmic counterparts of bouquet formation are mechanically regulated in rotating telomeres is unknown. It is unclear how rotation forces are generated, counterbalanced to allow movements, and then halted at the correct stage.

We previously characterized the nuclear and cytoplasmic components of the bouquet and its formation in zebrafish oogenesis (*19*, *24*) (fig. S1B). To obtain a better temporal resolution of bouquet formation, we performed live time-lapse analysis of bouquet chromosomal rotation in cultured ovaries (*24*) (fig. S2 and movie S1). This analysis revealed rapid rotational movements, specifically in leptotene-zygotene oocytes, in contrast to oogonia and somatic pre-granulosa follicle cell nuclei, which do not execute meiotic chromosomal pairing (fig. S2 and movie S1). These rapid rotational movements suggest the underlying action of substantial mechanical forces. Rotating telomeres then cluster, strictly juxtaposing the centrosome (*18*, *19*, *23*) (fig. S1A). Live recording of the centrosome during bouquet chromosomal rotations showed that it vibrates in place, remaining fixed at the same position in the cytoplasm (movie S2). Therefore, as in mice (*18*), telomeres rotate and are pulled by MTs toward the centrosome to cluster. These observations suggest that (i) MTs and the centrosome are subjected to mechanical strain during rotations, and (ii) the centrosome is likely to be physically anchored.

The zygotene cilium

We detected elongated fiber-like structures of acetylated tubulin that emanated from the centrosome in bouquet stage oocytes with clustered telomeres (*19*). These structures were highly reminiscent of cilia. A cilium is an MT-based organelle composed of an axoneme with stereotypically organized acetylated microtubule doublets that grow from the mother centriole (basal body) and extend extracellularly (*25*, *26*).

Several lines of evidence demonstrated that the bouquet acetylated tubulin structures are cilia: (i) The acetylated tubulin (AcTub)–positive structures colocalized with the specific ciliary membrane marker Arl13b (*27*, *28*) (Fig. 1, A and C); (ii) tubulin glutamylation (GluTub), a posttranslational MT modification of ciliary axonemes, showed similar structures (Fig. 1B) that colocalized with the AcTub signal (Fig. 1C); (iii) transgenic Arl13b-GFP in zygotene oocytes confirmed consistent ciliary structures in live ovaries (fig. S3B); and (iv) transmission electron microscopy (TEM) of ovaries identified structures that correspond to ciliary axonemes with typical MT doublets that are found in spaces between cell membranes of adjacent zygotene oocytes (Fig. 1D, bottom panels, and fig. S3A). Within oocytes, we identified the basal body, transition zone, and axoneme extending extracellularly through the ciliary pocket (Fig. 1D, top panels, and fig. S3A). Serial block-face scanning electron microscopy (SBF-SEM) confirmed axonemal structures that emanated from basal bodies in prophase oocytes (movies S3 to S5).

The cilia were stage specific: They were specifically present at the leptotene-zygotene stages as determined by our previously established staging criteria (*19*, *24*) (fig. S1B). This was confirmed by the prophase SC marker Sycp3 (Fig. 1E and fig. S1B). Cilia were absent from most premeiotic oogonial stages, but a

[1]Department of Developmental Biology and Cancer Research, Hebrew University of Jerusalem Faculty of Medicine, Ein-Kerem Campus, Jerusalem 9112102, Israel. [2]Institute for Medical Research-Israel-Canada (IMRIC), Ein-Kerem Campus, Jerusalem 9112102, Israel. [3]Institute of Molecular and Cell Biology, Proteos 138673, Singapore. [4]Department of Molecular Life Sciences, University of Zurich, 8057 Zurich, Switzerland. [5]Institute of Medical Genetics, University of Zurich, 8952 Schlieren, Switzerland. [6]Departments of Life Sciences, Ben-Gurion University of the Negev, Beer-Sheva 84105, Israel. [7]Department of Biological Sciences, National University of Singapore, 117543 Singapore. [8]Department of Pediatrics, Yong Loo Lin School of Medicine, National University of Singapore, 119288 Singapore.
*Corresponding author. Email: yaniv.elkouby@mail.huji.ac.il
†These authors contributed equally to this work.

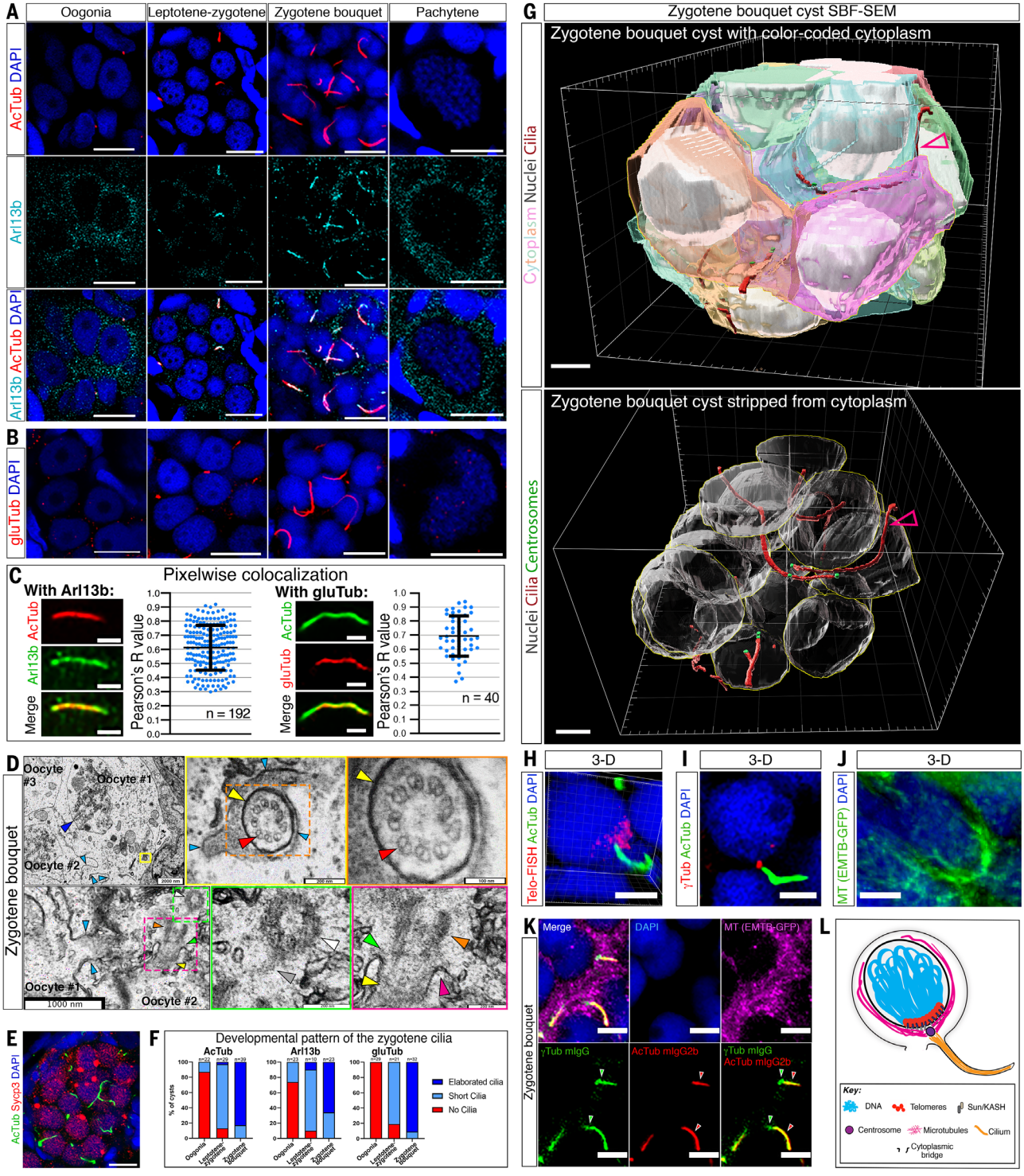

Fig. 1. A zygotene-specific oocyte cilium. (**A**) AcTub and Arl13b labeling shown at the indicated stages (n = 28 cysts in n = 8 ovaries). Scale bars for cyst panels, 5 μm. Scale bars for pachytene panels, 10 μm. (**B**) GluTub labeling shown as in (A) (n = 82 cysts in n = 7 ovaries). Scale bars are as in (A). (**C**) Pixelwise colocalization test for AcTub and Arl13b and for AcTub and gluTub. n, number of cilia. Bars are mean ± standard deviation (SD). (**D**) TEM images of cilia in leptotene-zygotene oocytes. Top left panel: leptotene-zygotene oocytes (dark-blue arrowhead indicates presumptive synapsed chromosomes interfacing the NE) within a germline cyst (light-blue arrowheads - cytoplasmic bridges. Right panels show cross-section of a ciliary axoneme, in higher magnifications (color-coded boxes), including ciliary membrane (yellow arrow) and MT doublets (red arrow), between oocyte membranes (light-blue arrowheads). Bottom panels: ciliary structures adjacent to a cytoplasmic bridge (light-blue arrows), including centriole (white), linker (gray), basal body (orange) transition zone (green), ciliary pockets (pink), axoneme (yellow), shown in higher magnifications (color-coded boxes in right panels). Scale bars are indicated. n = 23 oocytes in n = 5 ovaries. (**E**) AcTub and Sycp3 labeling shown in a zygotene cyst. n = 24 cysts in n = 2 ovaries. Scale bar, 10 μm. (**F**) The developmental distribution of the zygotene cilia as detected by AcTub (n > 100 ovaries), Arl13b (n = 18 ovaries), and GluTub (n = 11 ovaries). n = number of cysts. (**G**) 3D rendering of a

zygotene bouquet cyst from SBF-SEM data, showing: cytoplasm of cyst oocytes (different transparent colors), nuclei (gray), cilia (maroon; maroon-gray arrowhead), and basal body centrosomes (green). Bottom panel: same cyst render stripped from cytoplasm to show the cilia. Scale bars are 5 μm. (**H** to **J**) Zygotene bouquet oocytes from ovaries labeled for (Scale bars are 5 μm): (H) Telomeres (Telo-FISH) and AcTub showing that the cilium emanates from the cytoplasm apposing the telomere cluster. *n* = 3 ovaries. A snapshot from 3D construction in movie S7. (I) γTub and AcTub showing that the cilium emanates from the centrosome, which was shown to localize apposing the telomere cluster (10). *n* = 5 ovaries. (J) Microtubules [*Tg(βact:EMTB-3XGFP)*] showing perinuclear cables (nucleus is counterstained with DAPI). *n* = 7 ovaries. A snapshot from 3D construction in movie S8. Another example is shown in movie S9. (**K**) Co-labeling of microtubules (EMTB-GFP), γTub, AcTub, and DAPI, reveals that the zygotene cilium emanate from the centrosome, which is embedded in a perinuclear microtubule network. A merged image and all individual channels are shown. *n* = 5 ovaries. γTub (mIgG1) and AcTub (mIgG2b) antibodies are both isoforms of mIgG. We used mIgG secondary antibody that binds both primary γTub and AcTuB antibodies, and a mIgG2b secondary antibody that specifically binds to the AcTuB antibody and not γTub antibody (arrowheads in the three bottom panels). (**L**) Scheme showing the bouquet cytoplasmic cable system.

few short cilia were detected at the leptotene-zygotene stage. Cilia were then fully elaborated at the zygotene bouquet and disassembled at the pachytene stage (Fig. 1, A, B, and F). This developmental pattern was consistently detected using AcTub, Arl13b, or GluTub labeling (Fig. 1, A, B, and F). We conclude that we have identified a previously unknown cilium in early prophase oocytes that is specific to the leptotene-zygotene and zygotene bouquet stages.

Early prophase, including the leptotene and zygotene stages, is executed while oocytes develop within the germline cyst (*9*, *19*, *24*, *29*). The cyst is a compact and confined cellular organization in which cytoplasmic membranes of adjacent oocytes interface tightly (*19*). Zygotene cilia extended throughout the volume of the cyst (fig. S3, B to D). We characterized ciliary distribution in the cyst using SBF-SEM, which provided ultrastructural data of cysts at EM resolution in three dimensions (3D; movie S3). Tracking zygotene cilia in raw SBF-SEM data (movies S4 and S5) and in rendered leptotene and zygotene cysts in 3D (Fig. 1H and movies S3 and S6) confirmed that these organelles tangle tightly between oocyte cytoplasmic membranes and extend throughout the cyst (Fig. 1G). Measurements of zygotene cilia diameters showed the expected diameter of ciliary axonemes (~300 nm) (*30*) (fig. S5, A and B).

In the germline cyst, cytoplasmic bridges (CBs) are also based on MT cables (*19*, *31*). Several lines of evidence allowed us to distinguish cilia and CBs in our analysis: (i) Ciliary cytoplasm (TEM and SBF-SEM in Fig. 1D, fig. S5A, and movies S4 and S5) but not CB cytoplasm (fig. S4A) showed axonemal MT tracks and CB membranes were typically ruffled (fig. S4A); (ii) CB diameters (fig. S5, A and B) were consistent with those in *Xenopus* and mice [0.5 to 1 μm (*32*)] but not with the ciliary diameter; (iii) CBs were adjacent to the centrosomes/basal bodies (*19*) but never associated with them; and (iv) cilia did not extend through or colocalize with CBs as labeled by the midbody marker Cep55 (*33*) (figs. S4B and S5, C and D). Thus, zygotene cilia and CBs are distinct and separate structures.

We confirmed the organization of the zygotene cilium with the bouquet cytoplasmic machinery. Labeling bouquet-clustered telomeres, perinuclear MT, centrosome, and the zygotene cilia (Fig. 1, H to K, fig. S3E, and movies S7 to S9) confirmed the cytoskeletal arrangement of a cable system that extends from the zygotene cilium through the centrosome and MT to telomeres on the nuclear envelope. This cable system comprises a potential machinery for chromosomal pairing movements (Fig. 1L). Live time-lapse imaging confirmed that the zygotene cilium was present during bouquet chromosomal rotations (movie S10).

The zygotene cilium is required for telomere clustering in chromosomal bouquet formation

We next aimed to investigate the function of the zygotene cilium in oogenesis. Severe disruption to cilia differentiation causes embryonic lethality in zebrafish. However, mutations in certain cilia genes allow viability to the adult stage. We analyzed multiple such *loss-of-function* ciliary mutants that in humans cause ciliopathies, genetic disorders that are caused by ciliary defects (*9*), including *cep290* (*34*–*40*), *kif7* (*41*–*44*), and *cc2d2a* (*45*, *46*).

We analyzed zygotene cilia in juvenile ovaries of wild-type (wt) as well as *cep290*$^{-/-}$, *kif7*$^{-/-}$, and *cc2d2a*$^{-/-}$ mutants (Fig. 2, A to D). On the basis of these measurements in 3D (Fig. 2A and fig. S6), we defined "normal cilia" (4 to 8.5 μm), "short cilia" (<4 μm) and absent cilia [not detected (N.D.)]. We analyzed the individual ciliary length (Fig. 2A), average ciliary length per cyst (Fig. 2B), distribution of scored cysts (Fig. 2C), and scoring of entire ovaries (Fig. 2D). These established the shortening and loss of zygotene cilia in *cep290*$^{-/-}$ and *cc2d2a*$^{-/-}$ ovaries. *Kif7*$^{-/-}$ ovaries showed only mild partial ciliary shortening phenotypes (Fig. 2, A to D, and fig. S6). Attempting to abolish cilia altogether, we generated *cep290; kif7* double mutants. Indeed, we observed that in *cep290*$^{-/-}$;*kif7*$^{+/-}$ and *cep290*$^{-/-}$;*kif7*$^{-/-}$ ovaries, cilia were mostly or completely abolished (Fig. 2, A to D, and fig. S6).

We next analyzed bouquet formation upon ciliary loss in developing ovaries from juvenile wt and mutant fish. We first noticed fewer oocytes with clear telomere clusters in *cep290*$^{-/-}$ ovaries compared with wt, suggesting that prophase progression is defective. To distinguish between a delay versus failure in bouquet formation we investigated whether (i) oocytes at the leptotene-zygotene stages were delayed in bouquet formation, (ii) oocytes at bouquet stages formed proper telomere clusters, and (iii) late-bouquet oocytes eventually formed telomere clusters.

We addressed a delay in the leptotene-zygotene stages. We tested whether oocytes that showed radial telomere distribution on the NE typical of the leptotene-zygotene stages were abnormally larger as an indication for prophase progression delay. wt leptotene-zygotene oocytes are 7 to 9 μm in diameter and zygotene bouquet oocytes are 10 to 16 μm in diameter (Fig. 2, E and F, and fig. S1B) (*19*, *24*). In mutants, we identified oversized "leptotene-zygotene–like" oocytes, defined as oocytes with leptotene-zygotene–like radial telomere distribution that were larger than the largest detected wt oocyte at these stages (>9.1 μm; Fig. 2, E and F, and fig. S7B). Oocyte sizes were based on cytoplasmic staining by DiOC6 (*19*, *24*). In single and double *kif7/cep290* heterozygous, *kif7*$^{-/-}$ and *cep290*$^{+/-}$;*kif7*$^{-/-}$ ovaries, ~40 to 65% of oocytes with radial telomeres were mildly larger leptotene-zygotene–like oocytes (Fig. 2, E and F, and fig. S7A). In *cep290*$^{-/-}$ ovaries, 85% were much larger leptotene-zygotene–like oocytes (Fig. 2, E and F, and fig. S7A). In *cep290*$^{-/-}$;*kif7*$^{-/-}$ and *cep290*$^{-/-}$;*kif7*$^{+/-}$ ovaries, most were severely affected and contained low numbers of oocytes for analysis, and many ovaries of these genotypes converted to testes. In zebrafish, ovary conversion to testis is indicative of severe oocyte damage and loss (*47*–*49*), which we address and discuss below and in Fig. 5B and fig. S12. Nevertheless, we did capture ovaries for analysis. In *cep290*$^{-/-}$;*kif7*$^{-/-}$ and *cep290*$^{-/-}$;*kif7*$^{+/-}$ovaries, 100% of oocytes with radial telomeres were very large leptotene-zygotene–like oocytes (Fig. 2, E and F, and fig. S7A). Similar large leptotene-zygotene–like oocytes were detected in *cc2d2a*$^{-/-}$ ovaries (fig. S7B). This suggests that oocytes continued to grow in size, but bouquet formation was at least delayed. Such delay in progression from leptotene-zygotene to zygotene bouquet stages is consistent with the dynamics of meiotic checkpoint activation in females, which is different from males (*9*, *50*, *51*).

We tested whether bouquet stage oocytes properly formed telomere clusters. We blindly

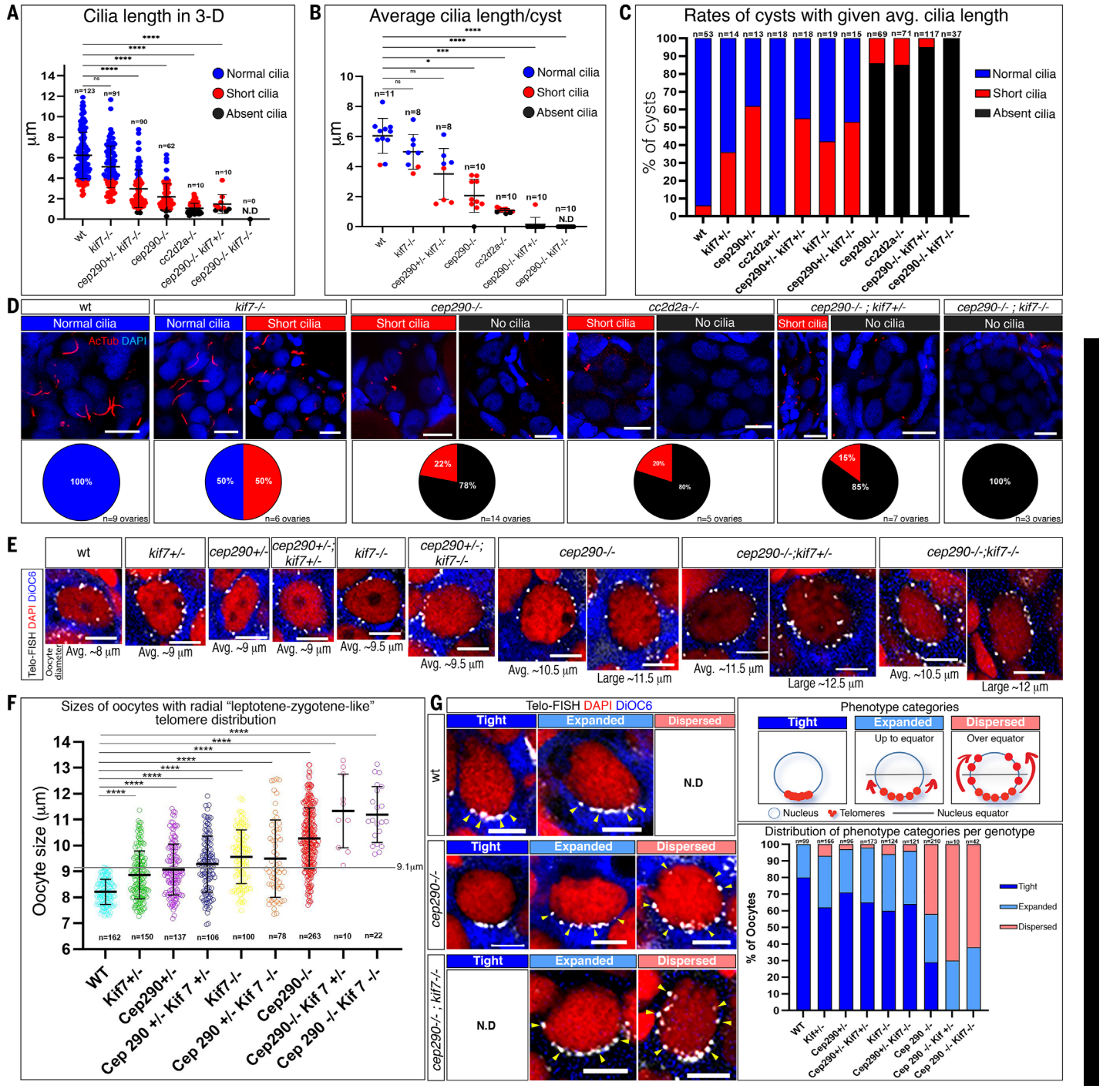

Fig. 2. The zygotene cilium is required for bouquet formation. (**A** and **B**) 3D measurements of ciliary lengths and average ciliary length per cyst. *n*, number of cilia. ND, not detected. Bars are mean ± SD. (**C**) Distribution of cysts with given ciliary length or absence. (**D**) Images of cysts from ciliary (AcTub) length categories as in (B) to (D). Percentage of ovaries with indicated categories are plotted. *n*, number of ovaries. Scale bars, 10 µm. (**E**) Images of "leptotene-zygotene-like" oocytes of average and large sizes. Scale bars, 5 µm. (**F**) "Leptotene-zygotene-like" oocyte sizes. *n*, number of oocytes. Bars are mean ± SD. 9.1 µm represents the largest wt leptotene oocytes. (**G**) Left panel: images of mid-bouquet-stage oocytes with tight, expanded, and dispersed telomeres (categories shown in top right panel). ND, nondetected. Scale bars, 5 µm. Right bottom panel: the percentage of each category in all genotypes. *n*, number of oocytes.

analyzed oocytes in sizes that were typical to midbouquet stages showing clear telomere clusters in wt (11.5 to 13 µm). Telomere distribution in wt midbouquet stages showed either a tight or slightly expanded telomere cluster (Fig. 2G). Ovaries of heterozygous, *kif7*$^{-/-}$ and *cep290*$^{+/-}$;*kif7*$^{-/-}$ fish were mostly similar to wt (Fig. 2G). However, in *cep290*$^{-/-}$ ovaries, in addition to the wt categories, we detected an abnormal "dispersed" category, in which telomeres were largely expanded beyond the nuclear equator (Fig. 2G). Moreover, in double-mutant *cep290*$^{-/-}$;*kif7*$^{+/-}$ and *cep290*$^{-/-}$;*kif7*$^{-/-}$ ovaries, we only detected "expanded" and "dispersed" category oocytes

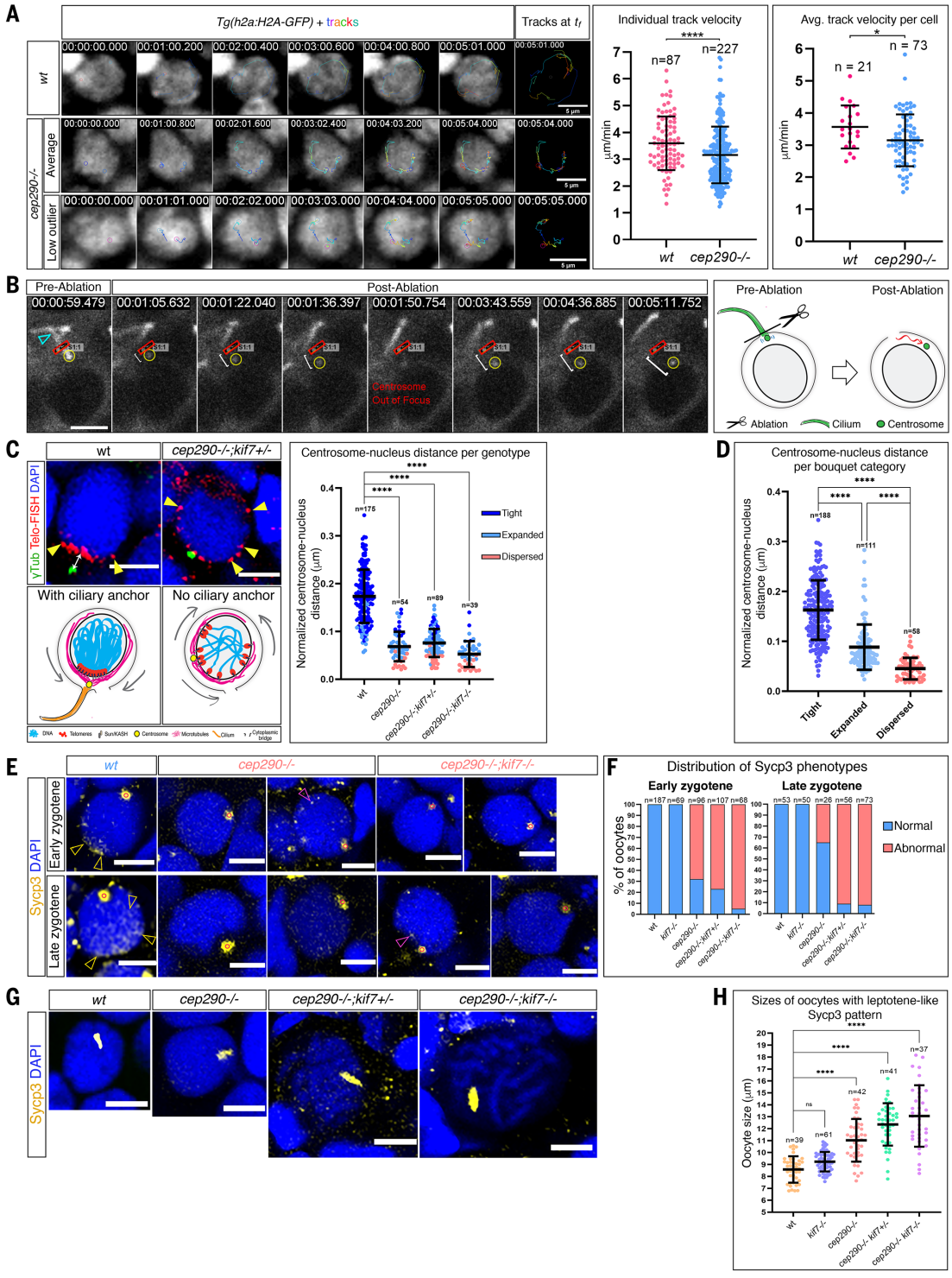

Fig. 3. Centrosome anchoring by the zygotene cilium is required for telomere clustering in bouquet formation and for proper synaptonemal complex formation. (**A**) Live time-lapse imaging of chromosomal bouquet rotations in *Tg(h2a:h2a-gfp);cep290*$^{+/+}$ and sibling *Tg(h2a:h2a-gfp);cep290*$^{-/-}$ ovaries. Chromosomal tracks and their sum at T_f are shown. Individual track velocities (*n*, number of tracks) and average track velocity per cell (*n*, number of cells) are plotted. Oocytes with mean and low outlier (below the SD) values of average track velocities are shown for *cep290*$^{-/-}$. Images are snapshots from movie S12. Scale bars, 5 µm. (**B**) Laser ablation of the zygotene cilium. The targeted cilium (teal arrowhead) is shown "pre-ablation" and the ablation region at its base (S1:1) is indicated throughout the time-lapse. The ablated ciliary associated centrosome (yellow circle) dislocates upon ablation in both XY and Z ("centrosome out of focus") axes (see cartoon, right). Time is indicated in mili-seconds. Scale bar, 5 µm. *n* = 17 cilia (oocytes) from *n* = 11 ovaries. Images are snapshots from movie S13; another example is shown in movie S14. (**C**) Images of mid-bouquet stage oocytes from wt and *cep290*$^{-/-}$;*kif7*$^{+/-}$ ovaries co-labeled for the centrosome (γTub) and telomeres (Telo-FISH). The distance between the centrosome and the nucleus (white arrow) in the wt is significantly decreased in mutant oocytes with defected telomere clustering (yellow arrowheads); see cartoons below. The normalized distances are plotted and bouquet phenotype

categories are color-coded. Scale bar, 5 μm. *n*, number of oocytes. (**D**) The normalized centrosome-nucleus distance in oocytes pooled from all genotypes in (C), categorized based on their bouquet phenotype. *n*, number of oocytes. (**E**) Images of Sycp3 localization patterns in early and late zygotene stages. Note normal Sycp3 patterns in wt oocytes (yellow arrowheads) and their absence in mutant oocytes (scattered foci, magenta arrowheads). Sycp3 signal accumulates in nucleoli (empty red circle) in all wt and mutant oocytes. Scale bars, 5 μm. (**F**) The distribution of normal and abnormal Sycp3 oocytes from (E). *n*, number of oocytes. (**G**) Images of "leptotene-like" oocytes shown in scale. Scale bars, 5 μm. (**H**) "Leptotene -like" oocyte sizes per genotype. *n*, number of oocytes. Bars are mean ± SD.

(Fig. 2G). Thus, telomere clustering is defective in bouquet-stage mutant oocytes. Mid-bouquet–stage oocytes in *cc2d2a*$^{-/-}$ ovaries also exhibited consistent telomere-clustering defects (fig. S7C).

We tested whether telomere clustering is delayed in mutant ovaries. We repeated the above analysis on oocytes at sizes of 13 to 15 μm in diameter, where the wt telomere clusters are "expanded" and "dispersed" (fig. S7, D and E) toward bouquet dissociation (*19*, *24*). Heterozygous *cep290* and *kif7*, as well as *cep290*$^{+/-}$; *kif7*$^{+/-}$ and *kif7*$^{-/-}$ ovaries, were similar to the wt (fig. S7D). In *cep290*$^{-/-}$ ovaries, telomeres were "expanded" and most were "dispersed," and in *cep290*$^{-/-}$;*kif7*$^{+/-}$ and *cep290*$^{-/-}$;*kif7*$^{-/-}$ ovaries all oocytes were "dispersed" (fig. S7, D and E). "Tight" telomere clusters were not detected at these stages, ruling out delayed clustering. Tight telomere clusters were similarly not detected in late-bouquet-stage oocytes in *cc2d2a*$^{-/-}$ ovaries (fig. S7E). Thus, with loss of cilia, telomeres do not cluster properly, remain distributed on the nuclear envelope, and fail to form the bouquet.

These ciliary loss–associated defects are similar to bouquet disruption by dynein inhibition (*10*–*17*). We treated ovaries with the specific dynein inhibitor ciliobrevin and performed the same bouquet analysis as above (fig. S8A). In contrast to control dimethyl sulfoxide (DMSO)–treated ovaries, dynein inhibition resulted in a dose-dependent increase in oocytes of the "expanded" and "dispersed" categories and a decrease in those of the "tight" category (fig. S8A). Thus, the loss of zygotene cilia phenocopied dynein inhibition in bouquet formation.

We next determined whether these bouquet phenotypes arose directly from ciliary defects. Cep290 localizations include the ciliary basal body and transition zone, as well as the centrosome (*36*, *40*, *52*–*56*). Cep290 is essential for cilia biogenesis (*35*–*40*), but whether it is required for centrosome MTOC functions in oocytes is unknown. The final step in MTOC maturation is γTub recruitment to the centrosome (*57*, *58*). In *cep290*$^{-/-}$ oogonia and early-prophase oocytes, γTub recruitment to the centrosome was intact even in the most severe cases, where cilia were completely absent (fig. S9B). Further, the MT perinuclear organization in *cep290*$^{-/-}$ early-prophase oocytes was not disrupted (fig. S8C). This demonstrates that the centrosome MTOC functions are unaltered, confirming that the observed bouquet defects arose directly from the loss of cilia.

Ciliary anchoring of the bouquet centrosome is required for telomere clustering and proper SC formation

We hypothesized that the zygotene cilium could generate and transmit forces for telomere rotations or provide counterbalance for their movements by anchoring the bouquet centrosome. Force generation by the cilium would require dynein and kinesin motor activity along the ciliary axoneme and could involve cilia motility. We thus addressed the motility of the zygotene cilium. Four lines of evidence suggest that the zygotene cilium is not a motile cilium: (i) Ultrastructure analysis of the zygotene cilium showed a 9+0 axoneme organization without obvious dynein arms (Fig. 1D), which is typical for nonmotile cilia (*59*, *60*); (ii) live time-lapse imaging did not reveal ciliary-beating movement, which is a characteristic of motile cilia (movies S10 and S11); (iii) reporter line expression of motile ciliary master transcriptional regulators of the Foxj1 family, *Tg(foxj1a:GFP)* and *Tg(foxj1b:GFP)* (*61*, *62*), was not detected in prophase oocytes within germline cysts where the zygotene cilium forms (fig. S9); and (iv) motility of zygotene cilia was not essential for fertility. Ccdc103 is a motile cilium dynein assembly factor essential for motility (*63*). *ccdc103*$^{-/-}$ adult females, rescued from embryonic lethality through mRNA injection, were fertile (five of six females mated spontaneously and each produced 50 to 300 eggs with a 50 to 100% fertilization rate). Taken together, these experiments show that the zygotene cilium is not a motile cilium.

To investigate whether the zygotene cilium is required to generate chromosomal movement, we performed live time-lapse imaging of chromosomal rotations in *cep290*$^{-/-}$ ovaries [*Tg(h2a:H2A-GFP);cep290*$^{-/-}$ fish; Fig. 3A and movie S12]. In *cep290*$^{-/-}$ oocytes, chromosomal rotations were still present and we only detected a very small decrease in track velocities (Fig. 3A and movie S12) compared with wt. Twenty percent of *cep290*$^{-/-}$ oocytes, including 13.6% outliers, were plotted lower than the lowest wt oocyte (Fig. 3A and movie S12). However, these *cep290*$^{-/-}$ oocytes still exhibited slower but clear rotations (Fig. 3A, left bottom panels, and movie S12). The persistence of gross chromosomal rotations in *cep290*$^{-/-}$ oocytes allows us to conclude that the zygotene cilium is not an essential generator of chromosomal rotation forces.

We next addressed a potential role for ciliary anchoring of the bouquet centrosome. The centrosome is stationary during chromosomal rotations in zebrafish (movie S2) and mice (*18*) while telomeres are being pulled on MT cables that are associated with it. This suggests that the centrosome is under strain. It is plausible that the centrosome end of the cables must be affixed for the telomeres to be pulled and clustered toward the centrosome and not vice versa. In this case, without such counterbalance, telomeres will fail to cluster and form the bouquet. We hypothesized that the zygotene cilium could function as a physical anchor required for counterbalancing telomere rotation forces and for telomere pulling and clustering.

We tested whether ciliary excision would result in dislocation of the centrosome. To experimentally eliminate potential ciliary anchoring, we performed laser excision experiments in ovaries of double-transgenic fish fluorescently co-labeled for cilia and centrosomes [*Tg(βact:Cetn2-GFP);Tg(βact:Arl13b-GFP)*; Fig. 3B]. We excised the ciliary base in zygotene-bouquet-stage oocytes while tracing the centrosome by live time-lapse imaging. These analyses showed that upon ciliary excision, the associated centrosome immediately dislocated away (Fig. 3B, yellow circle, and movies S13 and S14, red circles). By contrast, other centrosomes in the same cyst and frame that were associated with non-ablated cilia remained relatively stationary (movies S13 and S14, green circles). This supports the specific effect of precise ciliary excision of the targeted centrosome achieved in this experimental setting. Moreover, control experiments with twofold-higher laser power immediately resulted in clear and stereotypic cell death (movies S15 and S16). This phenomenon was clearly distinct from the localized centrosome dislocation observed, arguing against nonspecific consequences of laser treatment on centrosomal behavior. Thus, when disconnected from the cilium, the centrosome does not remain stationary but dislocates. Centrosome dislocation is likely caused by the rotational forces of hauled telomeres that act on its associated microtubules.

We addressed genetically the bouquet centrosome dynamics upon ciliary loss. We found that in the conditions were telomeres were dispersed upon ciliary loss in *cep290*$^{-/-}$, *cep290*$^{-/-}$ *kif7*$^{+/-}$, and *cep290*$^{-/-}$;*kif7*$^{-/-}$, the centrosome was much more juxtaposed to the nucleus compared with wt (Fig. 3C). We labeled ovaries for the centrosome (γTub) and telomeres [Telo-fluorescence in situ hybridization (Telo-FISH)] and measured the distance between the centrosome and the nucleus in the mid-

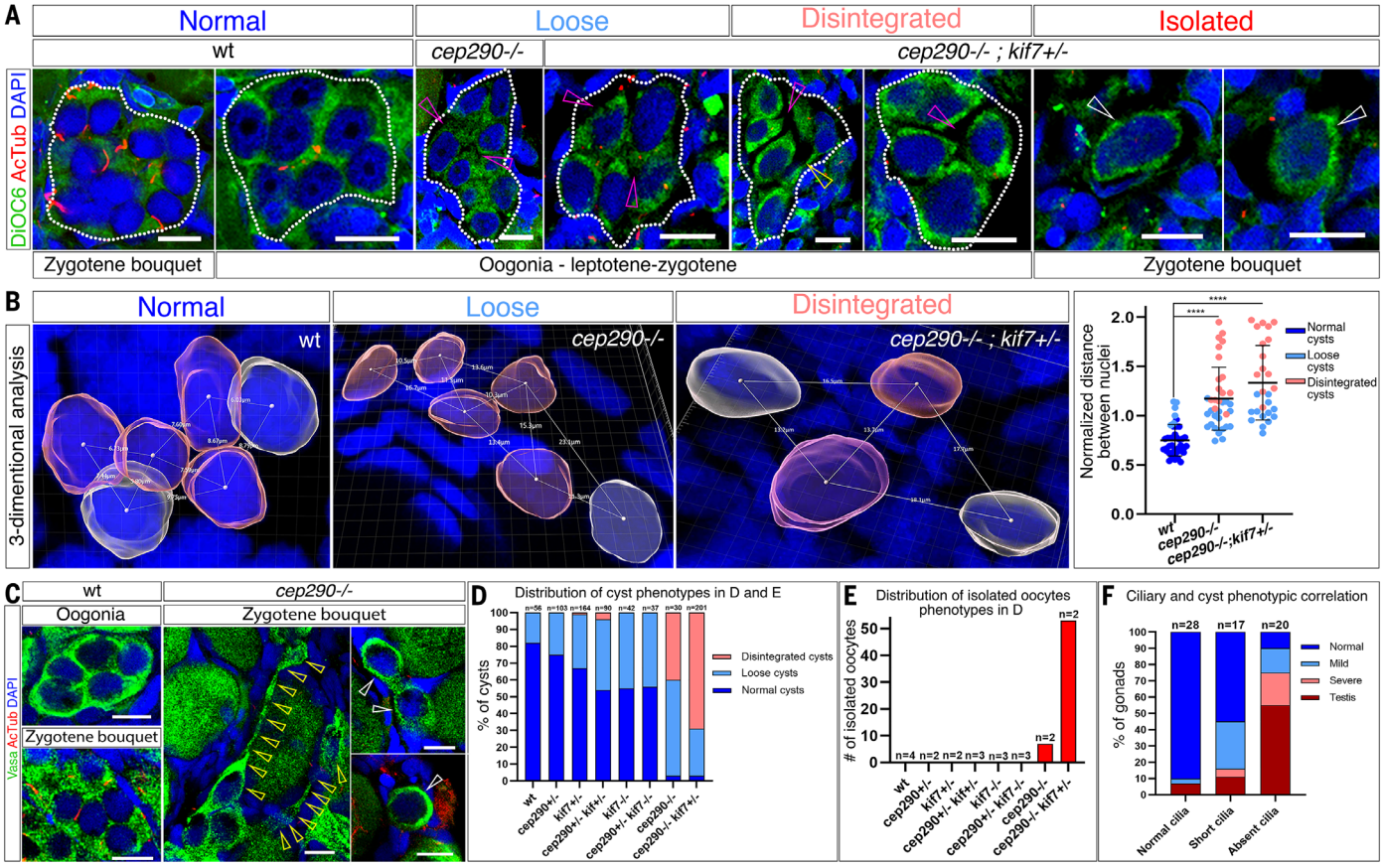

Fig. 4. The zygotene cilium is required for germline cyst morphogenesis. (**A**, **D**, and **E**) Images of cyst (white outlines) phenotype categories labeled for the cytoplasmic marker DiOC6 and AcTub (A), showing gaps between oocytes (magenta arrows), elongated cytoplasmic bridges (yellow arrows) and isolated oocytes (white arrows). Scale bars, 10 μm. The percentage of cyst phenotype categories and number of isolated oocytes are shown in (D) (*n*, number of cysts) and (E) (*n*, number of ovaries), respectively. (**B**) Images of 3D cyst morphology analysis per category. Normalized distances are plotted. *n* = 5 to 7 cysts from *n* = 2 to 3 ovaries per genotype. Bars are mean ± SD. (**C**) Vasa and AcTub labeling shows normal cysts in wt ovaries, and disintegrated cysts (elongated CBs, yellow arrows) as well as isolated zygotene oocytes (white arrows) in *cep290*$^{-/-}$ ovaries. Phenotype distribution is plotted in fig. S11. Scale bars, 10 μm. (**F**) Severity of cyst phenotypes and gonad conversions plotted for three categories of ciliary defects pooled from all genotypes. *n*, number of gonads.

zygotene-bouquet stage oocytes normalized to oocyte size (arrow in Fig. 3C). These normalized distances were significantly decreased in *cep290*$^{-/-}$, *cep290*$^{-/-}$;*kif7*$^{+/-}$, and *cep290*$^{-/-}$;*kif7*$^{-/-}$ oocytes compared with wt (Fig. 3C). In parallel, we independently scored telomere clustering in these oocytes. The shortest centrosome-nucleus distances were measured in oocytes with dispersed telomeres (telomere clustering categories are color coded in Fig. 3C). We reciprocally tested the centrosome-nucleus distance per telomere clustering category in pooled data from all genotypes above (Fig. 3D). We found that the centrosome-nucleus distance associated with telomere-clustering capability. Sufficient distance in "tight" correlated with successful clustering, whereas oocytes with "dispersed" failed clustering always showed the shortest distances (Fig. 3D). This further substantiates the view that a counterbalance between the centrosome and rotating telomeres is an inherently required feature of bouquet formation. Together, these results suggest that the zygotene cilium is required for anchoring the centrosome as a counterbalance for telomere rotations. When cilia are lost, the centrosome is instead pulled toward the nucleus, telomere pooling is less efficient, and bouquet formation fails.

We finally tested whether bouquet failure affected the formation of SCs between pairing chromosomes. It has been shown in zebrafish that the bouquet telomere cluster is a hub for chromosomal pairing (*22*). Double-strand breaks cluster in subtelomeric regions, and the loading of SC protein 3 (Sycp3) is initially seeded in these regions specifically at bouquet stages (*22*, *49*). Sycp3 then spreads from this position along the axes of pairing chromosomes (*22*, *49*). This suggests that telomere clustering in the bouquet configuration could be functionally required for SC formation. We analyzed Sycp3 localization patterns in whole-mount wt and mutant ovaries in the early zygotene-bouquet-stage (oocyte size 10 to 12 μm) and the late zygotene-bouquet-stage (oocyte size 12 to 14 μm) as defined in fig. S1, B and C. All wt and *kif7*$^{-/-}$ zygotene oocytes showed normal Sycp3 patterns, including initial polarized loading of Sycp3 at the early zygotene-bouquet stage (*22*, *49*), and the beginning of its extension along chromosome axes at the late zygotene-bouquet stage (*22*, *49*) (Fig. 3E, yellow arrowheads). By contrast, in most zygotene stage oocytes of *cep290*$^{-/-}$, *cep290*$^{-/-}$;*kif7*$^{+/-}$, and *cep290*$^{-/-}$;*kif7*$^{-/-}$ ovaries, these normal Sycp3 patterns were completely lost, with only few scattered foci remaining in some oocytes (Fig. 3, E and F, magenta arrowheads). All zygotene oocytes from all genotypes showed accumulation of Sycp3 signal in oocyte nucleoli (Fig. 3E, red empty circles). These results are consistent with the corresponding bouquet defects in these mutants (Fig. 2G).

Sycp3 labeling also confirmed the prophase delay observed in our Telo-FISH analyses (Fig. 2, E and F). Measuring the diameter of all oocytes exhibiting the Sycp3 oval patch pattern that is characteristic of the leptotene stage (*23*) (fig.

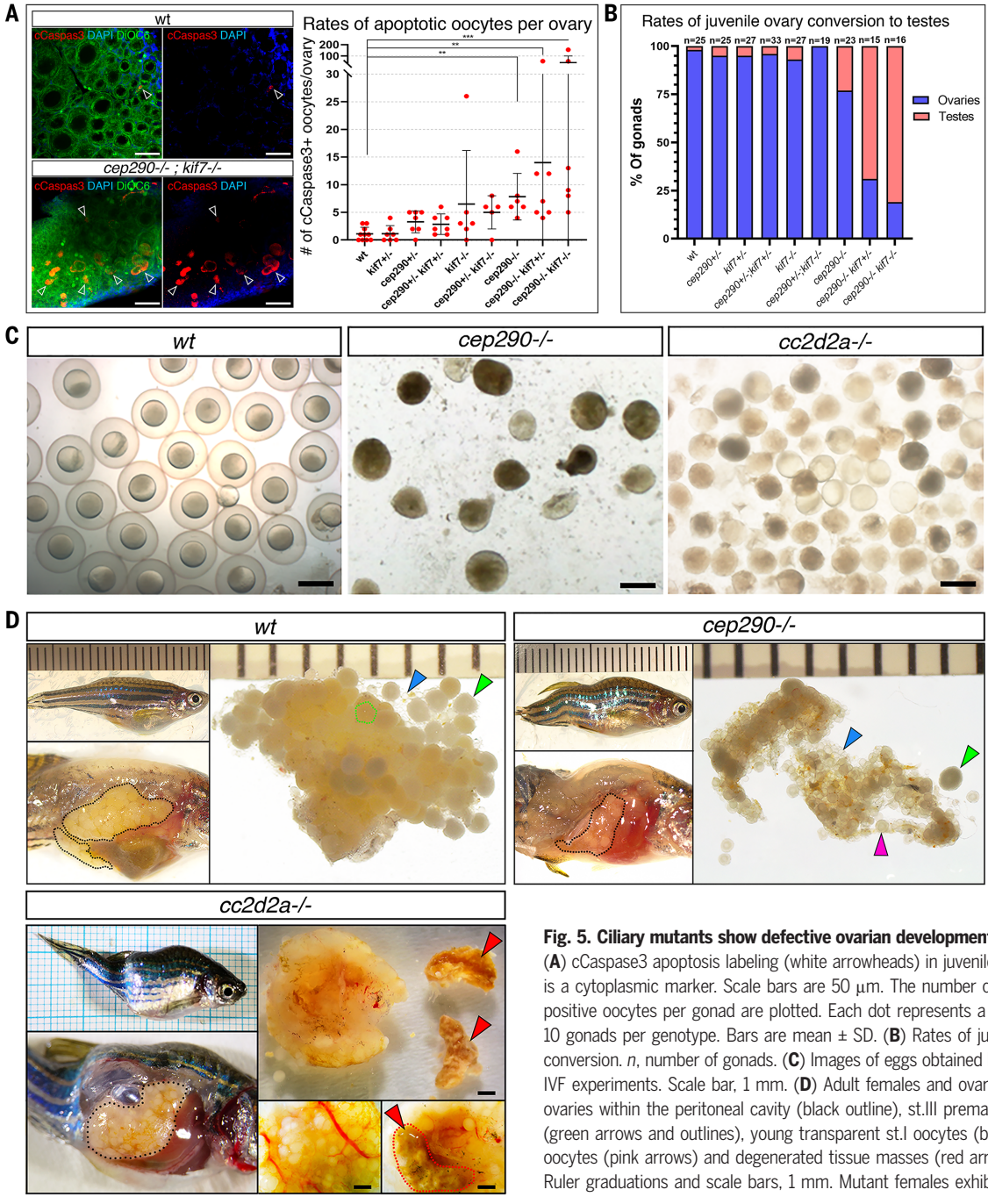

Fig. 5. Ciliary mutants show defective ovarian development and fertility. (**A**) cCaspase3 apoptosis labeling (white arrowheads) in juvenile ovaries. DiOC6 is a cytoplasmic marker. Scale bars are 50 μm. The number of cCaspase3-positive oocytes per gonad are plotted. Each dot represents a gonad, *n* = 5 to 10 gonads per genotype. Bars are mean ± SD. (**B**) Rates of juvenile gonad conversion. *n*, number of gonads. (**C**) Images of eggs obtained by squeezing for IVF experiments. Scale bar, 1 mm. (**D**) Adult females and ovaries showing: ovaries within the peritoneal cavity (black outline), st.III premature oocytes (green arrows and outlines), young transparent st.I oocytes (blue arrows), st.II oocytes (pink arrows) and degenerated tissue masses (red arrow and outline). Ruler graduations and scale bars, 1 mm. Mutant females exhibit scoliosis.

S1C), confirmed their typical sizes in wt and *kif7*$^{-/-}$ ovaries, and that most of these oocytes in *cep290*$^{-/-}$, *cep290*$^{-/-}$;*kif7*$^{+/-}$, and *cep290*$^{-/-}$;*kif7*$^{-/-}$ ovaries were oversized (Fig. 3, G and H). These results confirm defects in prophase progression, where defected oocytes continue to grow while delayed in prophase, as discussed above.

Altogether, these findings demonstrate that upon ciliary loss, failed telomere clustering resulted in failed Sycp3 loading to and along chromosome axes. Thus, the zygotene cilium is required for proper formation of SC, at least partly through bouquet centrosome anchoring.

Loss of the zygotene cilium perturbs germline cyst morphogenesis

We identified a second phenotype in the ciliary mutant ovaries in which germline cysts were disintegrated. The wt cysts are compact, with no gaps between cytoplasmic membranes of adjacent oocytes (*19*), as detected by DiOC6 cytoplasmic staining ("normal" in Fig. 4A). By contrast, in *cep290*$^{-/-}$ and *cep290*$^{-/-}$;*kif7*$^{+/-}$ ovaries, we observed abnormal cyst integrity (Fig. 4, A and D). We categorized cyst disintegration on the basis of severity: "Loose cysts" showed abnormal gaps between oocytes, whereas more severe "disintegrated cysts" showed larger gaps and exposed elongated CBs. In the compact wt cysts, CBs cannot be resolved without a specific marker. However, CBs were obvious in the increased spaces between oocytes in disintegrated cysts of mutants. To quantify cyst disintegration, we measured the normalized distance between all neighboring

nuclei in 3D in wt, *cep290*$^{-/-}$, and *cep290*$^{-/-}$;*kif7*$^{+/-}$ cysts (Fig. 4B, right panel, and movie S17). The normalized distances between neighboring nuclei in *cep290*$^{-/-}$, and *cep290*$^{-/-}$;*kif7*$^{+/-}$ cysts were significantly increased compared with wt (Fig. 4B). A similar cyst integrity phenotype with greater normalized distances between cyst nuclei was observed in *cc2d2a* mutant ovaries (fig. S10, A and B).

We observed a third and most severe category of "isolated oocytes" in *cep290*$^{-/-}$ and *cep290*$^{-/-}$;*kif7*$^{+/-}$ ovaries (Fig. 4, A and E). In wt ovaries, zygotene-bouquet-stage oocytes are never seen outside the germline cyst. Isolated oocytes are zygotene-bouquet-stage oocytes that were found individually scattered in *cep290*$^{-/-}$ and *cep290*$^{-/-}$;*kif7*$^{+/-}$ ovaries (Fig. 4A), indicating their disintegration from cysts. Telomere labeling (Telo-FISH) confirmed that "isolated oocytes" are abnormal zygotene bouquet oocytes (fig. S11A). In contrast to wt, heterozygous and *kif7*$^{-/-}$ ovaries, ovaries of *cep290*$^{-/-}$, *cc2d2a*$^{-/-}$, and *cep290*$^{-/-}$;*kif7*$^{+/-}$ fish barely contained normal cysts but instead harbored mostly disintegrated cysts and isolated oocytes (Fig. 4D and fig. S10A). The *cep290*$^{-/-}$;*kif7*$^{-/-}$ gonads converted to testes in these experiments, preventing oocyte analysis, but indicating oocyte loss caused by severe defects (see discussion below and Fig. 5 and fig. S12). Labeling ovaries with the germ-cell-specific marker Vasa confirmed the detection of isolated zygotene oocytes in doublets and singlets, as well as disintegrated cysts with long cytoplasmic bridges extending between distant oocytes (Fig. 4C and fig. S11, B and C). These oocytes exhibited oval and irregular cellular morphology that coincided with their likely abnormal separation (Fig. 4C). Later pachytene- and diplotene-stage oocytes exhibited irregular mesenchymal-like cellular morphology in *cep290*$^{-/-}$ ovaries instead of their smooth spherical morphology in the wt (fig. S11C). Disintegration of cysts in these Vasa experiments was mostly apparent in *cep290*$^{-/-}$ mutants, whereas *cep290*$^{-/-}$;*kif7*$^{+/-}$ and *cep290*$^{-/-}$;*kif7*$^{-/-}$ were converted to testes (discussed below) (fig. S11B). These results show that the zygotene cilium is required for cyst integrity and morphogenesis.

In all of the experiments above, we colabeled cilia by AcTub staining and simultaneously analyzed cyst integrity and ciliary phenotypes. We analyzed the correlation between these phenotypes. We categorized gonads from all genotypes (n = 43 gonads, n = 10 to 60 cysts per gonad) on the basis of their ciliary phenotype (as in Fig. 2, A to D) and separately their cyst integrity phenotypes (as in Fig. 4D). This revealed a strong correlation between the severity of ciliary loss and severity of cyst phenotypes (Fig. 4F and fig. S10C). This correlation is consistent with our findings that ciliary defects directly underlie bouquet phenotypes (fig. S8B). The most severe phenotype with complete ciliary loss predicts conversion to testes, which represents oocyte loss in zebrafish (discussed below), and was observed in ~60% of gonads (Fig. 4F). We found similar correlation between ciliary loss and cyst phenotypes in *cc2d2a* ovaries (fig. S10C).

Loss of the zygotene cilium is detrimental to oogenesis and fertility

The above bouquet and germline cyst phenotypes represent severe oocyte defects. We tested their consequences on oogenesis and whether they result in oocyte loss by apoptosis. In wt juvenile ovaries, apoptotic oocytes are rare (*64*), as detected by cleaved Caspase3 in wt, *cep290*, and *kif7* heterozygous fish (Fig. 5A). We detected more apoptotic oocytes in *cep290*$^{-/-}$, *kif7*$^{-/-}$ and in *cep290*$^{+/-}$;*kif7*$^{-/-}$ ovaries, and this was significantly increased in *cep290*$^{-/-}$;*kif7*$^{+/-}$ and *cep290*$^{-/-}$;*kif7*$^{-/-}$ ovaries (Fig. 5A). These results show that ciliary loss results in severe oocyte defects and consequently oocyte loss by apoptosis.

Substantial oocyte loss by apoptosis during ovarian development in zebrafish often results in gonad conversion to testis (*9*, *47*–*49*). Consistent with the increased apoptosis levels, we found that in juvenile *cep290*$^{-/-}$;*kif7*$^{+/-}$ and *cep290*$^{-/-}$;*kif7*$^{-/-}$ fish, most gonads converted to testes (Fig. 5B). In all of our analyses above, we examined oocyte phenotypes in normal and affected ovaries (fig. S12) across the reported genotypes before potential conversion. Gonads from these analyses that were converted and did not include oocytes were categorized separately as "converted to testis" (fig. S12) and are described here. In wt and heterozygous mutants, we detected up to ~5% conversion (Fig. 5B), which represents occasional earlier sex determination. By contrast, ~24% of *cep290*$^{-/-}$ ovaries were converted, whereas ~60% of *cep290*$^{-/-}$;*kif7*$^{+/-}$ and ~80% of *cep290*$^{-/-}$;*kif7*$^{-/-}$ ovaries were converted (Fig. 5B). *cep290*$^{-/-}$;*kif7*$^{+/-}$ and *cep290*$^{-/-}$;*kif7*$^{-/-}$ ovaries concomitantly exhibited the highest levels of apoptosis (Fig. 5A). We observed a male bias in adult *cep290*$^{-/-}$, *cep290*$^{-/-}$;*kif7*$^{+/-}$, and *cep290*$^{-/-}$;*kif7*$^{-/-}$ fish (fig. S13). Altogether, these results demonstrate that ciliary loss is detrimental to oogenesis.

Ciliary loss could directly cause the above bouquet and germline cyst phenotypes, which in turn induce apoptosis. Alternatively, they could induce oocyte apoptosis, which in turn causes these phenotypes downstream. Throughout our analyses above, bouquet and cyst phenotypes were detected in oocytes that otherwise appeared viable, suggesting that they preceded apoptosis. To confirm this, we crossed *cep290* fish to *tp53* mutants, which rescues apoptosis (*47*, *48*, *50*). We confirmed that loss of Tp53 completely rescued oocytes from apoptosis in *cep290*$^{-/-}$;*tp53*$^{-/-}$ ovaries (fig. S14A), as well as juvenile ovary conversion to testes (fig. S14B) and the male bias in adults (fig. S14C). Double-mutant juvenile ovaries continued to develop and contained later-stage oocytes with an extremely abnormal morphology that is never detected in *wt* or *cep290*$^{-/-}$ ovaries (fig. S14D). This demonstrates that in *cep290*$^{-/-}$;*tp53*$^{-/-}$ ovaries, defective oocytes, which in *cep290*$^{-/-}$ ovaries were otherwise cleared by apoptosis, survived but failed to develop normally. These results conclude that the loss of the zygotene cilium is detrimental to oocyte development. The defects in bouquet and germline cyst morphology likely activate a meiotic checkpoint (which in turn induces tp53-dependent apoptosis).

We reevaluated the ciliary bouquet and cyst phenotypes in *cep290*$^{-/-}$;*tp53*$^{-/-}$ gonads. We reasoned that if the bouquet and cyst phenotypes were caused by oocyte apoptosis, then they should be rescued in *cep290*$^{-/-}$;*tp53*$^{-/-}$ ovaries. However, if they were caused by the loss of cilia, then they should persist in *cep290*$^{-/-}$;*tp53*$^{-/-}$ ovaries. Bouquet phenotypes, including prophase delay and telomere-clustering defects, were consistently prominent in *cep290*$^{-/-}$ as well as in *cep290*$^{-/-}$;*tp53*$^{-/-}$ ovaries (fig. S15). These findings show that these bouquet phenotypes are caused independently of apoptosis. In *tp53*$^{-/-}$ ovaries, we detected slightly oversized "leptotene-zygotene-like" oocytes (fig. S15, A and B) and ~20% mid-bouquet oocytes with dispersed telomere clusters (fig. S15, C and D). These likely represent oocytes that are normally cleared by checkpoint-induced apoptosis in wt ovaries but are retained in *tp53*$^{-/-}$ ovaries.

We next examined the cyst phenotypes after *p53* knock-out. In both *cep290*$^{-/-}$ and *cep290*$^{-/-}$;*tp53*$^{-/-}$ ovaries, cysts were mostly loose or disintegrated compared with wt (fig. S16, A and C), as confirmed by 3D cyst analysis (fig. S16, B and D). This argues that apoptosis is not a primary cause for cyst disintegration. Although we detected more normal cysts in *cep290*$^{-/-}$;*tp53*$^{-/-}$ ovaries than in *cep290*$^{-/-}$ ovaries, >60% of cysts were defective in these ovaries compared with none in the wt and ~2% in *tp53*$^{-/-}$. The above analyses argue that bouquet and cyst phenotypes are not direct consequences of oocyte apoptosis. We conclude that ciliary loss causes bouquet and germline cyst defects that induce apoptosis, which is detrimental to oogenesis.

For an ultimate readout of oogenesis, we examined adult ovaries and female fertility. *kif7*$^{-/-}$ females, in which ovaries showed normal or only mildly shortened cilia (Fig. 2, A and B), were fully fertile. By contrast, we found that *cep290*$^{-/-}$ and *cc2d2a*$^{-/-}$ adult females did not mate spontaneously in either homozygous in-crosses or when homozygous females were crossed to wt males (fig. S17A). This indicates defective oogenesis, or abnormal spawning or mating behavior, which might be secondary to the characteristic cilia loss–scoliosis phenotype in mutants (*34*, *45*, *65*, *66*). However,

considering that rescued *ccdc103* mutants are fertile (above) despite having profound scoliosis, this is an unlikely possibility. To specifically test for abnormalities in oogenesis, we performed in vitro fertilization (IVF) assays between homozygous mutant females and wt males. Most *cep290*$^{-/-}$ and *cc2d2a*$^{-/-}$ females produced degenerated eggs or no eggs at all (Fig. 5C and fig. S17A). Consistent with their deficient fertility, *cep290*$^{-/-}$ and *cc2d2a*$^{-/-}$ females exhibited profound ovarian dysgenesis (Fig. 5D and fig. S17C). Compared with wt, mutant ovaries were smaller, underdeveloped, and exhibited degenerated masses of tissue (Fig. 5D and fig. S17C). We were able to confirm these phenotypes in a fifth ciliary mutant that is viable in zebrafish and causes human ciliopathies, *armc9* (*9*, *65*, *67*, *68*). *armc9*$^{-/-}$ females exhibited similar fertility deficiency in both spontaneous mating and IVF experiments, as well as ovarian dysgenesis (fig. S17, A to C). These data show that the zygotene cilium is required directly in oogenesis and is essential for ovarian development and fertility.

The zygotene cilium is conserved in male and female meiosis in zebrafish and mouse

Considering the importance of zygotene cilia in oogenesis, we investigated whether it also forms during spermatogenesis. In juvenile testes, co-labeling of AcTub with the cytoplasmic membrane marker β-catenin and with the prophase marker Sycp3 detected cilia-like structures in prophase spermatocytes within developing seminiferous tubules (fig. S18A). Sperm flagella are specialized ciliary structures with similar acetylated tubulin-positive axonemes (*69*). Flagella formation begins after prophase, at midround spermatid stages, and completes by the mature spermatozoa stage (*69*). To distinguish potential zygotene cilia from flagella, we analyzed seminiferous tubules in adult testes, where all spermatogenesis stages can be detected. We co-labeled AcTub with three prophase spermatocyte markers separately: telomere dynamics (Telo-FISH) (*23*), Sycp3 (*49*), and γH2Ax (*49*) (Fig. 6, A to C). Round spermatids had AcTub-positive flagella [E2 in Fig. 6, A to C; staging criteria in (*9*)], and flagella of spermatozoa were very long and swayed within the lumen of the tubules (E3 in Fig. 6, A to C). Zygotene-stage spermatocytes with the characteristic bouquet patterns of telomeres (Telo-FISH), Sycp3, and γH2Ax (*23*, *49*), showed clear AcTub-labeled cilia (Fig. 6, A to C). In pachytene spermatocytes and E1 early-round spermatid stages, some showed AcTub-positive cilia whereas others did not (Fig. 6, A and B). These stages likely represent an intermediate time window during and between zygotene cilia removal and flagella formation. TEM analysis confirmed ciliary structures in zygotene spermatocytes (Fig. 6D). These emanated from densely packed spermatocytes (Fig. 6D) that are distinct from the flagella structures in the lumen of seminiferous tubules (*69*) (fig. S18C). Thus, the zygotene cilium is a separate structure from the flagellum and occurs in the same meiotic stages in spermatogenesis as in oogenesis.

Bouquet mechanisms of meiotic chromosomal pairing are universal in sexually reproducing species (*10*–*18*, *70*–*73*). We thus investigated whether the zygotene cilium is conserved in mammals. In the mouse fetal ovary, oocyte development is synchronized (*74*–*77*). Sycp3 labeling showed that E14.5 ovaries contained mostly early-prophase oocytes (*74*–*77*) (Fig. 6E). AcTub labeling of E14.5 ovaries identified two structures in Vasa-positive germline cysts (Fig. 6F): One resembled a CB and the other a cilium. We confirmed the ciliary structures by co-labeling AcTub and Vasa with ciliary markers. γTub (Fig. 6G), Arl13b (Fig. 6H), GluTub (Fig. 6I), and Adcy3 (Fig. 6J) all confirmed AcTub-positive ciliary structures adjacent to negatively stained AcTub-positive CBs. Co-labeling for Vasa, Sycp3, and GluTub confirmed that the cilia form in prophase oocytes and, similar to zebrafish, within the germline cyst (Fig. 6K and fig. S18D). We also identified ciliary structures in spermatocytes in postnatal day 12 and 16 mouse testes using multiple ciliary markers including Arl13b and GluTub co-labeled with Sycp3 (fig. S19). Adcy3 further identified these ciliary structures and colocalized to the centrosome basal body as labeled with γTub (fig. S19A). These ciliary structures in mouse spermatocytes were very short and included mostly a shortly extended basal body (arrowheads in fig. S19, right panels). Highly similar atypical ciliary structures with yet unknown functions have been previously reported in *Drosophila* spermatocytes (*78*). These results demonstrate that the zygotene cilium is conserved between sexes and across multiple organisms, suggesting that it could be an inherent and fundamental part of the meiosis program.

Discussion

Our work identifies the cilium as a conserved player in meiosis that regulates chromosomal bouquet formation and germ cell morphogenesis. The bouquet telomere dynamics facilitate chromosomal homology searches for pairing and was first described in 1900 (*20*). However, fundamental principles of its activity and regulation are still being uncovered (*15*, *16*, *72*, *79*–*81*). Our work describes the complete framework of the cytoplasmic bouquet machinery as a cable system assembled by the zygotene cilium, centrosome, and microtubules. This machinery biomechanically facilitates telomere dynamics for chromosomal bouquet formation in meiosis. We have shown that as part of this machinery, the zygotene cilium anchors the centrosome to counterbalance telomere rotation and pulling to form the bouquet. Further, we have shown that bouquet telomere clustering is required for proper SC formation. In this machinery, the cilium could also contribute to meiotic progression and cyst organization by transducing an as-yet unknown signal, which will require further investigation.

Our findings suggest that telomere clustering in the bouquet is required for proper SC formation. Investigations in mice established that telomere rotations are essential for homology searches (*11*–*13*, *15*, *16*). However, mutants in these studies prevented proper loading of telomeres onto the NE and/or their association with MT, precluding the experimental uncoupling between telomere rotations and their clustering (*11*–*13*, *15*, *16*). We now show that upon ciliary loss, telomeres rotate on the NE but do not cluster. In these conditions, Sycp3 fails to load on chromosomes and oocytes undergo P53-dependent apoptosis. It is plausible that in the bouquet, telomere clustering could contribute to Sycp3 seeding in assembling the SC. Recent yeast-based mathematical modeling of meiotic chromosomal dynamics showed that pairing is faster if a bouquet configuration is added to the modeling simulation (*82*). In zebrafish, the bouquet telomere cluster was proposed as a hub for chromosomal pairing (*22*). DSB cluster in subtelomeric regions and Sycp3 and Sycp1 initially load adjacent to clustered telomeres, specifically at the bouquet stage (*22*, *49*), and from this position, Sycp3 and Sycp1 then extend along chromosomal axes (*22*, *49*). Our work provides functional evidence to support this mechanism.

Our findings shed new light on reproduction phenotypes in ciliopathies. These have so far been explained by sperm flagella defects and defective motile cilia lining the fallopian tubes and efferent ducts (*83*, *84*). Our study reveals ciliary functions in early differentiating gametes and in fetal ovaries. Severe pediatric ciliopathy syndromes are lethal or lead to acute developmental defects in young children before puberty (*37*–*40*, *85*–*89*), likely masking reproduction phenotypes. In milder ciliopathies, phenotypes could be variable. In our analyses, truncated cilia produced milder phenotypes than complete ciliary loss. Further, *cep290*, *cc2d2a*, and *armc9* females had deficient fertility, but some were able to produce fertilizable eggs. This is consistent with reported pleiotropic and variable ciliopathy phenotypes in humans (*37*–*40*, *85*, *86*). Thus, our findings uncover a mechanism that could additionally contribute to reproduction phenotypes in ciliopathies.

Finally, our work offers the paradigm that ciliary structures can control nuclear chromosomal dynamics. Most cells in metazoans are ciliated and many exhibit cell-type-specific nuclear and/or chromosomal dynamics, implying that ciliary regulation of nuclear events may be widely conserved.

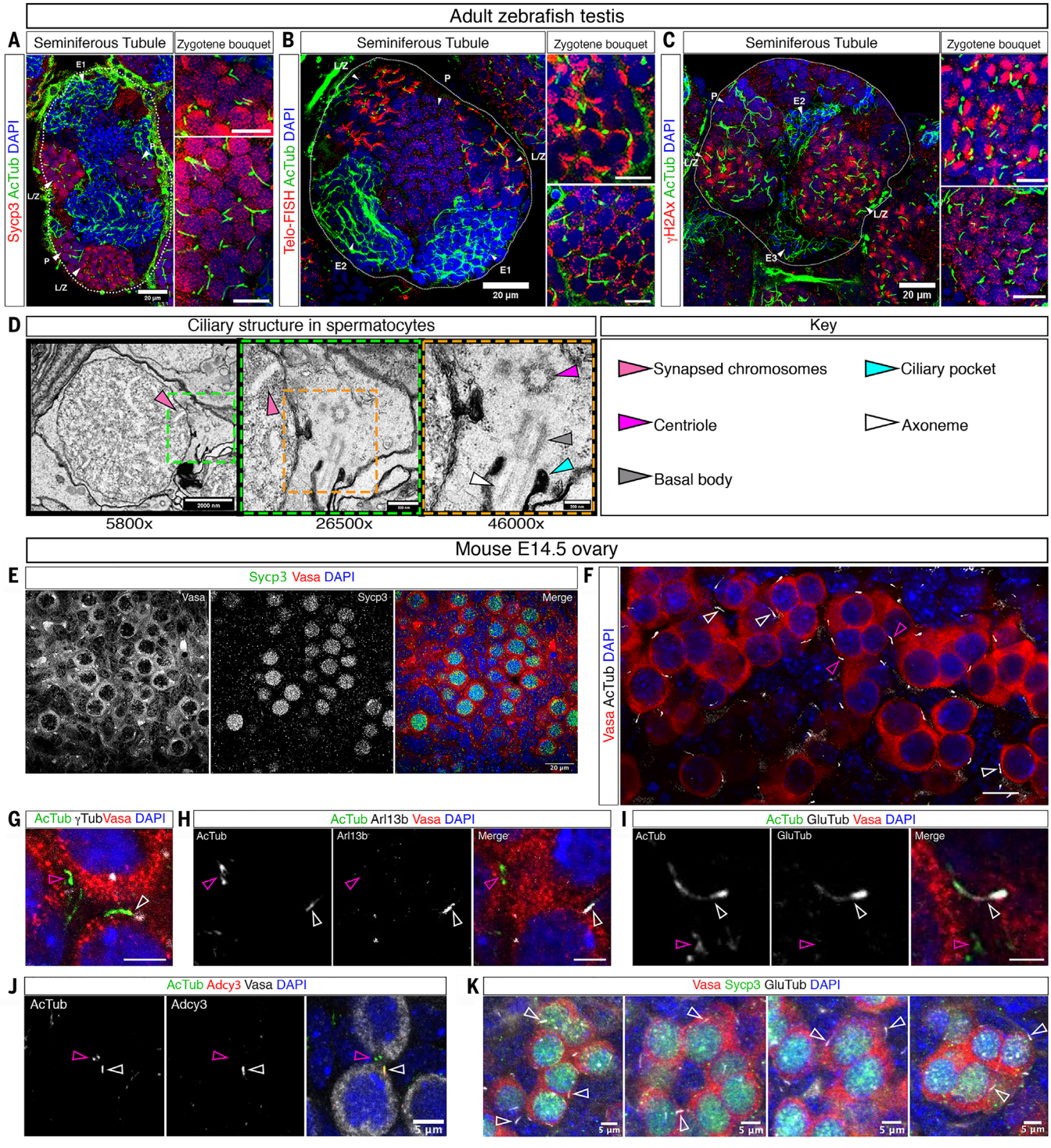

Fig. 6. The zygotene cilium is conserved in zebrafish male meiosis and mouse oogenesis. (**A** to **C**) Seminiferous tubules of adult zebrafish testes labeled with AcTub and Sycp3 [(A), *n* = 35 tubules in *n* = 3 testes] or Telo-FISH [(B), *n* = 29 tubules in *n* = 2 testes] or γH2Ax [(C), *n* = 34 tubules in *n* = 3 testes]. Left panels: optical sections of entire tubules (white outline; scale bars, 20 μm). Right panels: magnified images of zygotene bouquet spermatocytes (early zygotene bouquet in top panels, and late zygotene bouquet in bottom panels; scale bars, 10 μm). L/Z, leptotene/zygotene primary spermatocytes; P, pachytene spermatocytes; E1, initial spermatids; E2, intermediate spermatids; E3, final (mature) spermatids. (**D**) TEM images of adult testis showing ciliary structures (see arrowheads in key) within (left panels) prophase spermatocytes (synapsed chromosomes, pink arrowheads). Colored panels are magnifications of color-coded boxes. Magnifications and scale bars are as indicated. *n* = 25 spermatocytes in *n* = 2 testes. (**E**) Mouse E14.5 ovaries labeled with Vasa and Sycp3. Scale bar, 20 μm. (**F**) Mouse E14.5 ovaries labeled with Vasa and AcTub showing AcTub-positive CBs (pink arrows) and cilia (white arrows) in Vasa-labeled cysts. *n* = 4 ovaries. Scale bar, 15 μm. (**G** to **J**) E14.5 ovaries labeled with AcTub, Vasa, and γTub [(G), *n* = 2 ovaries], or Arl13b (H), *n* = 2 ovaries], or GluTub [(I), *n* = 2 ovaries], or Adcy3 [(J), *n* = 2 ovaries]. Scale bars, 5 μm. (**K**) E14.5 ovaries co-labeled with Vasa, Sycp3, GluTub, and DAPI. Individual channel images are shown in fig. S18 (*n* = 2 ovaries). Scale bars, 5 μm. In (E) to (J), cilia (white arrows) and CB-like structures (pink arrows) are indicated.

Materials and Methods

Ethics statement

All animal experiments were supervised by the Hebrew University Authority for Biological Models, the Veterinäramt Zürich, and the Singapore National Advisory Committee on Laboratory Animal Research according to the institutional animal care and use committee and accredited by AAALAC. All experiments were appropriately approved under ethics requests MD-2016222-1, MD-18-15600-2, ZH116/2021- 33632, 191419, and 191429.

Fish lines and gonad collections

Juvenile ovaries were collected from 5 to 7 weeks postfertilization (wpf) juvenile fish. Fish had a standard length (SL) measured according to (*90*) and were consistently ~10 to 15 mm in length. Ovary collection was done as in (*18*, *24*). Briefly, to fix the ovaries for immunostaining and DNA-FISH, fish were cut along the ventral midline and the lateral body wall was removed. The head and tail were removed, and the trunk pieces with the exposed abdomen containing the ovaries were fixed in 4% paraformaldehyde (PFA) at 4°C overnight with nutation. Trunks were then washed in phosphate-buffered saline (PBS), and ovaries were finely dissected in cold PBS. Ovaries were washed in PBS and then either stored in PBS at 4°C in the dark or dehydrated and stored in 100% MeOH at −20°C in the dark. Testes were collected similarly from 7-wpf juvenile fish and from adult fish and processed similarly. Adult ovaries were collected from wt and mutant fish using similar microdissection and imaged using a Leica S9i stereomicroscope and camera.

Fish lines used in this research were: TU wt, *cep290*^{fh297}(*34*), *kif7*^{i271}(*41*), *cc2d2a*^{w38} (*45*), *tp53*^{M214K}(*91*), *Tg(μ−act:Arl13b-GFP)* (*92*), *Tg(h2a:H2A-GFP)* (*93*), *Tg(μ−act:Cetn2- GFP* (*94*), *Tg(foxj1a:GFP)* (*62*), *Tg(foxj1b:GFP) (61)*, *Tg(μ−act: mCherry-Cep55l)*,and *armc9*^{zh505} (*68*). The *Tg(μ−act: mCherry-Cep55l)* line was generated using the *tol2* system. *mCherry-cep55l* was polymerase chain reaction amplified from a *mCherry-cep55l C1* vector (*95*) and cloned into *pDest-Tol2* plasmid under the *β-actin* promoter using Gibson assembly (E5510S; New England Biolabs).

Staging of prophase oocytes

Oocyte prophase stages were determined on the basis of established staging criteria (*18*, *24*) (fig. S1B). We established prophase staging criteria for zebrafish oocytes on the basis of the characteristic telomere dynamics at each stage (*18*, *24*). Briefly, telomeres are distributed intranuclearly in mitotic oogonia, then load on the NE at the onset of meiosis and remain radially distributed on the NE through the leptotene-zygotene stages (including during chromosomal rotations). Telomeres are clustered at one pole of the nucleus during zygotene bouquet stages. Later, they disperse radially and dissociate back into the nuclear vicinity (*18*, *24*). We characterized cellular features, including the typical oocyte size and nuclear morphology, that strictly and distinctively accompanied each telomere distribution, such that they identify each stage even without telomere labeling (*18*, *24*) (fig. S1B). We developed a reliable method for measuring oocyte size in diameter in 3D (*24*), which we routinely use for determining the oocyte size as part of its staging criteria. For example, oogonia with dispersed intranuclear telomere distribution was always ~10 μm with noncondensed 4′,6-diamidino-2-phenylindole (DAPI)–labeled DNA and central one to three nucleoli, leptotene-zygotene stages with telomere radially loaded on the NE were always 7 to 9 μm with central few nucleoli and zygotene bouquet with clustered telomeres on the NE were always 10 to 16 μm with condensed DAPI-labeled chromosomes and a peripheral single nucleolus (*18*, *24*) (fig. S1B).

In this study, to further precisely determine the specific leptotene-zygotene stages of prophase oocytes, we used the established nuclear patterns of the synaptonemal complex protein Sycp3. We identified the characteristic patterns to each prophase stage as established in (*22*, *23*). The leptotene stage is characterized by an elongated patch of Sycp3 signal in the oocyte nucleus (*22*, *23*) (fig. S1C). Early zygotene is characterized by a polarized Sycp3 signal that corresponds to the bouquet telomere cluster, where it begins to load on chromosomes in zebrafish (*22*, *23*) (fig. S1C). During late zygotene, the Sycp3 signal extends from its polarized location along chromosomal axes (*22*, *23*) (fig. S1C). We measured oocyte size per each Sycp3 pattern in three dimensions in wholemount ovaries, as described in (*24*). Figure S1C shows Sycp3 patterns and their corresponding oocyte sizes. Note that these Sycp3-based oocyte sizes are fully consistent with these based on Telo-FISH and morphological features above, further confirming our staging criteria. In all our analyses we always included cytoplasmic labeling (like DiOC6) or used the background of other labeling to visualize oocyte cytoplasm, measure oocyte size in three dimensions (*18*, *24*), and determine its prophase stage based on the size and morphological criteria.

Fluorescence immunohistochemistry (IHC) and DNA-Telo-FISH

IHC was performed as in (*18*, *24*). Briefly, ovaries were washed twice for 5 min in PBT (0.3% Triton X-100 in 1× PBS; if stored in MeOH, ovaries were gradually rehydrated first), then washed four times for 20 min in PBT. Ovaries were blocked for 1.5 to 2 hours in blocking solution (10% fetal bovine serum in PBT) at room temperature and then incubated with primary antibodies in blocking solution at 4°C overnight. Ovaries were washed four times for 20 min in PBT and incubated with secondary antibodies in fresh blocking solution for 1.75 hours; they were light protected from this step onward. Ovaries were washed four times for 20 min in PBT and then incubated in PBT containing DAPI (1:1000; Molecular Probes) with or without $DiOC_6$ (1:5000; Molecular Probes) for 50 min and washed twice for 5 min in PBT and twice for 5 min in PBS. All steps were performed with nutation. Ovaries were transferred into Vectashield (with DAPI; Vector Laboratories). Ovaries were finally mounted between two #1.5 coverslips using a 120-μm spacer (Molecular Probes).

Primary antibodies used were γ-tubulin (1:400; Sigma-Aldrich), green fluorescent protein (GFP; 1:400; Molecular Probes), Vasa (1:5000) (*96*), acetylated tubulin (1:200; Sigma-Aldrich), β-catenin (1:1000; Sigma-Aldrich), Arl13b (*97*), glutamylated tubulin (1:400; Adipogen), Sycp3 (1:200; Abcam), ψH2Ax (1:400; GeneTex), and cCaspase3 (1:300; Abcam). Secondary antibodies were used at 1:500 (Alexa Fluor; Molecular Probes).

Telo-FISH was performed using the PNA technique (PNA-Bio) following the manufacturer's protocol. Hybridization buffer was 70% formamide, 1 mM Tris, pH 7.2, 8.5% $MgCl_2$ buffer (25 mM magnesium chloride, 9 mM citric acid, and 82 mM sodium hydrogen phosphate, pH 7), 1× blocking reagent in maleic acid buffer (100 mM maleic acid, pH 7.5), 0.1% Tween 20, and 88 nM probe (*5 -CCCTAACCC-TAACCCTAA-3* ,Cy3-conjugated).

For a combination of IHC with Telo-FISH, IHC was performed first. At the end of the IHC procedure, ovaries were washed an extra time for 30 min in PBT and fixed quickly in 4% PFA for 15 to 20 min at room temperature. After staining was complete, DAPI (with or without $DiOC_6$) staining and mounting was performed as described above.

Confocal microscopy, image acquisition, and image processing

Images were acquired on a Zeiss LSM 880 confocal microscope using a 40× lens. The acquisition setting was set between samples and experiments to: XY resolution = 1104 × 1104 pixels, 12-bit, 2× sampling averaging, pixel dwell time = 0.59 s, zoom = 0.8×, pinhole adjusted to 1.1 μm of Z thickness. Increments between images in stacks were 0.5 3μm, and laser power and gain were set in an antibody-dependent manner to 7 to 11% and 400 to 650, respectively, below saturation condition. Unless otherwise noted, images shown are partial sum Z-projection. Acquired images were not manipulated, and only contrast and brightness were linearly adjusted. All figures were made using Adobe Photoshop CC 2014.

Confocal live and time-lapse imaging of cultured ovaries

Live imaging was performed as in (*24*). Briefly, ovaries were dissected from juvenile fish (5 to

7 wpf, SL ~10 to 15 mm) into fresh warm HL-15 medium [Hanks solution containing 60% L-15 with no phenol red (Sigma-Aldrich) and 1:100 Glutamax (Invitrogen) warmed to 28°C]. Ovaries were then embedded in 0.5% low-melt agarose in HL-15 on a glass-bottom dish and covered with warm HL-15. After the agarose polymerized, ovaries were incubated in HL-15 at 28°C. Time-lapse images of live ovaries were acquired using either a Zeiss LSM 880 or Nikon Ti2E spinning-disk confocal microscopes, both equipped with an environmental chamber set to 28°C and using 40× and 60× lenses, respectively. Images were acquired every 6 s for single Z sections or every 18 to 20 s for Z stacks for 5 to 10 minutes.

Chromosome rotation tracking in live time-lapse images

Live time-lapse imaging of *Tg(h2a:h2a-gfp)* cultured ovaries were performed as above, recording large frames of ovaries that included multiple zygotene oocytes, oogonia, and somatic pre-granulosa cells side by side and under identical conditions. Chromosomal dynamics in these cells were tracked on the basis of H2A-GFP intensities using the TrackMate plugin on ImageJ (*98*) with the following setting parameters. Blob diameter was set to 3 μm with an appropriate threshold, and Linking distance was set to 4 μm with a maximum permissibility of two frame gaps for gap closing and a gap-closing maximum distance of 1 μm. Identified tracks were confirmed manually. Selected tracks were identified over 20 to 30 consecutive time points; at least six consecutive time points were selected, and images with at least two appropriately identified tracks were analyzed. For track visualization, spot sizes were set to 0.2 of the original spot radius ratio (~0.6 μm), and tracks were set to show tracks backward and color-coded for time. Tracks were then recorded as an overlay on the original image using the "capture overlay" function. Track parameters, including velocity, displacement, and track duration, were exported to Excel and GraphPad Prism for statistical analysis.

Coloc2 analysis

A pixelwise quantitative test for colocalization of AcTub with Arl13b and with GluTub signals was performed using the Coloc 2 plug-in on Fiji as in (*18*). Cilia regions of interest (ROIs) were taken along individual cilia from representative images. The shapes of the ROIs vary according to the cilia orientation: ROI of straight cilia are narrower, whereas ROI of bent or curled cilia are wider. However, the spaces taken around the cilia were consistent in all ROIs. We calculated a point spread function of ~1.6 pixels on average for each channel and image based on PSF = 0.8 × exitation wavelength (nm)/objective's numerical aperture]/pixel size (nm). Minimum and maximum thresholds were automatically set by the plug-in for each image. The Pearson correlation coefficient (R) was calculated. R values were interpreted as follows: $-1 < R < 0$ for anticorrelation; $R = 0$ for no correlation; and $0 < R < 1$ for correlation. The plug-in then scrambled the pixels to generate a random image and test for the probability to yield the same Pearson coefficient from a random image. Scrambling was set to 100 iterations, generating 100 different random images from the tested image's pixels. The probability of receiving the calculated Pearson coefficient values for both AcTub and Arl13b and AcTub and GluTub were $P = 1$. A pixelwise quantitative test for colocalization of GluTub with Cep55 was performed similarly.

Image 3D reconstructions in IMARIS

ROIs of whole cysts were extracted from confocal raw data and used to reconstruct nuclei, cilia, and other cellular features with respect to each other using blend volume rendering mode. Signal brightness and object transparency were edited in all channels to optimize signal and reduce background. Animation frames were made using the key frame animation tool.

SBF-SEM

Resin-embedded ovaries were mounted onto a cryo pins using conductive silver epoxy, and targeted trimming was performed using an ultra-microtome (Leica) to expose specific areas of the ovaries. The trimmed block was painted with Electrodag silver paint and coated with 10 nm AuPd using a Q150T sputter coater (Quorum Technologies).

Cysts were imaged using a Gatan 3View mounted on a Quanta 250 SEM (FEI). Two areas containing cysts were imaged using the multiple ROI function, ROI-00 and ROI-01. Imaging conditions were as follows: for ROI 00, magnification 3445×, pixel size 5.9 nm in x and y, 75 nm in z, image dimensions 8189 × 5932 pixels; for ROI 01, magnification 3480×, pixel size 5.9 nm in x and y, 75 nm in z, and frame width 8192× 5932. The chamber pressure was 70 Pa. 2.8kV, dwell time per pixel 68 μs for both ROIs. Before converting the images into TIFF format with Digital Micrograph, they were binned by two, giving a final pixel size in x and y of 12 nm.

3D rendering of SBF-SEM images

Renders were made from over 330 75-nm sections for each cyst (movie S3). The image sequence generated from SBF-SEM was imported into ImageJ. The imported image was then adjusted with the correct voxel size, brightness, contrast, and alignment. The stack was imported into TrakEM2 canvas for segmentation. In TrakEM2, a project tree was made by adding area lists. Once the area list was made, cells were manually segmented at every seventh to eighth slice using the brush tool of ImageJ, and the gap was filled by using the interpolation function of TrakEM2. The segmented structure of the cyst was then exported as a TIFF file to IMARIS software, and image properties were set to the acquisition voxel size. Surfaces were created using the surface creation wizard, and color and transparency were set for individual cells. The segmented cells were then exported as "scenes." This pipeline was repeated for different structures of the cyst and exported a different scenes from the area lists. Then, the SBF-SEM image stack was imported to the arena area of IMARIS. The voxel size was corrected, and Scenes were imported. Once all the scenes were imported, color and transparency were set for individual elements for optimal representation. The reconstruction was finally saved using the animation function of IMARIS (movies S3 and S6).

Rescue of ccd103 mutant embryonic lethality

The mRNA of zebrafish ccdc103 was transcribed from template with the mMessage mMachine SP6 transcription kit (Invitrogen, AM1340). To rescue the mutants, a total of 0.5 nl of the mRNA with final concentration of 150 ng/μl was injected into the animal pole of one-cell-stage embryos. Rescued *ccd103*$^{-/-}$females were confirmed by genotyping and exhibited the characteristic scoliosis phenotype, which results from loss of ciliary motility from ependymal cells in the spine central canal.

Measurements of cilia and CBs in SBF-SEM data

The image sequence was imported as a stack in Fiji. The image voxel size was set as per the acquisition metadata by selecting image properties. Slices in which cytoplasmic bridges or cilia were widest were selected. Using the line tool from the Fiji menu bar, measuring lines were drawn across the width of the cilia or CBs. The lines drawn were color-coded red from overlay properties and added to the ROI manager. Three measurement lines were drawn across cilia and CB longitudinal sections. Two perpendicular lines were drawn across cilia cross-sections (along perpendicular diameters). All lines in ROI manager were measured, and the resulting table was saved as a CSV file, exported to Excel for calculating average width of CB and cilia, and graphical representation was produced using GraphPad Prism 8.

Measurements of cilia length in confocal data and defining ciliary length categories in wt and mutant ovaries

Ten representative cyst ROIs from each genotype were cropped in Fiji and used for image processing in the IMARIS 3D software. The filaments IMARIS feature was used to mark the cilia pathways, as follows. To create the cilium filament, the auto-depth semi-automatic

IMARIS algorithm was used, combining user's manual tracking and local signal intensity (fig. S6). After creating filaments for all cilia in a cyst, the filament lengths were extracted to Excel and GraphPad Prism for statistical analysis, and the images of cilia tracks were extracted as JPEG files (fig. S6).

We first measured ciliary lengths in wt cysts in 3D as described above and defined ciliary length categories. wt cilia mostly ranged between 4 and 8.5 μm, with the longest cilia reaching 12 mm (Fig. 2A). We defined ciliary lengths at 4 to 8.5 μm as "normal cilia" and cilia with outlier values <4 μm as "short cilia." Cilia that were only detected as an extremely short dot-like signal that was <1 μm or not detected at all were defined as "absent cilia" (ND in Fig. 2, A and B). Individual cilia were measured as described above in cysts from all genotypes (Fig. 2A), and the average ciliary length per cyst was calculated (Fig. 2B). Cysts with average cilia lengths >4 μm were scored as cysts with normal cilia, and cysts with average cilia lengths <4 μm were scored as cysts with short cilia (Fig. 2B). Distribution of scored cysts were plotted (Fig. 2C), entire ovaries were scored, and their distribution for the same categories was plotted (Fig. 2D).

Bouquet analysis

Zygotene bouquet stages span oocyte sizes of 10 to 16 μm in diameter (*18*, *24*). We reasoned that the telomere cluster may be less compact during its early formation (oocyte sizes of 10 to 11.5 μm in diameter) and its later dissociation (oocyte sizes 13 to 16 μm in diameter). We therefore focused on midbouquet stages (oocyte sizes 11.5 to 13 μm in diameter) that show clear clusters (*18*, *24*). We co-labeled telomeres by Telo-FISH and the cytoplasm with $DiOC_6$ (Fig. 2G). We scored all oocytes blinded to the Telo-FISH channel, measured their size in diameter on the basis of the $DiOC_6$ cytoplasmic labeling according to (*24*), and selected oocytes at midbouquet sizes (11.5 to 13 μm). We then used the Telo-FISH channel to analyze the distribution of telomeres in all Z sections spanning these entire oocytes. Categories were defined as "tight" for telomere clusters at one pole of the nucleus that spanned up to approximately 25% of the nuclear circumference, "expanded" for wider clusters that spread beyond 25% of the nuclear circumference and up to the nuclear equator, and "dispersed" for unclustered telomeres that spread over the nuclear equator, as shown in Fig. 2G. The analysis in fig. S7D, which addresses later bouquet stages, was performed identically, but selected oocytes were at a size range of 13 to 15 μm.

Ciliobrevin treatment

Ovaries were dissected from juvenile wt fish and cultured in HL-15 as described in the "Confocal live and time-lapse imaging of cultured ovaries" section above. The HL-15 medium was then replaced with HL-15 medium containing either DMSO or 15 or 50 μM ciliobrevin. Ovaries were incubated for 80 min at 28°C, and fixed for Telo-FISH, $DiOC_6$, and DAPI labeling. Bouquet analysis was performed on 11.5- to 13-μm oocytes as described above.

Ciliary laser excision

Ovaries were dissected from 6 wpf *Tg(βact:Arl13b-GFP);Tg(βact:Cetn2-GFP)* fish and mounted as described for live imaging above. Excisions were performed using a Leica TCS SP8 MP two-photon microscope with a 25× objective and equipped with an incubation chamber set to 28°C. An ROI with a good number of cilia in the field of view was selected. The laser stimulation region for excision was drawn manually using the "draw ROI" function. Time-lapse was recorded for 60 s before ablation, followed by a laser stimulation (900 nm, 2.79 W) for 20 s, and time-lapse recording for 8 min after ablation (movies S13 and S14). Control experiments (movies S15 and S16) were performed side by side with the experimental ablations under identical conditions and settings, except laser power was set to 4 W for 20 s.

Centrosome-nucleus distance measurements

The distance between the centrosome and the nucleus was measured in wt and mutant ovaries co-labeled for centrosome (γ-Tub antibody) and telomeres (Telo-FISH) and counterstained with DAPI. Oocyte at the mid-zygotene bouquet stage were selected as in the bouquet analysis above (oocyte size 11 to 13 μm). For centrosome-nucleus distance measurements, the optical section that includes the center of the centrosome was selected, and the distance between the centrosome and the closest point on the nucleus surface was measured in Fiji. Measurements were tracked using the Fiji ROI manager. We then independently scored the telomere clusters of measured oocytes to the tight, expanded, and dispersed categories according to the bouquet analysis above. Centrosome-nucleus distances were normalized to oocyte size (diameter), plotted per genotype, and color-coded for telomere cluster categories (Fig. 3C). Pooled oocytes from all genotypes in this analysis were also plotted per telomere cluster category (Fig. 3D).

Sycp3 phenotype analysis

To analyze effects on Sycp3 in wt and mutant whole-mount ovaries labeled for Sycp3 and DAPI, we scored oocytes at three stages and sizes based on our wt prophase staging in fig. S1, B and C: early zygotene (10 to 12 μm) and late zygotene (12 to 14 μm). For each stage, we selected oocytes of the appropriate size range, and then scored the Sycp3 signal as either normal or defected (Fig. 3E) compared with wt and as shown in fig. S1, B and C.

Quantitative analysis of cyst morphology and integrity

We defined phenotype categories for germline cyst morphology, as follows: The "loose cysts" category showed abnormal gaps between sister oocytes in cysts (Fig. 4A); the disintegrated cysts category phenotype was more severe, showing larger abnormal gaps between cyst oocytes (Fig. 4A) and clear elongated CBs extending between distant oocytes (Fig. 4A). Normally, at later stages when oocytes leave the cyst, their CBs are detected by MT labeling and appear elongated as they disjoin from their sister oocytes (*18*). Within normal cysts, CBs are very challenging to detect by either MT (*18*) or cytoplasmic labeling without a specific marker (Fig. 4A). This is likely because the cytoplasmic membranes of oocytes interface tightly, masking the fine and short structure of CBs (fig. S4). In disintegrated cysts, the elongated CBs are visible without labeling of MT or specific markers and are similar to the MT-detected CBs of oocytes that naturally leave the cyst later (*18*). They likely represent CBs of oocytes that are separating.

For quantitative analysis of category phenotypes, and because borders between tight cells in wt cysts are difficult to detect, we measured the distances between the centers of all the neighboring nuclei in 3D in wt, *cep290*$^{-/-}$,and *cep290*$^{-/-}$;*kif7*$^{+/-}$ cysts (Fig. 4B, fig. S10B, and movie S17). All distances were normalized to the average oocyte diameter per cyst (Fig. 4B and fig. S10B, right panels). Five to eight representative cysts ROIs from each phenotypic category were cropped in Fiji and used for image processing in IMARIS 3D software. We used a semiautomatic segmentation approach to create nuclei surfaces. Each nucleus was segmented in each Z layer to create a full 3D surface either by the software automatic segmentation (intensity based) or by marking the nucleus contour manually. After creating surfaces for all cyst nuclei, we used the measurement point feature to calculate the distances between the center of mass of all neighboring nuclei. Distance measurements were exported to an Excel sheet and normalized to the average oocyte size [diameter in micrometers, measured as in (*24*)] per given cyst. Normalized distances were exported to GraphPad Prism for statistical analysis between groups and generation of dot plots. Images of processed cysts were exported from IMARIS.

Correlation analysis of cyst integrity and ciliary phenotypes

In all cyst morphology experiments, we co-labeled cilia with AcTub staining and simultaneously analyzed cyst and cilia phenotypes. To analyze the correlation between cyst and ciliary phenotypes, we pooled gonads from across all examined genotypes and categorized

them by the effect on cilia, i.e., normal, short (truncated), or absent (as in Fig. 2, A to D) regardless of their genotype. We then investigated how many cysts per ciliary phenotypic category were observed in each ovary and, based on this distribution, labeled ovaries as normal, mildly affected, or severely affected (n = 43 gonads, n = 10 to 60 cysts analyzed per gonad). We next categorized cyst phenotypes in these ovaries and considered disintegrated and isolated oocytes categories as severe effects. In most ovaries, a certain cyst phenotype category was predominant in at least 50% of cysts. The ovary category was chosen according to this cyst category or to the most frequently detected one in few cases where no category was frequent in 50% of cysts. The frequency of cyst severity phenotypes was plotted for each ciliary phenotype (Fig. 4F). *cc2d2a* mutants were analyzed identically (fig. S10C).

Determining stages of spermatogenesis

We identified all spermatogenesis stages in tubules based on their characteristic nuclear morphology and size using DAPI counterstain according to (*99*), as well as the prophase markers telo-FISH, Sycp3, and gH2Ax, as described in the text. Briefly, round spermatids had small round nuclei (2.5 ± 0.1 μm in diameter) and were found toward the center of the tubule as expected. Spermatozoa had compact round nuclei (2.1 ± 0.1 μm in diameter) and were found in the lumen of the tubules as expected. Early round spermatids had a nuclear diameter of 3 ± 0.1 μm. Round spermatids and spermatozoa were negative to all three prophase markers. Nuclear diameter of leptotene-zygotene spermatocytes and pachytene spermatocytes were 5.1 ± 0.1 and 6 ± 0.1 μm, respectively, and both were positive for all prophase markers, showing the expected pattern of each stage (*23*, *49*).

TEM

Gonads were dissected from juvenile fish (5 to 7 wpf, SL ~10 to 15 mm) and fixed as described above in PBS containing 4% PFA and 2.5% glutaraldehyde overnight at 4°C. Gonads were then rinsed four times for 10 min in 0.1 M cacodylate buffer, pH 7.4, and postfixed and stained with 1% osmium tetroxide, 1.5% potassium ferricyanide in 0.1 M cacodylate buffer for 1 hour. Ovaries were washed four times in cacodylate buffer, followed by dehydration in increasing concentrations of ethanol consisting of 30, 50, 70, 80, 90, and 95% for 10 min each step, followed by 100% anhydrous ethanol three times for 20 min each step, and propylene oxide two times for 10 min each step. After dehydration, the ovaries were infiltrated with increasing concentrations of Agar 100 resin in propylene oxide, consisting of 25, 50, 75, and 100% resin for 16 hours each step. Gonads were embedded in fresh resin and left to polymerize in an oven at 60°C for 48 hours.

Embedded gonads in blocks were sectioned with a diamond knife on a Leica Reichert Ultracut S microtome, and ultrathin sections (80 nm) were collected onto 200-mesh, thin-bar copper grids. The sections on grids were sequentially stained with uranyl acetate for 10 min, and with lead citrate for 10 min, and imaged with Tecnai 12 TEM 100 kV (Phillips) equipped with a MegaView II CCD camera and Analysisversion 3.0 software (Soft Imaging System). For TEM images, only the brightness and contrast were slightly adjusted in Adobe Photoshop. These adjustments did not affect the biological properties of the imaged cellular features.

IVF

IVF was performed as in (*100*). Briefly, sperm were collected from anesthetized males into Hank's solution and stored on ice until eggs were collected. Sperm from two males of the same genotype were collected into a single tube and used to fertilize eggs collected from control wt, *cep290*^{fh297}, *cep290*^{fh378}, *cc2d2a*^{w38}, or *armc9*^{zh505}homozygous females. Anesthetized wt or mutant females were placed in a dish and squeezed for egg collection. On hundred to 150 μl of sperm solution was added to the collected eggs and incubated for 20 s. One milliliter of E3 containing 0.5% fructose was added to activate sperm, gently mixed, and incubated for 2 min. Two milliliters of E3 was added, followed by 5 min of incubation. The dish was then flooded with E3 and placed in a 28°C incubator until examination of fertilization rates.

Mouse gonads and IHC

The C57BL/6 inbred strain of mice was used for all experiments. Ovaries from fetal mice at embryonic day 14.5 were first fixed in trunk with 4% paraformaldehyde in PBS at room temperature for 2 hours before being dissected out and washed briefly in PBS. The ovaries were further permeabilized with 0.3% Triton X-100 in PBS for 30 min at room temperature, followed by blocking with 3% bovine serum albumin (BSA) in 0.3% Triton X-100 in PBS for 1 hour at room temperature. Primary antibody incubation was performed at 4 overnight. After washing for 20 min six times with 0.3% Triton X-100 in PBS, the ovaries were incubated with secondary antibodies at room temperature for 3 hours. The stained ovaries were finally washed for 20 min six times with 0.3% Triton X-100 in PBS and mounted in 70% glycerol.

Testes from postnatal day 12 and 16 mice were fixed in the trunk with 4% paraformaldehyde in PBS at room temperature for 2 hours, followed by dissection to isolate the testes. The whole testes were then processed with cryo-embedding. Representative cross-sections of the testes were acquired at anterior, posterior, and middle regions with a thickness of 20 μm. Testes cryo-sections on slides were first thawed and dried before drawing borders around the sections with a PAP pen (ab2601; Abcam). The slides were then fixed with 4% PFA for 15 min at room temperature in Coplin jars (all subsequent steps were performed in Coplin jars unless stated otherwise), rinsed twice with ice-cold PBS followed by permeabilization with 0.2% Triton X-100 in PBS for 15 min.

Next, slides were washed for 5 min three times in PBS and blocked with 2% BSA in PBS for 2 h at room temperature. The slides were then transferred to a humidified box. Primary antibodies in PBS (with 0.1% Tween 20 and 1% BSA) were pipetted onto the sections and incubated overnight at 4°C. Slides were washed with PBS on a shaker for 10 min six times at room temperature. Secondary antibodies in PBS (with 0.1% Tween 20 and 1% BSA) were then added, and the slides were incubated in the humidified box for 5 h at room temperature. Finally, the slides were washed for 10 min six times with PBS at room temperature, dried, and mounted before imaging.

Primary antibodies used to stain mice ovaries or testes cryo-sections were as follows: AcTub (1:500; Sigma-Aldrich), glutamylated tubulin (1:500; Adipogen), Vasa (1:500; R&D Systems), γTub (1:500; Adipogen), Arl13b (1:500; Proteintech), and Adcy3 (1:500; LSBio). Alexa Fluor fluorescent secondary antibodies (Invitrogen) were used at 1:500.

Statistical analysis

All statistical analysis and data plotting was performed using GraphPad Prism 7 software. Datasets were tested with two-tailed unpaired t test. In the figures, P values are indicated by asterisks as follows: *$P < 0.05$, **$P < 0.01$, ***$P < 0.001$, and ****$P < 0.0001$ (ns, not significant at $P > 0.05$). All bar graphs were tested with chi-squaredFisher's exact test, and P values were at least <0.0001 between *wt* and *cep290*$^{-/-}$, *cep290*$^{-/-}$;*kif7*$^{+/-}$, or *cep290*$^{-/-}$;*kif7*$^{-/-}$unless otherwise indicated.

REFERENCES AND NOTES

1. J. Fraune, S. Schramm, M. Alsheimer, R. Benavente, The mammalian synaptonemal complex: Protein components, assembly and role in meiotic recombination. *Exp. Cell Res.* **318**, 1340–1346 (2012). doi: 10.1016/j.yexcr.2012.02.018; pmid: 22394509
2. M. R. Gyuricza *et al*., Dynamic and stable cohesins regulate synaptonemal complex assembly and chromosome segregation. *Curr. Biol.* **26**, 1688–1698 (2016). doi: 10.1016/j.cub.2016.05.006; pmid: 27291057
3. K. A. Collins *et al*., Corolla is a novel protein that contributes to the architecture of the synaptonemal complex of *Drosophila*. *Genetics* **198**, 219–228 (2014). doi: 10.1534/genetics.114.165290; pmid: 24913682
4. S. Köhler, M. Wojcik, K. Xu, A. F. Dernburg, Superresolution microscopy reveals the three-dimensional organization of meiotic chromosome axes in intact *Caenorhabditis elegans* tissue. *Proc. Natl. Acad. Sci. U.S.A.* **114**, E4734–E4743 (2017). doi: 10.1073/pnas.1702312114; pmid: 28559338

5. C. M. Lake *et al*., Vilya, a component of the recombination nodule, is required for meiotic double-strand break formation in *Drosophila*. *eLife* **4**, e08287 (2015). doi: 10.7554/eLife.08287; pmid: 26452093
6. O. Rog, S. Köhler, A. F. Dernburg, The synaptonemal complex has liquid crystalline properties and spatially regulates meiotic recombination factors. *eLife* **6**, e21455 (2017). doi: 10.7554/eLife.21455; pmid: 28045371
7. K. Schücker, T. Holm, C. Franke, M. Sauer, R. Benavente, Elucidation of synaptonemal complex organization by super-resolution imaging with isotropic resolution. *Proc. Natl. Acad. Sci. U.S.A.* **112**, 2029–2033 (2015). doi: 10.1073/pnas.1414814112; pmid: 25646409
8. C. K. Cahoon, R. S. Hawley, Regulating the construction and demolition of the synaptonemal complex. *Nat. Struct. Mol. Biol.* **23**, 369–377 (2016). doi: 10.1038/nsmb.3208; pmid: 27142324
9. See the supplementary materials.
10. Y. Chikashige *et al*., Meiotic proteins bqt1 and bqt2 tether telomeres to form the bouquet arrangement of chromosomes. *Cell* **125**, 59–69 (2006). doi: 10.1016/j.cell.2006.01.048; pmid: 16615890
11. X. Ding *et al*., SUN1 is required for telomere attachment to nuclear envelope and gametogenesis in mice. *Dev. Cell* **12**, 863–872 (2007). doi: 10.1016/j.devcel.2007.03.018; pmid: 17543860
12. H. F. Horn *et al*., A mammalian KASH domain protein coupling meiotic chromosomes to the cytoskeleton. *J. Cell Biol.* **202**, 1023–1039 (2013). doi: 10.1083/jcb.201304004; pmid: 24062341
13. A. Morimoto *et al*., A conserved KASH domain protein associates with telomeres, SUN1, and dynactin during mammalian meiosis. *J. Cell Biol.* **198**, 165–172 (2012). doi: 10.1083/jcb.201204085; pmid: 22826121
14. A. Sato *et al*., Cytoskeletal forces span the nuclear envelope to coordinate meiotic chromosome pairing and synapsis. *Cell* **139**, 907–919 (2009). doi: 10.1016/j.cell.2009.10.039; pmid: 19913287
15. H. Shibuya *et al*., MAJIN links telomeric DNA to the nuclear membrane by exchanging telomere cap. *Cell* **163**, 1252–1266 (2015). doi: 10.1016/j.cell.2015.10.030; pmid: 26548954
16. H. Shibuya, K. Ishiguro, Y. Watanabe, The TRF1-binding protein TERB1 promotes chromosome movement and telomere rigidity in meiosis. *Nat. Cell Biol.* **16**, 145–156 (2014). doi: 10.1038/ncb2896; pmid: 24413433
17. E. Trelles-Sticken, M. E. Dresser, H. Scherthan, Meiotic telomere protein Ndj1p is required for meiosis-specific telomere distribution, bouquet formation and efficient homologue pairing. *J. Cell Biol.* **151**, 95–106 (2000). doi: 10.1083/jcb.151.1.95; pmid: 11018056
18. H. Shibuya, A. Morimoto, Y. Watanabe, The dissection of meiotic chromosome movement in mice using an in vivo electroporation technique. *PLOS Genet.* **10**, e1004821 (2014). doi: 10.1371/journal.pgen.1004821; pmid: 25502938
19. Y. M. Elkouby, A. Jamieson-Lucy, M. C. Mullins, Oocyte polarization is coupled to the chromosomal bouquet, a conserved polarized nuclear configuration in meiosis. *PLOS Biol.* **14**, e1002335 (2016). doi: 10.1371/journal.pbio.1002335; pmid: 26741740
20. H. Scherthan, A bouquet makes ends meet. *Nat. Rev. Mol. Cell Biol.* **2**, 621–627 (2001). doi: 10.1038/35085086; pmid: 11483995
21. Y. M. Elkouby, M. C. Mullins, Coordination of cellular differentiation, polarity, mitosis and meiosis - New findings from early vertebrate oogenesis. *Dev. Biol.* **430**, 275–287 (2017). doi: 10.1016/j.ydbio.2017.06.029; pmid: 28666956
22. Y. P. Blokhina, A. D. Nguyen, B. W. Draper, S. M. Burgess, The telomere bouquet is a hub where meiotic double-strand breaks, synapsis, and stable homolog juxtaposition are coordinated in the zebrafish, *Danio rerio*. *PLOS Genet.* **15**, e1007730 (2019). doi: 10.1371/journal.pgen.1007730; pmid: 30653507
23. K. Saito, C. Sakai, T. Kawasaki, N. Sakai, Telomere distribution pattern and synapsis initiation during spermatogenesis in zebrafish. *Dev. Dyn.* **243**, 1448–1456 (2014). doi: 10.1002/dvdy.24166; pmid: 25044979
24. Y. M. Elkouby, M. C. Mullins, Methods for the analysis of early oogenesis in Zebrafish. *Dev. Biol.* **430**, 310–324 (2017). doi: 10.1016/j.ydbio.2016.12.014; pmid: 27988227
25. J. F. Reiter, O. E. Blacque, M. R. Leroux, The base of the cilium: Roles for transition fibres and the transition zone in ciliary formation, maintenance and compartmentalization. *EMBO Rep.* **13**, 608–618 (2012). doi: 10.1038/embor.2012.73; pmid: 22653444
26. M. Mirvis, T. Stearns, W. J. Nelson, Cilium structure, assembly, and disassembly regulated by the cytoskeleton. *Biochem. J.* **475**, 2329–2353 (2018). doi: 10.1042/BCJ20170453; pmid: 30064990
27. N. A. Duldulao, S. Lee, Z. Sun, Cilia localization is essential for in vivo functions of the Joubert syndrome protein Arl13b/Scorpion. *Development* **136**, 4033–4042 (2009). doi: 10.1242/dev.036350; pmid: 19906870
28. H. Higginbotham *et al*., Arl13b-regulated cilia activities are essential for polarized radial glial scaffold formation. *Nat. Neurosci.* **16**, 1000–1007 (2013). doi: 10.1038/nn.3451; pmid: 23817546
29. J. Li, W. Ge, Zebrafish as a model for studying ovarian development: Recent advances from targeted gene knockout studies. *Mol. Cell. Endocrinol.* **507**, 110778 (2020). doi: 10.1016/j.mce.2020.110778; pmid: 32142861
30. T. Ishikawa, Axoneme structure from motile cilia. *Cold Spring Harb. Perspect. Biol.* **9**, a028076 (2017). doi: 10.1101/cshperspect.a028076; pmid: 27601632
31. M. P. Greenbaum, L. Ma, M. M. Matzuk, Conversion of midbodies into germ cell intercellular bridges. *Dev. Biol.* **305**, 389–396 (2007). doi: 10.1016/j.ydbio.2007.02.025; pmid: 17383626
32. K. Haglund, I. P. Nezis, H. Stenmark, Structure and functions of stable intercellular bridges formed by incomplete cytokinesis during development. *Commun. Integr. Biol.* **4**, 1–9 (2011). doi: 10.4161/cib.13550; pmid: 21509167
33. O. Gershony *et al*., Measuring abscission spatiotemporal dynamics using quantitative high-resolution microscopy. *Methods Cell Biol.* **137**, 205–224 (2017). doi: 10.1016/bs.mcb.2016.03.032; pmid: 28065306
34. E. M. Lessieur *et al*., Ciliary genes arl13b, ahi1 and cc2d2a differentially modify expression of visual acuity phenotypes but do not enhance retinal degeneration due to mutation of cep290 in zebrafish. *PLOS ONE* **14**, e0213960 (2019). doi: 10.1371/journal.pone.0213960; pmid: 30970040
35. E. Betleja, D. G. Cole, Ciliary trafficking: CEP290 guards a gated community. *Curr. Biol.* **20**, R928–R931 (2010). doi: 10.1016/j.cub.2010.09.058; pmid: 21056833
36. C. Li *et al*., MKS5 and CEP290 dependent assembly pathway of the ciliary transition zone. *PLOS Biol.* **14**, e1002416 (2016). doi: 10.1371/journal.pbio.1002416; pmid: 26982032
37. L. Baala *et al*., Pleiotropic effects of CEP290 (NPHP6) mutations extend to Meckel syndrome. *Am. J. Hum. Genet.* **81**, 170–179 (2007). doi: 10.1086/519494; pmid: 17564974
38. F. Coppieters, S. Lefever, B. P. Leroy, E. De Baere, CEP290, a gene with many faces: Mutation overview and presentation of CEP290base. *Hum. Mutat.* **31**, 1097–1108 (2010). doi: 10.1002/humu.21337; pmid: 20690115
39. V. Frank *et al*., Mutations of the CEP290 gene encoding a centrosomal protein cause Meckel-Gruber syndrome. *Hum. Mutat.* **29**, 45–52 (2008). doi: 10.1002/humu.20614; pmid: 17705300
40. E. M. Valente *et al*., Mutations in CEP290, which encodes a centrosomal protein, cause pleiotropic forms of Joubert syndrome. *Nat. Genet.* **38**, 623–625 (2006). doi: 10.1038/ng1805; pmid: 16682970
41. A. K. Maurya *et al*., Positive and negative regulation of Gli activity by Kif7 in the zebrafish embryo. *PLOS Genet.* **9**, e1003955 (2013). doi: 10.1371/journal.pgen.1003955; pmid: 24339784
42. D. Barakeh *et al*., The many faces of KIF7. *Hum. Genome Var.* **2**, 15006 (2015). doi: 10.1038/hgv.2015.6; pmid: 27081521
43. M. He *et al*., The kinesin-4 protein Kif7 regulates mammalian Hedgehog signalling by organizing the cilium tip compartment. *Nat. Cell Biol.* **16**, 663–672 (2014). doi: 10.1038/ncb2988; pmid: 24952464
44. A. Putoux *et al*., KIF7 mutations cause fetal hydrolethalus and acrocallosal syndromes. *Nat. Genet.* **43**, 601–606 (2011). doi: 10.1038/ng.826; pmid: 21552264
45. R. Bachmann-Gagescu *et al*., The ciliopathy gene cc2d2a controls zebrafish photoreceptor outer segment development through a role in Rab8-dependent vesicle trafficking. *Hum. Mol. Genet.* **20**, 4041–4055 (2011). doi: 10.1093/hmg/ddr332; pmid: 21816947
46. F. R. Garcia-Gonzalo *et al*., A transition zone complex regulates mammalian ciliogenesis and ciliary membrane composition. *Nat. Genet.* **43**, 776–784 (2011). doi: 10.1038/ng.891; pmid: 21725307
47. D. B. Dranow, R. P. Tucker, B. W. Draper, Germ cells are required to maintain a stable sexual phenotype in adult zebrafish. *Dev. Biol.* **376**, 43–50 (2013). doi: 10.1016/j.ydbio.2013.01.016; pmid: 23348677
48. A. Rodríguez-Marí *et al*., Sex reversal in zebrafish fancl mutants is caused by Tp53-mediated germ cell apoptosis. *PLOS Genet.* **6**, e1001034 (2010). doi: 10.1371/journal.pgen.1001034; pmid: 20661450
49. K. Saito, K. R. Siegfried, C. Nüsslein-Volhard, N. Sakai, Isolation and cytogenetic characterization of zebrafish meiotic prophase I mutants. *Dev. Dyn.* **240**, 1779–1792 (2011). doi: 10.1002/dvdy.22661; pmid: 21594953
50. E. Bolcun-Filas, V. D. Rinaldi, M. E. White, J. C. Schimenti, Reversal of female infertility by Chk2 ablation reveals the oocyte DNA damage checkpoint pathway. *Science* **343**, 533–536 (2014). doi: 10.1126/science.1247671; pmid: 24482479
51. M. Di Giacomo *et al*., Distinct DNA-damage-dependent and -independent responses drive the loss of oocytes in recombination-defective mouse mutants. *Proc. Natl. Acad. Sci. U.S.A.* **102**, 737–742 (2005). doi: 10.1073/pnas.0406212102; pmid: 15640358
52. J. S. Andersen *et al*., Proteomic characterization of the human centrosome by protein correlation profiling. *Nature* **426**, 570–574 (2003). doi: 10.1038/nature02166; pmid: 14654843
53. B. Chang *et al*., In-frame deletion in a novel centrosomal/ciliary protein CEP290/NPHP6 perturbs its interaction with RPGR and results in early-onset retinal degeneration in the rd16 mouse. *Hum. Mol. Genet.* **15**, 1847–1857 (2006). doi: 10.1093/hmg/ddl107; pmid: 16632484
54. J. A. Sayer *et al*., The centrosomal protein nephrocystin-6 is mutated in Joubert syndrome and activates transcription factor ATF4. *Nat. Genet.* **38**, 674–681 (2006). doi: 10.1038/ng1786; pmid: 16682973
55. W. Y. Tsang *et al*., CP110 suppresses primary cilia formation through its interaction with CEP290, a protein deficient in human ciliary disease. *Dev. Cell* **15**, 187–197 (2008). doi: 10.1016/j.devcel.2008.07.004; pmid: 18694559
56. T. R. Stowe, C. J. Wilkinson, A. Iqbal, T. Stearns, The centriolar satellite proteins Cep72 and Cep290 interact and are required for recruitment of BBS proteins to the cilium. *Mol. Biol. Cell* **23**, 3322–3335 (2012). doi: 10.1091/mbc.e12-02-0134; pmid: 22767577
57. J. Fu, I. M. Hagan, D. M. Glover, The centrosome and its duplication cycle. *Cold Spring Harb. Perspect. Biol.* **7**, a015800 (2015). doi: 10.1101/cshperspect.a015800; pmid: 25646378
58. E. A. Nigg, T. Stearns, The centrosome cycle: Centriole biogenesis, duplication and inherent asymmetries. *Nat. Cell Biol.* **13**, 1154–1160 (2011). doi: 10.1038/ncb2345; pmid: 21968988
59. L. Lee, L. E. Ostrowski, Motile cilia genetics and cell biology: Big results from little mice. *Cell. Mol. Life Sci.* **78**, 769–797 (2021). doi: 10.1007/s00018-020-03633-5; pmid: 32915243
60. P. Satir, S. T. Christensen, Overview of structure and function of mammalian cilia. *Annu. Rev. Physiol.* **69**, 377–400 (2007). doi: 10.1146/annurev.physiol.69.040705.141236; pmid: 17009929
61. P. P. D'Gama *et al*., Diversity and function of motile ciliated cell types within ependymal lineages of the zebrafish brain. *Cell Rep.* **37**, 109775 (2021). doi: 10.1101/2021.02.17.431442
62. T. Tian, L. Zhao, X. Zhao, M. Zhang, A. Meng, A zebrafish gene trap line expresses GFP recapturing expression pattern of foxj1b. *J. Genet. Genomics* **36**, 581–589 (2009). doi: 10.1016/S1673-8527(08)60150-2; pmid: 19840756
63. J. R. Panizzi *et al*., CCDC103 mutations cause primary ciliary dyskinesia by disrupting assembly of ciliary dynein arms. *Nat. Genet.* **44**, 714–719 (2012). doi: 10.1038/ng.2277; pmid: 22581229
64. D. M. Leerberg, K. Sano, B. W. Draper, Fibroblast growth factor signaling is required for early somatic gonad development in zebrafish. *PLOS Genet.* **13**, e1006993 (2017). doi: 10.1371/journal.pgen.1006993; pmid: 28873404
65. B. L. Latour *et al*., Dysfunction of the ciliary ARMC9/TOGARAM1 protein module causes Joubert syndrome. *J. Clin. Invest.* **130**, 4423–4439 (2020). doi: 10.1172/JCI131656; pmid: 32453716
66. E. A. Bearce, D. T. Grimes, On being the right shape: Roles for motile cilia and cerebrospinal fluid flow in body and spine morphology. *Semin. Cell Dev. Biol.* **110**, 104–112 (2021). doi: 10.1016/j.semcdb.2020.07.005; pmid: 32693941
67. D. K. Breslow *et al*., A CRISPR-based screen for Hedgehog signaling provides insights into ciliary function and

ciliopathies. *Nat. Genet.* **50**, 460–471 (2018). doi: 10.1038/s41588-018-0054-7; pmid: 29459677
68. J. C. Van De Weghe *et al*., Mutations in ARMC9, which encodes a basal body protein, cause Joubert syndrome in humans and ciliopathy phenotypes in zebrafish. *Am. J. Hum. Genet.* **101**, 23–36 (2017). doi: 10.1016/j.ajhg.2017.05.010; pmid: 28625504
69. M. S. Lehti, A. Sironen, Formation and function of sperm tail structures in association with sperm motility defects. *Biol. Reprod.* **97**, 522–536 (2017). doi: 10.1093/biolre/iox096; pmid: 29024992
70. A. M. Penkner *et al*., Meiotic chromosome homology search involves modifications of the nuclear envelope protein Matefin/SUN-1. *Cell* **139**, 920–933 (2009). doi: 10.1016/j.cell.2009.10.045; pmid: 19913286
71. M. N. Conrad, A. M. Dominguez, M. E. Dresser, Ndj1p, a meiotic telomere protein required for normal chromosome synapsis and segregation in yeast. *Science* **276**, 1252–1255 (1997). doi: 10.1126/science.276.5316.1252; pmid: 9157883
72. J. Long *et al*., Telomeric TERB1-TRF1 interaction is crucial for male meiosis. *Nat. Struct. Mol. Biol.* **24**, 1073–1080 (2017). doi: 10.1038/nsmb.3496; pmid: 29083416
73. D. F. Pendlebury *et al*., Dissecting the telomere-inner nuclear membrane interface formed in meiosis. *Nat. Struct. Mol. Biol.* **24**, 1064–1072 (2017). doi: 10.1038/nsmb.3493; pmid: 29083414
74. R. Arora *et al*., Meiotic onset is reliant on spatial distribution but independent of germ cell number in the mouse ovary. *J. Cell Sci.* **129**, 2493–2499 (2016). doi: 10.1242/jcs.189910; pmid: 27199373
75. D. C. Miles, J. A. van den Bergen, A. H. Sinclair, P. S. Western, Regulation of the female mouse germ cell cycle during entry into meiosis. *Cell Cycle* **9**, 408–418 (2010). doi: 10.4161/cc.9.2.10691; pmid: 20023406
76. Y. Q. S. Soh *et al*., Meioc maintains an extended meiotic prophase I in mice. *PLOS Genet.* **13**, e1006704 (2017). doi: 10.1371/journal.pgen.1006704; pmid: 28380054
77. N. Vernet *et al*., Meiosis occurs normally in the fetal ovary of mice lacking all retinoic acid receptors. *Sci. Adv.* **6**, eaaz1139 (2020). doi: 10.1126/sciadv.aaz1139; pmid: 32917583
78. M. G. Riparbelli, G. Callaini, T. L. Megraw, Assembly and persistence of primary cilia in dividing *Drosophila* spermatocytes. *Dev. Cell* **23**, 425–432 (2012). doi: 10.1016/j.devcel.2012.05.024; pmid: 22898783
79. J. M. Dunce *et al*., Structural basis of meiotic telomere attachment to the nuclear envelope by MAJIN-TERB2-TERB1. *Nat. Commun.* **9**, 5355 (2018). doi: 10.1038/s41467-018-07794-7; pmid: 30559341
80. Y. Wang *et al*., The meiotic TERB1-TERB2-MAJIN complex tethers telomeres to the nuclear envelope. *Nat. Commun.* **10**, 564 (2019). doi: 10.1038/s41467-019-08437-1; pmid: 30718482
81. J. Zhang, Z. Tu, Y. Watanabe, H. Shibuya, Distinct TERB1 domains regulate different protein interactions in meiotic telomere movement. *Cell Rep.* **21**, 1715–1726 (2017). doi: 10.1016/j.celrep.2017.10.061; pmid: 29141207
82. E. J. Navarro, W. F. Marshall, J. C. Fung, Modeling cell biological features of meiotic chromosome pairing. bioRxiv 475288 [Preprint] (2022); .doi: 10.1101/2022.01.06.475288
83. J. Wallmeier *et al*., Motile ciliopathies. *Nat. Rev. Dis. Primers* **6**, 77 (2020). doi: 10.1038/s41572-020-0209-6; pmid: 32943623
84. B. Terré *et al*., Defects in efferent duct multiciliogenesis underlie male infertility in GEMC1-, MCIDAS- or CCNO-deficient mice. *Development* **146**, dev.162628 (2019). doi: 10.1242/dev.162628; pmid: 30936178
85. S. Zahid *et al*., "*CEP290*," in *Retinal Dystrophy Gene Atlas* (Springer, 2018), pp. 47–49.
86. P. Moradi, W. L. Davies, D. S. Mackay, M. E. Cheetham, A. T. Moore, Focus on molecules: Centrosomal protein 290 (CEP290). *Exp. Eye Res.* **92**, 316–317 (2011). doi: 10.1016/j.exer.2010.05.009; pmid: 20493186
87. E. Forsythe, P. L. Beales, Bardet-Biedl syndrome. *Eur. J. Hum. Genet.* **21**, 8–13 (2013). doi: 10.1038/ejhg.2012.115; pmid: 22713813
88. V. Hartill, K. Szymanska, S. M. Sharif, G. Wheway, C. A. Johnson, Meckel-Gruber syndrome: An update on diagnosis, clinical management, and research advances. *Front Pediatr.* **5**, 244 (2017). doi: 10.3389/fped.2017.00244; pmid: 29209597
89. M. Romani, A. Micalizzi, E. M. Valente, Joubert syndrome: Congenital cerebellar ataxia with the molar tooth. *Lancet Neurol.* **12**, 894–905 (2013). doi: 10.1016/S1474-4422(13)70136-4; pmid: 23870701
90. D. M. Parichy, M. R. Elizondo, M. G. Mills, T. N. Gordon, R. E. Engeszer, Normal table of postembryonic zebrafish development: Staging by externally visible anatomy of the living fish. *Dev. Dyn.* **238**, 2975–3015 (2009). doi: 10.1002/dvdy.22113; pmid: 19891001
91. S. Berghmans *et al*., *tp53* mutant zebrafish develop malignant peripheral nerve sheath tumors. *Proc. Natl. Acad. Sci. U.S.A.* **102**, 407–412 (2005). doi: 10.1073/pnas.0406252102; pmid: 15630097
92. A. Borovina, S. Superina, D. Voskas, B. Ciruna, Vangl2 directs the posterior tilting and asymmetric localization of motile primary cilia. *Nat. Cell Biol.* **12**, 407–412 (2010). doi: 10.1038/ncb2042; pmid: 20305649
93. S. Pauls, B. Geldmacher-Voss, J. A. Campos-Ortega, A zebrafish histone variant H2A.F/Z and a transgenic H2A.F/Z: GFP fusion protein for in vivo studies of embryonic development. *Dev. Genes Evol.* **211**, 603–610 (2001). doi: 10.1007/s00427-001-0196-x; pmid: 11819118
94. C. Novorol *et al*., Microcephaly models in the developing zebrafish retinal neuroepithelium point to an underlying defect in metaphase progression. *Open Biol.* **3**, 130065 (2013). doi: 10.1098/rsob.130065; pmid: 24153002
95. S. Adar-Levor *et al*., Cytokinetic abscission is part of the midblastula transition in early zebrafish embryogenesis. *Proc. Natl. Acad. Sci. U.S.A.* **118**, e2021210118 (2021). doi: 10.1073/pnas.2021210118; pmid: 33837152
96. H. Knaut, F. Pelegri, K. Bohmann, H. Schwarz, C. Nüsslein-Volhard, Zebrafish vasa RNA but not its protein is a component of the germ plasm and segregates asymmetrically before germline specification. *J. Cell Biol.* **149**, 875–888 (2000). doi: 10.1083/jcb.149.4.875; pmid: 10811828
97. J.-Y. Tinevez *et al*., TrackMate: An open and extensible platform for single-particle tracking. *Methods* **115**, 80–90 (2017). doi: 10.1016/j.ymeth.2016.09.016; pmid: 27713081
98. M. C. Leal *et al*., Histological and stereological evaluation of zebrafish (*Danio rerio*) spermatogenesis with an emphasis on spermatogonial generations. *Biol. Reprod.* **81**, 177–187 (2009). doi: 10.1095/biolreprod.109.076299; pmid: 19339708
99. C. Dingare *et al*., The Hippo pathway effector Taz is required for cell morphogenesis and fertilization in zebrafish. *Development* **145**, dev167023 (2018). doi: 10.1242/dev.167023; pmid: 30327325
100. F. L. Marlow, M. C. Mullins, Bucky ball functions in Balbiani body assembly and animal-vegetal polarity in the oocyte and follicle cell layer in zebrafish. *Dev. Biol.* **321**, 40–50 (2008). doi: 10.1016/j.ydbio.2008.05.557; pmid: 18582455
101. L. Lei, A. C. Spradling, Mouse primordial germ cells produce cysts that partially fragment prior to meiosis. *Development* **140**, 2075–2081 (2013). doi: 10.1242/dev.093864; pmid: 23578925
102. D. H. Leu, B. W. Draper, The ziwi promoter drives germline-specific gene expression in zebrafish. *Dev. Dyn.* **239**, 2714–2721 (2010). doi: 10.1002/dvdy.22404; pmid: 20737503
103. M. E. Pepling, M. de Cuevas, A. C. Spradling, Germline cysts: A conserved phase of germ cell development? *Trends Cell Biol.* **9**, 257–262 (1999). doi: 10.1016/S0962-8924(99)01594-9; pmid: 10370240
104. K. Lu, L. Jensen, L. Lei, Y. M. Yamashita, Stay connected: A germ cell strategy. *Trends Genet.* **33**, 971–978 (2017). doi: 10.1016/j.tig.2017.09.001; pmid: 28947158
105. M. E. Pepling, Follicular assembly: Mechanisms of action. *Reproduction* **143**, 139–149 (2012). doi: 10.1530/REP-11-0299; pmid: 22065859
106. K. Selman, R. A. Wallace, A. Sarka, X. Qi, Stages of oocyte development in the zebrafish, Brachy*Danio rerio*. *J. Morphol.* **218**, 203–224 (1993). doi: 10.1002/jmor.1052180209; pmid: 29865471
107. L. Lei, A. C. Spradling, Mouse oocytes differentiate through organelle enrichment from sister cyst germ cells. *Science* **352**, 95–99 (2016). doi: 10.1126/science.aad2156; pmid: 26917595
108. C. M. Lake, R. S. Hawley, The molecular control of meiotic chromosomal behavior: Events in early meiotic prophase in *Drosophila* oocytes. *Annu. Rev. Physiol.* **74**, 425–451 (2012). doi: 10.1146/annurev-physiol-020911-153342; pmid: 22335798
109. A. J. MacQueen, A. Hochwagen, Checkpoint mechanisms: The puppet masters of meiotic prophase. *Trends Cell Biol.* **21**, 393–400 (2011). doi: 10.1016/j.tcb.2011.03.004; pmid: 21531561
110. P. S. Burgoyne, S. K. Mahadevaiah, J. M. Turner, The consequences of asynapsis for mammalian meiosis. *Nat. Rev. Genet.* **10**, 207–216 (2009). doi: 10.1038/nrg2505; pmid: 19188923
111. J. L. Anderson *et al*., Multiple sex-associated regions and a putative sex chromosome in zebrafish revealed by RAD mapping and population genomics. *PLOS ONE* **7**, e40701 (2012). doi: 10.1371/journal.pone.0040701; pmid: 22792396
112. G. Maack, H. Segner, Morphological development of the gonads in zebrafish. *J. Fish Biol.* **62**, 895–906 (2003). doi: 10.1046/j.1095-8649.2003.00074.x

ACKNOWLEDGMENTS

We thank M. C. Mullins, C. Moens, P. Ingham, S. Farber, Z. Sun, and B. Perkins for sharing fish lines; Z. Sun for the zebrafish Arl13b antibody; Y. Buganim for help with mouse ovary work; and S. Burgess and M. Kluetstein for help with Sycp3 labeling. TEM analysis was performed with the help of Y. Friedmann, The Bio-Imaging Unit, The Alexander Silberman Institute of Life Science of The Hebrew University of Jerusalem. The SBF-SEM analysis was performed with the help of A. Beckett, Biomedical EM Unit, The University of Liverpool. We thank Z. Manevich from the Faulty of Medicine Microscopy core and Y. Addadi from the Weizmann Institute core facility for their help with laser ablation experiments **Funding:** This work was supported by the Israel Science Foundation–Singapore National Research Foundation joint research program (grant no. 3291/19 to Y.M.E. and S.R.); the Ben Schender Fund for Outstanding Young Scientists (Y.M.E.); a Dr. Gabrielle Reem-Kayden Scholarship to A.M. and K.L.; a HUJI International PhD Talent Scholarship to V.K.; and an Abisch-Frenkel Scholarship for Scientific Excellence to N.H. **Author contributions:** Conceptualization: A.M., V.K., Q.T., R.B.G., S.R., Y.M.E.; Funding acquisition: S.R., Y.M.E.; Investigation: A.M., V.K., T.Q., R.D., N.H., K.L., M.M., F.N., H.E., S.R., A.S.; Methodology: A.M., V.K., T.Q., R.D., N.H., A.S., A.A., K.L., S.A.-L., R.Y.B., N.E., R.B.-G., S.R., Y.M.E.; Supervision: R.G.B., S.R., Y.M.E.; Visualization: A.M., V.K., Q.T., R.D., K.L., M.M., R.B.-G., S.R., Y.M.E.; Writing – original draft: A.M., V.K., T.Q., M.M., R.B.-G., S.R., Y.M.E. **Competing interests:** The authors declare no competing interests. **Data and materials availability:** All data are available in the main text or the supplementary materials. **License information:** Copyright © 2022 the authors, some rights reserved; exclusive licensee American Association for the Advancement of Science. No claim to original US government works. www.science.org/about/science-licenses-journal-article-reuse

SUPPLEMENTARY MATERIALS

science.org/doi/10.1126/science.abh3104
Materials and Methods
Supplementary Text
Figs. S1 to S19
Movies S1 to S17
References (*90*–*112*)
MDAR Reproducibility Checklist

View/request a protocol for this paper from *Bio-protocol*.

Submitted 1 March 2021; accepted 3 May 2022
10.1126/science.abh3104

RESEARCH ARTICLE SUMMARY

INNATE IMMUNITY

Human OTULIN haploinsufficiency impairs cell-intrinsic immunity to staphylococcal α-toxin

András N. Spaan*, Anna-Lena Neehus†, Emmanuel Laplantine†, Frederik Staels†, Masato Ogishi†, Yoann Seeleuthner†, Franck Rapaport†, Keenan A. Lacey, Erika Van Nieuwenhove, Maya Chrabieh, David Hum, Mélanie Migaud, Araksya Izmiryan, Lazaro Lorenzo, Tatiana Kochetkov, Dani A. C. Heesterbeek, Bart W. Bardoel, Ashley L. DuMont, Kerry Dobbs, Solenne Chardonnet, Søren Heissel, Timour Baslan, Peng Zhang, Rui Yang, Dusan Bogunovic, Herman F. Wunderink, Pieter-Jan A. Haas, Henrik Molina, Griet Van Buggenhout, Stanislas Lyonnet, Luigi D. Notarangelo, Mikko R. J. Seppänen, Robert Weil, Gisela Seminario, Héctor Gomez-Tello, Carine Wouters, Mehrnaz Mesdaghi, Mohammad Shahrooei, Xavier Bossuyt, Erdal Sag, Rezan Topaloglu, Seza Ozen, Helen L. Leavis, Maarten M. J. van Eijk, Liliana Bezrodnik, Lizbeth Blancas Galicia, Alain Hovnanian, Aude Nassif, Brigitte Bader-Meunier, Bénédicte Neven, Isabelle Meyts, Rik Schrijvers, Anne Puel, Jacinta Bustamante, Ivona Aksentijevich, Daniel L. Kastner, Victor J. Torres, Stéphanie Humblet-Baron‡, Adrian Liston‡, Laurent Abel‡, Bertrand Boisson§, Jean-Laurent Casanova*§

INTRODUCTION: *Staphylococcus aureus* is a bacterial pathogen with a global impact on human health. Most individuals carry *S. aureus* on their skin and in their nostrils, but a minority develop life-threatening staphylococcal disease. The molecular basis of interindividual clinical variability upon exposure to and infection with *S. aureus* is unclear. Inherited or acquired disorders affecting innate, myeloid immunity confer a predisposition to staphylococcal disease but account for only a small proportion of cases. Most cases of severe staphylococcal disease remain unexplained.

RATIONALE: Single-gene inborn errors of immunity are being implicated in a growing number of life-threatening infectious diseases. We performed a genome-wide study to identify the human genetic determinants of severe staphylococcal disease. We tested for genetic homogeneity in a cohort of patients with unexplained life-threatening staphylococcal disease by searching for variant enrichment in the exomes of 105 cases and 1274 controls. We considered rare variants and tested an autosomal dominant mode of inheritance with incomplete penetrance.

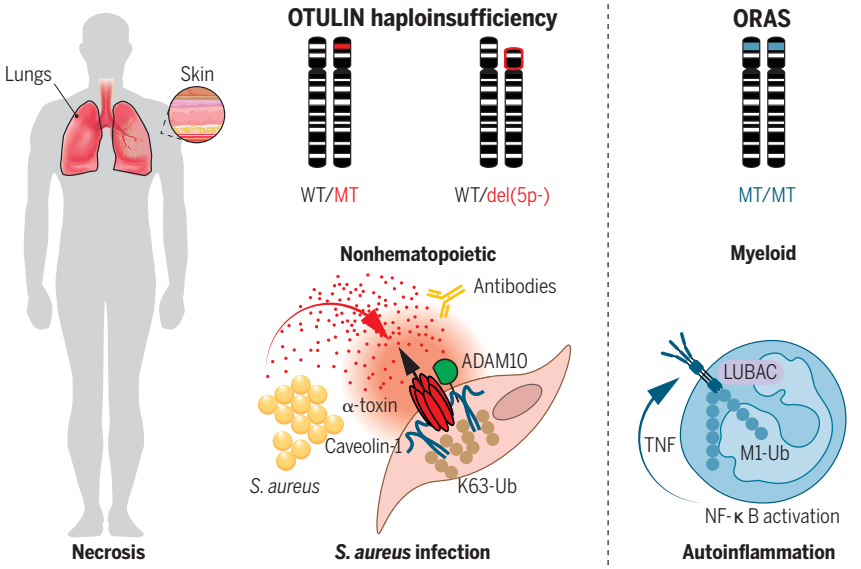

OTULIN haploinsufficiency is characterized by skin and pulmonary necrosis after *S. aureus* infection. The disorder is phenocopied in patients with 5p −syndrome. The cytotoxic damage to fibroblasts inflicted by the staphylococcal α-toxin is facilitated by caveolin-1 accumulation and ADAM10 retention at the cell surface. OTULIN haploinsufficiency is rescued by naturally elicited α-toxin–neutralizing antibodies. Autoinflammation in biallelic OTULIN deficiency is driven by excessive NF-κB activation in myeloid cells. WT, wild-type allele; MT, mutant allele; del, deletion; LUBAC, linear ubiquitin assembly complex; M1-Ub, M1-linked ubiquitin.

RESULTS: We found enrichment for heterozygous *OTULIN* variants in patients with severe staphylococcal disease. OTULIN is a linear deubiquitinase and negative regulator of nuclear factor κB (NF-κB) signaling encoded by a gene on chromosome 5p. Biallelic *OTULIN* mutations cause an early-onset autoinflammatory condition called OTULIN-related autoinflammatory syndrome (ORAS). Probands heterozygous for deleterious *OTULIN* variants suffered from life-threatening skin or pulmonary necrosis. Their disease was typically triggered by *S. aureus* infection and occurred from adolescence onward. Clinically, penetrance was incomplete, and expressivity was variable. The dominance mechanism was haploinsufficiency, which was both biochemically and clinically phenocopied in patients with the more common 5p– (Cri-du-Chat) chromosomal deletion syndrome. Blood leukocyte subsets were developmentally and functionally unaffected. In dermal fibroblasts, OTULIN haploinsufficiency increased the levels of linear ubiquitin, but tumor necrosis factor (TNF) receptor–mediated NF-κB signaling remained intact. Through crosstalk with CYLD, OTULIN haploinsufficiency caused the accumulation of caveolin-1 complexes modified with lysine-63–linked polyubiquitin (K63-Ub) chains. Caveolin-1 accumulation in the patients' dermal fibroblasts, but not leukocytes, enhanced the cytotoxicity of the staphylococcal virulence factor α-toxin. Upon α-toxin binding to its receptor, disintegrin and metalloprotease domain–containing protein 10 (ADAM10), the receptor was retained at the cell surface, enhancing cytotoxicity in the patients' dermal fibroblasts. Impaired cell-intrinsic immunity to α-toxin owing to OTULIN haploinsufficiency was rescued by α-toxin–neutralizing antibodies.

CONCLUSION: By disrupting cell-intrinsic immunity to α-toxin in fibroblasts and, perhaps, other nonleukocytic cells, human OTULIN haploinsufficiency underlies life-threatening staphylococcal disease of the skin and lungs. Naturally elicited α-toxin–neutralizing antibodies in heterozygotes may contribute to incomplete clinical penetrance. The study of OTULIN haploinsufficiency, a rare inborn error of immunity, helped clarify a phenotype seen in individuals with 5p– syndrome, a more common chromosomal abnormality. ■

The list of author affiliations is available in the full article online.
*Corresponding author. Email: a.n.spaan@umcutrecht.nl (A.N.S); casanova@rockefeller.edu (J.-L.C.)
†These authors contributed equally to this work.
‡These authors contributed equally to this work.
§These authors contributed equally to this work.
Cite this article as A. N. Spaan *et al.*, *Science* **376**, eabm6380 (2022). DOI: 10.1126/science.abm6380

READ THE FULL ARTICLE AT
https://doi.org/10.1126/science.abm6380

RESEARCH ARTICLE

INNATE IMMUNITY

Human OTULIN haploinsufficiency impairs cell-intrinsic immunity to staphylococcal α-toxin

András N. Spaan[1,2]*, Anna-Lena Neehus[3,4,5]†, Emmanuel Laplantine[6,7]†, Frederik Staels[8]†, Masato Ogishi[1]†, Yoann Seeleuthner[3,4]†, Franck Rapaport[1]†, Keenan A. Lacey[9], Erika Van Nieuwenhove[8,10], Maya Chrabieh[3,4], David Hum[1], Mélanie Migaud[3,4], Araksya Izmiryan[4,11], Lazaro Lorenzo[3,4], Tatiana Kochetkov[1], Dani A. C. Heesterbeek[2], Bart W. Bardoel[2], Ashley L. DuMont[9], Kerry Dobbs[12], Solenne Chardonnet[13], Søren Heissel[14], Timour Baslan[15], Peng Zhang[1], Rui Yang[1], Dusan Bogunovic[16], Herman F. Wunderink[2], Pieter-Jan A. Haas[2], Henrik Molina[14], Griet Van Buggenhout[17,18], Stanislas Lyonnet[4,19], Luigi D. Notarangelo[12], Mikko R. J. Seppänen[20], Robert Weil[6], Gisela Seminario[21], Héctor Gomez-Tello[22], Carine Wouters[8,23], Mehrnaz Mesdaghi[24], Mohammad Shahrooei[25,26], Xavier Bossuyt[25], Erdal Sag[27], Rezan Topaloglu[28], Seza Ozen[27], Helen L. Leavis[29], Maarten M. J. van Eijk[30], Liliana Bezrodnik[21], Lizbeth Blancas Galicia[31], Alain Hovnanian[4,11,32], Aude Nassif[33], Brigitte Bader-Meunier[4,34,35], Bénédicte Neven[4,34,35], Isabelle Meyts[36,37], Rik Schrijvers[38], Anne Puel[1,3,4], Jacinta Bustamante[1,3,4,39], Ivona Aksentijevich[40], Daniel L. Kastner[40], Victor J. Torres[9], Stéphanie Humblet-Baron[8]‡, Adrian Liston[8,41,42]‡, Laurent Abel[1,3,4]‡, Bertrand Boisson[1,3,4]§, Jean-Laurent Casanova[1,3,4,43,44]*§

The molecular basis of interindividual clinical variability upon infection with *Staphylococcus aureus* is unclear. We describe patients with haploinsufficiency for the linear deubiquitinase OTULIN, encoded by a gene on chromosome 5p. Patients suffer from episodes of life-threatening necrosis, typically triggered by *S. aureus* infection. The disorder is phenocopied in patients with the 5p− (Cri-du-Chat) chromosomal deletion syndrome. OTULIN haploinsufficiency causes an accumulation of linear ubiquitin in dermal fibroblasts, but tumor necrosis factor receptor–mediated nuclear factor κB signaling remains intact. Blood leukocyte subsets are unaffected. The OTULIN-dependent accumulation of caveolin-1 in dermal fibroblasts, but not leukocytes, facilitates the cytotoxic damage inflicted by the staphylococcal virulence factor α-toxin. Naturally elicited antibodies against α-toxin contribute to incomplete clinical penetrance. Human OTULIN haploinsufficiency underlies life-threatening staphylococcal disease by disrupting cell-intrinsic immunity to α-toxin in nonleukocytic cells.

Staphylococcus aureus is a major bacterial pathogen with a global impact on human health (*1*). Individuals with staphylococcal disease may suffer from a range of superficial (folliculitis, cellulitis, abscesses) to severe (e.g., necrotizing skin and soft tissue infections and necrotizing pneumonia, with or without septicemia) manifestations (*1*). Most individuals carry *S. aureus* asymptomatically on their skin and in their nostrils for long periods of their lives, but only a minority develop life-threatening staphylococcal disease. Severe disease has a poor prognosis, owing to its rapid invasive course (*2*–*5*). Acquired risk factors for staphylococcal disease include surgery and intravascular devices (*1*). Life-threatening staphylococcal disease can also result from single-gene inborn errors of immunity (IEIs) (*6*). Disorders affecting phagocyte development or function, such as severe congenital neutropenia, chronic granulomatous disease, and leukocyte adhesion deficiency, confer a predisposition to staphylococcal disease (*6*, *7*). Disorders of the Toll-like receptor (TLR) and interleukin-1 receptor (IL-1R) nuclear factor κB (TIR–NF-κB) pathway (*8*–*12*) and of IL-6– and signal transducer and activator of transcription 3 (STAT3)–dependent immunity (*13*–*17*) have also been identified in patients suffering from severe staphylococcal disease. All these defects preferentially affect innate, myeloid immunity, but, collectively, they account for only a small proportion of cases (*18*). Most cases of severe staphylococcal disease remain unexplained, because they strike otherwise healthy individuals with no detectable phagocyte defect (*2*, *19*). In this study, we aimed to elucidate human genetic and immunological etiologies of life-threatening staphylococcal disease.

Results

Genome-wide enrichment in rare OTULIN variants

Given the severity of their disease, we hypothesized that there would be at least some genetic homogeneity in our cohort of patients with unexplained life-threatening staphylococcal disease. We sequenced the exomes of 105 index cases. Given the rarity of severe staphylococcal disease in otherwise healthy individuals, and assuming a dominant mode of inheritance, we hypothesized that the disease-causing variants would be very rare [minor allele frequency (MAF) < 1×10^{-5}] (*20*). We also prioritized variants predicted to be deleterious [combined annotation-dependent depletion score (CADD) > mutation significance cutoff (MSC)] (*21*–*23*). We performed the same analysis on 1274 control exomes from patients with mycobacterial diseases (including individuals with Mendelian susceptibility to mycobacterial disease or those with tuberculosis), which rarely overlap with staphylococcal disease (*24*). After adjusting for ethnicity by principal components analysis (PCA), we used the results of these two analyses to test the null hypothesis that variants of a given gene were not specific to staphylococcal disease. *OTULIN* was the only gene satisfying the threshold for statistical significance on a genome-wide level, with a P value of 5.74×10^{-7} (Fig. 1A and tables S1 and S2). We repeated our analysis for *OTULIN*, adding 2504 individuals from the 1000 Genomes Project (*25*) to our control dataset (*26*); none of these individuals had developed life-threatening *S. aureus* infections. The enrichment in *OTULIN* variants was even stronger ($P = 3.85 \times 10^{-8}$) in this analysis, indicating that very rare variants of this gene were found specifically in patients with severe staphylococcal disease.

The patients carry heterozygous OTULIN variants

The linear deubiquitinase OTULIN is a negative regulator of inflammation (*27*, *28*). In humans, biallelic *OTULIN* mutations cause a potentially fatal early-onset autoinflammatory condition called OTULIN-related autoinflammatory syndrome (ORAS) (*29*–*33*). Closer inspection revealed that the signal for genetic homogeneity in the cohort of patients with severe staphylococcal disease was driven by three probands carrying heterozygous variants of *OTULIN* (Fig. 1B): one missense (p.D246V), one nonsense (p.E95X), and one frameshift (p.D268TfsX5) variant. In each of these probands, the clinical hallmark of disease after infection with *S. aureus* was life-threatening necrosis of the skin and/or lungs [fig. S1A; see supplementary materials (SM)]. Given the extreme inflammatory responses to infection with *S. aureus* in these patients, we investigated the possibility of other triggers generating similar disease. We identified three additional kindreds with very rare heterozygous missense variants of *OTULIN* (p.N341D, p.P254S, and p.R263Q) (Fig. 1C). The probands of these kindreds presented severe diseases triggered by infectious and unknown etiologies (fig. S1B; SM). The clinical course of disease in patients with no documented infection suggests that low-grade infections, or noninfectious triggers, might induce an inflammatory phenotype similar to that of patients with documented *S. aureus* infection (fig. S1, A and B; SM). In total, we identified six very rare variants in seven patients from six kindreds (fig. S1C). These seven patients did not carry

variants fitting the known modes of inheritance for any of the 430 genes already implicated in IEIs (*7*, *34*). In most patients, the first episode of disease occurred during adolescence (SM). Clinical data indicated a degree of phenotypic heterogeneity in the index cases, but with the skin and/or lungs consistently affected in all cases (Fig. 1, B and C, and fig. S1, A and B; SM). One-third of the heterozygous relatives (three of the nine for whom data were available) expressed a related but milder phenotype, the other six carriers being apparently healthy (Fig. 1, B and C; SM). We then hypothesized that the parents of the patients with biallelic OTULIN deficiency reported in previous studies (*29*–*32*), who themselves carried deleterious *OTULIN* alleles in the heterozygous state, might present phenocopies of the disorder observed in the patients of our cohort. One-third of the parents (3 of 10) did indeed express the phenotype (Fig. 1D; SM). Thus, very rare heterozygous mutations of *OTULIN* confer predisposition to severe necrosis of the skin and lungs, typically, but not exclusively, after infection with *S. aureus*, with variable expressivity and incomplete penetrance.

OTULIN is subject to negative selection

The severity of disease in the probands carrying very rare heterozygous *OTULIN* variants suggests that this gene is subject to evolutionary forces acting at the population level. The *f* parameter score for *OTULIN* is 0.36, indicating that this gene is under negative selection (fig. S1D) (*35*). Moreover, the consensus score for negative selection (CoNeS) for *OTULIN* is −0.78, within the reported range for genes underlying IEIs with both autosomal dominant (AD) and autosomal recessive (AR) inheritance (fig. S1E) (*36*). *OTULIN* has a LoFtool score of 0.115, suggesting that it does not tolerate haploinsufficiency (*37*). Predicted loss-of-function (pLOF) *OTULIN* variants are very rare in the general population, with a cumulative MAF of 1×10^{-4} (fig. S1F) (*20*). Consistent with the negative selection pressure acting on *OTULIN*, the alleles of the patients were found to be either ultra-rare or private (fig. S1F) (*20*). These population genetics parameters indicate that heterozygous pLOF variants of *OTULIN* are disadvantageous for the individual. This finding is consistent with the hypothesis that the very rare variants for which enrichment was detected in the patients studied are causal for the life-threatening necrosis of the skin and/or lungs triggered by *S. aureus* infection.

The OTULIN alleles of the patients are severely hypomorphic or amorphic

We overexpressed the cDNAs corresponding to the *OTULIN* alleles of the patients in human embryonic kidney (HEK) 293T cells. The truncated cDNAs of the patients demonstrated loss of expression, whereas the missense cDNAs of the patients and cDNAs corresponding to two *OTULIN* alleles commonly found in the general population (*20*) were expressed at normal levels (fig. S1G). No in-frame reinitiation was observed for truncated alleles from the patients (fig. S1H). We then assessed the deubiquitinase activity of the products of the alleles from the patients and their capacity to inhibit NF-κB signaling. Consistent with published findings in overexpression systems, some, but not all, protein products of the alleles concerned were defective for the linear deubiquitination of NF-κB essential modulator (NEMO) in the presence of linear ubiquitin assembly complex (LUBAC) (fig. S1I) (*32*, *33*). We assessed the capacity of the gene products to regulate receptor signaling, by investigating the functional consequences of the *OTULIN* alleles of the patients for NF-κB inhibition after stimulation with TNF in a cellular signaling system. All the alleles from patients were severely hypomorphic or amorphic (fig. S1J). In contrast to the alleles of the patients, the two alleles common in the general population (*20*) were found to be isomorphic (fig. S1J). The apparent differences between the two overexpression systems may reflect different impacts of the various *OTULIN* alleles on ubiquitin binding capacity (*27*, *32*, *33*). We then performed functional tests for all the other *OTULIN* coding sequence variants reported in public databases ($N = 120$ variants) (*20*). The cumulative MAF of amorphic and hypomorphic *OTULIN* alleles (with <25% wild-type levels of NF-κB signaling inhibitory activity) in the general population was 6×10^{-5} (Fig. 1E). The greater rarity of amorphic and hypomorphic *OTULIN* alleles than of pLOF variants highlights the importance of experimental validation for pLOF variants. Thus, the rare *OTULIN* variants found in the patients are deleterious, and AD OTULIN deficiency predisposes the patients to disease.

Autosomal dominant OTULIN deficiency acts through haploinsufficiency

We tested the genetic mechanism of AD OTULIN deficiency and found no negative dominance for the alleles expressed by the patients (fig. S1K). This implies that the genetic mechanism underlying AD OTULIN deficiency is haploinsufficiency. *OTULIN* is located on the short arm of chromosome 5. Depending on the breakpoint, almost all individuals with 5p– syndrome—the most common chromosomal deletion syndrome in humans, also known as Cri-du-Chat syndrome—are

[1]St. Giles Laboratory of Human Genetics of Infectious Diseases, Rockefeller Branch, The Rockefeller University, New York, NY 10065, USA. [2]Department of Medical Microbiology, University Medical Center Utrecht, Utrecht University, 3584 CX Utrecht, Netherlands. [3]Laboratory of Human Genetics of Infectious Diseases, Necker Branch, INSERM U1163, Necker Hospital for Sick Children, 75015 Paris, France. [4]Imagine Institute, Paris Cité University, 75015 Paris, France. [5]Institute of Experimental Hematology, REBIRTH Research Center for Translational and Regenerative Medicine, Hannover Medical School, 30625 Hannover, Germany. [6]Centre d'Immunologie et des Maladies Infectieuses, INSERM U1135, CNRS ERL8255, Sorbonne University, 75724 Paris, France. [7]Institut de Recherche St. Louis, Hôpital St. Louis, INSERM U944, CNRS U7212, Paris Cité University, 75010 Paris, France. [8]Laboratory for Adaptive Immunology, Department of Microbiology, Immunology and Transplantation, KU Leuven, 3000 Leuven, Belgium. [9]Department of Microbiology, New York University Grossman School of Medicine, New York, NY 10016, USA. [10]Department of Pediatric Rheumatology and Immunology, Wilhelmina Children's Hospital, University Medical Center Utrecht, Utrecht University, 3584 CX Utrecht, Netherlands. [11]Laboratory of Genetic Skin Diseases, INSERM U1163, 75015 Paris, France. [12]Laboratory of Clinical Immunology and Microbiology, Division of Intramural Research, NIAID, NIH, Bethesda, MD 20852, USA. [13]Plateforme Post-génomique de la Pitié-Salpêtrière, P3S, UMS Production et Analyse de données en Sciences de la vie et en Santé, PASS, INSERM, Sorbonne University, 75013 Paris, France. [14]Proteomics Resource Center, The Rockefeller University, New York, NY 10065, USA. [15]Cancer Biology and Genetics Program, Memorial Sloan Kettering Cancer Center, New York, NY 10065, USA. [16]Icahn School of Medicine at Mount Sinai, New York, NY 10029, USA. [17]Department of Human Genetics, KU Leuven, 3000 Leuven, Belgium. [18]Center for Human Genetics, University Hospitals Leuven, 3000 Leuven, Belgium. [19]Laboratory Embryology and Genetics of Malformations, INSERM U1163, Necker Hospital for Sick Children, 75015 Paris, France. [20]Rare Disease and Pediatric Research Centers, Children and Adolescents, University of Helsinki and HUS Helsinki University Hospital, 00260 Helsinki, Finland. [21]Center for Clinical Immunology, Immunology Group Children's Hospital Ricardo Gutiérrez, C1425EFD Buenos Aires, Argentina. [22]Immunology Department, Poblano Children's Hospital, 72190 Puebla, Mexico. [23]Department of Pediatrics, University Hospitals Leuven, 3000 Leuven, Belgium. [24]Department of Allergy and Clinical Immunology, Mofid Children's Hospital, Shahid Beheshti University of Medical Sciences, 15468-155514 Tehran, Iran. [25]Clinical and Diagnostic Immunology, Department of Microbiology, Immunology and Transplantation, KU Leuven, 3000 Leuven, Belgium. [26]Specialized Immunology Laboratory of Dr. Shahrooei, Sina Medical Complex, 15468-155514 Ahvaz, Iran. [27]Department of Pediatric Rheumatology, Hacettepe University, 06230 Ankara, Turkey. [28]Department of Pediatric Nephrology, Hacettepe University School of Medicine, Hacettepe University, 06230 Ankara, Turkey. [29]Department of Rheumatology and Clinical Immunology, University Medical Center Utrecht, Utrecht University, 3584 CX Utrecht, Netherlands. [30]Department of Intensive Care Medicine, University Medical Center Utrecht, Utrecht University, 3584 CX Utrecht, Netherlands. [31]Immune Deficiencies Laboratory National Institute of Pediatrics, 04530 Mexico City, Mexico. [32]Department of Genetics, Necker Hospital for Sick Children, AP-HP, 75015 Paris, France. [33]Centre Médical, Institut Pasteur, 75724 Paris, France. [34]Pediatric Immunology, Hematology and Rheumatology Unit, Necker Hospital for Sick Children, AP-HP, 75015 Paris, France. [35]Laboratory of Immunogenetics of Pediatric Autoimmunity, INSERM U1163, Necker Hospital for Sick Children, 75015 Paris, France. [36]Laboratory of Inborn Errors of Immunity, Department of Microbiology, Immunology and Transplantation, KU Leuven, 3000 Leuven, Belgium. [37]Department of Pediatrics, Jeffrey Modell Diagnostic and Research Network Center, University Hospitals Leuven, 3000 Leuven, Belgium. [38]Allergy and Clinical Immunology Research Group, Department of Microbiology, Immunology and Transplantation, KU Leuven, 3000 Leuven, Belgium. [39]Study Center for Primary Immunodeficiencies, Necker Hospital for Sick Children, AP-HP, 75015 Paris, France. [40]Inflammatory Disease Section, National Human Genome Research Institute, Bethesda, MD 20892, USA. [41]VIB Center for Brain and Disease Research, Leuven 3000, Belgium. [42]Immunology Programme, Babraham Institute, Babraham Research Campus, Cambridge CB22 3AT, UK. [43]Department of Pediatrics, Necker Hospital for Sick Children, AP-HP, 75015 Paris, France. [44]Howard Hughes Medical Institute, The Rockefeller University, New York, NY 10065, USA.

***Corresponding author. Email: a.n.spaan@umcutrecht.nl (A.N.S); casanova@rockefeller.edu (J.-L.C.)** †These authors contributed equally to this work. ‡These authors contributed equally to this work. §These authors contributed equally to this work.

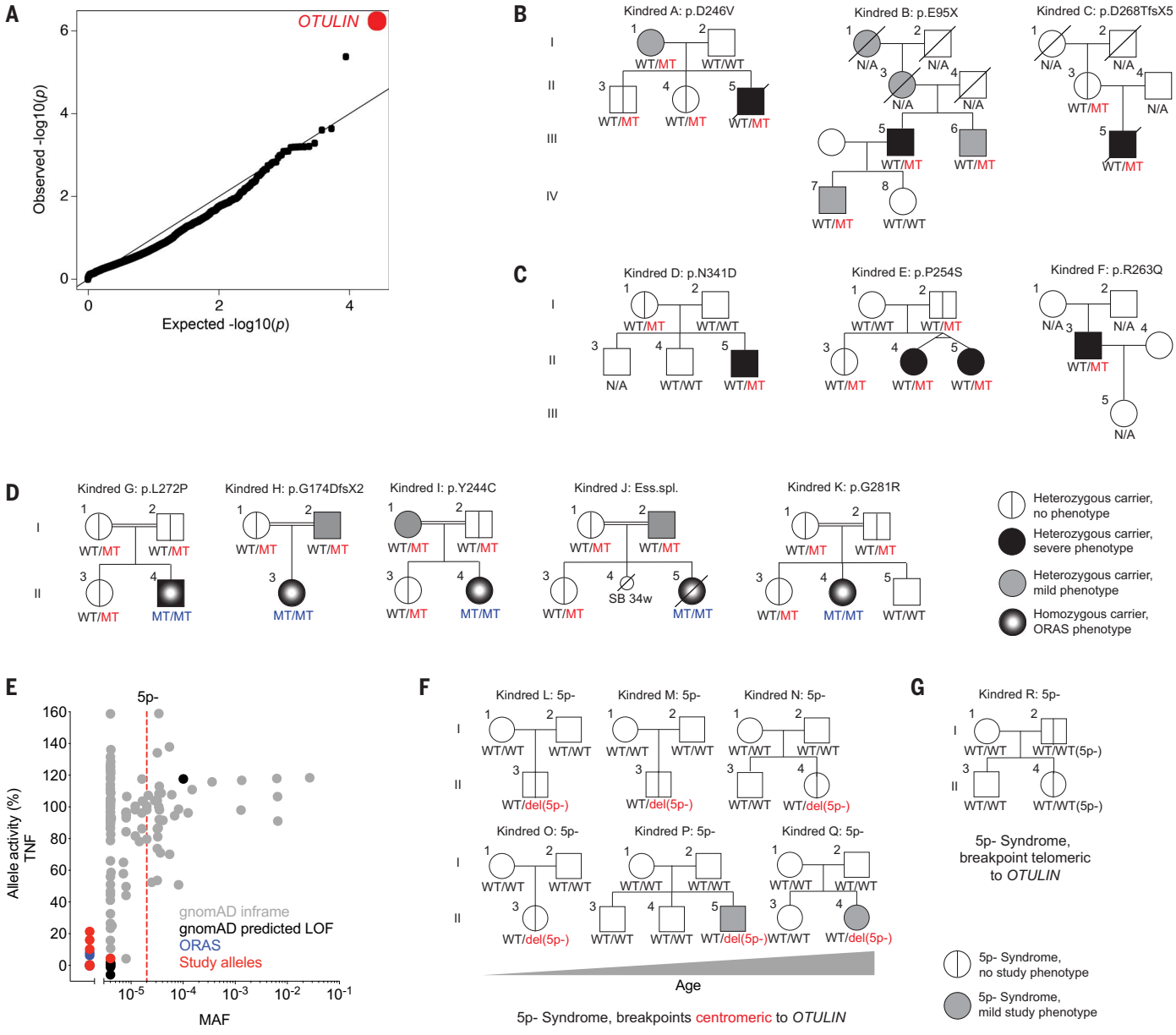

Fig. 1. OTULIN haploinsufficiency and its molecular characterization. (**A**) Genome-wide enrichment in rare, predicted deleterious variants in the cohort of 105 patients with severe staphylococcal disease, relative to 1274 patients with mycobacterial disease. (**B**) Pedigrees of the kindreds presenting severe necrotizing staphylococcal disease and carrying heterozygous mutations of *OTULIN*. (**C**) Pedigrees of the kindreds carrying heterozygous mutations of *OTULIN* and presenting necrosis triggered by other etiologies. (**D**) Pedigrees of the kindreds of ORAS probands carrying biallelic mutations of *OTULIN*. (**E**) Functional population genetics based on MAFs reported in gnomAD and the NF-κB inhibitory capacity of the OTULIN variants, as assessed with a luciferase reporter system in transiently transfected HEK293T cells stimulated with TNF (data points represent the mean of $N = 4$ to 5 per variant). (**F**) Pedigrees of the kindreds of the 5p− syndrome probands carrying deletions with a breakpoint centromeric to *OTULIN*. The patients are shown in ascending age order (left to right, top to bottom). (**G**) Pedigree of the 5p− syndrome kindred with probands carrying a deletion with a breakpoint telomeric to *OTULIN*. WT, wild-type allele; MT, mutant allele; LOF, loss of function. See also fig. S1 and tables S1 and S2.

haploinsufficient for OTULIN by definition (*38*–*40*). The prevalence of 5p− syndrome is ~1 in 50,000 live births, similar to the cumulative MAF for amorphic and hypomorphic *OTULIN* alleles (Fig. 1E) (*41*). Respiratory tract infections are one of the principal causes of hospitalization in individuals with 5p− syndrome, and pneumonia is among the most common causes of death in these individuals (*40*, *42*–*44*). We recruited six 5p− syndrome patients with a breakpoint centromeric to *OTULIN* (Fig. 1F and fig. S1L). Expressivity was variable and penetrance was incomplete, but one-third of these OTULIN-haploinsufficient 5p− syndrome patients (two of six) presented an age-dependent phenocopy of the disorder observed in patients with heterozygous *OTULIN* mutations (Fig. 1F; SM). We also identified two individuals from a multigeneration kindred affected by 5p− syndrome with an extremely rare breakpoint telomeric to *OTULIN* (Fig. 1G and fig. S1L) (*38*). Both these individuals carried two copies of *OTULIN* and did not display the phenotype studied here (SM). The clinical similarities between patients with heterozygous *OTULIN* mutations and those with 5p− syndrome suggest a common mechanism of

predisposition to infection due to haploinsufficiency for OTULIN.

Immunological characterization of OTULIN-haploinsufficient PBMCs

The autoinflammatory features seen in ORAS patients are largely driven by abnormally high levels of NF-κB activation in myeloid cells (*29*, *30*, *33*). We thus investigated whether patients with OTULIN haploinsufficiency presented any related immunological disturbances. OTULIN expression in monocytes differed between patients and healthy controls (fig. S2A). Routine immunological tests performed in diagnostic laboratories [including assessments of leukocyte differentiation and oxidative burst capacity—deficiencies of which are known to confer a predisposition to staphylococcal disease (*6*, *7*)] revealed no explanatory defects in patients with OTULIN haploinsufficiency (SM). We thus looked for more-subtle immunological features by testing peripheral blood mononuclear cells (PBMCs) from the patients using mass cytometry [cytometry by time-of-flight (CyTOF)] (*45*) and RNA sequencing. In comparisons with healthy controls, we observed no differences in the abundance of leukocyte subsets or in the expression of lineage markers (Fig. 2A and fig. S2, B to D). The development of myeloid and lymphoid subsets in patients with OTULIN haploinsufficiency was, therefore, apparently normal. At baseline, we observed a complex transcriptional signature not associated with NF-κB–driven inflammation in the PBMCs of the patients (Fig. 2B and fig. S2E). This difference between the patients and healthy controls disappeared after stimulation (Fig. 2B). Both at baseline and after stimulation, the PBMCs of the patients had a capacity to secrete various cytokines, including TNF and IL-1β, similar to that of PBMCs from healthy controls (fig. S2F). We detected no defect of IL-6 production (fig. S2F), deficiencies of which are known to be associated with staphylococcal disease (*6*). Single-cell RNA sequencing revealed a contribution of $CD14^+$ monocytes to the transcriptional signature in the PBMCs of the patients relative to healthy controls (fig. S2, G and H). However, consistent with their capacity to produce normal amounts of TNF and IL-1β (fig. S2I), the amounts of phosphorylated P65 in $CD14^+$ monocytes from the patients were normal both at baseline and after stimulation (fig. S2J). The $CD14^+$ monocytes of patients with OTULIN haploinsufficiency thus did not appear to be functionally affected. Finally, induced pluripotent stem cell (iPSC)–derived macrophages from patients had normal oxidative burst and phagocytic capacities relative to healthy controls (fig. S2, K and L). These observations suggest an absence of overt immunological disturbance in patients with OTULIN haploinsufficiency, contrasting with the autoinflammatory markers described in ORAS patients (*29*–*33*).

OTULIN gene dosage–dependent accumulation of linear ubiquitin in fibroblasts

We next performed a biochemical characterization of the nonhematopoietic compartment in the patients and assessed the levels of *OTULIN* expression in primary dermal fibroblasts (PDFs). *OTULIN* mRNA levels varied (fig. S3, A and B), but the levels of the corresponding protein were low in the patients and depended on the nature of the mutation (Fig. 3, A and B). OTULIN haploinsufficiency led to an accumulation of aggregates containing linear ubiquitin (M1-Ub) in immortalized fibroblasts from patients, including 5p– syndrome patients with a breakpoint centromeric to *OTULIN* (Fig. 3, C and D, and fig. S3C). These aggregates were sensitive to treatment with exogenous OTULIN (fig. S3D), and their accumulation was rescued by genetic complementation with wild-type *OTULIN* (Fig. 3E and fig. S3E). We used a combination of an M1-Ub–selective tandem Ub-binding entity (TUBE) and absolute quantification (AQUA) tandem mass spectrometry (MS/MS) to assess M1-Ub levels in immortalized fibroblasts from the patients. M1-Ub levels were much higher in the cells of both ORAS and OTULIN-haploinsufficient patients than in those of healthy controls and HOIL1-deficient patients (Fig. 3F) (*46*). Thus, OTULIN haploinsufficiency and recessive deficiency result in the cellular accumulation of M1-Ub in a gene dosage–dependent manner.

Normal TNF receptor signaling in OTULIN-haploinsufficient fibroblasts

In the PDFs of ORAS patients, expression of the components of LUBAC decreases to compensate for recessive OTULIN deficiency (Fig. 3A) (*29*, *30*, *32*). This compensatory mechanism impaired TNF receptor signaling in immortalized fibroblasts from ORAS patients (fig. S3F). By contrast, OTULIN haploinsufficiency did not lead to a loss of LUBAC expression in PDFs (Fig. 3A) or to impaired TNF receptor signaling (fig. S3F) or IL-6 and IL-8 secretion (fig. S3G). Indeed, no differential transcription patterns were evident in the patients' PDFs after stimulation with TNF (fig. S3H). The impairment of early NF-κB activation sensitizes PDFs from ORAS and LUBAC-deficient patients to TNF-induced apoptotic cell death under stress conditions (*29*, *46*). However, consistent with their normal LUBAC expression, PDFs from patients with OTULIN haploinsufficiency were not susceptible to stress-induced apoptosis upon exposure to TNF (fig. S3I). Thus, the functional dysregulation of TNF receptor signaling via NF-κB is limited to fibroblasts displaying a recessive OTULIN deficiency.

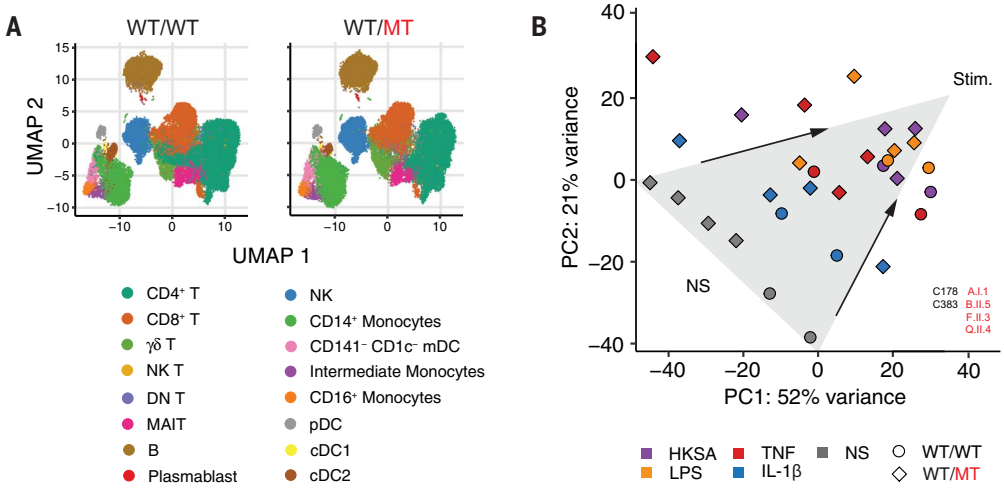

Fig. 2. OTULIN haploinsufficiency does not impair the hematopoietic immune system. (**A**) Aggregate uniform manifold approximation and projection (UMAP) plots of PBMCs from patients with AD OTULIN deficiency and healthy controls, as assessed by CyTOF. NK, natural killer T cells; DN T, double-negative T cells; MAIT, mucosal-associated invariant T cells; B, B cells; pDC, plasmacytoid dendritic cells; cDC, conventional dendritic cells. (**B**) Principal components analysis plot of the transcriptional profile of PBMCs at baseline and after incubation with various stimuli, in comparison with healthy controls. Arrows have been added to illustrate the direction of variance after stimulation. NS, not stimulated; HKSA, heat-killed *S. aureus*; LPS, lipopolysaccharide. See also fig. S2.

Global dysregulation of transcription in OTULIN-haploinsufficient fibroblasts

The presence of a biochemical phenotype in the absence of an immunological phenotype after stimulation in OTULIN-haploinsufficient fibroblasts led us to investigate transcriptional homeostasis in resting PDFs from the patients. Consistent with the gene dosage–dependent accumulation of M1-Ub in immortalized fibroblasts, this approach revealed a continuous genotype-dependent transcriptional phenotype in the basal state (Fig. 4A). Despite an absence of functional consequences of OTULIN haploinsufficiency (fig. S3, F to I), specific gene set enrichment analyses of the resting

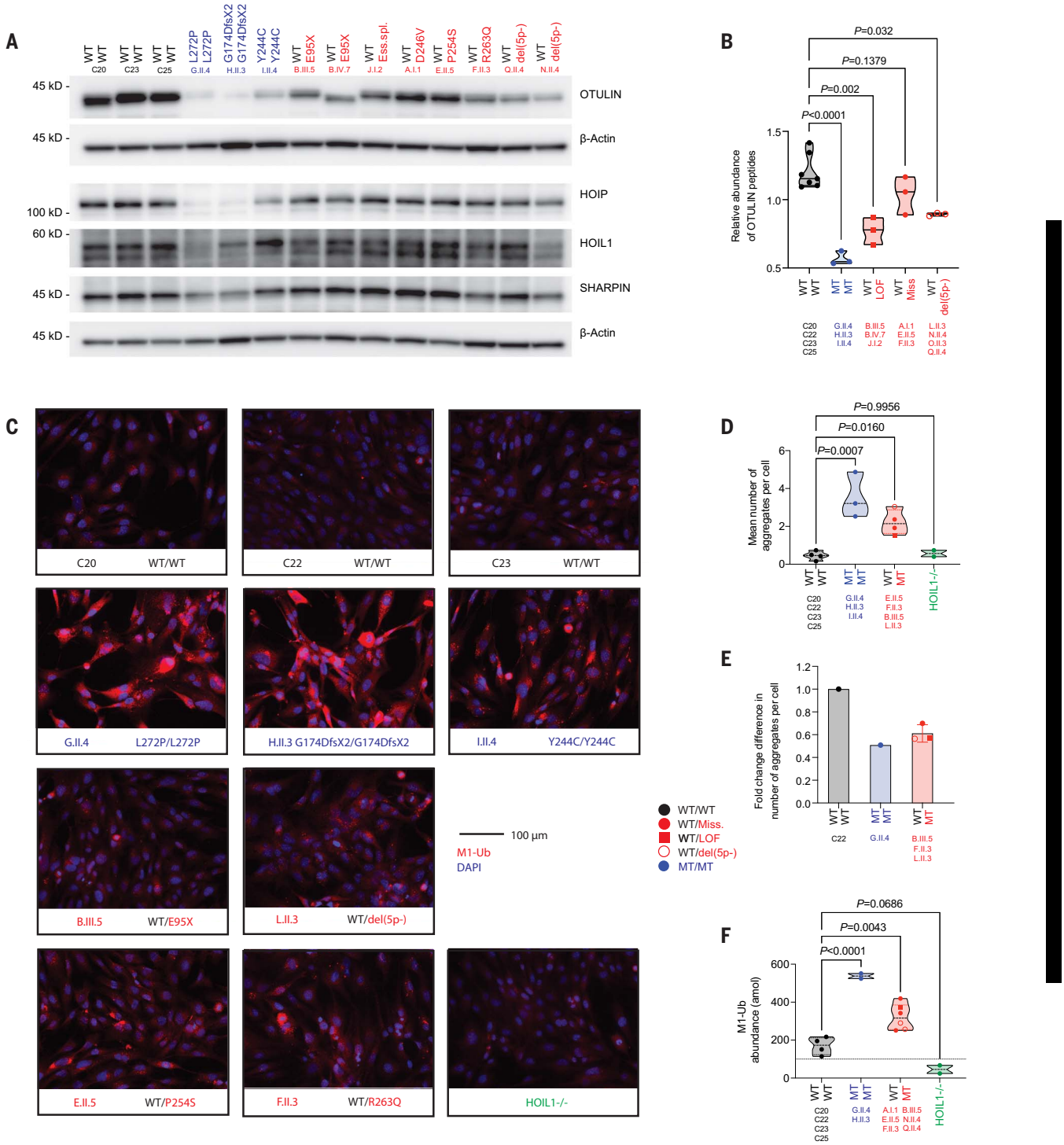

Fig. 3. *OTULIN* gene dosage–dependent accumulation of M1-Ub in fibroblasts. (**A**) Expression of OTULIN, HOIP, HOIL1, and SHARPIN in PDFs. (**B**) Relative abundance of OTULIN peptides in PDFs, as determined by mass spectrometry analysis (median). (**C**) Accumulation of aggregates containing M1-Ub in immortalized fibroblasts, as assessed by immunohistochemistry. Representative images. (**D**) Quantification of the aggregate accumulations seen in (D) (median). (**E**) Quantification of aggregates containing M1-Ub in immortalized fibroblasts after rescue with wild-type OTULIN, as compared with cells rescued with an empty virus (mean ± SD). (**F**) Abundance of M1-Ub, as determined by AQUA-MS/MS analysis of immortalized fibroblasts (median). Statistical significance was calculated by analysis of variance (ANOVA) with Dunnett's post hoc correction for multiple comparisons. See also fig. S3.

transcriptome revealed a subtle signal for TNF receptor signaling via NF-κB (fig. S4A). These analyses also revealed a transcriptional signature affecting various other cellular processes relative to cells from healthy controls (fig. S4A) (*47*). The affected processes included the MYC and E2F transcription factor systems and the G2/M cell cycle checkpoint system, the gene sets for these systems displaying a partial overlap (fig. S4B). These findings indicate a global dysregulation of transcription in resting OTULIN-haploinsufficient fibroblasts.

Accumulation of caveolin-1 in OTULIN-haploinsufficient fibroblasts

The observed patterns of transcription could not be explained by the known function of OTULIN as a linear deubiquitinase. We thus hypothesized that OTULIN haploinsufficiency affects cellular homeostasis posttranslationally, in an as yet unknown manner. The proteome of the resting PDFs from the patients displayed a continuous cellular phenotype, consistent with the transcriptome (Fig. 4B and fig. S4C). Focusing on this continuous proteomic phenotype, we observed a pattern of differential abundance for a cluster of 11 proteins including caveolin-2 and gelsolin (fig. S4, D to F). A STRING-interaction network analysis of this protein cluster identified a node connecting caveolin-2 and gelsolin: caveolin-1 (Fig. 4C). Conventional techniques revealed the accumulation of SDS-resistant high–molecular weight (MW) caveolin-1–containing complexes (*48*, *49*) in PDFs from the patients in comparison with those from healthy controls (Fig. 4, D and E). We analyzed caveolin-1 immunopurification products (IPs) from PDF whole-cell lysates (WCLs) from one healthy control and one patient with recessive OTULIN deficiency by liquid chromatography and tandem mass spectrometry (LC-MS/MS). Validating the STRING-interaction network (Fig. 4C), both sets of caveolin-1 IPs also contained caveolin-2, whereas gelsolin was detected in the OTULIN-deficient sample only (fig. S4G). Caveolin-1 levels vary between cell types and are highest in structural cells, such as fibroblasts (*50*, *51*). By contrast to our observations for PDFs, caveolin-1 was barely detectable in hematopoietic cells, and the abundance of caveolin-1 in monocytes did not differ between OTULIN-haploinsufficient patients and healthy controls (fig. S4H). We detected no accumulation of caveolin-1–containing complexes in PDFs from the 5p− syndrome patient carrying two copies of the *OTULIN* gene relative to healthy controls (Fig. 4E and fig. S4I). However, as in PDFs from the patients, caveolin-1 accumulated as a high-MW complex in an isogenic *OTULIN*-knockout PDF cell line (Fig. 4F and fig. S4J). Thus, OTULIN haploinsufficiency results in a selective accumulation of high-MW caveolin-1 in PDFs.

Lysine-63–linked polyubiquitination of caveolin-1

The differences in gelsolin abundance in PDFs were attributed to differences in *GSN* transcription, but no differential transcription was detected for *CAV1* and *CAV2* (fig. S5A). Caveolin-1 is a key component of cell membrane microdomains, in which it acts as a scaffold for other proteins and receptors (*47*, *52*). A signal for plasma membrane disturbance was detected at the proteomic but not the transcriptional level in the patients' PDFs (fig. S5B), suggesting a posttranslational role for OTULIN in the regulation of caveolin-1 expression in PDFs. Caveolin-1 is decorated with ubiquitin (*48*, *49*, *53*). We hypothesized that OTULIN haploinsufficiency and recessive deficiency affect the ubiquitination status of caveolin-1. We found that caveolin-1 IPs from PDF-WCLs from one healthy control and one patient with recessive deficiency of OTULIN contained a high-MW ubiquitin-containing complex (fig. S5C). We then used LC-MS/MS to characterize the ubiquitination profiles of purified caveolin-1 in solution, in the high-MW complex fraction, and in the monomeric fraction. Lysine-48–linked polyubiquitin (K48-Ub) chains were conjugated to the high-MW caveolin-1–containing complex regardless of genotype (fig. S5D). We detected no M1-Ub in any of the caveolin-1 IP fractions (fig. S5, C and D). Instead, the high-MW caveolin-1–containing complex was abundantly decorated with lysine-63–linked polyubiquitin (K63-Ub) chains in the OTULIN-deficient sample but not in the healthy control (Fig. 5A and fig. S5C) (*49*). No other branched polyubiquitin linkages were detected in the caveolin-1 IP fractions. The remaining unmodified ubiquitin was probably conjugated as a monomer to caveolin-1 (fig. S5D) (*53*). The OTULIN-dependent accumulation of caveolin-1 complexes modified with K63-Ub but not M1-Ub chains indicates cross-talk between OTULIN and other ubiquitin ligases and/or hydrolases.

CYLD binds linear ubiquitin

We characterized the cross-talk between OTULIN and K63-Ub chains by treating purified caveolin-1 from one ORAS patient with a panel of recombinant deubiquitinases. Consistent with the respective specificities of the various hydrolases, the K63-linked polyubiquitination of high-MW caveolin-1 was reduced by treatment with recombinant CYLD but not OTULIN (Fig. 5B and fig. S5E). Similarly, the overexpression of *CYLD* but not *OTULIN* in PDFs from a patient with ORAS rescued the K63-linked polyubiquitination of high-MW caveolin-1 (Fig. 5C and fig. S5F). Unexpectedly, a stronger rescue was observed when both *CYLD* and *OTULIN* were overexpressed (Fig. 5C and fig. S5F). Caveolin-1 colocalized with K63-Ub and, to some extent, with M1-Ub aggregates in PDFs (fig. S5G). We used a combination of TUBE and high-input AQUA-MS/MS in immortalized fibroblasts to identify proteins bound to M1-Ub. We detected LUBAC components (fig. S5H), which are known to be decorated with M1-Ub (*29*). We also identified caveolin-1 and CYLD as possibly binding to M1-Ub (fig. S5H) and used cells from a HOIL1-deficient patient to validate specificity (*46*). The detection of caveolin-1 was not specific (fig. S5I), consistent with the absence of M1-Ub in the caveolin-1 IP (Fig. 5A and fig. S5, C and D). We confirmed the specific binding of CYLD to M1-Ub in an *OTULIN* gene dosage–dependent manner (Fig. 5D and fig. S5I). The M1-Ub–bound CYLD species had a higher MW than that of the total CYLD pool (fig. S5I), suggesting posttranslational modification. We identified no Gly-Gly ubiquitination signature sites on CYLD by proteomic approaches, suggesting that the posttranslational modification is not ubiquitination itself and that the binding of CYLD to M1-Ub is noncovalent. Unlike an *OTULIN* gene-dosage effect, M1-Ub–bound HOIP was detected in cells from ORAS patients only (Fig. 5D and fig. S5, I and J). These data reveal a direct, LUBAC-independent but OTULIN-dependent binding of M1-Ub to CYLD.

Colocalization of caveolin-1 with S. aureus α-toxin

Caveolin-1 clusters in membrane microdomains (*52*) and has been reported to colocalize with a disintegrin and metalloprotease domain–containing protein 10 (ADAM10) (*54*). ADAM10 is a cell surface receptor used by the staphylococcal virulence factor α-toxin (*54*, *55*). α-Toxin is a pore-forming cytotoxin triggering ADAM10-mediated cell death in a process facilitated by caveolin-1 (*56*). We hypothesized that the OTULIN-dependent caveolin-1 accumulation in the PDFs from the patients would contribute to the adverse outcomes of their disease. We thus investigated the cellular kinetics of α-toxin binding. After its addition to PDFs, α-toxin colocalized with both ADAM10 and caveolin-1 (Fig. 6A and fig. S6, A and B). ADAM10 and caveolin-1 were colocalized to some extent in the presence or absence of toxin binding (Fig. 6A and fig. S6, A and B). The patients' PDFs displayed moderately higher levels of α-toxin binding than cells from healthy controls (Fig. 6B and fig. S6C). This observation could not be explained by differential ADAM10 expression at baseline (fig. S6, D and E). However, after α-toxin binding, the expression of ADAM10 at the cell surface was greater in PDFs from patients than in those from healthy controls (fig. S6F). These data suggest a role for caveolin-1 in retaining ADAM10 at the surface of the cell when OTULIN-haploinsufficient fibroblasts are exposed to α-toxin (*57*, *58*).

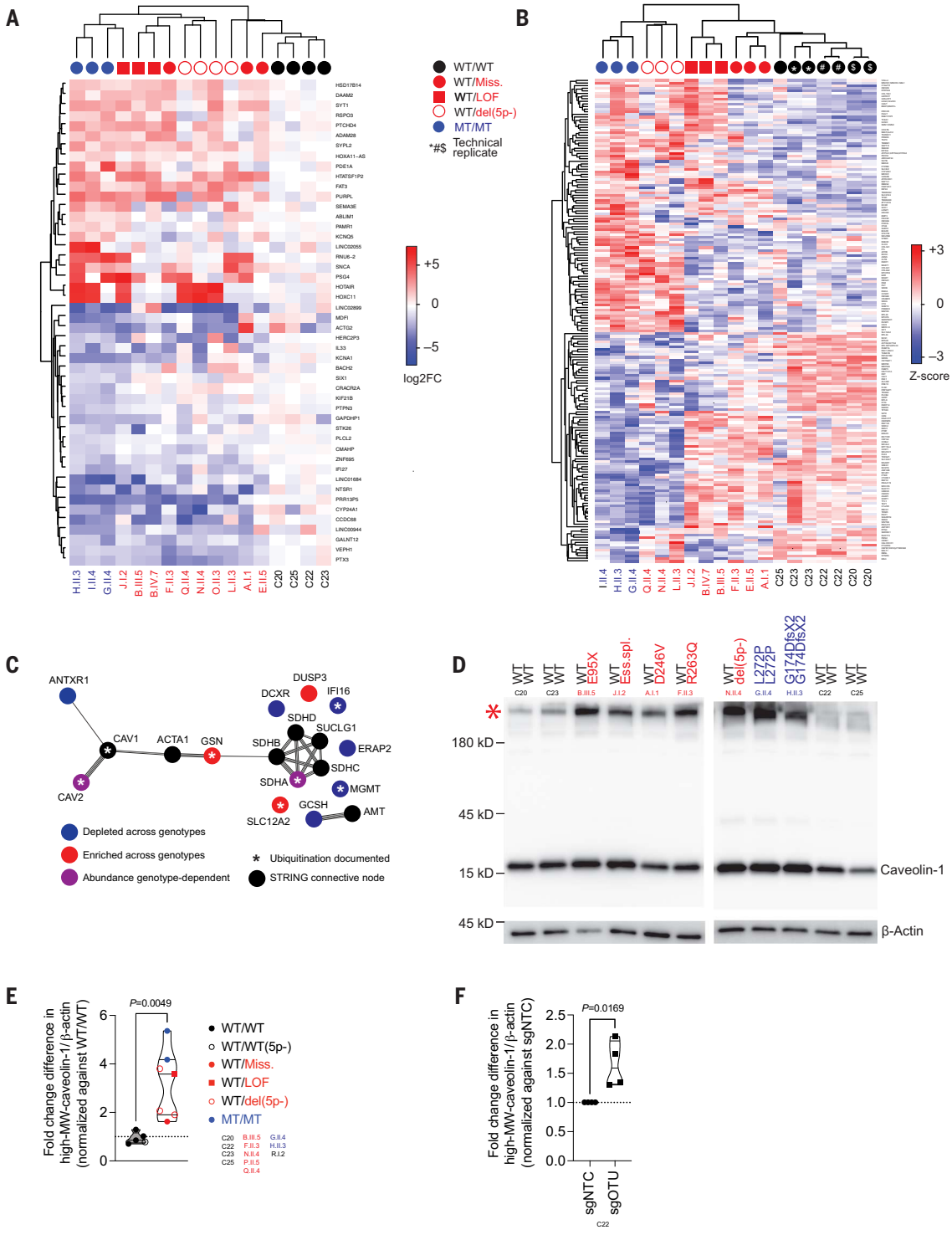

Fig. 4. *OTULIN*-dependent accumulation of caveolin-1 in fibroblasts. (**A**) Transcriptional profile of unstimulated PDFs, as assessed by RNA sequencing, expressed as $\log_2$ fold changes (FC) relative to the mean value for controls. Genes satisfying the threshold for statistical significance in comparisons of ORAS patients to controls are shown. (**B**) Proteomic profiles of unstimulated PDFs, as assessed by mass spectrometry on WCLs, expressed as Z-scores. Genes satisfying the threshold for statistical significance in comparisons of ORAS patients to controls are shown. (**C**) STRING analysis of the cluster of proteins with differential abundances in various genotypes identified in (B). (**D**) Accumulation of SDS-resistant high-MW caveolin-1–containing complexes in PDF-WCLs. (**E**) High-MW caveolin-1–containing complex intensities relative to β-actin intensities in PDF-WCLs, normalized against the mean value of healthy controls (data points indicate the mean of $N = 2$ replicates per patient, median per group). (**F**) High-MW caveolin-1–containing complex intensities relative to β-actin intensities in PDF-WCLs treated with an sgRNA pool targeting *OTULIN* (sgOTU), normalized against the mean value in those treated with a nontargeting control sgRNA (sgNTC) (median, $N = 4$). The statistical significance of differences was assessed in Student's *t* tests. See also fig. S4.

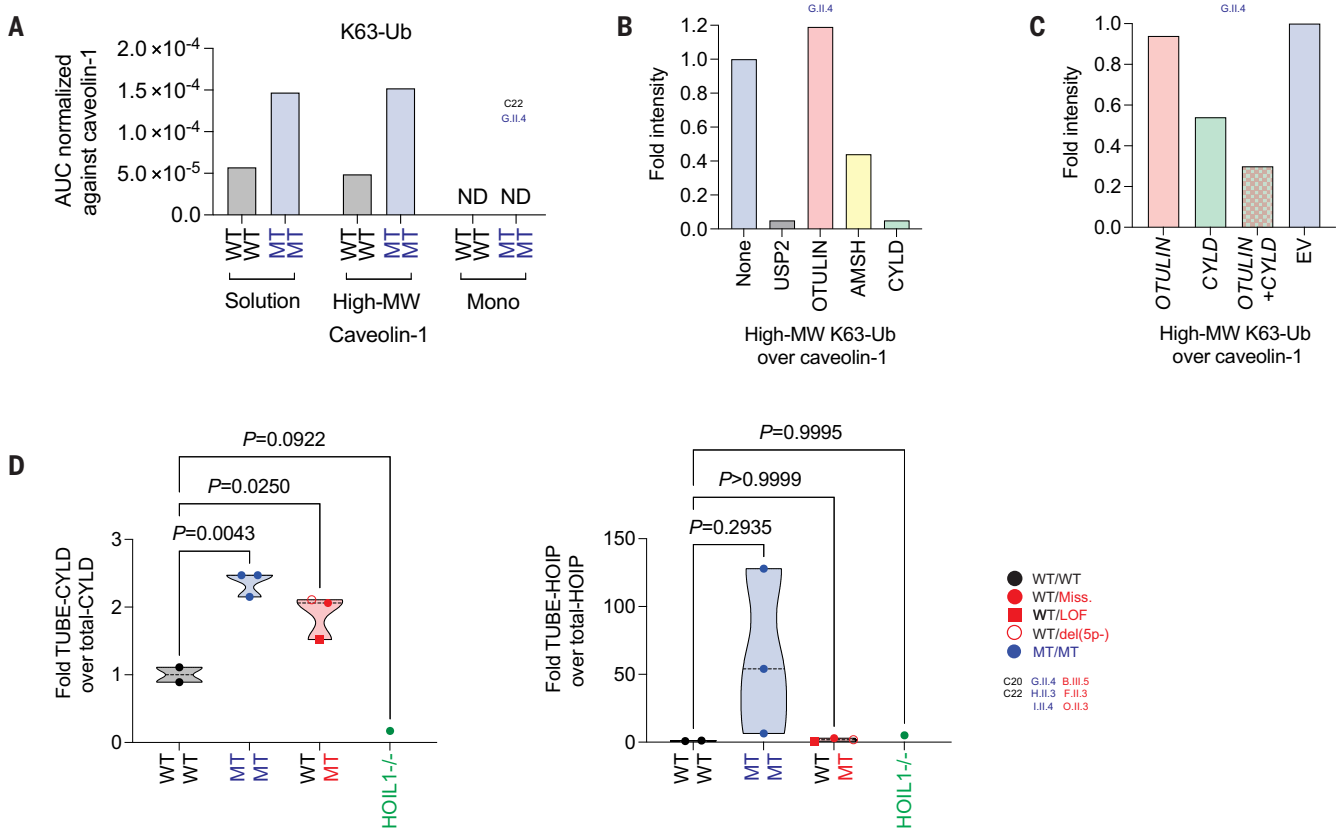

Fig. 5. Polyubiquitination of caveolin-1. (**A**) Analysis of K63-Ub on caveolin-1 by LC-MS/MS on purified caveolin-1 from PDF-WCLs. Caveolin-1 was analyzed in solution, in the high-MW complex fraction, and in the monomeric (Mono) fraction. (**B**) High-MW K63-Ub complex intensities relative to caveolin-1 intensities in recombinant deubiquitinase-treated purified caveolin-1 from PDFs. (**C**) High-MW K63-Ub complex intensities relative to caveolin-1 intensities in purified caveolin-1 from PDFs after rescue with *CYLD* and/or *OTULIN*. (**D**) Intensities of CYLD and HOIP bound to M1-Ub, as detected in TUBE pull-downs from immortalized fibroblasts, relative to intensities of total CYLD and HOIP, respectively. Statistical significance was calculated by ANOVA with Dunnett's post hoc correction for multiple comparisons. See also fig. S5.

OTULIN haploinsufficiency impairs intrinsic immunity to α-toxin

We hypothesized that OTULIN haploinsufficiency confers a predisposition to α-toxin–induced cell death in the PDFs of the patients. Indeed, these cells displayed an enhanced susceptibility to *S. aureus* culture supernatant–elicited cytotoxicity (Fig. 6C). This cytotoxicity was antagonized by prior treatment of the supernatant with α-toxin–neutralizing monoclonal antibodies (fig. S6G), indicating a major contribution of α-toxin to cytotoxicity in these cells. *OTULIN* genotype–dependent susceptibility to α-toxin was confirmed with recombinant α-toxin (Fig. 6D and fig. S6H). The absence of a particular phenotype after the treatment of cells from patients with streptolysin O (SLO) and aerolysin—microbial toxins produced by other bacteria and not requiring specific proteinaceous host-cell surface receptors (*59*)—indicates a specific susceptibility of the OTULIN-haploinsufficient PDFs from patients to α-toxin (Fig. 6D and fig. S6H). Normal susceptibility to α-toxin was observed in PDFs from a 5p– syndrome patient carrying two copies of the *OTULIN* gene, confirming the OTULIN-dependence of the phenotype (Fig. 6E and fig. S6I). α-Toxin elicited higher levels of cell surface metalloprotease activation in PDFs from the patients than in those of healthy controls (Fig. 6F) (*55*). Again, a 5p– syndrome patient carrying two copies of the *OTULIN* gene behaved like controls (Fig. 6F). Activity levels were correlated with ADAM10 levels after α-toxin binding (fig. S6J). Prior treatment of the PDFs with an ADAM10-selective inhibitor blocked α-toxin–induced metalloprotease activation completely in controls, but activation levels in patients were decreased only slightly, to levels seen in untreated controls (Fig. 6F). Moreover, to various extents, ADAM10 inhibition protected the patients' PDFs against α-toxin cytotoxicity (fig. S6K). Prior treatment with cyclodextrin, a chemical product disrupting caveolin-1–enriched membrane microdomains (*60*), protected PDFs from the patients against α-toxin–induced cytotoxicity (fig. S6K). The susceptibility of an OTULIN-deficient PDF cell line was partially rescued by knocking out *CAV1* but not by knocking out *CAV2* (Fig. 6G and fig. S6L), further supporting a facilitating role of caveolin-1 in α-toxin cytotoxicity (*54*). Consistent with the low levels of caveolin-1 in hematopoietic cells from the patients, these cells displayed no OTULIN-dependent susceptibility to α-toxin (fig. S6M). Murine PDFs, unlike their human counterparts, were resistant to α-toxin–elicited cell death regardless of *Otulin* genotype (fig. S6N). Thus, OTULIN haploinsufficiency results in a human-specific cell-intrinsic susceptibility of nonhematopoietic cells to the major *S. aureus* virulence factor α-toxin.

α-Toxin–neutralizing antibodies rescue OTULIN haploinsufficiency

Colonization and infection with *S. aureus* elicit α-toxin–neutralizing antibodies in an age-dependent manner (*61*). We hypothesized that α-toxin–neutralizing antibodies in the plasma of adult symptomatic and asymptomatic heterozygotes might contribute to the incomplete clinical penetrance of OTULIN haploinsufficiency (Fig. 1, B to D and F) (*12*). Routine

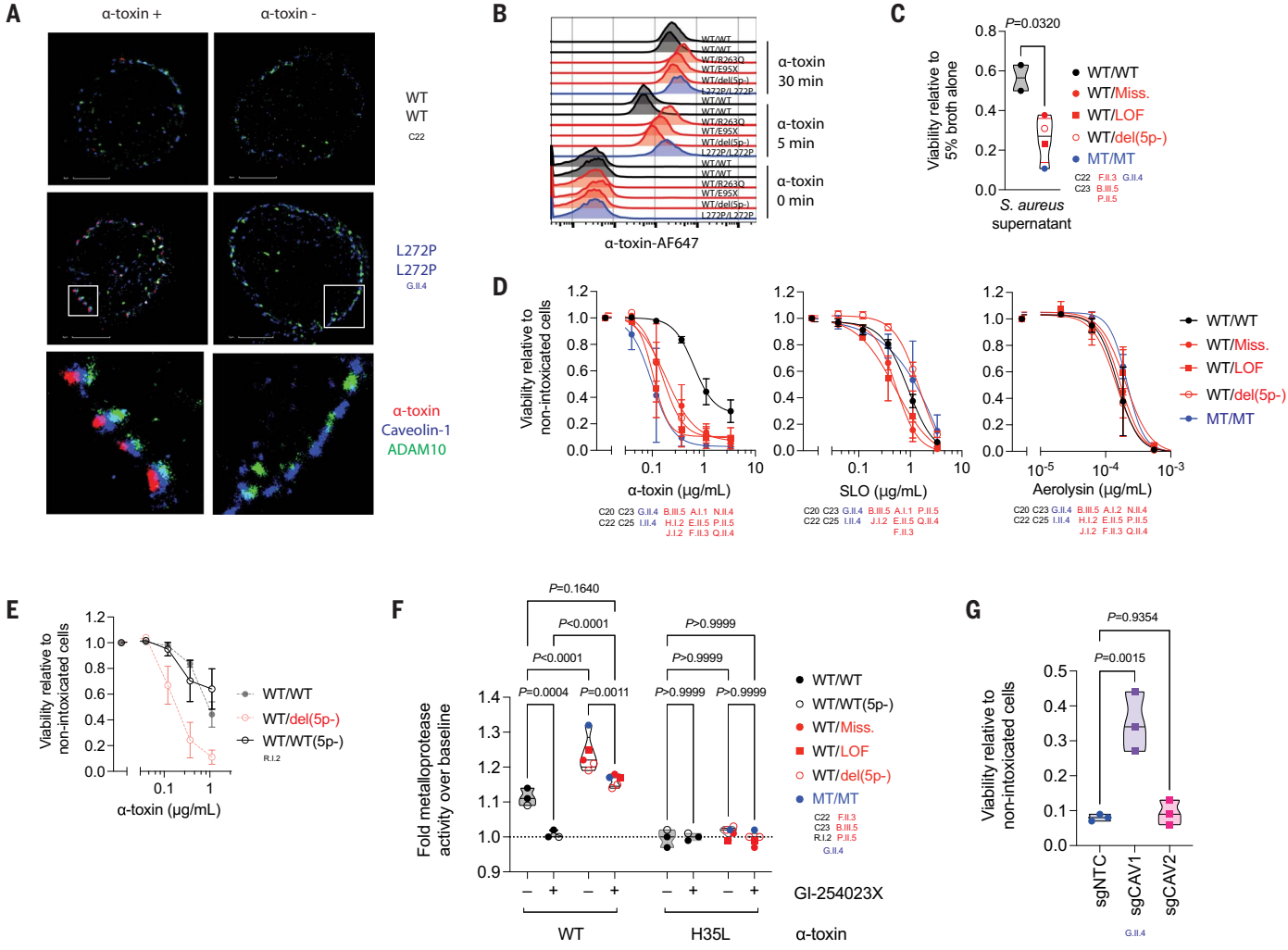

Fig. 6. OTULIN haploinsufficiency impairs intrinsic immunity to α-toxin in fibroblasts. (**A**) Colocalization of α-toxin with ADAM10 and caveolin-1 in PDFs, visualized in high-resolution images acquired by stochastic optical reconstruction microscopy, after 30 min of incubation in the presence or absence of α-toxin. (**B**) Binding of α-toxin in PDFs, as detected by flow cytometry. (**C**) Viability of PDFs after 2.5 hours of incubation with culture supernatant from *S. aureus* (data points indicate the mean of *N* = 3 replicates per patient, median per group). (**D**) Viability of PDFs after 24 hours of incubation with recombinant microbial toxins (*N* = 2 to 4 per group, mean ± SD per group). (**E**) Viability of PDFs from a 5p− syndrome patient with a breakpoint telomeric to *OTULIN* after 24 hours of incubation with recombinant α-toxin, superimposed on that for healthy controls and 5p− patients with a breakpoint centromeric to *OTULIN* from (F) (*N* = 3, mean ± SD). (**F**) Cell-surface metalloprotease activity in PDFs induced by wild-type α-toxin (WT) or a toxoid mutant (H35L) after the treatment of cells with an ADAM10 inhibitor or carrier (data points indicate the mean of *N* = 3 replicates per patient, median per group). (**G**) Viability of OTULIN-deficient PDFs treated with an sgRNA pool targeting *CAV1* (sgCAV1), *CAV2* (sgCAV2), or a nontargeting control sgRNA (sgNTC) after exposure to α-toxin (0.12 μg/ml; *N* = 3, median). The statistical significance of differences was assessed in Student's *t* tests (C), or by ANOVA with Bonferroni (F) or Dunnett's (G) post hoc corrections for multiple comparisons. See also fig. S6.

measurements of immunoglobulin (Ig) levels and vaccine responses revealed no defects in the patients (SM). Plasma α-toxin–neutralizing capacity in asymptomatic carriers was similar to that of healthy controls, whereas this capacity was significantly lower in patients (about one-fifth that in healthy controls) (Fig. 7A and fig. S7A). The lower neutralizing capacity in the patients was specific for α-toxin, because the plasma of the patients neutralized SLO and pneumolysin normally (Fig. 7A and fig. S7A). In healthy controls, plasma α-toxin–neutralizing capacity was largely driven by IgG (fig. S7B). In patients, anti–α-toxin IgG levels were significantly lower than those in healthy controls, whereas IgA and IgM levels were unaffected (Fig. 7B and fig. S7, C and D). The anti–α-toxin IgG levels in asymptomatic carriers were like those of healthy controls (Fig. 7B and fig. S7, C and D) (*61*). Similar observations were made after correction for sample-specific total IgG levels (fig. S7E). Thus, naturally elicited α-toxin–neutralizing antibodies can rescue OTULIN haploinsufficiency in vivo, thereby contributing to incomplete penetrance.

Discussion

We tested the hypothesis that some patients from our cohort with severe staphylococcal disease suffered from IEIs. Using an unbiased approach, we detected a genome-wide enrichment in very rare, deleterious heterozygous *OTULIN* variants in the cohort. We identified haploinsufficiency for OTULIN as a genetic etiology of severe staphylococcal disease. AR OTULIN deficiency results in life-threatening autoinflammation, manifesting early in life as ORAS (*29*–*32*). By contrast, patients with AD OTULIN deficiency typically presented with

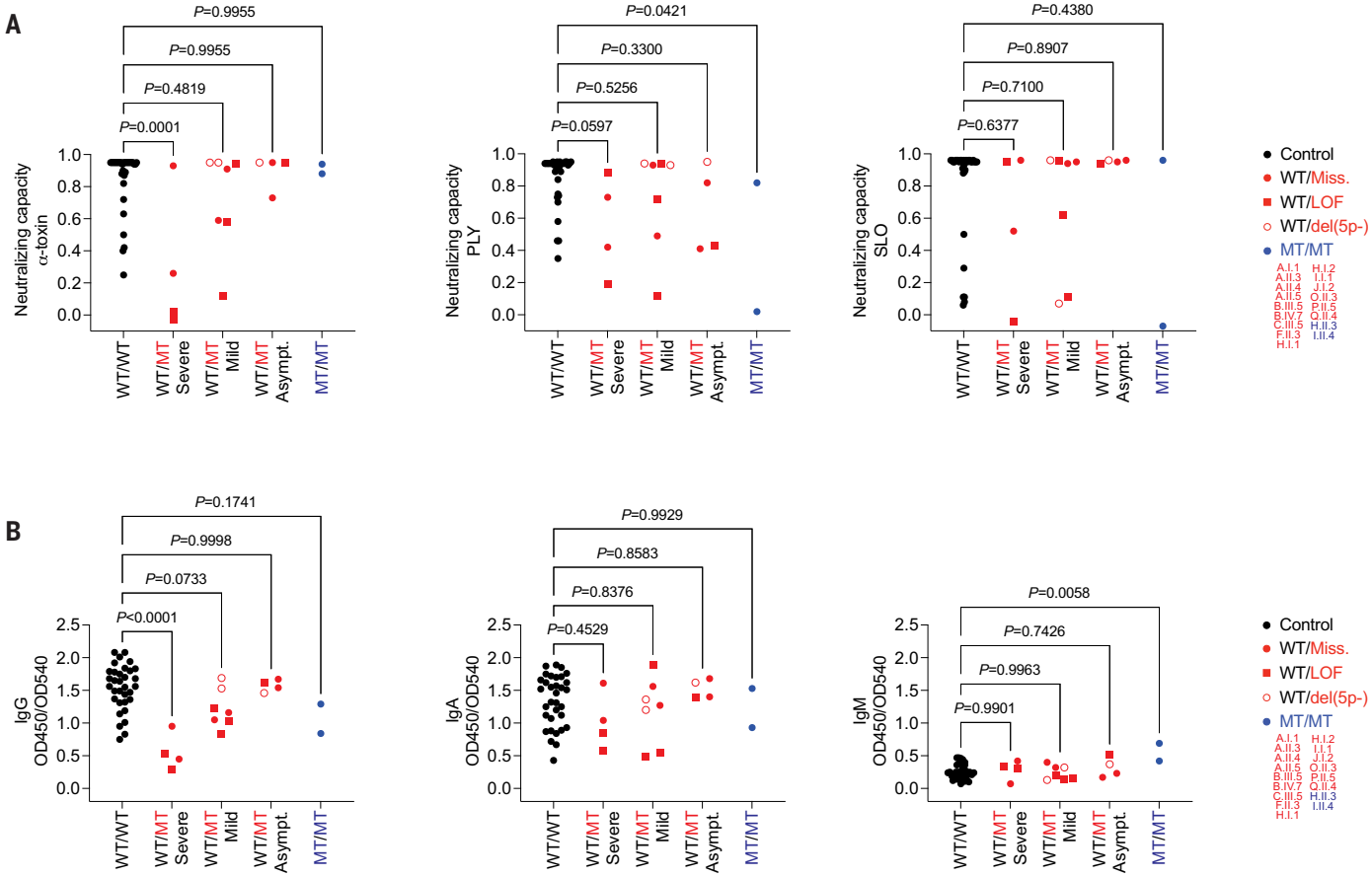

Fig. 7. α-Toxin–neutralizing antibodies rescue OTULIN haploinsufficiency. (**A**) Capacity of plasma at a dilution of 1:300 to neutralize the hemolytic activity of α-toxin (20 ng/ml), pneumolysin (PLY, 0.67 ng/ml), and streptolysin O (SLO, 42 ng/ml) in rabbit erythrocytes. (**B**) Anti–α-toxin immunoglobulin levels in plasma at a dilution of 1:750. We analyzed plasma from adult patients, relatives, and controls. The statistical significance of differences was determined by ANOVA with Dunnett's post hoc correction for multiple comparisons. See also fig. S7.

severe disease triggered by *S. aureus* infections. Most of the patients with OTULIN haploinsufficiency experienced their first episode of disease during adolescence. Necrosis was a clinical hallmark of disease in the probands. Some patients were not diagnosed with *S. aureus* infections, suggesting that low-grade infectious or, perhaps, noninfectious triggers might be at work. AD OTULIN deficiency is clinically expressed in a tissue-specific manner, because the skin and/or lungs are the affected organs in all patients. The pedigrees reported in our study displayed variable degrees of penetrance and expressivity. Such observations are common in situations of haploinsufficiency (*62*, *63*). We show that naturally elicited α-toxin–neutralizing antibodies can rescue OTULIN haploinsufficiency, and we suspect that declining levels of such antibodies may contribute to recurrent episodes of severe staphylococcal disease in some patients. We estimate the clinical penetrance of AD OTULIN deficiency at ~30%. This estimate of clinical penetrance mirrors our findings for individuals with 5p– syndrome. It is difficult to establish causal relationships between individual genes and specific phenotypes in patients with chromosomal deletion syndromes. Clinical manifestations of a monogenic disorder in a chromosomal deletion syndrome have also been reported for GATA3 haploinsufficiency (*64*). Our observations suggest that the study of rare IEIs can help to clarify phenotypes seen in individuals with more-common chromosomal abnormalities.

In ORAS patients, autoinflammation results from the defective down-regulation of NF-κB–dependent inflammatory signaling in hematopoietic cells, particularly those of the myeloid lineage (*29*–*32*). OTULIN deficiency causes a gene dosage–dependent accumulation of M1-Ub, but OTULIN haploinsufficiency is both clinically and biochemically silent for TNF-induced signaling events, instead causing a predisposition to infection. The apparent paradox of autoinflammation and immunodeficiency within the spectrum of clinical phenotypes of OTULIN deficiency is also observed in patients with HOIL1 and HOIP deficiencies, which greatly decrease the levels of M1-Ub (*46*, *65*). The combination of autoinflammation and immunodeficiency in HOIL1 and HOIP deficiencies highlights the complex role of LUBAC in maintaining the cell type–specific balance between inflammation and immunity. Inflammation is regulated by two other deubiquitinases in addition to OTULIN: A20 and CYLD. Phosphorylated A20 preferentially cleaves K63-Ub in cells (*66*, *67*). CYLD hydrolyzes K63-Ub and M1-Ub (*68*). AD A20 deficiency causes an autoinflammatory condition resembling Behçet's disease (*69*), whereas AD CYLD deficiency results in cylindromatosis of the skin (*70*). AR HOIL1, HOIP, and OTULIN deficiencies and AD A20 deficiency are systemic disorders. Conversely, AD OTULIN and CYLD deficiencies result in tissue-specific disease. OTULIN and CYLD bind HOIP in a mutually exclusive manner (*71*). The detection of CYLD bound to M1-Ub reveals another, LUBAC-independent, layer of cross-talk between the two deubiquitinases. CYLD activity and specificity were recently shown to be regulated by phosphorylation and ubiquitin-binding CAP-Gly domains (*72*). We speculate that, with insufficient amounts of OTULIN, phosphorylated CYLD primed for activity toward K63-Ub is quenched by M1-Ub. The

accumulation of caveolin-1 in dermal fibroblasts observed in patients with OTULIN deficiency probably results from disruption of the polyubiquitination of this molecule.

Human OTULIN haploinsufficiency is an inborn error of cell-intrinsic immunity to *S. aureus* infection. Staphylococcal disease displays a remarkable organ tropism, affecting the skin and lungs in particular (*1*). Tissue barrier disruption is a hallmark of severe staphylococcal disease (*73*). α-Toxin is a key staphylococcal virulence factor that contributes to severe disease (*73*–*76*) and can injure nonhematopoietic cells (*54*, *73*, *77*, *78*). The mechanism underlying the impairment of staphylococcal immunity in OTULIN haploinsufficiency is reminiscent of that involved in cell-intrinsic immunodeficiencies conferring susceptibility to viral infections (*79*–*81*). In the absence of sufficient levels of α-toxin–neutralizing antibodies, susceptibility to staphylococcal disease in patients with OTULIN haploinsufficiency is driven by a defect of cell-intrinsic immunity to the α-toxin of the pathogen. In patients with OTULIN haploinsufficiency, caveolin-1 accumulates specifically in nonhematopoietic cells. Caveolin-1 clusters with α-toxin, and the retention of ADAM10 at the surface of the patients' cells predisposes these cells to α-toxin–induced cell death (*82*, *83*). Caveolin-1 accumulation is observed in the cells of patients with either biallelic or monoallelic OTULIN deficiencies. The late-onset infectious phenotype in patients with AD OTULIN deficiency may be overshadowed by the early-onset severe autoinflammatory manifestations in ORAS or compensated for by the presence of α-toxin–neutralizing antibodies. Consistent with this view, we also identified a pediatric homozygous carrier of a moderately hypomorphic OTULIN variant with an infectious phenotype indistinguishable from that of our haploinsufficient probands, with no autoinflammatory features. This work provides a direct demonstration of a defined host characteristic predisposing humans to adverse events elicited by a specific bacterial virulence factor.

S. aureus is a pathogen of paramount significance in human health (*1*). In the face of a globally emerging epidemic of community-acquired methicillin-resistant *S. aureus* (MRSA) strains (*18*), innovative strategies for treating and preventing infection are needed (*84*). In the presence or absence of documented *S. aureus* infections, OTULIN-haploinsufficient patients with severe necrosis may benefit from combined antibiotic and steroid therapy, together with α-toxin–neutralizing monoclonal antibodies (*85*). Despite clear public health needs, no effective *S. aureus* vaccine has yet been approved (*86*). Humans are the main reservoir of *S. aureus*, and the pathogen is highly adapted to its human host (*77*, *78*). Mice are naturally resistant to *S. aureus* infection (*87*). The principal mechanistic differences in hematopoietic immunity to staphylococcal infections between humans and mice have been characterized (*77*, *78*). By contrast, the mechanisms of cell-intrinsic immunity in nonhematopoietic cells have been minimally studied in humans or mice (*80*, *88*–*90*). Staphylococcal virulence factors, such as α-toxin, are considered potential targets for strategies aiming to treat and prevent infection (*77*, *78*). For many of these virulence factors, and cytotoxins in particular, one or more aspects of the interaction with the host are human-specific (*78*, *91*). Murine ADAM10 can interact with α-toxin (*55*). However, OTULIN haploinsufficiency reveals a layer of human specificity at the interface between α-toxin and its human nonhematopoietic target cells. OTULIN haploinsufficiency demonstrates the contribution of *S. aureus* toxins to the pathophysiology of severe disease in humans. The experiment of nature described here identifies a mechanism of human cell–intrinsic immunity to *S. aureus* infections and highlights the potential for interfering with the staphylococcal α-toxin for treating and preventing disease (*85*, *92*).

Materials and methods summary

Human subjects

Informed consent was obtained from each patient, in accordance with local regulations, and a protocol for research on human subjects was approved by the institutional review boards of Institut National de la Santé et de la Recherche Médicale (INSERM, protocol C10-16) and The Rockefeller University (protocols JCA-0698 and JCA-0695).

Whole-exome sequencing, breakpoint determination, and variant enrichment analyses

Genomic DNA was extracted from whole blood. Whole-exome sequencing and breakpoint determinations are detailed in the SM. A gene-based enrichment analysis was performed on the cohort of 105 patients with severe staphylococcal disease, together with 1274 individuals with Mendelian susceptibility to mycobacterial disease or suffering from tuberculosis as controls. Rare variants [MAF < 1×10^{-5} in the Genome Aggregation Database (gnomAD) (*20*)] predicted to be damaging [CADD > MSC (*21*)] were retained (table S1) (*23*). The proportions of individuals with rare damaging variants in the cohort and the controls were compared by logistic regression with likelihood ratio tests (table S2). The first five principal components of the PCA were systematically included in the logistic regression model to account for the ethnic heterogeneity of the cohorts, as previously described (*93*). Genes were then tested under a dominant genetic model. Four carriers, three of whom carried heterozygous variants, were identified among the cases. No carriers were identified among the controls. We then performed the same analysis again, but with the addition of 2504 individuals from 1000 Genomes Project phase 3 (*25*) to our control dataset (*26*).

Cell culture

PDFs were obtained from skin biopsy specimens and cultured in Dulbecco's modified Eagle's medium (DMEM) (Gibco) supplemented with 10% heat-inactivated fetal bovine serum (HI-FBS) (Gibco) unless otherwise specified. PBMCs were isolated from whole blood by density gradient centrifugation on Ficoll-Paque PLUS (GE Healthcare Life Sciences) and maintained in Roswell Park Memorial Institute (RPMI) 1640 medium (Gibco) supplemented with 10% HI-FBS unless otherwise specified. Immortalized fibroblasts were generated by transformation with SV40 as previously described (*94*) and maintained in DMEM supplemented with 10% HI-FBS. HEK293T cells (American Type Culture Collection) were cultured in DMEM supplemented with 10% HI-FBS.

Generation of OTULIN constructs, transfection, transduction, and nucleofection

The human canonical *OTULIN* cDNA open reading frame clone was amplified from pCMV6-Entry FAM105B (OriGene) and inserted into the pCMV6-AN-Myc-DDK–tagged vector (OriGene) or pLentiIII-UBC (Abmgood). Site-directed mutagenesis to generate the *OTULIN* variants present in the patients was performed by a modified overlap-extension polymerase chain reaction (PCR)–based method (*95*). All constructs were validated by Sanger sequencing. HEK293T cells were transiently transfected in the presence of Lipofectamine LTX (Thermo Fisher Scientific). For lentiviral transductions, semi-confluent HEK293T cells were cotransfected with *OTULIN*, *GAG*, *POL*, and *ENV* plasmids. The supernatant was collected at 48 and 72 hours and concentrated with a Lenti-X concentrator (Clontech). A 10-fold dilution (by volume) of the lentivirus preparation was added to semi-confluent immortalized fibroblasts plated on six-well plates. Transduced cells were selected with puromycin (Invitrogen). PDFs were mixed with gene knockout kit V2 single guide RNA pools (Synthego) in the presence of TrueCut Cas9 protein V2 (Thermo Fisher Scientific), or with pCMV6 expression vectors, and nucleofected with the basic nucleofector kit for primary mammalian fibroblasts (Lonza) on a Nucleofector 2b device (Lonza).

NF-κB inhibition assay and linear deubiquitinase assay

HEK293T cells in 96-well plates were transiently cotransfected with pCMV6 vectors containing the *OTULIN* cDNA variants, the NF-κB

firefly luciferase plasmid pGL4.32, and the *Renilla* luciferase plasmid (pRLTK) as an internal control. The cells were stimulated, 24 hours after transfection, by incubation with 20 ng/ml TNF in minimal medium (1% FBS) for an additional 24 hours. The ratio of firefly-to-*Renilla* luciferase expression was assessed with the Dual-Glo Luciferase assay (Promega) on a bioluminescence plate reader. Data were normalized against the inhibitory activity of cells transfected with a vector encoding the *OTULIN* reference cDNA. For linear deubiquitination assays, HEK293T cells were co-transfected with pCMV6 vectors containing the *OTULIN* cDNA variants, *RBCK1*, *RNF31*, *SHARPIN*, and linear ubiquitin (*UBC*) and harvested after 48 hours. Whole-cell lysates were prepared with WCL buffer A (table S4). For immunoprecipitation, anti–M1-Ub antibody was added, and the lysates were incubated overnight at room temperature. Dynabeads Protein G (Thermo Fisher Scientific) beads were added to the samples, which were then incubated for 1 hour at room temperature. The beads were then washed with WCL buffer A (table S4) and resuspended in 2 x NuPAGE LDS sample buffer (Thermo Fisher Scientific) supplemented with dithiothreitol (DTT). The antibodies used are described in table S3.

Reverse transcription and PCR

Total RNA was extracted from transiently transfected HEK293T cells or from PDFs with the RNeasy Mini Kit (QIAGEN). Reverse transcription was performed with the SuperScript III First-Strand Synthesis System (Invitrogen) and random hexamers. Quantitative PCR was performed with the TaqMan Universal PCR Master Mix (Applied Biosystems) in the 7500 Fast Real-Time PCR System (Applied Biosystems). The following TaqMan Gene Expression assays (Thermo Fisher Scientific) were used: *OTULIN* (Hs01113237_m1), *GUSB* (Hs00939627_m1), and *GAPDH* (Hs99999905_m1).

Whole-cell lysates, SDS-PAGE, and Western blotting

Transiently transfected HEK293T cells were harvested and lysed in WCL buffer B (table S4). PDFs were synchronized by incubation in DMEM containing 1% FBS for 24 hours before trypsin treatment and were then lysed in WCL buffer C (table S4) with sonication to clear the supernatants. Immortalized fibroblasts were stimulated with 10 ng/ml TNF and lysed in WCL buffer D (table S4). Monocytes were obtained from freshly thawed PBMCs with the Pan Monocyte Isolation Kit (Miltenyi Biotec) and lysed in WCL buffer C (table S4) with sonication to clear the supernatants. Laemmli buffer (BioRad) supplemented with DTT was added to the clarified lysates. Proteins were separated by SDS–polyacrylamide gel electrophoresis (SDS-PAGE) transferred onto an Immobilon-P PVDF membrane (Millipore). The membrane was blocked by incubation in PBS supplemented with 0.1% Tween 20 and 5% bovine serum albumin (BSA) and incubated overnight with the primary antibody, followed by the appropriate horseradish peroxidase–conjugated secondary antibody. Immunoreactive proteins were visualized by enhanced chemiluminescence. Intensity analyses were performed with ImageStudioLite (LI-COR). The antibodies used are described in table S3.

Cytometry by time-of-flight

Freshly thawed PBMCs were incubated with Fc block and then with a panel of metal-conjugated antibodies, as described elsewhere (*96*). The antibodies used are described in table S3. Batch-integrated unsupervised clustering analysis was conducted with the iMUBAC pipeline (*45*). The analysis included 29 adult controls (nine studied in replicate) and nine pediatric controls (all under the age of 18 years) studied across seven batches of experiments, four patients with heterozygous mutations of *OTULIN* and two 5p− patients studied in two batches of experiments. Clusters were identified manually and renamed according to their marker expression patterns.

Flow cytometry

Freshly thawed PBMCs were rested for 3 hours and were then stimulated for 90 min with 20 ng/ml TNF (R&D Systems) or 1 ng/ml LPS (InvivoGen). The reaction was stopped by washing the cells with PBS, and the cells were then subjected to live/dead staining. Cells were subsequently stained with surface markers and washed. They were then permeabilized and stained with Phosflow Perm Buffer (BD) or Intracellular Staining Perm Wash Buffer (BioLegend). PDFs were synchronized by incubation in DMEM supplemented with 1% HI-FBS for 24 hours and were then harvested by trypsin treatment. The fibroblasts were stained, fixed, and acquired on an LSR-Fortessa cytometer (BD). All flow cytometry results were analyzed with FlowJo (version 10). The antibodies used are described in table S3.

Cytokine detection

PDFs were synchronized by incubation in DMEM supplemented with 1% HI-FBS for 24 hours before stimulation. At steady state and after 6 hours of stimulation with 20 ng/ml TNF (R&D Systems), supernatants were harvested, and the levels of IL-6 and IL-8 were assessed with the IL-6 and IL-8 Human enzyme-linked immunosorbent assay (ELISA) kits (Thermo Fisher Scientific). Freshly thawed PBMCs were left unstimulated or stimulated with 20 ng/ml TNF (R&D Systems), 10 ng/ml IL-1β (R&D Systems), HKSA (heat-killed *S. aureus*; MOI: 10; InvivoGen), or 1 ng/ml LPS (InvivoGen) for 6 hours. Supernatants were harvested, and chemokines and cytokines were detected with LEGENDPlex Human Inflammation Panel 1 (BioLegend).

Induced pluripotent stem cells

The generation and culture of iPSCs, their differentiation into macrophages, and the phagocytosis and H_2O_2 production assays are described in the SM.

Transcriptional and proteomic analyses

Transcriptional analyses in PDFs and PBMCs, single-cell RNA-sequencing on PBMCs, and global proteomics analyses of PDFs are described in the SM.

Caveolin-1 immune purification from whole-cell lysates

PDFs were synchronized by incubation in DMEM containing 1% HI-FBS for 24 hours and were then harvested by trypsin treatment. Cell pellets were lysed in WCL buffer C (table S4) with sonication to clear the supernatants. Cleared WCLs were incubated overnight at 4°C with Protein A Dynabeads (Thermo Fisher Scientific) conjugated to the monoclonal anti–caveolin-1 antibody or an isotype control. The samples were then eluted from the beads with 50 mM glycine, pH 2. The antibodies used are described in table S3. The IPs were then split into portions for loading onto a gel or direct in-solution proteomic analyses, as described in the SM.

Deubiquitination of purified caveolin-1

Caveolin-1 IPs were treated with recombinant deubiquitinases as described elsewhere (*97*). Briefly, immunopurified caveolin-1 was incubated with deubiquitinases at 37°C for 30 min. Recombinant USP2, AMSH, and OTULIN (UbiCREST Deubiquitinase Enzyme Set, R&D Systems) were used at a final concentration of 1x. Recombinant His-CYLD (R&D Systems) was used at a final concentration of 1 μM. Purified polyubiquitin chains were deubiquitinated by incubating tetra-M1-, K48-, and K63-Ub chains (R&D Systems) at a concentration of 3 μM with deubiquitinases. After the enzymatic reactions, sample buffer containing DTT was added, and the proteins were separated by SDS-PAGE, as described above.

Linear ubiquitin–selective tandem Ub-binding entity assay

For M1-Ub pull-down, immortalized fibroblasts were lysed in WCL buffer E (table S4) containing FLAG-tagged M1-Ub–selective TUBE (LifeSensors). Supernatants were cleared by centrifugation and incubated with Anti-FLAG M2 agarose beads (Sigma Aldrich) for 2 hours at 4°C. The beads were washed with WCL buffer E (table S4) and resuspended in 1 x Laemmli buffer without reducing agent.

For M1-Ub quantification, we used an input of ~0.5 mg per sample. For the identification of peptides bound to M1-Ub, we used an input of ~2 mg per sample. M1-Ub quantification and the identification of peptides bound to M1-Ub by means of AQUA-MS/MS are described in the SM. For Western blot analyses, beads were resuspended in sample buffer containing DTT, and samples were separated by SDS-PAGE, as described above.

Immunofluorescence assays

Immortalized fibroblasts were cultured on glass coverslips for the staining of M1-Ub, K63-Ub, and caveolin-1. The cells were fixed in methanol, blocked by incubation with 1% BSA, and incubated overnight with primary antibodies and CellMask deep red plasma membrane stain (Thermo Fisher Scientific), followed by secondary antibodies and 4′,6-diamidino-2-phenylindole (DAPI). Specimens were examined either with an Imager Z1 microscope (Carl Zeiss, for M1-Ub aggregate number quantifications) or a LSM800 laser scanning microscope (Carl Zeiss, for caveolin-1 and M1-Ub or K63-Ub colocalization experiments). The numbers of ubiquitin aggregates per cell were quantified using CellProfiler (https://cellprofiler.org/). Nuclei and cell boundaries were segmented to identify OTULIN-positive cells and to attribute M1-Ub–positive aggregates to parental cells. Immunofluorescence deubiquitination and competition assays are described in the SM. For α-toxin colocalization and binding experiments, PDFs were synchronized by incubation in DMEM containing 1% HI-FBS for 24 hours before trypsin treatment. PDFs were incubated with 10 μg/ml α-toxin-Cys-AF647, washed, and then fixed with methanol. After incubation with antibodies and DAPI, cells were seeded in a slide chamber. Images were acquired on a Leica SP5 confocal microscope (Leica Microsystems) and NanoImager (ONI). In parallel, the cells were recorded on a FACS Verse flow cytometer (BD). Confocal images were analyzed with Image J Fiji software and the JACoP colocalization analysis plugin (*98*). The antibodies used are described in table S3.

Cell viability assays

PDFs were plated in a microtiter plate and synchronized in DMEM containing 1% HI-FBS and 25 mM DMEM for 24 hours and were then incubated for 2.5 hours with 5 or 10% crude bacterial culture supernatant or for 24 hours with recombinant toxins, or with 100 ng/ml TNF (R&D Systems) plus 1 μM BV6 (ApexBio) at 37°C, under an atmosphere containing 5% CO_2. Bacterial supernatants were neutralized by incubation for 15 min in DMEM supplemented with 10% HI-FBS and 100 μg/ml monoclonal antibodies (*92*, *99*). PBMCs and iPSC-derived macrophages were incubated with α-toxin for 2 and 24 hours, respectively, at 37°C, under an atmosphere containing 5% CO_2. For the inhibition of α-toxin cytotoxicity, PDFs were treated for 1 hour with 20 μM GI-254023X (R&D Systems) or dimethyl sulfoxide (DMSO) before adding 1.1 μg/ml α-toxin, or for 2 hours with 1 mM methyl-β-cyclodextrin (Sigma) followed by washing and the addition of 1.1 μg/ml α-toxin. Viability was assessed with the CellTiterGlo Luminescent Cell Viability Assay (Promega) and expressed relative to cells not incubated with the toxin or supernatant. Four-parameter nonlinear regression analyses were performed to obtain half-maximum effective concentrations (EC_{50}). The expression of recombinant toxins and the generation of bacterial culture supernatant are described in the SM.

Metalloprotease activity assays

PDFs were plated in a microtiter plate and synchronized by incubation in DMEM containing 1% HI-FBS and 25 mM DMEM for 24 hours. They were then treated for 1 hour with 20 μM GI-254023X (R&D Systems) or DMSO before the addition of 3.3 μg/ml wild-type or H35L-toxoid α-toxin. After 2 hours of incubation at 37°C, under an atmosphere containing 5% CO_2, cells were washed with 25 mM Tris (pH 8) and 10 μM Mca-PLAQAV-Dpa-RSSSR-NH2 Fluorogenic Peptide Substrate (R&D Systems) was added. After incubation for 30 min, fluorescence intensity was measured on a monochromator-based microplate reader and expressed relative to cells not incubated with the toxin.

Mice

The generation and use of *Otulin*-haploinsufficient mice are described in the SM.

Anti–α-toxin immunoglobulins

The capacity of the plasma to neutralize microbial toxins was assessed with rabbit erythrocytes, as described in the SM. Pooled plasma was depleted of IgG with HiTrap Protein G HRP columns (GE Healthcare). Anti–α-toxin immunoglobulin levels were measured by ELISA, as described in the SM.

REFERENCES AND NOTES

1. F. D. Lowy, *Staphylococcus aureus* infections. *N. Engl. J. Med.* **339**, 520–532 (1998). doi: 10.1056/NEJM199808203390806; pmid: 9709046
2. Y. Gillet *et al*., Association *between Staphylococcus aureus* strains carrying gene for Panton-Valentine leukocidin and highly lethal necrotising pneumonia in young immunocompetent patients. *Lancet* **359**, 753–759 (2002). doi: 10.1016/S0140-6736(02)07877-7; pmid: 11888586
3. A. I. Hidron, C. E. Low, E. G. Honig, H. M. Blumberg, Emergence of community-acquired meticillin-resistant *Staphylococcus aureus* strain USA300 as a cause of necrotising community-onset pneumonia. *Lancet Infect. Dis.* **9**, 384–392 (2009). doi: 10.1016/S1473-3099(09)70133-1; pmid: 19467478
4. G. Lina *et al*., Involvement of Panton-Valentine leukocidin-producing *Staphylococcus aureus* in primary skin infections and pneumonia. *Clin. Infect. Dis.* **29**, 1128–1132 (1999). doi: 10.1086/313461; pmid: 10524952
5. F. Vandenesch *et al*., Community-acquired methicillin-resistant *Staphylococcus aureus* carrying Panton-Valentine leukocidin genes: Worldwide emergence. *Emerg. Infect. Dis.* **9**, 978–984 (2003). doi: 10.3201/eid0908.030089; pmid: 12967497
6. B. Boisson, The genetic basis of pneumococcal and staphylococcal infections: Inborn errors of human TLR and IL-1R immunity. *Hum. Genet.* **139**, 981–991 (2020). doi: 10.1007/s00439-020-02111-z; pmid: 31980906
7. S. G. Tangye *et al*., The ever-increasing array of novel inborn errors of immunity: An interim update by the IUIS Committee. *J. Clin. Immunol.* **41**, 666–679 (2021). doi: 10.1007/s10875-021-00980-1; pmid: 33598806
8. C. Picard *et al*., Pyogenic bacterial infections in humans with IRAK-4 deficiency. *Science* **299**, 2076–2079 (2003). doi: 10.1126/science.1081902; pmid: 12637671
9. C. Picard *et al*., Clinical features and outcome of patients with IRAK-4 and MyD88 deficiency. *Medicine* **89**, 403–425 (2010). doi: 10.1097/MD.0b013e3181fd8ec3; pmid: 21057262
10. C. Picard, J. L. Casanova, A. Puel, Infectious diseases in patients with IRAK-4, MyD88, NEMO, or IκBα deficiency. *Clin. Microbiol. Rev.* **24**, 490–497 (2011). doi: 10.1128/CMR.00001-11; pmid: 21734245
11. H. von Bernuth *et al*., Pyogenic bacterial infections in humans with MyD88 deficiency. *Science* **321**, 691–696 (2008). doi: 10.1126/science.1158298; pmid: 18669862
12. L. Israel *et al*., Human adaptive immunity rescues an inborn error of innate immunity. *Cell* **168**, 789–800.e10 (2017). doi: 10.1016/j.cell.2017.01.039; pmid: 28235196
13. A. Puel *et al*., Recurrent staphylococcal cellulitis and subcutaneous abscesses in a child with autoantibodies against IL-6. *J. Immunol.* **180**, 647–654 (2008). doi: 10.4049/jimmunol.180.1.647; pmid: 18097067
14. T. Schwerd *et al*., A biallelic mutation in *IL6ST* encoding the GP130 co-receptor causes immunodeficiency and craniosynostosis. *J. Exp. Med.* **214**, 2547–2562 (2017). doi: 10.1084/jem.20161810; pmid: 28747427
15. V. Béziat *et al*., A recessive form of hyper-IgE syndrome by disruption of ZNF341-dependent STAT3 transcription and activity. *Sci. Immunol.* **3**, eaat4956 (2018). doi: 10.1126/sciimmunol.aat4956; pmid: 29907691
16. Y. Minegishi *et al*., Dominant-negative mutations in the DNA-binding domain of STAT3 cause hyper-IgE syndrome. *Nature* **448**, 1058–1062 (2007). doi: 10.1038/nature06096; pmid: 17676033
17. S. Spencer *et al*., Loss of the interleukin-6 receptor causes immunodeficiency, atopy, and abnormal inflammatory responses. *J. Exp. Med.* **216**, 1986–1998 (2019). doi: 10.1084/jem.20190344; pmid: 31235509
18. F. R. DeLeo, M. Otto, B. N. Kreiswirth, H. F. Chambers, Community-associated meticillin-resistant *Staphylococcus aureus*. *Lancet* **375**, 1557–1568 (2010). doi: 10.1016/S0140-6736(09)61999-1; pmid: 20206987
19. L. J. Shallcross, E. Fragaszy, A. M. Johnson, A. C. Hayward, The role of the Panton-Valentine leucocidin toxin in staphylococcal disease: A systematic review and meta-analysis. *Lancet Infect. Dis.* **13**, 43–54 (2013). doi: 10.1016/S1473-3099(12)70238-4; pmid: 23103172
20. K. J. Karczewski *et al*., The mutational constraint spectrum quantified from variation in 141,456 humans. *Nature* **581**, 434–443 (2020). doi: 10.1038/s41586-020-2308-7; pmid: 32461654
21. Y. Itan *et al*., The mutation significance cutoff: Gene-level thresholds for variant predictions. *Nat. Methods* **13**, 109–110 (2016). doi: 10.1038/nmeth.3739; pmid: 26820543
22. M. Kircher *et al*., A general framework for estimating the relative pathogenicity of human genetic variants. *Nat. Genet.* **46**, 310–315 (2014). doi: 10.1038/ng.2892; pmid: 24487276
23. P. Zhang *et al*., PopViz: A webserver for visualizing minor allele frequencies and damage prediction scores of human genetic variations. *Bioinformatics* **34**, 4307–4309 (2018). doi: 10.1093/bioinformatics/bty536; pmid: 30535305
24. L. D. Notarangelo, R. Bacchetta, J. L. Casanova, H. C. Su, Human inborn errors of immunity: An expanding universe. *Sci. Immunol.* **5**, eabb1662 (2020). doi: 10.1126/sciimmunol.abb1662; pmid: 32651211
25. 1000 Genomes Project Consortium, A global reference for human genetic variation. *Nature* **526**, 68–74 (2015). doi: 10.1038/nature15393; pmid: 26432245
26. S. Boisson-Dupuis *et al*., Tuberculosis and impaired IL-23–dependent IFN-γ immunity in humans homozygous for a common *TYK2* missense variant. *Sci. Immunol.* **3**, eaau8714 (2018). doi: 10.1126/sciimmunol.aau8714; pmid: 30578352

27. K. Keusekotten *et al*., OTULIN antagonizes LUBAC signaling by specifically hydrolyzing Met1-linked polyubiquitin. *Cell* **153**, 1312–1326 (2013). doi: 10.1016/j.cell.2013.05.014; pmid: 23746843
28. E. Rivkin *et al*., The linear ubiquitin-specific deubiquitinase gumby regulates angiogenesis. *Nature* **498**, 318–324 (2013). doi: 10.1038/nature12296; pmid: 23708998
29. R. B. Damgaard *et al*., OTULIN deficiency in ORAS causes cell type-specific LUBAC degradation, dysregulated TNF signalling and cell death. *EMBO Mol. Med.* **11**, e9324 (2019). doi: 10.15252/emmm.201809324; pmid: 30804083
30. R. B. Damgaard *et al*., The deubiquitinase OTULIN is an essential negative regulator of inflammation and autoimmunity. *Cell* **166**, 1215–1230.e20 (2016). doi: 10.1016/j.cell.2016.07.019; pmid: 27523608
31. M. Nabavi *et al*., Auto-inflammation in a patient with a novel homozygous OTULIN mutation. *J. Clin. Immunol.* **39**, 138–141 (2019). doi: 10.1007/s10875-019-00599-3; pmid: 30796585
32. Q. Zhou *et al*., Biallelic hypomorphic mutations in a linear deubiquitinase define otulipenia, an early-onset autoinflammatory disease. *Proc. Natl. Acad. Sci. U.S.A.* **113**, 10127–10132 (2016). doi: 10.1073/pnas.1612594113; pmid: 27559085
33. J. Zinngrebe *et al*., Compound heterozygous variants in OTULIN are associated with fulminant atypical late-onset ORAS. *EMBO Mol. Med.* **14**, e14901 (2022). doi: 10.15252/emmm.202114901; pmid: 35170849
34. A. Bousfiha *et al*., Human inborn errors of immunity: 2019 update of the IUIS phenotypical classification. *J. Clin. Immunol.* **40**, 66–81 (2020). doi: 10.1007/s10875-020-00758-x; pmid: 32048120
35. K. E. Eilertson, J. G. Booth, C. D. Bustamante, SnIPRE: Selection inference using a Poisson random effects model. *PLOS Comput. Biol.* **8**, e1002806 (2012). doi: 10.1371/journal.pcbi.1002806; pmid: 23236270
36. F. Rapaport *et al*., Negative selection on human genes underlying inborn errors depends on disease outcome and both the mode and mechanism of inheritance. *Proc. Natl. Acad. Sci. U.S.A.* **118**, e2001248118 (2021). doi: 10.1073/pnas.2001248118; pmid: 33408250
37. J. Fadista, N. Oskolkov, O. Hansson, L. Groop, LoFtool: A gene intolerance score based on loss-of-function variants in 60 706 individuals. *Bioinformatics* **33**, 471–474 (2017). pmid: 27563026
38. X. Zhang *et al*., High-resolution mapping of genotype-phenotype relationships in cri du chat syndrome using array comparative genomic hybridization. *Am. J. Hum. Genet.* **76**, 312–326 (2005). doi: 10.1086/427762; pmid: 15635506
39. J. Lejeune *et al*., Trois cas de d'el'etion partielle du bras court d'un chromosome 5 [3 cases of partial deletion of the short arm of a 5 chromosome]. *C. R. Hebd. Seances Acad. Sci.* **257**, 3098–3102 (1963). pmid: 14095841
40. E. Niebuhr, The Cri du chat syndrome: Epidemiology, cytogenetics, and clinical features. *Hum. Genet.* **44**, 227–275 (1978). doi: 10.1007/BF00394291; pmid: 365706
41. P. Cerruti Mainardi, Cri du Chat syndrome. *Orphanet J. Rare Dis.* **1**, 33 (2006). doi: 10.1186/1750-1172-1-33; pmid: 16953888
42. P. C. Mainardi *et al*., The natural history of Cri du Chat Syndrome. A report from the Italian Register. *Eur. J. Med. Genet.* **49**, 363–383 (2006). doi: 10.1016/j.ejmg.2005.12.004; pmid: 16473053
43. R. Seger *et al*., Defects in granulocyte function in various chromosome abnormalities (Down's-, Edwards'-, Cri-du-chat syndrome). *Klin. Wochenschr.* **54**, 177–183 (1976). doi: 10.1007/BF01468883; pmid: 176505
44. L. E. Wilkins, J. A. Brown, W. E. Nance, B. Wolf, Clinical heterogeneity in 80 home-reared children with cri du chat syndrome. *J. Pediatr.* **102**, 528–533 (1983). doi: 10.1016/S0022-3476(83)80179-6; pmid: 6834187
45. M. Ogishi *et al*., Multibatch cytometry data integration for optimal immunophenotyping. *J. Immunol.* **206**, 206–213 (2021). doi: 10.4049/jimmunol.2000854; pmid: 33229441
46. B. Boisson *et al*., Immunodeficiency, autoinflammation and amylopectinosis in humans with inherited HOIL-1 and LUBAC deficiency. *Nat. Immunol.* **13**, 1178–1186 (2012). doi: 10.1038/ni.2457; pmid: 23104095
47. A. Subramanian *et al*., Gene set enrichment analysis: A knowledge-based approach for interpreting genome-wide expression profiles. *Proc. Natl. Acad. Sci. U.S.A.* **102**, 15545–15550 (2005). doi: 10.1073/pnas.0506580102; pmid: 16199517
48. A. Hayer *et al*., Caveolin-1 is ubiquitinated and targeted to intralumenal vesicles in endolysosomes for degradation. *J. Cell Biol.* **191**, 615–629 (2010). doi: 10.1083/jcb.201003086; pmid: 21041450
49. M. Sato, R. Konuma, K. Sato, K. Tomura, K. Sato, Fertilization-induced K63-linked ubiquitylation mediates clearance of maternal membrane proteins. *Development* **141**, 1324–1331 (2014). doi: 10.1242/dev.103044; pmid: 24595290
50. M. Uhlén *et al*., Tissue-based map of the human proteome. *Science* **347**, 1260419 (2015). doi: 10.1126/science.1260419; pmid: 25613900
51. P. J. Thul *et al*., A subcellular map of the human proteome. *Science* **356**, eaal3321 (2017). doi: 10.1126/science.aal3321; pmid: 28495876
52. K. G. Rothberg *et al*., Caveolin, a protein component of caveolae membrane coats. *Cell* **68**, 673–682 (1992). doi: 10.1016/0092-8674(92)90143-Z; pmid: 1739974
53. W. Kim *et al*., Systematic and quantitative assessment of the ubiquitin-modified proteome. *Mol. Cell* **44**, 325–340 (2011). doi: 10.1016/j.molcel.2011.08.025; pmid: 21906983
54. G. A. Wilke, J. Bubeck Wardenburg, Role of a disintegrin and metalloprotease 10 in *Staphylococcus aureus* α-hemolysin–mediated cellular injury. *Proc. Natl. Acad. Sci. U.S.A.* **107**, 13473–13478 (2010). doi: 10.1073/pnas.1001815107; pmid: 20624979
55. I. Inoshima *et al*., A *Staphylococcus aureus* pore-forming toxin subverts the activity of ADAM10 to cause lethal infection in mice. *Nat. Med.* **17**, 1310–1314 (2011). doi: 10.1038/nm.2451; pmid: 21926978
56. E. S. Seilie, J. Bubeck Wardenburg, *Staphylococcus aureus* pore-forming toxins: The interface of pathogen and host complexity. *Semin. Cell Dev. Biol.* **72**, 101–116 (2017). doi: 10.1016/j.semcdb.2017.04.003; pmid: 28445785
57. J. Moreno-Càceres *et al*., Caveolin-1 is required for TGF-β-induced transactivation of the EGF receptor pathway in hepatocytes through the activation of the metalloprotease TACE/ADAM17. *Cell Death Dis.* **5**, e1326 (2014). doi: 10.1038/cddis.2014.294; pmid: 25032849
58. E. M. Khan *et al*., Epidermal growth factor receptor exposed to oxidative stress undergoes Src- and caveolin-1-dependent perinuclear trafficking. *J. Biol. Chem.* **281**, 14486–14493 (2006). doi: 10.1074/jbc.M509332200; pmid: 16407214
59. M. Dal Peraro, F. G. van der Goot, Pore-forming toxins: Ancient, but never really out of fashion. *Nat. Rev. Microbiol.* **14**, 77–92 (2016). doi: 10.1038/nrmicro.2015.3; pmid: 26639780
60. R. Zidovetzki, I. Levitan, Use of cyclodextrins to manipulate plasma membrane cholesterol content: Evidence, misconceptions and control strategies. *Biochim. Biophys. Acta Biomembr.* **1768**, 1311–1324 (2007). doi: 10.1016/j.bbamem.2007.03.026; pmid: 17493580
61. Y. Wu *et al*., Prevalence of IgG and neutralizing antibodies against *Staphylococcus aureus* alpha-toxin in healthy human subjects and diverse patient populations. *Infect. Immun.* **86**, e00671-17 (2018). doi: 10.1128/IAI.00671-17; pmid: 29263109
62. C. Gruber, D. Bogunovic, Incomplete penetrance in primary immunodeficiency: A skeleton in the closet. *Hum. Genet.* **139**, 745–757 (2020). doi: 10.1007/s00439-020-02131-9; pmid: 32067110
63. F. Rieux-Laucat, J. L. Casanova, Autoimmunity by haploinsufficiency. *Science* **345**, 1560–1561 (2014). doi: 10.1126/science.1260791; pmid: 25258064
64. H. Van Esch *et al*., GATA3 haplo-insufficiency causes human HDR syndrome. *Nature* **406**, 419–422 (2000). doi: 10.1038/35019088; pmid: 10935639
65. B. Boisson *et al*., Human HOIP and LUBAC deficiency underlies autoinflammation, immunodeficiency, amylopectinosis, and lymphangiectasia. *J. Exp. Med.* **212**, 939–951 (2015). doi: 10.1084/jem.20141130; pmid: 26008899
66. I. E. Wertz *et al*., De-ubiquitination and ubiquitin ligase domains of A20 downregulate NF-κB signalling. *Nature* **430**, 694–699 (2004). doi: 10.1038/nature02794; pmid: 15258597
67. D. L. Boone *et al*., The ubiquitin-modifying enzyme A20 is required for termination of Toll-like receptor responses. *Nat. Immunol.* **5**, 1052–1060 (2004). doi: 10.1038/ni1110; pmid: 15334086
68. M. S. Ritorto *et al*., Screening of DUB activity and specificity by MALDI-TOF mass spectrometry. *Nat. Commun.* **5**, 4763 (2014). doi: 10.1038/ncomms5763; pmid: 25159004
69. Q. Zhou *et al*., Loss-of-function mutations in *TNFAIP3* leading to A20 haploinsufficiency cause an early-onset autoinflammatory disease. *Nat. Genet.* **48**, 67–73 (2016). doi: 10.1038/ng.3459; pmid: 26642243
70. G. R. Bignell *et al*., Identification of the familial cylindromatosis tumour-suppressor gene. *Nat. Genet.* **25**, 160–165 (2000). doi: 10.1038/76006; pmid: 10835629
71. P. Draber *et al*., LUBAC-recruited CYLD and A20 regulate gene activation and cell death by exerting opposing effects on linear ubiquitin in signaling complexes. *Cell Rep.* **13**, 2258–2272 (2015). doi: 10.1016/j.celrep.2015.11.009; pmid: 26670046
72. P. R. Elliott *et al*., Regulation of CYLD activity and specificity by phosphorylation and ubiquitin-binding CAP-Gly domains. *Cell Rep.* **37**, 109777 (2021). doi: 10.1016/j.celrep.2021.109777; pmid: 34610306
73. B. J. Berube, J. Bubeck Wardenburg, *Staphylococcus aureus* α-toxin: Nearly a century of intrigue. *Toxins* **5**, 1140–1166 (2013). doi: 10.3390/toxins5061140; pmid: 23888516
74. F. R. DeLeo *et al*., Molecular differentiation of historic phage-type 80/81 and contemporary epidemic *Staphylococcus aureus*. *Proc. Natl. Acad. Sci. U.S.A.* **108**, 18091–18096 (2011). doi: 10.1073/pnas.1111084108; pmid: 22025717
75. L. Stulik *et al*., α-Hemolysin activity of methicillin-susceptible *Staphylococcus aureus* predicts ventilator-associated pneumonia. *Am. J. Respir. Crit. Care Med.* **190**, 1139–1148 (2014). doi: 10.1164/rccm.201406-10120C; pmid: 25303310
76. J. Bubeck Wardenburg, T. Bae, M. Otto, F. R. Deleo, O. Schneewind, Poring over pores: α-hemolysin and Panton-Valentine leukocidin in *Staphylococcus aureus* pneumonia. *Nat. Med.* **13**, 1405–1406 (2007). doi: 10.1038/nm1207-1405; pmid: 18064027
77. V. Thammavongsa, H. K. Kim, D. Missiakas, O. Schneewind, Staphylococcal manipulation of host immune responses. *Nat. Rev. Microbiol.* **13**, 529–543 (2015). doi: 10.1038/nrmicro3521; pmid: 26272408
78. A. N. Spaan, B. G. Surewaard, R. Nijland, J. A. van Strijp, Neutrophils versus *Staphylococcus aureus*: A biological tug of war. *Annu. Rev. Microbiol.* **67**, 629–650 (2013). doi: 10.1146/annurev-micro-092412-155746; pmid: 23834243
79. S. Y. Zhang, Herpes simplex virus encephalitis of childhood: Inborn errors of central nervous system cell-intrinsic immunity. *Hum. Genet.* **139**, 911–918 (2020). doi: 10.1007/s00439-020-02127-5; pmid: 32040615
80. S. Y. Zhang, O. Harschnitz, L. Studer, J. L. Casanova, Neuron-intrinsic immunity to viruses in mice and humans. *Curr. Opin. Immunol.* **72**, 309–317 (2021). doi: 10.1016/j.coi.2021.07.004; pmid: 34425410
81. J. L. Casanova, L. Abel, Mechanisms of viral inflammation and disease in humans. *Science* **374**, 1080–1086 (2021). doi: 10.1126/science.abj7965; pmid: 34822298
82. F. Galbiati, B. Razani, M. P. Lisanti, Emerging themes in lipid rafts and caveolae. *Cell* **106**, 403–411 (2001). doi: 10.1016/S0092-8674(01)00472-X; pmid: 11525727
83. S. D. Conner, S. L. Schmid, Regulated portals of entry into the cell. *Nature* **422**, 37–44 (2003). doi: 10.1038/nature01451; pmid: 12621426
84. E. Tacconelli *et al*., Discovery, research, and development of new antibiotics: The WHO priority list of antibiotic-resistant bacteria and tuberculosis. *Lancet Infect. Dis.* **18**, 318–327 (2018). doi: 10.1016/S1473-3099(17)30753-3; pmid: 29276051
85. B. François *et al*., Efficacy and safety of suvratoxumab for prevention of *Staphylococcus aureus* ventilator-associated pneumonia (SAATELLITE): A multicentre, randomised, double-blind, placebo-controlled, parallel-group, phase 2 pilot trial. *Lancet Infect. Dis.* **21**, 1313–1323 (2021). doi: 10.1016/S1473-3099(20)30995-6; pmid: 33894131
86. W. Salgado-Pabón, P. M. Schlievert, Models matter: The search for an effective *Staphylococcus aureus* vaccine. *Nat. Rev. Microbiol.* **12**, 585–591 (2014). doi: 10.1038/nrmicro3308; pmid: 24998740
87. M. von Köckritz-Blickwede *et al*., Immunological mechanisms underlying the genetic predisposition to severe *Staphylococcus aureus* infection in the mouse model. *Am. J. Pathol.* **173**, 1657–1668 (2008). doi: 10.2353/ajpath.2008.080337; pmid: 18974303
88. F. Randow, J. D. MacMicking, L. C. James, Cellular self-defense: How cell-autonomous immunity protects against pathogens. *Science* **340**, 701–706 (2013). doi: 10.1126/science.1233028; pmid: 23661752
89. R. G. Gaudet *et al*., A human apolipoprotein L with detergent-like activity kills intracellular pathogens. *Science* **373**, eabf8113 (2021). doi: 10.1126/science.abf8113; pmid: 34437126
90. C. Nathan, Rethinking immunology. *Science* **373**, 276–277 (2021). doi: 10.1126/science.abj5637; pmid: 34437138
91. A. N. Spaan, J. A. G. van Strijp, V. J. Torres, Leukocidins: Staphylococcal bi-component pore-forming toxins find their receptors. *Nat. Rev. Microbiol.* **15**, 435–447 (2017). doi: 10.1038/nrmicro.2017.27; pmid: 28420883
92. H. Rouha *et al*., Five birds, one stone: Neutralization of α-hemolysin and 4 bi-component leukocidins of *Staphylococcus*

aureus with a single human monoclonal antibody. *mAbs* **7**, 243–254 (2015). doi: 10.4161/19420862.2014.985132; pmid: 25523282
93. S. Belkaya *et al*., Autosomal recessive cardiomyopathy presenting as acute myocarditis. *J. Am. Coll. Cardiol.* **69**, 1653–1665 (2017). doi: 10.1016/j.jacc.2017.01.043; pmid: 28359509
94. S. Y. Zhang *et al*., Inborn errors of RNA lariat metabolism in humans with brainstem viral infection. *Cell* **172**, 952–965.e18 (2018). doi: 10.1016/j.cell.2018.02.019; pmid: 29474921
95. S. Belkaya *et al*., Inherited IL-18BP deficiency in human fulminant viral hepatitis. *J. Exp. Med.* **216**, 1777–1790 (2019). doi: 10.1084/jem.20190669; pmid: 31213488
96. R. Yang *et al*., Human T-bet governs innate and innate-like adaptive IFN-γ immunity against mycobacteria. *Cell* **183**, 1826–1847.e31 (2020). doi: 10.1016/j.cell.2020.10.046; pmid: 33296702
97. M. K. Hospenthal, T. E. T. Mevissen, D. Komander, Deubiquitinase-based analysis of ubiquitin chain architecture using Ubiquitin Chain Restriction (UbiCRest). *Nat. Protoc.* **10**, 349–361 (2015). doi: 10.1038/nprot.2015.018; pmid: 25633630
98. S. Bolte, F. P. Cordelières, A guided tour into subcellular colocalization analysis in light microscopy. *J. Microsc.* **224**, 213–232 (2006). doi: 10.1111/j.1365-2818.2006.01706.x; pmid: 17210054
99. A. Ruzin *et al*., Characterisation of anti-alpha toxin antibody levels and colonisation status after administration of an investigational human monoclonal antibody, MEDI4893, against *Staphylococcus aureus* alpha toxin. *Clin. Transl. Immunology* **7**, e1009 (2018). doi: 10.1002/cti2.1009; pmid: 29484186

ACKNOWLEDGMENTS

We thank the patients, their families, and the US 5p− Syndrome Society for their trust and collaboration. We thank M. van Aartrijk, S. Delafontaine, M. Muona, E. Jouanguy, Y. Nemirovskaya, M. Woollett, M. Wassenberg, M. Bonten, S. Rooijakkers, K. van Kessel, and J. van Strijp for their assistance and support. We thank the Flow Cytometry and Genomics Resource Centers at The Rockefeller University. **Funding:** This work was supported by the National Center for Advancing Translational Sciences of the National Institutes of Health (NIH) (UL1TR001866 to The Rockefeller University), the Sackler Center for Biomedicine and Nutrition at the Center for Clinical and Translational Science at The Rockefeller University and the Shapiro-Silverberg Fund for the Advancement of Translational Research (to A.N.S.), NIH P01AI061093 (to J.-L.C.), the Square Foundation, the French National Research Agency (ANR-10-IAHU-01, ANR-21-CE17-0014-03, ANR 14-CE15-0009-01, and ANR-15-CE17-0014), the Integrative Biology of Emerging Infectious Diseases Laboratory of Excellence (ANR-10-LABX-62-IBEID), the French Foundation for Medical Research (EQU201903007798), the Howard Hughes Medical Institute, the St. Giles Foundation, The Rockefeller University, Institut National de la Santé et de la Recherche Médicale (INSERM), the Paris Cité University, the Laura and Isaac Perlmutter Cancer Center and the National Institutes of Health/National Cancer Institute (P30CA016087 to NYU Langone's Rodent Genetic Engineering Laboratory), the Bettencourt Schueller Foundation and the International PhD program of the Imagine Institute (to A.-L.N.), the David Rockefeller Graduate Program (to M.O.), the New York Hideyo Noguchi Memorial Society (to M.O.), the Funai Foundation for Information Technology (to M.O.), the Honjo International Scholarship Foundation (to M.O.), the Cystic Fibrosis Foundation Postdoctoral Research Fellowship award (LACEY19FO to K.A.L.), the William C. and Joyce C. O'Neil Charitable Trust (to T.B.), the Memorial Sloan Kettering Single Cell Sequencing Initiative (to T.B.), the Hospital Research Funds at the Pediatric Research Center at the Helsinki University Hospital (to M.R.J.S.), and the Foundation for Pediatric Research of Finland (to M.R.J.S.). C.W. serves as a member of the European Reference Network for Rare Immunodeficiency, Autoinflammatory and Autoimmune Diseases (739543). The work was supported in part by the ERC Start grant IMMUNO (ERC-2010-StG_20091118 to A.L.), the VIB Grand Challenges (to A.L., S.H.-B., and R.S.), the KU Leuven BOFZAP start-up grant (to S.H.-B.), National Fund for Scientific Research senior clinical investigator fellowships (1805518N to R.S. and G0B5120N to I.M.), National Fund for Scientific Research grants (G0E8420N and G0C8517N to I.M.), a KU Leuven C1 grant (to I.M.), and the ERC Start grant MORE2ADA2 (ERC-2020-StG_ 948959 to I.M.). I.M. is a member of ERN-RITA. D.B. is supported by the NIH (R01 AI148963) and a founder of Lab11 Therapeutics Inc. The *S. aureus* work in the Torres laboratory is funded by the NIH (R01 AI099394, R01 AI105129, R01 AI121244, R01 AI137336, and R01 AI140754 to V.J.T.). V.J.T. is a Burroughs Wellcome Fund Investigator in the pathogenesis of infectious diseases. A.N.S. was supported in part by the European Union's Horizon 2020 Research and Innovation Program (Marie Skłodowska-Curie grant 789645), the Dutch Research Council Talent Program (NWO Rubicon grant 019.171LW.015, partially nonstipendiary), and the European Molecular Biology Organization (EMBO Long-Term Fellowship grant ALTF 84-2017, nonstipendiary). **Author contributions:** A.N.S., L.A., B.B., and J.-L.C. conceptualized the project. A.N.S., D.B., H.M., S.C., L.A., B.B., and J.-L.C. designed the methods. A.N.S., A.-L.N., E.L., F.R., M.O., Y.S., P.Z., S.C., and B.B. performed formal analyses. A.N.S., A.-L.N., E.L., F.S., K.A.L., E.V. N., M.C., D.H., M.Mi., A.I., L.L., T.K., M.R.J.S., D.A.C.H., S.H., T.B., and R.Y. performed investigations. A.L.D., K.D., H.F.W., G.V.B., R.W., G.S., H.G.-T., H.L.L., B.W.B., S.L., L.D.N., M.Me., M.S., X.B., E.S., R.T., S.O., P.-J.A.H., A.H., M.M.J.v.E., L.B., L.B.G., A.L., A.N., B.B.-M., B.N., I.M., C.W., M.R.J.S., R.S., A.P., J.B., I.A., and D.L.K. provided resources. A.N.S., B.B., and J.-L.C. wrote the manuscript. A.N.S., V.J.T., A.L., S.H.-B., L.A., B.B., and J.-L.C. supervised the project. A.N.S., V.J.T., A.L., S.H.-B., L.A., B.B., and J.-L.C. acquired funding for the project. **Competing interests:** V.J.T. is an inventor on patents and patent applications filed by New York University, which are currently under commercial license to Janssen Biotech Inc. Janssen Biotech Inc. provides research funding and other payments associated with the licensing agreement. D.B. is a founder of Lab11 Therapeutics Inc. None of the other authors have any conflicts of interest to declare. **Data and materials availability:** Plasma, cells, and genomic DNA are available from J.-L.C. under a material transfer agreement with The Rockefeller University. The materials and reagents used are almost exclusively commercially available and nonproprietary. Raw RNA sequencing data have been deposited to the NCBI BioProject database and are available under project number PRJNA818002. Proteomic data have been deposited to the ProteomeXchange Consortium via the PRIDE partner repository and are available with dataset identifier PXD032727. All other data are available in the main text or in the supplementary materials. **License information:** Copyright © 2022 the authors, some rights reserved; exclusive licensee American Association for the Advancement of Science. No claim to original US government works. https://www.science.org/about/science-licenses-journal-article-reuse

SUPPLEMENTARY MATERIALS

science.org/doi/10.1126/science.abm6380
Case Reports for the Patients Studied
Materials and Methods
Figs. S1 to S7
Tables S1 to S4
References (*100*–*128*)
MDAR Reproducibility Checklist

View/request a protocol for this paper from *Bio-protocol*.

Submitted 30 September 2021; accepted 5 May 2022
Published online 19 May 2022
10.1126/science.abm6380

RESEARCH ARTICLE

ROBOTIC MATERIALS

Design and printing of proprioceptive three-dimensional architected robotic metamaterials

Huachen Cui[1], Desheng Yao[1], Ryan Hensleigh[1], Haotian Lu[2], Ariel Calderon[1], Zhenpeng Xu[1], Sheyda Davaria[3], Zhen Wang[1], Patrick Mercier[4], Pablo Tarazaga[5], Xiaoyu (Rayne) Zheng[1,2,3,6]*

Advances in additive manufacturing techniques have enabled the creation of stimuli-responsive materials with designed three-dimensional (3D) architectures. Unlike biological systems in which functions such as sensing, actuation, and control are closely integrated, few architected materials have comparable system complexity. We report a design and manufacturing route to create a class of robotic metamaterials capable of motion with multiple degrees of freedom, amplification of strain in a prescribed direction in response to an electric field (and vice versa), and thus, programmed motions with self-sensing and feedback control. These robotic metamaterials consist of networks of piezoelectric, conductive, and structural elements interwoven into a designed 3D lattice. The resulting architected materials function as proprioceptive microrobots that actively sense and move.

Advances in additive manufacturing techniques have enabled the fabrication of materials with ultrahigh stiffness (*1*) and damage tolerance (*2*, *3*), exotic mechanical behaviors (*4*, *5*), negative thermal expansion coefficients (*6*), fluid control (*7*), and wave transmissions (*8*). These materials can be digitally designed by placing structural elements as bits and atoms in a three-dimensional (3D) layout. The potential of architecting electronic and multifunctional materials and their combinations is still elusive, as most additive fabrication techniques have focused on single structural materials such as polymers, metals, and ceramics. Architecting functional materials could offer exotic and configurable properties in functional space, such as directional sensing (*9*), morphing (*10*), and reconfigurability (*11*, *12*).

Piezoelectric materials, which are capable of converting an electrical field into mechanical strain and vice versa (*13*), are ideal candidates for providing both sensing and actuation functions in a robotic system. These materials are widely employed in precision actuators (*14*), manipulators (*15*), accelerometers (*16*), and tactile sensors (*17*, *18*) to generate robotic motions and sensing feedback. However, their electric field–induced strain, as a result of asymmetric displacement of ions in crystal dimensions, is derived from and thus limited by the naturally existing crystal structures, leading to a magnitude of <0.5% [i.e., the strain range in lead zirconate titanate (PZT) ceramic and single-crystalline lead magnesium niobate–lead titanate (PMN-PT) is <0.1 and <0.5%, respectively] in only the normal and shear directions (*13*). To use piezoelectric materials as transducers in robotic systems, the manufacturing process must involve extensive processing and assembly steps—such as ceramic machining (*19*), lamination (*20*), attaching planar electrodes for both activation and driving (*21*), and integration with transmission mechanisms (*22*)—to amplify the piezoelectric strain and transform the strain into motion in desired directions. These manufacturing routes usually process solid piezoelectric materials only and cannot precisely pattern electrodes, making it difficult to reduce the weight of an actuation element and activate bidirectional piezoelectric effects at small scales (*23*).

We show that a two-way conversion from an electric field to an arbitrary mechanical strain in a prescribed direction (and vice versa) can be achieved via a 3D network of interconnected piezoactive, conductive, and structural phases (Fig. 1A). Through analytical, numerical, and experimental validations, we show that these 3D microarchitected piezoelectric materials exhibit piezoelectric strain constants that cannot be achieved in standard materials and result in a wealth of electric field–induced strain conversions—including tension, shear, twisting, and flexure degrees of freedom (DoFs) and their combinations—as well as amplification of strain and logic-related subtraction and addition of strains. We developed a charge-programmed multimaterial additive manufacturing technique capable of directly assembling conductive, piezoactive, and structural materials into a complex 3D microarchitecture, which leads to a class of robotic metamaterials. We use the term "robotic metamaterials" to represent materials with designed 3D microarchitectures that directly serve as microrobots capable of performing many robotic tasks, including locomotion, steering, stepping, and two-way sound and ultrasonic transductions, as well as decision-making via feedback control (*24*).

Rational design of robotic metamaterials with arbitrary strain modes

The core concept of architected materials is the unrestricted placement of materials in a 3D cellular topology that either bypasses limitations inherent in natural crystals or mimics them to achieve desired properties. We introduce a convenient and robust strategy to architect piezoactive, conductive, and structural phases (Fig. 1A) in 3D space. Such multimaterial metamaterials are capable of receiving an input electric field and outputting a desired mode of strain that includes DoFs beyond the Cauchy strain components (normal and shear strains) (*25*), such as normal, shear, twisting, and flexure modes as well as their combinations and amplifications.

Because the existing piezoelectric tensors are not sufficient to describe all DoFs, we define the generalized piezoelectric tensors d_{nm} and $\bar{d}_{nm}$ on the basis of Cosserat solids (*26*) to describe the strain conversions of the architected piezoelectric materials (Fig. 1B)

$$\varepsilon_m = d_{nm}E_n;\ \varphi_m = \bar{d}_{nm}E_n \qquad (1)$$

where E_n is the electric field along the n direction in Cartesian coordinates (n = 1 to 3); ε_m and φ_m (m = 1 to 6) are the directional strain and coupled strain tensors (*25*), respectively; d_{nm} is the piezoelectric tensor that describes only the correlation between the normal or shear strain and the electric field; and $\bar{d}_{nm}$ is the extended piezoelectric tensor with components that denote the additional strain modes, including twist and flexure.

To design a piezoelectric microarchitecture that displays a desired global strain mode d_{nm} (or $\bar{d}_{nm}$) (Fig. 1B; see movie S1 for 36 distinguished strain modes), we start by identifying the motion of a stack of virtual characteristic planes within a unit cell of the microarchitecture (Fig. 1, C and D) and the local strain of the piezoactive struts that make up the unit cell (Fig. 1E and movie S1). The virtual characteristic planes can be considered "pinned" by the piezoactive struts to allow unconstrained motion and display a motion representing the desired global strain. As shown in fig. S1, A to D, the characteristic planes undergo distance changes, slip, rotation, and tilt corresponding to strain modes such as normal strain (ε_m, with m = 1 to 3), shear (ε_m, with m = 4 to 6),

[1]Department of Civil and Environmental Engineering, University of California, Los Angeles, CA 90095, USA. [2]Department of Mechanical and Aerospace Engineering, University of California, Los Angeles, CA 90095, USA. [3]Department of Mechanical Engineering, Virginia Tech, Blacksburg, VA 24061, USA. [4]Department of Electrical and Computer Engineering, University of California, San Diego, CA 92093, USA. [5]Department of Mechanical Engineering, Texas A&M University, College Station, TX 77843, USA. [6]California NanoSystems Institute, University of California, Los Angeles, CA 90095, USA.
*Corresponding author: Email: rayne@seas.ucla.edu

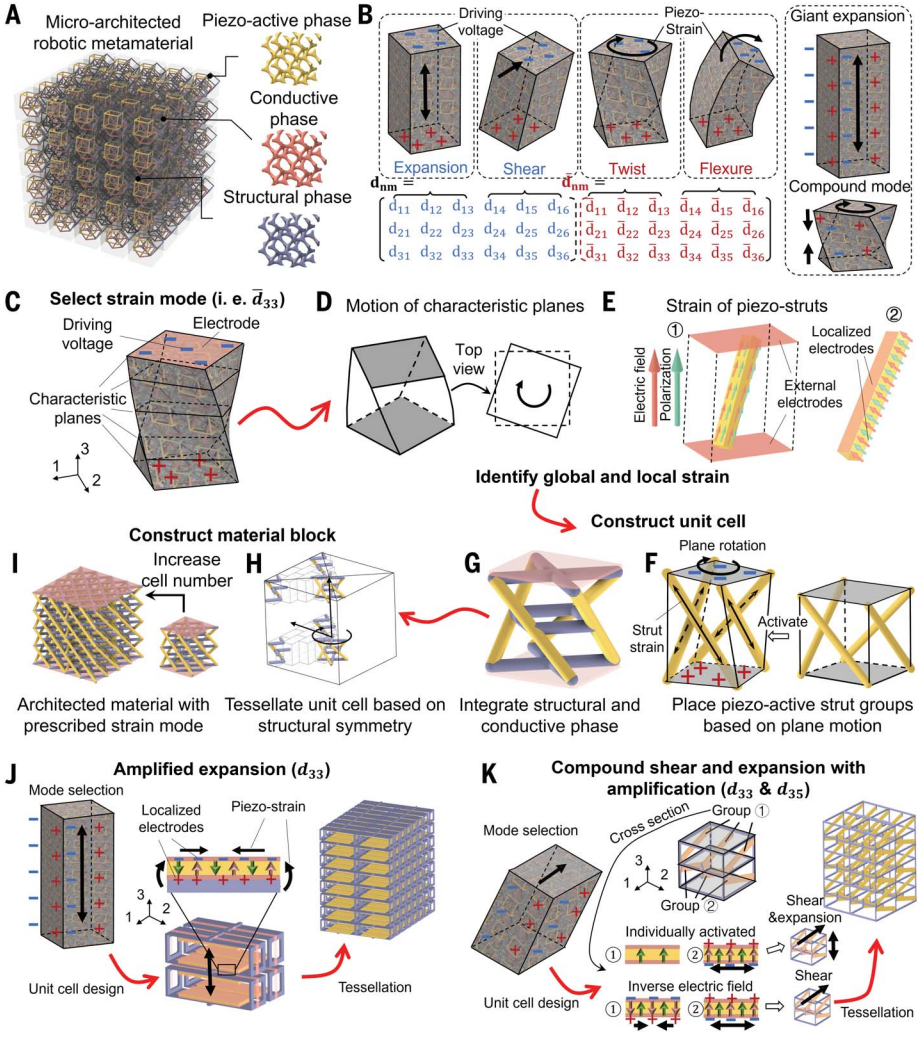

Fig. 1. Rational designs of robotic metamaterials with arbitrary strain modes. (**A**) Schematic of the piezoelectric metamaterial consisting of piezoactive, conductive, and structural phases. (**B**) Schematic of various strain modes and a piezoelectric strain matrix with extended tensors (red), enabled by metamaterial design and compared with the 18 tensors in natural piezoelectric ceramics (blue). (**C** to **I**) Schematic of the design rationale for the piezoelectric metamaterials. The example shown here is for the $\bar{d}_{33}$ (twisting) mode. (**J**) Designs of a piezoelectric robotic metamaterial with amplified expansion. (**K**) Schematic of the compound and decoupled expansion-shear mode with strain amplification. ①, external electrodes; ②, localized electrodes.

twist (φ_m, with m = 1 to 3), and flexure (φ_m, with m = 4 to 6). Figure 1D shows an example of a cube that twists upon application of an electric field in the direction of the 3-axis ($\bar{d}_{33}$ mode), which is represented by the in-plane rotation of the characteristic planes (Fig. 1D). The local strain of a piezoactive strut within the unit cell, either expanding or contracting, is determined by the direction of the strut, polarization, and electric field (see materials and methods for details on local strain identification). The electric field is generated by a conducting phase that either covers the sides of the lattice topology [external electrodes (Fig. 1E, ①)] or penetrates the topology [localized electrodes (Fig. 1E, ②)], covering both sides of the active struts and resulting in a shorter distance between electrodes and a stronger electric field.

The next design step is to place the piezoactive struts in a spatial layout such that their local strain drives the virtual characteristic planes to display the motion path corresponding to the target global strain mode (d_{nm} or $\bar{d}_{nm}$) (movie S1). Figure 1F presents the design of the piezoactive struts that generate a clockwise rotation of the characteristic planes, resulting in a twist strain mode and corresponding to a nonzero piezoelectric twist coefficient, $\bar{d}_{33}$. The 3D microarchitectural layouts of piezoactive struts for other strain modes (including expansion, shear, and flexure) are summarized in fig. S1, E to H. The full unit cell design is then completed by adding a structural phase and a conductive phase (Fig. 1G) in a layout that matches the symmetry of the piezoactive struts (see materials and methods for details on different phases).

In the last step, we tessellate the unit cells into a "metacrystal" that reflects the effective response of the unit cell (see materials and methods and fig. S1, I to L, for the choice of tessellation orientations). For example, to generate a twisting metamaterial, we tessellate the unit cell in cylindrical coordinates along the radial (r), angular (θ), and height (z) directions (Fig. 1, H and I, and movie S1). This aperiodic tessellation is scalable to an infinite number of unit cells and bypasses the effect of the number of unit cells when tessellated in Cartesian coordinates, for which the twist strain would vanish when reduced to a Cauchy continuum as the unit cell number increases (*27*) (fig. S2). As such, these metamaterial concepts are scalable, and the coefficient is invariant of the number of unit cells in all directions. Designs with all strain modes shown in the extended matrix are summarized in table S1.

The interpenetrating piezoactive, structural, and conductive phases allow amplification and logic-related subtraction and addition of strains, leading to the coupling and suppression of selected strain modes. Figure 1J shows the unit cell design featuring amplified expansion by tessellating pairs of piezoactive and structural struts (*28*). Figure 1K demonstrates the design with localized electrodes. The localized electrode architecture that covers selected groups of struts allows for programming of the polarization and electric field direction within the unit cell (Fig. 1K; see fig. S3 for polarization and driving voltage programming), thereby achieving a compound strain mode with both shear and expansion strain output or a decoupled strain mode with doubled shear strain and suppressed expansion.

We implemented a computational framework that predicts and verifies the piezoelectric coefficients—d_{nm} and $\bar{d}_{nm}$, respectively—of the metacrystal designs. This is achieved by calculating the total induced-load contribution of the connected piezoactive struts within the cubic volume under an electric field [materials and methods and supplementary text section 1 (SM 1)]. SM 2 and fig. S4 show the finite element analysis results that verify the actuation modes.

Additive manufacturing of robotic metamaterials

We developed a charge-programmed multimaterial additive manufacturing technique capable of assembling piezoactive, structural, and conducting phases into a complex 3D microarchitecture. First, a negatively charged resin [which can be selectively deposited with metals (*29*)] and a highly loaded nanoparticle

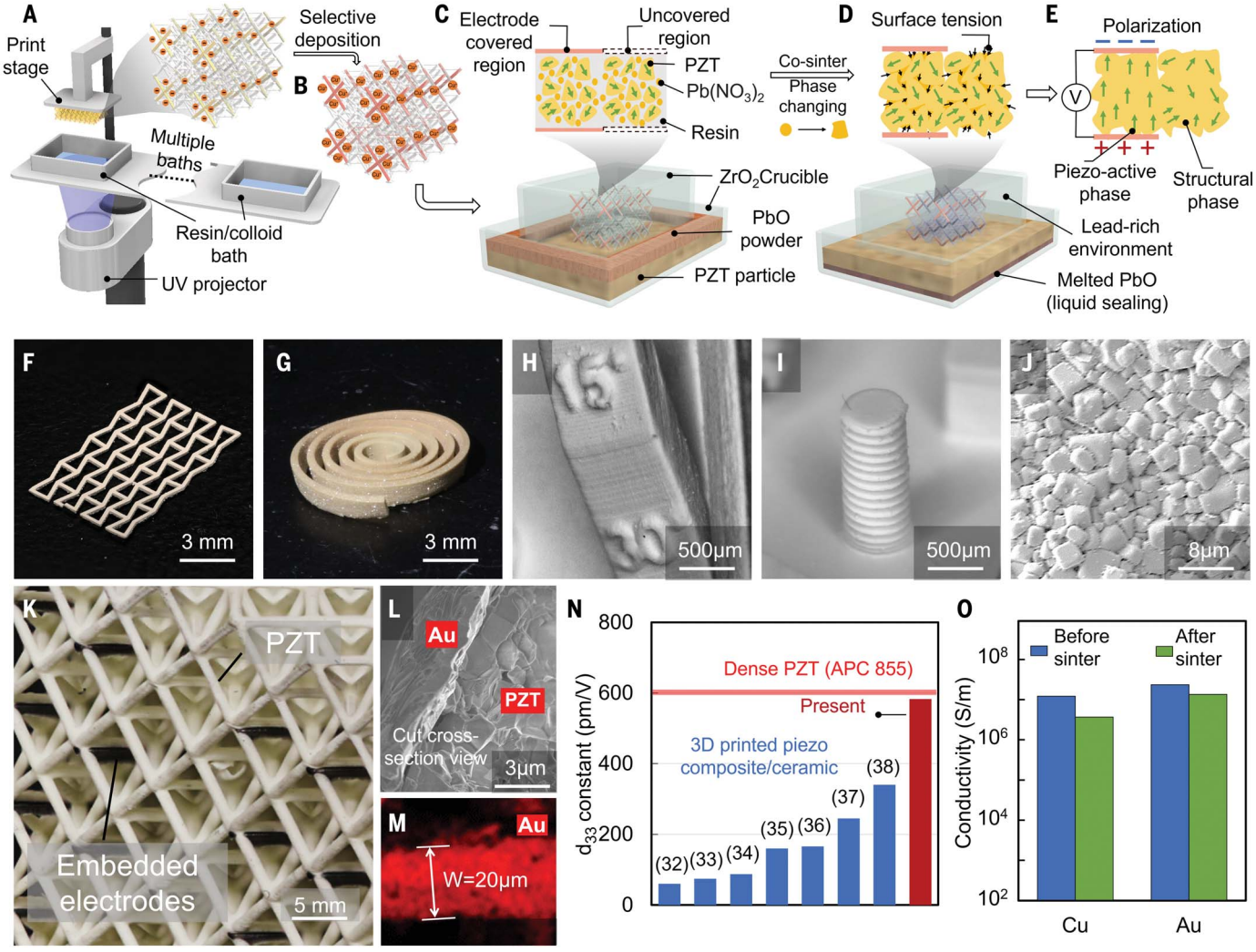

Fig. 2. Multimaterial fabrication platform. (**A** and **B**) Schematic illustrations of the charge-programmed multimaterial additive fabrication of 3D piezoelectric ceramics with embedded electrodes. UV, ultraviolet. (**C** and **D**) Schematics of the sintering process of highly loaded piezoelectric ceramics with localized electrodes. (**E**) Schematic of the selective activation (polarization) process of the piezoactive phase. (**F** to **I**) Optical images of as-fabricated samples. (**J**) Scanning electron microscopy (SEM) image of the cross section of the sintered PZT. (**K**) Optical image of a printed piezoelectric metamaterial block with embedded 3D electrodes. (**L**) SEM image of the boundary between the PZT and Au electrode. (**M**) Elemental mapping of a selectively deposited thin wire, showing the minimum deposition width (W). (**N**) Comparison of piezoelectric charge coefficients between piezoceramics presented in this study and current 3D-printed piezoelectric materials (*32*–*38*). (**O**) Conductivity of Cu and Au conductive phases before and after sintering.

colloid were printed via the multimaterial 3D printing system (materials and methods), as shown in Fig. 2A. The nanoparticle colloid consists of 15 to 50 vol % PZT (APC 855), featuring a high piezoelectric strain constant (d_{33} = 600 pm/V) and 5 to 15% lead nitrate, which is used as a liquid-phase–sintering agent (*30*). The conductive phase was then selectively deposited onto the charged resins, forming a 3D microarchitecture with electrodes (Fig. 2B and materials and methods). The deposited architectures were cosintered with an optimized temperature profile in a gas environment (fig. S5) to prevent degradation of the piezoelectricity of the piezoceramics and conductivity of the electrodes (Fig. 2C). Additionally, lead oxide was used to provide a liquid seal and lead-rich environment to suppress lead evaporation of PZT at temperatures higher than 800°C (Fig. 2D and SM 3). The lead nitrate particles within the printed architecture melted and induced contraction of the PZT particles as a result of their surface tension, which densified the PZT and reduced the porosity. Next, the architected piezoceramics were polarized by applying a strong electric field through the deposited metals at an elevated temperature (SM 3 and fig. S5). After polarization, the regions not covered with electrodes remained inactive (unpolarized) and were employed as the structural phase (Fig. 2E). Other ceramics, such as silicon oxycarbide (SiOC) (*31*), could also be employed as the structural phase to enhance the stiffness of the metamaterial.

This 3D fabrication approach allows the fabrication of piezoactive materials with precise, microscale 3D architectures and low porosity (Fig. 2, F to H). Figure 2K shows a robotic metamaterial block with embedded electrodes. The gapless bonding between the piezoactive and conductive phases (Fig. 2L) results in minimal dielectric loss when an electric field is applied. The minimum achievable feature size of the conductive phase reaches 20 μm (Fig. 2M), ensuring precise control of the localized electric field when voltages are applied through these conductive phases. The

as-printed piezoelectric solids reach a measured piezoelectric constant (d_{33}) as high as 583 pm/V (measured with a d33 meter, APC 90-2030), indicating that these materials outperform existing 3D printable piezoelectric composites or ceramics (Fig. 2N) (*32*–*38*). The selectively patterned conductive phases are highly conductive (SM 4), achieving values of 3.7×10^6 and 1.35×10^7 S/m (where 1 S = 1 A/V) after sintering for Cu and Au, respectively (Fig. 2O), which makes them suitable for subsequent actuation with negligible energy loss. The surface texture and roughness of different materials of the as-fabricated samples are summarized in SM 6 and fig. S7. See SM 5 and fig. S6 for the characterization of mechanical properties of the as-printed lattice materials, including strength, elastic modulus, and durability. The high-precision fabrication, highly responsive 3D-printed PZT, and highly conductive deposited metals enable the implementation of metamaterial designs.

Multi-DoF amplified and programmed strain

To verify the designed strain modes of the robotic metamaterials, we measured the electric field–activated deformation of the as-fabricated and polarized samples via high-precision full-field scanning laser Doppler vibrometry (Polytec, PSV-500) (Fig. 3A). A sinusoidal sweep signal with 50-V amplitude was applied through the layered external electrodes, whereas the activated deformation was measured by tracing the side surface of the metamaterial (Fig. 3A) and reconstructed as operational deflectional shapes in the quasi-static region for visualization. Figure 3, B and C, displays an optical image of a twist ($\bar{d}_{33}$) mode lattice with external electrodes and its side-surface deformation,

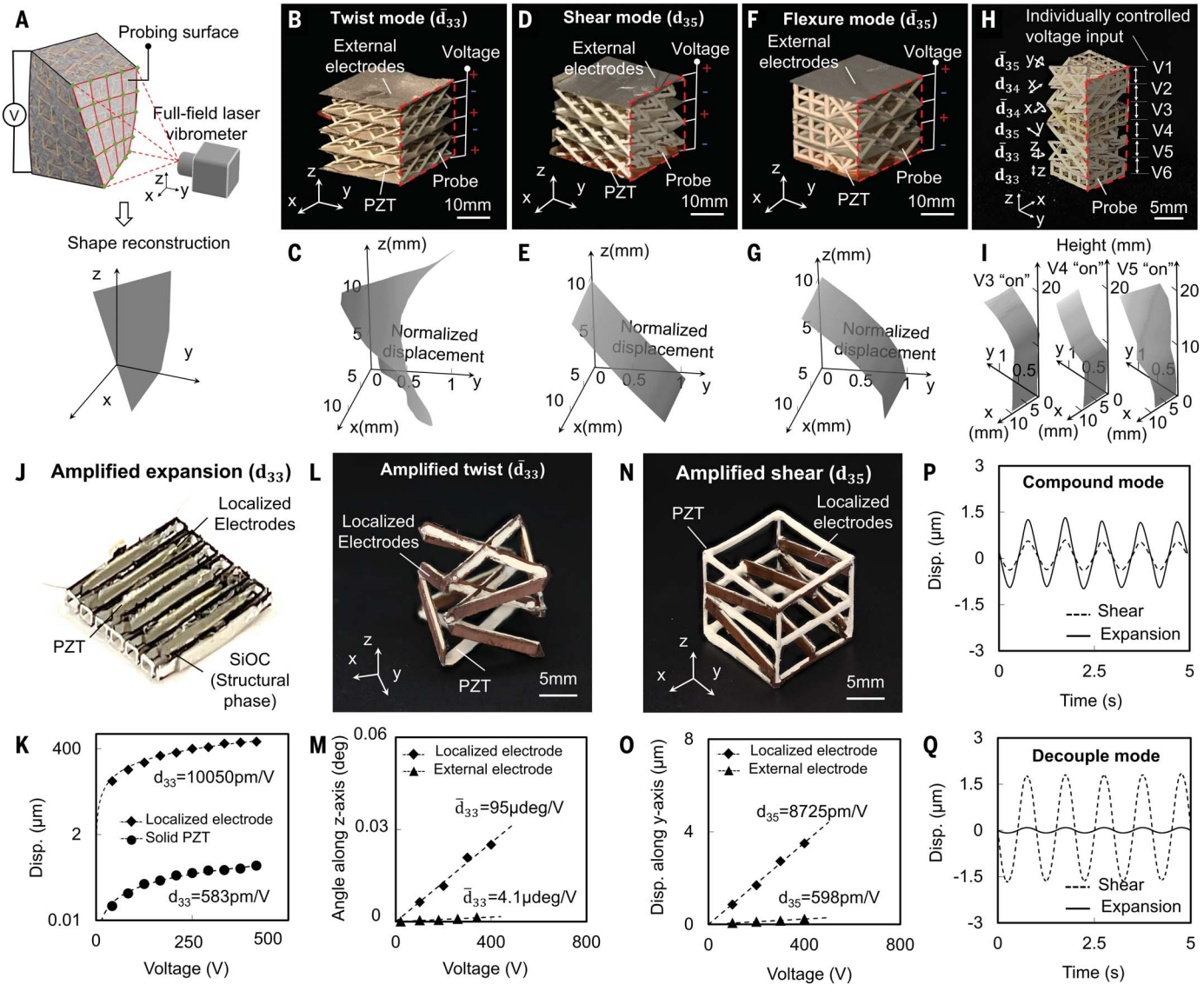

Fig. 3. Experimental verification of robotic metamaterial designs. (**A**) Schematic of the test setup with a laser vibrometer to measure the deformation of the side surface of the lattice. (**B** to **G**) Optical images of the twist, shear, and flexure mode lattice and their side-surface deformation. (**H**) Optical image of a modularized piezoelectric actuator with six DoFs. (**I**) Deformation of the side surface of the 6-DoF piezoelectric actuator working in three representative operating modes ($\bar{d}_{34}$, d_{35}, and $\bar{d}_{33}$ modes). (**J**) Optical image of a piezoelectric metamaterial with amplified expansion. (**K**) Displacement of the metamaterial with localized electrodes and solid PZT material with external electrodes as a function of the input voltage. (**L**) Optical image of the piezoelectric metamaterial with amplified twist and suppressed expansion. (**M**) Twist angle of the metamaterial with external and localized electrodes as a function of input voltage. (**N**) Optical image of the piezoelectric metamaterial with amplified shear. (**O**) Shear displacement of the metamaterial with external electrodes and localized electrodes as a function of input voltage. (**P** and **Q**) Displacement of compound and decoupled expansion-shear modes with sinusoidal voltage input.

showing a wrapped shape that corresponds to a twisted solid (Fig. 1C). Operational deflectional shapes for shear (d_{34}) and flexure ($\bar{d}_{35}$) mode lattices are summarized in Fig. 3, D and E, and Fig. 3, F and G, respectively. Different strain modes can be combined into a single-element piezoelectric lattice to achieve a multi-DoF metamaterial actuator with six individually actuatable architecture designs with six DoFs, including the d_{33}, d_{34}, d_{35}, $\bar{d}_{33}$, $\bar{d}_{34}$, and $\bar{d}_{35}$ modes (Fig. 3, H and I, and movie S2). This multi-DoF actuator has a density of 0.88/cm^3, which is an order of magnitude lower than that of existing piezoactuators with dense PZT (*23*) (fig. S8). We demonstrate a high-speed galvanometer actuated by two multi-DoF actuators assembled with two reflective mirrors (movie S3). Figure S9 shows a star pattern drawn by the guided laser beam (10 cycles at 20 Hz, root mean square precision of 50 ± 13 μm). This is achieved by programming the input voltage that controls the tilt angle of the metamaterial (see SM 7 for details of the laser pattern reconstruction).

We fabricated microarchitectures with embedded electrodes and demonstrated strain amplification, strain compounding, and strain addition and subtraction enabled by the localized electrodes and microarchitecture design. Figure 3, J, L, and N, present as-fabricated lattices with localized electrodes that feature amplified expansion (d_{33}; Fig. 1J), amplified twist ($\bar{d}_{33}$; fig. S3), and amplified shear (d_{34}; Fig. 1K), respectively. The displacement versus the driving voltage of the lattices was measured by the laser vibrometer and plotted (Fig. 3, K, M, and O) to derive the corresponding strain coefficients. Compared with the strain coefficients of lattices with layered external electrodes, the piezoelectric coefficients of the localized electrodes (i.e., d_{33} = 10,050 pm/V) are amplified, with values two orders of magnitude higher than that of their native material (583 pm/V). The compound expansion-shear strain and the decoupled pure shear strain are demonstrated, using designs from Fig. 1K, by programming the local polarization and driving electric field within the embedded electrode architectures (Fig. 3, P and Q).

Robotic metamaterials as proprioceptive microrobots

These piezoceramic architectures have bidirectional electrical-to-mechanical energy conversion—namely, direct and inverse piezoelectric effects. These metamaterials can be exploited as a proprioceptive microrobotic system with feedback control and without the need to combine transmissions and external sensors. Within a single piece of piezoelectric architecture, selected regions serve as actuation limbs using the inverse piezoelectric effect, whereas other regions that use the direct and bidirectional piezoelectric effects serve as strain sensors and pulse-echo elements, respectively (Fig. 4A).

We fabricated one piece of metamaterial with an amplified d_{33} mode (Fig. 1J) as a multimodal microrobot (Fig. 4B; see SM 8 and figs. S10 and S11 for an alternative version consisting of compound flexure-twist mode lattices). Selected regions serve as robotic limbs capable of actuation and load carrying, with the ability to sense both contact forces and remote objects. The microrobot is controlled by a closed-loop system via its sensing components (fig. S12). The microrobot consists of three individually actuatable regions that serve as its body, rear legs, and front legs (Fig. 4B). The coordinated motion of these three regions enables three distinguishable modes described as walking, turning, and jumping (Fig. 4B; see materials and methods and fig. S14, A and B, for motion planning based on the three limbs). The 3D localized electrode interconnects all piezoactive elements within one region and minimizes the number of connection leads, enabling a compact design (without additional circuit boards or leads wired to individual piezoactive elements) and making the microrobot lightweight (740 mg).

In contrast to existing piezoelectric actuation mechanisms in which leveraging or transmission methods are employed to amplify displacement at the cost of reducing blocking force, a feature of the actuation performance of the robotic metamaterial is its simultaneously increased blocking force and displacement via its skeletal actuator layout. An actuator connected with a transmission system for robotic motions typically leads to a trade-off between blocking force and step length, owing to the compliant levering mechanism involved (*39*, *40*). We show that these architected piezoelectric robotic limbs (Fig. 4A), composed of a network of microscale actuation units distributed throughout the robot body in a fashion similar to skeletal muscles, breaks this trade-off and simultaneously produce long steps and high blocking force with high system stiffness. A comparison between the skeletal actuation architecture and actuator-transmission mechanism is described in fig. S13 and SM 9. Although a transmission system effectively amplifies the displacement, its additional levering inevitably reduces the system stiffness and therefore the blocking force (Fig. 4C; N denotes the number of unit cells of the metamaterial block), resulting in a decreased payload capability of the robot when driven at higher speeds. The interconnected microactuator and embedded electrode microarchitecture allow the driving voltage to be applied locally at each element, enabling a higher driving electric field and thus an amplified displacement. This is achieved while maintaining the overall stiffness through the interconnections of the unit cells without compliant transmissions. These features enhance the performance of the microrobot, including high speed, payload, and resonance.

The long steps and high resonance of the metamaterial limb enable a maximum speed of 128 mm/s in the walking mode and a turning rate of 90°/s (Fig. 4D and movie S4; see fig. S14 for the frequency response of the limb and speed benchmark). With its broadband response (fig. S14), the robotic metamaterial achieves a short rise time to impulse voltage inputs (*41*). This enables the release of actuation energy within 1 ms, resulting in the microrobot lifting its front legs into the air and then lifting its body and rear legs, thus allowing it to step up from the ground (movie S4). The jumping mode enables the microrobot to climb over elevated and rough surfaces (Fig. 4E and movie S4), movement that is not achievable by piezoelectric microrobots with small strokes (*42*, *43*). The stiffness of the piezoelectric metamaterial elements enables a large system payload. Various weights (1 to 5.6 g) are loaded on the microrobot, and its speed is measured by digital image correlation. More than 80% of the original speed is retained for a 500% payload, compared with a >80% speed reduction with a <200% payload for microrobotic systems using a compliant mechanism (Fig. 4F) (*39*, *44*).

By assigning sections of the piezoactive phases as the sensing element and using its direct piezoelectric effects via 3D embedded electrodes, we demonstrate that the robotic metamaterial is capable of self-sensing its strain change and responding to external stimuli, which allows closed-loop control and quick reactions to external stimuli. As shown in Fig. 4B, the selectively deposited electrodes separate a strain-sensing section from a piezoactive element with a 100-μm isolation gap, which eliminates electrical coupling. This section is integrated with a microcontroller to form a closed-loop control system that receives the sensing voltage and sends the control voltage to the actuation regions. The self-sensing voltage signal updates as the actuator element deforms, allowing real-time monitoring of the gait status and response to stimuli (see fig. S12 for control loop design; see SM 10 and fig. S15 for more details on proprioception and exteroception). Figure 4G demonstrates the gait-monitoring signal, detection of the external impact, and programmed reaction within 0.1 ms upon a drop-weight impact during locomotion (SM 11). Movie S5 shows other programmed reactions that include stopping or turning upon detecting an obstacle. The high payload of the metamaterial-enabled robot allows for the integration of an onboard power (7.4 V), a driver, and a microcontroller, paving the way for fully untethered operations with closed-loop control (SM 12, fig. S16, and movies S6 and S7).

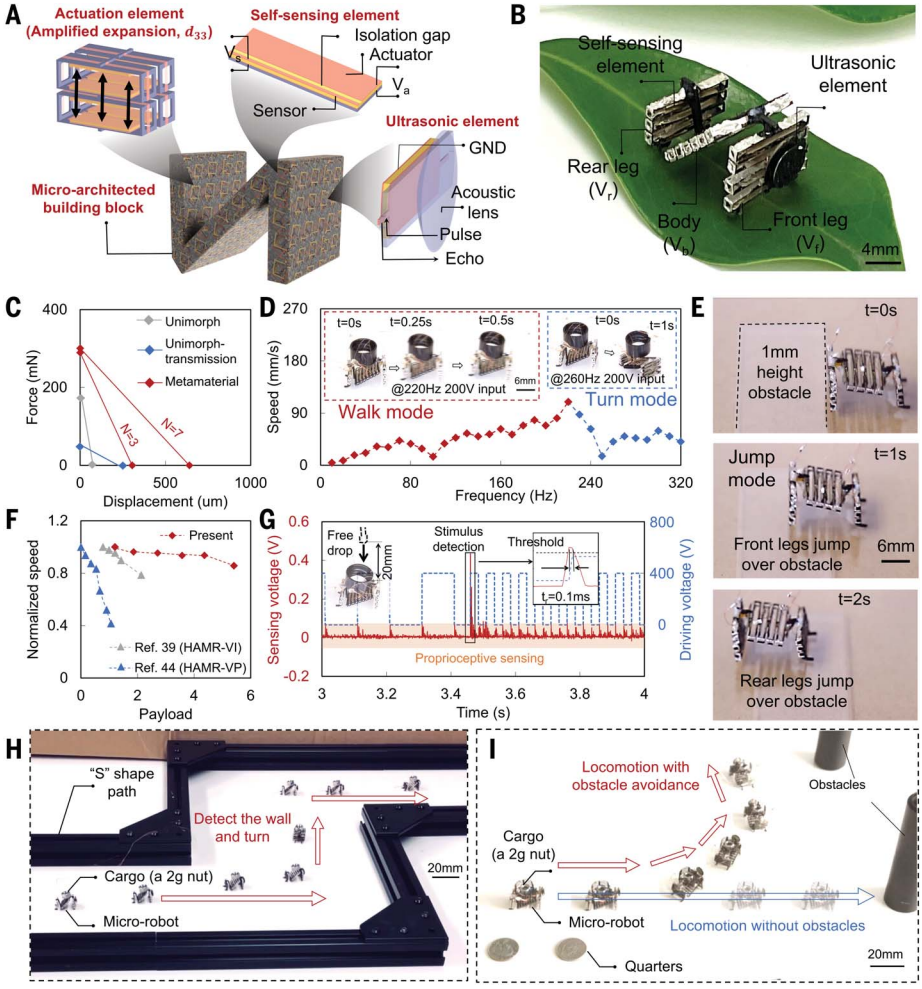

Fig. 4. Stimuli-responsive multimodal mobile microrobot. (**A**) Schematic of the microarchitected piezoelectric metamaterial building block with an embedded actuation element, an embedded self-sensing element, and a contactless detection element. GND, ground. (**B**) Optical image of the mobile robot. (**C**) Working curves of a unimorph, a unimorph assembled with a transmission mechanism, and the fabricated piezoactuator with multiple unit cells. N, number of unit cells of the metamaterial block. (**D**) Speed as a function of stepping frequency. (**E**) Optical image of the microrobot climbing over a 1-mm-high obstacle in jumping mode. (**F**) Normalized speed of the microrobot under various payload conditions. HAMR-VI and HAMR-VP denote two versions of the Harvard Ambulatory Microrobot. (**G**) Sensing voltage and mobile voltage as a function of time during the impact test. (Inset) Optical image of the drop-weight impact test of the microrobot with a basket. (**H**) Trajectory of the microrobot navigating an S-shaped path. (**I**) Trajectory of the microrobot with and without obstacle.

The robotic metamaterial is also capable of sensing and reacting to noncontact stimuli when the pulse-echo element functions with bidirectional piezoelectric effects. As shown in Fig. 4B, an element on a frontal leg is capable of emitting and receiving focused ultrasonic waves with a semispherical acoustic lens printed with the structural phase. The echo signal (fig. S17 and materials and methods) from the remote object is processed by the closed-loop control system that updates the driving voltage to navigate through an S-shaped path and avoid remote obstacles (Fig. 4, H and I, and movie S8).

Discussion and outlook

We introduced a strategy to design and construct a class of robotic metamaterials that incorporate electronic, structural, and conducting microscale strut elements in a 3D architecture. These multifunctional metamaterials revealed a myriad of strain modes, including twisting, flexure, compound, decoupled, and amplified strains. The microarchitecture designs surpass the limitations of natural piezoelectric crystals in which the piezoelectric strain relies on the available natural crystalline structures. The design strategy can be combined with a topology-optimization algorithm to generate arbitrary piezoelectric tensors.

The multimaterial additive manufacturing technique reported herein combines piezoceramic, metallic, and structural materials into a complex 3D architecture. The resulting metamaterial blocks with milli- to centimeter dimensions are capable of outputting multi-DoF motions with high blocking force as well as sensing contact and remote stimuli. This is accomplished without any external sensors and transmissions. Compared with other actuation materials (e.g., dielectric elastomers), the robotic metamaterials have low driving voltage, broad frequency range, two-way sensing, and actuation. The reported design framework and manufacturing methods have direct implications for the future development of miniaturized robots, transducers, and robotic materials; it will be possible to achieve desired motions and decision-making via simplified artificial materials.

REFERENCES AND NOTES

1. X. Zheng *et al.*, *Science* **344**, 1373–1377 (2014).
2. A. J. D. Shaikeea, H. Cui, M. O'Masta, X. R. Zheng, V. S. Deshpande, *Nat. Mater.* **21**, 297–304 (2022).
3. M.-S. Pham, C. Liu, I. Todd, J. Lertthanasarn, *Nature* **565**, 305–311 (2019).
4. X. Zheng *et al.*, *Nat. Mater.* **15**, 1100–1106 (2016).
5. Y. Kim, H. Yuk, R. Zhao, S. A. Chester, X. Zhao, *Nature* **558**, 274–279 (2018).
6. H. Xu, D. Pasini, *Sci. Rep.* **6**, 34924 (2016).
7. N. A. Dudukovic *et al.*, *Nature* **595**, 58–65 (2021).
8. N. J. Gerard *et al.*, *Appl. Phys. Lett.* **114**, 231902 (2019).
9. H. Cui *et al.*, *Nat. Mater.* **18**, 234–241 (2019).
10. K. Liu, F. Hacker, C. Daraio, *Sci. Robot.* **6**, eabf5116 (2021).
11. J. T. B. Overvelde *et al.*, *Nat. Commun.* **7**, 10929 (2016).
12. J. T. B. Overvelde, J. C. Weaver, C. Hoberman, K. Bertoldi, *Nature* **541**, 347–352 (2017).
13. S. Trolier-McKinstry, S. Zhang, A. J. Bell, X. Tan, *Annu. Rev. Mater. Res.* **48**, 191–217 (2018).
14. Z. Li *et al.*, *Adv. Sci.* **7**, 2001155 (2020).
15. H. Götze, L. Pagel, *Microelectron. Eng.* **84**, 1333–1336 (2007).
16. P. Scheeper, J. O. Gulløv, L. M. Kofoed, *J. Micromech. Microeng.* **6**, 131–133 (1996).
17. P. Zhu *et al.*, *Adv. Energy Mater.* **10**, 2001945 (2020).
18. M. Han *et al.*, *Nat. Electron.* **2**, 26–35 (2019).
19. H. Kiso, T. Taguchi, M. Fukuhara, T. Kimura, *Bull. Jpn. Soc. Precis. Eng.* **21**, 142–143 (1987).
20. M. F. M. Sabri, T. Ono, S. M. Said, Y. Kawai, M. Esashi, *J. Microelectromech. Syst.* **24**, 80–90 (2015).
21. Y. P. Singh, V. K. Jain, P. Kumar, D. C. Agrawal, *J. Mater. Process. Technol.* **58**, 24–31 (1996).
22. Y. Chen, N. Doshi, B. Goldberg, H. Wang, R. J. Wood, *Nat. Commun.* **9**, 2495 (2018).
23. Z. Li *et al.*, *Adv. Mater.* **34**, e2107236 (2022).
24. M. A. McEvoy, N. Correll, *Science* **347**, 1261689 (2015).
25. A. C. Eringen, *Microcontinuum Field Theories: I. Foundations and Solids* (Springer, 1999); https://www.springer.com/gp/book/9780387986203.
26. E. M. P. Cosserat, F. Cosserat, *Theory of Deformable Bodies* (NASA, 1970).

27. T. Frenzel, M. Kadic, M. Wegener, *Science* **358**, 1072–1074 (2017).
28. B. Rodriguez, H. Kalathur, R. Lakes, *Phys. Stat. Sol. B* **251**, 349–353 (2014).
29. R. Hensleigh *et al*., *Nat. Electron.* **3**, 216–224 (2020).
30. R. M. German, P. Suri, S. J. Park, *J. Mater. Sci.* **44**, 1–39 (2009).
31. H. Cui, R. Hensleigh, H. Chen, X. Zheng, *J. Mater. Res.* **33**, 360–371 (2018).
32. Y. Zeng *et al*., *Micromachines* **11**, 713 (2020).
33. S. M. Gaytan *et al*., *Ceram. Int.* **41**, 6610–6619 (2015).
34. X. Song *et al*., *Rapid Prototyping J.* **23**, 44–53 (2017).
35. Z. Chen *et al*., *Nano Energy* **27**, 78–86 (2016).
36. J. Cheng, Y. Chen, J.-W. Wu, X.-R. Ji, S.-H. Wu, *Sensors* **19**, 4078 (2019).
37. H. Chabok *et al*., in *Proceedings of the ASME/ISCIE 2012 International Symposium on Flexible Automation* (American Society of Mechanical Engineers, 2013), pp. 433–444.
38. Y.-Z. Ji *et al*., *Adv. Eng. Mater.* **19**, 1600803 (2017).
39. N. Doshi *et al*., in *2015 IEEE/RSJ International Conference on Intelligent Robots and Systems (IROS)* (IEEE, 2015), pp. 4119–4126.
40. K. Jayaram, J. Shum, S. Castellanos, E. F. Helbling, R. J. Wood, in *2020 IEEE International Conference on Robotics and Automation (ICRA)* (IEEE, 2020), pp. 10305–10311.
41. S. J. Rupitsch, *Piezoelectric Sensors and Actuators: Fundamentals and Applications* (Topics in Mining, Metallurgy and Materials Engineering series, Springer, 2019); https://www.springer.com/gp/book/9783662575321.
42. H. H. Hariri *et al*., in *2016 IEEE International Conference on Robotics and Automation (ICRA)* (IEEE, 2016), pp. 4743–4749.
43. A. G. Dharmawan, H. H. Hariri, S. Foong, G. S. Soh, K. L. Wood, in *2017 IEEE International Conference on Robotics and Automation (ICRA)* (IEEE, 2017), pp. 6008–6013.
44. A. T. Baisch, O. Ozcan, B. Goldberg, D. Ithier, R. J. Wood, *Int. J. Robot. Res.* **33**, 1063–1082 (2014).

ACKNOWLEDGMENTS

We acknowledge D. Maurya and P. Kuma for assistance with the laser vibrometer and power amplifier and S. Chamanian and B. Liu for assistance with the power system. We thank H. Hemminger for setting up the laser sensor circuits and Z. Wong for the coding of the Seeeduino microcontroller. **Funding:** This work was supported by US Defense Advanced Research Projects Agency (D20AP00001-02; Program Managers: R. Polcawich and W. Carter) and US Office of Naval Research (N00014-19-1-2723; Program Managers: F. Blackmon and M. Wardlaw). The authors would like to thank the US Office of Naval Research (N00014-20-1-2504), Air Force Office of Scientific Research (FA9550-18-1-0299 and FA9550-21-1-0241), and National Science Foundation (2048200 and 2119643) for funding support. **Author contributions:** Conceptualization: X.Z. and H.C. Methodology: X.Z., H.C., D.Y., R.H., A.C., and P.M. Investigation: H.C., D.Y., R.H., H.L, Z.W., Z.X., S.D., and P.M. Visualization: H.C., H.L., S.D., P.T., Z.X., and A.C. Funding acquisition: X.Z. Project administration: X.Z. and H.C. Supervision: X.Z. Writing – original draft: H.C., D.Y., R.H., and X.Z. Writing – review & editing: H.C., D.Y., R.H., Z.X., H.L., S.D., Z.W., P.T., and X.Z. **Competing interests:** R.H. and X.Z. are inventors on a patent application (PCT/US2019/033385) held/submitted by Virginia Tech that covers multimaterial printing of 3D electronics. The authors certify that they have no affiliations with or involvement in any organization or entity with any financial interest or nonfinancial interest in the subject matter or materials discussed in this manuscript. **Data and materials availability:** All data are available in the manuscript or the supplementary materials. **License information:** Copyright © 2022 the authors, some rights reserved; exclusive licensee American Association for the Advancement of Science. No claim to original US government works. https://www.science.org/about/science-licenses-journal-article-reuse

SUPPLEMENTARY MATERIALS

science.org/doi/10.1126/science.abn0090
Materials and Methods
Supplementary Text
Figs. S1 to S21
Tables S1 and S2
References (*45*–*64*)
Movies S1 to S8

Submitted 15 November 2021; accepted 27 April 2022
10.1126/science.abn0090

PLANT SCIENCE

A genetic module at one locus in rice protects chloroplasts to enhance thermotolerance

Hai Zhang[1,2,3,4], Ji-Fu Zhou[1,3], Yi Kan[1,2], Jun-Xiang Shan[1,2], Wang-Wei Ye[1,2], Nai-Qian Dong[1,2], Tao Guo[1], You-Huang Xiang[1,2,3], Yi-Bing Yang[1,2,3], Ya-Chao Li[1,3,4], Huai-Yu Zhao[1,3], Hong-Xiao Yu[1,3], Zi-Qi Lu[1,4], Shuang-Qin Guo[1,2,3], Jie-Jie Lei[1,2,3], Ben Liao[1,4], Xiao-Rui Mu[1,2,3], Ying-Jie Cao[1,2,3], Jia-Jun Yu[1,4], Youshun Lin[5]*, Hong-Xuan Lin[1,2,3,4]*

How the plasma membrane senses external heat-stress signals to communicate with chloroplasts to orchestrate thermotolerance remains elusive. We identified a quantitative trait locus, *Thermo-tolerance 3* (*TT3*), consisting of two genes, *TT3.1* and *TT3.2*, that interact together to enhance rice thermotolerance and reduce grain-yield losses caused by heat stress. Upon heat stress, plasma membrane–localized E3 ligase TT3.1 translocates to the endosomes, on which TT3.1 ubiquitinates chloroplast precursor protein TT3.2 for vacuolar degradation, implying that TT3.1 might serve as a potential thermosensor. Lesser accumulated, mature TT3.2 proteins in chloroplasts are essential for protecting thylakoids from heat stress. Our findings not only reveal a *TT3.1-TT3.2* genetic module at one locus that transduces heat signals from plasma membrane to chloroplasts but also provide the strategy for breeding highly thermotolerant crops.

Plants have developed multiple resistance mechanisms (*1*–*3*), including the ubiquitin proteasome system (*4*–*7*), and chloroplast stress responses (*8*–*11*) to buffer themselves against temperature fluctuations. The process of ubiquitination plays a key role in eliminating denatured proteins and thus improves plants thermotolerance (*6*, *12*). Chloroplasts are photosynthetic organelles that also contribute to heat-stress responses (*8*, *10*, *13*, *14*). Chloroplast proteins damaged by stress need to be rapidly degraded through chloroplastic hydrolases or extraplastidic pathways (26*S*-proteasome and autophagy), which are well described (*15*–*17*). However, how heat signals are transduced from the plasma membrane into chloroplasts to control plant thermotolerance remains unknown. We found that a *Thermo-tolerance 3.1* (*TT3.1*)–*TT3.2* genetic module in rice links the plasma membrane to chloroplasts to protect chloroplasts from heat-stress damage and increases grain yield under heat stress.

Results

Identification of TT3 *locus for thermotolerance*

To identify potential quantitative trait loci (QTLs) conferring rice thermotolerance, we tested a set of chromosome segment substitution lines with the African rice variety CG14 as the donor parent and the Asian rice variety Wuyunjing (WYJ) as the recurrent parent (fig. S1A) (*18*). We selected a QTL, designated *TT3*, for further fine-mapping and delimited *TT3* to a 36.6-kb region (fig. S1, B to D). We then constructed the nearly isogenic line (NIL) that contains this region and carries *TT3* by backcrossing with WYJ (NIL-$TT3^{CG14}$). NIL-$TT3^{CG14}$ was more tolerant than its isogenic control, NIL-$TT3^{WYJ}$, upon heat stress (Fig. 1, A and B), indicating that *TT3* is a QTL contributing to rice thermotolerance.

In the *TT3* region, three genes were annotated: *LOC_Os03 g49900*, *LOC_Os03 g49930*, and *LOC_Os03 g49940*, whereas three other genes encode retrotransposon or expressed proteins (Fig. 1C). Knocking out *LOC_Os03 g49930* exhibited the same hypersensitive phenotypes as WYJ, implying that *LOC_Os03 g49930* had no effects on thermotolerance (fig. S2, A and B). Nevertheless, the *LOC_Os03 g49900* knockout lines exhibited more sensitivity to heat than WYJ, whereas the *LOC_Os03 g49940* knockout seedlings were more thermotolerant than WYJ (Fig. 1, D and E, and fig. S2, C to F), indicating that *LOC_Os03 g49900* and *LOC_Os03 g49940* were both thermotolerance-related candidate genes at *TT3*. The *LOC_Os03 g49900* gene was defined as *TT3.1* and *LOC_Os03 g49940* as *TT3.2* for further investigation. Sequence comparisons of NIL-$TT3^{WYJ}$ and NIL-$TT3^{CG14}$ within *TT3.1* and *TT3.2* uncovered one amino acid substitution in *TT3.1* (Ala^{128}→Val) and *TT3.2* (Ser^{242}→Gly), respectively (Fig. 1C). Further protein sequence alignments of TT3.1, TT3.2, and their homologs revealed that TT3.1 and TT3.2 are conserved in many monocots (fig. S3). We also found that heat treatment induced the expression of *TT3.1* and *TT3.2* and that their expression levels between NIL-$TT3^{WYJ}$ and NIL-$TT3^{CG14}$ were not significantly different (fig. S4, A and B), which was consistent with the absence of heat-responsive elements among polymorphic regulatory elements in the *TT3.1* and *TT3.2* promotors (fig. S4, C and D).

We then overexpressed the coding region of $TT3.1^{WYJ}$ and $TT3.1^{CG14}$ in WYJ, respectively, and found that the overexpression lines were both more thermotolerant than WYJ (Fig. 1, F and G, and fig. S2, G and H). We also found that with the increased expression levels of $TT3.1^{WYJ}$ and $TT3.1^{CG14}$ in overexpression lines, seedlings exhibited enhanced thermotolerance (fig. S2, I to K). However, at similar levels of gene expression, overexpression-$TT3.1^{CG14}$ was more tolerant than overexpression-$TT3.1^{WYJ}$ under heat stress, which indicates that $TT3.1^{CG14}$ possessed the stronger effect on heat tolerance and is an elite allele for improving thermotolerance. Next, we overexpressed the coding sequence (CDS) of $TT3.2^{CG14}$ in WYJ and found that the transgenic plants displayed weaker heat tolerance than WYJ (fig. S2L). Together, these results suggested that *TT3.1* and *TT3.2* are both candidate genes for *TT3* locus and that *TT3.1* is a positive regulator to promote thermotolerance, whereas *TT3.2* plays a negative role.

We generated the *tt3.1tt3.2* double mutant by crossing *tt3.1* with *tt3.2*. The *tt3.1* mutant was sensitive to heat stress; the *tt3.2* mutant was tolerant to heat stress, and the *tt3.1tt3.2* double mutant resembled the *tt3.2* mutant in terms of thermotolerance (fig. S2, M and N), suggesting that *TT3.1* acts upstream of *TT3.2* to regulate heat tolerance.

TT3 *enhances thermotolerance at reproductive stages*

To test whether the heat tolerance response of *TT3* comes at the cost of growth and yields, we performed yield-trait evaluation. Field experiments showed that NIL-$TT3^{WYJ}$ and NIL-$TT3^{CG14}$ had no significant difference in yield traits (fig. S5, A and B). Overexpression-$TT3.1^{CG14}$ and *tt3.2* mutant also exhibited no significant differences in yield traits compared with those of WYJ (fig. S5, C to E), which indicates that the *TT3* locus and the genetic modification of *TT3* candidate genes increased thermotolerance without obvious growth and yield penalties.

Next, we evaluated the thermotolerance of NIL-*TT3* at the reproductive stage in the artificial greenhouse with high-temperature treatments. At the heading stage, all leaves and tillers in NIL-$TT3^{CG14}$ plants remained green and alive, whereas those of the NIL-$TT3^{WYJ}$ plants were dried and almost dead (Fig. 2A). The NIL-$TT3^{CG14}$ plants showed a marked increase in seed setting rate and 1000-grain weight and an approximately onefold increase in grain yield per plant compared with that of NIL-$TT3^{WYJ}$ (Fig. 2, B to D). At the grain-filling stage, no significant differences were observed in leaves and tiller status between NIL-$TT3^{WYJ}$ and NIL-$TT3^{CG14}$ (fig. S5F). However, NIL-$TT3^{CG14}$ plants had significantly increased in

[1]National Key Laboratory of Plant Molecular Genetics, CAS Centre for Excellence in Molecular Plant Sciences, Shanghai Institute of Plant Physiology and Ecology, Chinese Academy of Sciences, Shanghai 200032, China. [2]Guangdong Laboratory for Lingnan Modern Agriculture, Guangzhou 510642, China. [3]University of the Chinese Academy of Sciences, Beijing 100049, China. [4]School of Life Science and Technology, ShanghaiTech University, Shanghai 201210, China. [5]Joint Center for Single Cell Biology, School of Agriculture and Biology, Shanghai Jiao Tong University, Shanghai 200240, China.
*Corresponding author. Email: linyoushun@sjtu.edu.cn (Y.L.); hxlin@cemps.ac.cn (H.-X.L.)

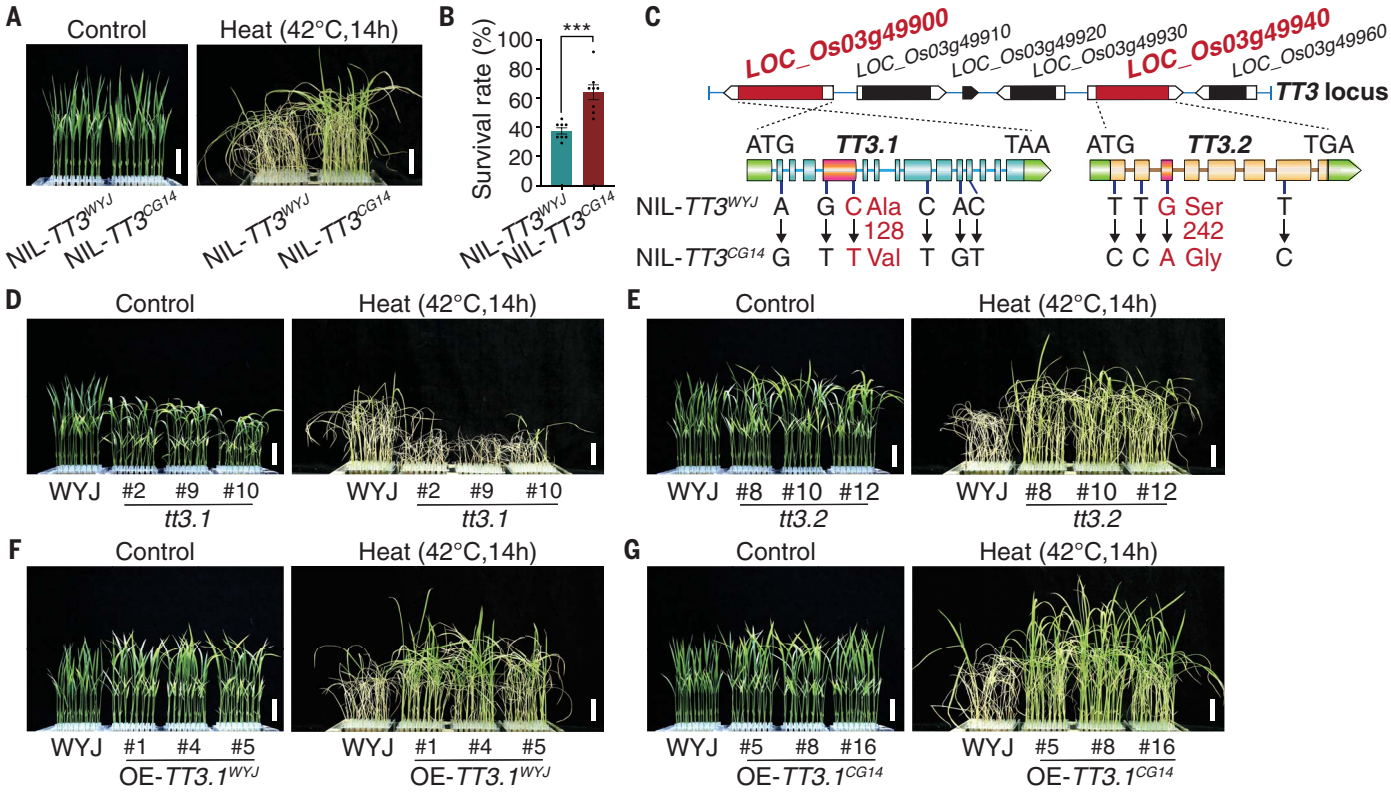

Fig. 1. Identification of *TT3* locus for rice thermotolerance. (**A** and **B**) Photos (A) and survival rate (B) of 12-day-old NIL-*TT3* rice plants under normal (control) or recovery conditions for 7 days after heat stress (42°C, 14 hours). Scale bars, 5 cm. Data are mean ± SEM (n = 8 biological replicates; each replicate is 24 plants). Significant differences were determined by a two-tailed t test. ***P < 0.001. (**C**) *TT3* was localized to a 36.6-kb region that contains six genes. Single-nucleotide mutations and the corresponding amino acid changes in NIL-$TT3^{CG14}$ are shown beneath the schematic illustration of *TT3.1* and *TT3.2* genes; red boxes below indicate the positions of the corresponding amino acid changes. (**D** to **G**) Photos of *tt3.1* mutants (D), *tt3.2* mutants (E), overexpression-$TT3.1^{WYJ}$ (OE-$TT3.1^{WYJ}$) (F), and overexpression-$TT3.1^{CG14}$ (OE-$TT3.1^{CG14}$) (G) transgenic rice plants under normal (control) or recovery conditions for 7 days after heat stress (42°C, 14 hours). Scale bars, 5 cm.

seed setting rate and 1000-grain weight and had an approximately onefold increase in grain yield per plant compared with that of NIL-$TT3^{WYJ}$ (fig. S5, G to I). Field experiments also confirmed that the *TT3* locus improved heat tolerance at the reproductive stage. In field conditions (fig. S5J), no significant differences were observed in phenotypes and average plot yield between NIL-$TT3^{WYJ}$ and NIL-$TT3^{CG14}$ (fig. S5, K and L). However, under high-temperature treatment at the field, with sunlight-heated greenhouses covered with plastic film (fig. S5, M and N), NIL-$TT3^{CG14}$ showed a 20% increase in average plot yield compared with that of NIL-$TT3^{WYJ}$ (fig. S5O). These results further support the notion that the $TT3^{CG14}$ allele has potential for improving heat tolerance.

We also determined the thermotolerance of *TT3* transgenic and mutant lines at the heading stage in the artificial greenhouse and showed that heat treatment had no impact on phenotypes of overexpression-$TT3.1^{CG14}$ and *tt3.2*, whereas in WYJ, leaves were barely green and almost dead (Fig. 2E). Overexpression-$TT3.1^{CG14}$ and *tt3.2* exhibited a significant increase in seed setting rate and 1000-grain weight and 2.6- to 3.8-fold increases in grain yield per plant compared with that of WYJ (Fig. 2, F to H). Under normal conditions, pollen fertility was similar in WYJ, overexpression-$TT3.1^{CG14}$, and *tt3.2* (fig. S5, P and Q), whereas after heat treatment, pollen fertility of overexpression-$TT3.1^{CG14}$ and *tt3.2* was significantly higher than that of WYJ (fig. S5, P and R). Collectively, these results indicated that overexpressing *TT3.1* or knocking out *TT3.2* conferred significant yield increases under heat stress, thus providing the strategies for breeding highly heat-tolerant crops.

Heat stress triggers TT3.1 and TT3.2 translocation to endosomes

TT3.1 was predicted to encode a RING-type E3 ligase with transmembrane domains (fig. S6A). Subcellular localization assays found that TT3.1–green fluorescent protein (GFP) showed plasma membrane localization with cytosolic puncta (Fig. 3A and fig. S6B). To investigate the nature of those puncta, we performed FM4-64 staining in *pTT3.1::TT3.1*-GFP transgenic rice roots, showing that TT3.1-GFP localized to endosomes (fig. S6C), which was confirmed by colocalization with the early [SCAMP1–red fluorescent protein (RFP)] and late endosome markers (ARA7-RFP) in *Nicotiana benthamiana* (fig. S6, D and E). These results suggested that TT3.1 localized to the plasma membrane and endosomes.

TT3.2 was an unknown transmembrane protein that contained a chloroplast transit peptide (fig. S6F). Transient expression assays showed that TT3.2 mainly localized to the chloroplast (Fig. 3B and fig. S6G). We also found a few TT3.2 puncta colocalized with FM4-64–labeled endosomes in *TT3.2*-GFP transgenic rice roots (fig. S6H). Therefore, we speculated that TT3.1 might recruit newly synthesized TT3.2 chloroplast precursors in the cytosol to endosomes. This hypothesis was verified by the colocalization of TT3.1-GFP and TT3.2-mCherry on intracellular puncta, likely to be endosomes (Fig. 3C, left).

We tracked TT3.1 dynamics and found that under normal conditions, TT3.1 largely showed

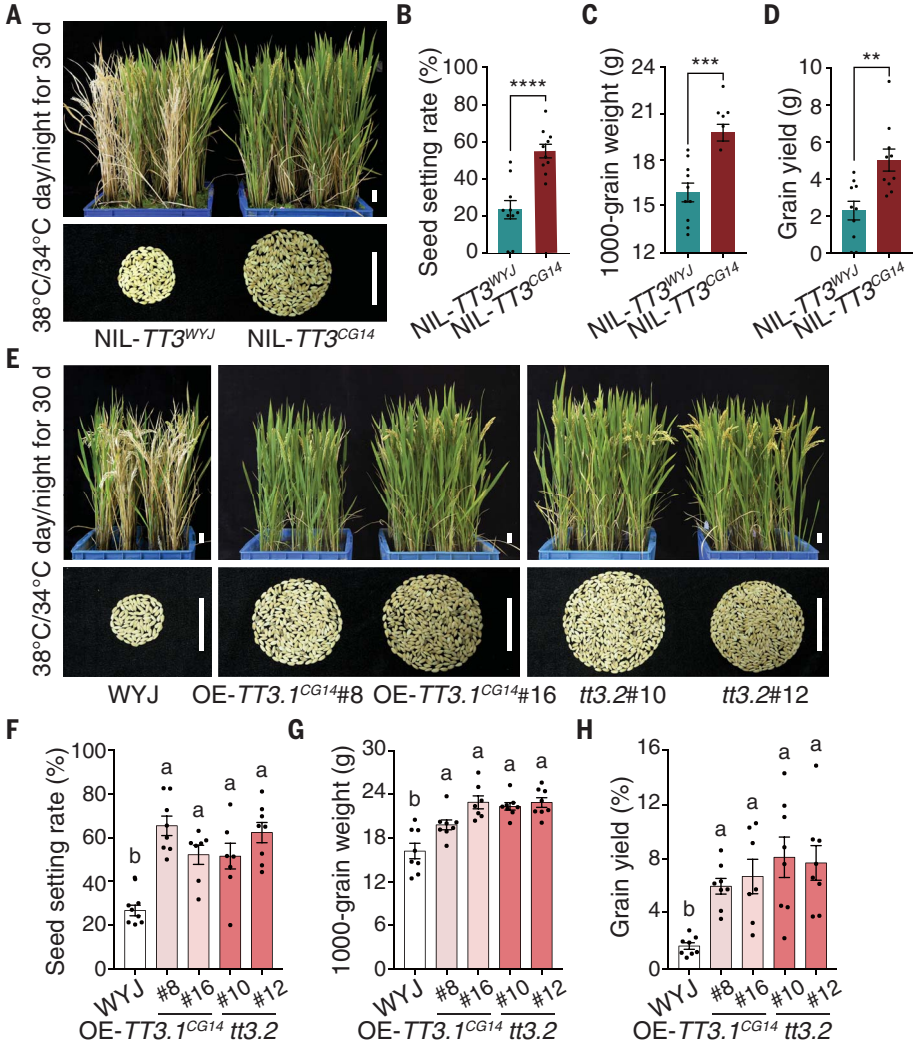

Fig. 2. *TT3* enhances rice thermotolerance at reproductive stages. (**A**) Phenotypes of mature plants and total grains per plant in NIL-*TT3* after 30 days of high-temperature treatment (38° and 34°C, day and night) at the heading stage. Scale bars, 5 cm. (**B** to **D**) Comparison of seed setting rate (B), 1000-grain weight (C), and grain yield per plant (D) between NIL-$TT3^{WYJ}$ and NIL-$TT3^{CG14}$ after 30 days of high-temperature treatment (38° and 34°C, day and night) at heading stage. Data are mean ± SEM (n = 10 plants). Significant differences were determined by a two-tailed t test. $^{**}P < 0.01$, $^{***}P < 0.001$, $^{****}P < 0.0001$. (**E**) Phenotypes of mature plants and total grains per plant in WYJ, overexpression-$TT3.1^{CG14}$, and *tt3.2* mutant plants after 30 days of high-temperature treatment (38° and 34°C, day and night) at the heading stage. Scale bars, 5 cm. (**F** to **H**) Comparison of seed setting rate (F), 1000-grain weight (G), and grain yield per plant (H) between WYJ and transgenic rice plants after 30 days of high-temperature treatment (38° and 34°C, day and night) at heading stage. Data are mean ± SEM (n = 8 plants). Significant differences were determined by one-way analysis of variance with post hoc Dunnett's multiple comparisons test, with different letters at $P < 0.01$.

plasma membrane localization (Fig. 3D, left), whereas under heat stress, TT3.1 translocated from the cell surface into intracellular compartments and eventually lost its plasma membrane localization patterns in *N. benthamiana* (Fig. 3D, middle and right) and in rice (fig. S7). We further investigated the dynamic relationship between TT3.1 and TT3.2 and found that heat treatment promoted the cotranslocation of TT3.1 and TT3.2 to endosomes (Fig. 3C, middle and right). Together, heat stress triggered TT3.1 internalization from the plasma membrane to endosomes to associate with TT3.2.

TT3.1 relocalizes TT3.2 to endosomes under heat stress

We characterized the spatial relationship between TT3.1 and TT3.2 on endosomes at nanometer resolution. Under normal conditions, $TT3.2^{WYJ}$ was observed on the thylakoid membranes and exhibited a similar number of gold particles when compared to $TT3.2^{CG14}$ (fig. S8, A to C). After heat treatment, TT3.2 accumulated on thylakoid membranes of NIL-$TT3^{WYJ}$ (Fig. 4, A and C), whereas few TT3.2 gold particles were detected on thylakoid membranes of NIL-$TT3^{CG14}$ (Fig. 4, B and C). These results implied that TT3.2 localized to the thylakoid membranes and that TT3.2 protein abundance decreased in chloroplasts in NIL-$TT3^{CG14}$ but not in NIL-$TT3^{WYJ}$ upon heat stress.

By contrast, the results of immunogold labeling showed that upon heat stress, TT3.2 was more accumulated on multivesicular endosomes in NIL-$TT3^{CG14}$ than in NIL-$TT3^{WYJ}$ (Fig. 4, D to F). These results suggested that TT3.2 precursor proteins destined to chloroplasts can be selected into multivesicular endosomes by TT3.1 for the vacuolar degradation, and the sorting efficiency was higher in NIL-$TT3^{CG14}$ than in NIL-$TT3^{WYJ}$. Thus, the mature TT3.2 proteins of NIL-$TT3^{CG14}$ accumulated less on thylakoid membranes than those of NIL- $TT3^{WYJ}$ under heat stress.

Plasma membrane– and endosome-localized TT3.1-GFP proteins were also confirmed by transmission electron microscopy imaging (fig. S8, D to I). Furthermore, double immunogold–labeling assays showed that few gold particles of TT3.1 and TT3.2 were observed on multivesicular endosomes under normal conditions (Fig. 4, G and I). However, the numbers of TT3.1 and TT3.2 gold particles were increased on multivesicular endosomes upon heat stress (Fig. 4, H and I), which supports the hypothesis that TT3.1 relocalizes TT3.2 chloroplast precursor protein to multivesicular endosomes under heat stress.

TT3.1 ubiquitinates TT3.2 on endosomes for degradation

We performed in vitro ubiquitination assays to detect the ubiquitin ligase activity of truncated TT3.1 (TT3.1C) (fig. S9A). Polyubiquitination conjugation was observed in TT3.1C–maltose binding protein (MBP)– purified proteins, whereas site mutation of the TT3.1C RING domain (MTT3.1C) abolished the ligase activity (fig. S9, A and B). This result indicated that TT3.1 was a functional E3 ligase, and the ligase activity was dependent on the 441 and 443 amino acids sites of the RING domain.

To test the functional relationship between TT3.1 and TT3.2, we first verified their interactions by yeast two-hybrid (Y2H) assays. $TT3.1^{WYJ}$ and $TT3.2^{WYJ}$ exhibited a strong interaction; unexpectedly, the interaction of $TT3.1^{CG14}$ with $TT3.2^{CG14}$ and that of $TT3.1^{CG14}$ with $TT3.2^{WYJ}$ were weaker than that of $TT3.1^{WYJ}$ with $TT3.2^{WYJ}$ (Fig. 5A). However, site mutations of $TT3.1^{CG14}$ in the ubiquitin functional RING domain ($MTT3.1^{CG14}$) (fig. S9A) restored the strong interaction between $MTT3.1^{CG14}$ and TT3.2 (Fig. 5A). Moreover, the split firefly luciferase complementation assay

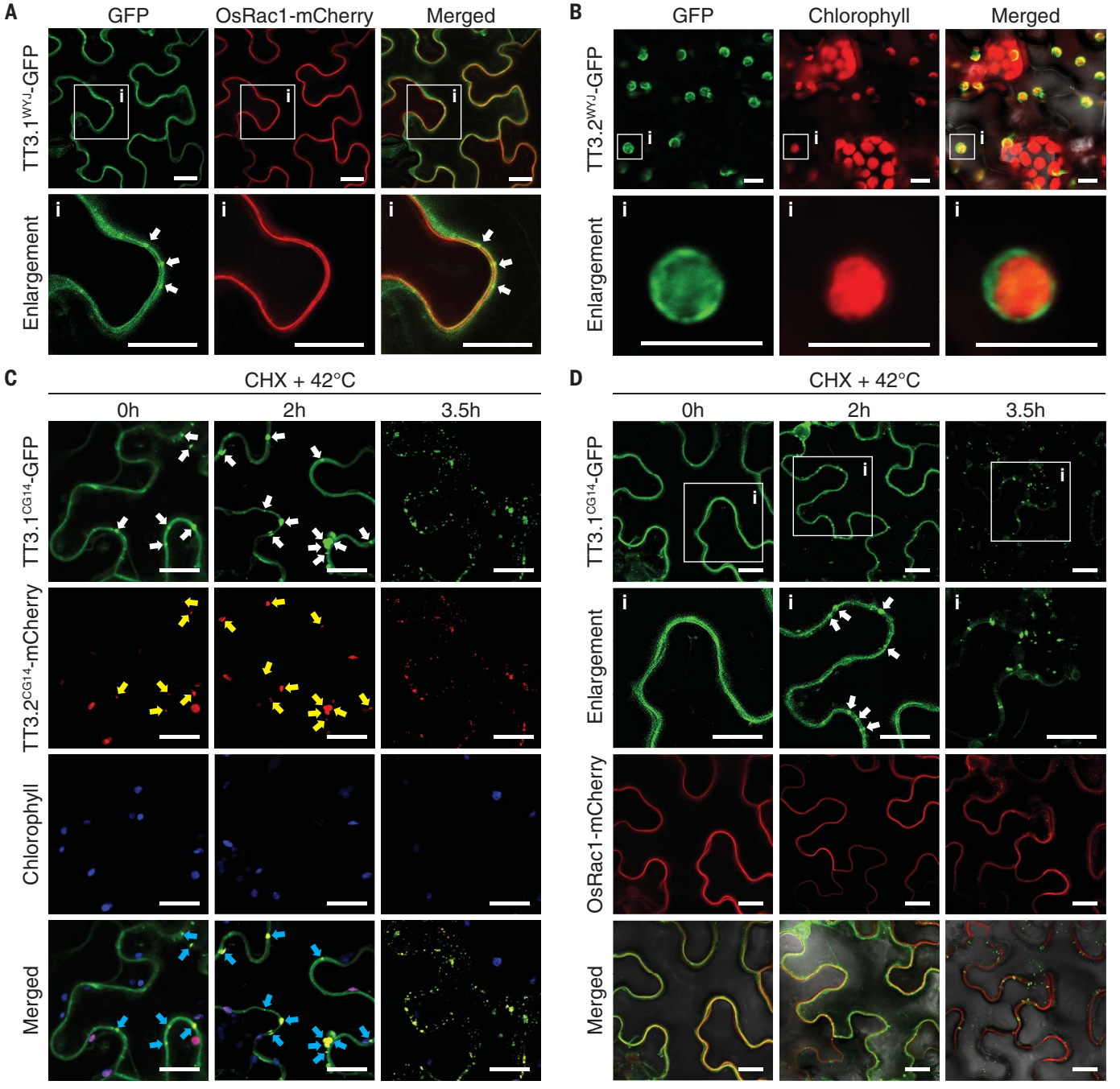

Fig. 3. TT3.1 senses high temperature and internalizes to colocalize with TT3.2. (**A**) Plasma membrane localization of TT3.1-GFP in *N. benthamiana* leaf cells. TT3.1-GFP colocalized with the plasma membrane–localized guanosine triphosphatase OsRac1-mCherry. White arrows indicate the punctate signals of TT3.1-GFP. The rectangle indicates the enlarged part. Scale bars, 20 μm. (**B**) Localization of TT3.2-GFP to the chloroplast. The rectangle indicates the enlarged part. Scale bars, 10 μm. (**C**) Colocalization of TT3.1-GFP and TT3.2-mCherry in *N. benthamiana* leaf cells after high-temperature treatment (42°C for 0, 2, and 3.5 hours) in the presence of cycloheximide (CHX, 50 μM, 2 hours before heat treatment). White arrows indicate the punctate signals of TT3.1-GFP in the cytoplasm; yellow arrows indicate the punctate signals of TT3.2-mCherry; blue arrows indicate the colocalization of TT3.1-GFP and TT3.2-mCherry. Scale bars, 20 μm. (**D**) Localization of TT3.1-GFP after high-temperature treatment (42°C for 0, 2, and 3.5 hours) in the presence of CHX (50 μM, 2 hours before heat treatment). OsRac1-mCherry is a plasma membrane marker. White arrows indicate the punctate signals of TT3.1-GFP in the cytoplasm. The rectangle indicates the enlarged part. Scale bars, 20 μm. Experiments were repeated three times with similar results.

confirmed that TT3.1 interacted with TT3.2 (fig. S9C). We next performed an in vitro ubiquitination assay, which showed that TT3.1C-MBP could polyubiquitinate TT3.2^{WYJ}-Flag and TT3.2^{CG14}-Flag, respectively (fig. S9D). These results demonstrated that TT3.1 targets TT3.2 for polyubiquitination.

We next examined whether TT3.1 determined the degradation of TT3.2 in vivo and found that under heat stress, TT3.1^{CG14} in NIL-*TT3*^{CG14} promoted TT3.2 degradation, whereas the degradation efficiency of TT3.2 declined in the *TT3.1*^{WYJ} background (Fig. 5B). This result indicated that TT3.1^{CG14} had a stronger function for TT3.2 degradation than TT3.1^{WYJ}.

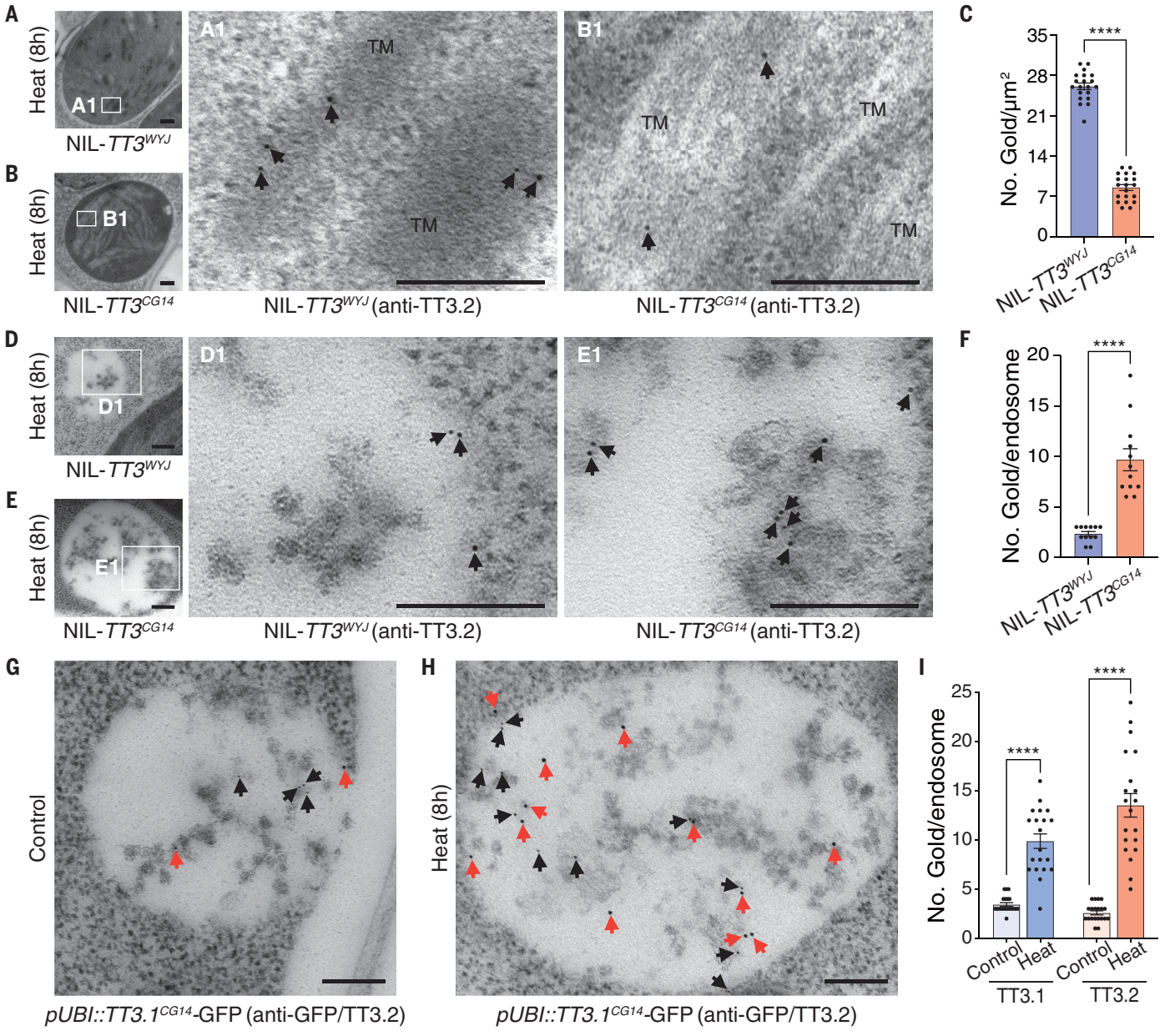

Fig. 4. Heat stress triggers TT3.1 and TT3.2 sorting into multivesicular endosomes. (**A** to **C**) Immunogold electron microscopy with the anti-TT3.2 antibody (raised in rabbit) showing gold particles of TT3.2 localized in thylakoid membranes in chloroplasts of NIL-*TT3*^{WYJ} (A) and NIL-*TT3*^{CG14} (B) leaf cells, and quantitative analysis (C) under heat treatment (42°C for 8 hours). The images with labels A1 and B1 (right) are enlargements of the frames in white (left). The black arrows indicate TT3.2 immunogold particles at the thylakoid membrane (TM). Scale bars, 400 nm in (A) and (B) and 200 nm in (A1) and (B1). Data are mean ± SEM (n = 20 regions; each region is 1 μm^2). Significant differences were determined by a two-tailed t test. ****P < 0.0001. (**D** to **F**) TT3.2 immunogold particles localized to endosomes of NIL-*TT3*^{WYJ} (D) and NIL-*TT3*^{CG14} (E) leaf cells, and quantitative analysis (F) under heat treatment (42°C for 8 hours). Images labeled D1 and E1 (right) are enlargements of the frames in white (left). The black arrows indicate TT3.2 immunogold particles in endosomes. Scale bars, 200 nm. Data are mean ± SEM (n = 12 endosomes). Significant differences were determined by a two-tailed t test. ****P < 0.0001. (**G** to **I**) Immunogold electron microscopy with anti-TT3.2 antibody (raised in rabbit) against TT3.2 (5 nm gold) and anti-GFP antibody (raised in mice) against GFP (10 nm gold), showing gold particles of TT3.2 and TT3.1-GFP localized in endosomes in *pUBI::TT3.1*^{CG14}-GFP transgenic rice plants under control (G) or heat treatment (42°C for 8 hours) (H), and quantitative analysis (I). The black and red arrows indicate TT3.2 and TT3.1-GFP immunogold particles in endosomes, respectively. Scale bars, 200 nm. Data are mean ± SEM (n = 20 endosomes). Significant differences were determined by a two-tailed t test. ****P < 0.0001.

To clarify the degradation pathway of TT3.2, we performed immunoblot assays with drug treatments. In NIL-*TT3*^{CG14}, the degradation rate of TT3.2 remained similar under treatments with cycloheximide and cycloheximide + MG132 (proteasome inhibitor) (Fig. 5C), which suggests that TT3.2 degradation is not mediated by the 26S proteasome pathway. However, treatment with cycloheximide + E64d (vacuolar hydrolases inhibitor) suppressed both TT3.2 degradation (Fig. 5C) and the thermotolerance of NIL-*TT3*^{CG14} (fig. S9E), indicating that the endosome-to-vacuole pathway participated in TT3.2 degradation. Although the tendency of TT3.2 degradation is similar in the *TT3.1*^{WYJ}

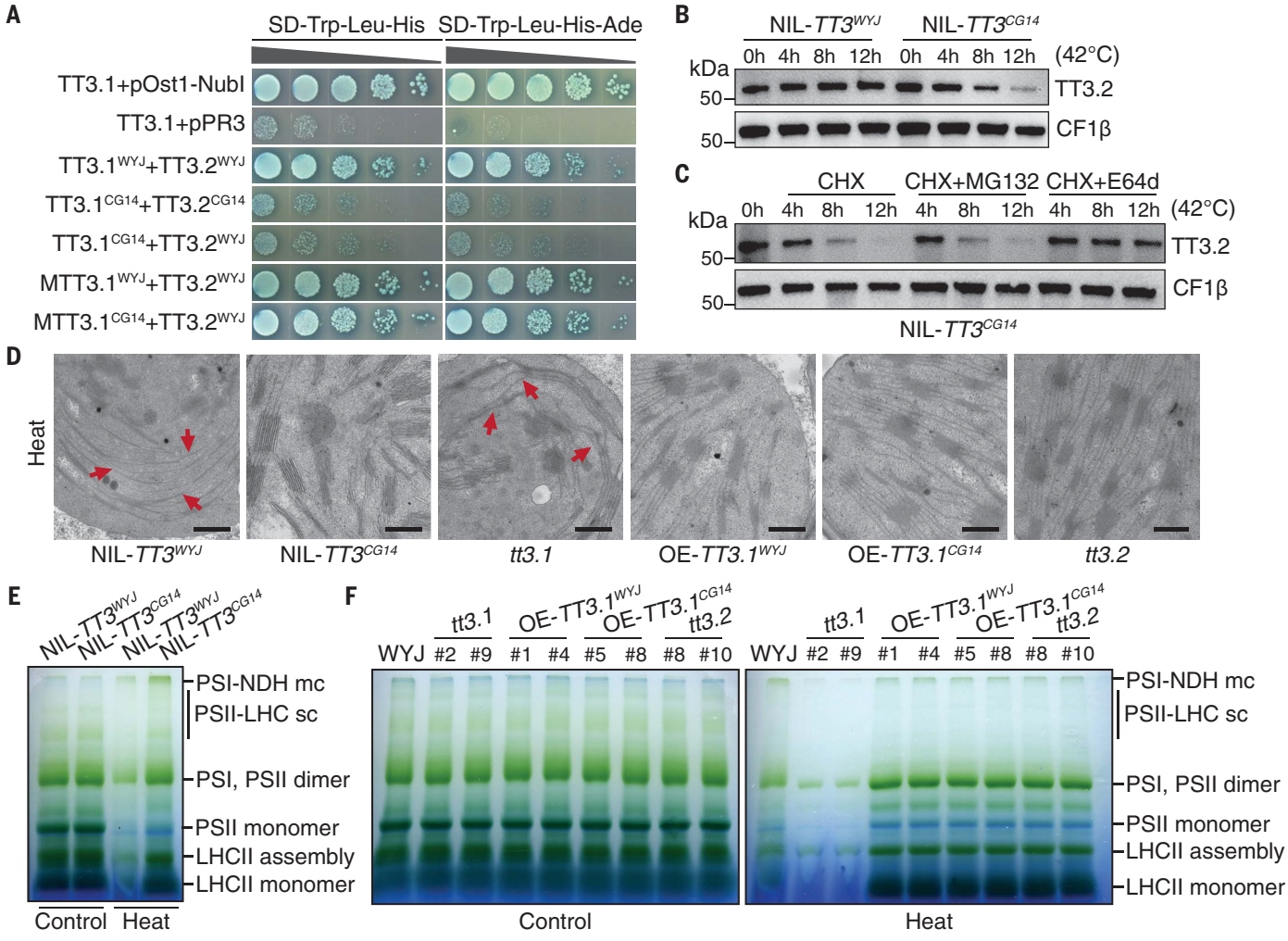

Fig. 5. TT3.1 interacts with TT3.2 for degradation, and overexpression-*TT3.1* and *tt3.2* protect thylakoids. (**A**) Interaction of TT3.1 and TT3.2 in Y2H assay. TT3.1 and MTT3.1 (point mutations of TT3.1) CDSs were cloned into the pBT3-STE vector. TT3.2 CDSs were cloned into the pPR3-N vector. The combination of TT3.1-STE and pOst1-NubI was used as a positive control. The combination of TT3.1-STE and pPR3-N was used as a negative control. Medium contained 15 mM 3-aminotriazole. (**B**) Degradation efficiency of TT3.2 in NIL-*TT3*^{WYJ} and NIL-*TT3*^{CG14} plants upon heat stress (0, 4, 8, and 12 hours). Equal protein loading was confirmed with the anti-CF1β antibody. (**C**) Heat promoted the degradation of TT3.2 via the endosomes-to-vacuole degradation pathway. Twelve-day-old NIL-*TT3*^{CG14} rice seedlings were collected after 42°C heat treatment in the presence of CHX (protein synthesis inhibitor in eukaryotes, 50 μM), CHX with MG132 (proteasome inhibitor, 50 μM), and CHX with E64d (vacuolar hydrolases inhibitor, 50 μM), respectively. TT3.2 protein was confirmed with anti-TT3.2 antibody, and equal protein loading was confirmed with anti-CF1β antibody. (**D**) Transmission electron micrographs of chloroplast ultrastructure from leaves of NIL-*TT3*, *tt3.1* mutant, overexpression-*TT3.1*^{WYJ}, overexpression-*TT3.1*^{CG14}, and *tt3.2* mutant plants after 42°C heat treatment for 14 hours. Red arrows indicate collapsed thylakoids. Scale bars, 400 nm. (**E** and **F**) Blue native–polyacrylamide gel electrophoresis analysis of thylakoid membrane proteins from detached leaves of NIL-*TT3* (E), WYJ, transgenic, and mutant plants (F) under normal growth and heat-stress conditions (42°C, 14 hours). PSI, photosystem I; NDH, [NAD(P)H dehydrogenase]; LHC, light-harvesting complex; mc, megacomplex; sc, supercomplex.

and *TT3.1*^{CG14} backgrounds, the total degradation efficiency is much lower in *TT3.1*^{WYJ} than in *TT3.1*^{CG14} (fig. S9F). In short, TT3.1^{CG14} was more efficient than TT3.1^{WYJ} in promoting TT3.2 degradation via the endosome-to-vacuole pathway.

TT3.2 degradation protects thylakoids against heat-stress damage

To investigate the effect of TT3.2 on chloroplasts, we carried out transmission electron microscopy analysis. Under normal conditions, the chloroplasts in NIL-*TT3*, transgenic, and mutant plants developed normally (fig. S9G). After heat treatment, chloroplasts in NIL-*TT3*^{WYJ} and *tt3.1* mutant were disrupted with distorted and impaired stroma lamellae (Fig. 5D). However, in NIL-*TT3*^{CG14}, overexpression-*TT3.1*^{WYJ}, overexpression-*TT3.1*^{CG14}, and *tt3.2* mutant plants, the thylakoids retained their initial configurations (Fig. 5D). We also found that a similar abundance of photosynthetic protein complexes was observed in NIL-*TT3* (Fig. 5E), WYJ (wild type), transgenic, and mutant plants under normal conditions (Fig. 5F), whereas under heat stress, the abundance of photosynthetic protein complexes was decreased in NIL-*TT3*^{WYJ}, WYJ, and *tt3.1* but remained stable in NIL-*TT3*^{CG14}, overexpression-*TT3.1*^{WYJ}, overexpression-*TT3.1*^{CG14}, and *tt3.2* (Fig. 5, E and F).

We further detected the abundance of core subunits of photosystem II (PSII) (e.g., D1 and D2), showing that D1 and D2 abundance remained similar in NIL-*TT3*^{WYJ} and NIL-*TT3*^{CG14} under normal conditions (fig. S9H). Upon heat stress, D1 and D2 abundance was decreased in NIL-*TT3*^{WYJ} but stabilized in NIL-*TT3*^{CG14} (fig. S9H). Furthermore, the abundance of D1 and D2 was stable in overexpression-*TT3.1*^{WYJ}, overexpression-*TT3.1*^{CG14}, and *tt3.2* but decreased in WYJ and *tt3.1* under heat stress

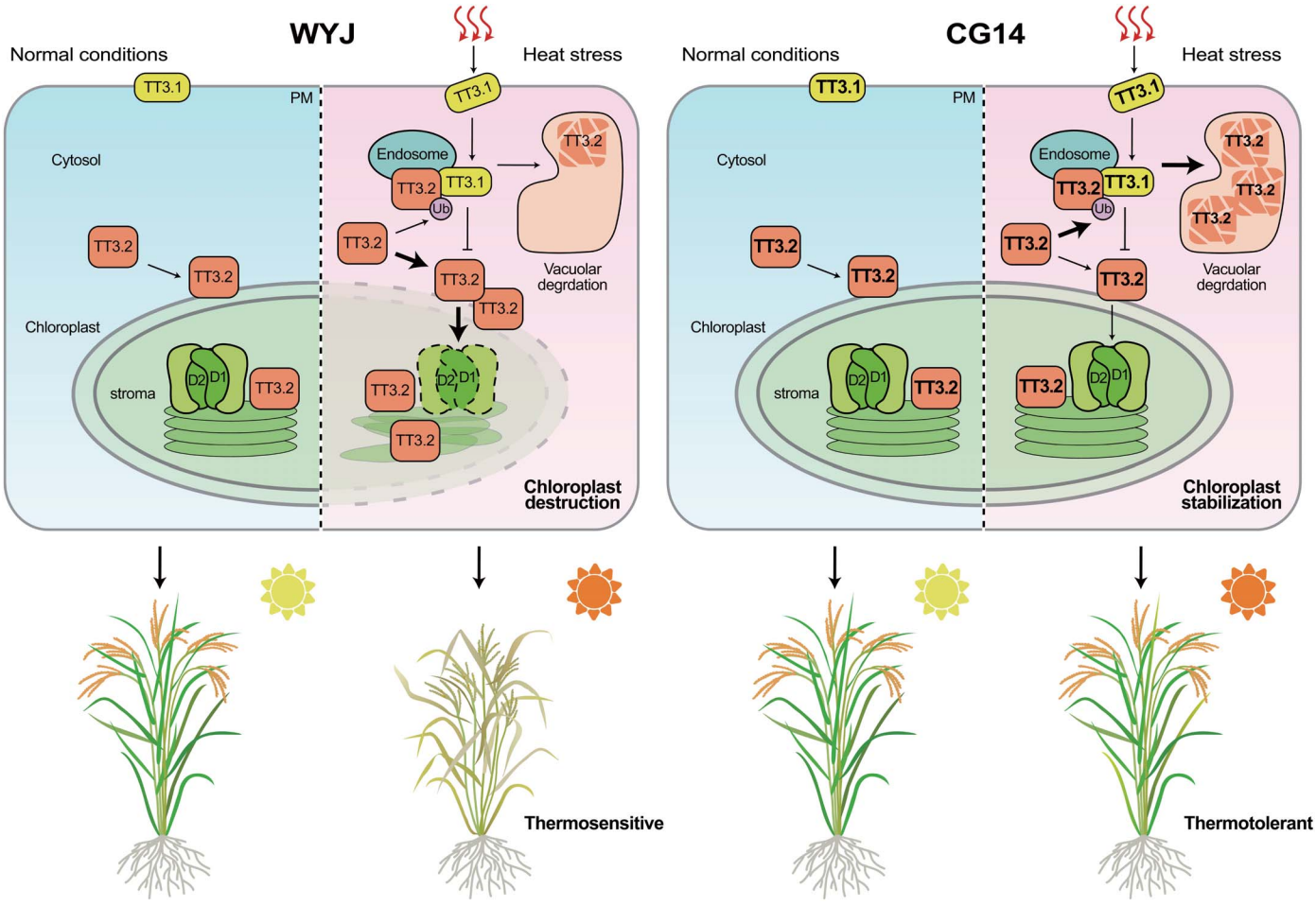

Fig. 6. Proposed model for TT3.1 and TT3.2 function in thermotolerance. Under normal conditions, TT3.1^{WYJ} and TT3.1^{CG14} mainly localize to the plasma membrane; TT3.2^{WYJ} and TT3.2^{CG14} precursor proteins are imported from the cytosol to chloroplasts and do not influence plant growth. Upon heat stress, TT3.1^{CG14} with high ligase activity is sorted into endosomes, where it interacts with TT3.2^{CG14} precursor proteins for ubiquitination, and the latter is delivered to endosomes for vacuolar degradation. Lesser imported TT3.2^{CG14} in chloroplasts avoid the disruption of the PSII complex and thylakoids, thus enhancing thermotolerance and increasing rice productivity (right). By contrast, low ligase activity of TT3.1^{WYJ} results in reduced degradation of TT3.2^{WYJ}. Overaccumulation of TT3.2^{WYJ} in chloroplasts disrupts the PSII complex and thylakoid stability, leading to thermosensitivity with growth inhibition and yield loss (left).

(fig. S9I). Together, these results suggested that the accumulation of chloroplast-localized TT3.2 is detrimental to the PSII complex and thylakoids, and TT3.1 favors maintenance of chloroplast stability by mediating the degradation of the chloroplast precursor protein TT3.2 during heat stress.

Discussion

Thermosensing is the first step in heat-stress responses (*19*–*21*), and the identification of thermosensors is challenging (*22*). In this study, we showed that heat-triggered translocation of TT3.1 from the plasma membrane to endosomes was likely to transduce environmental signals from the cell surface into intracellular organelles. The endosome-localized TT3.1 protein ubiquitinated the TT3.2 chloroplast precursor protein, which was then sorted into endosomes for vacuolar degradation. In the African rice CG14 variety, TT3.1 has high E3 ubiquitin ligase activity to rapidly degrade the TT3.2 chloroplast precursor protein, which can reduce TT3.2-triggered chloroplast damage caused by heat stress, exhibiting high thermotolerance under heat stress (Fig. 6, right). However, in the Asian rice WYJ variety, TT3.1 has low E3 ubiquitin ligase activity, resulting in the accumulation of TT3.2 and consequent destruction of chloroplasts under heat stress, which manifests as a heat-sensitive phenotype (Fig. 6, left). In all, we proposed that TT3.1 might be a potential thermosensor involved in heat-stress responses (*22*). TT3.2 is a chloroplast membrane protein with unknown functions. How TT3.2 accumulation promotes chloroplast damage induced by heat stress is an intriguing question for future research. In addition, we uncovered a mechanism for chloroplast precursor protein degradation mediated by the endosome-to-vacuole pathway upon heat stress.

TT3^{WYJ} (*TT3.1*^{WYJ}/*TT3.2*^{WYJ}) from *temperate japonica* rice conferred a heat-sensitive phenotype, which is related to the distribution of *temperate japonica* rice in temperate and cooler regions (*23*). By contrast, *TT3*^{CG14} (*TT3.1*^{CG14}/*TT3.2*^{CG14}) from African rice contributed a heat-tolerant phenotype, which is related to the distribution of African rice in tropical regions (*24*). Therefore, we speculated that *TT3* was selected as an adaptation to different temperature climates. The *TT3* natural allele or genetic editing of *TT3.1/TT3.2* in rice enhanced heat tolerance and reduced loss of grain yield caused by heat stress. These genes are conserved in other major crops, such as maize and wheat, and are considered to be valuable resources for breeding highly heat stress–tolerant crops.

REFERENCES AND NOTES

1. Y. Ma *et al*., *Cell* **160**, 1209–1221 (2015).
2. Y. Kan *et al*., *Nat. Plants* **8**, 53–67 (2022).
3. Y. Li, X. Li, J. Yang, Y. He, *Nat. Commun.* **11**, 5351 (2020).
4. F. Q. Xu, H. W. Xue, *Plant Cell Environ.* **42**, 2931–2944 (2019).
5. S. K. Cho *et al*., *BMB Rep.* **50**, 393–400 (2017).
6. X. M. Li *et al*., *Nat. Genet.* **47**, 827–833 (2015).
7. X. Wang *et al*., *Dev. Cell* **51**, 222–235.e5 (2019).
8. S. Hu, Y. Ding, C. Zhu, *Front. Plant Sci.* **11**, 375 (2020).
9. Y. Song, L. Feng, M. A. M. Alyafei, A. Jaleel, M. Ren, *Int. J. Mol. Sci.* **22**, 13464 (2021).
10. S. Ji, A. Siegel, S. O. Shan, B. Grimm, P. Wang, *Nat. Plants* **7**, 1420–1432 (2021).
11. L. Zhong *et al*., *Plant Cell* **25**, 2925–2943 (2013).
12. K. E. Gil *et al*., *Plant Cell* **29**, 2882–2894 (2017).
13. P. Paul *et al*., *Genes* **11**, 650 (2020).
14. X. T. Zheng *et al*., *New Phytol.* 10.1111/nph.18121 (2022).
15. Y. N. Tian *et al*., *Mol. Plant* **14**, 1149–1167 (2021).
16. J. D. Woodson, *New Phytol.* **212**, 36–41 (2016).
17. M. S. Otegui, *J. Exp. Bot.* **69**, 741–750 (2018).
18. J. J. Luo, W. Hao, J. Jin, J. P. Gao, H. X. Lin, *Mol. Plant* **1**, 830–838 (2008).
19. J. H. Jung *et al*., *Science* **354**, 886–889 (2016).
20. S. Hayes, J. Schachtschabel, M. Mishkind, T. Munnik, S. A. Arisz, *Plant Cell Environ.* **44**, 2018–2033 (2021).
21. J.-H. Jung *et al*., *Nature* **585**, 256–260 (2020).
22. L. D. Vu, K. Gevaert, I. De Smet, *Trends Plant Sci.* **24**, 210–219 (2019).
23. C. Gardener, S. V. Kumar, *Mol. Plant* **8**, 1439–1441 (2015).
24. M. Wang *et al*., *Nat. Genet.* **46**, 982–988 (2014).

ACKNOWLEDGMENTS

We thank M. Shi for technical supports of transgenic assay; W. J. Cai, S. N. Yin, Z. P. Zhang, X. Y. Gao, J. Q. Li, L. N. Xu, and L. Liu for technical support; F. Q. Guo and Q. H. Ling for suggestions and technical assistance; and Y. G. Liu for the donation of CRISPR/Cas9 plasmids. **Funding:** This work was supported by grants from the National Natural Science Foundation of China (31788103 and 31630052), Chinese Academy of Sciences (XDB27010104, QYZDY-SSW-SMC023, and 159231KYSB20200008), Laboratory of Lingnan Modern Agriculture Project (NT2021002), Shanghai Jiao Tong University (ZXWH3150101/006), CAS-Croucher Funding Scheme for Joint Laboratories, and National Key Laboratory of Plant Molecular Genetics. **Author contributions:** H.-X.L. and Y.L. conceived and supervised the project, and H.-X.L., Y.L., and H.Z. designed the experiments. H.Z. performed most of the experiments. J.-F.Z., Y.K., J.-X.S., W.-W.Y., N.-Q.D., T.G., Y.-H.X., Y.-B.Y., Y.-C.L., H.-Y.Z., H.-X.Y., Z.-Q.L., S.-Q.G., J.-J.L., B.L., X.-R.M., Y.-J.C., J.-J.Y., Y.L., and H.-X.L. performed some of the experiments. H.Z., Y.L., and H.-X.L. analyzed data and wrote the manuscript. **Competing interests:** The authors declare no competing interests. **Data and materials availability:** All data are available in the main text or the supplementary materials. **License information:** Copyright © 2022 the authors, some rights reserved; exclusive licensee American Association for the Advancement of Science. No claim to original US government works. https://www.science.org/about/science-licenses-journal-article-reuse

SUPPLEMENTARY MATERIALS

science.org/doi/10.1126/science.abo5721
Materials and Methods
Figs. S1 to S9
Table S1
References (*25*–*32*)
MDAR Reproducibility Checklist

View/request a protocol for this paper from *Bio-protocol*.

Submitted 11 February 2022; accepted 4 May 2022
10.1126/science.abo5721

REPORT

OIL POLLUTION

Chronic oiling in global oceans

Yanzhu Dong[1,2], Yongxue Liu[1]*, Chuanmin Hu[3], Ian R. MacDonald[4], Yingcheng Lu[5]

Ocean oil slicks can be attributed to natural seepages or to anthropogenic discharges. To date, the global picture of their distribution and relative natural and anthropogenic contributions remains unclear. Here, by analyzing 563,705 Sentinel-1 images from 2014–2019, we provide the first global map of oil slicks and a detailed inventory of static-and-persistent sources (natural seeps, platforms, and pipelines). About 90% of oil slicks were within 160 kilometers of shorelines, with 21 high-density slick belts coinciding well with shipping routes. Quantified by slick area, the proportion of anthropogenic discharges was an order of magnitude greater than natural seepages (94 versus 6%), in contrast to the previous estimate quantified by volume during 1990–1999 (54 versus 46%). Our findings reveal that the present-day anthropogenic contribution to marine oil pollution may have been substantially underestimated.

Ocean oil slicks are microscopically thin and highly transient floating layers of liquid hydrocarbons (*1*). They can seep naturally from seafloor hydrocarbon reservoirs or be intentionally or accidentally discharged from ships, offshore oil/gas infrastructures, and land-based sources (*2*, *3*) (Fig. 1). Oil pollution has been a global concern because of its adverse impacts on marine biology (*4*, *5*) and ecology (*6*, *7*). The indirect consequences, such as the toxicity along the food chain (*4*) and the loss of ecological diversity (*8*–*10*), will persist for a long time and further weaken regional sustainable development capacity (*5*, *11*). A comprehensive investigation of the global oil slick distribution can benefit studies analyzing the environmental and socioeconomic effects and practices that provide crucial knowledge for related authorities and multiple stakeholders to predict trajectories of oil slicks and further implement more effective and informed regulations (*12*, *13*).

Establishing a better understanding of oil slicks on a global scale, including their extent, hotspots, and natural and anthropogenic contributions, is usually compromised because of the extensive areas and tremendous data involved. It is also challenging to locate oil slicks because of their ephemeral and errant nature: Their advection and evolution heavily depend on winds, currents, waves, and other sea conditions (*14*). It is especially acute for accidental human-induced oil slicks occurring at random positions: Only a tiny percentage of these have been recorded, and even fewer cases have come into the sight of research. Likewise, previous estimates of natural seep contributions were variable, from ~10% in the 1980s (*15*) to ~46% in 1990–1999 (*16*, *17*), and dubious—for example, the global extrapolation was based on limited known cases (*16*). In the context of the increasing human impact on the oceans in the present time (*18*), a sound baseline of global oil slicks will be meaningful for protecting the ocean we need for the future we want.

Synthetic aperture radar (SAR) offers an effective means with which to acquire spatially explicit information about oil slicks over a large area, and this method has been widely adopted in oil spill monitoring (*1*, *2*). From all offshore Sentinel-1A/1B SAR images of 2014–2019 (n = 563,705 images), we identified 452,057 locations of oil slicks and extracted their extents (see the materials and methods: SAR data, oil slick extraction; figs. S1 to S3). We detected a cumulative oil slick area of 1.51×10^6 km^2 (more than twice the area of France) in global oceans and established an extensive global oil slick dataset that enables an up-to-date understanding of their distributions and sources. This information allowed us to address the following three questions: Where and at what magnitude did oil slicks occur globally? Where and how frequently did the static and persistent sources seep or leak oil? What proportions did natural seeps and human activities contribute to the total slick area on regional and global scales?

In answering the first question, we used three metrics, distance, zonal, and gridded statistics (see the materials and methods: oil slicks spatial analysis), to demonstrate the spatial pattern of the global oil slicks. Our analysis showed that the spatial distribution of oil slicks was exceptionally uneven in the following ways.

Oil slicks were primarily distributed along the coasts. Approximately 50% of the cumulative oil slick area was observed within 38 km from the coastline, with the peak at 7 km, and ~90% of the slicks were within 160 km (Fig. 2A). When oil slick areas were normalized by the SAR observation areas (purple shadows in Fig. 2A), the slick areas decreased overall with greater distance from the coast. Patterns of source distribution also became clear. The greatest magnitude of platform slicks occured between 20 and 40 km from the coast, whereas natural oil seeps were prevalent within 90 km. These peaks reflect the high frequency of present-day offshore production and seepage zones from the outer continental slope (*2*).

The area of oil slicks varied considerably among different coasts and seas. For the 31 offshore regions (Fig. 2B and fig. S4), >30% of

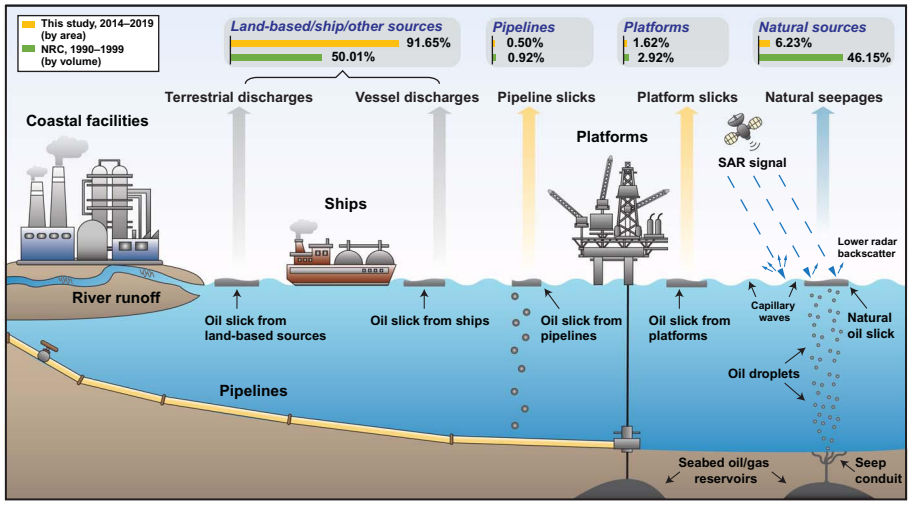

Fig. 1. Oil slicks from different sources entering into the marine environment. The orange bars in the legend refer to the contributions of natural and anthropogenic sources during 2014–2019 derived in this study, and the green bars are those of 1990–1999 estimated by the NRC.

[1]School of Geography and Ocean Science, Nanjing University, Nanjing 210023, China. [2]Collaborative Innovation Center of South China Sea Studies, Nanjing University, Nanjing 210093, China. [3]College of Marine Science, University of South Florida, St. Petersburg, FL 33701, USA. [4]Department of Earth, Ocean, and Atmospheric Science, Florida State University, Tallahassee, FL 32306, USA. [5]International Institute for Earth System Sciences, Nanjing University, Nanjing 210023, China.
*Corresponding author. Email: yongxue@nju.edu.cn

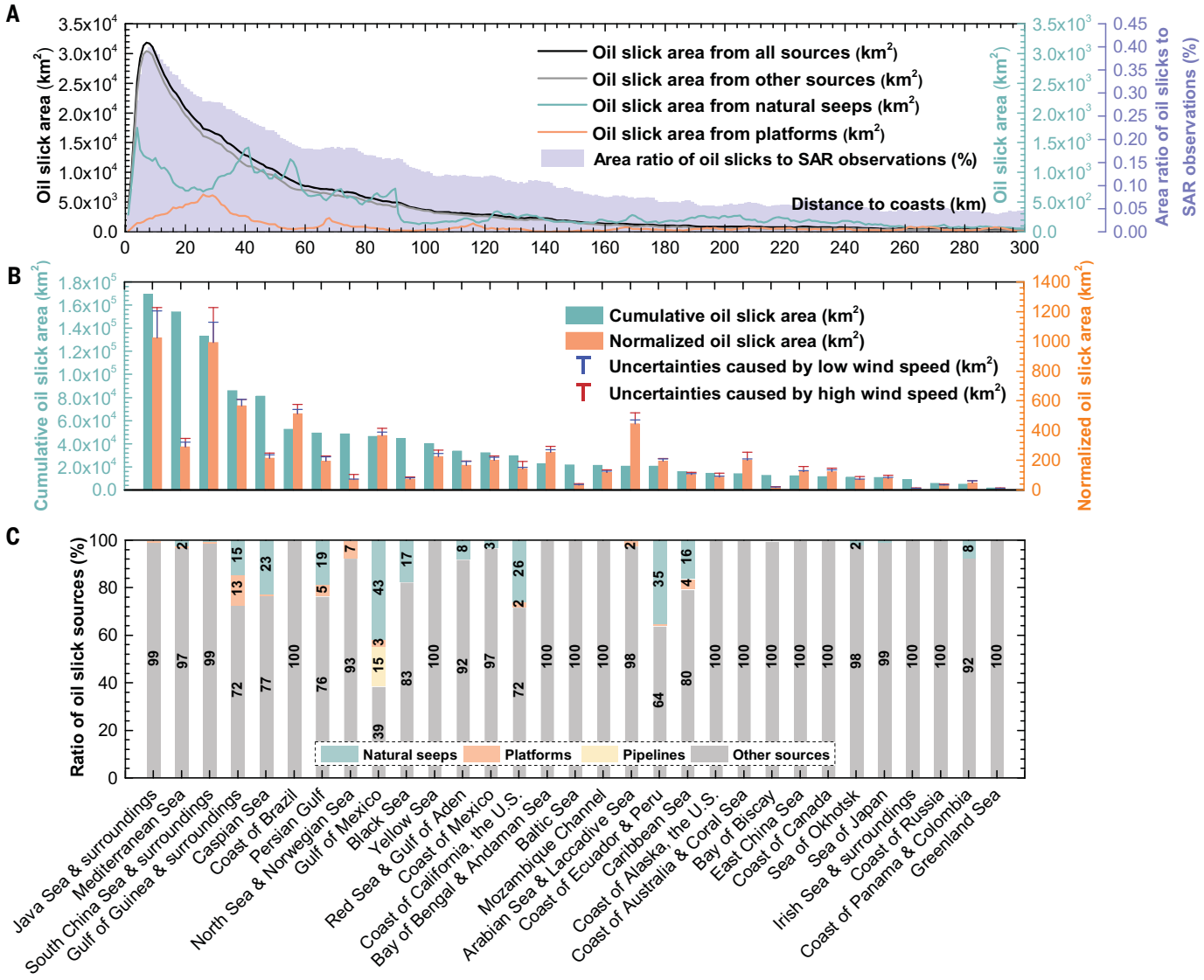
A
Oil slick area (km²)
Oil slick area from all sources (km²)
Oil slick area from other sources (km²)
Oil slick area from natural seeps (km²)
Oil slick area from platforms (km²)
Area ratio of oil slicks to SAR observations (%)
Distance to coasts (km)
Area ratio of oil slicks to SAR observations (%)
B
Cumulative oil slick area (km²)
Normalized oil slick area (km²)
Cumulative oil slick area (km²)
Normalized oil slick area (km²)
Uncertainties caused by low wind speed (km²)
Uncertainties caused by high wind speed (km²)
C
Ratio of oil slick sources (%)
Natural seeps
Platforms
Pipelines
Other sources
Java Sea & surroundings
Mediterranean Sea
South China Sea & surroundings
Gulf of Guinea & surroundings
Caspian Sea
Coast of Brazil
Persian Gulf
North Sea & Norwegian Sea
Gulf of Mexico
Black Sea
Yellow Sea
Red Sea & Gulf of Aden
Coast of Mexico
Coast of California, the U.S.
Bay of Bengal & Andaman Sea
Baltic Sea
Mozambique Channel
Arabian Sea & Laccadive Sea
Coast of Ecuador & Peru
Caribbean Sea
Coast of Alaska, the U.S.
Coast of Australia & Coral Sea
Bay of Biscay
East China Sea
Coast of Canada
Sea of Okhotsk
Sea of Japan
Irish Sea & surroundings
Coast of Russia
Coast of Panama & Colombia
Greenland Sea

Fig. 2. Oil slick statistics (2014–2019). (**A**) Oil slick area histogram by their distances to the coasts (*x*-axis step: 1 km, left *y*-axis: oil slick areas from all sources, right cyan *y*-axis: oil slick areas from natural seeps and platform sources). (**B**) Cumulative and normalized oil slick areas in the 31 regions. Here, "cumulative area" means oil slick areas from all available SAR images, and "normalized" means oil slick areas per full-coverage observation. (**C**) Proportions of the four oil slick sources in these regions.

all oil slicks were found in the Java Sea and surroundings (1.69×10^5 km^2), the Mediterranean Sea (1.54×10^5 km^2), and the South China Sea and surroundings (1.33×10^5 km^2). After normalizing oil slick area per region (see the materials and methods: oil slick spatial analysis), the top three regions were the Java Sea, the South China Sea, and the Gulf of Guinea and surroundings (1.03×10^3, 9.94×10^2, and 5.68×10^2 km^2 per full-coverage observation, respectively). For the Gulf of Mexico, we detected an oil slick area of 367.19 km^2 per full-coverage observation during 2014–2019, ~50% less than previous estimates (*2*), although regions of persistent oil slicks observed were identical. The difference probably results from the higher spatial resolutions of the SAR data used in this study (predominantly 10 m for Sentinel-1 versus the previous 100 to 400 m).

Oil slick footprints showed hotspots globally. Although oil slicks were found widely, the hotspots were primarily located in natural seep zones (such as the Caspian Sea and the Black Sea) and offshore oil and gas development areas (such as the coast of California and the Persian Gulf) (Fig. 3A and fig. S5). Additionally, in the gridded map (0.1° × 0.1° cell size) of oil slicks, 21 distinct high-density belts were visually found to coincide well with shipping routes, even though oil slicks may drift under winds and currents. These included 10 prominent oil pollution belts in the Mediterranean Sea and the Black Sea (Fig. 3B) and 11 other ship-induced oil pollution belts in the Strait of Hormuz, the Bay of Bengal, the Strait of Malacca, the Java Sea, and the Yellow Sea (Fig. 3, C to G). Outside of these belts, we also recognized 82,982 linear oil slicks that were likely from ship discharges, and these slicks and the belts together account for at least 19.8% of the global total. Although the International Convention for the Prevention of Pollution from Ships (MARPOL 73/78) has been in place since 1983 (*19*), the substantial contribution of the ship discharges still suggests the urgent need for more effective international cooperation and informed regulation.

The second question we wanted to address is what are the distribution and occurrence rates of oil slicks from static and persistent sources? The global oil slick footprints during 2014–2019 revealed 586 aggregation centers with recurrent oil slicks (Fig. 4A and table S1).

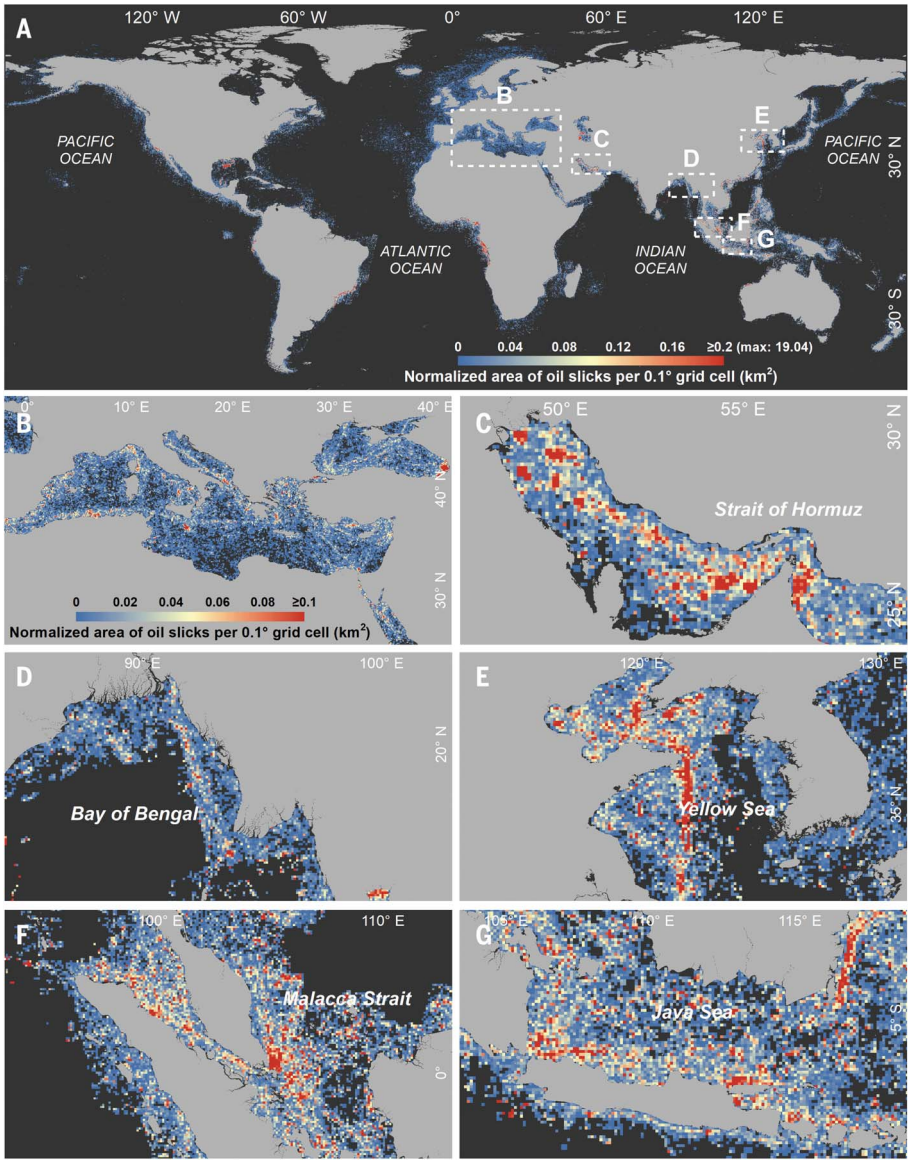

Fig. 3. Global distribution of oil slicks (2014–2019). (**A**) Normalized area of oil slicks in a 0.1° × 0.1° grid representing oil slick area per full-coverage SAR observation. (**B** to **G**) Enlarged views of areas marked by white dashed boxes in (A). High-density belts caused by oil pollution from ships can be observed, and their shape coincides well with the shipping routes over these areas. Color bar is the same for (A) and (C) to (G).

Among them, 14 were related to offshore aquaculture net cages that produced biogenic slicks (fig. S6) and therefore were excluded from further analysis.

Natural seepages from seafloor hydrocarbon reservoirs have long been regarded as a primary source of oil slicks (*17*, *20*), and some hotspots have been analyzed in detail (*2*, *21*, *22*). Here, a total of 435 aggregation centers were recognized as natural seep centers (NSCs) (see the materials and methods: oil slick classification). These NSCs were located within 3.36 to 363.57 km of the shorelines, with water depths ranging from 4 to 5526 m. The Gulf of Mexico had >40% of NSCs (with a total of 176 aggregation centers found) (fig. S7), followed by the Gulf of Guinea (62 centers), the Caspian Sea (43 centers), the coasts of Ecuador and Peru (31 centers), and other areas (figs. S8 to S18). The oil slick detection rate of NSCs varied greatly even in an identical region (Fig. 4, B to L), suggesting complicated controlling factors among natural seeps. On the basis of recurrent detection over time, we discovered that the most active natural seepage rates were in the western Caspian Sea (61.4%) and at the entrance of the Red Sea (59.3%), rather than the Gulf of Mexico (58.6%) or the coast of California (53. 5%), as previously reported (*16*, *23*).

Compared with the last global natural seepage map compiled in the 1970s (containing a total of 190 offshore seepage sites) (*20*), we discovered 245 additional NSCs in global oceans (fig. S19A). Approximately 25% (48 sites) of the previously recorded seepage sites were not identified in our results, mainly in the coastal waters of Alaska, Canada, Argentina, India, Myanmar, Russia, Australia, New Zealand, and the Mozambique Channel. However, considering that the minimum SAR observation over these areas was 138 times, we suspect that the oil seepage rates of these sites may be too intermittent to exhibit recognizable aggregation patterns (fig. S20). Another possible reason is that these seepages may have been misinterpreted because of technical limitations or local environment peculiarities. For example, the 30-year investigation over offshore basins of Australia showed a few natural hydrocarbon seeps (*24*) instead of the five sites reported previously (*20*). Furthermore, taking the Gulf of Mexico and the Lower Congo Basin as examples, we found that ~80% of the seepage locations documented in the previous studies (*2*, *21*) coincide well with our results (fig. S19, B and C).

Oil slicks from the expanding offshore oil and gas development activities (*25*) have been deemed to occur accidentally, and research attention has largely been limited to reported cases or those around damaged or misoperated platforms (*26*–*28*). However, our time-series analyses revealed frequent oil leakages and discharges from offshore infrastructures worldwide. We found that 111 oil slick aggregation centers (recognized as platform slick centers, PSCs) were closely related to energy production platforms (figs. S21 to S27), including one decommissioned platform (fig. S28). The North Sea and the Norwegian Sea contributed nearly a fourth (34 centers) of PSCs, followed by the Gulf of Guinea (33 centers), South China Sea and Java Sea (15 centers), and other regions (Fig. 4A and figs. S7 to S18). The detection rates of PSCs in the North Sea and Norwegian Sea were low to moderate, varying from 0.7% to 11.8%, with a mean value of 4.4% (fig. S14). For comparison, the PSCs in the Gulf of Guinea exhibited a higher mean detection rate of 17.4%, and the highest rate (in the Lower Congo Basin) reached 69.3% (fig. S8). We suggest that the numerous PSCs and the alarming oil slick detection rates in some areas reflect ineffectual or absent marine environmental supervision, where time-series satellite monitoring could play a vital role.

Additionally, 26 aggregation centers were found to be close (mean distance 0.98 km) to pipelines (fig. S29) and were therefore classified as pipeline slick centers (PiSCs). Note that in the northern-central Gulf of Mexico, 18 PiSCs were not far from the known natural

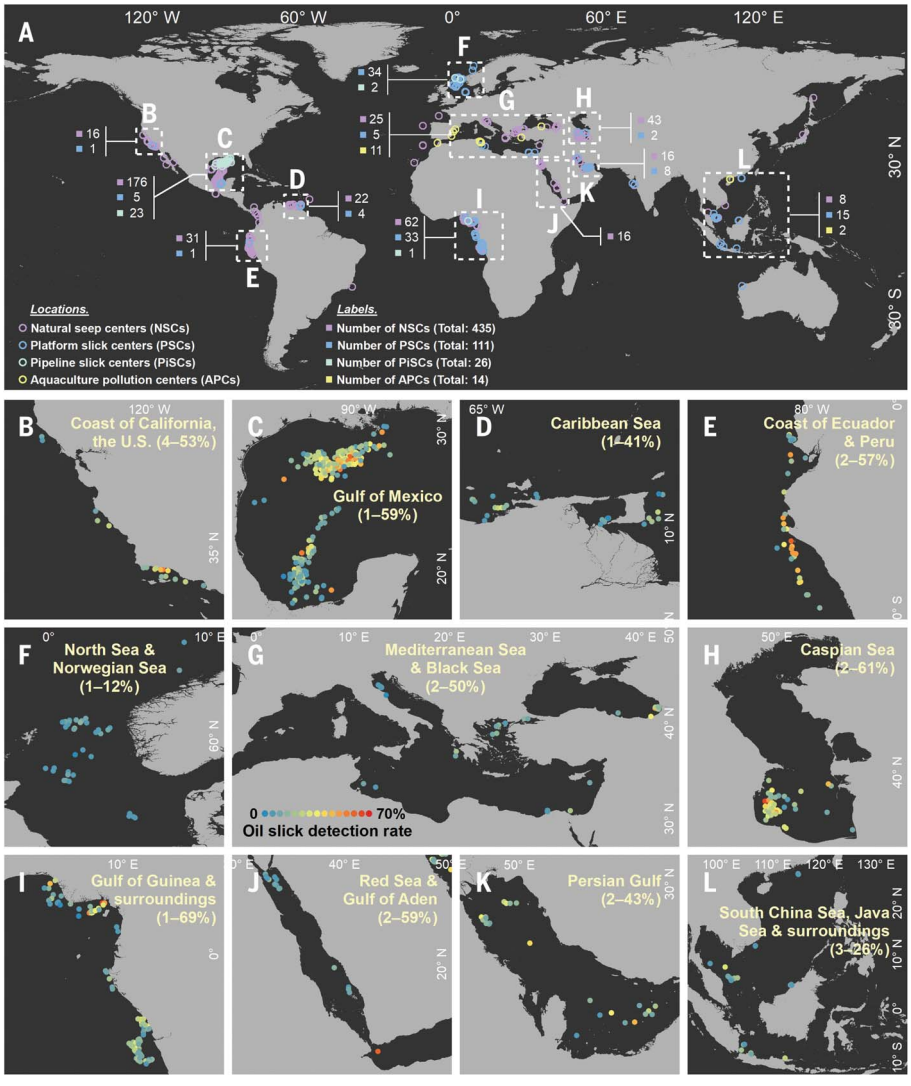
A
120° W
60° W
0°
60° E
120° E
30° N
30° S
Locations.
Natural seep centers (NSCs)
Platform slick centers (PSCs)
Pipeline slick centers (PiSCs)
Aquaculture pollution centers (APCs)
Labels.
Number of NSCs (Total: 435)
Number of PSCs (Total: 111)
Number of PiSCs (Total: 26)
Number of APCs (Total: 14)
B Coast of California, the U.S. (4–53%)
C Gulf of Mexico (1–59%)
D Caribbean Sea (1–41%)
E Coast of Ecuador & Peru (2–57%)
F North Sea & Norwegian Sea (1–12%)
G Mediterranean Sea & Black Sea (2–50%)
H Caspian Sea (2–61%)
I Gulf of Guinea & surroundings (1–69%)
J Red Sea & Gulf of Aden (2–59%)
K Persian Gulf (2–43%)
L South China Sea, Java Sea & surroundings (3–26%)
0
70%
Oil slick detection rate

Fig. 4. Global oil slick aggregation centers. (**A**) Distribution of NSCs, PSCs, PiSCs, and APCs. (**B** to **L**) More detailed views in selected regions. The numbers in the brackets represent the range of detection rates.

seep locations (mean distance 14.23 km) and need further investigation to confirm whether they resulted from pipelines or from natural seeps (see the materials and methods: limitations and uncertainties). Regardless, oil slicks from all PiSCs accounted for only 0.5% of the global total.

To address the third question of what proportions natural and anthropogenic sources contributed to the global total slick area, we classified oil slick origins into four categories: natural seeps, pipelines, platforms, and other anthropogenic sources (ships and land-based discharges). On the global scale, their proportions were 6.2%, 0.5%, 1.6%, and 91.7%, respectively (Fig. 1). At the regional scale, their proportions varied. For example, natural seeps accounted for 43.3% in the Gulf of Mexico, 35.1% off the coast of Ecuador and Peru, and 26.2% off the coast of California (Fig. 2C). Nevertheless, oil slicks from anthropogenic sources dominate global oil slicks at present. Considering each region's diverse area and observation area, we found that the weighted proportion of anthropogenic sources exceeds 98% (see the materials and methods: oil slick classification; fig. S30). Additionally, massive oil spills such as the 2010 Deepwater Horizon oil spill would release much more oil than other spills. No such oil spill disasters occurred during 2014–2019; otherwise, they would result in a higher proportion of anthropogenic sources.

According to the National Research Council (NRC) estimate of 1990–1999 (*16*), natural and anthropogenic sources contributed 46.15% and 53.85% to global oil discharge volume, respectively. Although we discovered more than twice the number of natural seepage sites than that reported previously, their contribution (6.2% in this study) to the global oil slick area is still an order of magnitude lower than the NRC estimate (46.2%). We attribute this to the improved global data and methodology and to the following. First, the NRC estimates were based on several assumptions and global extrapolation, and the three major inputs (natural seeps, land-based, and operational discharges from vessels) had especially high levels of uncertainties (*16*). Second, there were increased discharges from anthropogenic sources in recent years. Our statistics demonstrate that the area of high-confidence oil slicks from ship discharges was at least three times that of natural oil slicks. We attribute this to the expansion of world maritime transportation, the carrying capacity of which has risen by 2.5 times from 2000 to 2019 (fig. S31). Additionally, oil contamination was particularly noteworthy from the coasts of emerging economies (including China, Vietnam, Indonesia, Malaysia, and Brazil), which have contributed ~25% of the global total economic growth during the past two decades (fig. S32). Thus, we argue that the adverse effects of the marine ecosystem's chronic exposure to human-induced oil slicks may have been substantially underestimated. Indeed, exposure to polycyclic aromatic hydrocarbons in concentrations of 1 to 10 μg/liter has been shown to impair cardiac development in larval fishes (*10*); even minor releases of oil may have immediate impacts on marine biota (*5*). In addition, given the nature of oil slicks and SAR data coverage, as well as the various factors influencing their detection accuracies (such as unfavorable wind conditions and detection limit of oil slick size; see the materials and methods: limitations and uncertainties), the estimate of anthropogenic contribution in this study is likely to be conservative. Therefore, the distribution and magnitude of oil slicks from anthropogenic origins, as well as their potential effects on marine ecosystem health, require comprehensive monitoring and research.

Overall, we have established a comprehensive and up-to-date understanding of global oil slicks based on all offshore Sentinel-1 SAR images acquired from 2014 to 2019. Our analysis reveals the highly concentrated distribution of oil slicks in nearshore waters and global hotspots of oil contaminations. Regulation and control of anthropogenic oil slicks are challenging because in many cases we cannot identify the specific pollution event. We also compiled a global inventory of static and persistent sources (both natural and anthropogenic), including their exact locations and oil slick detection rates, which could then be used to help guide future offshore oil and gas exploration and pollution management. The derived oil slick dataset can provide a training set for computer-based deep-learning techniques requiring big data to summarize the paradigm and automatically extract oil slicks. Finally, our results reveal the overwhelming

contributions of anthropogenic oil slicks compared with those from natural seeps that are probably due to increased human activities. Under a changing climate and projected increasing anthropogenic stresses on the health of the ocean ecosystem, the findings of this study will serve as a scientific and normative basis for achieving the Sustainable Development Goal 14 of the United Nations: to conserve and sustainably use the oceans, seas, and marine resources for sustainable development.

REFERENCES AND NOTES

1. I. Leifer *et al*., *Remote Sens. Environ.* **124**, 185–209 (2012).
2. I. R. MacDonald *et al*., *J. Geophys. Res. Oceans* **120**, 8364–8380 (2015).
3. M. K. McNutt *et al*., *Proc. Natl. Acad. Sci. U.S.A.* **109**, 20222–20228 (2012).
4. I. Berenshtein *et al*., *Sci. Adv.* **6**, eaaw8863 (2020).
5. C. P. D. Brussaard *et al*., *Nat. Commun.* **7**, 11206 (2016).
6. C. H. Peterson *et al*., *Science* **302**, 2082–2086 (2003).
7. C. Hu *et al*., *Geophys. Res. Lett.* **38**, 2011GL047184 (2011).
8. B. R. Silliman *et al*., *Proc. Natl. Acad. Sci. U.S.A.* **109**, 11234–11239 (2012).
9. L. A. Henkel *et al*., *Mar. Pollut. Bull.* **79**, 155–163 (2014).
10. J. P. Incardona *et al*., *Proc. Natl. Acad. Sci. U.S.A.* **111**, E1510–E1518 (2014).
11. C. M. Reddy *et al*., *Environ. Sci. Technol.* **36**, 4754–4760 (2002).
12. E. E. Cordes *et al*., *Front. Environ. Sci.* **4**, 58 (2016).
13. X. Li, C. Li, Z. Yang, W. Pichel, *Remote Sens. Environ.* **130**, 182–187 (2013).
14. M. Razaz, D. Di Iorio, B. Wang, S. Daneshgar Asl, A. M. Thurnherr, *Sci. Rep.* **10**, 12654 (2020).
15. National Research Council, *Petroleum in the Marine Environment* (National Academies Press, 1975).
16. National Research Council, *Oil in the Sea III: Inputs, Fates, and Effects* (National Academies Press, 2003).
17. K. A. Kvenvolden, C. K. Cooper, *Geo-Mar. Lett.* **23**, 140–146 (2003).
18. B. S. Halpern *et al*., *Sci. Rep.* **9**, 11609 (2019).
19. International Maritime Organization, "International Convention for the Prevention of Pollution from Ships (MARPOL)" (2021); https://www.imo.org/en/About/Conventions/Pages/International-Convention-for-the-Prevention-of-Pollution-from-Ships-(MARPOL).aspx.
20. R. D. Wilson, P. H. Monaghan, A. Osanik, L. C. Price, M. A. Rogers, *Science* **184**, 857–865 (1974).
21. R. Jatiault, D. Dhont, L. Loncke, D. Dubucq, *Remote Sens. Environ.* **191**, 258–272 (2017).
22. C. Hu, X. Li, W. G. Pichel, F. E. Muller-Karger, *Geophys. Res. Lett.* **36**, L01604 (2009).
23. J. S. Hornafius, D. Quigley, B. P. Luyendyk, *J. Geophys. Res.* **104** (C9), 20703–20711 (1999).
24. G. A. Logan, A. T. Jones, J. M. Kennard, G. J. Ryan, N. Rollet, *Mar. Pet. Geol.* **27**, 26–45 (2010).
25. Y. Liu *et al*., *Remote Sens. Environ.* **222**, 244–266 (2019).
26. S. Daneshgar Asl, J. Amos, P. Woods, O. Garcia-Pineda, I. R. MacDonald, *Deep Sea Res. Part II Top. Stud. Oceanogr.* **129**, 187–195 (2016).
27. C. Hu *et al*., *Eos* **84**, 313–319 (2003).
28. M. Silva *et al*., *Front. Earth Sci.* **10**, 833661 (2022).

ACKNOWLEDGMENTS

We thank the Google Earth Engine (GEE) for providing Sentinel-1 SAR GRD data and the online computation and all of the data providers listed in table S2 for their continuous efforts and data sharing. **Funding:** This work was supported by the Key Research and Development Program of China (grant no. 2016YFB0501502). **Author contributions:** Conceptualization: Y.L., C.H.; Funding acquisition: Y.L.; Investigation: Y.D.; Methodology: Y.D., Y.L., C.H., I.R.M., Y.L.; Project administration: Y.L.; Supervision: Y.L.; Visualization: Y.D.; Writing: Y.D., Y.L., C.H., I.R.M., Y.L. **Competing interests:** The authors declare no competing interests. **Data and materials availability:** All data are available in the main text or the supplemental materials. **License information:** Copyright © 2022 the authors, some rights reserved; exclusive licensee American Association for the Advancement of Science. No claim to original US government works. https://www.science.org/about/science-licenses-journal-article-reuse

SUPPLEMENTARY MATERIALS

science.org/doi/10.1126/science.abm5940
Materials and Methods
Figs. S1 to S46
Tables S1 to S6
References (*29*–*43*)

Submitted 12 October 2021; accepted 29 April 2022
10.1126/science.abm5940

QUANTUM GASES

Spin-charge separation in a one-dimensional Fermi gas with tunable interactions

Ruwan Senaratne[1]†, Danyel Cavazos-Cavazos[1]†, Sheng Wang[2,3], Feng He[3,4], Ya-Ting Chang[1], Aashish Kafle[1], Han Pu[1], Xi-Wen Guan[2,5]*, Randall G. Hulet[1]*

Ultracold atoms confined to periodic potentials have proven to be a powerful tool for quantum simulation of complex many-body systems. We confine fermions to one dimension to realize the Tomonaga-Luttinger liquid model, which describes the highly collective nature of their low-energy excitations. We use Bragg spectroscopy to directly excite either the spin or charge waves for various strengths of repulsive interaction. We observe that the velocity of the spin and charge excitations shift in opposite directions with increasing interaction, a hallmark of spin-charge separation. The excitation spectra are in quantitative agreement with the exact solution of the Yang-Gaudin model and the Tomonaga-Luttinger liquid theory. Furthermore, we identify effects of nonlinear corrections to this theory that arise from band curvature and back-scattering.

Unlike three-dimensional (3D) metals whose low-energy excitations are fermionic quasiparticles, the low-energy excitations of 1D fermions are collective bosonic spin- and charge-density waves (SDWs and CDWs) that disperse linearly, as described by the Tomonaga-Luttinger liquid (TLL) theory (*1*–*5*). Notably, the SDWs and the CDWs of an interacting 1D Fermi gas propagate at different speeds, causing a spatial separation of the spin and charge excitations in the gas.

Spin-charge separation has been studied in quasi-1D solid-state materials in several ground-breaking experiments that used either momentum-resolved tunneling to determine the dispersions (*6*–*8*) or angle-resolved photoemission spectroscopy (*9*–*11*). Although these experiments observe splitting into spin and charge excitations, a quantitative analysis of these data has proved challenging because of the complexity of the electronic structure and the unavoidable presence of impurities and defects. Recently, a series of experiments with ultracold atoms in an optical lattice was performed on a single-site resolved 1D Hubbard chain, leading to the observation of the fractionalization of spin and charge quantum numbers at equilibrium (*12*), the modification of the SDW wave vector by density doping and by spin polarization (*13*), and the study of simultaneous spin and charge dynamics outside the Luttinger liquid regime that result from a deconfinement-induced quench (*14*). These experiments demonstrated the ability to perform quantum simulation of interacting fermions in one dimension with unprecedented control in cold-atom systems, but they did not measure the collective low-energy excitation spectrum inherent to spin-charge separation.

The excitation spectrum of the charge (density) mode of fermionic atoms confined to quasi-1D tubes has been previously measured for fixed (*15*) and variable interaction strengths (*16*). These experiments used two-photon stimulated Bragg spectroscopy (Fig. 1, A and B) to impart an observable momentum $\hbar q$, with energy $\hbar\omega$, while keeping the internal state of the atom unchanged (*17*–*20*) ($\hbar$ is the reduced Planck's constant). The response of the 1D gas at a particular q and ω is related to the dynamic structure factor (DSF) $S(q, \omega)$, which characterizes the low-energy excitation spectrum for $q \ll k_F$, where k_F is the Fermi wave vector. In our previous work the charge-mode structure factor $S_c(q, \omega)$ was measured and quantitatively compared with theory with good results (*16*). Measurement of the spin-wave spectrum $S_s(q, \omega)$ remained out of reach because, without appropriate modifications, such a measurement induces single-photon scattering events that produce substantial atom loss.

We have developed improvements to our implementation of Bragg spectroscopy to reduce spontaneous scattering to an acceptable

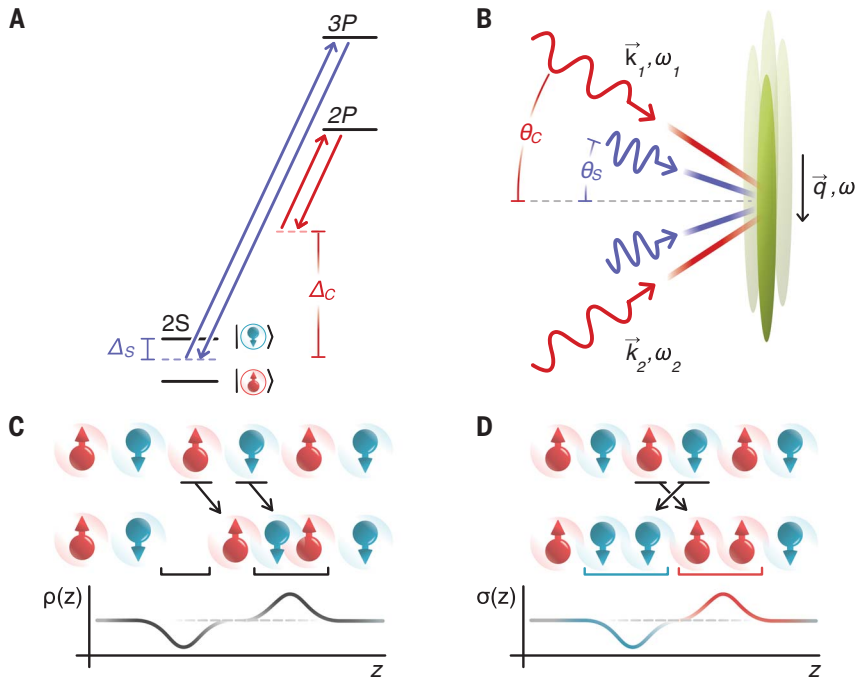

Fig. 1. Spin and charge excitations from Bragg spectroscopy. (**A**) Partial energy-level diagram of ^{6}Li showing relevant transitions and laser detunings for spin (Δ_s, violet) and charge (Δ_c, red) excitations. (**B**) Relative orientation ($\theta_{c,s}$) of each Bragg beam (1 and 2) with respect to the axis perpendicular to the 1D tube direction. A momentum transfer $\vec{q} = \vec{k}_1 - \vec{k}_2 \approx 0.2\, k_F$ for the central tubes is delivered to the sample for a given relative detuning $\omega = \omega_1 - \omega_2$ between the beams. (**C** and **D**) Diagram of the charge and spin excitations, showing an excitation of (C) a particle-hole pair and (D) a spinon pair. The effect on the total density $\rho(z)$ and spin density $\sigma(z)$ is shown for each case at the bottom. The excitations are depicted, for clarity, as starting from a classical zero-temperature antiferromagnetic ground state in the strongly repulsive regime.

[1]Department of Physics and Astronomy, Rice University, Houston, TX 77005, USA. [2]State Key Laboratory of Magnetic Resonance and Atomic and Molecular Physics, Wuhan Institute of Physics and Mathematics, APM, Chinese Academy of Sciences, Wuhan 430071, China. [3]University of Chinese Academy of Sciences, Beijing 100049, China. [4]International School for Advanced Studies (SISSA) and National Institute of Nuclear Physics (INFN), Sezione di Trieste, 34136 Trieste, Italy. [5]Department of Theoretical Physics, RSPE, Australian National University, Canberra, ACT 0200, Australia.
*Corresponding author. Email: randy@rice.edu (R.G.H.); xiwen.guan@anu.edu.au (X.-W.G.)
†These authors contributed equally to this work.

level while selectively exciting either the SDW or the CDW with tunable repulsive interactions. The measurements are compared with the TLL theory, which describes the low-energy excitations of the more general Yang-Gaudin model of a spin-1/2, 1D Fermi gas with repulsive delta-function interactions in the continuum limit (*21*, *22*). They provide a quantitative test of spin-charge separation in the Luttinger liquid regime. Additionally, we quantitatively show that our results for $S_s(q, \omega)$ provide evidence for deviations from the linear TLL theory caused by low-energy back-scattering interactions, which are usually neglected to obtain a linear spin-mode dispersion (*5*).

Bragg spectroscopy is well suited to studying spin-charge separation because the CDW or SDW may be isolated by the choice of detuning of the Bragg beams from resonance with an electronic excited state (Fig. 1). The detuning determines the sign of the light-shift potential, which can be used to create a symmetrical light shift that exclusively excites charge waves or an asymmetrical potential that only excites spin waves. For a system composed of a balanced mixture of two spin components (↑, ↓) we can identify two independent contributions to the DSF, $S_{\uparrow\uparrow}$ and $S_{\uparrow\downarrow}$, and thus define a charge- and spin-density DSF given by (*5*)

$$S_{c,s}(q,\omega) \equiv 2\left[S_{\uparrow\uparrow}(q,\omega) \pm S_{\uparrow\downarrow}(q,\omega)\right]$$

where the "+" sign corresponds to charge and the "–" sign corresponds to spin. At zero temperature, the momentum transfer to the system from the Bragg beams is given by (*20*, *23*)

$$P(q,\omega) \propto \left(\frac{1}{\Delta_\uparrow^2} + \frac{1}{\Delta_\downarrow^2}\right) S_{\uparrow\uparrow} + \frac{2}{\Delta_\uparrow \Delta_\downarrow} S_{\uparrow\downarrow}$$

where Δ_σ is the relative detuning of the Bragg beam from the excited state with respect to each ground spin state σ. If the condition $\Delta_\uparrow \approx \Delta_\downarrow \gg \Delta_{\uparrow\downarrow}$ is satisfied, where $\Delta_{\uparrow\downarrow}$ is the splitting of the spin states, then $P(q, \omega) \propto S_c(q, \omega)$ and a CDW is excited, as depicted in Fig. 1C. On the other hand, if $\Delta_\uparrow = -\Delta_\downarrow = |\Delta_{\uparrow\downarrow}|/2$, then $P(q, \omega) \propto S_s(q, \omega)$ and an SDW is excited, as depicted in Fig. 1D. The detuning required for measuring $S_s(q, \omega)$ is thus fixed by $\Delta_{\uparrow\downarrow}$, unlike in the case for measuring $S_c(q, \omega)$, where, in principle, the detuning may be arbitrarily large. In the finite temperature case, a reverse Bragg process must also be considered, for which the momentum transfer is modified as $P(q, \omega) \propto S(q, \omega) - S(-q, -\omega) = S(q, \omega)[1 - \exp(-\hbar\omega/k_B T)]$ (*24*, *25*), where k_B is the Boltzmann constant.

To reduce spontaneous scattering during the Bragg measurement, the ratio of $\Delta_{\uparrow\downarrow}$ to Γ, the linewidth of the transition, must be increased. We approximately doubled $\Delta_{\uparrow\downarrow}$ by choosing $|1\rangle$ and $|3\rangle$ as our pseudo–spin-1/2 states, rather than $|1\rangle$ and $|2\rangle$ as used previously (states $|1\rangle$, $|2\rangle$, and $|3\rangle$ are the three lowest hyperfine states of ^{6}Li) (*16*, *19*). For the excitation of the SDW, we took the additional step of reducing Γ by detuning the Bragg beams from the $3P_{3/2}$ excited state at a wavelength of 323 nm, rather than the usual 671-nm transition to the $2P_{3/2}$ state that we use to excite the CDW (see Fig. 1A). The spontaneous-decay linewidth of the ultraviolet transition is nearly eight times smaller than that for the red transition (*26*). We compensate for the difference in wavelength by simply adjusting the angle between the Bragg beams ($\theta_c \simeq 4.5°$ and $\theta_s \simeq 2.2°$; see Fig. 1B), such that for both cases, the Bragg wave vector is parallel to the tube axis and has a magnitude $|\vec{q}| = 1.47\ \mu m^{-1}$, corresponding to $0.2k_F$ for a peak-occupancy tube. Thus, the net effect of this change is to further reduce the rate of incoherent scattering. The combination of these two steps reduces the spontaneous scattering by more than a 10-fold factor for a given Bragg coupling, as compared with (*16*), and is sufficient to measure $S_s(q, \omega)$.

A more detailed description of our experimental methods may be found in the supplementary materials (*27*). We prepare a spin-balanced mixture of ^{6}Li atoms in the two energetically lowest hyperfine sublevels, states $|1\rangle$ and $|2\rangle$, and confine them in an isotropic optical trap. We evaporatively cool the atoms to a temperature $T \approx 0.1T_F$, where T_F is the Fermi temperature. We create an effectively 1D system that realizes the Yang-Gaudin model by loading the atoms into a 2D optical lattice with depth of $15E_r$, where E_r is the recoil energy of a lattice photon of wavelength 1.064 μm. The resulting trap configuration is an array of quasi-1D tubes that are elongated in the axial dimension with an aspect ratio of ~170.

The number of atoms per tube is nonuniform across the ensemble of tubes because of the Gaussian curvature of the optical beams.

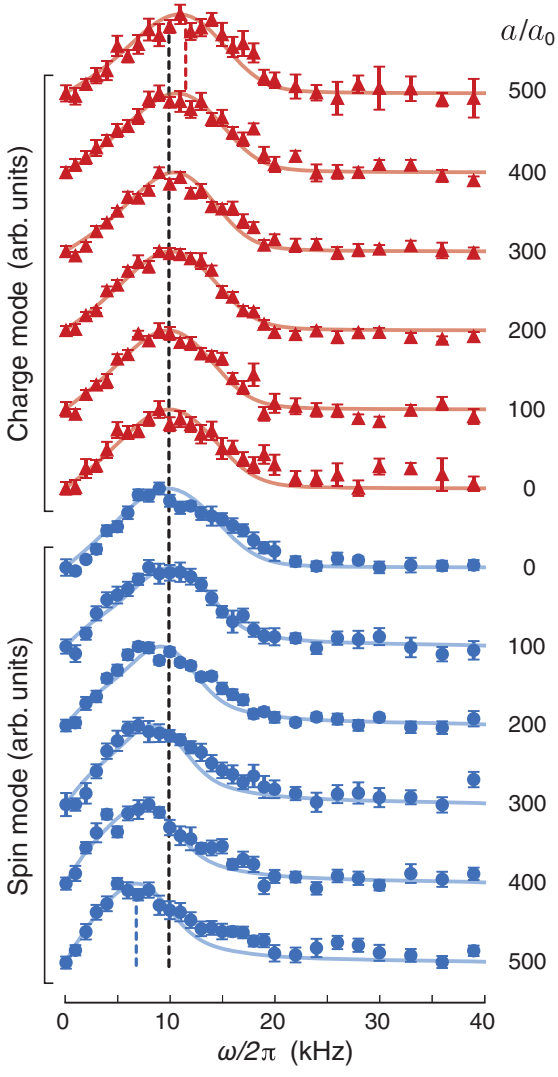

Fig. 2. Bragg spectra. Normalized Bragg signals related to $S_c(q, \omega)$ (red triangles) and $S_s(q, \omega)$ (blue circles) for the range of 3D scattering length a from 0 to $500a_0$. Each data point is the average of at least 20 separate experimental shots. Error bars represent standard error, obtained by bootstrapping (*40*). Vertical dashed lines show the extracted peak frequency ω_p for the noninteracting case (black) and the strongest probed interactions for the spin and charge modes (blue and red, respectively). Solid lines are the calculated Bragg spectra for a global temperature T = 250 nK with no additional fitting parameters other than overall scaling. Theory includes the nonlinear effects of band curvature in the charge mode and back-scattering in the spin mode (for linear theory, see figs. S7 and S8). Deviations from theory at high frequency may be due to unaccounted-for corrections of order q^3.

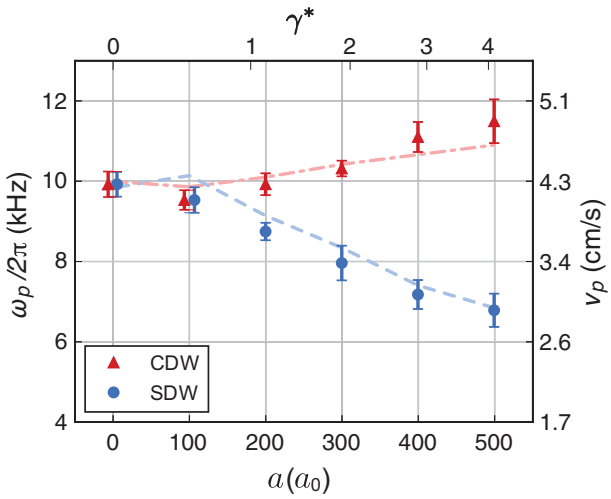

Fig. 3. Spin-charge separation. Peaks of measured Bragg spectra for charge (red triangles) and spin (blue circles) configurations for a ranging from 0 to 500a_0. Peak frequency values were determined through fits of a parabolic function to the data points above 50% of the maximum measured value, and error bars are statistical standard errors of the relevant fit parameters. The corresponding speed of sound $v_p = \omega_p/q$ is given by the right axis. The upper horizontal axis gives the interaction strength in terms of the Lieb-Liniger parameter γ*, evaluated at the center of a tube with an occupancy of 30 atoms. Lines show the calculated values for ω_p for the charge and spin modes (dash-dotted red and dashed blue lines, respectively). Symbols for a = 0 and 100a_0 have been slightly displaced horizontally from one another for clarity. Nonmonotonicity in the charge-mode data and theory at low interaction is caused by small residual differences in the number profiles prepared at different interaction strengths. Nonmonotonicity in the spin-mode theory is likely a consequence of neglecting the effects of band curvature, a q^3 correction.

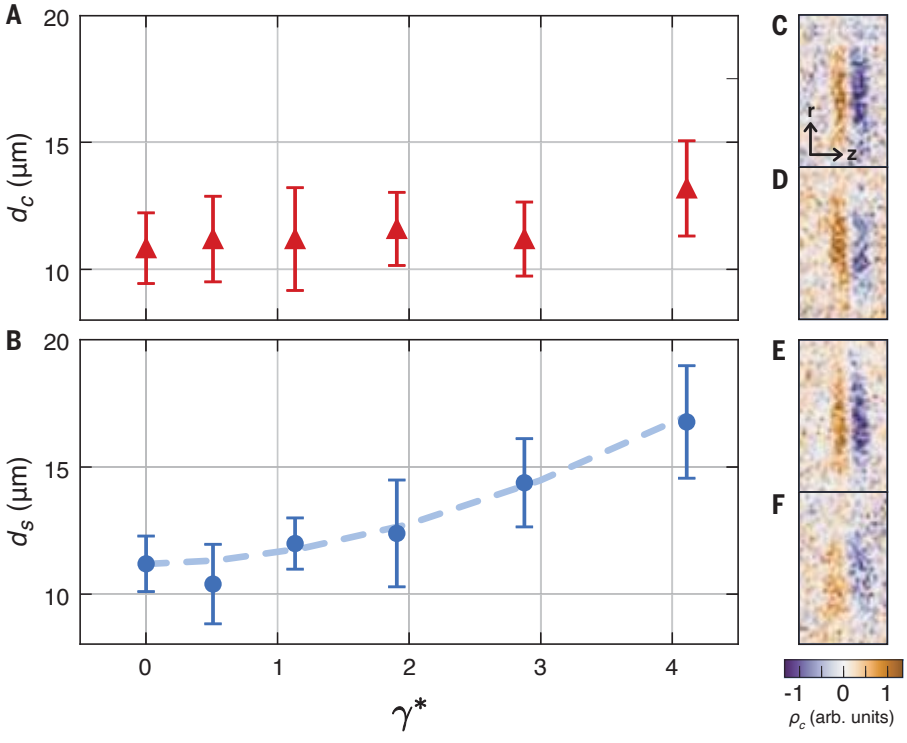

Fig. 4. Dispersion of SDWs and CDWs. (**A** and **B**) The $1/e^2$ axial width of outcoupled atoms after a Bragg pulse and 150-μs time of flight for (A) charge (d_c, red triangles) and (B) spin (d_s, blue circles) excitations, with a ranging from 0 to 500a_0. The widths are the Gaussian fits to the positive outcoupled signal at ω_p. Error bars are standard errors determined by bootstrapping for at least 20 independent images (*40*). The horizontal axis gives the Lieb-Liniger parameter γ* calculated for a median tube occupancy of 30 atoms (*27*). The blue dashed line shows an estimation for d_s derived from the finite lifetime of the spin bosons. (**C** to **F**) Representative samples of column-density (ρ_c) images of the atom cloud after the Bragg pulse and time of flight. Shown are the charge-mode excitations with (C) a = 0 and (D) a = 500a_0, and the spin-mode excitations with (E) a = 0 and (F) a = 500a_0. Each frame corresponds to 40 μm by 65 μm.

The number distribution from tube to tube is also dependent on interaction strength; the central tube occupancy is highest for a noninteracting gas and decreases as repulsive interactions increase. We actively control for these variations by applying a focused repulsive green (532 nm) laser beam during the lattice ramp up along each of the three orthogonal axes (*28*). Varying the depth of this harmonic antitrapping potential allows us to adjust the amount of confinement produced by the optical lattice and thus make the density profiles comparable between different interaction strengths while keeping the total atom number constant. We measure the tube occupancy by taking in situ phase-contrast images of the atom cloud (*29*) and performing an inverse Abel transform to obtain the 3D distribution. A typical ensemble consists of a total of 6.5×10^4 atoms, has a peak tube occupancy of ~50 atoms, and has a most probable tube occupancy of ~30 atoms.

We perform Bragg spectroscopy by applying the pair of Bragg beams on the atoms in a 200-μs pulse. The intensity per beam is fixed to limit the loss of atoms caused by spontaneous scattering to 6 to 8% during the spin-mode measurement and to ensure that the momentum transfer is in the linear-response regime for either mode over the entire range of interaction strengths that we study (*27*). There is no discernible atom loss during the charge-mode measurement. Immediately after the Bragg pulse, the atoms are released from the lattice and are imaged using phase-contrast imaging after 150 μs of time of flight, after which atoms receiving the Bragg kick are noticeably displaced from the center of the cloud (fig. S1). We define the Bragg signal to be proportional to the number of outcoupled atoms.

The interaction strength is readily tunable using the Feshbach resonance between states $|1\rangle$ and $|3\rangle$ located at 690 G (*30*). The 3D scattering length a may be tuned between a = 0 and a = 500a_0, where a_0 is the Bohr radius, without appreciable atom loss. Figure 2 shows the measured (symbols) and calculated (solid lines) Bragg spectra for both modes in the range of a from 0 to 500a_0. Our DSF calculations take into account the effect of the inhomogeneous density that stems from the harmonic confinement along each tube by use of the local density approximation (LDA). The strength of interactions is density dependent and is given by the dimensionless Lieb-Liniger parameter $\gamma = mg_1(a)/\hbar^2\rho_{1D}$, where $g_1(a)$ is the coupling strength of the quasi-1D pseudopotential (*31*) and m is the atomic mass. The local density ρ_{1D} determines the local Fermi velocity and momentum (v_F and $\hbar k_F$), the Luttinger parameters ($K_{c,s}$), and the local velocities of the charge and spin waves (v_c and v_s, respectively). Because the Bragg signal

is proportional to the total transferred momentum, we sum up the local values of the DSF along each tube, by invoking the LDA, to obtain the calculated spectra. Finally, we account for the frequency broadening caused by the finite duration of the Bragg pulses. A global temperature of 250 nK is the only free parameter in this model, other than an independent normalization of each calculated and measured spectrum.

To calculate the charge and spin DSFs, we use the exact Bethe ansatz solution of the Yang-Gaudin model at zero temperature (*21*, *32*). For $|q| \ll k_F$, the low-energy charge and spin excitations have approximately linear dispersion and, in this approximation, $S_{c,s}(q,\omega) \propto |q|\ \delta(\omega - v_{c,s}q)$. However, at finite temperature and q, these DSFs are broadened when nonlinear effects are considered (*33*). For the strength of interactions probed in this experiment and for $T \ll T_F$, $S_c(q, \omega)$ is well approximated by the noninteracting DSF because the latter also exhibits a particle-hole excitation spectrum with width $\propto q^2$. As in (*16*), the effect of interactions is accounted for by replacing k_F with $k_c = m^* v_c/\hbar$, where m^* is the effective mass. The leading correction to the spin-mode dispersion at finite temperature is a consequence of a low-energy back-scattering process that is expected for contact interactions in 1D (*34*). Here, distinguishable spins permute between the two Fermi points by exchanging $2k_F$. This process is exclusive to the spin sector and disrupts the linearization of the spin dispersion in the bosonization approach of TLL theory (*5*, *32*). We obtain the retarded spin-spin correlation function at finite temperature from the dressed spin-boson propagator (*35*). By comparing our measurements to the nonlinear Luttinger liquid (NLL) theory, we find that accounting for nonlinearities caused by back-scattering is necessary to model the spin Bragg spectra, particularly for large interactions. The linear TLL model fails to reproduce the observed high-frequency tails of the spin-mode Bragg spectra (*27*).

The frequency at which the Bragg signal reaches a maximum, ω_p, corresponds to the most probable value of the mode velocity, $v_p = \omega_p/q$, in the ensemble. We determine the peaks of each of the measured spectra by fitting a parabola to the data points that are above 50% of the maximum measured value for each spectrum. The locations of the peaks of the spectra obtained for our range of interaction are shown in Fig. 3 along with the peaks of the calculated spectra for each mode, which are in excellent agreement. For the noninteracting gas, the spin and charge collective modes have the same speed, resulting in nearly identical measured spectra for the two cases (*27*). The congruence between the two spectra also confirms that the atom loss suffered during the spin-mode measurement has no discernible effect on the measured Bragg spectrum. As the strength of the interaction is increased, the charge-mode velocity v_c increases, whereas the spin-mode velocity v_s decreases. This is seen in the shifts of the peaks of the two spectra: to a lower frequency for the spin mode, and to a higher frequency for the charge mode.

We further explored the NLL regime by extracting the axial width of the out-coupled atom packet after time-of-flight expansion, as shown in Fig. 4 as functions of interaction for both modes. As expected, the out-coupled widths increase with γ for measurements of the spin mode, whereas they remain approximately constant for the charge mode. We are able to model the increase in the out-coupled width for the spin mode by calculating the spread in velocities implied by the finite spin-boson lifetime due to back-scattering (*27*).

Having harnessed the tunability of interactions available in the cold-atom setting, we reveal the role of interactions in spin-charge separation by tuning between a spin-charge separated regime and one where there is no separation. Further, the selectivity of the Bragg process in exciting either the CDW or the SDW allows us to provide a clear demonstration of the division of the TLL Hamiltonian into distinct spin and charge sectors. Bragg spectroscopy may be used to probe the ultracold-atom TLL beyond the demonstration of spin-charge separation contained in this work. Measurements with variable q can be conducted to further study the NLL and to benchmark calculations that include effects of band curvature and spin-charge coupling (*33*, *35*, *36*). Additionally, at increased temperatures and interactions, a spin-incoherent Luttinger liquid is expected, which supports a propagating charge mode but not a spin mode (*37*, *38*). Spin-imbalanced mixtures and attractive interactions are also of interest and are accessible by using this technique (*39*). Experiments with shallower lattices will allow for the study of dimensionality effects due to tunneling between tubes (*5*). It is increasingly clear that the oft-admired mathematical elegance of 1D many-body physics is well complemented by the purity and tunability of ultracold atoms.

REFERENCES AND NOTES

1. S.-I. Tomonaga, *Prog. Theor. Phys.* **5**, 544–569 (1950).
2. J. Luttinger, *J. Math. Phys.* **4**, 1154–1162 (1963).
3. F. D. M. Haldane, *J. Phys. C Solid State Phys.* **14**, 2585–2609 (1981).
4. J. Voit, *J. Phys. Condens. Matter* **5**, 8305–8336 (1993).
5. T. Giamarchi, *Quantum Physics in One Dimension* (Oxford Univ. Press, 2003).
6. O. M. Auslaender *et al.*, *Science* **295**, 825–828 (2002).
7. O. M. Auslaender *et al.*, *Science* **308**, 88–92 (2005).
8. Y. Jompol *et al.*, *Science* **325**, 597–601 (2009).
9. P. Segovia, D. Purdie, M. Hengsberger, Y. Baer, *Nature* **402**, 504–507 (1999).
10. C. Kim *et al.*, *Phys. Rev. Lett.* **77**, 4054–4057 (1996).
11. B. Kim *et al.*, *Nat. Phys.* **2**, 397–401 (2006).
12. T. A. Hilker *et al.*, *Science* **357**, 484–487 (2017).
13. G. Salomon *et al.*, *Nature* **565**, 56–60 (2019).
14. J. Vijayan *et al.*, *Science* **367**, 186–189 (2020).
15. G. Pagano *et al.*, *Nat. Phys.* **10**, 198–201 (2014).
16. T. L. Yang *et al.*, *Phys. Rev. Lett.* **121**, 103001 (2018).
17. J. Stenger *et al.*, *Phys. Rev. Lett.* **82**, 4569–4573 (1999).
18. J. Steinhauer, R. Ozeri, N. Katz, N. Davidson, *Phys. Rev. Lett.* **88**, 120407 (2002).
19. G. Veeravalli, E. Kuhnle, P. Dyke, C. J. Vale, *Phys. Rev. Lett.* **101**, 250403 (2008).
20. S. Hoinka, M. Lingham, M. Delehaye, C. J. Vale, *Phys. Rev. Lett.* **109**, 050403 (2012).
21. C. N. Yang, *Phys. Rev. Lett.* **19**, 1312–1315 (1967).
22. M. Gaudin, *Phys. Lett. A* **24**, 55–56 (1967).
23. D. Pines, *Theory of Quantum Liquids: Normal Fermi Liquids* (CRC Press, 2018).
24. A. Brunello, F. Dalfovo, L. Pitaevskii, S. Stringari, F. Zambelli, *Phys. Rev. A* **64**, 063614 (2001).
25. A. Y. Cherny, J. Brand, *Phys. Rev. A* **73**, 023612 (2006).
26. P. M. Duarte *et al.*, *Phys. Rev. A* **84**, 061406 (2011).
27. See supplementary materials.
28. R. A. Hart *et al.*, *Nature* **519**, 211–214 (2015).
29. R. G. Hulet, J. H. V. Nguyen, R. Senaratne, *Rev. Sci. Instrum.* **91**, 011101 (2020).
30. G. Zürn *et al.*, *Phys. Rev. Lett.* **110**, 135301 (2013).
31. M. Olshanii, *Phys. Rev. Lett.* **81**, 938–941 (1998).
32. F. He *et al.*, *Phys. Rev. Lett.* **125**, 190401 (2020).
33. A. Imambekov, T. L. Schmidt, L. I. Glazman, *Rev. Mod. Phys.* **84**, 1253–1306 (2012).
34. F. D. M. Haldane, *J. Phys. C Solid State Phys.* **12**, 4791–4799 (1979).
35. R. G. Pereira, E. Sela, *Phys. Rev. B* **82**, 115324 (2010).
36. A. Imambekov, L. I. Glazman, *Science* **323**, 228–231 (2009).
37. G. A. Fiete, *Rev. Mod. Phys.* **79**, 801–820 (2007).
38. P. Kakashvili, S. Bhongale, H. Pu, C. Bolech, *Phys. Rev. A* **78**, 041602 (2008).
39. X.-W. Guan, M. T. Batchelor, C. Lee, *Rev. Mod. Phys.* **85**, 1633–1691 (2013).
40. B. Efron, *Ann. Stat.* **7**, 1 (1979).
41. R. Senaratne *et al.*, Data for "Spin-charge separation in a 1D Fermi gas with tunable interactions." Zenodo (2022).

ACKNOWLEDGMENTS

We thank T. L. Yang for his contributions to the apparatus. **Funding:** This work was supported in part by the Army Research Office Multidisciplinary University Research Initiative (grant no. W911NF-17-1- 0323), the NSF (grant nos. PHY-1707992 and PHY-2011829), and the Welch Foundation (grant no. C-1133). H.P. acknowledges support from the NSF (PHY-1912068) and the Welch Foundation (grant no. C-1669). X.-W.G. is supported by National Natural Science Foundation of China (NSFC) key grant no. 12134015, NSFC grant nos. 11874393 and 12121004, and National Key Research and Development Program of China (NKRDPC) grant no. 2017YFA0304500. D.C.-C. acknowledges financial support from Consejo Nacional de Ciencia y Tecnología (CONACyT) (Mexico, scholarship no. 472271). **Author contributions:** R.S. and D.C.-C. built the experimental setup, performed the measurements, and analyzed data. S.W. and F.H. performed the modeling of the experimental data and the theoretical calculations. Y.-T.C. and A.K. assisted with experiments. All work was supervised by H.P., X.-W.G., and R.G.H. All authors discussed the results and contributed to the manuscript. **Competing interests:** The authors declare no competing interests. **Data and materials availability:** All data needed to evaluate the conclusions in the paper are archived on Zenodo (*41*). **License information:** Copyright © 2022 the authors, some rights reserved; exclusive licensee American Association for the Advancement of Science. No claim to original US government works. https://www.science.org/about/science-licenses-journal-article-reuse

SUPPLEMENTARY MATERIALS

science.org/doi/10.1126/science.abn1719
Materials and Methods
Supplementary Text
Figs. S1 to S10
References (*42*–*45*)

Submitted 11 November 2021; accepted 16 May 2022
10.1126/science.abn1719

PHOTONICS

A photonic integrated circuit–based erbium-doped amplifier

Yang Liu[1,2]†, Zheru Qiu[1,2]†, Xinru Ji[1,2], Anton Lukashchuk[1,2], Jijun He[1,2], Johann Riemensberger[1,2], Martin Hafermann[3], Rui Ning Wang[1,2], Junqiu Liu[1,2], Carsten Ronning[3], Tobias J. Kippenberg[1,2]*

Erbium-doped fiber amplifiers revolutionized long-haul optical communications and laser technology. Erbium ions could provide a basis for efficient optical amplification in photonic integrated circuits but their use remains impractical as a result of insufficient output power. We demonstrate a photonic integrated circuit–based erbium amplifier reaching 145 milliwatts of output power and more than 30 decibels of small-signal gain—on par with commercial fiber amplifiers and surpassing state-of-the-art III-V heterogeneously integrated semiconductor amplifiers. We apply ion implantation to ultralow–loss silicon nitride (Si_3N_4) photonic integrated circuits, which are able to increase the soliton microcomb output power by 100 times, achieving power requirements for low-noise photonic microwave generation and wavelength-division multiplexing optical communications. Endowing Si_3N_4 photonic integrated circuits with gain enables the miniaturization of various fiber-based devices such as high–pulse-energy femtosecond mode-locked lasers.

The invention of erbium-doped fiber amplifiers (EDFAs) in the 1980s (*1*, *2*) revolutionized long-haul optical communications, profoundly affecting the transmission of information in society. EDFAs have replaced complex and bandwidth-limited electrical repeaters, enabling transatlantic fiber-based optical communication networks (*3*). Erbium amplifiers have a number of properties highly suitable for optical communications, such as a broadband gain of ~1550 nm-wavelength that coincides with the lowest optical fiber propagation loss band, a long millisecond (ms)-lifetime of the parity forbidden intra–4f shell $^4I_{15/2}-{}^4I_{13/2}$ transition that leads to slow gain dynamics and negligible interchannel crosstalk in multiwavelength amplification, high-temperature stability, and a low-noise figure approaching the quantum mechanical limit of 3 decibels (dB) for phase-insensitive amplification (*4*). Today, EDFAs have underpinned the development of narrow-linewidth and mode-locked lasers that are widely deployed in applications such as coherent communications (*3*), interferometric sensing, and optical frequency metrology (*5*). Rare-earth ion doping (*6*, *7*) can provide the basis for compact erbium-doped waveguide amplifiers (EDWAs) (*8*). In the 1990s efforts were made to implement EDWAs on the basis of oxide glass waveguides (*9*, *10*), but these were hindered by large waveguide background losses, large device footprints, and incompatibility with contemporary photonic integrated circuits, and thus were ultimately abandoned. Interest in EDWAs reemerged with the Si_3N_4 complementary metal-oxide-semiconductor–compatible photonic integrated circuit platform, with advantages over silicon including a wider transparency window (*11*), absence of two-photon absorption in telecommunication bands, lower temperature sensitivity, high power handling of >10 watts (*12*), and most crucially, low propagation losses of <3 dB/m, maintained over meter-scale lengths (*13*).

[1]Institute of Physics, Swiss Federal Institute of Technology Lausanne (EPFL), CH-1015 Lausanne, Switzerland. [2]Center for Quantum Science and Engineering, Swiss Federal Institute of Technology Lausanne (EPFL), CH-1015 Lausanne, Switzerland. [3]Institute of Solid State Physics, Friedrich Schiller University Jena, Max-Wien-Platz 1, 07743 Jena, Germany.
*Corresponding author. Email: tobias.kippenberg@epfl.ch
†These authors contributed equally to this work.

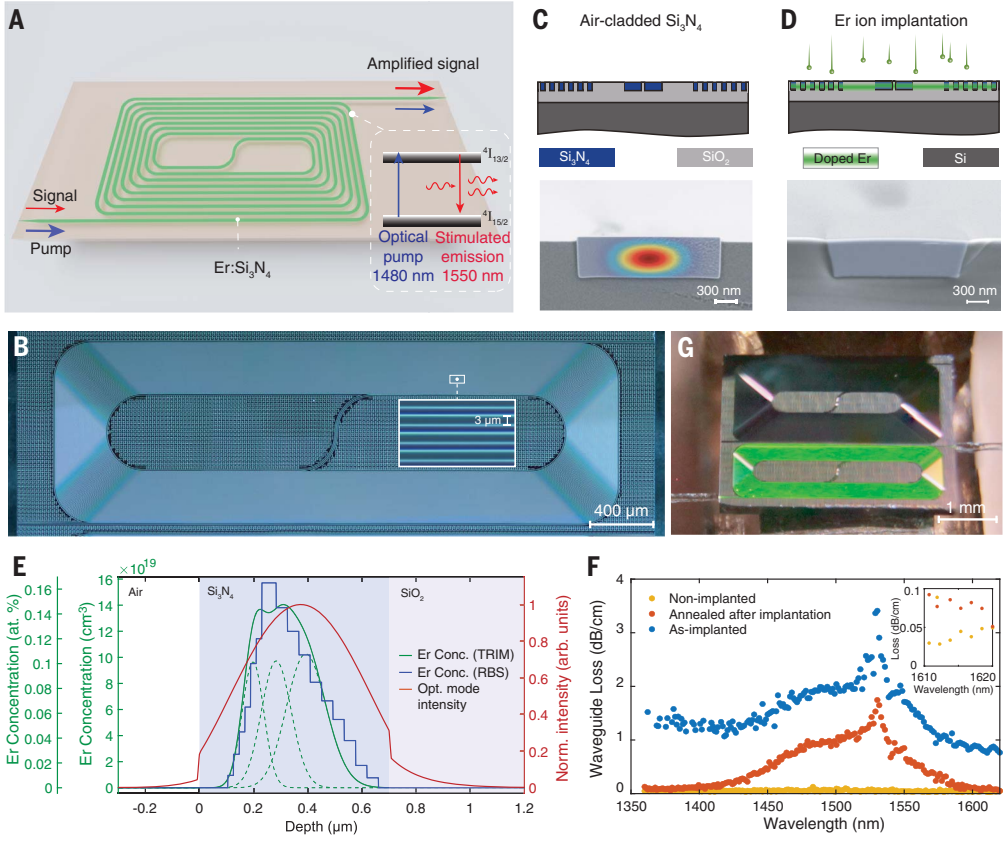

Fig. 1. Integrated erbium-implanted Si_3N_4 waveguide amplifier. (**A**) A Si_3N_4 waveguide amplifier with erbium ions optically excited by a 1480-nm pump. (**B**) Optical image of a 0.5-m-long Er: Si_3N_4 waveguide coil. (**C**) Schematics of key fabrication processes and SEM images of waveguide cross sections overlaid with the simulated optical transverse electric (TE) mode before and (**D**) after ion implantation. (**E**) Vertical profiles of calculated erbium concentration (green), simulated optical TE mode intensity (red), and measured concentration (blue) by Rutherford backscattering spectrometry (RBS) across the waveguide center. (**F**) Measured optical losses before ion implantation, as-implanted, and after annealing. (**G**) Optical image of an intensely pumped Er: Si_3N_4 chip butt-coupled with optical fibers.

One challenge in realizing photonic integrated circuit–based erbium amplifiers is the limited achievable gain stemming from constraints in doping concentration due to cooperative upconversion (*14*). This limitation necessitates waveguides with low propagation losses and long waveguides with lengths ranging from tens of centimeters to meters, to achieve large gain and high output power. Although net gain has been shown, all prior work using erbium-doped Al_2O_3 (*15*, *16*), TeO_2 (*17*), and erbium chloride silicate nanowires (*18*) typically achieved low output power of <<1 mW, below the level demanded by many applications and below that achieved with heterogeneous III-V integration in silicon photonics (*19*, *20*).

We demonstrate a photonic integrated circuit–based erbium-implanted Si_3N_4 (Er: Si_3N_4) amplifier based on meter scale ultralow-loss Si_3N_4 waveguides (Fig. 1A). We fabricate densely-packed Si_3N_4 spiral waveguides of 0.5 m in length (Fig. 1B) with 3-μm gap spacing and cross sections measuring 0.7 × 2.1 μm^2, achieving a compact footprint of only 1.2 × 3.6 mm^2 and a propagation loss of <5 dB/m through the photonic damascene process (*13*) (Fig. 1C and fig. S1). We use devices without top cladding to enable direct ion implantation into the waveguide core (Fig. 1D). Next, we apply ion implantation (*6*)—a wafer-scale process that benefits from much lower cooperative upconversion compared with cosputtered films (*14*)—to the Si_3N_4 integrated circuits (fig. S1). To achieve a large overlap of $\Gamma \approx 50\%$ between embedded ions with the fundamental optical waveguide mode, we use three successive implantation steps with ion energies of 2.0, 1.416, and 0.966 mega–electron volts (MeV) and corresponding ion fluences of 4.50×10^{15}, 3.17×10^{15}, and 2.34×10^{15} cm^{-2}, respectively. The simulated concentration profile (Fig. 1E, green) with a maximum depth of 400 nm in Si_3N_4 (*21*) matches well with Rutherford backscattering spectrometry (RBS) measurement (fig. S2).

Upon implantation the waveguide background loss increases from <5 to 100 dB/m because of implantation defects (Fig. 1F). The background loss outside the erbium absorption band is reduced after annealing at 1000°C in oxygen for 1 hour and approaches the same level as undoped waveguides (*21*). Green luminescence is observed stemming from cooperative upconversion (Fig. 1G). Notably, such a loss only contributes <2.5 dB of background attenuation for a 0.5-m-long waveguide, appreciably lower than the 30 dB passive loss for waveguides of equal lengths in prior work (*15*, *16*), which depletes the pump early and prevents efficient amplification. Moreover, we investigate selective masking (using a photoresist) during ion implantation (figs. S4 and S5). Crucially, lateral claddings can provide mechanical support to mitigate severe cross section deformations observed in the waveguides without lateral claddings (figs. S1 and S6).

The emission and absorption cross sections [$\sigma_e(\lambda)$ and $\sigma_a(\lambda)$] are important parameters for modelling gain performance and extracting cooperative upconversion coefficients. Figure 2A shows the emission spectrum when pumping the $^4I_{11/2}$ state (980 nm) in a 0.46-cm-long Er: Si_3N_4 waveguide, from which the emission cross section (Fig. 2C) can be derived (*22*) through $\frac{1}{\tau} = 8\pi n^2 c \int \frac{\sigma_e(\lambda)}{\lambda^4} d\lambda$, in which n is the waveguide refractive index and τ = 3.4 ms

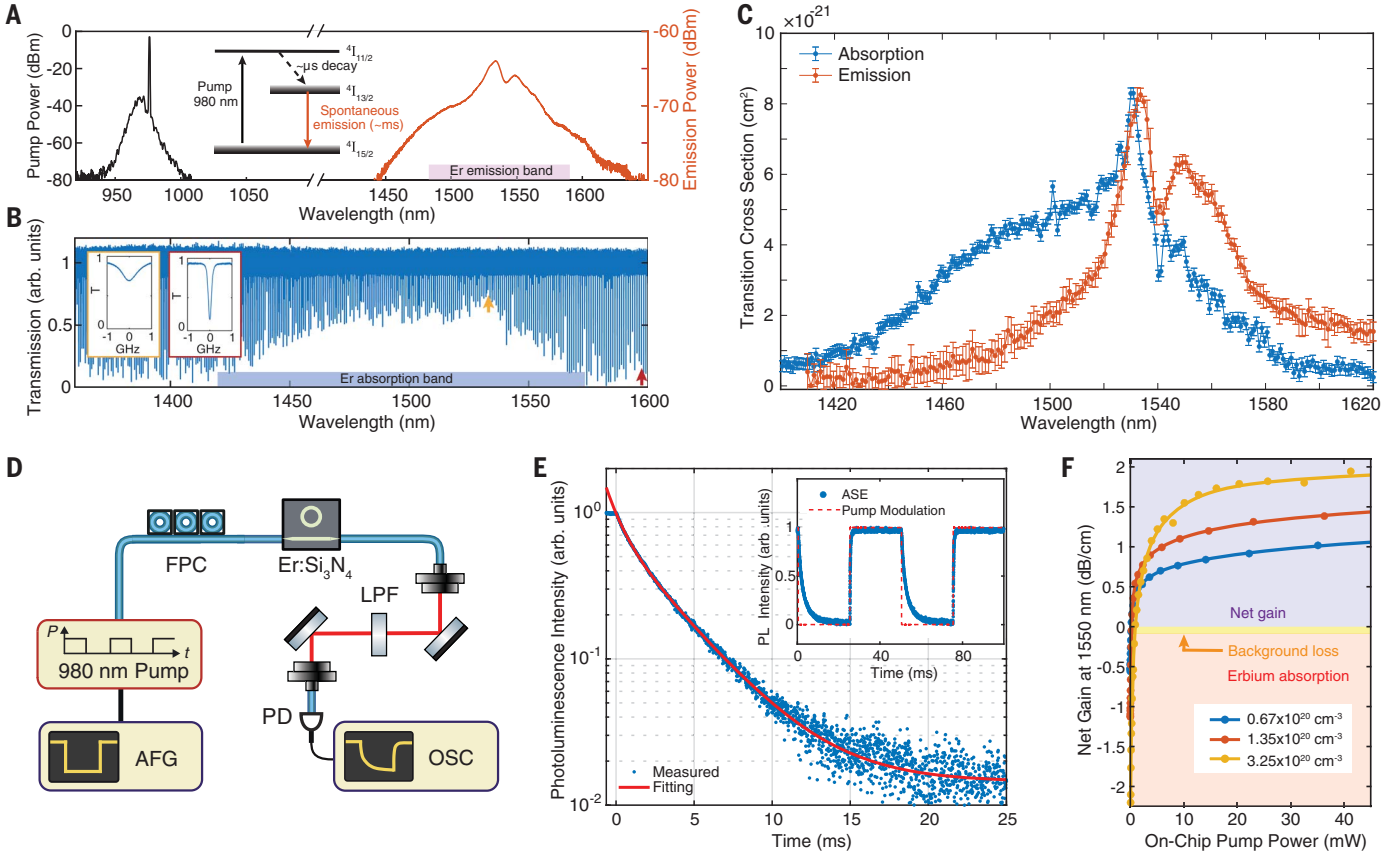

Fig. 2. Light emission and absorption properties of Er: Si_3N_4 photonic waveguides. (**A**) Fluorescence emission spectrum (red) from an Er: Si_3N_4 waveguide. (**B**) Measured resonance linewidths of an Er: Si_3N_4 microring resonator for extracting erbium absorption. The insets exemplify two resonances with intrinsic loss of 2 and 0.08 dB/cm. (**C**) Extracted emission and absorption cross sections. (**D**) Experimental setup for fluorescence lifetime measurement. AFG, arbitrary function generator; FPC, fiber-based polarization controller; LPF, optical long pass filter; PD, photodetector; OSC, oscilloscope. (**E**) Measured fluorescence decay from the $^4I_{13/2}$ level. The inset shows the gated pump and emission. (**F**) Measured net gain coefficients with different erbium concentrations upon 1480-nm pumping.

is the photoluminescence lifetime fitted from temporal measurement (Fig. 2, D and E), assuming the modification (~0.93) of the density of states has limited effects on the emission rate (*21*). The wavelength-dependent erbium absorption loss α_{Er} is derived from the intrinsic resonance linewidths of an Er: Si_3N_4 microring resonator and is calibrated by optical frequency domain reflectometry measurements (fig. S3). The loss is proportional to the erbium absorption cross section given by $\sigma_a(\lambda) = \frac{\alpha_{Er}(\lambda)}{\Gamma \cdot N_0}$, in which N_0 is the effective peak erbium ion concentration and Γ is the overlap factor (*23*). The absorption cross section $\sigma_a(\lambda)$ is obtained by scaling its peak value to approximately that of the derived $\sigma_e(\lambda)$, which in turn gives $N_0 = 1.35 \times 10^{20}$ cm^{-3}, indicating that almost all the incorporated erbium ions are optically active compared with the RBS measurement (Fig. 1E). Comparisons of measured gain coefficients are made under different ion concentrations (Fig. 2F), pump wavelengths, and waveguide widths (fig. S7).

Next, we demonstrate high output power and large net gain upon 1480 nm pumping in a 0.21-meter-long Er: Si_3N_4 waveguide with an erbium concentration of ~3.25×10^{20} cm^{-3} (Fig. 3A), showing a broadband on-chip net gain of 30 dB (Fig. 3B). Figure 3C shows measured net gain at 1550 nm along with simulations reproduced for parameter fitting. The on-chip output power reaches 60 mW for 0.07 mW input, indicating an off-chip net gain of 24 dB considering ~5.8-dB coupling loss. The on-chip output power reaches 145 mW for an increased input power of 2.61 mW at 245 mW coupled pump power (Fig. 3D, inset), indicating an on-chip power conversion efficiency approaching 60% (signal power increment divided by pump power). Similar gain performance is achieved in a 0.5-meter-long Er: Si_3N_4 waveguide with a lower erbium concentration of ~1.35×10^{20} cm^{-3} (figs. S9 and S10). A noise figure of ~7 dB is measured at a net gain of >20 dB (fig. S11) and the excess EDWA RIN approaches the same level (ca. −156 dBc/Hz) as the EDFA for >10 MHz offset Fourier frequency (fig. S12). Simulations suggest that the low cooperative upconversion ($C_{24} = 3.0 \times 10^{-18}$ cm^3s^{-1} and 13.0×10^{-18} cm^3s^{-1} fitted for low and high concentrations, respectively) does not impose limitation on the EDWA gain performance at high pump power >245 mW (*21*). The observed fluctuations in measured gain are caused by the gain clamping effect when parasitic lasing occurs in an optical Fabry-Pérot cavity formed by waveguide facets (fig. S13).

As an example of the utility, we apply the Er: Si_3N_4 EDWA to the amplification of soliton microcombs (Fig. 4A) (*24*), which typically exhibit low conversion (~1%) efficiency (*25*) and require amplification in virtually all applications. First, a 19.8-GHz single-soliton microcomb generated in a Si_3N_4 Euler-bend racetrack microresonator (*26*) with 0.08 mW output power [Fig. 4B, panel (i)], is amplified to 8.4 mW of off-chip power by the EDWA [panel (ii)]. This leads to a reduction in single-sideband phase noise of a soliton repetition rate to ca. −144 dBc/Hz at >1 MHz offset Fourier frequency, compared with −104 dBc/Hz (before amplification) limited by photon shot noise (Fig. 4C). Comb line spikes [panel (ii)] are induced by the regenerative feedback from EDWA chip facets. A commercial EDFA is deployed to amplify the same soliton microcomb to a similar power level [panel (iii)], giving identical performance.

Second, we demonstrate a telecommunication experiment using an amplified soliton

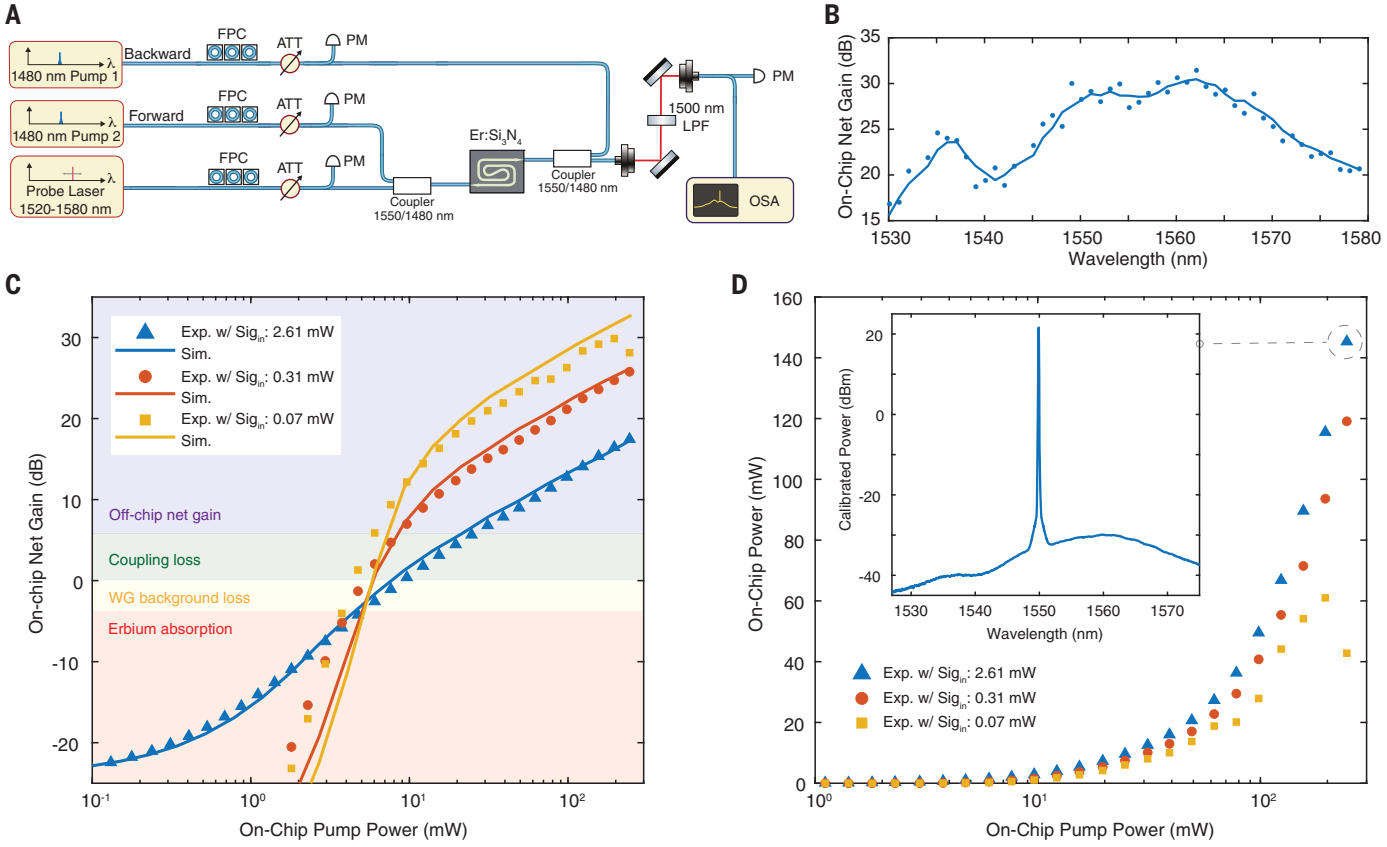

Fig. 3. Intense optical amplification in an Er: Si_3N_4 waveguide amplifier. (**A**) Experimental setup for optical amplification with a free-space filter for pump suppression. ATT, tunable optical attenuator; PM, power meter; OSA, optical spectrum analyzer. (**B**) Measured gain spectrum. (**C**) Measured (scatters) and simulated (curves) gain at 1550 nm. The color-shaded areas indicate the region of off-chip net gain and sources of loss. (**D**) Measured output power at 1550 nm. The inset shows the calibrated optical spectrum at 145 mW signal output.

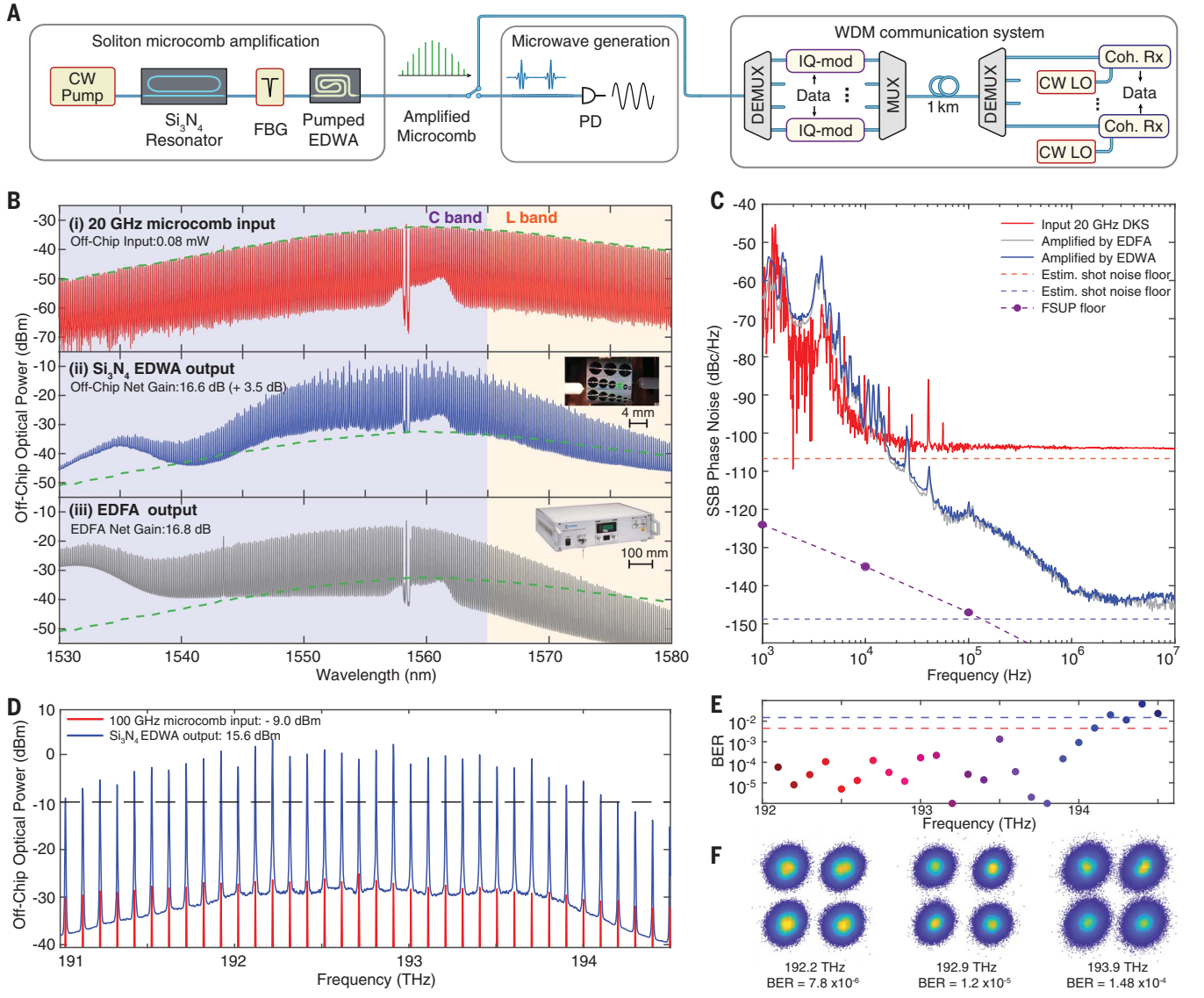

Fig. 4. On-chip amplification of soliton microcombs. (**A**) Experimental setup for soliton amplification, microwave generation, and wavelength-division multiplexing optical communication. FBG, fiber Bragg grating; DEMUX, demultiplexer; LO, local oscillator. (**B**) Amplification of 19.8 GHz microcomb. (i) Generated single-soliton state microcomb, (ii) amplified microcomb by the EDWA (inset), and (iii) amplified microcomb by a commercial EDFA (inset). The EDWA output power is measured with ~3.5 dB insertion loss of fiber couplers and filters. (**C**) Measured single–sideband phase noises of generated microwave signals. (**D**) Optical spectra of amplified 100 GHz soliton microcomb and input. (**E**) Measured bit error ratio (BER). Blue (red) dashed line corresponds to 7% soft decision (20% hard decision) forward error correction overhead. (**F**) Reconstructed QPSK constellation diagrams.

microcomb with 100-GHz channel spacing in which a commercial wavelength-division multiplexer allows for individual access to the comb lines (Fig. 4, A and D). We modulate optical carriers with quadrature phase-shift keying (QPSK) bit stream at a symbol rate of 10 gigabaud and coherently detect the data transmitted over 1 km of standard single-mode fiber (*21*). More than 0.1 mW of optical power per line enables reliable data transmission for >20 channels (Fig. 4, E and F). We envision our EDWAs to act either as compact booster amplifiers after signal modulation or as pre-amplifiers at receivers, meeting the requirements of the optical power and SNR budget. The EDWA is also capable of amplifying mode-locked lasers with 1 pJ pulse energy and 100-MHz repetition rate (fig. S14).

Our photonic integrated circuit–based EDWA can provide >145 mW on-chip output power and >30 dB of small-signal gain. The technique of ion implantation in Si_3N_4 can provide a basis for the gain medium in a variety of integrated laser sources such as high-power soliton microcombs, low-noise rare-earth-ion-based CW lasers, femtosecond mode-locked lasers (*27*) or cavity soliton lasers (*28*). Moreover, it could allow for co-doping of other rare-earth ions such as ytterbium (emission at 1 μm) and thulium (2 μm), thereby providing optical gain in other wavelength regions. Further, this active Si_3N_4 photonic platform is compatible with heterogeneous integration of thin-film lithium niobate, enabling the combination of both high-speed electro-optic modulation and amplification on the same chip for coherent communications (*29*) or radio frequency photonics (*30*).

REFERENCES

1. S. B. Poole, D. N. Payne, R. J. Mears, M. E. Fermann, R. I. Laming, *J. Lightwave Technol.* **4**, 870–876 (1986).
2. R. Mears, L. Reekie, I. Jauncey, D. Payne, *Electron. Lett.* **23**, 1026 (1987).
3. P. J. Winzer, D. T. Neilson, A. R. Chraplyvy, *Opt. Express* **26**, 24190–24239 (2018) [Invited].

4. P. Becker, A. Olsson, J. Simpson, *Erbium-Doped Fiber Amplifiers* (Elsevier, 1999).
5. C. Xu, F. W. Wise, *Nat. Photonics* **7**, 875–882 (2013).
6. A. Polman, D. C. Jacobson, D. J. Eaglesham, R. C. Kistler, J. M. Poate, *J. Appl. Phys.* **70**, 3778–3784 (1991).
7. A. Polman, *J. Appl. Phys.* **82**, 1–39 (1997).
8. J. Bradley, M. Pollnau, *Laser Photonics Rev.* **5**, 368–403 (2011).
9. G. Nykolak, M. Haner, P. Becker, J. Shmulovich, Y. Wong, *IEEE Photonics Technol. Lett.* **5**, 1185–1187 (1993).
10. K. Hattori, T. Kitagawa, M. Oguma, Y. Ohmori, M. Horiguchi, *Electron. Lett.* **30**, 856 (1994).
11. D. J. Moss, R. Morandotti, A. L. Gaeta, M. Lipson, *Nat. Photonics* **7**, 597–607 (2013).
12. V. Brasch *et al*., *Science* **351**, 357–360 (2016).
13. J. Liu *et al*., *Nat. Commun.* **12**, 2236 (2021).
14. P. G. Kik, A. Polman, *J. Appl. Phys.* **93**, 5008–5012 (2003).
15. J. Mu, M. Dijkstra, J. Korterik, H. Offerhaus, S. M. García-Blanco, *Photon. Res.* **8**, 1634 (2020).
16. J. Rönn *et al*., *Nat. Commun.* **10**, 432 (2019).
17. H. C. Frankis *et al*., *Photon. Res.* **8**, 127 (2020).
18. H. Sun *et al*., *Nat. Photonics* **11**, 589–593 (2017).
19. M. L. Davenport *et al*., *IEEE J. Sel. Top. Quantum Electron.* **22**, 78–88 (2016).
20. K. Van Gasse, R. Wang, G. Roelkens, *Opt. Express* **27**, 293–302 (2019).
21. See supplementary materials.
22. D. E. McCumber, *Phys. Rev.* **136**, A954–A957 (1964).
23. R. C. Giles, E. Desurvire, *J. Lightwave Technol.* **9**, 271–283 (1991).
24. T. J. Kippenberg, A. L. Gaeta, M. Lipson, M. L. Gorodetsky, *Science* **361**, eaan8083 (2018).
25. C. Bao *et al*., *Opt. Lett.* **39**, 6126–6129 (2014).
26. X. Ji *et al*., *Commun. Phys.* **5**, 84 (2022).
27. N. Singh, E. Ippen, F. X. Kärtner, *Opt. Express* **28**, 22562–22579 (2020).
28. H. Bao *et al*., *Nat. Photonics* **13**, 384–389 (2019).
29. P. Marin-Palomo *et al*., *Nature* **546**, 274–279 (2017).
30. D. Marpaung, J. Yao, J. Capmany, *Nat. Photonics* **13**, 80–90 (2019).
31. Y. Liu *et al*., A photonic integrated circuit based erbium-doped amplifier, Version 1, Zenodo (2022); https://zenodo.org/record/6515905#.YpZdCijMI2w.

ACKNOWLEDGMENTS

Silicon nitride samples were fabricated in the EPFL Center of MicroNanoTechnology (CMi). We thank A.S. Raja and W. Weng for discussions on experiments. We thank E. Wendler for help in analyzing the RBS data. **Funding:** This work was supported by contract HR0011-20-2-0046 (NOVEL) from the Defense Advanced Research Projects Agency (DARPA), by the Air Force Office of Scientific Research (AFOSR) under award FA9550-19-1-0250, by the SNSF under grant 176563 (BRIDGE) and grant 201923 (Ambizione), and by the collaborative research center CRC 1375 NOA (Project C5). This work is also funded by the EU H2020 research and innovation programme under grant 696656 (Graphene Core3), grant 965124 (FEMTOCHIP), and Marie Sklodowska-Curie IF grant 898594 (CompADC). **Author contributions:** Y.L. and Z.Q. conceived and performed the experiments, data analysis, and simulations. X.J., A.L., J.H., and J.R. provided experimental support. Y.L. and Z.Q. designed the Si_3N_4 samples (D85). J.L., R.N.W., Z.Q., and X.J. designed and fabricated the passive Si_3N_4 samples. M.H. and C.R. performed the RBS measurements. Y.L. and T.J.K. wrote the manuscript with input from all coauthors. T.J.K. supervised the project. **Competing interests:** T.J.K. is a cofounder and shareholder of LiGenTec SA, a startup company offering Si_3N_4 photonic integrated circuits as a foundry service. T.J.K., Y.L., Z.Q., and X.J. are inventors on patent application (PCT/IB2022/052668) submitted by Swiss Federal Institute of Technology Lausanne (EPFL) that covers "Waveguide amplifier and waveguide amplifier fabrication method". **Data and materials availability:** The datasets used to produce the results of this paper are available at (*31*).

License information: Copyright © 2022 the authors, some rights reserved; exclusive licensee American Association for the Advancement of Science. No claim to original US government works. https://www.sciencemag.org/about/science-licenses-journal-article-reuse

SUPPLEMENTARY MATERIALS

science.org/doi/10.1126/science.abo2631
Materials and Methods
Supplementary Text
Figs. S1 to S14
Tables S1 to S3
References (*32*–*65*)

Submitted 6 February 2022; accepted 10 May 2022
10.1126/science.abo2631

TRANSCRIPTION

Structural basis of nucleosome retention during transcription elongation

Martin Filipovski[1], Jelly H. M. Soffers[1], Seychelle M. Vos[2], Lucas Farnung[1]*

In eukaryotes, RNA polymerase (Pol) II transcribes chromatin and must move past nucleosomes, often resulting in nucleosome displacement. How Pol II unwraps the DNA from nucleosomes to allow transcription and how DNA rewraps to retain nucleosomes has been unclear. Here, we report the 3.0-angstrom cryo–electron microscopy structure of a mammalian Pol II-DSIF-SPT6-PAF1c-TFIIS-nucleosome complex stalled 54 base pairs within the nucleosome. The structure provides a mechanistic basis for nucleosome retention during transcription elongation where upstream DNA emerging from the Pol II cleft has rewrapped the proximal side of the nucleosome. The structure uncovers a direct role for Pol II and transcription elongation factors in nucleosome retention and explains how nucleosomes are retained to prevent the disruption of chromatin structure across actively transcribed genes.

Transcription requires the passage of RNA polymerase (Pol) II through chromatin. The nucleosome is a substantial barrier to Pol II because of an extensive network of contacts between histone proteins and the DNA that is wrapped around them (*1*). In vitro, Pol II is either unable to move past these obstacles or needs to displace at least one H2A-H2B dimer to transcribe through a nucleosome (*2*–*6*). By contrast, in vivo experiments have demonstrated that most transcribed genes have intact nucleosomes, and only very highly transcribed genes show nucleosomal loss (*7*, *8*). Nucleosome maintenance during transcription is critical for cell survival, and disruption of chromatin structure during transcription elongation has a major impact on transcription fidelity; even partial loss of nucleosomes results in aberrant transcription initiation events from nonpromoter regions within gene bodies (*9*, *10*). Thus, nucleosomes play a fundamental role in suppressing cryptic transcription events and restricting transcription initiation to gene promoters. Moreover, nucleosome displacement leads to a loss of posttranslational histone modifications that have a central regulatory role in demarcating transcriptionally active gene loci (*11*).

Understanding how nucleosomes are overcome and retained during transcription is a fundamental objective. Recently, cryo–electron microscopy (cryo-EM) structures of Pol II–nucleosome complexes have begun to elucidate how transcription through nucleosomes is mediated (*12*–*15*). They have not, however, addressed the question of how nucleosomes are retained during transcription. Biochemical and in vivo data suggest that the formation of an intranucleosomal Pol II containing a template loop (the "0-loop") could play an important role in nucleosome retention (*6*, *16*–*19*).

[1]Department of Cell Biology, Blavatnik Institute, Harvard Medical School, Boston, MA, USA. [2]Department of Biology, Massachusetts Institute of Technology, Cambridge, MA, USA.
*Corresponding author. Email: lucas_farnung@hms.harvard.edu

To investigate how Pol II traverses the nucleosome and concurrently maintains nucleosome integrity, we designed a nucleosomal substrate that allows for transcription of Pol II close to the nucleosomal dyad, a position previously described as a major stall site for Pol II (*20*). The nucleosomal DNA template contains a modified Widom 601 sequence that lacks deoxythymidine in the template strand from the transcription start site to a position 64 base pairs (bp) within the nucleosome (+64) (fig. S1A). An RNA primer can be annealed to a 3′-DNA overhang at the entry site, forming a nine-nucleotide DNA·RNA hybrid to allow for primer extension by Pol II upon the addition of nucleoside triphosphates. Mononucleosomes were assembled on this DNA template and then the following were added: (i) purified *Sus scrofa* Pol II and *Homo sapiens* elongation factor PAF1c composed of subunits CTR9, CDC73, WDR61, PAF1, LEO1, and RTF1; (ii) DRB-sensitivity-inducing factor (DSIF) composed of subunits SPT4 and SPT5; and (iii) SPT6, TFIIS, the kinase-positive transcription elongation factor b (P-TEFb), and 3′-deoxy-adenosine 5′-triphosphate (fig. S1B). The transcription reaction was initiated by the addition of cytosine 5′-triphosphate, guanasine 5′-triphosphate, and uridine 5′-triphosphate (fig. S1C). 3′-Deoxy-adenosine 5′-trisphosphate enabled robust stalling at the engineered stall site while serving as a P-TEFb substrate to allow for phosphorylation-dependent complex formation (fig. S1, C and D) (*21*). Subsequently, the transcription reaction mixture was subjected to size-exclusion chromatography, which revealed the formation of a Pol II-DSIF-PAF1c-SPT6-TFIIS-nucleosome complex (Fig. 1A and fig. S1, D to F). Analysis of the transcription products by denaturing gel electrophoresis revealed that RNA fragments corresponding to nucleosomal stall sites +38, +54, and +64 were the predominant products (Fig. 1B) (*20*). Peak fractions containing the nucleosome-bound elongation complex were mildly cross-linked with glutaraldehyde and prepared for single-particle cryo-EM.

The structure of the activated elongation complex bound to a nucleosome was determined at an overall resolution of 3.0 Å from 105,420 particles (Fig. 1C, figs. S2 to S4, movie S1, and table S1 and S3). A final composite map was assembled from masked refinements of the nucleosome, Pol II, and the PAF1 complex, with local resolutions ranging from 2.9 to 11.1 Å (figs. S2 to S4). Known structures of the complete mammalian activated elongation complex, TFIIS, and the nucleosome were placed into this map, and the structures were adjusted locally (*21*). The reconstruction shows DNA density extending from the upstream DNA toward the nucleosome. We observed a change in the location of the downstream DNA in the Pol II cleft compared with the DNA location of previously obtained elongation complexes (*13*, *15*, *21*, *22*) (Figs. 1, C and D, and 2, and fig. S4F). We de novo built the DNA to accommodate the observed changes in the DNA path. The model was real-space refined and shows good stereochemistry (table S3).

High-resolution features of the DNA·RNA hybrid and visualization of the complete transcription bubble allowed unambiguous assignment of the nucleic acid register (fig. S4, C, G, and H). In our structure, Pol II has unraveled DNA up to nucleosomal superhelical location (SHL) −0.5, and the Pol II active site is located at nucleosomal bp +54 (Fig. 2A). It adopts a mixture of pretranslocated states (nucleotide-binding site occupied by newly extended RNA 3′ end) and posttranslocated states (nucleotide-binding site not occupied) (fig. S4C). The +54 site that we observed was selected by the transcribing Pol II because the engineered stall site is only at nucleosomal bp +64. This implies that stalling at +54 is a major barrier to Pol II.

The transcribed upstream DNA adopts a new path when exiting the Pol II cleft. The upstream DNA projects away from Pol II toward the nucleosome, and ~55 bp of transcribed DNA rewraps the proximal side of the nucleosome from SHL −6.5 to SHL −1 (Figs. 1D and 2, A and B, and figs. S5 and S6). The path of the rewrapped DNA follows the DNA conformation of a canonical nucleosome. The upstream DNA stabilizes the proximal H2A-H2B dimer that plays a critical role in nucleosome retention during transcription (Fig. 2, A and B) (*2*). The DNA rewrapping also has consequences for the path of the downstream DNA. Usually, the downstream DNA duplex and the DNA·RNA hybrid emanate at a 105° angle from the Pol II active site, where the downstream DNA lies in the cleft between the clamp and RPB2 (fig. S5) (*22*). Farther downstream, the DNA contacts the Pol II jaw domain of RPB5. In our structure, the downstream

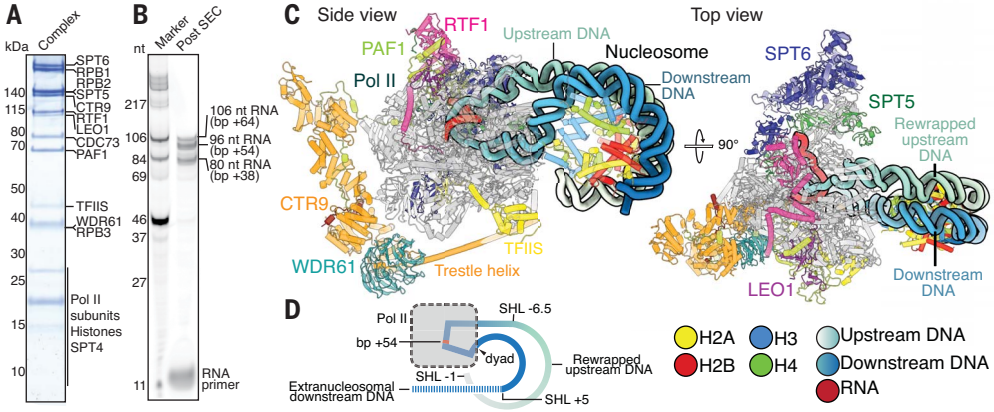

Fig. 1. Mammalian Pol II-DSIF-SPT6-PAF1c-TFIIS complex with rewrapped nucleosome. (**A**) SDS-polyacrylamide gel electrophoresis of peak fraction used for cryo-EM analysis showing the assembly of the Pol II-DSIF-SPT6-PAF1c-TFIIS-nucleosome complex. (**B**) Denaturing gel of purified complex showing primer extension and accumulation of the elongation complex at nucleosomal bp +38, +54, and +64. Stall sites within the nucleosome and corresponding RNA lengths are indicated. (**C**) Two views of the mammalian Pol II-DSIF-PAF1c-TFIIS-nucleosome complex with rewrapped transcribed DNA. The views are related by a 90° rotation. Pol II, SPT5, SPT6, CTR9, WDR61, PAF1, LEO1, CDC73, RTF1, TFIIS, H2A, H2B, H3, and H4 are shown in gray, forest green, dark blue, orange, teal, limon, purple, dark red, pink, yellow, light yellow, red, light blue, and chartreuse, respectively. The DNA template is colored upstream to downstream as a gradient from white to blue, respectively. The same colors are used throughout. (**D**) Schematic of the complex. Unresolved downstream DNA is shown as a dotted line.

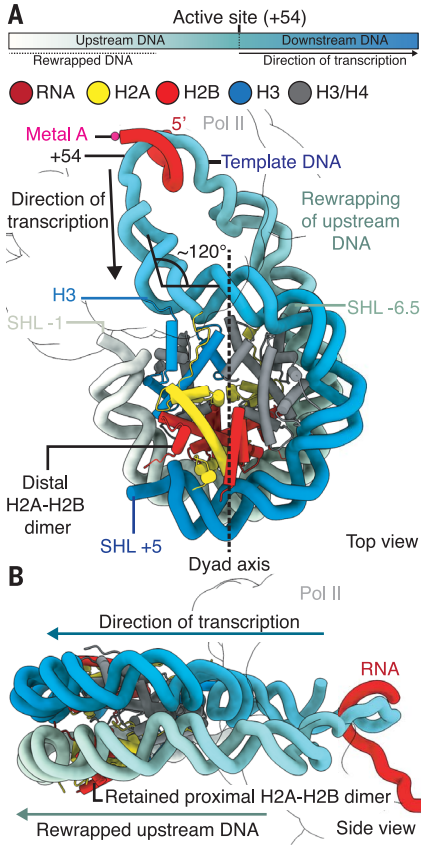

Fig. 2. Details of nucleosome rewrapping during transcription. (**A**) Rewrapping of transcribed upstream DNA from SHL −6.5 to SHL −1 on the histone octamer and unwrapping of downstream DNA from SHL +5 to SHL +7. H3 inserts between rewrapped upstream and downstream DNA. (**B**) Nucleosome side view showing template looping with the transcribed upstream DNA rewrapping the nucleosome. Directions of transcription and rewrapping are indicated.

DNA duplex is bent away from the jaw domain into the cleft by ~30°, losing contact with RPB5 (fig. S5B) (*22*). After exiting the Pol II cleft, the downstream DNA is then contorted by ~120° and is bound by the histones from SHL −0.5 to SHL +5 (Fig. 2, A and B, and fig. S5C). This DNA path differs from previous downstream DNA conformations of Pol II–nucleosome complexes in which the downstream DNA projects in a straight B-DNA conformation toward the nucleosome (*12*–*15*). The small gap between downstream DNA at SHL −0.5 and rewrapped nucleosomal DNA at SHL −1 is filled by histone H3 N-terminal residues 39 to 43 (Fig. 2A). Additionally, we observed that downstream DNA starting at SHL +5 to SHL +7 was no longer bound by the nucleosome and projects away from the complex (fig. S5D).

On the upstream side of Pol II, the rewrapped DNA displaces SPT4 and the SPT5 NGN and KOW1 domains of DSIF from their previously observed binding positions on Pol II (Fig. 3A) (*21*, *23*). However, we observed densities for the SPT5 domains KOW2-3, KOWx-4, and KOW5 (fig. S4, K and L). This suggests that the partial displacement of SPT4 and SPT5 from the tip of the Pol II clamp and from the RPB2 protrusion domain is required for rewrapping of nucleosomal DNA and supports nucleosome retention, as reported biochemically (*24*). Consistent with this observation, functional genomics data show changes in cross-linking patterns for Spt4/5 as Pol II transcribes through a nucleosome (*25*). We observed a second Pol II-DSIF-PAF1c-SPT6-TFIIS-nucleosome complex in our data stalled at nucleosomal bp +38 (figs. S7 to S9 and tables S2 and S3). This complex shows no rewrapping, but SPT4 and the SPT5 NGN and KOW1 domains are present and are positioned at the Pol II clamp as observed in previous studies (fig. S9, F and G).

In the rewrapped nucleosome, we observed interactions among Pol II, the PAF1c subunit CTR9, and the nucleosome (Fig. 3, B to D, and figs. S4, I to L). These contacts actively stabilized the observed nucleosome conformation by contacting the rewrapped DNA. First, we observed an interaction between the RPB2 protrusion residue lysine 427 (K427) and the upstream DNA (Fig. 3B). RPB2 K427 is widely conserved among eukaryotes but is not found in the corresponding *Escherichia coli* RNA polymerase subunit (fig. S10). Thus, the protrusion domain may have evolved to support chromatin transcription by mediating DNA rewrapping. Second, like previous *Saccharomyces cerevisiae* Pol II–nucleosome structures (*13*, *15*), RPB1 clamp head residue

K203 contacts downstream nucleosomal DNA at SHL −0.5 (Fig. 3C). Third, we observed that the C-terminal end of the CTR9 trestle helix lies near the rewrapped DNA at SHL −1, potentially stabilizing the rewrapped DNA (Fig. 3D). These contacts formed by Pol II and transcription elongation factors with the retained nucleosome suggest that the transcription elongation machinery actively supports nucleosome retention by stabilizing the nucleosomal DNA through multiple contacts with the DNA phosphate backbone.

Together, our data show that Pol II can help to retain nucleosomes during transcription by facilitating DNA rewrapping back onto the histone octamer surface (Fig. 4). This rewrapping and template looping supports the 0-loop hypothesis that was proposed on the basis of biochemical data (*6*, *16*). This model proposes that Pol II transcribes nucleosomes while DNA both upstream and downstream of Pol II is bound to the nucleosome. Our structure supports a loop size of ~90 bp (fig. S6), comparable to atomic force microscopy measurements (*6*). Unambiguous assignment of the DNA register and comparison with canonical nucleosomes showed that 30 bp of previously linear entry side DNA rewrap the nucleosome from SHL −4 to SHL −1 (fig. S6), resulting in an upstream nucleosomal shift after transcription (*6*, *26*). Such a retrograde movement of nucleosomes has been observed both in vivo and in vitro (*19*, *26*).

Previous structural studies have shown that stabilization of the proximal H2A-H2B dimer can be achieved by the binding of a secondary, "foreign" DNA molecule in *trans* (*14*, *15*). By contrast, our structure, in which Pol II is accompanied by the transcription factors DSIF, SPT6, and PAF1c, now reveals that rewrapping of upstream DNA can also occur in *cis*, where the same DNA molecule rewraps the histone core (Fig. 4). This has wide implications for our understanding of the mechanism of nucleosome retention during transcription.

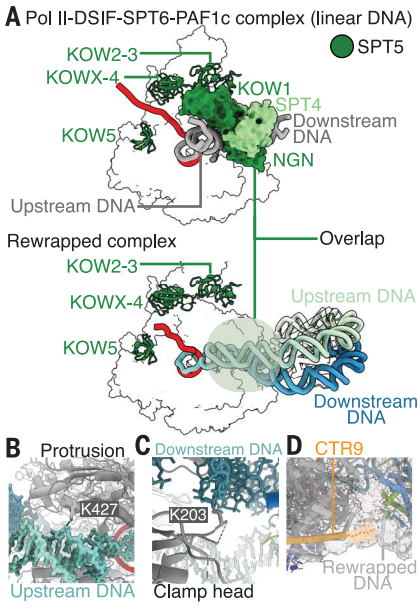

Fig. 3. Interactions and changes in elongation complex conformation. (**A**) Comparison of the Pol II-DSIF-SPT6-PAF1c complex on the linear DNA template (gray, PDB 6TED) with the Pol II-DSIF-SPT6-PAF1c-TFIIS-nucleosome structure stalled at +54 revealing displacement of SPT4 and SPT5 NGN and KOW1 domains in the rewrapped complex. The trajectory of the upstream DNA duplex is altered compared with the Pol II-DSIF-SPT6-PAF1c complex on a linear DNA template. SPT5 KOW2-3, x-4, and 5 (forest green) are retained in the rewrapped complex. (**B**) Interaction of Pol II RPB2 protrusion domain residue K427 with nucleosomal DNA at the dyad. (**C**) Interaction of the Pol II clamp head (residue K203) with nucleosomal DNA. (**D**) The CTR9 C terminus is positioned near the rewrapped nucleosomal DNA at SHL −1. Density is shown in gray.

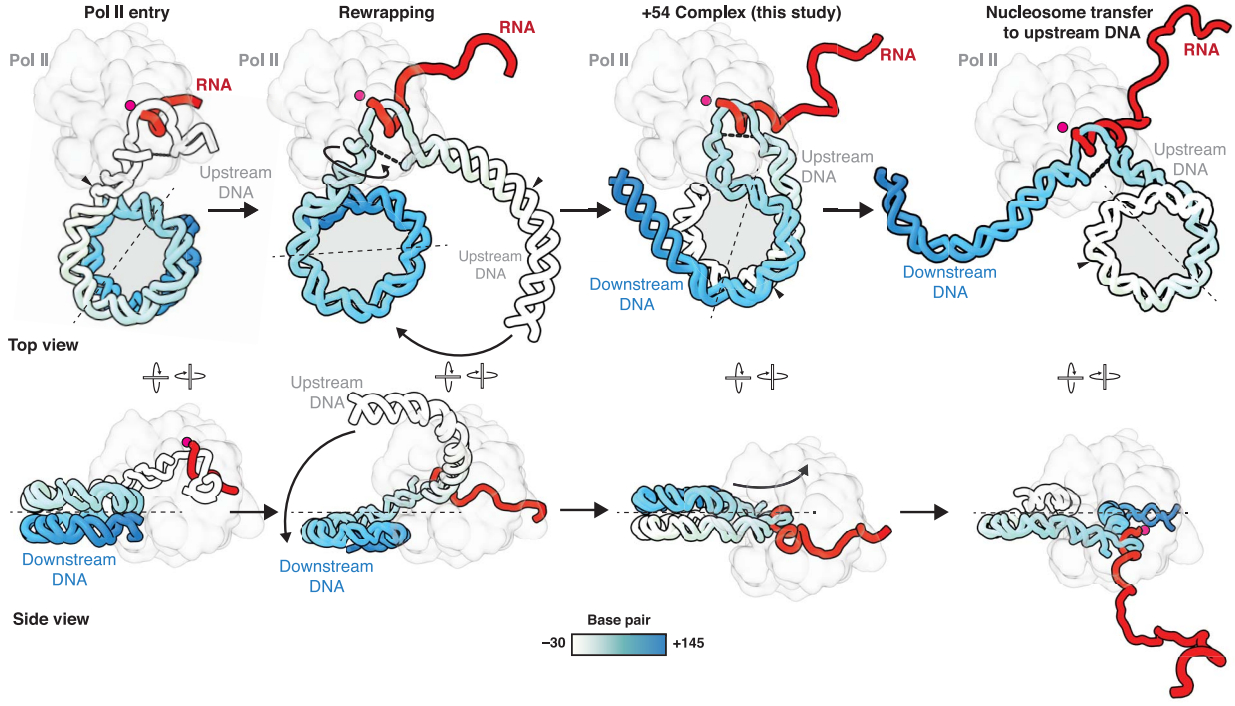

Fig. 4. Model of nucleosome retention. Model depicting Pol II transcription through a nucleosome. After Pol II has transcribed sufficiently into the nucleosome, the DNA rewraps. Further transcription may result in a complete transfer of the nucleosome to upstream DNA. The transfer may result in a positional shift of the nucleosome. Pol II is shown as an outline. Metal A is shown as a magenta sphere. The histone octamer is shown as a gray circle. Nucleosomal entry bp +1 is indicated with a black arrow. The dyad axis is indicated as a dotted line.

Whereas binding of a secondary molecule in *trans* suggests a mechanism involving stabilization of the nucleosome to distal DNA, our structure provides evidence that nucleosomes are not fully disassembled during transcription (*6*, *17*–*19*) (see the supplementary text).

We propose a model that explains nucleosome transfer to the upstream side of Pol II (Fig. 4). Transcription of Pol II past the dyad is likely to result in complete unraveling of the ~50 bp of downstream DNA that are still wrapped around the nucleosome from SHL −0.5 to SHL +5. Release of the downstream DNA from the octamer will result in a complete transfer of the nucleosome to the upstream DNA. At this point, Pol II only transcribes linear downstream DNA, which may explain why the distal part of the nucleosome does not pose any major transcriptional barrier (*12*, *20*). The proximal and distal sides of the histone octamer switch during the transfer process.

Further rewrapping of upstream DNA may result in a reduced linker length between the transcribed nucleosome and the preceding nucleosome. Chromatin remodelers belonging to the CHD and ISWI families might be needed to reestablish nucleosome spacing (*27*). The chromatin remodeler CHD1, for example, could be readily recruited by the upstream-positioned PAF1c subunit RTF1 to engage the retained nucleosome and correct nucleosome spacing (*28*).

Nucleosomes are critical for transcription fidelity by limiting transcription initiation to promoter regions and by maintaining transcriptional memory through epigenetic modifications. Our structure provides a structural foundation to explain how nucleosomes are retained during transcription elongation, and it also provides a framework to understand the actions of the transcription machinery in a chromatin environment.

REFERENCES AND NOTES

1. K. Luger, A. W. Mäder, R. K. Richmond, D. F. Sargent, T. J. Richmond, *Nature* **389**, 251–260 (1997).
2. F.-K. Hsieh *et al*., *Proc. Natl. Acad. Sci. U.S.A.* **110**, 7654–7659 (2013).
3. H. A. Cole, J. Ocampo, J. R. Iben, R. V. Chereji, D. J. Clark, *Nucleic Acids Res.* **42**, 12512–12522 (2014).
4. M. L. Kireeva *et al*., *Mol. Cell* **9**, 541–552 (2002).
5. S. Bevington, J. Boyes, *EMBO J.* **32**, 1381–1392 (2013).
6. L. Bintu *et al*., *Nat. Struct. Mol. Biol.* **18**, 1394–1399 (2011).
7. C.-K. Lee, Y. Shibata, B. Rao, B. D. Strahl, J. D. Lieb, *Nat. Genet.* **36**, 900–905 (2004).
8. S. Ramachandran, K. Ahmad, S. Henikoff, *Mol. Cell* **68**, 1038–1053.e4 (2017).
9. G. Schlissel, J. Rine, *Proc. Natl. Acad. Sci. U.S.A.* **116**, 20605–20611 (2019).
10. C. D. Kaplan, L. Laprade, F. Winston, *Science* **301**, 1096–1099 (2003).
11. M. Smolle, J. L. Workman, *Biochim. Biophys. Acta* **1829**, 84–97 (2013).
12. L. Farnung, M. Ochmann, M. Engeholm, P. Cramer, *Nat. Struct. Mol. Biol.* **28**, 382–387 (2021).
13. L. Farnung, S. M. Vos, P. Cramer, *Nat. Commun.* **9**, 5432 (2018).
14. H. Ehara *et al*., *Science* **363**, 744–747 (2019).
15. T. Kujirai *et al*., *Science* **362**, 595–598 (2018).
16. O. I. Kulaeva *et al*., *Nat. Struct. Mol. Biol.* **16**, 1272–1278 (2009).
17. V. M. Studitsky, D. J. Clark, G. Felsenfeld, *Cell* **76**, 371–382 (1994).
18. J. Bednar, V. M. Studitsky, S. A. Grigoryev, G. Felsenfeld, C. L. Woodcock, *Mol. Cell* **4**, 377–386 (1999).
19. C. Hodges, L. Bintu, L. Lubkowska, M. Kashlev, C. Bustamante, *Science* **325**, 626–628 (2009).
20. Z. Chen *et al*., *eLife* **8**, e48281 (2019).
21. S. M. Vos, L. Farnung, A. Linden, H. Urlaub, P. Cramer, *Nat. Struct. Mol. Biol.* **27**, 668–677 (2020).
22. C. Bernecky, F. Herzog, W. Baumeister, J. M. Plitzko, P. Cramer, *Nature* **529**, 551–554 (2016).
23. C. Bernecky, J. M. Plitzko, P. Cramer, *Nat. Struct. Mol. Biol.* **24**, 809–815 (2017).
24. J. B. Crickard, J. Lee, T.-H. Lee, J. C. Reese, *Nucleic Acids Res.* **45**, 6362–6374 (2017).
25. Ü. Uzun, T. Brown, H. Fischl, A. Angel, J. Mellor, *Cell Rep.* **36**, 109755 (2021).
26. M. Radman-Livaja *et al*., *PLOS Biol.* **9**, e1001075 (2011).
27. P. R. Eriksson, D. J. Clark, *Sci. Rep.* **11**, 4195 (2021).
28. R. Simic *et al*., *EMBO J.* **22**, 1846–1856 (2003).

ACKNOWLEDGMENTS

We thank all members of the Farnung laboratory; members of the Cramer laboratory for histone proteins; D. Moazed, K. Adelman, S. Buratowski, T. Rapoport, and F. Winston for discussions and critical reading of the manuscript and valuable input; and the Harvard Cryo-EM Center for Structural Biology at Harvard Medical School for support with data collection. **Funding:** L.F. is supported by the Dorsett L. Spurgeon, MD (HMS 1929) Distinguished Research Award at Harvard Medical School and by The Smith Family Awards Program for Excellence in Biomedical Research. S.M.V is supported by The Smith Family Awards Program for Excellence in Biomedical Research, the NIH Director's New Innovator Award (grant no. DP2-GM146254), and Alex's Lemonade Stand Foundation Crazy 8 Initiative (grant no. 20071760). **Author contributions:** Conceptualization: L.F.; Funding acquisition: S.M.V., L.F.; Investigation: M.F., J.H.M.S., S.M.V., L.F.; Methodology: M.F., LF; Project administration: L.F.; Supervision: L.F.; Visualization: M.F., L.F.; Writing – original draft: M.F., L.F.; Writing – review and editing: M.F., S.M.V., L.F. **Competing interests:** The authors declare no competing interests. **Data and materials availability:** All data are available in the main text or the supplementary materials. The cryo-EM reconstructions and final models for the complex stalled at +54 were deposited with the Electron Microscopy Database (EMD- 26620) and the Protein Data Bank (PDB 7UNC). The cryo-EM reconstructions and final models for the complex stalled at +38 were deposited with the Electron Microscopy Database (EMD-26621) and the Protein Data Bank (PDB 7UND). **License information:** Copyright © 2022 the authors, some rights reserved; exclusive licensee American Association for the Advancement of Science. No claim to original US government works. https://www.science.org/about/science-licenses-journal-article-reuse

SUPPLEMENTARY MATERIALS

science.org/doi/10.1126/science.abo3851
Materials and Methods
Supplementary Text
Figs. S1 to S10
Tables S1 to S4
Movie S1
MDAR Reproducibility Checklist
References (*29*–*40*)

View/request a protocol for this paper from *Bio-protocol*.

Submitted 31 January 2022; accepted 12 May 2022
10.1126/science.abo3851

HISTORICAL DROUGHT

Droughts and societal change: The environmental context for the emergence of Islam in late Antique Arabia

Dominik Fleitmann[1]*, John Haldon[2]*, Raymond S. Bradley[3], Stephen J. Burns[3], Hai Cheng[4,5,6], R. Lawrence Edwards[7], Christoph C. Raible[8,9], Matthew Jacobson[10], Albert Matter[11]

In Arabia, the first half of the sixth century CE was marked by the demise of Himyar, the dominant power in Arabia until 525 CE. Important social and political changes followed, which promoted the disintegration of the major Arabian polities. Here, we present hydroclimate records from around Southern Arabia, including a new high-resolution stalagmite record from northern Oman. These records clearly indicate unprecedented droughts during the sixth century CE, with the most severe aridity persisting between ~500 and 530 CE. We suggest that such droughts undermined the resilience of Himyar and thereby contributed to the societal changes from which Islam emerged.

The Himyarite kingdom was the dominant power in Arabia from the late third to the early sixth century CE (Fig. 1A). Its dissolution over the course of the sixth century CE marked the end of a 1400-year-long pre-Islamic period of supratribal polities in Arabia (*1*–*6*), but the reasons for its demise remain debated. Himyar's decline was characterized by political disorder, socioeconomic change, shifting settlement patterns and demography (Fig. 1, B and C), and the decline of major irrigation systems (*2*, *4*, *5*, *7*, *8*). The annexation of Himyar by Aksum (today's Ethiopia) in 525 CE and frequent interventions from the Byzantine and Sasanian Empires were additional factors that contributed to profound social, economic, and political transformations during the sixth century CE in Arabia (*1*, *5*, *6*). Explanations for these changes focus on sociopolitical factors (*4*, *5*). The possibility that drought played a role has been largely ignored (*4*, *6*, *9*, *10*), despite the fact that Himyar and the southern Arabian region more widely were extremely vulnerable to droughts because their economy was based on rain-fed and irrigated agriculture (*5*, *6*, *9*).

[1]Department of Environmental Sciences, University of Basel, 4054 Basel, Switzerland. [2]Department of History, Princeton University, Princeton, NJ 08544, USA. [3]Department of Geosciences, University of Massachusetts, Amherst, MA 01003, USA. [4]Institute of Global Environmental Change, Xi'an Jiatong University, Xi'an 710054, China. [5]State Key Laboratory of Loess and Quaternary Geology, Institute of Earth Environment, Chinese Academy of Sciences, Xi'an 710061, China. [6]Key Laboratory of Karst Dynamics, MLR, Institute of Karst Geology, CAGS, Guilin 541004, China. [7]Department of Earth and Environmental Sciences, University of Minnesota, Minneapolis, MN 55455, USA. [8]Climate and Environmental Physics, Physics Institute, University of Bern, 3012 Bern, Switzerland. [9]Oeschger Centre for Climate Change Research, University of Bern, 3012 Bern, Switzerland. [10]Department of Archaeology, University of Reading, Reading RG6 6AB, UK. [11]Institute of Geological Sciences, University of Bern, 3012 Bern, Switzerland.
*Corresponding author. Email: dominik.fleitmann@unibas.ch (D.F.); jhaldon@princeton.edu (J.H.)

The lack of highly resolved and precisely dated palaeoclimate records from southern Arabia has prevented an assessment of whether droughts were a factor that contributed to Himyar's decline. Here, we combine hydrological, historical, and archaeological records from the Middle East and East Africa with a new stalagmite record of winter-spring precipitation and effective moisture (EM) in northern Oman to demonstrate that severe and persistent droughts may have been an important factor in the changes that took place in southern Arabia in the sixth century CE (*2*, *4*, *5*, *11*).

Stalagmite H12 from Hoti Cave in northern Oman (57°21′E, 23°05′N; 800 m above sea level) (Fig. 1A and figs. S1 and S2) provides a well-dated hydroclimatic record that spans this critical period of history. Rainfall in northern Oman and most of Arabia originates predominantly from Mediterranean frontal systems, whereas summer monsoon (SM) precipitation affects only the Yemeni highlands and southern Oman (*12*). Thunderstorms during summer and occasional cyclones are additional sources of rainfall. Regional precipitation varies between 50 and 255 mm year^{-1} (Al Hamra; 1978–1997) and occurs in winter and spring (~65% of annual rainfall) and summer (fig. S3). Importantly for this study, changes in rainfall (fig. S4) are consistent across southern Arabia, particularly for extreme droughts, which are often supraregional (*13*).

The chronology of H12 is based on 20 U-Th ages, with an average growth rate of ~0.23 mm year^{-1} over the past 2650 years (fig. S5 and tables S1 and S2). The oxygen ($\delta^{18}O$) and carbon ($\delta^{13}C$) isotope records have a ~2-year resolution and reflect fluctuations in rainfall amount and EM, respectively (*14*), as indicated by several observations. First, H12 $\delta^{18}O$ values correlate [correlation coefficient (r) = −0.69; $p \leq 0.001$] with mean annual rainfall in Oman and are consistent with rainfall anomalies for the entire Arabian Peninsula (*15*, *16*), with higher rainfall related to more negative $\delta^{18}O$ values (Fig. 2, A and B). Second, more positive H12 $\delta^{18}O$ values correspond to a reduced diameter of the stalagmite cap (Fig. 2C), indicative of lower drip rates and winter-spring precipitation, respectively (*17*). Third, the strong correlation between H12 $\delta^{18}O$ and $\delta^{13}C$ values (r^2 = 0.52) indicates that calcite did not precipitate in isotopic equilibrium with its parent drip water. Because $\delta^{13}C$ values are strongly governed by CO_2 degassing, more positive $\delta^{13}C$ values indicate lower drip rates and a lower partial pressure of CO_2 (P_{CO_2}) of cave air because of enhanced ventilation of Hoti Cave at times of lower precipitation and cave lake levels (fig. S1). Additionally, reduced vegetation density and soil microbial activity during drier

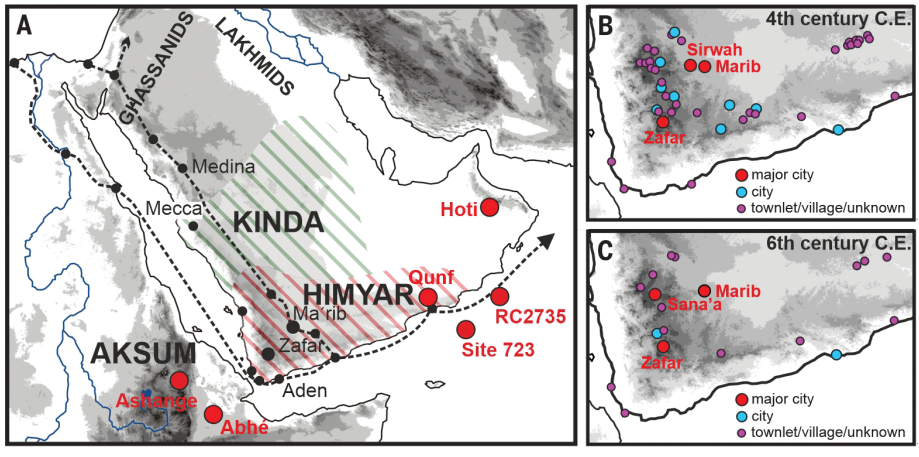

Fig. 1. Location and settlement maps. (**A**) Map showing the location of key proxy records and the suggested extent of Himyar (red line) and Kinda (green line) at the beginning of the sixth century CE (*6*). Black dashed lines denote the main trading routes (*6*). (**B** and **C**) Settlement patterns in Himyar in the (B) fourth and (C) sixth centuries CE (*8*).

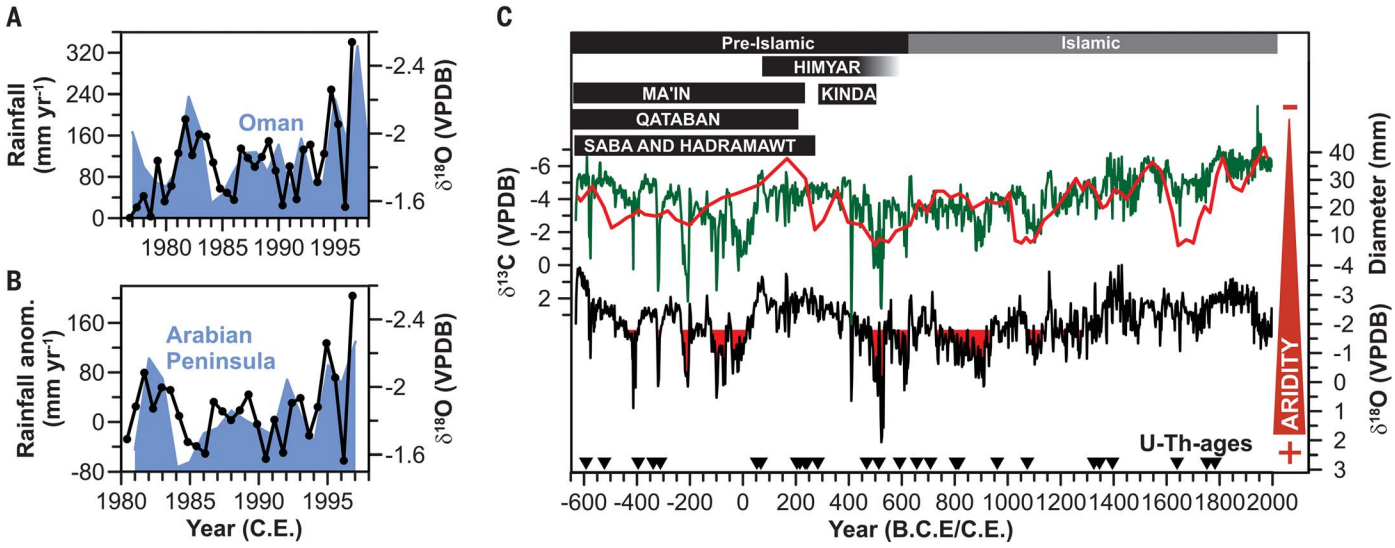

Fig. 2. Hoti Cave and meteorological records. (**A** and **B**) Comparison of H12 $\delta^{18}O$ values and (A) mean annual rainfall for Oman (*15*) and (B) precipitation anomalies [with respect to the 1978–1997 average of −1.8 per mil (‰)] averaged for the Arabian Peninsula (*16*). VPDB, Vienna Pee Dee Belemnite international standard. (**C**) H12 $\delta^{18}O$ (black), $\delta^{13}C$ (green), and stalagmite diameter (red line) records. The red-shaded area shows EM anomalies with respect to the 1978–1997 mean (−1.8‰). Black triangles denote ^{230}Th dates (tables S1 and S2). Black-shaded bars denote the estimated lifetime of kingdoms in southern and central Arabia (*11*).

years leads to lower biogenic soil P_{CO_2} and more positive calcite $\delta^{13}C$ values (*18*). Thus, H12 $\delta^{18}O$ and $\delta^{13}C$ values are primarily governed by precipitation and EM.

The H12 $\delta^{18}O$ profile displays high variability in EM over the past ~2600 years, with two periods of persistently lower EM from ~250 BCE to 25 CE and from ~480 to 1400 CE, on which distinct decadal to multidecadal fluctuations in $\delta^{18}O$ were superimposed (Fig. 2C). The most pronounced minimum in EM occurred from ~520 to 532 CE, with the most severe drought conditions of the entire H12 record centered at ~523 CE ± 30 years (Fig. 3B). This date is in excellent agreement with other independently dated winter-spring rainfall records from the Middle East (Fig. 3). In the Neor Lake record from northern Iran (*19*), a sharp rise in titanium (high dust flux) starts at the beginning of the sixth century CE. The lake level of the Dead Sea (*20*) declined from ~490 CE onward, and more positive $\delta^{13}C$ values (reduced EM) are observed in the Jeita Cave $\delta^{13}C$ record from Lebanon at ~510 CE (*21*). Likewise, the frequency of historical accounts of droughts in the Middle East peaks between 520 and 530 CE (Fig. 3F), with the spring of Siloam in Jerusalem reportedly drying up at ~520 CE (*22*, *23*). Overall, key hydrological records from the Middle East indicate drought conditions related to a decline in winter-spring precipitation and a substantial decrease in EM from ~480 CE onward. By contrast, the Nar Lake $\delta^{18}O$ record from Turkey (*24*) documents a substantial increase in precipitation, which is most likely related to a northward displacement of storm tracks in the eastern Mediterranean at the beginning of the sixth century CE, with fewer rain-bearing storms reaching the Fertile Crescent and Arabia.

Though winter-spring precipitation is the main source of annual rainfall throughout the Middle East, SM precipitation is an additional crucial source of rainfall in southern Arabia and Yemen (Himyar) in particular. SM records from southern Oman (Qunf Cave) (*12*, *14*), Ethiopia (Lake Ashange and Lake Abhé) (*25*, *26*), the Arabian Sea (sites RC2735 and 723) (*27*, *28*), India (Sahiya Cave) (*29*), and China (Dongge Cave) (*30*) indicate that SM wind strength and precipitation reached their absolute minimum during the sixth century CE as boreal summer insolation, a primary driver of monsoon intensity (*14*), reached its lowest Holocene values (Fig. 4). Furthermore, an abrupt decline in precipitation between 450 and 500 CE is evident in the SM records from Ethiopia (Lake Ashange) (*25*), the Arabian Sea (sites RC735 and 723) (*27*, *28*), and India (core 16A) (*31*), and, taking age uncertainties of the individual records into account, these are broadly concurrent with decreasing winter-spring precipitation in the H12 $\delta^{18}O$ and other hydroclimate records displayed in Fig. 4. In addition, the precisely dated Sahiya Cave (India) SM record (*29*) reveals a decrease in SM rainfall after ~490 CE (Fig. 3H). Taken together, mean annual precipitation in Arabia and northeastern Africa reached an absolute minimum at the beginning of the sixth century CE, with the most severe drought conditions persisting between ~500 and 530 CE (Fig. 4).

The synchronicity between peak aridity in southern Arabia and the sudden decline of Himyar points to a possible causal relationship between both. Himyar, with its centralized political system of kingship and subordinate chiefdoms, was the dominant power in southern and central Arabia (Fig. 1) (*2*, *6*). Though international trade in aromatics and metals had earlier also been a major source of revenue, agricultural production was fundamental to both central and regional economies (*5*, *7*, *32*). The importance of agriculture is evidenced by widespread terraced fields in the highlands, numerous irrigation systems along the desert margin, and a considerable expansion of hydraulic structures between the first and fourth centuries CE (*5*, *33*–*35*) (figs. S6 and S7). The dams, for instance, were a symbol and instrument through which Himyarite rulers exerted their authority, as indicated by inscriptions. Dams and terraced fields were designed to harvest rainfall and runoff ("runoff irrigation") because water was the most limited agricultural resource. The structural integrity of the terraced fields depended on the proper maintenance of the whole system of hillside terraces, and dams required constant repairs, which only a well-organized workforce and stable society could provide (*2*, *6*, *7*). Furthermore, a stable society and a functioning political entity were crucial to manage the proper allocation of water for the irrigated plots, particularly during drier years with more frequent water disputes (*36*). Himyar's agricultural productivity depended on a consistent rainfall cycle, with two rainy seasons in spring and summer (fig. S8). These factors combined made Himyar vulnerable to droughts, and low agricultural yields would have had a negative impact on Himyar's socioeconomic and political stability and thus the

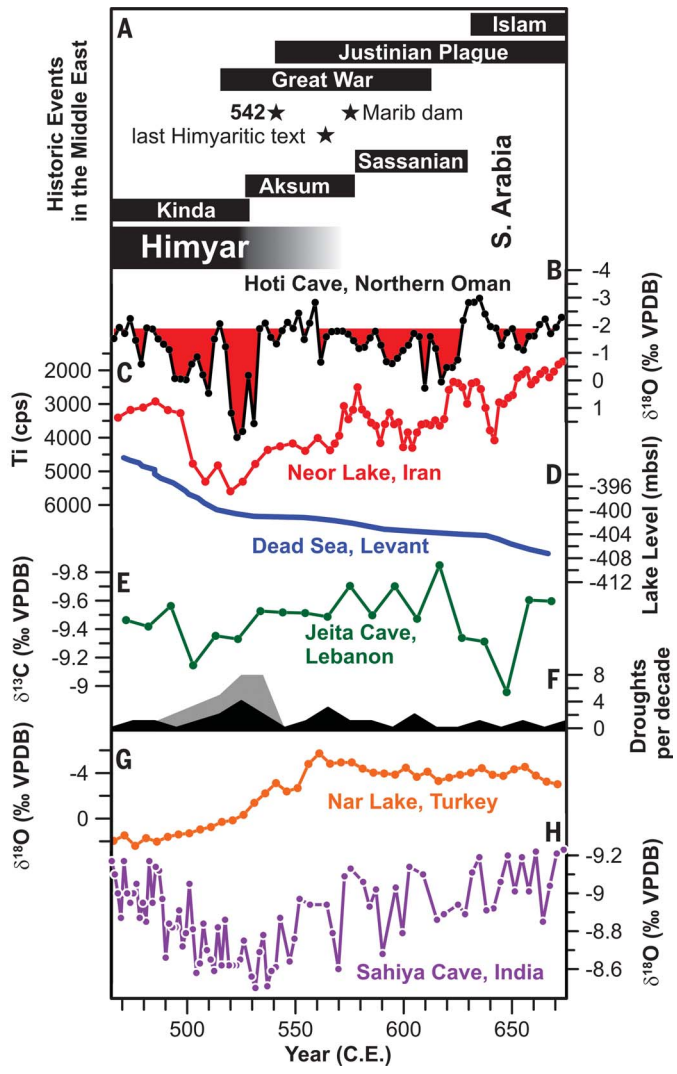

Fig. 3. Climate proxy records and historic events. (**A**) Key historic and cultural events in southern Arabia. Black bars denote ruling powers in southern Arabia, sociocultural events (star symbols) such as the disappearance of Himyarite inscriptions (*39*, *48*), and the destruction of the dam of Marib (*7*). (**B**) H12 $\delta^{18}O$ record from Hoti Cave. The red-shaded area marks periods of below-normal precipitation (with respect to the 1978–1997 average of −1.8‰). (**C**) Lake Neor titanium record from Iran (*19*). cps, counts per second. (**D**) Dead Sea level (*20*). mbsl, meters below sea level. (**E**) Jeita Cave $\delta^{13}C$ record (*21*). (**F**) Historic accounts (plotted as droughts per decade) derived from the Middle East after (*22*) (black-shaded curve) and (*23*) (gray-shaded curve). (**G**) Nar Lake $\delta^{18}O$ record from Turkey (*24*). (**H**) Sahiya Cave $\delta^{18}O$ record from India (*29*).

proper management of all water-harvesting structures. Thus, the abrupt and persistent decrease in rainfall and EM, respectively, throughout Arabia at the end of the fifth and beginning of the sixth century CE must have been a substantial stressor, undermining Himyar's resilience to both internal and external socioeconomic and geopolitical conflicts, particularly Christian Aksumite attempts to control the lucrative trading routes along the Red Sea and Arabian Sea coasts. Such stress may well have been further exacerbated by the possible effects of the global cooling that marked the beginning of the so-called Late Antique Little Ice Age that is visible in proxy data from the later 530s CE (*37*).

From the 480s CE, Himyar faced a number of problems. Internal conflict between rival elite lineages, partly informed by religious affiliations to either Judaism or Christianity, was exacerbated by Aksumite intervention between 518 and 530 CE that reduced Himyar to vassal status (*5*, *11*, *38*–*40*). This was followed by a brief revival of Himyarite power (but under an Aksumite general, Abreha) (*5*), to which a short-lived increase in winter-spring precipitation between 530 and 545 CE (Figs. 2 and 3) may perhaps have contributed. Yet it took this new regime at least four expeditions over more than 15 years to reestablish Himyarite political hegemony outside Yemen and Hadramaut, suggestive of both the weakening of its power and the extent of fragmentation of the traditional order in the region (*38*). Further indications of this include evidence for drought-induced migration across the region into Persian- and Byzantine-controlled Syria and Iraq, as well as southward into Yemen and Hadramaut, and the failure to maintain the dam of Marib, leading to a collapse of the system in ~580 CE and its final destruction in ~600 CE (an event important enough to find mention in the Koran 34:15–17) (*2*, *5*, *7*). The disappearance of Himyarite inscriptions after ~559 CE (*5*) may also indicate a breakdown of political authority and the established order. From about 570 CE, Himyar came under Persian domination and effectively ceased to exist as an independent polity (*1*–*3*, *5*, *6*, *40*).

The weakening of Himyar from the 480s CE onward, and its rapid conquest by Aksum in 525 CE, were thus directly coincident with both internal conflict as well as increasing aridity and declining agricultural yields that were due to a simultaneous reduction in winter-spring and SM precipitation, culminating in the most severe drought conditions of the entire Holocene in the early sixth century CE. Himyar's continued weakening through the middle decades of the sixth century CE, in spite of the temporary resurgence under Abreha, and its final dissolution in the 570s CE should thus be understood in the context of these conditions and the evidence for the persistence of drought conditions during the sixth century CE (Fig. 4). Aksum, however, was less affected by the drought because rainfall amounts were generally much higher (fig. S9) and a reduction in rainfall was therefore less detrimental to agricultural productivity. Although correlation is not necessarily causation, the singular magnitude and persistence of sixth-century drought, superimposed on a region that was highly dependent on rain-fed agriculture, is coincident with a clear turning point in Arabian history (*2*, *4*–*6*), when a cascade of regional political and socioreligious transformations occurred over the following decades.

Whether Himyar's decline as the dominant Arabian polity induced a sociopolitical vacuum remains unclear, although this is often assumed (*4*–*7*). But it has been plausibly argued that one result of the changed situation throughout Arabia during the sixth and early seventh centuries CE was a growth in the importance of pilgrimage and economic centers. Of these, Mecca (Muhammad's birthplace) gained considerable influence in central and southern Arabia in the first half of the sixth century CE (*41*). Furthermore, the reduction in the reach of Himyarite power drew the competing Byzantine and Sasanian empires into increasing and intensified competition for political and religious influence in the region as well as for economic resources, including precious metals (*42*, *43*). Such involvement was long-standing, and their influence was exercised both through their client kingdoms, the Ghassanid and Lakhmid confederacies (and their earlier equivalents) in northern Arabia, and through Aksum. Direct intervention was thus not new and had indeed occurred on several occasions from the third century on (*44*–*46*). But the crucial difference from the middle of the sixth century was precisely the absence of a stable Himyarite kingdom. Finally, external interventions stimulated a hostile

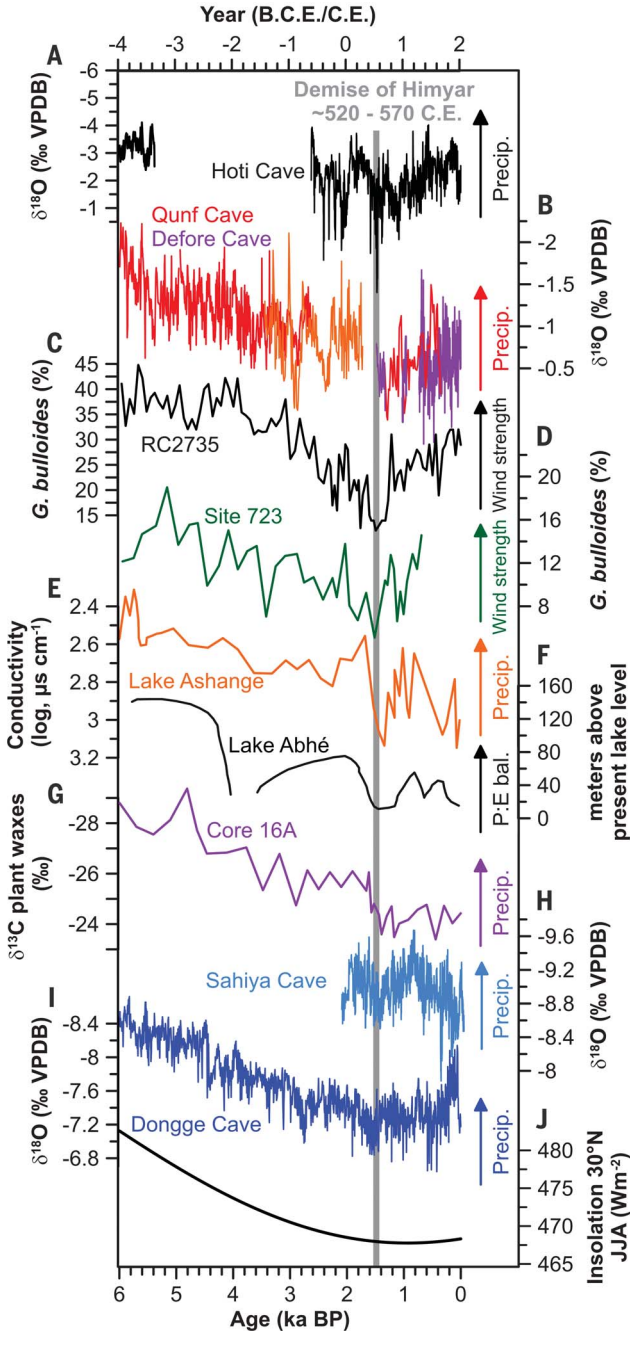

Fig. 4. Comparison of the H12 $\delta^{18}O$ record with SM records. (**A**) Hoti Cave $\delta^{18}O$ record. (**B**) Defore Cave (purple) and Qunf Cave (red and orange) $\delta^{18}O$ records from southern Oman (*12*). (**C** and **D**) *Globigerina bulloides*, a heterotrophic planktonic foraminifer, monsoon upwelling records from the Arabian Sea (*27*, *28*). (**E**) Lake Ashange conductivity record from Ethiopia (*25*). (**F**) Lake level record from Lake Abhé at the Etiopia-Djibouti border (*26*). P.E. bal., precipitation minus evaporation balance. (**G**) $\delta^{13}C$ plant-wax record from core 16A offshore of India (*31*). (**H**) Sahiya Cave $\delta^{18}O$ record from India (*29*). (**I**) Dongge Cave $\delta^{18}O$ record from China (*30*). (**J**) Insolation curve at 30°N, averaged from June to August (*49*). All records reflect either SM wind strength or precipitation. The vertical gray bar marks the time interval between ~520 and 570 CE, which covers the period of Himyar's demise. ka BP, thousand years before present.

reaction, both to Christian Aksumite proselytizing and to the political maneuvering of the neighboring empires (*11*), although that this promoted a search for a new "Arab" identity remains questionable (*2*, *10*, *41*). Regardless, after 525 CE and the Aksumite invasion, both Arabian reactions and outside interventions occurred in a geopolitical context without an effective centralizing power. The decline and dissolution of Himyar was thus a critical element in the socioeconomic, political, and religious-cultural transformations in Arabia that ultimately framed the emergence of a range of new religious leaders or movements, many focused around monotheistic beliefs, including Islam. The challenges faced by the Islamic leadership in unifying the Arabian Peninsula in the 620s CE, in spite of substantial opposition from such competitors as well as from tribes that had converted to Judaism or were hostile to the Quraysh (Muhammad's tribe), reflected this situation (*2*–*4*, *6*, *47*). But by the late 620s CE, with Himyarite authority a distant memory and both Persia and Byzantium exhausted by their long war, the early Islamic leadership had the field to itself with respect to its ability to mount long-distance military expeditions.

We do not suggest that the extreme droughts of the late fifth to early seventh century CE in Arabia were the direct trigger for these fundamental changes (*43*), which were complex and, in several respects, of long duration. But we can now confirm from an entirely independent proxy that the Arabian Peninsula suffered from unusual and extreme aridity in the period between ~500 and 530 CE. This constituted an important, and hitherto largely neglected, factor that can only have undermined Himyarite resilience to both longer-term and more immediate internal and external stresses (*2*, *4*).

REFERENCES AND NOTES

1. M. Lecker, in *The Formation of the Islamic World, Sixth to Eleventh Centuries*, vol. 1 of *The New Cambridge History of Islam*, C. F. Robinson, Ed. (Cambridge Univ. Press, 2010), pp. 153–169.
2. C. J. Robin, in *The Oxford Handbook of Late Antiquity*, S. F. Johnson, Ed. (Oxford Univ. Press, 2012), pp. 247–332.
3. G. Bowersock, *The Throne of Adulis: Red Sea Wars on the Eve of Islam* (Oxford Univ. Press, 2013).
4. A. Korotayev, V. Klimenko, D. Proussakov, *Acta Orientalia Academiae Scientiarum Hungaricae* **52**, 243–276 (1999).
5. K. Schippmann, *Ancient South Arabia – From the Queen of Sheba to the Advent of Islam* (Markus Wiener Publishers, 2001).
6. P. A. Yule, *Late Antique Yemen* (Linden Soft, 2007).
7. U. Brunner, *Arab. Archaeol. Epigr.* **8**, 190–202 (1997).
8. J. Schiettecatte, in *L'Arabie à la veille d l'Islam*, C. Robin, J. Schiettecatte, Eds. (CNRS, 2008), pp. 217–249.
9. T. J. Wilkinson, in *Landscapes and Societies: Selected Cases*, I. P. Martini, W. Chesworth, Eds. (Heidelberg, 2011), pp. 135–151.
10. F. M. Donner, *The Early Islamic Conquests* (Princeton Univ. Press, 1981).
11. R. G. Hoyland, *Arabia and the Arabs from the Bronze Age to the Coming of Islam* (Princeton Univ. Press, 2001).
12. D. Fleitmann *et al.*, *Science* **300**, 1737–1739 (2003).
13. M. Barlow *et al.*, *J. Clim.* **29**, 8547–8574 (2016).
14. D. Fleitmann *et al.*, *Quat. Sci. Rev.* **26**, 170–188 (2007).
15. A. Y. Kwarteng, A. S. Dorvlo, G. T. Vijaya Kumar, *Int. J. Climatol.* **29**, 605–617 (2009).
16. S. AlSarmi, R. Washington, *J. Geophys. Res.* **116**, D11109 (2011).
17. J. Martín-Chivelet, M. B. Muñoz-García, J. A. Cruz, A. I. Ortega, M. J. Turrero, *Sediment. Geol.* **353**, 28–45 (2017).
18. D. Fleitmann *et al.*, *Quat. Sci. Rev.* **23**, 935–945 (2004).
19. A. Sharifi *et al.*, *Quat. Sci. Rev.* **123**, 215–230 (2015).
20. R. Bookman, Y. Enzel, A. Agnon, M. Stein, *Geol. Soc. Am. Bull.* **116**, 555–571 (2004).
21. H. Cheng *et al.*, *Geophys. Res. Lett.* **42**, 8641–8650 (2015).
22. M. McCormick *et al.*, *J. Interdiscip. Hist.* **43**, 169–220 (2012).
23. I. G. Telelis, *Jahrbuch der Österreichischen Byzantinistik* **58**, 167–208 (2008).
24. M. D. Jones, C. N. Roberts, M. J. Leng, M. Turkes, *Geology* **34**, 361–364 (2006).
25. M. H. Marshall *et al.*, *Palaeogeogr. Palaeoclimatol. Palaeoecol.* **279**, 114–127 (2009).
26. F. Gasse, *Quat. Sci. Rev.* **19**, 189–211 (2000).
27. A. K. Gupta, D. M. Anderson, J. T. Overpeck, *Nature* **421**, 354–357 (2003).
28. D. M. Anderson, C. K. Baulcomb, A. K. Duvivier, A. K. Gupta, *J. Quaternary Sci.* **25**, 911–917 (2010).
29. A. Sinha *et al.*, *Nat. Commun.* **6**, 6309 (2015).
30. Y. Wang *et al.*, *Science* **308**, 854–857 (2005).
31. C. Ponton *et al.*, *Geophys. Res. Lett.* **39**, L03704 (2012).
32. I. Shahid, *Byzantium and the Arabs in the Sixth Century, Volume 2, Part 2: Economic, Social, and Cultural history* (Dumbarton Oaks Research Library and Collection, 2009).
33. J. Schiettecatte, in *Yémen, Terre d'archéologiee*, G. Charloux, J. Schiettecatte, Eds. (Geuthner, 2016), pp. 190–199.

34. J. Charbonnier, *Proc. Seminar Arabian Studies* **41**, 35–46 (2011).
35. J. Charbonnier, *Proc. Seminar Arabian Studies* **39**, 81–93 (2009).
36. D. M. Varisco, *Hum. Ecol. Interdiscip. J.* **11**, 365–383 (1983).
37. U. Büntgen *et al*., *Nat. Geosci.* **9**, 231–236 (2016).
38. G. Hatke, thesis, Princeton University, Princeton, NJ, (2011).
39. M. B. Piotrovsky, in *Land Use and Settlement Patterns*, vol. 2 of *The Byzantine and Early Islamic Near East*, G. R. D. King, A. Cameron, Eds. (Gerlach Press, 1994), pp. 213–220.
40. C. J. Robin, in *Arabs and Empires Before Islam*, G. Fisher, Ed. (Oxford Univ. Press, 2015), pp. 127–171.
41. P. Crone, *Meccan Trade and the Rise of Islam* (Princeton Univ. Press, 1987).
42. H. Kennedy, *The Prophet and the Age of the Caliphates* (Pearson-Longman, 2004).
43. G. W. Heck, *J. Econ. Soc. Hist. Orient* **42**, 364–395 (1999).
44. P. Edwell, in *Arabs and Empires Before Islam*, G. Fisher, Ed. (Oxford Univ. Press, 2015), pp. 214–275.
45. J. Wiesehöfer, in *The Formation of the Islamic World, Sixth to Eleventh Centuries*, vol. 1 of *The New Cambridge History of Islam*, C. F. Robinson, Ed. (Cambridge Univ. Press, 2010), pp. 98–152.
46. M. Whittow, in *The Formation of the Islamic World, Sixth to Eleventh Centuries*, vol. 1 of *The New Cambridge History of Islam*, C. F. Robinson, Ed. (Cambridge Univ. Press, 2010), pp. 72–97.
47. C. Robinson, in *The Formation of the Islamic World, Sixth to Eleventh Centuries*, vol. 1 of *The New Cambridge History of Islam*, C. F. Robinson, Ed. (Cambridge Univ. Press), pp. 173–225.
48. D. Nebes, in *The Qur'ān in Context: Historical and Literary Investigations into the Qur'ānic Milieu*, A. Neuwirth, N. Sinai, M. Marx, Eds., (Brill, 2010), pp. 27–59.
49. A. Berger, M. F. Loutre, *Quat. Sci. Rev.* **10**, 297–317 (1991).

ACKNOWLEDGMENTS

We thank M. Cook, A. Izdebski, L. Mordechai, T. Newfield, and J. Tannous for their thoughtful comments. We also thank H. Mohammad al Azri of the Oman Ministry of Industry and Commerce and Z. Al Suleimani of the Ministry of Water Resources for their support during fieldwork. We are very grateful to A. Al Kathiri for showing us the location of Defore Cave. **Funding:** This work was supported by the Swiss National Science Foundation (grants PP002-110554/1 and CRSI22_132646/1 to D.F.), the National Natural Science Foundation of China (grant NSFC 41888101 to H.C.), the National Science Foundation (grant NSF 1701628 to R.L.E.), and the National Socio-Environmental Synthesis Center (SNF grant DBI-1639145 to J.H.). **Author contributions:** D.F. designed this study with input from J.H., R.S.B., and A.M.; D.F. and S.J.B. collected stalagmite H12; D.F. performed stable isotope analysis; H.C. and R.L.E. performed uranium-series dating; D.F. and M.J. performed diameter measurements; C.C.R. analyzed meteorological data; and D.F., J.H., and R.S.B. wrote the paper with contributions from all other authors. **Competing interests:** The authors declare no competing interests. **Data availability:** The data are available on the National Oceanic and Atmospheric Association (NOAA) National Centers for Environmental Information (NCEI) palaeoclimatology server (www.ncdc.noaa.gov/data-access/paleoclimatology-data/datasets). **License information:** Copyright © 2022 the authors, some rights reserved; exclusive licensee American Association for the Advancement of Science. No claim to original US government works. https://www.science.org/about/science-licenses-journal-article-reuse

SUPPLEMENTARY MATERIALS

science.org/doi/10.1126/science.abg4044
Materials and Methods
Figs. S1 to S10
Tables S1 to S3
References (*50*–*58*)

Submitted 4 January 2021; accepted 6 May 2022
10.1126/science.abg4044

BIOCONJUGATION

A chemoenzymatic strategy for site-selective functionalization of native peptides and proteins

Anna Fryszkowska[1]*, Chihui An[1]*, Oscar Alvizo[2], Goutami Banerjee[2]†, Keith A. Canada[1], Yang Cao[1], Duane DeMong[1], Paul N. Devine[1]‡, Da Duan[2], David M. Elgart[2], Iman Farasat[1]§, Donald R. Gauthier[1], Erin N. Guidry[3], Xiujuan Jia[1], Jongrock Kong[1], Nikki Kruse[2], Katrina W. Lexa[3]¶, Alexey A. Makarov[1], Benjamin F. Mann[1], Erika M. Milczek[1]#, Vesna Mitchell[2], Jovana Nazor[2], Claudia Neri[1], Robert K. Orr[1], Peter Orth[3]**, Eric M. Phillips[1], James N. Riggins[2], Wes A. Schafer[1], Steven M. Silverman[1], Christopher A. Strulson[1], Nandhitha Subramanian[2]††, Rama Voladri[2]‡‡, Hao Yang[1], Jie Yang[2]†, Xiang Yi[2]§§, Xiyun Zhang[2]†, Wendy Zhong[1]

The emergence of new therapeutic modalities requires complementary tools for their efficient syntheses. Availability of methodologies for site-selective modification of biomolecules remains a long-standing challenge, given the inherent complexity and the presence of repeating residues that bear functional groups with similar reactivity profiles. We describe a bioconjugation strategy for modification of native peptides relying on high site selectivity conveyed by enzymes. We engineered penicillin G acylases to distinguish among free amino moieties of insulin (two at amino termini and an internal lysine) and manipulate cleavable phenylacetamide groups in a programmable manner to form protected insulin derivatives. This enables selective and specific chemical ligation to synthesize homogeneous bioconjugates, improving yield and purity compared to the existing methods, and generally opens avenues in the functionalization of native proteins to access biological probes or drugs.

With the increasing number of new modalities and biologics in pharmaceutical pipelines (*1*–*4*), the selective transformation of biomolecules, such as proteins and peptides, has emerged as an important challenge in organic synthesis. The need to maintain the complex tertiary structure of biological polymers, combined with the diversity and repetition of functional groups, demands both mild conditions and high chemoselectivity, each of which is difficult to achieve with existing methods (*5*–*7*). Current strategies to directly modify native proteins rely on the inherent reactivity of functional groups within the molecule, either by targeting modifications at the termini (*8*) or by exploiting subtle differences in the nucleophilicity, pK_a (*9*), or redox potential (*10*, *11*) of the repeating amino acid residues, which necessarily restricts the scope and selectivity of such methodologies (*5*–*7*) (Fig. 1A).

Consequently, genetic modifications of the proteins where an (un)natural amino acid or recognition motif is inserted as a handle for site-selective functionalization have gained great interest (*5*–*7*). However, the introduction of recognition tags invariably alters the biomolecule, which may affect the very function that it performs as well as narrowing the scope of such approaches. These limitations have created a high demand for the invention of scalable strategies for site-selective bioconjugation of native proteins to accelerate the discovery and development of biological probes and therapeutics (*4*, *12*–*16*). Here we show that strategies based on enzyme catalysis can enable improved bioconjugation of native proteins such as insulin (**1**, Fig. 1, A and B).

Over the past several decades, the growing epidemic of diabetes mellitus has motivated many research laboratories to search for therapies that exhibit improved safety and pharmacology (*17*). The inherently low therapeutic index of insulin-based medicines, where overdosing can lead to hypoglycemia, remains a substantial medical risk and necessitates complex dosing regimens (*17*). Modified insulin molecules will advance understanding of how the insulin receptor is activated and the structure-activity relationships of its binders (*18*) and may ultimately lead to safer insulin-based medicines for glycemic controls (*17*). Our laboratories have been pursuing diverse human insulin bioconjugates with promising therapeutic potential and improved pharmacodynamic profiles, including insulin receptor partial agonists MK-1092 and MK-5160 (*19*) or glucose-responsive insulin MK-2640 (*20*) (Fig. 1C, **5a** to **5c**).

These medicinal chemistry efforts targeted the modification of free amino groups on the native peptide. In the case of recombinant human insulin **1**, this approach required discriminating among three distinct amine functionalities: the N-terminal glycine A1 (pK_a 8.4), the N-terminal phenylalanine B1 (pK_a 7.1), and the side-chain ε-amino group of lysine B29 (pK_a 11.1) [Fig. 1A; pK_a values based on (*21*)]. Our initial conjugation strategy to access insulin analogs was driven primarily by differences in pK_a, which afforded only modest site selectivity (*19*). As a result, a challenging chromatographic purification was required to separate structurally related compounds, leading to moderate yields of the bioconjugates. The complexity of implementing pK_a-based modification of human insulin drove the need for a general, scalable ligation strategy to obtain homogeneous conjugates and facilitate further discovery and development efforts.

We envisaged an approach similar to that of protecting group strategies used in small-molecule chemistry, where selectively protected insulins **3** (Fig. 1B) could enable their site-selective conjugation with any molecule of interest (e.g., sugar, polyethylene glycol, peptide), expediting the synthesis of a diverse array of modified insulins **5** (Fig. 1C) (*19*). To translate this vision into practice, we planned to exploit the specificity displayed by enzymes to prepare derivatives **3**. Enzymes are particularly suited to catalyze site-specific modifications that preserve the structure of biomolecules, as they can act under mild aqueous reaction conditions to confer high chemo- and regioselectivity (*13*–*16*). One key advantage of these methods is the ability to engineer properties of enzymes through directed evolution to enhance catalytic efficiency and to achieve exquisite selectivity toward the structural motif of choice (*22*, *23*). As a result, the growing number of enzymatic bioconjugation strategies provides a powerful extension to the scope of existing chemical approaches (*5*). Diverse hydrolases have been applied to site-selective protein modification to access antibody-drug conjugates, vaccines, and linear and macrocyclic peptides (*13*–*16*). We were encouraged by early reports on the deprotection of N-phenylacetyl–protected peptides using penicillin G acylase from *Escherichia coli* (*Ec*PGA, E. C. 3.5.1.11) (*24*, *25*). This enzyme displayed selective activity toward phenylacetyl amides, leaving peptide bonds and C-terminal esters intact. Wider adoption of PGA-catalyzed functionalization of proteins was hampered by the enzyme's low activity and its inhibition by both substrates and products (*25*, *26*). At the outset, we planned to explore natural PGAs for their ability to discriminate among the free amino groups in insulin (Fig. 2) to prepare orthogonally

[1]Process Research and Development, Merck & Co., Inc., Rahway, NJ 07065, USA. [2]Codexis Inc., 200 Penobscot Drive, Redwood City, CA 94063, USA. [3]Discovery Chemistry, Merck & Co., Inc., Kenilworth, NJ 07033, USA.
***Corresponding author. Email: anna.fryszkowska@merck.com (A.F.); chihui.an@merck.com (C.A.)**
†Present address: Fornia BioSolutions, Inc., 3876 Bay Center Place, Hayward, CA 94545, USA. ‡Present address: Schrödinger, Inc., 120 W 45th St, 17th Floor, New York, NY 10036, USA. §Present address: Janssen Pharmaceutical Companies of Johnson & Johnson, 1125 Trenton Harbourton Road, Titusville, NJ 08560, USA. ¶Present address: Denali Therapeutics Inc., 161 Oyster Point Blvd., South San Francisco, CA 94080, USA. #Present address: Curie Co., Inc., 6 Davis Dr., Durham, NC 27709, USA. **Present address: Proteovant Therapeutics, 151 W 42nd St, New York, NY 10036, USA. ††Present address: Lonza Biologics Plc, Gonville Building (B200), Chesterford Research Park, Little Chesterford CB10 1XL, UK. ‡‡Present address: The Clorox Company, 4900 Johnson Dr., Pleasanton, CA 94080, USA. §§Present address: Amgen Inc., 1120 Veterans Blvd., South San Francisco, CA 94080, USA.

protected (phenylacetyl)insulins **3a** to **3f**. If successful, such a "toolbox" would enable well-defined chemical ligation to access the full suite of insulin bioconjugates **5** (Fig. 1C).

We began by testing a library of >100 commercially available PGA homologs, screening for the hydrolysis of tri(phenylacetyl)insulin **2a**, chemically synthesized from insulin **1** with activated phenylacetyl derivative **6** (Fig. 2, see supplementary materials, Chemistry section for details). The screening revealed the existence of several selective enzyme preparations, such as immobilized acylases from *Achromobacter* sp. (Fermase PS150 and PS750), which displayed high selectivity toward hydrolysis of the A1- and B29-amides, yielding mono-protected B1-phenylacetylinsulin **3a** (Fig. 2). Yet, the majority of active acylases, such as the PGA from *Kluyvera cryocrescens* (*Kc*PGA), yielded complex mixtures of all possible mono and di-(phenylacetyl) products **3a** to **3f** (fig. S52), before converging at fully deprotected insulin **1** upon prolonged incubation (fig. S55). A time course study revealed that the *Kc*PGA enzyme displayed different hydrolysis rates of phenylacetamide groups of **2a**: B29 > A1 > B1. Encouraged by the existing hierarchy in hydrolysis, we envisaged that the regioselectivity conferred by this acylase could be modulated with directed evolution, providing enzymes that could catalyze site-selective hydrolysis. We decided to test this hypothesis by engineering *Kc*PGA to identify variants specific for B29-lysine (Fig. 2).

We introduced changes to the *Kc*PGA construct to simplify recombinant expression and directed evolution in *E. coli* as the host. PGAs are periplasmic heterodimeric enzymes composed of two subunits, which require an autoproteolytic processing step to form an active enzyme [fig. S1A (*27*)]. Consequently, the signal peptide and the 54 amino acid interdomain region were removed, and a short linker between the β and α domains was added, similar to a previous report for the *Ec*PGA

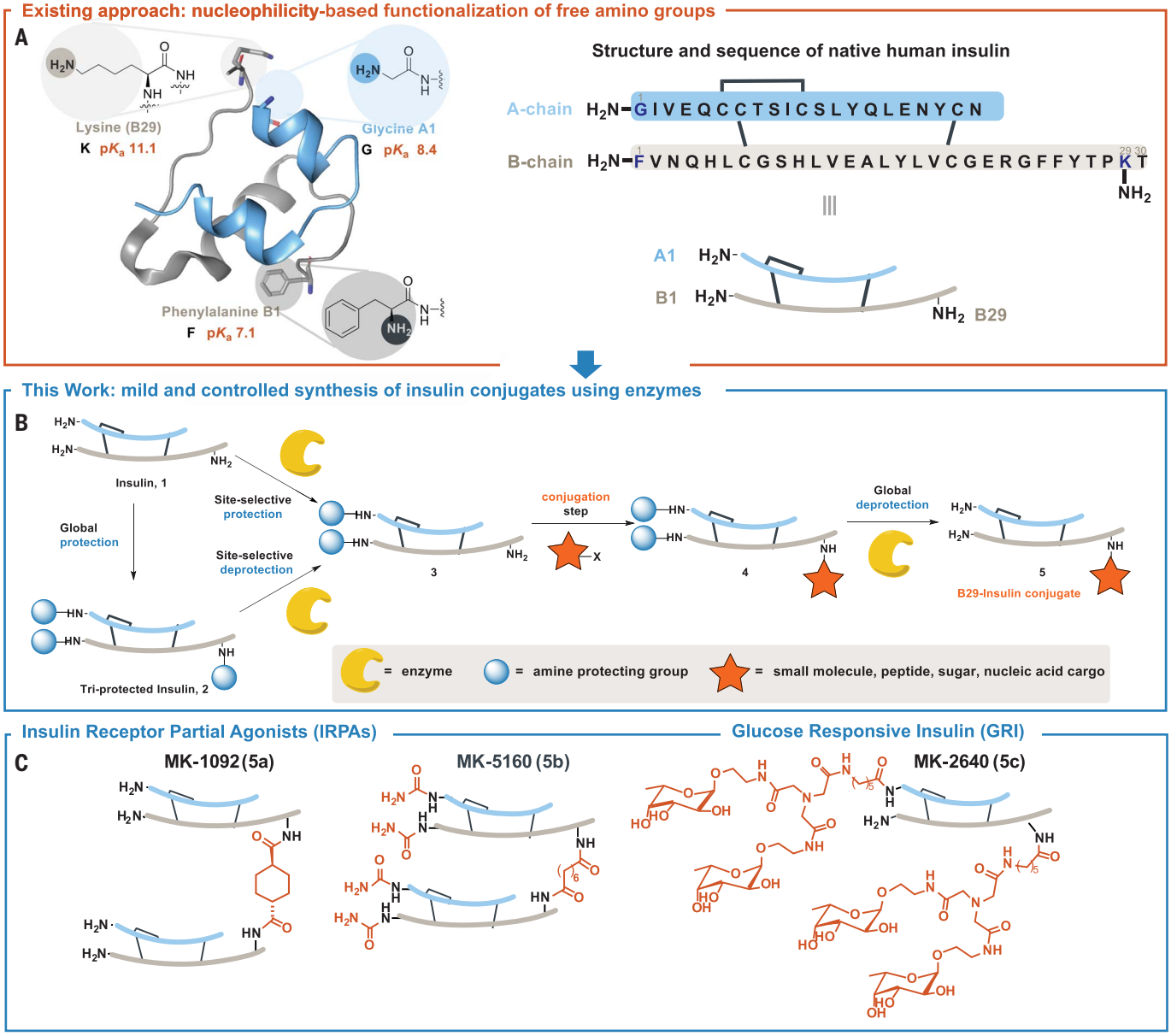

Fig. 1. Strategies for site-selective insulin functionalization. (**A**) Structure (left) and sequence (right) of human insulin with highlighted free amino groups at A1 (glycine, G^{α}), B1 (phenylalanine, F^{α}), and B29 positions (N^{6}-lysine, K^{ε}), which can be functionalized through a pK_a-based paradigm [pK_a values based on (*21*)]. The disulfide bonds are marked in dark gray. (**B**) A general strategy for well-defined insulin conjugation using biocatalytic protecting group strategy. (**C**) Insulin conjugate drug candidates (*19*, *20*).

homolog [fig. S1B (*28*)]. In this way, we constructed a single-chain enzyme, referred to as PGA^{Rd0}, where the catalytic residue serine is positioned at the N terminus, which obviated the need for its posttranslational processing to provide catalytically competent, mature enzyme.

PGA^{Rd0} became a parent enzyme (backbone) in the directed evolution programs (fig. S3, phylogenetic tree). With a high-throughput analytical assay in place (supplementary materials section 5), we focused on improving the selectivity for hydrolysis of tri(phenylacetyl)insulin **2a** at the B29 position (Fig. 2). After four rounds of enzyme evolution and high-throughput

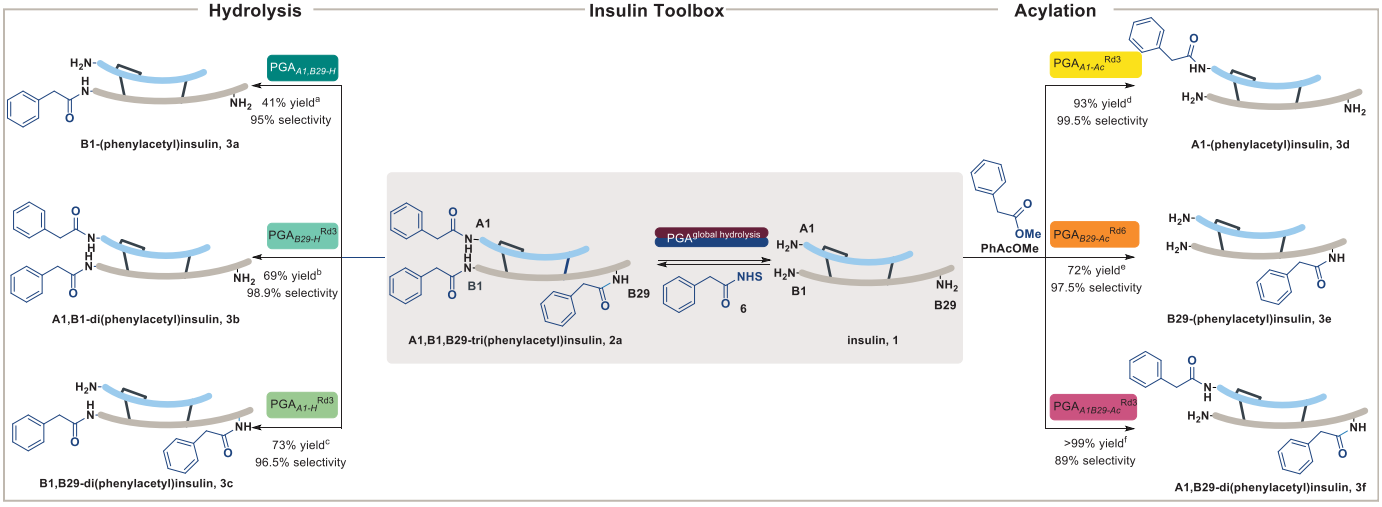

Fig. 2. Generation of phenylacetyl insulin toolbox. Enzymatic synthesis of (phenylacetyl)insulins **3a** to **3f** through hydrolysis of (triphenylacetyl)insulin **2a** or direct acylation of insulin **1**. All yields are reported as isolated yields. [a]0.78 mM **2a**, Fermase PS150 beads (PGA$_{A1B29\text{-}H}$), 100 mM Tris•HCl, pH 8.0, 10 vo l% MeCN, 30°C, 2 hours. [b]6.4 mM **2a**, 5.7 wt % PGA$_{B29\text{-}H}^{Rd3}$, water, pH 8.5, 30°C, 20 hours. [c]7.27 mM **2a**, 2.8 wt % PGA$_{A1\text{-}H}^{Rd3}$, 100 mM triethanolamine, pH 8.0, 30°C, 22 hours. [d]7.91 mM **1**, 20 equiv PhAcOMe, 2.25 wt % PGA$_{A1\text{-}Ac}^{Rd3\text{-}CHis}$, 20 vol % MeCN in water, pH 8.35, 27.5°C, 6 hours. [e]8.0 mM **1**, 20 equiv PhAcOMe, 5 wt% PGA$_{B29\text{-}Ac}^{Rd7\text{-}CHis}$, 20 vol % MeCN in water, pH 9.25, 30°C, 3 hours. [f]8.0 mM **1**, 20 equiv PhAcOMe, 5 wt % PGA$_{A1B29\text{-}Ac}^{Rd3\text{-}CHis}$, 20 vol % MeCN in water, pH 8.85, 27.5°C, 1.5 hours.

Table 1. Properties and performance of evolved acylases used in regioselective insulin functionalization compared to the starting (parent) variant (assays performed at 1- to 50-ml scale, with no pH control). The detailed phylogenetic tree is presented in fig. S3.

	STARTING ENZYME				EVOLVED ENZYME				
Evolution focus/ Reaction	**Parent variant**	**Conv. (select.)**	**Enz$_{wt}$ (%)[b]**	**Substr. (mM)[c]**	**Top-performing variant**	**Conv. (select)**	**Enz$_{wt}$ (%)[b]**	**Substr. (mM)[c]**	**Amino acids changed (no.)[a]**
B29-hydrolysis **2a** to **3b**	PGA^{Rd0}	21%[d] (36%)	10	0.8	PGA$_{B29\text{-}H}^{Rd4}$	99%[d] (99%)	1	8.2	16 (2.3%)
A1-hydrolysis **2a** to **3c**	PGA^{Rd0}	32%[e] (83%)	25	5.1	PGA$_{A1\text{-}H}^{Rd3}$	85%[e] (96%)	2.5	8.2	13 (1.7%)
A1-acylation **1** to **3d**	PGA$_{global\text{-}H}^{Rd1}$	48%[f] (97%)	2.5	6.9	PGA$_{A1\text{-}Ac}^{Rd3\text{-}CHis}$	92%[g] (98%)	0.8	8.6	15 (2.0%)
B29-acylation **1** to **3e**	PGA$_{B29\text{-}H}^{Rd4v2}$	0.5%[h] (nd)	12	4.3	PGA$_{B29\text{-}Ac}^{Rd6\text{-}CHis}$	64%[i] (92%)	2.5	12.9	26 (3.4%)
A1,B29-acylation **1** to **3f**	PGA$_{B29\text{-}Ac}^{Rd3\text{-}CHis}$	88[j] (9%)	4	8.6	PGA$_{A1B29\text{-}Ac}^{Rd3\text{-}CHis}$	99.5[k] (37%)	5	8.6	27 (3.5%)
Global hydrolysis (monomer) **3** to **1**	PGA^{Rd0}	12%[l]	16	0.8	PGA$_{global\text{-}H}^{Rd3\text{-}CHis}$	>99%[l]	16	0.8	8 (1.0%)
Global hydrolysis (dimer) **4a** or **4b** to **5a**	PGA$_{global\text{-}H}^{Rd3\text{-}CHis}$	34%[m]	2.5	1.2	PGA$_{global\text{-}dimer\text{-}H}^{Rd3\text{-}CHis}$	93%[m]	5	2.5	20 (2.6%)

[a]Number of mutations compared to PGA^{Rd0}; enzyme variants are color-coded based on their lineage in the phylogenetic tree (fig. S3). Crystal structures and computational models of top evolutionary variants are presented in supplementary materials. [b]Enzyme loading refers to the mass of lyophilized clarified cell lysate relative to the mass of the reaction substrate. Results may reflect improvements in enzyme expression as well as activity. [c]Starting insulin or insulin derivative concentration. [d]**2a,** 200 mM Tris•HCl, pH 8.0, 30°C, 24 hours. [e]**2a**, 200 mM Tris HCl, pH 8.0, 30°C, 5 hours. [f]**1**, 97 equiv PhAcOMe, 100 mM Tris•HCl, pH 8.5, 20 vol % MeCN, 30°C, 2 hours. [g] 1, 77 equiv PhAcOMe, 250 mM Tris•HCl, pH 9.25, 20 vol % MeCN, 30°C, 2 hours. [h]**1,** 26 equiv PhAcOMe, 100 mM Tris•HCl, pH 9.25, 20 vol % MeCN, 30°C, 3 hours. [i]**1**, 9 equiv PhAcOMe, 200 mM Tris•HCl, pH 9.25, 20 vol % MeCN, 30°C, 3 hours. [j]**1**, 14 equiv PhAcOMe, pH 9.25, 20 vol % MeCN, 30°C, 1 hour. [k]**1**, 20 equiv PhAcOMe, pH 9, 20 vol % MeCN, 27.5°C, 1 hour, data obtained in a high-throughput screening assay with no pH control. If pH was maintained throughout the reaction, 89% selectivity for **3f** was achieved (see Fig. 2). [l]**2a**, 100 mM Tris•HCl, pH 8.0, 30°C, 22 hours. [m]**4a**, 250 mM triethanolamine, 30°C, 24 hours. Conversion and selectivity were determined using the following equations: conversion (%) = Area$_{(desired\ product\mathbf{3x})}$/ΣArea$_{(all\ products\mathbf{1+\ 2a+\ 3a\text{-}f})}$ × 100%; selectivity (%) = Area $_{(desired\ product\mathbf{3x})}$/ΣArea$_{(all\ products\mathbf{3a\text{-}f})}$ × 100%.

screening, we identified mutant $PGA_{B29\text{-}H}^{Rd4}$ (Table 1), which displayed improved activity and 99% selectivity, providing access to A1,B1-di(phenylacetyl)insulin **3b** in excellent yield and purity (Table 1; see supplementary materials section 5 for details). Encouraged by this result, we began a divergent evolution program targeting A1-selective hydrolysis. Two rounds of evolution led to identification of $PGA_{A1\text{-}H}^{Rd3}$ with 95% selectivity, which enabled the synthesis of B1,B29-di(phenylacetyl)insulin **3c** (Table 1; see supplementary materials section 5 for details).

Although the above approach successfully afforded two of the desired insulin conjugates,

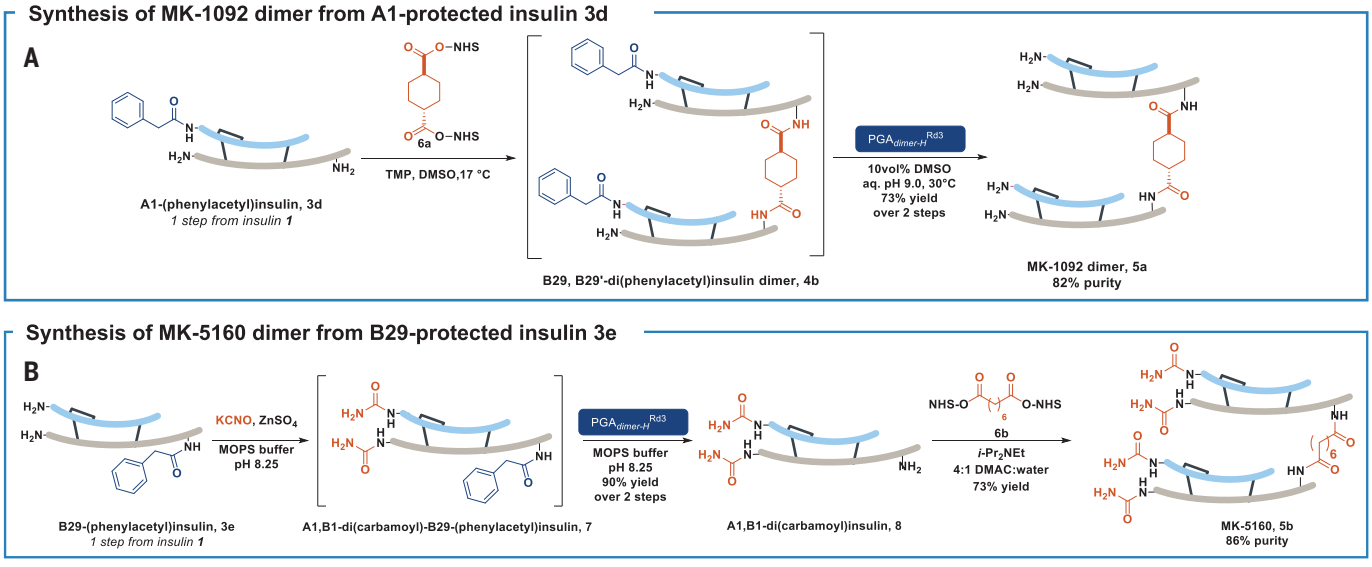

Fig. 3. Synthesis of B29,B29' insulin dimers. (**A**) MK-1092 in 73% yield over two steps from **3d**; (**B**) MK-5160 in 66% yield over three steps from **3e**.

Table 2. Activity and selectivity of evolved acylating PGA variants used in functionalization of native proteins. nd, – not determined.

NUCLEOPHILE	SEQUENCE	ENZYME	CONVERSION (modified site)[a]	SELECTIVITY[a]
Insulin (**1**) p*I* 5.4	A-chain H_2N-GIVEQCCTSICSLYQLENYCN B-chain H_2N-FVNQHLCGSHLVEALYLVCGERGFFYTPKT-NH_2	$PGA_{A1\text{-}Ac}^{Rd3\text{-}CHis}$ $PGA_{B29\text{-}Ac}^{Rd6\text{-}CHis}$ $PGA_{A1B29\text{-}Ac}^{Rd2\text{-}CHis}$	70% (A1) 74% (B29), 26% (A1B29) 7% (A1), 36% (B29), 54% (A1B29), 2% (A1B1B29)	>99% 74% 55%
Glargine (**9**) p*I* 6.7	A-chain H_2N-GIVEQCCTSICSLYQLENYCG B-chain H_2N-FVNQHLCGSHLVEALYLVCGERGFFYTPKTRR-NH_2	$PGA_{A1\text{-}Ac}^{Rd3\text{-}CHis}$ $PGA_{B29\text{-}Ac}^{Rd6\text{-}CHis}$ $PGA_{A1B29\text{-}Ac}^{Rd2\text{-}CHis}$	75% (A1) 32% (A1) 65% (A1)	>99% >99% >99%
Glucagon (**10**) p*I* 6.75[b]	H_2N-HSQGTFTSDYSKYLDSRRAQDFVQWLMNT-NH_2	$PGA_{A1\text{-}Ac}^{Rd3\text{-}CHis}$ $PGA_{B29\text{-}Ac}^{Rd6\text{-}CHis}$ $PGA_{A1B29\text{-}Ac}^{Rd2\text{-}CHis}$	14% (H1) trace trace	>99% nd nd
Melittin (**11**) p*I* 4.7[b]	H_2N-GIGAVLKVLTTGLPALISYIKRKRNN-NH_2	$PGA_{A1\text{-}Ac}^{Rd3\text{-}CHis}$ $PGA_{B29\text{-}Ac}^{Rd6\text{-}CHis}$ $PGA_{A1B29\text{-}Ac}^{Rd2\text{-}CHis}$	96% (G1) 33% (G1) 54% (G1)	>99% >99% >99%
Apamin (**12**) p*I* 5.5[b]	H_2N-CNCKAPETALCARRCQQH-NH_2	$PGA_{A1\text{-}Ac}^{Rd3\text{-}CHis}$ $PGA_{B29\text{-}Ac}^{Rd6\text{-}CHis}$ $PGA_{A1B29\text{-}Ac}^{Rd2A9\text{-}CHis}$	trace trace trace	nd nd nd
Somatostatin (**13**) p*I* 5.6[b]	H_2N-AGCKNFFWKTFTSC	$PGA_{A1\text{-}Ac}^{Rd3\text{-}CHis}$ $PGA_{B29\text{-}Ac}^{Rd6\text{-}CHis}$ $PGA_{A1B29\text{-}Ac}^{Rd2\text{-}CHis}$	2% (A1), 1% (K4), 1% (K9) 4% (A1), 0.5% (K4), 3% (K9) 1% (A1), 1% (K4), 5% (K9);	nd nd nd

[a]Reactions were conducted at 10 to 20 mg/ml peptide concentration in 100 mM triethanolamine buffer (pH 8.5) at 5 wt% enzyme loading and analyzed after 6 hours. Conversion and selectivity were determined using the following equations: conversion (%) = $Area_{(acylated\ product)}/\Sigma Area_{(all\ acylated\ products\ +\ native\ protein)} \times 100\%$; selectivity (%) = $Area_{(acylated\ product)}/\Sigma Area_{(all\ acylated\ products)} \times 100\%$. Site selectivity was determined by top-down MS analysis. [b]Calculated using Expasy Compute pI tool (https://web.expasy.org/compute_pi/).

we recognized that the selective deprotection of phenylacetyl groups requires chemical synthesis of tri(phenylacetyl)insulin **2a**, adding steps. By contrast, a direct selective installation of phenylacetyl groups on insulin **1** (Fig. 1B and 2) could offer a streamlined route to protected insulins **3**. PGA-catalyzed amide hydrolysis is a reversible process that has also been applied in amide synthesis by thermodynamically (*29*) or kinetically (*30*) controlled processes in aqueous media (*27*). Previous reports have shown that protein engineering can be used to increase the rate of enzymatic acyl transfer from phenylacetyl esters to amines (V_s) to outcompete the rate of the ester hydrolysis (V_h) (*31*, *32*). We tested the kinetically driven site-selective acylation of insulin using methyl phenylacetate (PhAcOMe) as a donor (Fig. 2) to access the remaining derivatives **3d** to **3f** and complete the build of our "insulin toolbox." Variants from early rounds of PGA evolution catalyzed the formation of A1-(phenylacetyl)insulin **3d** using an excess of methyl phenylacetate at pH 8.0 with acetonitrile as a cosolvent (20 vol %) with high (97%) selectivity, albeit low conversion (Table 1; see supplementary materials section 5 for evolutionary details). Two subsequent rounds of evolutionary screening yielded the $PGA_{A1\text{-}Ac}^{Rd3}$ variant, which catalyzed the formation of A1-(phenylacetyl)insulin **3d** by direct acylation of insulin **1** in 92% yield and 98% selectivity (Table 1 and supplementary materials section 5). At this point, to facilitate large-scale process development, as well as the structural studies, we introduced a hexa-histidine tag at the C terminus of the acylase (CHis) to provide the $PGA_{A1\text{-}Ac}^{Rd3\text{-}CHis}$ variant.

Encouraged by these results, our protein engineering efforts next targeted the evolution of the acylases to prepare B29-protected and A1,B29-di-protected peptides **3e** and **3f**. The B29-selective variant $PGA_{B29\text{-}H}^{Rd4.2}$ became the evolutionary starting point (see fig. S3, evolutionary tree). The initial studies highlighted the importance of pH in achieving a high V_s/V_h ratio for kinetically controlled processes (*33*). The higher pK_a of ε-terminal amino group of lysine (pK_a 11.1^{Lysine} versus $7.1^{Phenylalanine}$, Fig. 1A) required increasing the reaction pH to 9.25 to achieve >95% conversion to B29-amide. Using these conditions, directed evolution campaigns enabled the identification of two variants: $PGA_{B29\text{-}Ac}^{Rd6\text{-}CHis}$ for B29-acylation and $PGA_{A1B29\text{-}Ac}^{Rd3\text{-}CHis}$ for A1,B29-diacylation (Table 1 and fig. S3, evolutionary tree).

With five engineered variants of PGA from *K. cryocrescens* and the complementary activity of the PGA from *Achromobacter* sp., we gained access to all six combinations of protected mono- and di(phenylacetyl)insulin analogs (**3a** to **3f**, Fig. 2) for site-selective conjugation. Our protecting-group strategy additionally required a complementary enzyme to catalyze a robust and highly selective deprotection of protected insulins (Fig. 1C). Additional rounds of directed evolution of the parent PGA with a focus on improving hydrolysis at all three positions of tri(phenylacetyl)insulin **2a** yielded variant $PGA_{global\text{-}H}^{Rd3}$ with fourfold higher activity on the monomeric insulin (Table 1).

Our work highlights the flexibility and efficiency with which protein engineering can alter the specificity of a promiscuous parent acylase PGA^{Rd0}, whose native substrate is a small-molecule 6-aminopenicillanic acid, and enable site-selective activity on non-native substrates such as insulin **1** and its derivatives **2** to **4**. The six divergent directed evolution campaigns demonstrate that we can successfully tune both regioselectivity and kinetic rates of enzymatic transformations, i.e., V_s/V_h ratio of hydrolysis versus acylation. The final evolutionary variants required the incorporation of 11 to 26 amino acid mutations across the entire protein length (from 1.4 to 3.4% of a 764–amino acid single peptide, Table 1 and supplementary materials sections S4 and S5). To gain insights into how the specific mutations affect the selectivity and activity of the top-performing variants, we acquired crystal structures of the variants $PGA_{global\text{-}H}^{Rd3\text{-}CHis}$ (PDB ID 7reo, 1.81 Å) and $PGA_{A1\text{-}Ac}^{Rd3\text{-}CHis}$ (PDB ID 7rep, 2.19 Å), and for the other top-performing PGA variants we created computational models (Fig. 2B and figs. S9 to S20) The crystal structures closely match that of the heterodimeric *K. cryocrescens* PGA [PDB ID: 4pem (*34*), figs. S5 to S8]. Many mutations were in the flexible loops next to the active site and on the protein surface. The mutations introduced in the binding pocket and within 10 Å of its entrance are most likely critical for insulin recognition (Fig. 2B), whereas the changes that are remote from the active site might play a role in improving the overall enzyme fitness, such as stability in the presence of organic cosolvents. Some mutations, including silent DNA mutations, contributed toward the improvements in soluble protein expression in *E. coli*, which lowered the enzyme load to achieve scalable biotransformations (see supplementary materials, protein engineering and directed evolution section for details). Bioinformatic analysis of the gene sequence-function data of >200,000 variants screened across all six evolution programs highlighted the critical role of F701W and N2L mutations in the active site (fig. S8) to achieve A1 selectivity (see supplementary materials section 3 for a detailed discussion); however, the exact role of many other mutations was difficult to rationalize.

After the development of the insulin toolbox (Fig. 2 and Table 1), we explored the application and generality of this protecting-group strategy in the synthesis of our two clinical candidates MK-1092 (**5a**) and MK-5160 (**5b**) (Fig. 3) (*19*). These conjugates are insulin dimers stapled at the B29,B29′ positions with either a *trans*-1,4-cyclohexyldicarboxyamide or a suberoyl amide linker, respectively. Protected insulins **3** could provide a well-defined chemical dimerization and obviate the chromatographic purification at a large scale, facilitating process development, as well as further exploration of any structural insulin analog of interest.

We first studied the synthesis of MK-1092 through dimerization of A1,B1-di(phenylacetyl)insulin **3b**, followed by global hydrolysis of phenylacetamides catalyzed by deprotecting variant $PGA_{global\text{-}H}^{Rd3\text{-}CHis}$ (scheme S22). Initial trials showed clean, yet slow, enzymatic phenylacetamide deprotection, requiring >3 days to reach completion. A single round of evolution provided $PGA_{global\text{-}dimer\text{-}H}^{Rd1\text{-}CHis}$ with 2.5-fold improved activity. With this variant, both reactions proceeded in high conversion to afford MK-1092 **5a** in 93% purity, compared to <50% purity of the direct dimerization driven by differences in the pK_a of B29-lysine (*35*). Despite the improvements in product purity, this bioconjugation route suffered from a relatively high overall step count (four steps from insulin **1** through chemically prepared tri(phenylacetyl)insulin **2a**). A more efficient approach would be the direct dimerization of A1-(phenylacetyl)insulin **3d** (Fig. 3A). The derivative **3d** could be prepared from insulin **1** in one step with high selectivity that enabled its isolation by precipitation in 93% yield (Fig. 2A) and obviated the need for its chromatographic purification. Notably, the conjugation of **3d** with *N*-hydroxysuccinimide (NHS)–ester **6a** proceeded with high selectivity to form the desired A1,A1′-dimer **4b** (Fig. 3A). We hypothesize that the phenylacetamide on A1 is reducing surface accessibility of the unprotected N-terminal B1-phenylalanine residue, which did not participate in conjugation. Once dimerization was complete, the reaction stream could simply be diluted with water and subjected to the PGA-catalyzed deprotection. To facilitate large-scale delivery of MK-1092, we further engineered the deprotection enzyme to act on the dimer **4a**. Two evolutionary rounds afforded $PGA_{global\text{-}dimer\text{-}H}^{Rd3\text{-}CHis}$, which displayed a 2.5-fold increase in activity (Table 1; see supplementary materials section 10 for details). Using $PGA_{global\text{-}dimer\text{-}H}^{Rd3\text{-}CHis}$ variant, we generated >120 g of MK-1092 in 82% purity and 73% isolated yield over just two steps. This two-pot synthesis substantially improved the yield as compared to the direct conjugation used in the initial chemistry route (*19*, *36*).

The synthesis of MK-5160 **5b** required a different protected insulin to selectively install the carbamoyl groups capping both A1

and B1 N-terminal amines. The pK_a-driven strategy proved challenging to selectively make insulin derivative **8** [<70% purity, (*19*, *36*)]. Consequently, we subjected B29-(phenylacetyl)insulin **3e**, synthesized from insulin **1** using $PGA_{B29\text{-}Ac}^{Rd7\text{-}CHis}$ in acylation, to the chemical carbamoylation using potassium isocyanate under aqueous conditions to give derivative **7** (Fig. 3B). The subsequent enzymatic deprotection step was performed in a single pot without intermediate isolation to provide A1,B1-(dicarbamoyl)insulin **8** in 90% yield and 92% purity over the two steps. The dimerization with suberoyl NHS-ester (**6b**) afforded the target molecule MK-5160 **5b** an overall 86% purity and 66% yield from B29-(phenylacetyl)insulin **3e**, twofold higher in yield compared to the initial route (*19*). Synthesis of the two clinical candidates MK-1092 and MK-5160 demonstrates the value of our chemoenzymatic strategy to provide homogeneous protein conjugates at scale.

The enzymatic toolbox enables a simple, modular approach to the synthesis of structurally diverse insulin bioconjugates, allowing for efficient exploration of structure-activity relationships (*37*). The engineered PGAs can also accept other acyl donors such as phenoxy- or (4-ethynylphenyl)acetates (see supplementary materials section 10 and table S11), which can provide functional handles for further structural diversification, i.e., click chemistry. In addition, this strategy could be extended to the site-selective bioconjugation of other native proteins as well. Accordingly, we tested five other small peptides with the three acylating PGA variants ($PGA_{A1\text{-}Ac}^{Rd3\text{-}CHis}$, $PGA_{B29\text{-}Ac}^{Rd6\text{-}CHis}$, and $PGA_{A1B29\text{-}Ac}^{Rd2\text{-}CHis}$) (Table 2; see supplementary materials section 3.4 for details). For our studies, we selected insulin homolog glargine (**9**); two linear single-chain peptides, glucagon (**10**) and melittin (**11**); and two single-chain cyclic peptides containing disulfide bridges, apamin (**12**) and somatostatin (**13**), while insulin (**1**) was used as a control (scheme S21 and fig. S26).

Whereas the acylating PGAs were evolved for their activity and selectivity toward insulin (**1**), the enzymes could modify other peptides (**9** to **13**), albeit with lower activity and different site selectivity. For example, insulin-glargine (**9**) was acylated exclusively at A1 position by all three tested enzymes. Compared to human insulin (**1**), glargine contains two additional C-terminal arginines at B-chain, R31, and R32, and this change in the amino acid context was sufficient to completely abolish the enzymatic activity on γ-amine of the adjacent lysine B29. Similarly, the two linear peptides were only functionalized at their N termini: glycine of melittin **9** (33 to 96% conversion) and histidine of glucagon **10** (14% conversion with $PGA_{A1\text{-}Ac}^{Rd3\text{-}CHis}$ only). No or trace activity was noted with internal lysine residues. With cyclic peptides, apamin (**13**) proved least amenable to modifications with trace activity. By contrast, PGAs modified all three free amines of somatostatin (**12**), albeit with low conversions and varying site regioselectivity. The differences in reactivity among these peptides are challenging to rationalize or predict. Three-dimensional structure of the peptide substrates, steric and electronic context of the adjacent amino acids, character and pK_a of the modified residue: All of these factors undoubtedly play a role in site selectivity and protein-protein recognition. Isoelectric point pI and solubility of the substrate peptide under given pH may also contribute to the observed selectivities and efficiency of the modifications. Future efforts to obtain structural data could advance our understanding of peptide-enzyme recognition, enabling the rapid construction of structurally diverse peptide conjugates.

Our biocatalytic protecting-group strategy has provided well-defined, scalable ligation of insulin amines and enabled the construction of structurally complex bioconjugates of native peptides **5a** and **5b** with efficiency far exceeding that of existing synthetic approaches (*5*, *19*). The development of our enzymatic toolbox demonstrated the distinctive ability of enzyme catalysis to differentiate among amino acid residues in peptide substrates, which otherwise display similar chemical reactivity. Directed evolution remains a key tool to reprogram enzymes to perform site-specific conjugation on a peptide of interest, providing a control strategy previously unachievable with traditional methods for ligation of native proteins or other large molecules. We expect that bioconjugation strategies using naturally occurring and engineered enzymes to act on native proteins and peptides will continue to grow (*13*–*15*), accelerating the discovery and development of diagnostic probes and therapeutics (*1*–*4*). Progress in structural elucidation, as well as emerging machine learning approaches to predict the structure of interacting protein chains and complexes (*38*–*41*), will play a key role in the protein engineering and bioconjugation fields.

REFERENCES AND NOTES

1. C. Morrison, *Nat. Biotechnol.* **38**, 126–131 (2020).
2. R. J. Malonis, J. R. Lai, O. Vergnolle, *Chem. Rev.* **120**, 3210–3229 (2020).
3. E. Valeur *et al*., *Angew. Chem. Int. Ed.* **56**, 10294–10323 (2017).
4. K. R. Campos *et al*., *Science* **363**, eaat0805 (2019).
5. E. A. Hoyt, P. M. S. D. Cal, B. L. Oliveira, G. J. L. Bernardes, *Nat. Rev. Chem.* **3**, 147–171 (2019).
6. Q. Y. Hu, F. Berti, R. Adamo, *Chem. Soc. Rev.* **45**, 1691–1719 (2016).
7. P. Akkapeddi *et al*., *Chem. Sci.* **7**, 2954–2963 (2016).
8. C. B. Rosen, M. B. Francis, *Nat. Chem. Biol.* **13**, 697–705 (2017).
9. X. Chen, K. Muthoosamy, A. Pfisterer, B. Neumann, T. Weil, *Bioconjug. Chem.* **23**, 500–508 (2012).
10. S. Lin *et al*., *Science* **355**, 597–602 (2017).
11. J. Kim *et al*., *J. Am. Chem. Soc.* **142**, 21260–21266 (2020).
12. C. Bottecchia, T. Noël, *Chemistry* **25**, 26–42 (2019).
13. E. M. Milczek, *Chem. Rev.* **118**, 119–141 (2018).
14. T. Nuijens, A. Toplak, M. Schmidt, A. Ricci, W. Cabri, *Front Chem.* **7**, 829 (2019).
15. Y. Zhang, K. Y. Park, K. F. Suazo, M. D. Distefano, *Chem. Soc. Rev.* **47**, 9106–9136 (2018).
16. D. Kadereit, H. Waldmann, Enzymatic Protecting Group Techniques, *Chem. Rev.* **101**, 3367–3396 (2001).
17. A. N. Zaykov, J. P. Mayer, R. D. DiMarchi, *Nat. Rev. Drug Discov.* **15**, 425–439 (2016).
18. G. Scapin *et al*., *Nature* **556**, 122–125 (2018).
19. M. Wu *et al*., *Nat. Commun.* **13**, 942 (2022).
20. N. C. Kaarsholm *et al*., *Diabetes* **67**, 299–308 (2018).
21. J. Gao, M. Mrksich, F. A. Gomez, G. M. Whitesides, *Anal. Chem.* **67**, 3093–3100 (1995).
22. K. Chen, F. H. Arnold, *Nat. Catal.* **3**, 203–213 (2020).
23. A. Fryszkowska, P. N. Devine, *Curr. Opin. Chem. Biol.* **55**, 151–160 (2020).
24. F. Brtník, T. Barth, K. Jošt, *Collect. Czech. Chem. Commun.* **46**, 1983–1989 (1981).
25. Q. C. Wang, J. Fei, D. F. Cui, S. G. Zhu, L. G. Xu, *Biopolymers* **25** (Suppl), S109–S114 (1986).
26. L. Záková *et al*., *J. Pept. Sci.* **13**, 334–341 (2007).
27. R. C. Giordano, M. P. A. Ribeiro, R. L. C. Giordano, *Biotechnol. Adv.* **24**, 27–41 (2006).
28. G. Flores, X. Soberón, J. Osuna, *Protein Sci.* **13**, 1677–1683 (2004).
29. M. Cole, *Biochem. J.* **115**, 757–764 (1969).
30. M. J. Zmijewski Jr., B. S. Briggs, A. R. Thompson, I. G. Wright, *Tetrahedron Lett.* **32**, 1621–1622 (1991).
31. W. B. L. L. Alkema, A. J. Dijkhuis, E. De Vries, D. B. Janssen, *Eur. J. Biochem.* **269**, 2093–2100 (2002).
32. C. Carboni *et al*., *Tetrahedron Asymmetry* **17**, 245–251 (2006).
33. F. Bordusa, *Chem. Rev.* **102**, 4817–4868 (2002).
34. N. K. Varshney, S. Ramasamy, J. A. Brannigan, A. J. Wilkinson, C. G. Suresh, *Acta Crystallogr. Sect. F Struct. Biol. Cryst. Commun.* **69**, 925–929 (2013).
35. D. A. Pissarnitski *et al*., *J. Med. Chem.*, **65**, 5593–5605 (2022).
36. S. Lin *et al*., *Insulin Receptor Partial Agonists,* US Patent 10183981-B2 (2019).
37. D. Pissarnitski, S. Lin, Insulin Receptor Partial Agonists PCT/US21/47313 (2022).
38. M. Eisenstein, *Nature* **599**, 706–708 (2021).
39. R. Evans *et al*., bioRxiv 2021.10.04.463034 (2021). https://doi.org/10.1101/2021.10.04.463034.
40. I. R. Humphreys *et al*., *Science* **374**, eabm4805 (2021).
41. P. Bryant, G. Pozzati, A. Elofsson, *Nat. Commun.* **13**, 1256 (2022).

ACKNOWLEDGMENTS

We acknowledge the help and support of the following people from Merck & Co., Inc., Kenilworth, NJ, USA team: J. C. Moore for his scientific guidance; M. D. Truppo, L.-C. Campeau, M. A. Huffman, R. T. Ruck, K. M. Maloney, D. Thaisrivongs, and J. McIntosh for their feedback on the manuscript; B. Xiang, F. Meng, F. Mattrey, X. Yin, F.-R. Tsay, M. Biba, L. F. Frey, J. Kim, P. Reichert, W. Prosise, I. Lee, and D. Verma for experimental support and analysis; and Codexis team: R. D. Garcia, A. Sowell-Kantz, A. Ortega, S. Sivaramakrishnan, J. V. Viduya, S. J. Jenne, M. Mayo, and G. Cope for their support of directed evolution. **Funding:** This work was funded by Merck Sharp & Dohme Corp., a subsidiary of Merck & Co., Inc., Kenilworth, NJ, USA. **Author contributions:** A.F. and C.A. wrote the manuscript. P.N.D., and D.R.G. supervised chemistry development. O.A. and K.A.C. supervised enzyme evolution. C.A., A.F., E.M., R.K.O., and H.Y. carried out biocatalytic reaction development. C.A., D.D., E.G., J.K., R.K.O., E.P., S.M.S., and Y.C. carried out synthetic reaction development. G.B., D.D., D.M.E., I.F., V.M., J.N., J.N.R., R.V., J.Y., and X.Y. carried out enzyme engineering. X.J., A.A.M., C.N., B.F.M., J.N.R., C.S., W.S., and W.Z. developed analytical methods to allow chemistry development. N.K., K.W.L., and O.A. carried out computational work to support enzyme evolution. N.S. and D.V. performed computational modeling and evolutionary data analysis. P.O. obtained and solved crystal structures of evolved enzymes. **Competing interests:** Codexis, Inc. has filed patent applications covering the evolved enzymes: PCT/US2016/0326508, PCT/US2017/0321202, and PCT/US2018/0187180. **Data and materials availability:** The data supporting the findings of this

study are available within the paper and supplementary materials. Coordinates for the $PGA_{gloFbal\text{-}H}^{Rd3\text{-}CHis}$ and $PGA_{A1\text{-}Ac}^{Rd3\text{-}CHis}$ structures have been deposited in the PDB (PDB ID: 7reo and 7rep, respectively). DNA sequences of wild-type and evolved enzymes used in this study are available in the supplementary data files and have been deposited in GenBank (see table S13 for the accession numbers). The enzymes are commercially available from Codexis, Inc., subject to existing license obligations and restrictions. **License information:** Copyright © 2022 the authors, some rights reserved; exclusive licensee American Association for the Advancement of Science. No claim to original US government works. https://www.science.org/about/science-licenses-journal-article-reuse

SUPPLEMENTARY MATERIALS

science.org/doi/10.1126/science.abn2009
Materials and Methods
Chemistry, Analytical Chemistry, and Bioinformatics
Figs. S1 to S94
Tables S1 to S22
Schemes S1 to S25
DNA and Amino Acid Sequences of the Enzymes
MS and MS/MS Spectra
References (*42*–*66*)

View/request a protocol for this paper from *Bio-protocol*.

Submitted 10 November 2021; accepted 20 April 2022
10.1126/science.abn2009

CORONAVIRUS

Analysis of 6.4 million SARS-CoV-2 genomes identifies mutations associated with fitness

Fritz Obermeyer[1,2]*†, Martin Jankowiak[1,2], Nikolaos Barkas[1], Stephen F. Schaffner[1,3,4], Jesse D. Pyle[1]‡, Leonid Yurkovetskiy[5], Matteo Bosso[5], Daniel J. Park[1], Mehrtash Babadi[1], Bronwyn L. MacInnis[1,4,6], Jeremy Luban[1,5,6,7], Pardis C. Sabeti[1,3,4,6,8]§, Jacob E. Lemieux[1,6,9]*§

Repeated emergence of severe acute respiratory syndrome coronavirus 2 (SARS-CoV-2) variants with increased fitness underscores the value of rapid detection and characterization of new lineages. We have developed PyR_0, a hierarchical Bayesian multinomial logistic regression model that infers relative prevalence of all viral lineages across geographic regions, detects lineages increasing in prevalence, and identifies mutations relevant to fitness. Applying PyR_0 to all publicly available SARS-CoV-2 genomes, we identify numerous substitutions that increase fitness, including previously identified spike mutations and many nonspike mutations within the nucleocapsid and nonstructural proteins. PyR_0 forecasts growth of new lineages from their mutational profile, ranks the fitness of lineages as new sequences become available, and prioritizes mutations of biological and public health concern for functional characterization.

The severe acute respiratory syndrome coronavirus 2 (SARS-CoV-2) pandemic has been characterized by repeated waves of cases driven by the emergence of new lineages with higher fitness, in which fitness encompasses any trait that affects the lineage's growth, including its basic reproduction number (R_0), ability to evade existing immunity, and generation time. Rapid identification of such lineages as they emerge along with accurate forecasting of their dynamics is critical for guiding outbreak response. The ability to interrogate the entirety of the global SARS-CoV-2 genomic dataset would be greatly beneficial in doing this effectively. The large size (currently >7.5 million virus genomes) and geographic and temporal variability of the available data present considerable challenges that will become greater as more viruses are sequenced. Current phylogenetic approaches are computationally inefficient on datasets with more than ~5000 samples and take days to run at that scale. Ad hoc methods to estimate the relative fitness of particular SARS-CoV-2 lineages are a computationally efficient alternative (*1*–*3*) but have typically relied on models in which one or two lineages of interest are compared with all others and do not capture the complex dynamics of multiple cocirculating lineages.

Furthermore, estimates of relative fitness based on lineage frequency data alone (*2*–*5*), which can be extended to multiple lineages (*1*, *3*–*5*), do not take advantage of additional statistical power that can be gained from analyzing the independent appearance and growth of the same mutation in multiple lineages. Performing a mutation-based analysis of lineage prevalence has the additional advantage of identifying specific genetic determinants of a lineage's phenotype, which is critical both for understanding the biology of transmission and pathogenesis and for predicting the phenotype of new lineages. The SARS-CoV-2 pandemic has already been dominated by several genetic changes of functional and epidemiological importance, including the spike (S) D614G mutation associated with higher SARS-CoV-2 loads (*6*, *7*). Mutations found in Variants of Concern (VoC), such as S:N439R, S:N501Y, and S:E484K, have been linked to increased transmissibility (*8*), enhanced binding to ACE2 (*9*), and antibody escape, respectively (*10*, *11*). Despite these successes identifying functionally important mutations in the context of a large background of genetic variants of little or no phenotypic consequence remains challenging.

In modeling the relative fitness of SARS-CoV-2 lineages, we estimated their growth as a linear combination of the effects of individual mutations. To this end we developed PyR_0, a hierarchical Bayesian regression model that enables scalable analysis of the complete set of publicly available SARS-CoV-2 genomes, which can be applied to any viral genomic dataset and to other viral phenotypes. The model—which is summarized in fig. S1 and described in detail in the supplementary materials—avoids the complexity of full phylogenetic inference by first clustering genomes by genetic similarity (refining PANGO lineages) (*12*) and estimating the incremental effect on growth rate of each of the most common amino acid changes on the lineages in which they appear. By regressing growth rate on genome sequence, the model shares statistical strength among genetically similar lineages without explicitly relying on phylogeny. By modeling only the multinomial proportion of different lineages rather than the absolute number of samples for each lineage (*13*, *14*) and by doing so within 14-day intervals in 1560 globally-distributed geographic regions, the model achieves robustness to a number of sources of bias that affect all lineages across regions and over time, including differences in data collection and changes in transmission due to factors such as social behavior, public health policy, and vaccination.

We fit PyR_0 to 6,466,300 SARS-CoV-2 genomes available on GISAID (*15*) as of 20 January 2022, in a model that contained 3000 clusters derived from 1544 PANGO lineages and 2904 nonsynonymous mutations. The output of the model is a posterior distribution for the relative fitness (exponential growth rate) of each lineage and for the contribution to the fitness from each mutation. Fitting this large model is computationally challenging, so we used stochastic variational inference—an approximate inference method that reduced our task to solving an optimization problem with 75 million dimensions on a GPU. Inference was implemented in the Pyro (*16*) probabilistic programming framework (see supplemental materials). The trained model can be used to infer lineage fitness, predict the fitness of completely new lineages, forecast future lineage proportions, and estimate the effects of individual mutations on fitness.

The model's lineage fitness estimates (Fig. 1) show a modest upward trend over time among all lineages, interrupted by several lineages with much higher fitness. Sensitivity analyses revealed qualitative consistency of fitness estimates across spatial data subsets (fig. S2). The upward trend may in part reflect an upward bias caused by the lineage assignment process as can be seen in simulation studies (fig. S3); however, the high tail of the distribution exhibits elevated fitness values far in excess of this trend. The spread of the virus into human populations in late 2019 and early 2022 was marked by periods of rapid evolution in fitness and waves of increased case counts (Fig. 1). Although PANGO lineages facilitate communication by providing a stable nomenclature, we observed some PANGO lineages with multiple successive peaks in some regions, suggesting that sublineages within them had differing levels of fitness. We

[1]Broad Institute of MIT and Harvard, Cambridge, MA 02142, USA. [2]Pyro Committee, Linux AI & Data Foundation; San Francisco, CA 94104, USA. [3]Department of Organismic and Evolutionary Biology, Harvard University, Cambridge, MA 02138, USA. [4]Department of Immunology and Infectious Diseases, Harvard T. H. Chan School of Public Health, Harvard University, Boston, MA, USA. [5]Research Department, Molecular Enzymology Division, New England Biolabs, Ipswich, MA 01938, USA. [6]Massachusetts Consortium on Pathogen Readiness, Boston, MA 02115, USA. [7]Ragon Institute of MGH, MIT, and Harvard, Cambridge, MA 02139, USA. [8]Howard Hughes Medical Institute, Chevy Chase, MD 20815, USA. [9]Division of Infectious Diseases, Massachusetts General Hospital, Boston, MA, USA.
*Corresponding author. lemieux@broadinstitute.org (J.E.L.); fritz.obermeyer@gmail.com (F.O.)
†Present address: Generate Biomedicines, Inc., 26 Landsdowne Street, Cambridge, MA 02139, USA.
‡Present address: Research Department, Molecular Enzymology Division, New England Biolabs, Ipswich, MA 01938, USA.
§These authors contributed equally to this work.

therefore algorithmically refined the 1544 PANGO lineages into 3000 finer clusters and found that our model identified substantial heterogeneity within some PANGO lineages (fig. S4). When we tested the model's predictive ability (fig. S5), we found that forecasts were reliable for 1 to 2 months into the future for variants of concern—but not necessarily other variants—when they tended to be disrupted by the emergence of a completely new strain (table S1 and fig. S6). The accuracy of forecasts that stabilized typically did so within two weeks after the emergence of a new competitive lineage in a region (fig. S6).

The model correctly infers World Health Organization classification variant Omicron (PANGO BA.2) to have the highest fitness to date: 8.9 times [95% confidence interval (CI) 8.6 to 9.2] higher than the original A lineage (Fig. 1, inset), accurately foreshadowing its rise in regions where it is circulating (fig. S7). Through systematic backtesting we found that the model would have provided early warning and aided in the identification of VoCs had it been routinely applied to SARS-CoV-2 samples, confirming its utility for public health and underscoring the value of rapid sharing of genomic data. For example, the elevated fitness of BA.2 was identified by mid-December 2021 on the basis of 76 reported sequences (fig. S8); sharing statistical strength over mutations enabled an earlier and more confident prediction that BA.2 was the fittest lineage yet observed (fig. S14). Likewise, PyR_0 would have forecast the dominance of B.1.1.7 in late November 2020 (fig. S9), AY.4 by May 2021 (fig. S10), and BA.1 by early December 2021 (fig. S8). Although variant-specific models were accurate and useful in predicting the rise of these lineages (*2*), each modeling effort was specific to a particular lineage and geographic region. PyR_0's global approach provides similar early detection while also offering automated, rapid, and standardized consideration of all variants and lineages together with ranking based on relative fitness.

Compared to standard multinomial regression models, PyR_0 estimates of lineage fitness were similar (Pearson's R = 0.95, figs. S11 and S12), but inclusion of mutations in the model enables PyR_0 to infer elevated fitness of Omicron lineages BA.1 and BA.2 faster than the model without mutations (fig. S14). In contrast to nonhierarchical binomial logistic regression (fig. S13), PyR_0 estimates displayed less variability as data accumulated, benefitting from the sharing of information across regions and the regularizing effect of the prior probability distributions for the model coefficients. Lineage fitness estimates were also stable between our initial analysis of 2.1 million genomes in August 2021 (*17*), shortly after the emergence of the Delta lineages and before the emergence of Omicron (Spearman's rho = 0.78; fig. S15C). The correlation between individual amino acids in the two models was weaker than that for lineages (fig. S15, D and E; rho = 0.48) but still significant (test of no association for rho, $P < 2 \times 10^{-16}$), reflecting both the inherent difficulty of estimating high-dimensional mutational coefficients observed indirectly through lineage counts (supplementary note 1) as well as the addition of 4.3 million sequences, including highly fit Omicron lineages distinguished by their enhanced immune escape.

By jointly modeling fitness estimates with lineage counts and individual mutations PyR_0 harnesses convergent evolution (Table 1 and fig. S16) to infer the fitness of new constellations of mutations based on the trajectories of other lineages in which they have previously emerged. This predictive capability has the potential to aid public health efforts because the model has the potential to learn faster by incorporating mutations than it would by relying on lineage counts alone (fig. S14). To test the reliability of this kind of estimate we fit leave-one-out estimators for PANGO lineages on subsets of the dataset with that entire lineage removed, based solely on the mutational content of the omitted lineage (fig. S17). These estimators showed excellent agreement with estimators based on the observed behavior of the lineages; they were also more accurate than naive phylogenetic estimators that assume that the fitness of each new strain is equal to its parent lineage's fitness (Pearson's R = 0.983 after correcting for parent fitness; fig. S17). Together these analyses suggest that PyR_0 has the potential to aid genomic surveillance efforts by providing an automated early warning system on a time scale similar to that of sophisticated regional surveillance efforts (*18*, *19*).

Genome-wide estimates of the effect of SARS-CoV-2 mutations on fitness also provide a powerful tool for better understanding the biology of fitness. Our model allowed us to estimate the contribution of 2904 amino acid substitutions (Fig. 2A and Table 1) to lineage fitness and to rank them by inferred statistical significance (fig. S18). Cross-validation confirmed that these results replicate qualitatively across different geographic regions (fig. S19).

The highest concentrations of fitness-associated mutations were found in the S, N, M, and ORF1 polyprotein genes (ORF1a and ORF1b; Fig. 2, A and B, and figs. S20 and S21). Using spatial autocorrelation as a measure of spatial structure, we found evidence of functional hotspots in the S, N, ORF7a, ORF3a, and ORF1a genes (table S2). Within S, we confirmed three hotspots of fitness-enhancing mutations, each within a defined functional region: the N-terminal domain, the receptor-binding domain (RBD), and the furin-cleavage site (Fig. 2B). We

Table 1. Amino acid substitutions most significantly associated with increased fitness. Significance is defined as posterior mean or posterior standard deviation. Fitness is per 5.5 days (estimated generation time of the Wuhan (A) lineage) (*1*, *23*). The final column is the number of PANGO lineages in which each substitution emerged independently.

Rank	Gene	Substitution	Fold increase in fitness	Number of lineages
1	S	H655Y	1.051	33
2	S	T95I	1.046	30
3	ORF1a	P3395H	1.039	5
4	S	N764K	1.04	6
5	ORF1a	K856R	1.039	2
6	S	S371L	1.041	3
7	E	T9I	1.04	5
8	S	Q954H	1.04	5
9	ORF9b	P10S	1.039	25
10	S	L981F	1.04	2
11	N	P13L	1.04	25
12	S	G339D	1.039	4
13	S	S375F	1.04	5
14	S	S477N	1.039	47
15	S	N679K	1.04	11
16	S	S373P	1.04	5
17	M	Q19E	1.039	5
18	S	D796Y	1.038	11
19	S	N969K	1.04	5
20	S	T547K	1.038	3

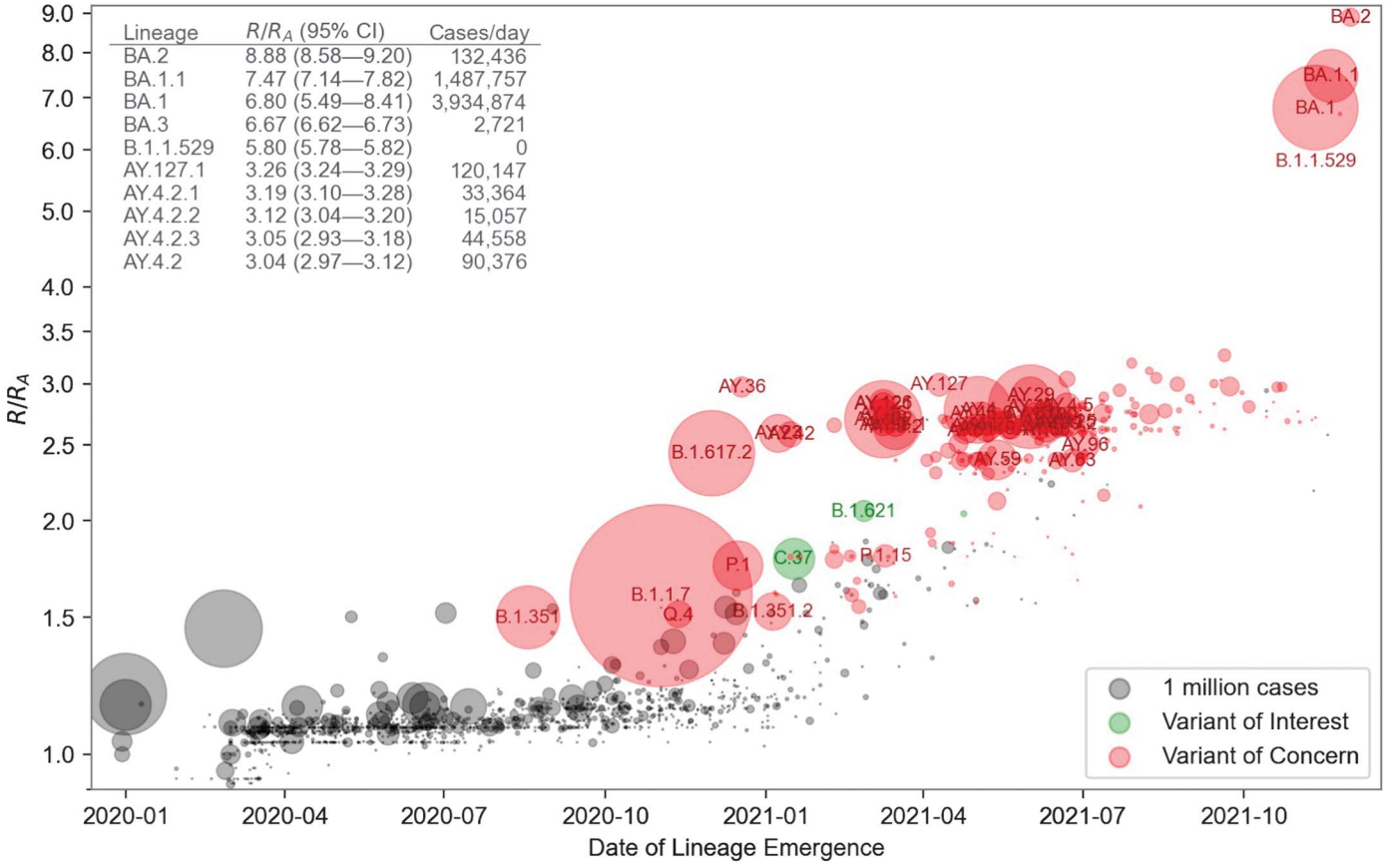

Fig. 1. Relative fitness versus date of lineage emergence. Circle size is proportional to cumulative case count inferred from lineage proportion estimates and confirmed case counts. The inset table lists the 10 fittest lineages inferred by the model. R/R_A is the fold increase in relative fitness over the Wuhan (A) lineage, assuming a fixed generation time of 5.5 days.

assessed mutational enrichment in the top-ranked set of mutations and identified enrichment for lysine to asparagine mutations in the S gene (fig. S22C). We visualized top-scoring mutations within atomic structures for the spike protein (Fig. 2, D to E), the nucleocapsid's N-terminal domain (Fig. 2F), the polymerase (fig. S23), and two proteases (fig. S24). Many of the top mutations in the S gene occurred in the receptor binding domain (RBD) that makes direct contact with the ACE2 receptor, including K417N/T and E484K (Fig. 2, D to E). Two top-ranked mutations, T478K and S477N, occur in a flexible loop adjacent to the S-ACE2 interface (Fig. 2E), suggesting that these mutations may affect the kinetics of receptor engagement or the Spike conformational changes that follow. Other mutations occurred in regions proximal to essential enzymatic active sites of viral replication (fig. S23) or protein processing (fig. S24) machinery.

We tested several of the high-scoring mutations in single-cycle infectivity assays as performed previously (*7*), focusing on the RBD (Fig. 3A). We found that although some individual mutations increased infectivity, on average high-scoring RBD mutations did not promote infectivity per se. We considered an alternate possibility that fitness of Spike mutations is driven by immune escape. Using RBD-aggregated mutations as a proxy for immune escape we found that the fitness effect of these Spike mutations correlates well with antibody escape estimates from Greaney *et al.* (*20*) (Fig. 3B). Together with the observed jump in fitness beginning in late 2021 (Fig. 3C) associated with Spike mutations—but not mutations elsewhere in the genome (Fig. 3E)—these results suggest that immune escape is the dominant driver of current fitness increases. BA.1 and BA.2 had similar estimated fitness from Spike mutations—potentially consistent with similar Spike antibody neutralization of these variants (*21*)—whereas PyR_0 inferred that the elevated fitness of BA.2 is attributed to non-Spike mutations (fig. S25). In contrast to mutations in Spike, those in the serine-arginine rich region of N were linked to increased efficiency of SARS-CoV-2 genomic RNA packaging (*22*). Within ORF1 we found fitness-associated mutations across all viral enzymes and clusters within additional nonstructural proteins (nsps). The highest concentration of fitness-associated mutations is found in nsp4, nsp6, and nsps12 to 14 (figs. S20B and S21, C and D), suggesting unexplored function at those sites. For example, nsp4 and nsp6 have roles in assembly of replication compartments and substitutions in these regions may influence the kinetics of replication (see supplemental note 3). We caution that although convergent evolution makes it possible to identify candidate functional mutations, observational data alone is insufficient to declare mutations as causal rather than merely correlated. Our uncertainty-ranked list of important mutations can be used to prioritize hits identified by our study for functional follow-up.

Some lineages increased in fitness more than others over the course of the pandemic (fig. S4). Notably, B.1.1 displayed the greatest variability among sublineages, followed by B.1. Fitness appeared to reach a plateau over time for most lineages (Fig. 1 and fig. S4). In contrast to Omicron sublineages Alpha and Delta showed little variability in Spike-attributable fitness (fig. S25), suggesting that the propensity to acquire new Spike mutations depends

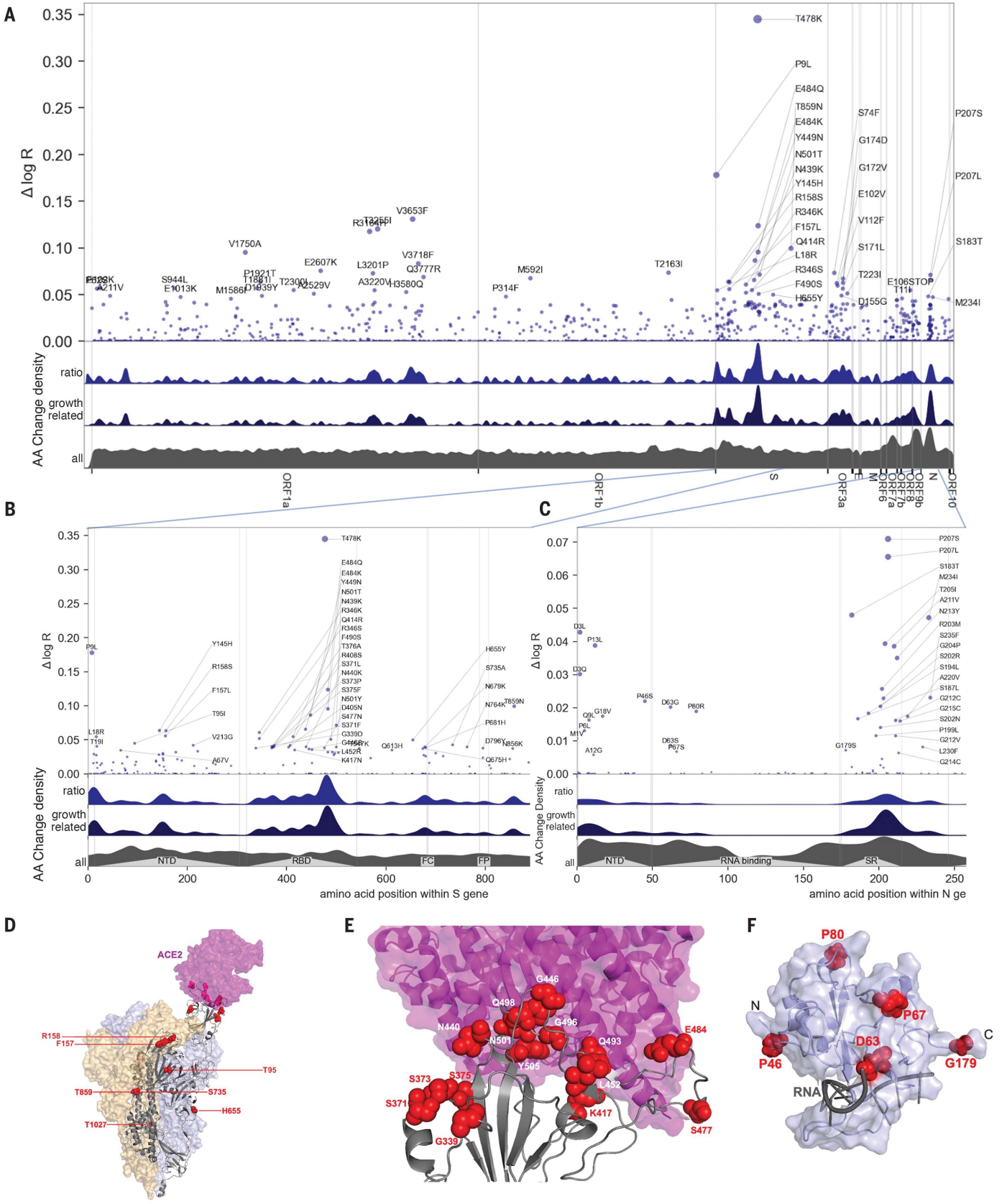

Fig. 2. Summary of amino acid changes assessed in this study. (**A**) Manhattan plots of amino acids and changes across the entire genome. (**B**) Changes in the first 850 amino acids of S. (**C**) Changes in the first 250 amino acids of N. The y axis in (A) to (C) shows effect size Δ log R, the estimated change in log relative fitness resulting from each amino acid change. The bottom three axes show the background density of all observed amino acid changes, the density of those associated with growth

fig 2 continued

(weighted by |Δ log R|), and the ratio of the two. The top 55 amino acid changes are labeled. See fig. S21 for detailed views of S, N, ORF1a, and ORF1b. (**D**) Structure of the spike-ACE2 complex (PDB: 7KNB). Spike subunits are colored light purple, light orange, and gray, top-ranked mutations are shown as red spheres, and ACE2 is shown in magenta. (**E**) Close-up view of the RBD interface. (**F**) Top-ranked mutations in the N-terminal RNA-binding domain of N. Residues 44 to 180 of N (PDB: 7ACT) are shown in light purple. Amino acid positions corresponding to top mutations in this region are shown as red spheres. A 10-nucleotide (nt)- bound RNA is shown in gray.

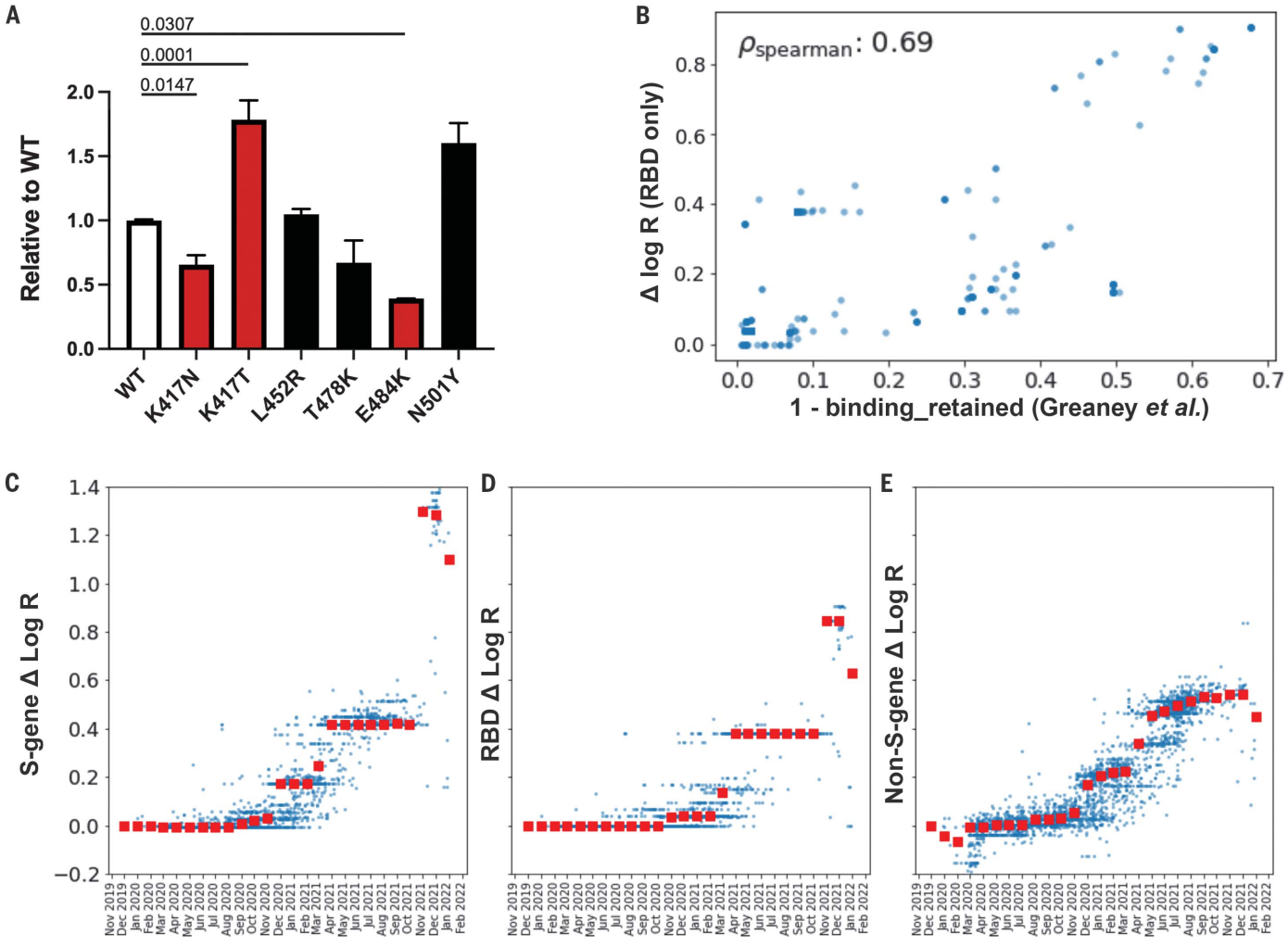

Fig. 3. Characterization of mutation-specific effects. (**A**) Infectivity relative to wild type (WT) of lentiviral vectors pseudotyped with the indicated Spike mutants. Target cells were HEK293T cells expressing ACE2 and TMPRSS2 transgenes. The genetic background of the Spike was Wuhan-Hu-1, bearing D614G. Red bars were significantly different from WT (adjusted p values shown) and black bars were not significantly different from WT. (**B**) For the 1701 SARS-CoV-2 clusters with at least one amino acid substitution in the RBD domain we compare: (i) the PyR_0 prediction for the contribution with Δ log R from RBD substitutions only; with (ii) antibody binding computed with the antibody-escape calculator in (*20*). The escape calculator is based on an intuitive nonlinear model parameterized with deep mutational scanning data for 33 neutralizing antibodies elicited by SARS-CoV-2. PyR_0 predictions exhibit high (Spearman) correlation with predictions from Greaney *et al*. (*20*) (**C** to **E**) We dissect PyR_0 Δ log R estimates into the S-gene (C), RBD (D), and non–S-gene (E) contributions for 3000 SARS-CoV-2 clusters (blue dots). The horizontal axis corresponds to the date at which each cluster first emerged. Red squares denote the median Δ log R within each monthly bin. The increased importance of S-gene mutations (notably in the RBD) over non–S-gene mutations starting around November 2021 is apparent.

on the constellation of mutations that constitute a lineage, consistent with epistasis. A limitation of PyR_0 is that it does not incorporate epistatic interactions between mutations (supplemental note 1); however, our results demonstrate the feasibility of inferring genetic determinants and lineage fitness with the simplest possible linear-additive model and provide a foundation for future research for more complex modeling that includes epistatic effects between mutations and migration across geographic regions.

In summary, PyR_0 provides a genome-wide, automated approach for detecting viral lineages with increased fitness. By combining a model-based assessment of lineage fitness with absolute case counts, our model provides a global picture of the events of the first two

years of the pandemic. Because it assesses the contribution of individual mutations and aggregates across all lineages and geographic regions, it can identify mutations and gene regions that likely increase fitness; additionally, mutation-level information may help detect fitter lineages earlier than case counts alone. Applied to the full set of publicly available SARS-CoV-2 genomes, it provides a genomic view of the mutations driving increased fitness of the virus, identifying experimentally established driver mutations in S and highlighting the key role of non-S mutations particularly in N, ORF1b, and ORF1a, which have received relatively less research attention than mutations in S. By modeling millions of viral sequences across thousands of regions, PyR_0 yields mechanistic insight into viral fitness and offers a panoramic view of viral evolution, revealing a pattern whereby major circulating lineages fragment into sublineages with modest differences in fitness before they are collectively displaced by the sudden emergence of markedly fitter variants.

REFERENCES AND NOTES:

1. N. G. Davies *et al*., *Science* **372**, eabg3055 (2021).
2. E. Volz *et al*., *Nature* **593**, 266–269 (2021).
3. P. Stefanelli *et al*., *Euro Surveill.* **27**, (2022).
4. F. Campbell *et al*., *Euro Surveill.* **26**, 2100509 (2021).
5. H. S. Vöhringer *et al*., *Nature* **600**, 506–511 (2021).
6. B. Korber *et al*., *Cell* **182**, 812–827.e19 (2020).
7. L. Yurkovetskiy *et al*., *Cell* **183**, 739–751.e8 (2020).
8. X. Deng *et al*., *Cell* **184**, 3426–3437.e8 (2021).
9. T. N. Starr *et al*., *Cell* **182**, 1295–1310.e20 (2020).
10. B. Choi *et al*., *N. Engl. J. Med.* **383**, 2291–2293 (2020).
11. A. J. Greaney *et al*., *Cell Host Microbe* **29**, 44–57.e9 (2021).
12. A. Rambaut *et al*., *Nat. Microbiol.* **5**, 1403–1407 (2020).
13. H. S. Vöhringer *et al*., bioRxiv 2021.05.22.21257633 [Preprint] (2021).
14. F. Campbell *et al*., *Euro Surveill.* **26**, (2021).
15. S. Elbe, G. Buckland-Merrett, *Glob. Chall.* **1**, 33–46 (2017).
16. E. Bingham *et al*., *J. Mach. Learn. Res.* **20**, 973–978 (2019).
17. F. Obermeyer *et al*., medRxiv 2021.09.07.21263228 [Preprint] (2021).
18. A. Rambaut *et al*., ARTIC Network, "Preliminary genomic characterisation of an emergent SARS-CoV-2 lineage in the UK defined by a novel set of spike mutations" (2020); https://virological.org/t/preliminary-genomic-characterisation-of-an-emergent-sars-cov-2-lineage-in-the-uk-defined-by-a-novel-set-of-spike-mutations/563).
19. R. Viana *et al*., *Nature* **603**, 679–686 (2022).
20. A. J. Greaney, T. N. Starr, J. D. Bloom, *Virus Evol.* **8**, veac021 (2022).
21. J. Yu *et al*., *N. Engl. J. Med.* **386**, 1579–1580 (2022).
22. A. M. Syed *et al*., *Science* **374**, 1626–1632 (2021).
23. L. Ferretti *et al*., bioRxiv 2020.09.04.20188516 [Preprint] (2020).
24. F. Obermeyer, N. Barkas, M. Jankowiak, J. Lemieux, C. Roemer, Zenodo (2022); https://zenodo.org/record/6399987).

ACKNOWLEDGMENTS

We acknowledge crucial assistance in data preprocessing from A. Hinrichs. We thank T. Bedford and C. Roemer for visualizing the outputs of our model on nextstrain.org. We acknowledge helpful discussions and feedback from D. Phan, W. Hanage, C. Tomkins-Tinch, S. Weingarten-Gabbay, K. Siddle, S. Gosai, S. Reilly, E. Bingham, H. Soutter, D. Marks, N. Youssef, S. Gurev, and N. Thadani. We gratefully acknowledge the authors from the originating laboratories and the submitting laboratories, who generated and shared via GISAID genetic sequence data on which this research is based (Supplementary Data File 3). This work is licensed under a Creative Commons Attribution 4.0 International (CC BY 4.0) license, which permits unrestricted use, distribution, and reproduction in any medium, provided the original work is properly cited. To view a copy of this license, visit https://creativecommons.org/licenses/by/4.0/. This license does not apply to figures/photos/artwork or other content included in the article that is credited to a third party; obtain authorization from the rights holder before using such material. **Funding:** This work was sponsored by the U.S. Centers for Disease Control and Prevention (BAA 75D30120C09605 to B.L.M.), as well as support from the Doris Duke Charitable Foundation (J.E.L.), the Howard Hughes Medical Institute (P.C.S.), the National Institute of Allergy and Infectious Diseases R37AI147868 (J.L.) and U19AI110818 (P.C.S.), and the Evergrande COVID-19 Response Fund Award from the Massachusetts Consortium on Pathogen Readiness (J.L.).
Competing interests: P.C.S. is a cofounder of and consultant to Sherlock Biosciences and a Board Member of Danaher Corporation, and holds equity in the companies. The authors declare no other conflicts of interest. **Author contributions:** Conceptualization: F.O., S.F.S., J.E.L., and M.J. Data curation: F.O. and N.B. Formal Analysis: F.O., S.F.S, M.J., N.B., and J.E.L. Funding acquisition: D.J.P., B.M., P.C.S, J.L., and J.E.L. Investigation: all authors. Methodology: F.O., S.F.S, M.J., J.E.L., L.Y., and M.B. Project administration: all authors. Software: F.O., N.B., and M.J. Supervision: D.J.P., B.M., J.L., P.C.S., and J.E.L. Validation: F.O., N.B., M.J., and S.F.S. Visualization: F.O., J.E.L., N.B., J.P., and S.F.S. Writing – original draft: F.O., S.F.S., B.M., P.C.S, and J.E.L. Writing – review and editing: All authors. **Data and materials availability:** Code is available at (*24*). We gratefully acknowledge all data contributors, i.e., the authors and their originating laboratories responsible for obtaining the specimens, and their submitting laboratories for generating the genetic sequence and metadata and sharing via the GISAID initiative (*15*) on which this research is based. A total of 6,466,300 submissions are included in this study. A complete list of 6.4 million accession numbers is included as data S3. **License information:** Copyright © 2022 the authors, some rights reserved; exclusive licensee American Association for the Advancement of Science. No claim to original US government works. https://www.sciencemag.org/about/science-licenses-journal-article-reuse

SUPPLEMENTARY MATERIALS

science.org/doi/10.1126/science.abm1208
Materials and Methods
Figs. S1 to S34
Tables S1 to S5
References (*25*–*56*)
MDAR Reproducibility Checklist
Data S1 to S5
GISAID Acknowledgments Table (table S3)

View/request a protocol for this paper from *Bio-protocol*.

Submitted 26 August 2021; resubmitted 16 February 2022
Accepted 10 May 2022
10.1126/science.abm1208

CONSERVATION

Glacial ice supports a distinct and undocumented polar bear subpopulation persisting in late 21st-century sea-ice conditions

Kristin L. Laidre[1,2]*, Megan A. Supple[3], Erik W. Born[2], Eric V. Regehr[1], Øystein Wiig[4], Fernando Ugarte[2], Jon Aars[5], Rune Dietz[6], Christian Sonne[6], Peter Hegelund[2], Carl Isaksen[2], Geir B. Akse†, Benjamin Cohen[1], Harry L. Stern[1], Twila Moon[7], Christopher Vollmers[8], Russ Corbett-Detig[8], David Paetkau[9], Beth Shapiro[3,10]

Polar bears are susceptible to climate warming because of their dependence on sea ice, which is declining rapidly. We present the first evidence for a genetically distinct and functionally isolated group of polar bears in Southeast Greenland. These bears occupy sea-ice conditions resembling those projected for the High Arctic in the late 21st century, with an annual ice-free period that is >100 days longer than the estimated fasting threshold for the species. Whereas polar bears in most of the Arctic depend on annual sea ice to catch seals, Southeast Greenland bears have a year-round hunting platform in the form of freshwater glacial mélange. This suggests that marine-terminating glaciers, although of limited availability, may serve as previously unrecognized climate refugia. Conservation of Southeast Greenland polar bears, which meet criteria for recognition as the world's 20th polar bear subpopulation, is necessary to preserve the genetic diversity and evolutionary potential of the species.

The impact of human-mediated climate warming on biodiversity is a global conservation concern (*1*). Shifts in species phenology, distribution, and abundance are altering ecological communities and increasing extinction risk (*2*). Understanding how life history strategies affect species persistence, including the role of within-species diversity at multiple spatial scales, is critical for conservation (*3*, *4*).

The ongoing and predicted decrease in Arctic sea ice (*1*) raises concerns for ice-dependent species such as polar bears (*5*), whose survival will depend on establishing populations in fragmented habitats and maintaining genetic connectivity among them (*6*). Recent forecasts of reduced polar bear distribution and abundance (*7*) are based on broad-scale climate projections and the estimated number of days that bears can fast without sea ice, which they require for hunting. These forecasts do not consider the role of small-scale habitat features that, although of limited availability, could serve as climatic refugia. Here, we combine 36 years of movement, genetic, and demographic data to describe a genetically distinct and functionally isolated group of polar bears in Southeast Greenland. We use these data to explore the prospects for polar bear survival in a warmer, ice-free Arctic.

The East Greenland subpopulation, one of 19 recognized subpopulations of polar bears, occupies a marine area of ~700,000 km^2 along a mostly uninhabited ~3200-km coastline (*8*, *9*). In 2011, we initiated a multiyear project to assess the status of East Greenland bears using movements, genetics, and demography (Fig. 1 and figs. S1 and S2). Intriguingly, satellite telemetry revealed that bears living south of 64°N, hereafter Southeast Greenland (n = 27 adult females, 2015–2021; table S1), did not interact with bears living north of 64°N, hereafter Northeast Greenland (n = 56 adult females, 1993–2021; Fig. 2A). Instead, female bears in Southeast Greenland made localized movements in fjords and at marine-terminating glacier fronts (Fig. 2B) with a median 4-day movement rate of 10 km (8.4 to 13.1 km, 25 and 75% quartiles; fig. S3). Some bears remained in one fjord for years, while others moved between adjacent fjords, traveling over mountains via the ice sheet and peripheral glaciers (fig. S4). In contrast, the median 4-day movement rate of female bears in Northeast Greenland was 40 km (30.0 to 49.0 km; fig. S3), with annual movements of >1500 km on the offshore sea ice. Recaptures of males indicated similar movement patterns (*10*). The degree of geographic isolation of Southeast Greenland bears distinguishes them from other subpopulations (*11*).

Current sea-ice conditions in Southeast Greenland, like those projected for the late 21st century in the High Arctic, appear unsuitable to support polar bears. Pack ice (freely floating sea ice) is intermittently flushed into fjords but is largely unusable owing to its low concentration and transience (Fig. 2C and figs. S5 to S10). Southeast Greenland bears use fast ice (sea ice frozen to the coastline) when it is available in winter and spring (figs. S11 to S15), but the number of days per year with fast-ice coverage is low and variable (between 0 and 153 days; mean: 89 days) (fig. S15 and table S2). Fast ice typically forms in February and disappears by late May, so the region is sea ice–free for more than 250 days per year, exceeding polar bears' estimated seasonal fasting threshold of 100 to 180 days (*7*). Our data show that Southeast Greenland bears use glacial mélange (freshwater ice at glacier fronts) as a platform for hunting during the sea ice–free season (Fig. 2, D and E), whereas in most parts of the Arctic, polar bears must move onto land or track the receding sea ice northward into the less productive polar basin (*11*).

Southeast Greenland bears appear to have adapted their movements to the region's specific physical geography. The high-velocity East Greenland Coastal Current (*12*) seasonally brings a narrow band of low-concentration pack ice south of 64°N and around the southern tip of Greenland (figs. S8 to S10) (*13*). All tracked Southeast Greenland bears that moved out of the fjords (n = 11) became caught in this current's drift ice and were transported southward toward Cape Farewell, drifting an average of 189 km in <2 weeks (fig. S4). Notably, all swam ashore and walked via land to their home fjord within 1 to 2 months, demonstrating high site fidelity. Bears in Southeast Greenland must remain inside fjords or risk export to human-inhabited areas of South Greenland or into the North Atlantic.

Southeast Greenland bears are the most genetically isolated polar bears in the Arctic (figs. S16 to S25 and tables S3 to S8). Principal components analyses showed a distinct Southeast Greenland cluster across 20 microsatellite loci isolated from 372 bears (Fig. 3A, fig. S16, and table S3), 40 whole genomes (Fig. 3B, fig. S21, and table S7), and whole-blood transcriptomic data from 16 bears (Fig. 3C and table S8) (*10*). In a Bayesian clustering analysis of 3064 bears from all subpopulations except the Arctic Basin, Southeast Greenland bears were distinct from all subpopulations across the species' circumpolar range when the model assumed four clusters (Fig. 3D and figs. S18 to S20) (*10*). Norwegian Bay bears, previously identified as the most distinct subpopulation (*14*–*16*), emerged at five clusters. Southeast Greenland bears also have the lowest levels of heterozygosity across microsatellites (table S4) and whole genomes (fig. S25), as well as the

[1]Polar Science Center, Applied Physics Laboratory, University of Washington, Seattle, WA 98105, USA. [2]Greenland Institute of Natural Resources, 3900 Nuuk, Greenland. [3]Department of Ecology and Evolutionary Biology, University of California, Santa Cruz, Santa Cruz, CA 95064, USA. [4]Natural History Museum, University of Oslo, Blindern, NO-0318 Oslo, Norway. [5]Norwegian Polar Institute, Fram Centre, NO-9296 Tromsø, Norway. [6]Department of Ecoscience and Arctic Research Centre, Aarhus University, DK-4000 Roskilde, Denmark. [7]National Snow and Ice Data Center, Cooperative Institute for Research In Environmental Sciences (CIRES), University of Colorado, Boulder, CO 80309, USA. [8]Department of Biomolecular Engineering, University of California, Santa Cruz, Santa Cruz, CA 95064, USA. [9]Wildlife Genetics International, Nelson, BC V1L 5P9, Canada. [10]Howard Hughes Medical Institute, University of California, Santa Cruz, Santa Cruz, CA 95064, USA.
*Corresponding author. Email: klaidre@uw.edu
†Independent researcher, NO-5237 Rådal, Norway.

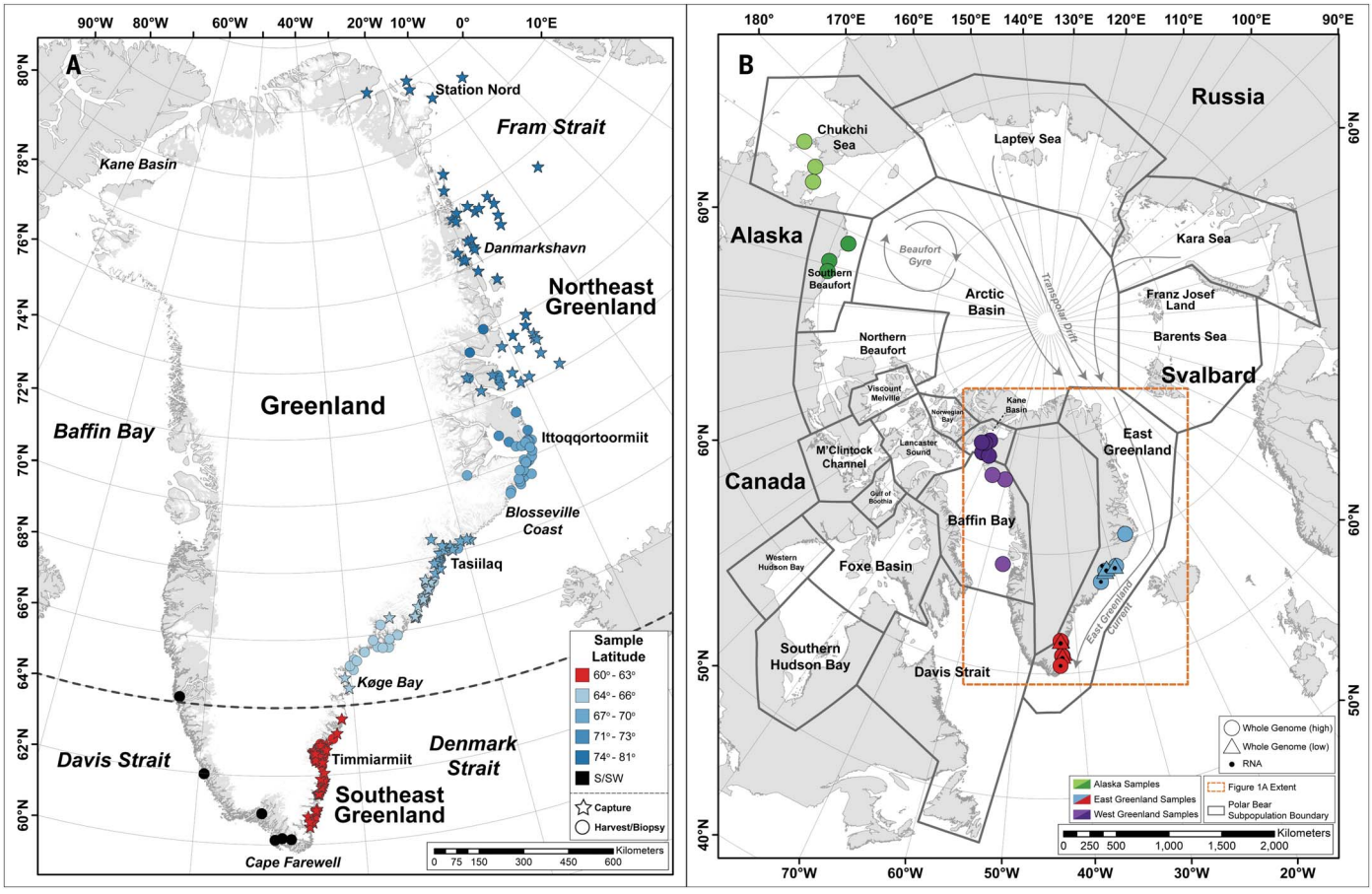

Fig. 1. Place names and distribution of samples. (**A**) Locations of physical captures, biopsies, and subsistence harvest samples used for genetic (1983–2017) and movement (1993–2021) analyses from polar bears collected within Southeast Greenland and Northeast Greenland, separated by 64°N. (**B**) Geographic locations of whole-genome and RNA samples (2015–2017) and subpopulation boundaries.

highest proportion of their genomes in runs of homozygosity (fig. S25) compared with other polar bear subpopulations.

Estimates of genetic divergence measured as F_{ST} showed that Southeast Greenland bears are more genetically diverged from neighboring groups of bears [in Northeast Greenland (F_{ST} = 0.059) and the Davis Strait subpopulation (F_{ST} = 0.086)] than any other neighboring subpopulation pair (table S5). The pair with the next-highest F_{ST} (M'Clintock Channel and Foxe Basin, F_{ST} = 0.039) are separated by a land boundary, which is less conducive to polar bear movement than a water–ice boundary. Norwegian Bay has even lower F_{ST} values with its neighbors (Kane Basin, F_{ST} = 0.026; Lancaster Sound, F_{ST} = 0.027). The genetic distinctiveness of Southeast Greenland bears may be due in part to the rapid directional flow of the East Greenland Coastal Current, which limits both northward emigration and southward immigration. In support of this hypothesis, bears genotyped from South and Southwest Greenland did not cluster with Southeast Greenland, their nearest neighbor. Instead, they clustered with Northeast Greenland bears (Figs. 1 and 3A), suggesting that they originated in Northeast Greenland and were subsequently transported south on the sea ice, past Southeast Greenland's fjords and around Cape Farewell. Davis Strait bears also were more similar to Northeast Greenland bears than to Southeast Greenland bears (table S5), suggesting gene flow from Davis Strait around the northern coast of Greenland.

Demographic data are consistent with Southeast Greenland bears functioning as a distinct subpopulation. Birth rates were low compared with Northeast Greenland and most other polar bear subpopulations (*10*, *17*). We found no differences in litter sizes between Southeast Greenland and Northeast Greenland subpopulations, which suggests similar cub survival (tables S9 and S10). Adult female body mass, an important determinant of cub production and survival (*18*), was lower in Southeast Greenland than in several other subpopulations but was similar to that of Northeast Greenland bears and the Barents Sea subpopulation (fig. S26 and table S11), both of which use glacial fjords (*19*). It is possible that low birth rates are influenced by highly fractured fjord and mountain habitats that reduce bear movements and impede breeding pair formation (*20*).

The distinctive movement, genetic, and demographic patterns of Southeast Greenland bears may have evolved over several hundred years of isolation. The earliest reference to polar bears in South Greenland dates to the 1300s (*21*), and the first written Western record of bears in Southeast Greenland fjords is from the 1830s (*22*). These records are consistent with analyses of rare single-nucleotide polymorphisms [maximum allele frequency of 5%; (*10*)] in the whole-genome data, which suggested that sampled Southeast Greenland bears share a common ancestor ~200 years ago (95% confidence interval: 189 to 264 years ago; fig. S22) and thus have been genetically isolated for at least this long.

Southeast Greenland bears have few opportunities for dispersal. Their habitat comprises steep coastal topography with fjords separated by >2000-m mountains and narrow glaciers. To the west, dispersal is restricted by the Greenland Ice Sheet. To the east is the open water of the Denmark Strait. Northward movement is limited by the East Greenland Coastal

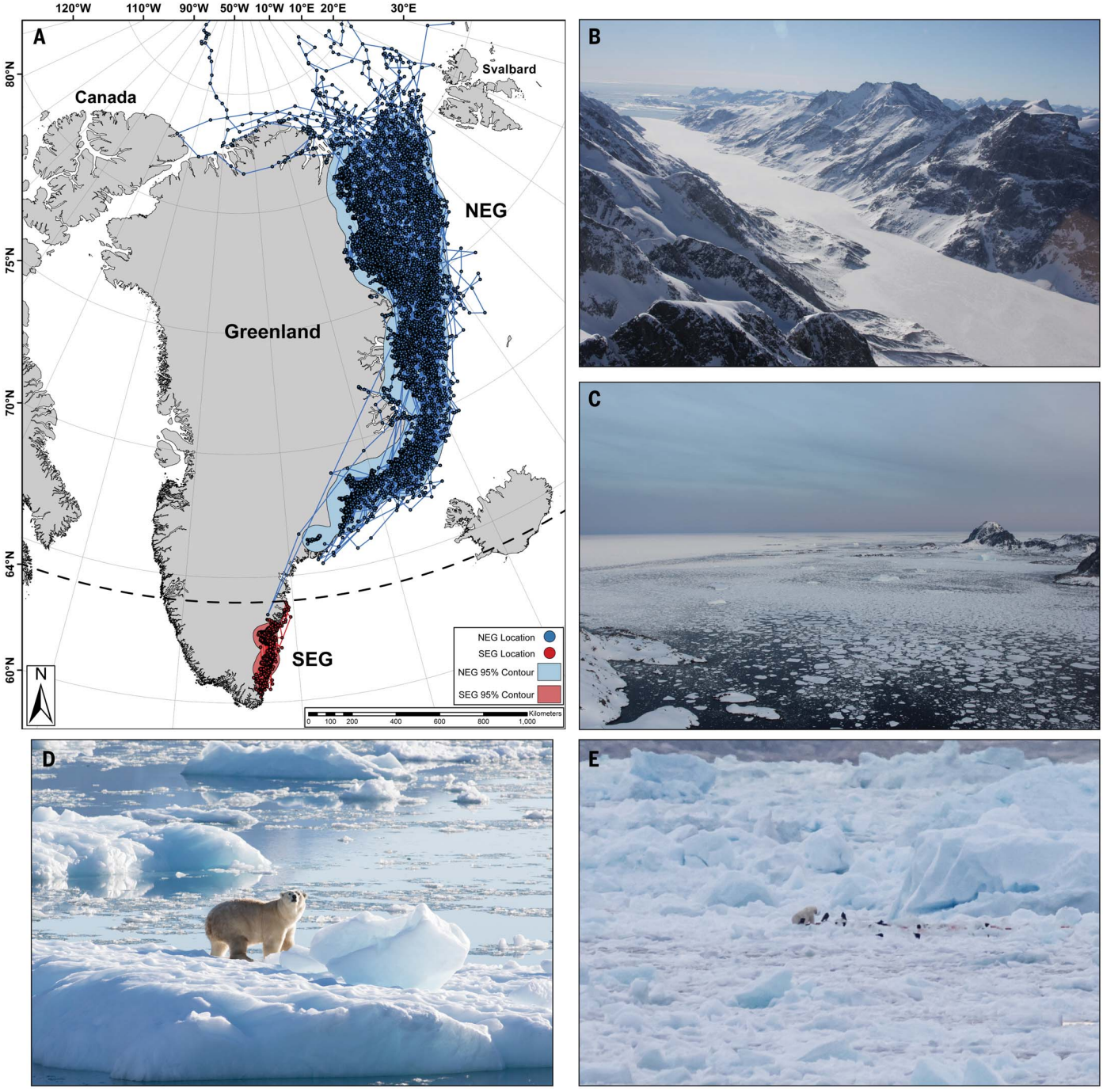

Fig. 2. Polar bear movements and habitat types. (**A**) Area use for Northeast Greenland (NEG) and Southeast Greenland (SEG) polar bears based on satellite telemetry from 1993 to 2021. SEG bears range over ~400 linear km of mountainous and glaciated coastal habitat (~27,749 km^2 within 95% probability contours), whereas NEG bears range over >2000 linear km of pack ice and fast ice and 671,208 km^2 (95% probability contours). NEG and SEG are separated at about 64°N latitude. (**B**) Fjord fast-ice habitat in SEG, present <4 months per year. (**C**) Low-concentration drift ice with open water on the horizon in Denmark Strait. (**D**) SEG polar bear using glacial ice at 62°N in September 2016. (**E**) Polar bear with a fresh seal kill at 61°N in September 2016.

PHOTOS: KRISTIN LAIDRE [(B) AND (C)]; THOMAS W. JOHANSEN/NASA OMG [(D) AND (E)]

Current (*12*), by katabatic winds that flush the region of sea ice around Køge Bay (65°N), and by subsistence hunting around the community of Tasiilaq. To the south, polar bear habitat disappears at the southern tip of Greenland, and both South and Southwest Greenland are inhabited by humans who hunt polar bears.

Despite limited options for dispersal, Southeast Greenland bears occasionally capture genetic diversity from other subpopulations, and our observations suggest that immigrants can adapt to the distinctive environment. Research-marked bears have been observed in Southeast and Southwest Greenland after being tagged in Franz Josef Land (Russia), Svalbard, Baffin Island, and the eastern Beaufort Sea (*9*). Our whole-genome dataset identifies two individuals as potential immigrants: one that clusters closer to the Southern Beaufort Sea and Chukchi Sea subpopulations in Alaska, and another that clusters closer to Northeast Greenland (Fig. 3B).

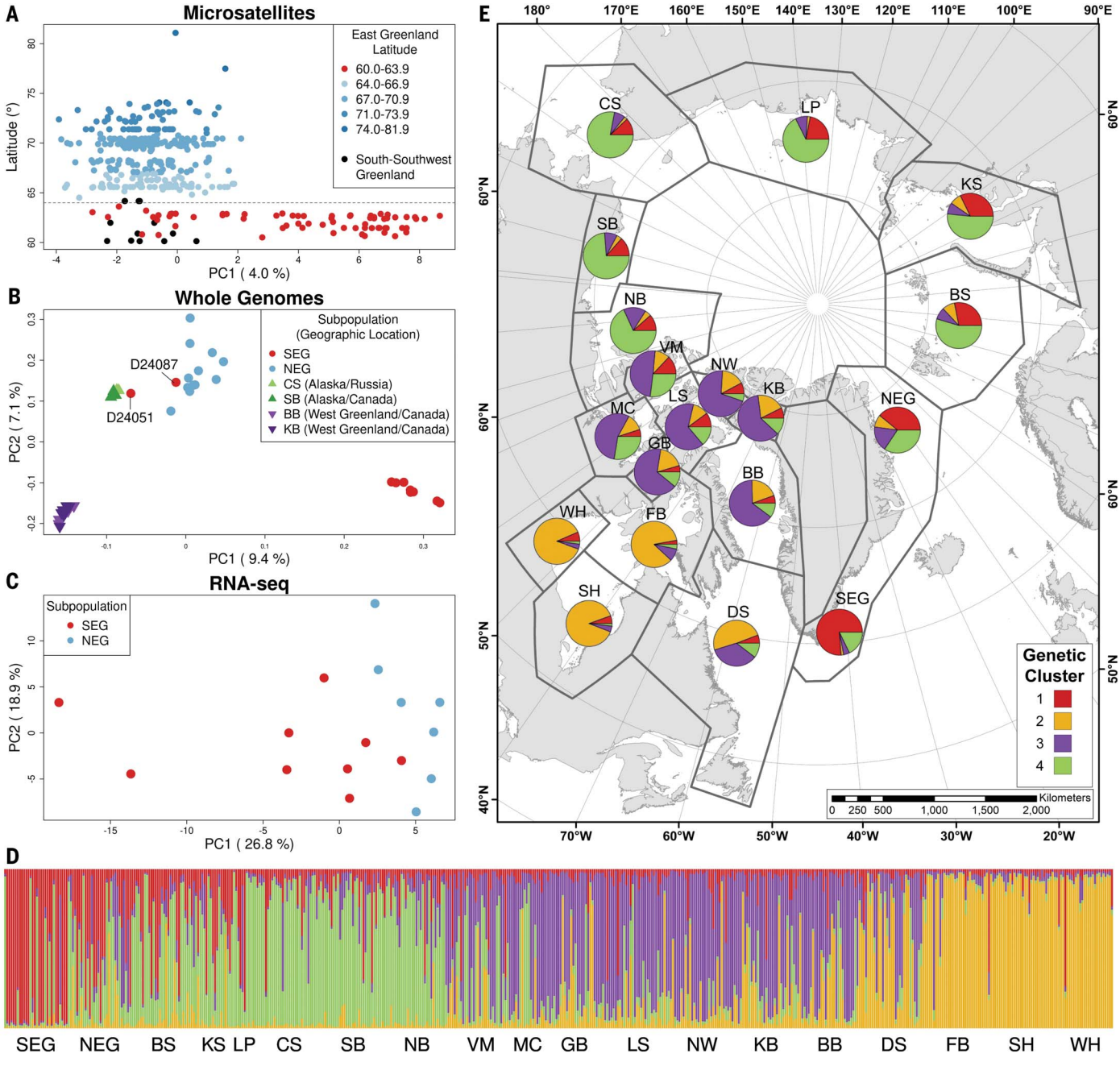

Fig. 3. Population structure. (**A**) Primary axis of genetic principal components analysis (PCA) versus latitude of Greenland bears. Most SEG bears (red) cluster separately from NEG bears (blue). Bears from South and Southwest Greenland (black) cluster with NEG bears. (**B**) Genomic PCA showing that SEG bears cluster separately from other subpopulations, except individuals D24051 and D24087, which cluster with Chukchi Sea (CS)/Southern Beaufort (SB) and NEG bears, respectively. (**C**) Transcriptomic PCA of East Greenland samples. SEG (red) and NEG (blue) bears show different gene expression profiles. Axes in (A) to (C) show the percentage of variation explained. (**D**) Bayesian clustering assuming four clusters. Each column represents a sample. (**E**) Summary by subpopulation of the individual-based results from (D). SEG bears are genetically distinct from other subpopulations. BS, Barents Sea; KS, Kara Sea; LP, Laptev Sea; NB, Northern Beaufort Sea; VM, Viscount Melville Sound; MC, M'Clintock Channel; GB, Gulf of Boothia; LS, Lancaster Sound; NW, Norwegian Bay; KB, Kane Basin; BB, Baffin Bay; DS, Davis Strait; FB, Foxe Basin; SH, Southern Hudson Bay; WH, Western Hudson Bay.

We detected little evidence of admixture in either bear (Fig. 4 and fig. S23). Combined with ancestry analysis (fig. S22), this suggests that these individuals were recent immigrants into Southeast Greenland. While these data do not establish successful gene flow into Southeast Greenland, microsatellites identify some Southeast Greenland bears with mixed ancestry (Fig. 3A and figs. S18 to S20), suggesting that immigrant bears adapt sufficiently to interbreed with resident bears.

Although our study was not designed to estimate abundance, data from marked individuals suggest that a few hundred animals currently inhabit Southeast Greenland, similar to other small polar bear subpopulations (*10*, *11*). Human-caused mortality is unlikely to limit the numbers of Southeast Greenland bears. Human settlements in the Skjoldungen-Timmiarmiit area were abandoned in the mid-1960s. Small numbers of subsistence hunters lived along

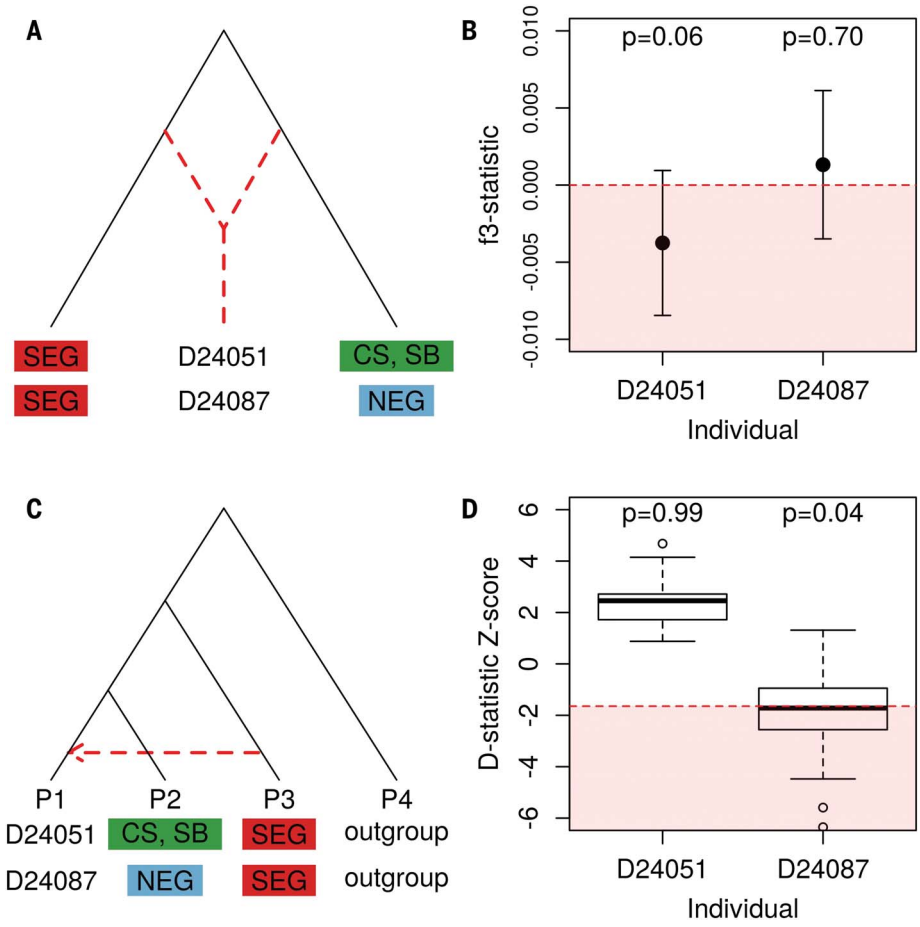

Fig. 4. Genomic tests of admixture in D24051 and D24087. (**A**) The f3 statistics explore whether D24051 and D24087 are mixtures of two source populations. (**B**) We find no statistical evidence at ±1.96 SE that either individual is admixed. Negative values (red region) indicate admixture. (**C**) The D-statistics investigate whether either D24051 or D24087 has excess ancestry from SEG as compared with the subpopulations they cluster with genetically. (**D**) Box plots showing all combinations of individuals from the specified subpopulations show little evidence that either individual is admixed. The region of statistical significance for a single comparison is highlighted in red.

the coast until the late 1970s (*23*), but it is uncommon for polar bear hunters to go to Southeast Greenland today (*24*).

We propose that Southeast Greenland polar bears are a resident, functionally and demographically isolated group that warrants consideration as the 20th subpopulation of polar bears by the International Union for Conservation of Nature. Southeast Greenland bears are distinct according to the same lines of evidence used to delineate other subpopulations, most of which exhibit substantially more genetic mixing (*11*, *16*). Maintenance of the distinctive Southeast Greenland lineage is necessary to preserve the genetic diversity of the species.

The existence of the Southeast Greenland subpopulation has implications for conservation. In most of the Arctic, glacial mélange habitats are uncommon, and the future of polar bears will be closely tied to the availability of sea ice (*5*–*7*). However, in Greenland and Svalbard, glacial mélange habitat is available and occupied year-round by ringed seals, the polar bear's primary prey (*25*) (Fig. 2, D and E). We show that some polar bears can become established and adapt to this distinctive environment, which, in some areas, may provide a buffer to sea-ice loss. The long-term role of refugia in the persistence of polar bears is unknown (*26*). Even glacial mélange habitat is changing, because the Greenland Ice Sheet coastal margin is undergoing widespread reconfiguration (*27*). Continued monitoring of Southeast Greenland bears will be critical to understand how the species will be affected by, and respond to, anthropogenic climate warming.

REFERENCES AND NOTES

1. H.-O. Pörtner *et al.*, Eds., "IPCC Special Report on the Ocean and Cryosphere in a Changing Climate" (Intergovernmental Panel on Climate Change, 2019); https://www.ipcc.ch/srocc/.
2. G. T. Pecl *et al.*, *Science* **355**, eaai9214 (2017).
3. S. A. Levin, *Ecology* **73**, 1943–1967 (1992).
4. D. E. Schindler *et al.*, *Nature* **465**, 609–612 (2010).
5. E. V. Regehr *et al.*, *Biol. Lett.* **12**, 20160556 (2016).
6. S. N. Maduna *et al.*, *Proc. Biol. Sci.* **288**, 20211741 (2021).
7. P. K. Molnár *et al.*, *Nat. Clim. Chang.* **10**, 732–738 (2020).
8. E. W. Born, Ø. Wiig, J. Thomassen, *J. Mar. Syst.* **10**, 67–77 (1997).
9. Ø. Wiig *et al.*, *Polar Biol.* **42**, 461–474 (2018).
10. Materials and methods are available as supplementary materials.
11. G. M. Durner, K. L. Laidre, G. S. York, Eds., *Polar Bears: Proceedings of the 18th Working Meeting of the IUCN/SSC Polar Bear Specialist Group, 7 to 11 June 2016, Anchorage, Alaska* (IUCN, 2018).
12. D. A. Sutherland, R. S. Pickart, *Prog. Oceanogr.* **78**, 58–77 (2008).
13. N. P. Foukal, R. Gelderloos, R. S. Pickart, *Sci. Adv.* **6**, eabc4254 (2020).
14. D. Paetkau *et al.*, *Mol. Ecol.* **8**, 1571–1584 (1999).
15. E. Peacock *et al.*, *PLOS ONE* **10**, e112021 (2015).
16. R. M. Malenfant, C. S. Davis, C. I. Cullingham, D. W. Coltman, *PLOS ONE* **11**, e0148967 (2016).
17. E. V. Regehr, R. R. Wilson, K. D. Rode, M. C. Runge, H. L. Stern, *J. Appl. Ecol.* **54**, 1534–1543 (2017).
18. K. D. Rode *et al.*, *PLOS ONE* **15**, e0237444 (2020).
19. A. E. Derocher, Ø. Wiig, *J. Zool.* **256**, 343–349 (2002).
20. P. K. Molnár, A. E. Derocher, M. A. Lewis, M. K. Taylor, *Proc. Biol. Sci.* **275**, 217–226 (2008).
21. F. Jónsson, *Det gamle Grønlands beskrivelse af Ívar Bárðarson* (Levin and Munksgaard, 1930).
22. W. A. Graah, *Narrative of an Expedition to the East Coast of Greenland, Sent by Order of the King of Denmark, in Search of the Lost Colonies, Under the Command of Captn. W. A. Graah* (J. W. Parker, 1837).
23. H. T. Sandell, B. Sandell, E. W. Born, R. Dietz, C. Sonne-Hansen, "Isbjørne i Østgrønland. En interviewundersøgelse om forekomst og fangst, 1999" (Teknisk rapport nr. 40, Pinngortitaleriffik, Grønlands Naturinstitut, Nuuk., 2001); https://natur.gl/forskning/rapporter/.
24. K. L. Laidre, A. D. Northey, F. Ugarte, *Front. Mar. Sci.* **5**, 135 (2018).
25. C. D. Hamilton, K. M. Kovacs, R. A. Ims, J. Aars, C. Lydersen, *J. Anim. Ecol.* **86**, 1054–1064 (2017).
26. G. W. K. Moore, A. Schweiger, J. Zhang, M. Steele, *Geophys. Res. Lett.* **46**, 11,237–11,243 (2019).
27. T. A. Moon, A. S. Gardner, B. Csatho, I. Parmuzin, M. A. Fahnestock, *J. Geophys. Res. Earth Surf.* **125**, (2020).
28. K. L. Laidre *et al.*, Glacial ice supports a distinct and undocumented polar bear subpopulation persisting in late 21st-century sea-ice conditions, Dryad (2022); https://doi.org/10.5061/dryad.9zw3r22h3.

ACKNOWLEDGMENTS

We thank the crews of RV *Polarstern*, MV *Nordsyssel*, RV *Lance*, Air Greenland, TeleGreenland, Prins Christians Sund weather station, Danmarkshavn weather station, the Villum Research Station, and the Danish military at Station Nord. Indigenous subsistence hunters from East Greenland provided local knowledge and samples from the subsistence catch. We thank J. Estes for fruitful discussions and M. C. Ngô and R. Guldborg Hansen for assistance with samples. The Norwegian Polar Institute and the Institute of Marine Research assisted during fieldwork in 2007 and 2008. The fieldwork in 1993 and 1994 was made possible by logistical support from Alfred Wegener Marine Research Institute. Three anonymous reviewers provided helpful comments and constructive criticism. **Funding:** This work was supported by the Environmental Protection Agency (Ministry of Environment and Food of Denmark), DANCEA Programme (E.W.B., K.L.L., and R.D.); Danish Ministry of the Environment under Miljøstøtte til Arktis, the Northeast Greenland Environmental Study Program (E.W.B. and K.L.L.); Greenland Bureau of Mineral and Petroleum (F.U.); Commission for Scientific Research in Greenland (E.W.B., F.U., and K.L.L.); Greenland Institute of Natural Resources (F.U., E.W.B., and K.L.L.); University of Oslo (Ø.W.); University of Washington (K.L.L. and E.V.R.); Leo Model Foundation (K.L.L.); Vetlesen Foundation (K.L.L.); NASA Biological Diversity and Ecological Forecasting Programs and Cryospheric Sciences (NNX11AO63G, NNX13AN28G, and 80NSSC18K1229) (K.L.L., H.L.S., and T.M.);

US National Science Foundation (NSF) DEB-1754451 (B.S.). **Author contributions:** Conceptualization: K.L.L. and E.W.B. Funding acquisition: K.L.L., E.W.B, and F.U. Fieldwork: K.L.L., E.W.B., E.V.R., Ø.W., J.A., F.U., R.D., C.S., P.H., C.I., and G.B.A. Laboratory work: M.A.S., C.V., R.C.-D., and B.S. Data analysis: K.L.L., M.A.S., E.V.R., B.C., H.L.S., D.P., C.V., R.C.-D., and B.S. Interpretation of results: K.L.L., M.A.S., E.V.R., and B.S., with input from E.W.B., Ø.W., F.U., J.A., H.L.S., and T.M. Writing – original draft: K.L.L., M.A.S., and B.S. Writing – review & editing: all authors. **Competing interests:** The authors declare that they have no competing interests. **Data and materials availability:** Detailed lists of samples are provided in the supplementary materials. Microsatellite genotypes are available in Dryad (*28*). Genomic data are available at NCBI under BioProject ID PRJNA669153. **License information:** Copyright © 2022 the authors, some rights reserved; exclusive licensee American Association for the Advancement of Science. No claim to original US government works. https://www.science.org/about/science-licenses-journal-article-reuse

SUPPLEMENTARY MATERIALS

science.org/doi/10.1126/science.abk2793
Materials and Methods
Figs. S1 to S26
Tables S1 to S11
References (*29*–*146*)

Submitted 2 July 2021; accepted 29 April 2022
10.1126/science.abk2793

MOLECULAR BIOLOGY

Structure of the mammalian ribosome as it decodes the selenocysteine UGA codon

Tarek Hilal[1]*†, Benjamin Y. Killam[2], Milica Grozdanović[2]‡, Malgorzata Dobosz-Bartoszek[2]§, Justus Loerke[1], Jörg Bürger[1,3], Thorsten Mielke[3], Paul R. Copeland[4], Miljan Simonović[2]*¶, Christian M. T. Spahn[1]*

The elongation of eukaryotic selenoproteins relies on a poorly understood process of interpreting in-frame UGA stop codons as selenocysteine (Sec). We used cryo-electron microscopy to visualize Sec UGA recoding in mammals. A complex between the noncoding Sec-insertion sequence (SECIS), SECIS-binding protein 2 (SBP2), and 40*S* ribosomal subunit enables Sec-specific elongation factor eEFSec to deliver Sec. eEFSec and SBP2 do not interact directly but rather deploy their carboxyl-terminal domains to engage with the opposite ends of the SECIS. By using its Lys-rich and carboxyl-terminal segments, the ribosomal protein eS31 simultaneously interacts with Sec-specific transfer RNA ($tRNA^{Sec}$) and SBP2, which further stabilizes the assembly. eEFSec is indiscriminate toward L-serine and facilitates its misincorporation at Sec UGA codons. Our results support a fundamentally distinct mechanism of Sec UGA recoding in eukaryotes from that in bacteria.

Translating ribosomes pause at stop codons—UAA, UAG, and UGA—which allows a protein release factor (RF) to bind and terminate protein synthesis. In a subset of mRNAs from most organisms across all domains of life, in-frame UGA codons recruit selenocysteinyl-tRNA (Sec-$tRNA^{Sec}$) to facilitate the stop-to-Sec recoding. The recoding leads to the synthesis of selenoproteins, which are required for a myriad of functions, notably the maintenance of redox and thyroid hormone homeostasis and protection of the cell membrane and DNA from oxidative damage (*1*). An embryonically lethal phenotype of the mouse mutant in which $tRNA^{Sec}$ was deleted (*2*) and systematic analyses of genetic rodent models of selenoprotein deficiency (*3*, *4*) demonstrate that selenoproteins are essential for vertebrate survival. Selenoprotein deficiency and mutations in selenoproteins cause systemic, often lethal diseases in humans (*5*). Despite the biological importance, the mechanism of Sec UGA recoding in eukaryotes is not well understood.

Stop-to-Sec recoding relies on a Sec-insertion sequence (SECIS) in the selenoprotein mRNA and a Sec-specific elongation factor—SelB in prokaryotes and eEFSec in eukaryotes. Although the bacterial SECIS follows Sec UGA within the open reading frame, the phylogenetically unrelated eukaryotic SECIS is in the 3′-untranslated region (3′-UTR). Prokaryotic SelB facilitates recoding on its own, but eEFSec requires a eukaryote-specific protein factor, SECIS-binding protein 2 (SBP2). Despite some conservation, the prokaryotic mechanism (*6*) cannot be extrapolated to eukaryotes (*7*). This raises questions about the architecture of the eukaryotic UGA recoding assembly (the "selenosome"), the role of SECIS and SBP2, and the molecular choreography that governs discrete steps of the process. To address these questions, we reconstituted human eEFSec, SBP2, and Ser-$tRNA^{Sec}$ on mammalian 80*S* ribosomes that were programmed with an mRNA containing an authentic SECIS element. Using cryo–electron microscopy (cryo-EM), we visualized the early steps of Sec UGA recoding in higher eukaryotes, providing a structural basis for the distinct mechanism of selenoprotein elongation.

To produce a stable complex and position the UGA codon in the ribosomal decoding center (DC), we used a chimeric mRNA construct that harbored a cricket paralysis virus (CrPV) internal ribosome entry site (IRES) on its 5′ end (*8*). Sec UGA, the first coding triplet, is followed by ~900 nucleotides (nt) of firefly luciferase coding region and the 3′-UTR of rat glutathione peroxidase 4 (Gpx4) that contains the SECIS. We combined the chimeric mRNA, purified rabbit ribosomal subunits, and the functional C-terminal half of human SBP2 (residues 409–854), which is composed of a Sec-insertion domain (SID) and an RNA-binding domain (RBD) (Fig. 1A). Concurrently, we assembled a ternary complex of the guanosine triphosphatase (GTPase)–defective His^{96}→Ala mutant of eEFSec (eEFSec-H96A), Ser-$tRNA^{Sec}$, and guanosine 5′-triphosphate (GTP). We chose eEFSec-H96A to avoid complex disassembly from GTP hydrolysis and Ser-$tRNA^{Sec}$ because of its similarity with Sec-$tRNA^{Sec}$. In the end, programmed ribosomes and ternary complex were assembled into the recoding complex immediately before vitrification (Fig. 1A).

From 13,921 selected micrographs, a total of 1,685,923 particle images were extracted and analyzed by means of multiparticle refinement (figs. S1 to S3 and table S1). A subpopulation of 77,142 particle images that corresponded to the intact selenosome yielded a reconstruction of 2.8 Å resolution (Fig. 1 and figs. S1 and S2). All recoding factors form an extended network of interactions (Fig. 1, B to E). The density for SECIS, a member of the kink-turn family of RNA structural motifs, is well resolved and is adjacent to the beak domain of the 40*S*. Near the SECIS core, densities for a segment of the SID and the entire RBD of SBP2 are readily visible (Figs. 1E and 2A). The opposite end of the SECIS contacts the C-terminal domain 4 (D4) of eEFSec, whereas D1, D2, and D3 reside at the GTPase-associated center (GAC). The acceptor and variable arms of Ser-$tRNA^{Sec}$ are bound to eEFSec (Fig. 2A), and the anticodon loop is properly positioned in the A site of the DC, which suggests that we captured the preaccommodated state of the selenosome with the $tRNA^{Sec}$ in the A/T conformation (fig. S4). The long mRNA segment that connects UGA and the SECIS is partially disordered and could not be modeled. The CrPV IRES is in the translocated state (*8*), which points away from the DC and rests against ES30L of the L1 stalk in the 60*S* (Fig. 1, C and D). We did not observe any interactions between the CrPV IRES and eEFSec, SBP2, Ser-$tRNA^{Sec}$, or the SECIS element. The absence of such interactions and the general similarity of our visualized recoding complex to canonical mammalian decoding complexes (*9*, *10*) suggest its physiological relevance.

Our reconstruction revealed the structure of the eEFSec•GTP•Ser-$tRNA^{Sec}$ complex (Figs. 1E and 2A). eEFSec-H96A resembles crystal structures of wild-type (WT) eEFSec (*11*) and archaeal SelB (*12*) (fig. S5A). When compared with the bacterial SelB, the structural conservation is preserved in D1, D2, and D3 but absent in D4 (fig. S5B). GTP is bound to the GTPase pocket in D1, but the side chains of switch 2 are disordered, which confirms the catalytically incompetent conformation of eEFSec-H96A (fig. S6A). D1 and D2 are sandwiched between H95 and uL14 of the 60*S* and h5 and h14 of the 40*S* (Fig. 2B), whereas D4 is wedged between the apical loop of SECIS and h33 of the 40*S* (Fig. 2D). The CCA end of $tRNA^{Sec}$ positions the Ser group into the proposed Sec-binding pocket. Highly conserved

[1]Institut für Medizinische Physik und Biophysik, Charité-Universitätsmedizin Berlin, 10117 Berlin, Germany. [2]Department of Biochemistry and Molecular Genetics, University of Illinois at Chicago, Chicago, IL 60607, USA. [3]Max-Planck Institut für Molekulare Genetik, 14195 Berlin, Germany. [4]Department of Biochemistry and Molecular Biology, Rutgers-Robert Wood Johnson Medical School, Piscataway, NJ 08854, USA.
*Corresponding author. Email: tarek.hilal@fu-berlin.de (T.H.); miljan.simonovic@nih.gov (M.S); christian.spahn@charite.de (C.M.T.S)
†Present address: Research Center of Electron Microscopy and Core Facility BioSupraMol, Institute of Chemistry and Biochemistry, Freie Universität Berlin, Berlin, Germany. ‡Present address: Vaccines Analytical Development, Merck & Co., Inc., West Point, PA 19486, USA. §Present address: Cytiva, Marlborough, MA 01752, USA. ¶Present address: National Institute of General Medical Sciences, National Institutes of Health, Bethesda, MD 20892, USA.

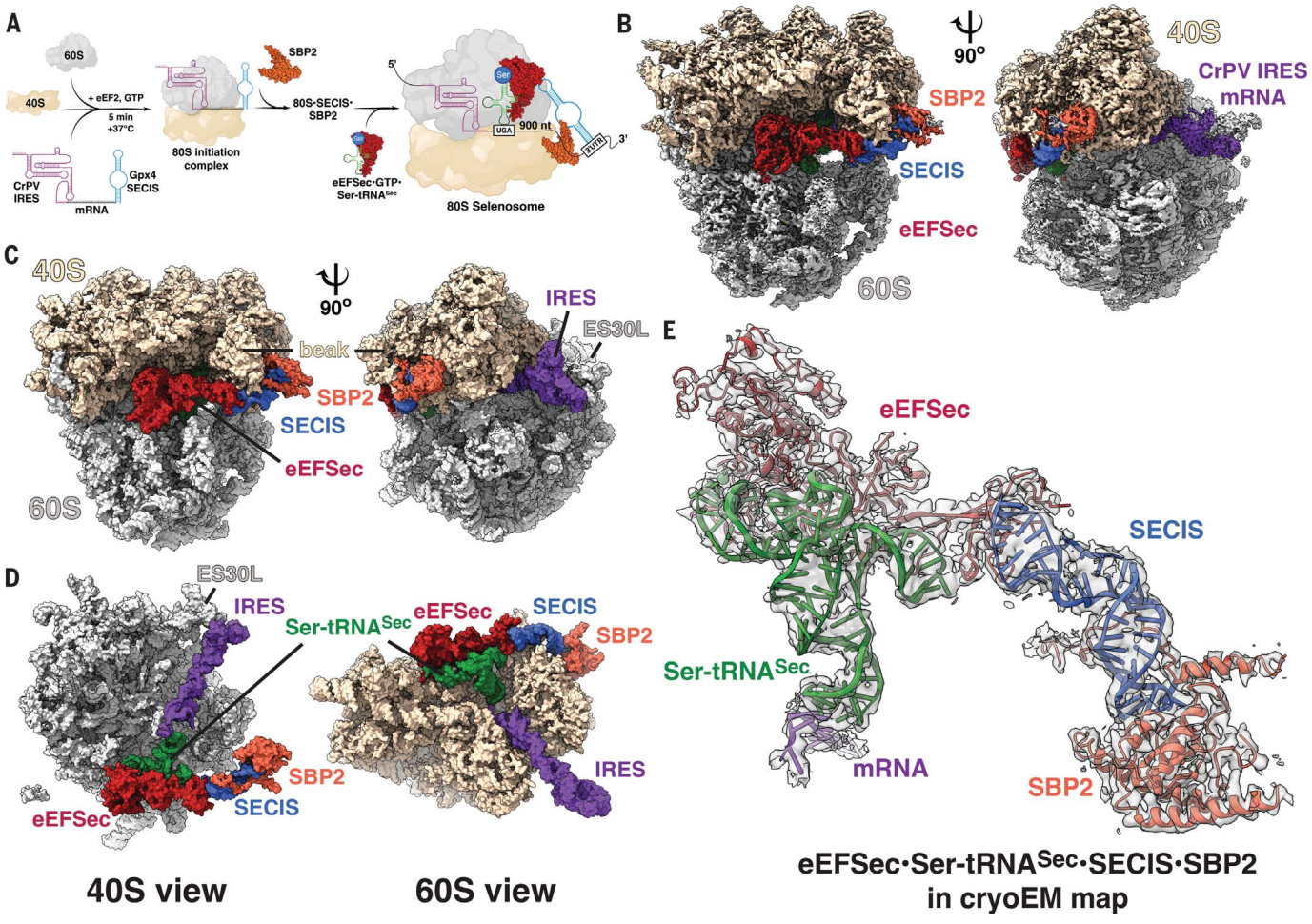

Fig. 1. The mammalian Sec UGA recoding assembly. (**A**) Reconstitution of complexes used in this study. (**B**) Three dimensional (3D) reconstruction of the assembly shown in two views related by ~90° clockwise rotation around the vertical axis. (**C**) The same views of the final model shown as a surface diagram. (**D**) The recoding complex as seen from the vantage points of the 40*S* (left) and 60*S* (right) subunits. (**E**) 3D map covering the eEFSec•GTP•Ser-tRNA^{Sec}•SECIS•SBP2 complex (cartoon). 60*S* is gray, 40*S* is sand, eEFSec•GTP is dark red, Ser-tRNA^{Sec} is dark green, SECIS is blue, SBP2 is dark orange, and the mRNA harboring CrPV IRES is purple.

Ser^{269}, Gln^{271}, and His^{274} surround Ala^{76} (fig. S7), and H-bonds with Gln^{237} lock its nucleobase in place (Fig. 2C). Phe^{273} and Arg^{285} cap the Sec-binding pocket, with Arg^{285} stabilizing the pocket through interactions with Thr^{242}. This explains the loss of function in Arg^{285}→Ala (R285A) and Arg^{285}→Asn (R285N) mutants (*11*). The hydroxyl of Thr^{242} is ~3.7 Å from the hydroxyl of Ser on Ser-tRNA^{Sec} (Fig. 2C), which suggests its importance for amino-acid selection. When accounting for the longer C-Se bond, the Se atom of Sec would be at the optimal distance of ~2.6 to 3.2 Å from Thr^{242}. Last, the eukaryote-specific loop β24–β25 (residues 522–524) in D4 of eEFSec forms an interface with the backbone of the AAR motif of SECIS (residues 1128–1130) and h33 (residues 1305–1308) of the 40*S* subunit (Fig. 2, D and E). Using a well-established Sec UGA readthrough reporter assay (Fig. 2F) (*13*), we show that eEFSec promotes recoding in an SBP2- and SECIS-dependent manner in the presence of Ser-tRNA^{Sec} but not Ser-tRNA^{Ser} (Fig. 2G). Also, replacing Thr^{242} with either Val (T242V) or Leu (T242L) and Phe^{522} and Gln^{524} with Gly (F522G and Q524G) causes impairment of the readthrough activity (Fig. 2H). Taken together, our results argue that Thr^{242} is a key selectivity residue in human eEFSec. Also, just as Cys is misincorporated at Sec UGA in TXNRD1 under low Se levels (*14*), the same may occur with Ser. However, it remains to be seen whether Ser misinsertion occurs in vivo and whether selenoenzyme activity is affected.

Human eEFSec uses all its domains to engage the tRNA^{Sec} (fig. S6, center). D1, D2, and D3 bind to the acceptor-TΨC arm (fig. S6, B and C), whereas the D3–D4 linker and D4 contact the variable stem and loop (fig. S6, D and E). The side chain of Glu^{299} establishes the tRNA^{Sec} identity through H-bonds with the Watson-Crick face of the Gly^{73} recognition base (fig. S6B). Arg^{432} and Asp^{434} from loop β19–β20 of D3 contact the minor groove of the TΨC arm (fig. S6C). The D3–D4 linker runs parallel to the variable arm where Lys^{471} interacts with a nonbridging oxygen between G47a and U47b (fig. S6D), and the variable loop is lodged against loop β22–α12 (residues 495–499) of D4 (fig. S6E). These interactions explain why mutations in and deletion of D4 had detrimental effects on eEFSec activity and selenoprotein synthesis (*15*). Although they share a conserved biological role, the eukaryotic selenosome is distinct from the bacterial one (fig. S8A), which suggests divergent UGA recoding mechanisms. In particular, the C-terminal D4 of eEFSec interacts with the variable arm of tRNA^{Sec} and

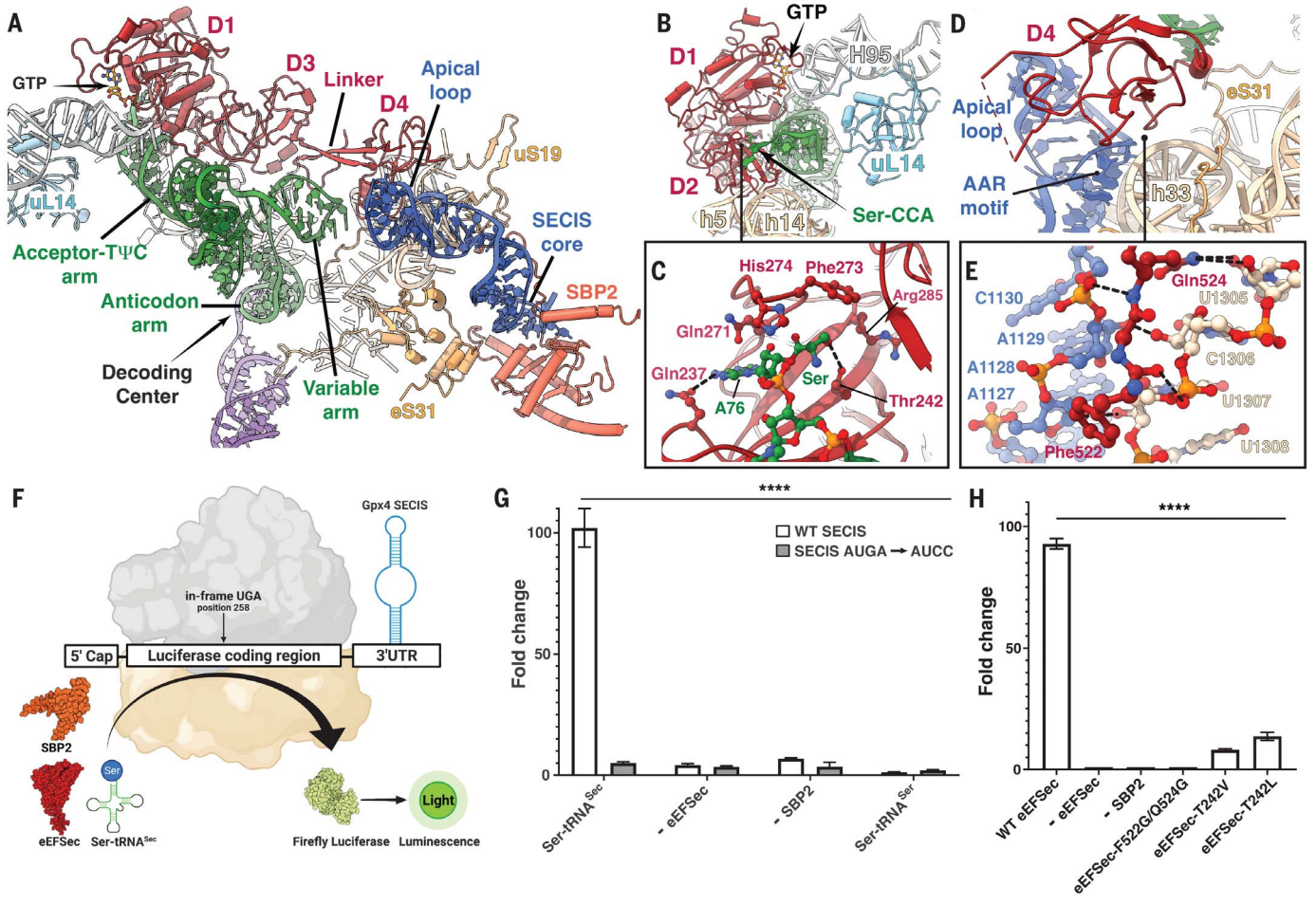

Fig. 2. Human eEFSec•GTP•Ser-tRNA^{Sec} on the 80*S* ribosome. (**A**) Side view of the eEFSec complex (cartoon) as bound to the 80*S*. (**B**) D1 and D2 of eEFSec rest against H95 of the 60*S* and h5 and h14 of the 40*S*. The Ser-CCA is bound to the Sec-binding pocket. The view is rotated 90° counterclockwise around the vertical axis relative to (A). (**C**) Close-up view of the Sec-binding pocket with Ser, Ala^{76}, and residues of the Sec-binding site shown as stick-and-ball. Dashed lines indicate H-bonds. (**D**) D4 of eEFSec is between the AAR motif of SECIS and h33 of the 40*S*. The view is rotated 90° clockwise around the vertical axis relative to (A). (**E**) Close-up view of the interface between AAR motif, h33, and D4. (**F**) The Sec UGA readthrough assay based on the luciferase reporter. (**G**) Ser-tRNA^{Sec}, but not Ser-tRNA^{Ser}, supports the SBP2-SECIS–dependent Sec UGA readthrough. Activity levels are presented as fold change over the control sample. White and gray bars correspond to WT and AUCC mutant SECIS, respectively. (**H**) T242L, T242V, and F522G/Q524G mutants lost the readthrough activity.

points away from the mRNA channel (fig. S8, A and B), whereas the bacterial D4 is rotated ~90° around the linker, does not interact with the variable arm, and binds near the mRNA entry channel (fig. S8C) (*6*).

The mammalian SECIS, which is derived from the 3′-UTR of Gpx4 (Fig. 3A), adopts a Form II structure that is characterized by two nearly coaxial stems that connect the GA quartet and AUGA bulge on one end and two loops and the essential AAR motif on the opposite, apical end (Fig. 2G). The basal stem, or helix I, is disordered in our map. The AUGA bulge, or the SECIS core, folds into a kink-turn motif, which serves as the SBP2-binding site (Fig. 3, A and B). Sitting atop Leu^{707}, U1112 forms H-bonds with the invariant Arg^{731} of SBP2, which suggests its relevance for complex formation (Fig. 3C). The rest of the bulge is structurally important, as illustrated by the inability of the AUGA→AUCC mutant to support recoding (Fig. 2G). On the opposite end are the apical stem, the apical loop, and the AAR motif, which is characterized by three unpaired adenosines (Fig. 3A). Replacing unpaired AAA with AUG hinders recoding (*16*), but the absence of sequence-specific interactions with the AAR motif may rationalize why some SECIS elements carry the CCR motif instead (*17*). Nonetheless, our structure uncovered insights about SECIS, a noncoding RNA element that regulates selenoprotein synthesis in higher organisms.

We modeled the N-terminal segment of the SID (residues 429–475) and RBD (residues 625–780) of SBP2 (Fig. 3B). Residues 429–437 fold into a fishhook-like structure that anchors against h33 of the 18*S* ribosomal RNA (rRNA). The subsequent segment (residues 441–446) forms a parallel β-strand that leans against the C terminus of eS31, which effectively expands the β sheet of the zinc-finger motif of this ribosomal protein (Fig. 3B). With its Lys-rich motif, eS31 reaches the anticodon arm of tRNA^{Sec} (fig. S9), but the 84 N-terminal residues are disordered, which allows expansion of the A site and accommodation of an enlarged tRNA^{Sec} variable arm. Residues 448–455 of the SID run along the major groove of SECIS (Fig. 3B) without establishing sequence-specific contacts. The SID in our structure ends with an α helix (residues 456–475), which is almost perpendicular to helix II of SECIS and is near the β1–α3 loop (^{701}IQSKG^{705}) of the RBD (Fig. 3B). The ribosomal protein uS19 binds to the opposite side of helix II, which further stabilizes the complex (Fig. 3B). Using

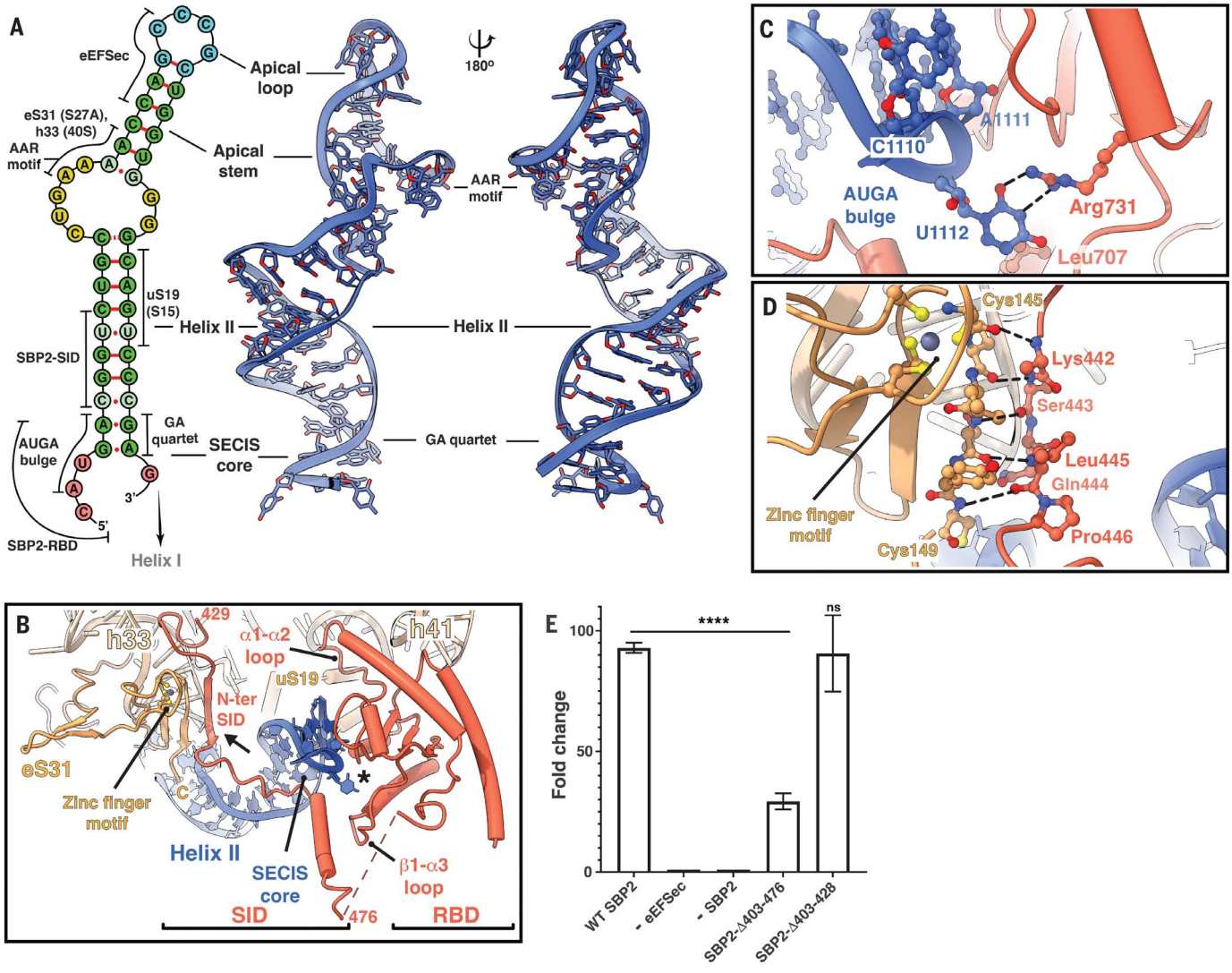

Fig. 3. Human SBP2•SECIS captured on the translating ribosome. (**A**) Secondary structure diagram (left) and two views of the 3D structure of the Form II Gpx4 SECIS (right). Major interactions are marked; base pairs are green; and loops are pink, yellow, and light blue. Solid red lines indicate Watson-Crick base pairs, dashed lines are non–Watson-Crick pairs, and red dots are wobble pairs. Color coding is the same as in Fig. 1. (**B**) RBD binds to the SECIS core (asterisk). The SID interacts with the zinc finger of eS31 (arrow). Contacts between helix II of the SECIS and uS19 and eS31 stabilize the complex. (**C**) Close-up view of interactions between Arg^{731} of RBD and U1112 of SECIS. (**D**) N-terminal segment of SID (residues 442–446) forms a parallel β-strand to the C terminus of eS31. (**E**) Only deletion of residues 403–476 from SBP2 (Δ403-476) abolishes Sec UGA readthrough activity.

luciferase reporter assay (Fig. 2F), we show that SBP2 that lacks residues 403–428 (SBP2-Δ428), but not 403–476 (SBP2-Δ476), supports Sec UGA readthrough (Fig. 3E). This suggests that residues 429–476 of the SID are important for binding of SBP2 to the ribosome and explains why mutations in the same region of rat SBP2 substantially diminished Sec incorporation efficiency (*18*, *19*). Furthermore, RBD of SBP2 adopts an L7Ae protein fold and binds to the conserved kink-turn motif of the SECIS. The RBD is locked in place through interactions of conserved ^{654}RFQDR^{658}, ^{663}DPVKA^{667}, and ^{680}VLKHLKL^{686} motifs (fig. S10) with ribosomal protein uS19 and h41 of the 40*S* (Fig. 3B). This illuminates why mutations in these motifs hindered ribosome binding and Sec incorporation activity, but not SECIS binding (*19*). Last, we rationalize effects of the disease-associated missense mutations Glu^{679}→Asp (E679D) and Cys^{691}→Arg (C691R) (fig. S11A) (*20*, *21*). Although the effects of E679D are neutral, C691R probably compromises SBP2 structure because of steric clashes of Arg^{691} with Ile^{693}, Pro^{724}, Val^{726}, Ile^{749}, Phe^{759}, and Met^{762} (fig. S11, B and C).

We investigated whether binding to the 80*S* of SBP2•SECIS alone could poise the ribosome for Sec UGA recoding. To this end, we determined the structure of the 80*S*•SBP2•SECIS complex at 3.1 Å resolution (Fig. 4A and fig. S3). We found that SBP2 and SECIS are bound to the beak of the 40*S* in the same manner as in the preaccommodated state structure of the complete selenosome (Fig. 4A). The mRNA follows a similar trajectory, which suggests that its conformation is independent from the eEFSec ternary complex binding and the recoding step itself. We thus conclude that the SBP2• SECIS binding to 80*S* is a prerequisite for the eEFSec•GTP•Sec-$tRNA^{Sec}$ ternary complex anchoring, which is consistent with the observation that the eukaryotic SECIS promotes Sec incorporation in cis when placed >55 nt downstream of the Sec codon (*22*). Last, SBP2•SECIS is not found in a position to prevent translation termination, which explains why RFs terminate selenoprotein

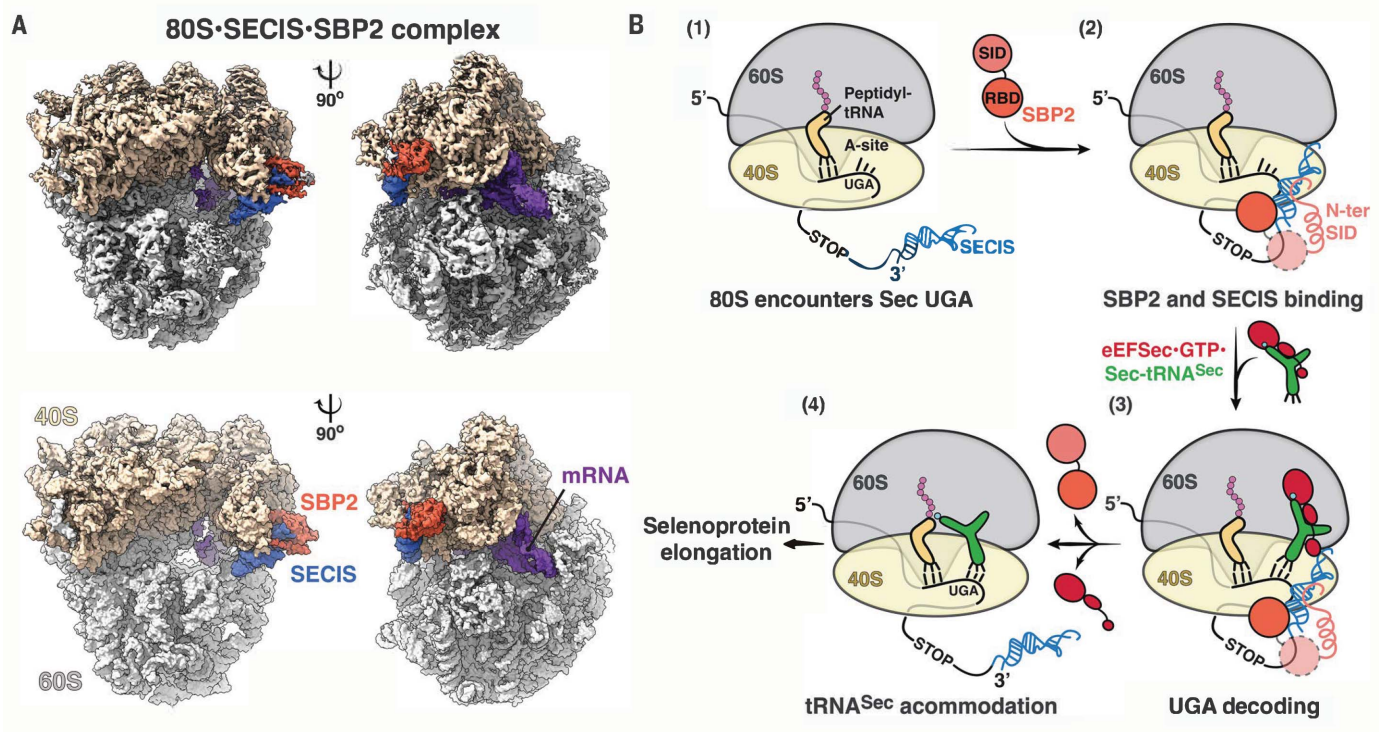

Fig. 4. Eukaryotic selenoprotein elongation at Sec UGA codons. (**A**) Cryo-EM map (top) and surface diagram (bottom) of 80S•SECIS•SBP2. (**B**) Proposed mechanism of Sec UGA recoding in eukaryotes. (1) 80*S* stalls at an in-frame UGA codon. (2) The RBD binds to the apical loop of SECIS, the mRNA folds over, SBP2•SECIS binds to the 40*S*, and the N terminus of the SID contacts eS31. This step could occur before ribosome stalling. (3) eEFSec•GTP delivers Sec-tRNA^{Sec} to the 80*S* and adopts a preaccommodated state conformation. (4) After GTP hydrolysis, eEFSec dissociates from the assembly, Sec-tRNA^{Sec} accommodates, and peptide bond synthesis and selenoprotein elongation occur. Steps 2 and 3 are visualized in this work.

synthesis at UGA codons when Sec insertion fails (*23*, *24*).

Although we cannot rule out that IRES and Ser-tRNA^{Sec} may have imposed kinetic and conformational constraints on programmed ribosomes, our structures allowed visualization of the long-sought early steps of selenoprotein elongation at Sec UGA codons in eukaryotes, leading to a revised model of the process (Fig. 4B). During translation of selenoprotein mRNAs, the SBP2•SECIS complex binds to the head domain of the 40*S* subunit. The RBD of SBP2 binds to the SECIS base, whereas the N-terminal part of the SID latches onto the 40*S* through contacts with the rRNA and eS31. The prebound SBP2•SECIS forms a docking site on the stalled ribosome for eEFSec•GTP•Sec-tRNA^{Sec} (Fig. 4B). The EF-Tu–like domain of eEFSec binds to the GAC, and D4 binds to the apical loop of the SECIS, opposite from the RBD. eEFSec clasps the A/T conformation of Sec-tRNA^{Sec} with the variable arm contacting the Lys-rich domain of eS31, which completes the preaccommodated state of the selenosome. Subsequent events remain unclear, which warrants detailed structural analyses. After adopting the GTPase activated state, the CCA end of Sec-tRNA^{Sec} is liberated from eEFSec. eEFSec dissociates from the ribosome, which leads to the departure of SECIS and SBP2. Sec-tRNA^{Sec} accommodates, and the peptide bond forms between an incoming Sec and the P-site peptidyl-tRNA, which ultimately completes the elongation step of a nascent selenoprotein at the UGA codon.

REFERENCES AND NOTES

1. Y. Zhang *et al.*, *Antioxidants* **9**, 383 (2020).
2. M. R. Bösl, K. Takaku, M. Oshima, S. Nishimura, M. M. Taketo, *Proc. Natl. Acad. Sci. U.S.A.* **94**, 5531–5534 (1997).
3. M. V. Kasaikina, D. L. Hatfield, V. N. Gladyshev, *Biochim. Biophys. Acta* **1823**, 1633–1642 (2012).
4. G. K. Sarangi, L. R. White, S. Castellano, *eLS* 10.1002/9780470015902.a0026518 (2017).
5. U. Schweizer, N. Fradejas-Villar, *FASEB J.* **30**, 3669–3681 (2016).
6. N. Fischer *et al.*, *Nature* **540**, 80–85 (2016).
7. J. N. Gonzalez-Flores, S. P. Shetty, A. Dubey, P. R. Copeland, *Biomol. Concepts* **4**, 349–365 (2013).
8. M. Muhs *et al.*, *Mol. Cell* **57**, 422–432 (2015).
9. T. V. Budkevich *et al.*, *Cell* **158**, 121–131 (2014).
10. S. Shao *et al.*, *Cell* **167**, 1229–1240.e15 (2016).
11. M. Dobosz-Bartoszek *et al.*, *Nat. Commun.* **7**, 12941 (2016).
12. M. Leibundgut, C. Frick, M. Thanbichler, A. Böck, N. Ban, *EMBO J.* **24**, 11–22 (2005).
13. N. Gupta, L. W. DeMong, S. Banda, P. R. Copeland, *J. Mol. Biol.* **425**, 2415–2422 (2013).
14. X. M. Xu *et al.*, *Proc. Natl. Acad. Sci. U.S.A.* **107**, 21430–21434 (2010).
15. J. N. Gonzalez-Flores, N. Gupta, L. W. DeMong, P. R. Copeland, *J. Biol. Chem.* **287**, 38936–38945 (2012).
16. M. J. Berry, L. Banu, J. W. Harney, P. R. Larsen, *EMBO J.* **12**, 3315–3322 (1993).
17. K. V. Korotkov, S. V. Novoselov, D. L. Hatfield, V. N. Gladyshev, *Mol. Cell. Biol.* **22**, 1402–1411 (2002).
18. J. Donovan, K. Caban, R. Ranaweera, J. N. Gonzalez-Flores, P. R. Copeland, *J. Biol. Chem.* **283**, 35129–35139 (2008).
19. K. Caban, S. A. Kinzy, P. R. Copeland, *Mol. Cell. Biol.* **27**, 6350–6360 (2007).
20. E. Schoenmakers *et al.*, *J. Clin. Invest.* **120**, 4220–4235 (2010).
21. J. Fu *et al.*, *J. Clin. Endocrinol. Metab.* **105**, e6–e11 (2020).
22. G. W. MartinIII, J. W. Harney, M. J. Berry, *RNA* **2**, 171–182 (1996).
23. A. Mehta, C. M. Rebsch, S. A. Kinzy, J. E. Fletcher, P. R. Copeland, *J. Biol. Chem.* **279**, 37852–37859 (2004).
24. S. B. Kotini, F. Peske, M. V. Rodnina, *Nucleic Acids Res.* **43**, 6426–6438 (2015).

ACKNOWLEDGMENTS

The authors thank H. Seibel for assistance with cloning. We acknowledge access to electron microscopic equipment and computational resources at the Core Facility for cryo–Electron Microscopy (CFcryoEM) of the Charité–Universitätsmedizin Berlin and the Core Facility BioSupraMol of Freie Universität Berlin. The authors thank T. Sprink for acquisition of the 80S-Selonosome dataset. **Funding:** This work was supported by grants from Deutsche Forschungsgemeinschaft (SFB740 and FOR1805 to C.M.T.S.), Deutsche Forschungsgemeinschaft and the state of Berlin for large equipment according to Article 91b GG (INST 335/588-1 FUGG, INST 335/589-1 FUGG, INST 335/590- 1 FUGG) and the Berlin University Alliance, National Institutes of Health (NIGMS GM097042 to M.S. and GM077073 to P.R.C. and M.S.), ACS-IL (225752 to M.S.), UIC Center for Clinical and Translational Sciences (to M.D.B.), and North-German Supercomputing Alliance (to T.H.). USCF Chimera X was developed by the Resource for Biocomputing, Visualization and Informatics at the University of California, San Francisco, with support from NIH (GM129325) and the Office of Cyber Infrastructure and Computational Biology, National Institute of Allergy, and Infectious Diseases. **Author contributions:** T.H., C.M.T.S., P.R.C., and M.S. conceived the

project; T.H., M.G., and M.D.-B. prepared the components of the complex; B.Y.K. prepared mutants and performed readthrough assays; T.H. reconstituted complexes and prepared cryo-EM samples; J.B. helped with grid preparation and screening of cryoEM samples; J.B. and T.M. imaged the 80S•SECIS•SBP2 sample; T.H. carried out cryo-EM data analysis and three-dimensional (3D) reconstruction; T.H. and M.S. built and refined atomic models; and C.M.T.S., T.M., P.R.C., and M.S. provided overall guidance during the project. All authors contributed to the experimental design and wrote the manuscript. **Competing interests:** The authors declare no competing interests. **Data and materials availability:** All data are available in the main text or the supplementary materials. Coordinates and electron density maps are deposited in the Protein Data Bank and Electron Microscopy Data Bank with the following accession numbers: 7ZJW and EMD-14751 for the 80*S*-selenosome structure and 7ZJX and EMD-14752 for the 80S•SBP2•SECIS complex structure. **Disclaimer:** This article was prepared while M.S. was employed at the University of Illinois at Chicago. The opinions expressed in this article are the author's own and do not reflect the view of the National Institutes of Health, the Department of Health and Human Services, or the United States government. **License information:** Copyright © 2022 the authors, some rights reserved; exclusive licensee American Association for the Advancement of Science. No claim to original US government works. https://www.science.org/about/science-licenses-journal-article-reuse

SUPPLEMENTARY MATERIALS

science.org/doi/10.1126/science.abg3875
Materials and Methods
Figs. S1 to S11
Table S1
References (*25*–*45*)
MDAR Reproducibility Checklist

View/request a protocol for this paper from *Bio-protocol*.

Submitted 2 January 2021; resubmitted 4 February 2022
Accepted 10 May 2022
10.1126/science.abg3875

HEART REPAIR

Meteorin-like promotes heart repair through endothelial KIT receptor tyrosine kinase

Marc R. Reboll[1,2], Stefanie Klede[1,2], Manuel H. Taft[3], Chen-Leng Cai[4], Loren J. Field[5], Kory J. Lavine[6], Andrew L. Koenig[6], Jenni Fleischauer[7], Johann Meyer[7], Axel Schambach[7], Hans W. Niessen[8], Maike Kosanke[9], Joop van den Heuvel[10], Andreas Pich[11], Johann Bauersachs[2], Xuekun Wu[1,2], Linqun Zheng[1,2], Yong Wang[1,2], Mortimer Korf-Klingebiel[1,2], Felix Polten[1,2], Kai C. Wollert[1,2]*

Effective tissue repair after myocardial infarction entails a vigorous angiogenic response, guided by incompletely defined immune cell–endothelial cell interactions. We identify the monocyte- and macrophage-derived cytokine METRNL (meteorin-like) as a driver of postinfarction angiogenesis and high-affinity ligand for the stem cell factor receptor KIT (KIT receptor tyrosine kinase). METRNL mediated angiogenic effects in cultured human endothelial cells through KIT-dependent signaling pathways. In a mouse model of myocardial infarction, METRNL promoted infarct repair by selectively expanding the KIT-expressing endothelial cell population in the infarct border zone. *Metrnl*-deficient mice failed to mount this KIT-dependent angiogenic response and developed severe postinfarction heart failure. Our data establish METRNL as a KIT receptor ligand in the context of ischemic tissue repair.

Acute myocardial infarction (MI) is a common cardiac emergency triggered by sudden coronary artery thrombosis and occlusion (*1*). The adult mammalian heart has limited regenerative capacity (*2*). Ischemic tissue injury sustained during acute MI therefore leads to scar formation and may result in left ventricular (LV) chamber remodeling and heart failure (*3*).

Effective tissue repair after MI involves a vigorous angiogenic response that commences in the infarct border zone and extends into the necrotic infarct core. Neovessel formation after MI mitigates scarring and worsening of heart function and may represent a therapeutic target (*4*). Monocytes (Mos) and macrophages (Mphs) accumulating in the infarct region drive postinfarction angiogenesis (*5*) by secreting proteins that impart signals to nearby endothelial cells (ECs) expressing their cognate receptors (*6*, *7*). The full complexity of this intercellular cross-talk that shapes angiogenesis and functional adaptation after MI remains incompletely understood (*8*, *9*).

We conducted a bioinformatic secretome analysis in a mouse model of acute MI to discover previously uncharacterized myeloid cell–derived growth factors that drive infarct repair (fig. S1, A and B). We thus identified the 30-kDa protein METRNL (meteorin-like) as being strongly expressed by myeloid cells in the infarct region of the left ventricle (table S1). METRNL is known to be secreted by Mphs during inflammation (*10*–*12*) and to promote metabolic adaptation and tissue protection under stressful conditions (*12*–*14*). The METRNL receptor is unknown.

METRNL was weakly expressed in the heart under sham-operated baseline conditions but strongly induced after MI (fig. S2A). METRNL was also abundantly expressed in myocardial tissue specimens from patients with acute MI (fig. S2B). As shown by confocal microscopy, METRNL-expressing cells coexpressed the myeloid cell marker CD11b and were often located in the vicinity of ECs in the infarct border zone (Fig. 1A). Quantitative reverse transcription polymerase chain reaction analysis identified Mos and Mphs as the main *Metrnl* mRNA–expressing cell types in the infarct region, bone marrow, spleen, and peripheral blood (fig. S3A). *Metrnl* was broadly expressed in Mo and Mph clusters defined by single-cell RNA sequencing in the infarcted heart (fig. S3B). Delineating Mo and Mph subsets on the basis of chemokine (C-C motif) receptor 2 (CCR2) and chemokine (C-X3-C motif) receptor 1 (CX3CR1) expression (*15*), we found *Metrnl* to be more strongly expressed in $CCR2^{high}$ Mos and $CCR2^{high}$ $CX3CR1^{high/low}$ Mphs than in $CCR2^{low}$ $CX3CR1^{high}$ Mphs (fig. S3C).

We subjected *Metrnl*-deficient ($Metrnl^{-/-}$) mice to acute MI to explore METRNL's function during infarct repair. $Metrnl^{-/-}$ mice breed normally and display no apparent phenotype (*11*, *12*). Indeed, $Metrnl^{-/-}$ mice had a normal heart size and preserved LV function under sham-operated baseline conditions (table S2). After MI, however, $Metrnl^{-/-}$ mice developed larger infarct scars than their wild-type (WT) littermates (fig. S4A), with more-pronounced LV dilatation and contractile dysfunction, as demonstrated by microcatheterization (fig. S4B and table S2) and high-resolution echocardiography (fig. S4, C and D). This deleterious response was not related to differences in infarct size or cardiomyocyte apoptosis in the infarct border zone 24 hours after injury (fig. S4, E and F) or to altered inflammatory cell accumulation in the infarct region (fig. S4G). Yet new capillary formation in the infarct border zone was impaired in $Metrnl^{-/-}$ mice (Fig. 1B and fig. S4H). Myocardial capillary density under baseline conditions (Fig. 1B) or remote from the infarct region (fig. S4I) was not reduced in $Metrnl^{-/-}$ mice, indicating that *Metrnl* deletion specifically impaired angiogenesis after ischemic injury.

Transplanting $Metrnl^{-/-}$ mice with WT bone marrow cells reversed the angiogenic defect (Fig. 1C) and ameliorated LV scarring and remodeling after MI (fig. S5, A to C). Conversely, transplanting WT mice with $Metrnl^{-/-}$ bone marrow cells or deleting *Metrnl* selectively in myeloid cells by crossing $Metrnl^{fl/fl}$ mice with $LysM^{Cre/+}$ mice (fig. S6, A and B) impaired postinfarction angiogenesis (Fig. 1, C and D) and worsened LV scarring and remodeling (figs. S5, A to C, and S6, C to E). Together, these findings show that myeloid cell–derived METRNL promotes angiogenesis, tissue repair, and functional adaptation after MI.

METRNL dose-dependently stimulated human coronary artery endothelial cell (HCAEC) proliferation and migration after scratch injury (fig. S7, A and B), indicating that the protein directly acts on ECs. The sigmoidal dose–response relationships and METRNL's low half-maximal effective concentration (<1 ng/ml) suggested that METRNL signals through a high-affinity receptor. Using chemical cross-linking mass spectrometry, we identified KIT (KIT receptor tyrosine kinase) as a METRNL cell surface receptor candidate in ECs (fig. S8, A and B). KIT is the receptor for stem cell factor (SCF; also known as KIT ligand). KIT is expressed by various cell types, including hematopoietic stem and progenitor cells and germ cells. SCF signaling via KIT plays multifaceted roles during development and is important for normal hematopoiesis and fertility (*16*). Most KIT-expressing cells in the adult mouse myocardium are ECs that retain their endothelial identity after MI (*17*–*20*).

[1]Division of Molecular and Translational Cardiology, Hans Borst Center for Heart and Stem Cell Research, Hannover Medical School, 30625 Hannover, Germany. [2]Department of Cardiology and Angiology, Hannover Medical School, 30625 Hannover, Germany. [3]Institute for Biophysical Chemistry, Hannover Medical School, 30625 Hannover, Germany. [4]Department of Pediatrics, Herman B Wells Center for Pediatric Research, Indiana University School of Medicine, Indianapolis, IN 46202, USA. [5]Krannert Cardiovascular Research Center and the Herman B Wells Center for Pediatric Research, Indiana University School of Medicine, Indianapolis, IN 46202, USA. [6]Center for Cardiovascular Research, Department of Medicine, Washington University School of Medicine, St. Louis, MO 63110, USA. [7]Institute of Experimental Hematology, Hannover Medical School, 30625 Hannover, Germany. [8]Department of Pathology and Department of Cardiac Surgery, Institute for Cardiovascular Research, Amsterdam University Medical Center, 1007 MB Amsterdam, Netherlands. [9]Research Core Unit Genomics, Hannover Medical School, 30625 Hannover, Germany. [10]Technology Platform Recombinant Protein Expression, Helmholtz Center for Infection Research, 38124 Braunschweig, Germany. [11]Core Unit Proteomics and Institute of Toxicology, Hannover Medical School, 30625 Hannover, Germany.
*Corresponding author. Email: wollert.kai@mh-hannover.de

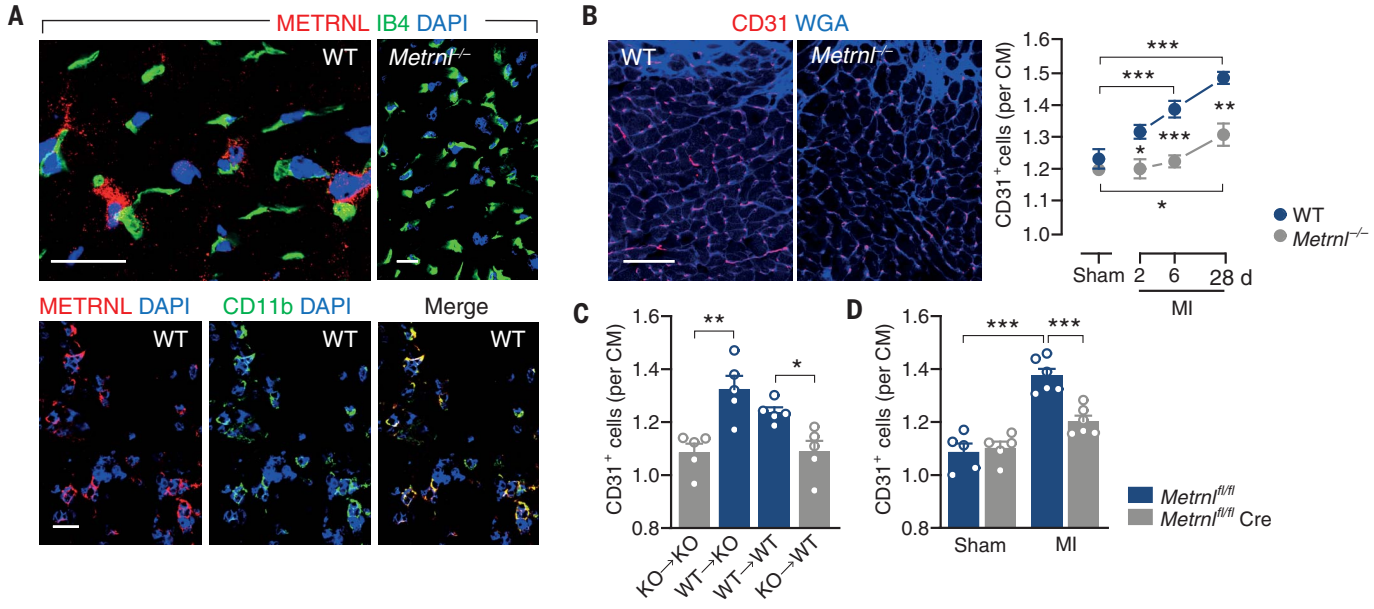

Fig. 1. Myeloid cell–derived METRNL promotes angiogenesis after myocardial infarction. (**A**) Confocal immunofluorescence microscopy images taken from the infarct border zone 3 days after MI in WT or *Metrnl*$^{-/-}$ mice. Sections were stained with 4′,6-diamidino-2-phenylindole (DAPI), fluorescein-labeled isolectin B4 (IB4), and antibodies against METRNL and CD11b. Of all METRNL-expressing cells, 92 ± 5% coexpressed CD11b (data from four mice). Scale bars, 25 μm. (**B**) WT and *Metrnl*$^{-/-}$ mice underwent sham or MI surgery and were followed for 6 days (sham) or up to 28 days (MI). Fluorescent images depict CD31^{+} ECs in the infarct border zone on day 28. Extracellular matrix and cardiomyocyte (CM) borders are highlighted by wheat germ agglutinin (WGA) staining. Scale bar, 50 μm. Summary data are from five mice per group. One-way analysis of variance (ANOVA) was performed with Dunnett test (MI versus same genotype sham), as well as independent-samples *t* test (WT versus *Metrnl*$^{-/-}$). (**C**) Bone marrow cells from *Metrnl*$^{-/-}$ [knockout (KO)] or WT mice were transplanted into (→) lethally irradiated KO or WT recipients. MI was induced after bone marrow reconstitution, and CD31^{+} capillary density in the infarct border zone was determined on day 28. Independent-samples *t* test was performed. (**D**) CD31^{+} capillary density in the infarct border zone in *Metrnl*$^{fl/fl}$ mice and *Metrnl*$^{fl/fl}$ *LysM*$^{Cre/+}$ (*Metrnl*$^{fl/fl}$ Cre) mice on day 28. Two-way ANOVA with Tukey test was performed. (B to D) Data are means ± SEM. **P* < 0.05, ***P* < 0.01, ****P* < 0.001.

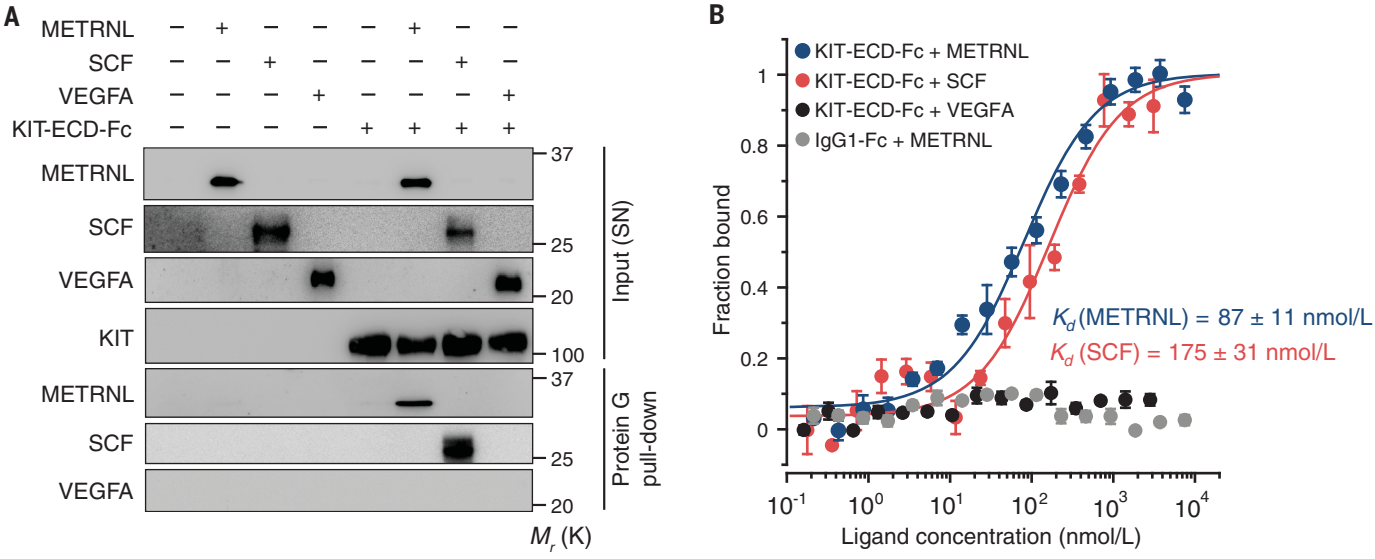

Fig. 2. METRNL binds to the extracellular domain of KIT. (**A**) Conditioned supernatants (SN) were prepared from HEK-293 cells transfected with expression plasmids encoding human KIT-ECD-Fc, METRNL, SCF, and/or VEGFA. Pull-down of KIT-ECD-Fc using protein G-coated beads copurified METRNL and SCF. Exemplary results from three experiments are shown. M_r, relative molecular mass. (**B**) Protein-protein interaction analysis by microscale thermophoresis. Binding curves illustrate the interaction of human METRNL and SCF with human KIT-ECD-Fc. Human VEGFA did not interact with KIT-ECD-Fc, nor did METRNL with an IgG1-Fc control protein. Data are means ± SEM from three or four technical replicates; two additional experiments yielded similar results. K_d, dissociation constant.

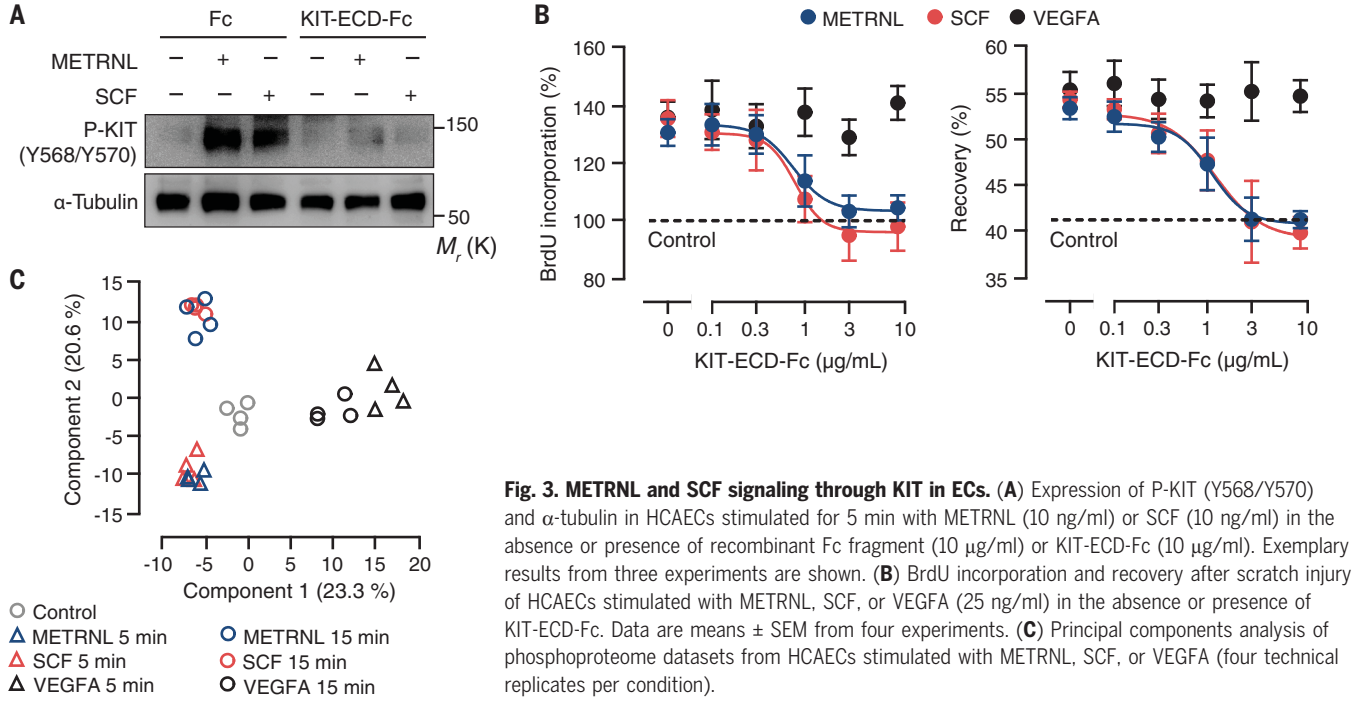

Fig. 3. METRNL and SCF signaling through KIT in ECs. (**A**) Expression of P-KIT (Y568/Y570) and α-tubulin in HCAECs stimulated for 5 min with METRNL (10 ng/ml) or SCF (10 ng/ml) in the absence or presence of recombinant Fc fragment (10 μg/ml) or KIT-ECD-Fc (10 μg/ml). Exemplary results from three experiments are shown. (**B**) BrdU incorporation and recovery after scratch injury of HCAECs stimulated with METRNL, SCF, or VEGFA (25 ng/ml) in the absence or presence of KIT-ECD-Fc. Data are means ± SEM from four experiments. (**C**) Principal components analysis of phosphoproteome datasets from HCAECs stimulated with METRNL, SCF, or VEGFA (four technical replicates per condition).

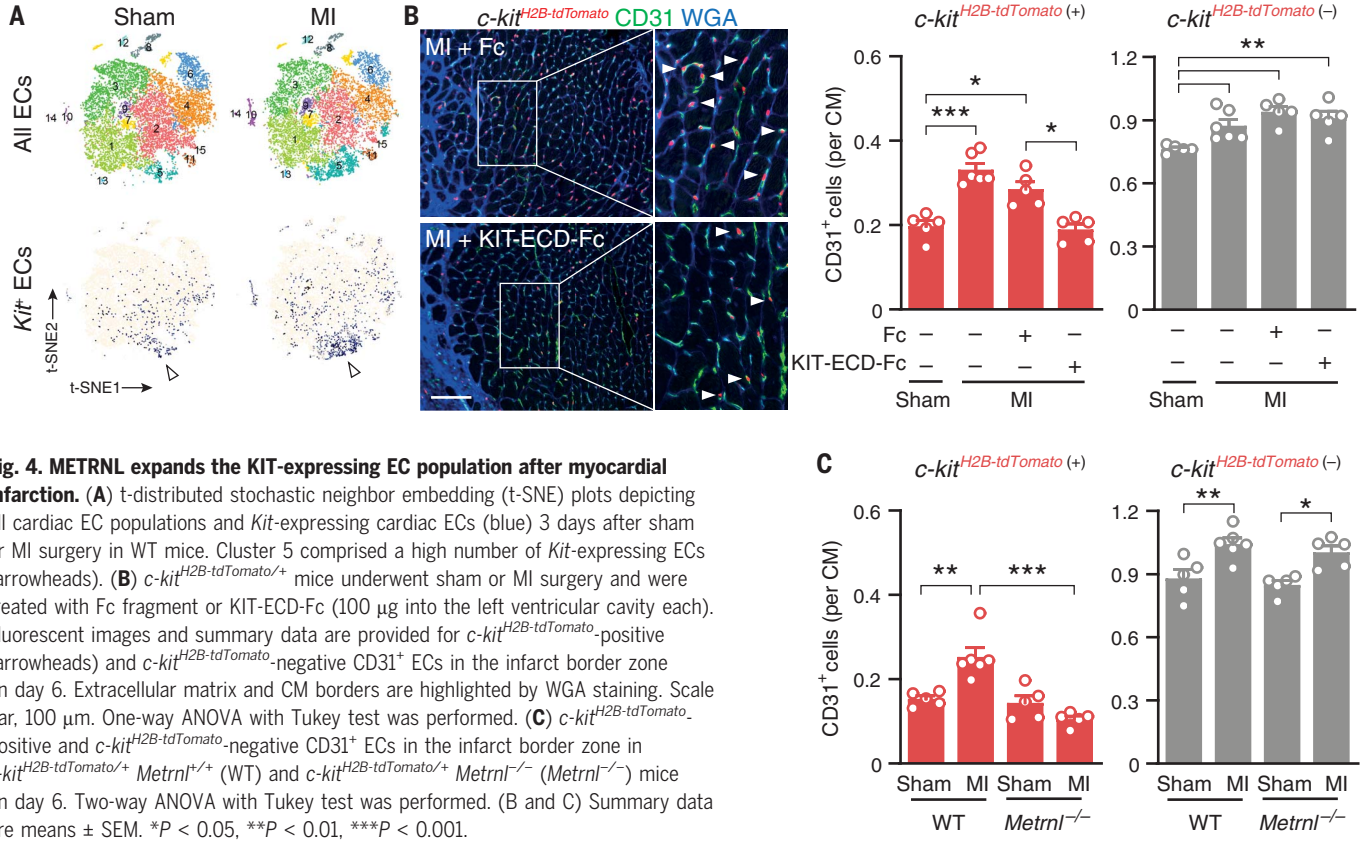

Fig. 4. METRNL expands the KIT-expressing EC population after myocardial infarction. (**A**) t-distributed stochastic neighbor embedding (t-SNE) plots depicting all cardiac EC populations and *Kit*-expressing cardiac ECs (blue) 3 days after sham or MI surgery in WT mice. Cluster 5 comprised a high number of *Kit*-expressing ECs (arrowheads). (**B**) *c-kit*$^{H2B\text{-}tdTomato/+}$ mice underwent sham or MI surgery and were treated with Fc fragment or KIT-ECD-Fc (100 μg into the left ventricular cavity each). Fluorescent images and summary data are provided for *c-kit*$^{H2B\text{-}tdTomato}$-positive (arrowheads) and *c-kit*$^{H2B\text{-}tdTomato}$-negative CD31$^+$ ECs in the infarct border zone on day 6. Extracellular matrix and CM borders are highlighted by WGA staining. Scale bar, 100 μm. One-way ANOVA with Tukey test was performed. (**C**) *c-kit*$^{H2B\text{-}tdTomato}$-positive and *c-kit*$^{H2B\text{-}tdTomato}$-negative CD31$^+$ ECs in the infarct border zone in *c-kit*$^{H2B\text{-}tdTomato/+}$ *Metrnl*$^{+/+}$ (WT) and *c-kit*$^{H2B\text{-}tdTomato/+}$ *Metrnl*$^{-/-}$ (*Metrnl*$^{-/-}$) mice on day 6. Two-way ANOVA with Tukey test was performed. (B and C) Summary data are means ± SEM. *P < 0.05, **P < 0.01, ***P < 0.001.

Coimmunoprecipitation experiments in human embryonic kidney 293 (HEK-293) cells expressing METRNL and KIT confirmed the physical interaction between the two proteins (fig. S9, A and B). After incubating human umbilical vein EC lysates containing endogenous KIT (*21*) with METRNL or SCF, we copurified both ligands by immunoprecipitating KIT (fig. S9C). To assess whether METRNL binds to KIT's extracellular domain, we prepared conditioned supernatants from HEK-293 cells expressing METRNL, SCF, vascular endothelial growth factor A (VEGFA), and/or a secreted KIT–extracellular domain–Fc fragment fusion protein (KIT-ECD-Fc). Pulling down KIT-ECD-Fc from the supernatants, we copurified METRNL and SCF, but not VEGFA (Fig. 2A). Microscale thermophoresis showed that METRNL and SCF bind to KIT's extracellular domain with similarly high affinity (Fig. 2B and fig. S9D).

We next explored whether METRNL mediates its angiogenic effects via KIT. In line with previous studies linking endothelial KIT activation to angiogenesis (*21*, *22*), SCF stimulated HCAEC proliferation and migration after scratch injury (fig. S7, C and D), as we had observed with METRNL (fig. S7, A and B). Small interfering RNA–mediated downregulation of KIT curtailed METRNL and SCF's angiogenic effects but did not affect EC responses to VEGFA (fig. S7, E and F).

SCF stimulation induces KIT homodimerization and transphosphorylation of tyrosine residues 568 and 570 (Y568/Y570) in the juxtamembrane region of the receptor (*23*), thus creating a docking site for SRC family kinases (*24*). Treating HCAECs with METRNL or SCF induced KIT (Y568/Y570) phosphorylation with similar kinetics (fig. S10A). Adding recombinant KIT-ECD-Fc to the culture medium prevented METRNL and SCF from inducing KIT (Y568/Y570) phosphorylation (Fig. 3A), consistent with the idea that transmembrane KIT and KIT-ECD-Fc compete for METRNL and SCF binding. Indeed, recombinant KIT-ECD-Fc dose-dependently inhibited the angiogenic effects of METRNL and SCF, but not those of VEGFA (Fig. 3B).

Downstream of KIT, both METRNL and SCF induced SRC (Y416) and AKT1 (S473) phosphorylation, again following comparable signaling kinetic trajectories (fig. S10, B and C). To gain a broader perspective, we applied high-resolution mass spectrometry to examine protein phosphorylation dynamics in HCAECs stimulated with METRNL, SCF, or VEGFA. In a principal components analysis based on 4750 phosphosites distributed among 1891 different proteins, the phosphoproteome signatures of METRNL and SCF clustered together and were segregated from VEGFA's signatures in principal component space (Fig. 3C). Unsupervised hierarchical clustering and plotting the data in a correlation matrix confirmed that the phosphoproteomic responses to METRNL and SCF were closely related and distinct from the response to VEGFA (fig. S11, A and B). The angiogenic effects of METRNL and SCF are thus mediated through KIT and shared downstream signaling pathways.

We used single-cell RNA sequencing to identify *Kit*-expressing ECs in the adult mouse myocardium. Whereas few ECs, scattered across several EC clusters, expressed *Kit* under baseline conditions, the number of *Kit*-expressing ECs markedly increased after MI (Fig. 4A). *Kit* was the only gene that was differentially expressed ($\log_2$ ratio > 1, $P < 0.05$) in *Kit*-expressing versus *Kit*-nonexpressing ECs under baseline conditions. After MI, however, genes related to cell proliferation and migration were highly enriched in *Kit*-expressing ECs, indicating that the cells had become activated (table S3).

To explore whether KIT expression determines EC susceptibility to METRNL and SCF stimulation, we isolated cardiac ECs from *c-kit*$^{H2B\text{-}tdTomato/+}$ knock-in mice. The nuclear tdTomato signal in these mice faithfully recapitulates the expression pattern of endogenous KIT (*17*). Using click chemistry to fluorescently label EdU^+ proliferating ECs, we found that METRNL and SCF stimulated *c-kit*$^{H2B\text{-}tdTomato}$-positive but not *c-kit*$^{H2B\text{-}tdTomato}$-negative EC proliferation (fig. S12). To survey KIT-expressing EC behavior in the infarct border zone, we subjected *c-kit*$^{H2B\text{-}tdTomato/+}$ mice to acute MI. As we had observed by single-cell RNA sequencing (Fig. 4A), *c-kit*$^{H2B\text{-}tdTomato}$-negative ECs outnumbered *c-kit*$^{H2B\text{-}tdTomato}$-positive ECs under baseline conditions and after MI (Fig. 4B). Yet expansion of both populations contributed about equally to the increase in capillary density in the infarct border zone (Fig. 4B). Treating *c-kit*$^{H2B\text{-}tdTomato/+}$ mice with KIT-ECD-Fc (100 μg into the LV cavity immediately after MI) selectively prevented *c-kit*$^{H2B\text{-}tdTomato}$-positive EC expansion in the infarct border zone (Fig. 4B) and worsened LV dysfunction after MI (table S4), indicating that growth factor(s) signaling through KIT stimulate KIT-expressing EC expansion and help preserve heart function after MI.

Unlike METRNL, SCF was expressed by ECs, fibroblasts, and cardiomyocytes in the infarct region (fig. S13A), and its expression did not increase after MI (fig. S13B). Further, we observed no up-regulation of SCF in the infarct region of *Metrnl*$^{-/-}$ mice (fig. S13C). To explore whether METRNL drives KIT-expressing EC expansion after MI, we crossed the *c-kit*$^{H2B\text{-}tdTomato}$ allele into *Metrnl*$^{-/-}$ mice. *Metrnl* deletion did not affect *c-kit*$^{H2B\text{-}tdTomato}$-positive or -negative EC densities in the myocardium under baseline conditions (Fig. 4C), indicating that METRNL is not necessary for establishing either cell population during development. After MI, however, *c-kit*$^{H2B\text{-}tdTomato}$-positive EC numbers failed to increase in *Metrnl*$^{-/-}$ mice, whereas *c-kit*$^{H2B\text{-}tdTomato}$-negative EC expansion was not affected (Fig. 4C).

To explore METRNL's therapeutic potential, we treated heart failure–prone FVB/N mice (*25*) with METRNL after MI (bolus injection into the LV cavity immediately after MI, followed by subcutaneous infusion) (fig. S14A). METRNL treatment enhanced infarct border zone capillarization (fig. S14B), limited scar formation (fig. S14C), and exerted sustained beneficial effects on LV function (table S5). In *c-kit*$^{H2B\text{-}tdTomato/+}$ reporter mice, these therapeutic effects were associated with selective expansion of *c-kit*$^{H2B\text{-}tdTomato}$-positive ECs in the infarct border zone (fig. S14D), showing that endogenous METRNL's effects on angiogenesis and heart function after MI can be therapeutically enhanced. METRNL therapy did not affect infarct size and cardiomyocyte apoptosis in the infarct border zone 24 hours after injury (fig. S14, E and F) or cardiomyocyte cell cycle activity in the left ventricle during the first week after MI (fig. S14, G and H). Notably, treating *c-kit*$^{H2B\text{-}tdTomato/+}$ mice with SCF expanded the *c-kit*$^{H2B\text{-}tdTomato}$-positive EC population in the infarct border zone and improved systolic function, as did treating the mice with METRNL (fig. S14, I and J). Increasing the availability of either ligand therefore promotes similar beneficial effects after MI.

In summary, we define a METRNL-based cross-talk between myeloid cells and ECs that promotes tissue repair after MI. We identify KIT as the cell surface receptor that mediates METRNL's angiogenic effects. While METRNL and SCF both bind to KIT with high affinity, engendering concordant phosphoproteome signatures in cultured human ECs, the two ligands exert nonredundant functions during development and after injury. In contrast to *Scf*-deficient mice, which die of severe anemia around the time of birth (*26*), *Metrnl*-deficient mice develop normally with no overt hematological abnormalities (fig. S15 and table S6). After MI, myeloid cell–derived METRNL drives expansion of the KIT-expressing EC population in the infarct border zone. This KIT-dependent angiogenic response is severely blunted in *Metrnl*-deficient mice, indicating a limited role for SCF in this setting, a conclusion in line with SCF's persistently low cardiac expression after MI (fig. S13) (*27*). Myeloid cell production of METRNL may thus provide a mechanism for activating endothelial KIT in the context of tissue injury and inflammation. Further studies may reveal other cell types and pathological conditions in which METRNL-KIT signaling is important.

REFERENCES AND NOTES

1. S. S. Virani *et al*., *Circulation* **143**, e254–e743 (2021).
2. T. Eschenhagen *et al*., *Circulation* **136**, 680–686 (2017).
3. S. D. Prabhu, N. G. Frangogiannis, *Circ. Res.* **119**, 91–112 (2016).

4. X. Wu, M. R. Reboll, M. Korf-Klingebiel, K. C. Wollert, *Cardiovasc. Res.* **117**, 1257–1273 (2021).
5. F. K. Swirski, M. Nahrendorf, *Nat. Rev. Immunol.* **18**, 733–744 (2018).
6. W. Walter *et al*., *Cell Rep.* **23**, 622–636 (2018).
7. N. Farbehi *et al*., *eLife* **8**, e43882 (2019).
8. M. Korf-Klingebiel *et al*., *Nat. Med.* **21**, 140–149 (2015).
9. M. R. Reboll *et al*., *Circulation* **136**, 1809–1823 (2017).
10. I. Ushach *et al*., *Clin. Immunol.* **156**, 119–127 (2015).
11. I. Ushach *et al*., *J. Immunol.* **201**, 3669–3676 (2018).
12. G. S. Baht *et al*., *Nat. Metab.* **2**, 278–289 (2020).
13. R. R. Rao *et al*., *Cell* **157**, 1279–1291 (2014).
14. C. Rupérez *et al*., *J. Exp. Med.* **218**, e20201206 (2021).
15. G. Bajpai *et al*., *Circ. Res.* **124**, 263–278 (2019).
16. J. Lennartsson, L. Rönnstrand, *Physiol. Rev.* **92**, 1619–1649 (2012).
17. N. Sultana *et al*., *Nat. Commun.* **6**, 8701 (2015).
18. J. H. van Berlo *et al*., *Nature* **509**, 337–341 (2014).
19. L. He *et al*., *Nat. Med.* **23**, 1488–1498 (2017).
20. K. Kretzschmar *et al*., *Proc. Natl. Acad. Sci. U.S.A.* **115**, E12245–E12254 (2018).
21. J. Matsui, T. Wakabayashi, M. Asada, K. Yoshimatsu, M. Okada, *J. Biol. Chem.* **279**, 18600–18607 (2004).
22. K. L. Kim *et al*., *Arterioscler. Thromb. Vasc. Biol.* **39**, 2120–2131 (2019).
23. C. D. Mol *et al*., *J. Biol. Chem.* **278**, 31461–31464 (2003).
24. J. Lennartsson *et al*., *Oncogene* **18**, 5546–5553 (1999).
25. S. W. M. van den Borne *et al*., *Cardiovasc. Res.* **84**, 273–282 (2009).
26. L. Ding, T. L. Saunders, G. Enikolopov, S. J. Morrison, *Nature* **481**, 457–462 (2012).
27. S. Vandervelde *et al*., *Cardiovasc. Res.* **73**, 783–793 (2007).

ACKNOWLEDGMENTS

We thank O. Dittrich-Breiholz for advice on the transcriptome and single-cell RNA-sequencing analyses, M. Ballmaier for support with flow cytometry, and A. Kanwischer and E. Brinkmann for technical assistance. **Funding:** This work was supported by German Research Foundation grants WO 552/10-2 and KFO311 WO 552/11-2 (K.C.W.), German Research Foundation Excellence Cluster REBIRTH-2 grant EXC62 (A.S. and K.C.W.), Lower Saxony Ministry of Science and Culture grant Niedersächsisches Vorab VW-ZN3440 (A.S. and K.C.W.), and China Scholarship Council grants 201606210134 (X.W.) and 202008080224 (L.Z.). K.J.L. is supported by funding provided by the Children's Discovery Institute of Washington University and St. Louis Children's Hospital, the Foundation of Barnes-Jewish Hospital, the Burroughs Foundation Welcome Fund, the Leducq Foundation, and the National Institutes of Health (R35 HL161185 and RO1 HL151078). J.F. is funded by German Research Foundation grant RO 5102/1-2. **Author contributions:** Conceptualization: M.R.R., S.K., and K.C.W. Methodology: M.R.R., S.K., M.H.T., C.-L.C., L.J.F., K.J.L., J.M., A.S., H.W.N., M.K., J.v.d.H., A.P., and F.P. Investigation: M.R.R., S.K., M.H.T., L.J.F., A.L.K., J.F., M.K., X.W., L.Z., Y.W., M.K.-K., and F.P. Funding acquisition: K.C.W. Supervision: M.R.R., S.K., and K.C.W. Writing – original draft: K.C.W. Writing – review & editing: M.R.R., C.-L.C., L.J.F., J.B. **Competing interests:** The authors declare that they have no competing interests. **Data and materials availability:** *c-kit*$^{H2B\text{-}tdTomato/+}$ mice are available from Icahn School of Medicine at Mount Sinai, New York City, under a material transfer agreement with that institution. Microarray and single-cell RNA-sequencing raw data have been deposited in Gene Expression Omnibus (GEO) with accession numbers GSE198376 and GSE198401. All other data are available in the main text or the supplementary materials.
License information: Copyright © 2022 the authors, some rights reserved; exclusive licensee American Association for the Advancement of Science. No claim to original US government works. https://www.science.org/about/science-licenses-journal-article-reuse

SUPPLEMENTARY MATERIALS

science.org/doi/10.1126/science.abn3027
Materials and Methods
Figs. S1 to S15
Tables S1 to S7
References (*28*–*36*)
MDAR Reproducibility Checklist

View/request a protocol for this paper from *Bio-protocol*.

Submitted 17 November 2021; accepted 6 May 2022
10.1126/science.abn3027

By **Ilya Smolensky**

More than my hands

I was sitting in a chemistry lab class during my first year of university, nervous about the experiment we were to perform. The procedure required us to transfer a solution from one tube to another. I grabbed a pipette and, as I feared, my hand started to shake—a symptom of cerebral palsy. I asked my lab partner whether they could perform the task instead. The experience was disheartening: I was hoping to pursue a career in science, but I started to wonder whether that would be possible if I had trouble completing simple lab experiments. I thought my dreams had crashed to the ground.

I was born after my twin brother. His birth was free of complications, but I was strangled by an umbilical cord and born with severe hypoxia. After a few weeks in the neonatal intensive care unit, I was diagnosed with cerebral palsy. My family managed to find good doctors where we lived, in Leningrad (now St. Petersburg), Russia, and I took part in clinical trials testing new interventions. Shortly after my first birthday, I started walking and it became clear my cognitive functions were unaffected. So in some sense I was lucky.

I couldn't do some things growing up. My left hand was (and still is) much worse than my right—I was mostly limited to using two fingers as pincers. I learned to write and do simple tasks with my right hand, but it wasn't dexterous enough to do anything that required precision. Both hands also shook, especially when I was nervous or embarrassed.

As a teenager, I faced a lot of bullying at school. Feeling alone, I joined a study group focused on the natural world, thinking I would like to live far from any people, studying animals. That's how I came into the field of biology.

At university, I enjoyed the lectures in my science classes. Many lab tasks proved impossible, however. Once, during a field course on an island in the White Sea, in the far north of Russia, I struggled to put a small marine worm in a petri dish. I spent that night walking around in the woods, wondering what else I could do other than biology.

As I struggled with my mood, I read a book about depression. From then on, the physiology of mental disorders became my scientific passion. I looked into what was being done locally and was excited to discover a lab that did behavioral experiments in rats to study depression. I thought that even with my shaking hands, I was capable of putting a rat into a maze and observing its behavior. I wanted to join that lab.

At the end of my second year, I approached the professor to see whether I could work with her. I was afraid to admit I couldn't do some lab tasks. To my relief, she was completely supportive. "Don't worry, we will find work to occupy you," she said.

"There's much more to being a scientist than performing the physical labor."

She set me to work performing behavioral experiments for others in the lab. Later, when the time came for me to produce a senior thesis, I used data I collected and hormonal data collected with the help of a colleague who completed the pipetting steps. I loved the supportive atmosphere so I stayed there to complete my master's and Ph.D.

When I graduated, I felt an itch to focus on molecular mechanisms of mental disorders. I landed a position that involved computer modeling, but I quit after 8 months because writing computer code was both frustrating and boring for me. After that I switched to a lab studying epilepsy in rats. I could do the work, but it wasn't my passion.

Eventually I started to look for positions abroad, buoyed by advice a doctor once gave me: "If you are smart enough, you will be a scientist regardless of your hands." During an interview for a postdoc in Switzerland, I revealed that I have cerebral palsy and can only do behavioral experiments. A few days later I received a job offer, which included a detail that the lab would hire a technician for any delicate tasks associated with my project.

I've been in that lab now for 2 years, and I've come to realize that my hands aren't the impediment I thought they were. By finding the right people, being open about my abilities, and working as part of a team, I've been able to follow my passions. I've also realized that there's much more to being a scientist than performing the physical labor. I may not collect all the data in my papers, but I'm fully capable of devising experiments and interpreting results—which, to me, is the most exciting part of science. ■

Ilya Smolensky is a postdoc at the University of Fribourg and the University of Basel. Send your career story to SciCareerEditor@aaas.org.

ILLUSTRATION: ROBERT NEUBECKER